PROCEEDINGS

Tenth International Symposium on Space Terahertz Technology

March 16 – 18, 1999

On the Grounds of
The University of Virginia
Charlottesville, Virginia

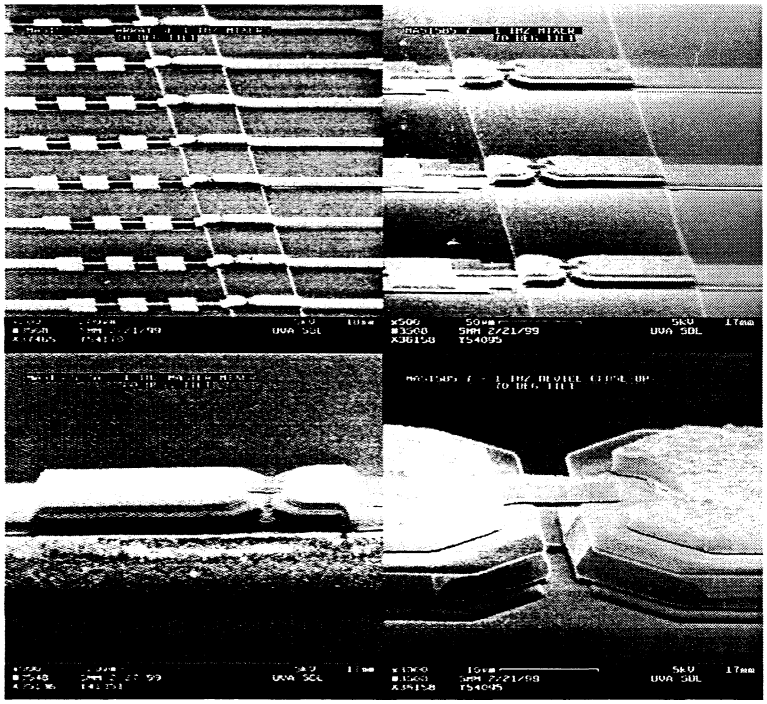

GaAs Mixers Integrated on a Quartz Substrate

Organized by: University of Virginia, Applied Electrophysical Laboratory

PROCEEDINGS

of the

TENTH INTERNATIONAL SYMPOSIUM ON

SPACE TERAHERTZ TECHNOLOGY

Tuesday – Thursday, March 16 – 18, 1999

University of Virginia
Charlottesville, Virginia

Organized by: University of Virginia, Applied Electrophysics Laboratory

Organizing Committee

Thomas W. Crowe, University of Virginia
Robert M. Weikle, II, University of Virginia

PREFACE

The Tenth International Symposium on Space Terahertz Technology was held on the Grounds of the University of Virginia on March 16-18, 1999. A total of sixty-two papers were presented, including thirteen poster papers. There were about 150 attendees from over a dozen countries representing academia, industry and national laboratories. The topics ranged from terahertz mixers and sources through new circuit architectures, materials and antennas. Continuing a recent trend, research on Hot Electron Bolometric Mixers contributed the most papers. However, SIS mixers remain dominant below about 1 THz and Schottky mixers continue to improve for applications that either can not afford or do not require cooling. Although there continues to be much work on terahertz sources, including frequency multipliers, flux-flow oscillators and photomixers, this remains the major obstacle to greater implementation of terahertz technology. Clearly, new ideas are still needed and the existing technologies must be better supported if they are to reach their full potential in time for major upcoming programs such as ESA's Far-Infrared and Submillimeter Telescope and NRAO's Millimeter Array.

Recently, there has been much discussion about the future of the symposium. Although there is strong consensus that it provides a vital service to the community and should continue, it lacks a strong base of administrative support. To address this problem, we have formed an administrative steering committee consisting of the six most recent conference hosts. These include Gabriel Rebeiz, Jonas Zmuidzinas, Robert Weikle, Ray Blundell, Rob McGrath and Tom Crowe. The first action of the committee has been to approve Jack East of the University of Michigan as the host of the eleventh symposium to be held in May 2000. Other issues to be addressed include an organized method to determine future sites, possible extension of the symposium beyond space applications and reaching out to include the direct detector community or pulsed terahertz technology. We also must consider forging closer ties to agencies that have supported the symposium, such as NASA and IEEE, as well as other agencies. If you have any suggestions with regard to these or other STT issues, please forward them to any member of the steering committee.

Thomas W. Crowe
Robert M. Weikle

For Information on the eleventh symposium, please contact:

Dr. Jack East
Elec. Engr. & Comp. Science
University of Michigan
1301 Beal Avenue
Ann Arbor, MI 48109-2122
FAX: (734) 763-9324
jeast@eecs.umich.edu

The SEMs on the cover show several views of GaAs mixer circuits integrated on a quartz substrate by the MASTER process, courtesy S.M. Marazita, University of Virginia.

Due to a printer's error, page 47 was duplicated on page 28. Therefore, all page numbers after page 28 are off by one.

TENTH INTERNATIONAL SYMPOSIUM ON SPACE TERAHERTZ TECHNOLOGY

Tuesday – Thursday, March 16 – 18, 1999

On the Grounds of the
University of Virginia
Charlottesville, Virginia

Organized by: University of Virginia, Applied Electrophysical Laboratory

DAY 1 – TUESDAY, MARCH 16

Opening Session

Welcoming Remarks	Tom Crowe	UVa	

Session 1: Sources 1 — **Chair: Phil Koh**

Time Resolved Measurements of Flux-Flow Oscillator Linewidth	U. Mueller, K. Jacobs	KOSMA, U. Cologne	13
Design of a Distributed Terahertz Photomixer	E. Duerr, K. McIntosh, S. Verghese	MIT	28
Traveling-Wave Photomixers Based On Noncollinear Optical/Terahertz Phase-Matching	S. Matsuura, G. Blake, J. Pearson, R. Wyss, C. Kadow, A. Jackson, A. Gossard	Caltech, JPL, UCSB	37
Heterostructure Barrier Varactors on Copper Substrate for Generation of Millimeter- and Submillimeter-Waves	L. Dillner, J. Stake, S. Hollung, C. Mann, E. Kollberg	Chalmers, RAL	47
The Complete Analytical Simulation of Heterostructure Barrier Varactor Frequency Multipliers	L. Dillner, M. Oldfield, C. Mann B. Alderman	Chalmers, RAL, U. Nottingham	57

Session 2: Schottky Mixers — **Chair: Richard Bradley**

177-207 GHz Radiometer Front End, Single-Side-Band Measurements	I. Galin, C. Schnitzer, R. Dengler,O. Quintero	Aerojet, JPL	69
Progress in Submillimeter Wavelength Integrated Mixer Technology	S. Marazita, K. Hui, J. Hesler, W. Bishop, T. Crowe	UVa	73
Anti-Parallel Planar Schottky Diodes for Subharmonically-Pumped 220 GHz/Mixer	C.-I. Lin, M. Rodriguez-Girones, A. Simon, J. Zhang, P. Piironen, V. Mottonen, J. Louhi,	Darmstadt, HUT	85

Day 3 – Wednesday, March 18

Session 9: Sources II — **Chair: Gerhard Schwaab**

Session 10: Circuits and Components — **Chair: Sigfrid Yngvesson**

Session 11: HEB III – Analysis **Chair: Stafford Withington**

TIME RESOLVED MEASUREMENTS OF FLUX-FLOW OSCILLATOR LINEWIDTH

U. Müller, K. Jacobs
KOSMA, I. Physikalisches Institut, University of Cologne
Zuelpicher Str. 77, 50937 Cologne, Germany

ABSTRACT

Superconducting Flux-Flow Oscillators (FFO) as local oscillators for radio astronomy are perfectly suited to be combined with SIS-mixing-devices in standard Nb/Al-AlO_X/Nb technology, having the potential to result in highly sophisticated integrated receivers up to the terahertz region. Oscillator linewidth and -stability are of exceptional importance for radio astronomical applications.
A spectroscopic measurement setup for the 350GHz-band has been built up to investigate the radiation properties of superconducting oscillators. We report on unique time resolved measurements of Flux-Flow Oscillator radiation characteristics using a modified KOSMA Acousto-Optical Spectrometer (AOS). Measurements with an integration time of 1μs result in a FFO linewidth of less than 1MHz at 350GHz. A simultaneously recorded spectrum analyzer trace with a sweep time of 40ms shows a FFO-linewidth of more than 20MHz. It is concluded that the time averaged linewidth of the Flux-Flow Oscillator - as can be seen on the spectrum analyzer - is due to frequency modulation of the intrinsic FFO-signal by low frequency pickup. A series of time resolved FFO-spectra gives a detailed impression of the evolution of the intrinsic FFO lineshape with time.

I. INTRODUCTION

In the frequency range up to 1THz radio astronomical receivers nowadays are based on superconductor-insulator-superconductor (SIS) tunnel-detectors, which offer the highest possible sensitivity. Because of the high frequencies and the demanded spectral resolution of $f/\Delta f \approx 10^6$ the receivers make use of the heterodyne principle. Linewidth as well as frequency stability of the local oscillator have to be far smaller than the resolution of the employed spectrometer. Only a radiation-linewith of significantly less than 1MHz qualifies a local oscillator (LO) for the spectroscopy of radio astronomical signals at frequencies of several hundred GHz and typical 3dB-linewidths of 1MHz-10MHz.

The Flux-Flow Oscillator has developed to a promising alternative to the commonly used gunn-oscillator/multiplier combination as a local oscillator for the mm- and submm-wave region. The fabrication of the FFO-devices is fully compatible to the standard Nb/Al-AlO_X/Nb-technology used for SIS-mixing elements. The combination of both devices on one chip will result in highly sophisticated integrated receivers for radio astronomical applications.

In comparison with gunn-oscillator/multiplier combinations Flux-Flow Oscillators distinguishes themselves by low weight and volume, extremely low power consumption, a wide operation band and the easy frequency tuning of an ideal voltage controlled oscillator. Especially the low power dissipation and the low weight makes them very interesting candidates for satellite based heterodyne systems. For array receivers the conventional distribution of available LO-power onto the detector elements make high demands on the complex optical setup and gets increasingly difficult with growing pixel number. Here the small dimensions of the FFOs offer the possibility to integrate an own local oscillator with every SIS-junction and to separately optimize the LO-level for every element.

In this work we report on the investigation of the radiation characteristics of Flux-Flow Oscillators with regard to their radio astronomical application.

II. Flux-Flow Oscillators

Superconducting Flux-Flow Oscillators (FFO) are traveling wave type oscillators for the mm- and submm-wave region. They are based on the unidirectional and viscous flow of magnetic flux quanta in a Josephson junction.

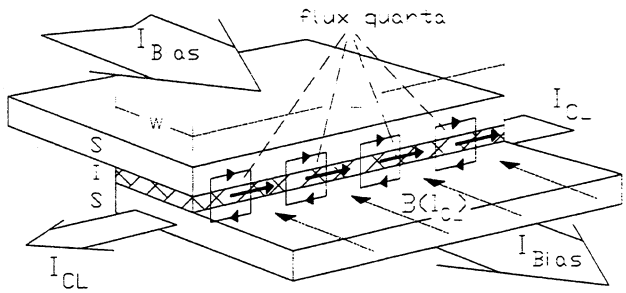

Figure 1: Flux-Flow Oscillator. Bias current through Josephson contact drives fluxon-chain towards junction end.

According to the Josephson penetration length λ_J Flux-Flow Oszillators are long and even quasi-one-dimensional superconductor-insulator-superconductor (SIS) contacts (LxW≈ 400µmx3µm) with $L>>\lambda_J$ and $W<<\lambda_J$ (figure 1). A control line current I_{CL} through the base electrode produces a magnetic field $B(I_{CL})$ penetrating through the barrier. It nucleates equidistant magnetic flux-quanta in the junction. The acting Lorentz force produced by the bias current I_{Bias} through the element accelerates the vortices to one junction end. In balance with the quasiparticle losses this leads to a constant propagation velocity u of the traveling fluxons. When the velocity of the vortex-array approaches the speed of light $\bar{c}$ in the junction this results in a steep

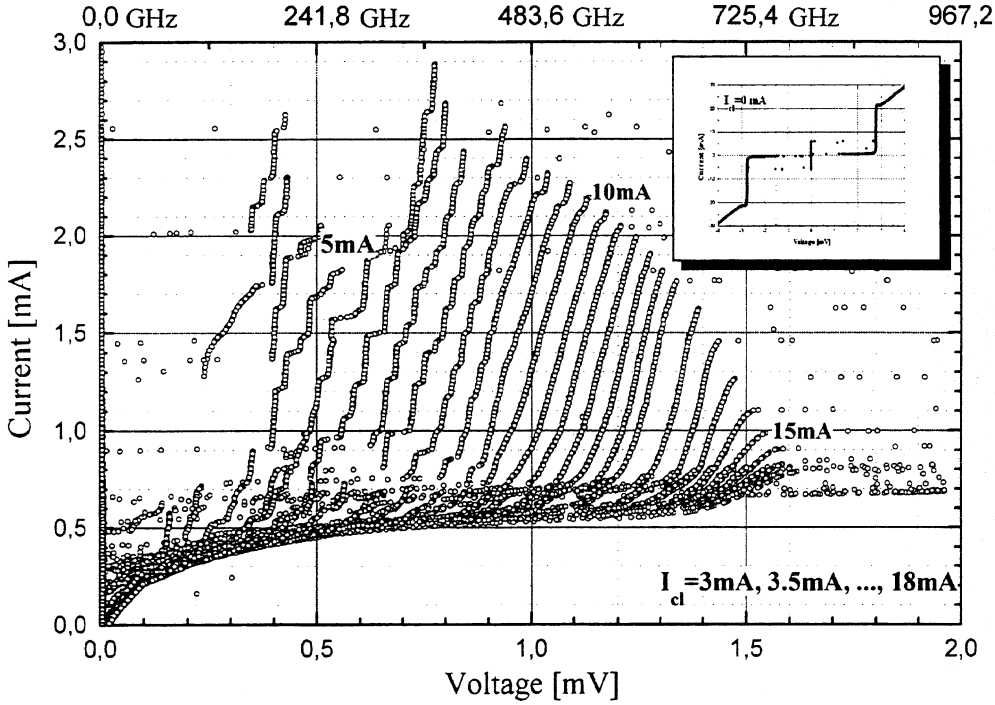

Figure 2: Measured I-V characteristics of a FFO for different applied control current 3mA, 3.5mA...18mA. The currents correspond to a magnetic field of ~1.2G to 11.3G in the tunnel barrier or 3 to 17 trapped magnetic flux quanta respectively. The inset displays the complete I-V in absence of a control current.

current step in the I-V characteristic of the oscillator, the so-called flux-flow step (FFS). The oscillation frequency is related to the dc-voltage drop across the junction by the Josephson relation: $f = V_{dc} / \Phi_0$ (flux quantum $\Phi_0 = h/2e$). The frequency can be continuously tuned over a wide range by changing the applied magnetic field and bias parameters. Figure 2 shows an overlay of measured I-V curves of a FFO for different applied control currents. For operating the Flux-Flow Oscillator in the 350GHz band a bias voltage of around ~0.7mV is required.

The linewidth of the emitted FFO-signal is mainly affected by the dc differential resistance R_d at the bias point [1]. For low R_d the linewidth is limited by external low frequency interferences (due to RF-signal pickup, hum etc.) with $\Delta f_{FFO} \sim R_d$. At high differential resistance the value of Δf_{FFO} is determined by a superposition of shot noise and thermal noise in the junction: $\Delta f_{FFO} \sim R_d^2$. Therefore the smallest linewidth is obtained for operating the FFO on the Fiske steps (geometric resonances of oscillating fluxons in the tunnel junction) with especially low R_d , which are superimposed on the FFS for $V_{bias} < 900\mu V$ in figure 2. Above that bias value the effect of Josephson self-coupling leads to an abrupt increase of the quasiparticle

damping [2] where the FFO enters the pure flux-flow regime and the linewidth increases.

III. Measurement Setup

To investigate the FFO-linewidth and -stability in a radio astronomically interesting frequency range, a spectroscopical measurement system based on a KOSMA 345GHz SIS-mixer [3] has been set up. The FFO-radiation represents the signal to be detected whereas the mixer is operated by a PLL stabilized Gunn-oscillator as a heterodyne receiver. Mixer and Flux-Flow Oscillator are placed together in an immersion cryostat and are cooled with liquid helium. The FFO-Chip is embedded in a separate waveguide environment with integrated diagonal horn (see chapter IV). The signals are coupled to the SIS-mixer quasioptically.

Figure 3 shows an outline of the cryogenic system. The FFO-radiation is imaged by the elliptical mirror „1" and is superimposed with the local oscillator signal at the beamsplitter. The beam is then focused onto the aperture of the diagonal horn antenna and detected in the SIS-mixer.

Figure 4 depicts a photograph of the central part of the cryogenic setup. The dimensions are roughly 10cm in diameter and 30cm in height. Hidden by the sidewalls the lower level contains the beamsplitter and the two elliptical mirrors. It is solidly attached to the following level which holds SIS-mixer (left) and FFO (right). The HEMT amplifier is located on top of the setup, separated from the lower levels by teflon poles. It is connected to the SIS-mixer via a semi-rigid coax-cable and ensures an amplification of the IF-signal by 20dB at the cold stage. The majority of the optical paths of the system are capsuled in teflon. The FFO is magnetically shielded during measurements by three layers of MUMETALL®, which posses a high permeability of $\mu_r \approx 10000$ at 4.2K.

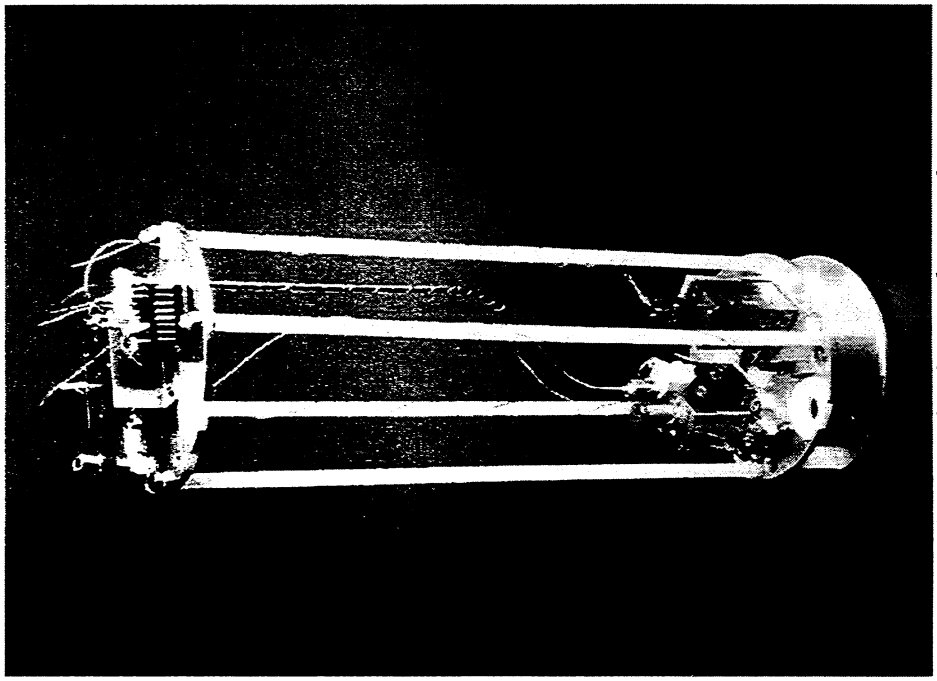

Figure 4: Photograph of central part of measurement setup with SIS-mixer (left), Flux-Flow Oscillator block (right) and HEMT amplifier (top)

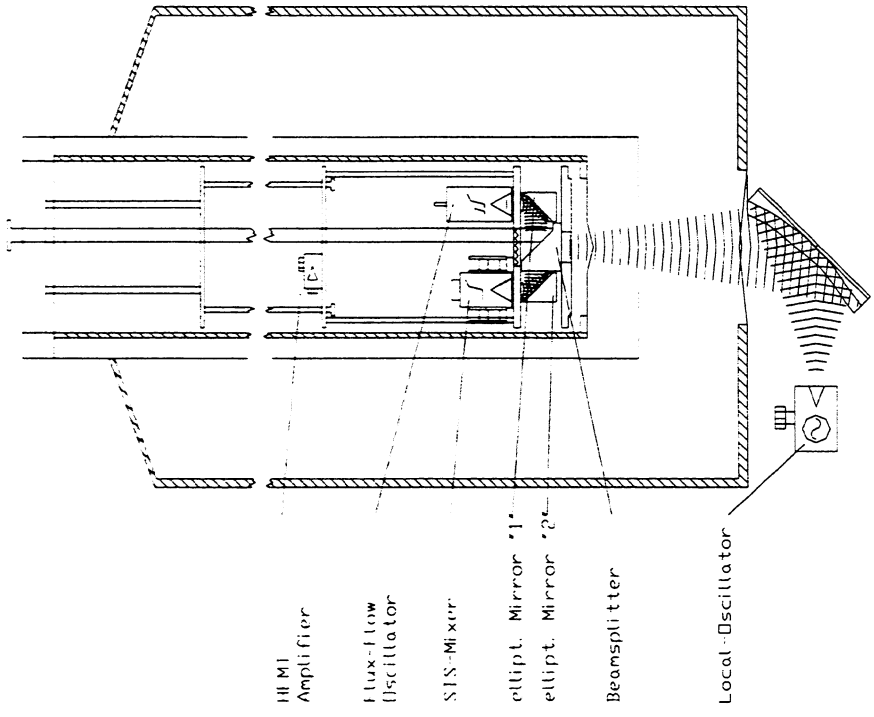

Figure 3: Schematic diagram of the cryogenic measurement setup for the investigation of the spectral radiation properties of Flux-Flow Oscillators.

IV. RF-LAYOUT AND WAVEGUIDE ENVIRONMENT OF FFO-CHIP

For the detection in the SIS-mixer the FFO-radiation has to couple to the Gaussian optics of the measurement setup. For that purpose, a FFO-chip and corresponding waveguide environment for a central frequency of 350GHz have been developed.

For the RF-design of the chip the Flux-Flow Oscillator can be described in good approximation as a linear Josephson transmission line with characteristic impedance Z_c. Figure 5 illustrates the cross sectional view of a FFO in Nb/Al-AlO_X/Nb overlap geometry. The capacitive electrode overhang affects the impedance per unit length significantly. For the given values in figure 5 the characteristic impedance evaluates to $Z_c = 0.33\Omega$ [4].

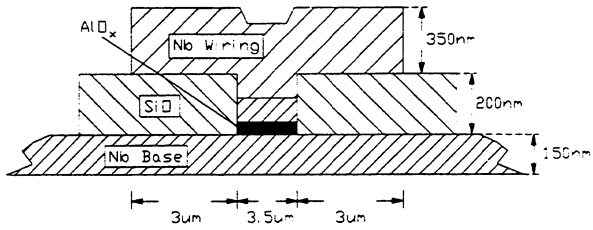

Figure 5: Schematic cross-sectional view of FFO-layers.

Figure 6 displays an schematic sketch of the FFO-quartz-chip. The layout uses an optimized microstrip-to-waveguide transition for 350GHz developed at MRAO University of Cambridge [5]. It has been designed for operation in low noise radio astronomical SIS-mixers and shows excellent coupling to the waveguide over a wide frequency band. The low impedance of the FFO in figure 6 is matched to a 19Ω microstrip line via a two-step impedance transformer and couples to the waveguide by the microstrip-to-finline transition. The quartz taper matches the empty to the filled waveguide. The implemented projection length of the Flux-Flow Oscillator at the junction end results in an improved bias feed and reduces the oscillator linewidth [6]. The magnetic control line current is fed through the base-electrode.

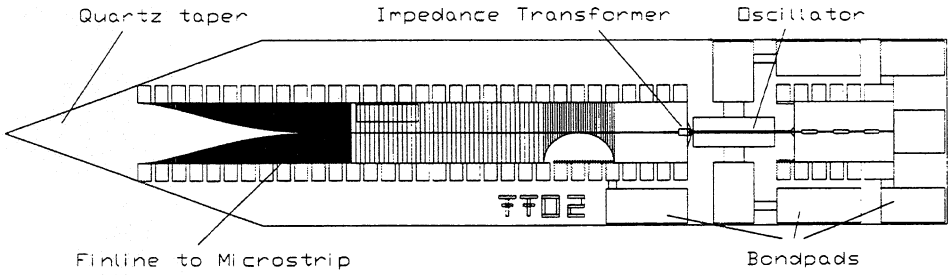

Figure 6: Plot of FFO-chip. FFO is matched to 19Ω microstrip-line via a two-step impedance transformer. The optimized microstrip-to-finline transition [5] couples to the waveguide.

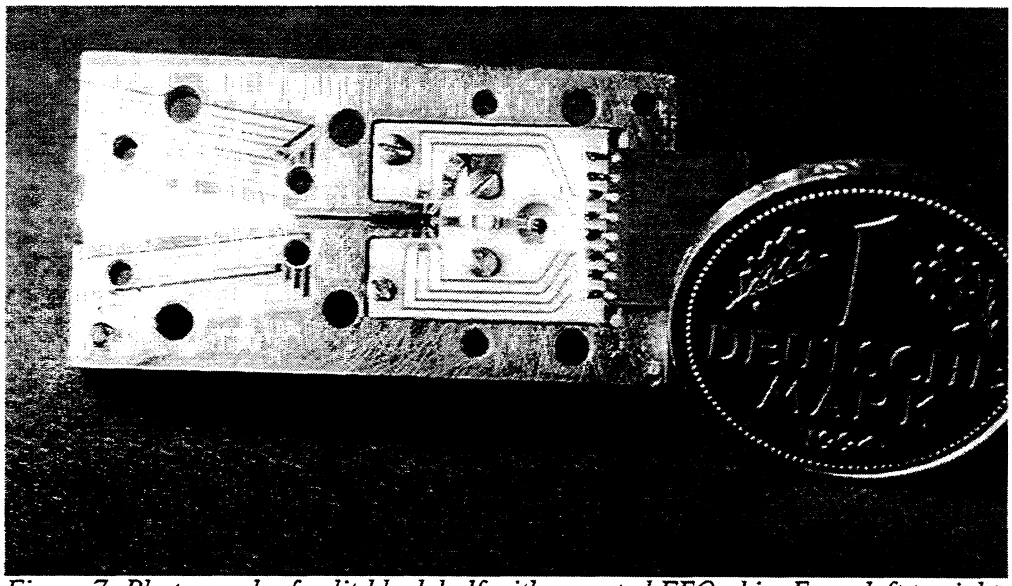

Figure 7: Photograph of split-block half with mounted FFO-chip. From left to right: diagonal horn, waveguide, FFO-chip, SMA-connector and dc-feeds.

The waveguide environment of the FFO-devices has been manufactured in split-block technology. Figure 7 shows a photograph of the split-block half with the mounted FFO-device. The outer dimensions of the block-half are 20mmx37.5mmx10mm (WxLxH). The FFO-chip couples to the TEM_{01}-mode of the waveguide which feeds the integrated diagonal horn visible at the far left in figure 7.

The FFO-elements in Nb/Al-AlO_X/Nb-technology were fabricated in house. The process has been proven to be fully compatible with the standard 4-layer process used for the production of SIS-mixing elements. It has already been used for the fabrication of combined SIS/FFO-devices [7].

V. KOSMA Acousto-Optical Spectrometer

The Acousto-Optical Spectrometers (AOS) which have been developed at the University of Cologne [8] are used both as real time spectrometers and receiver backends in radio astronomy. They can easily be modified for use in time resolved spectroscopy.

Acousto-optical spectrometers are based on the diffraction of light at ultrasonic waves. A schematic drawing is given in figure 8. A RF-signal (e.g.. the 1-2GHz IF-signal coming from the SIS-mixer) drives a piezoelectric transducer, which generates an acoustic wave in a crystal. The acoustic wave modulates the refractive index of the crystal and induces a phase grating. The deflector (Bragg cell) is illuminated by a collimated laser beam. The refracted light than is collected and imaged onto a linear

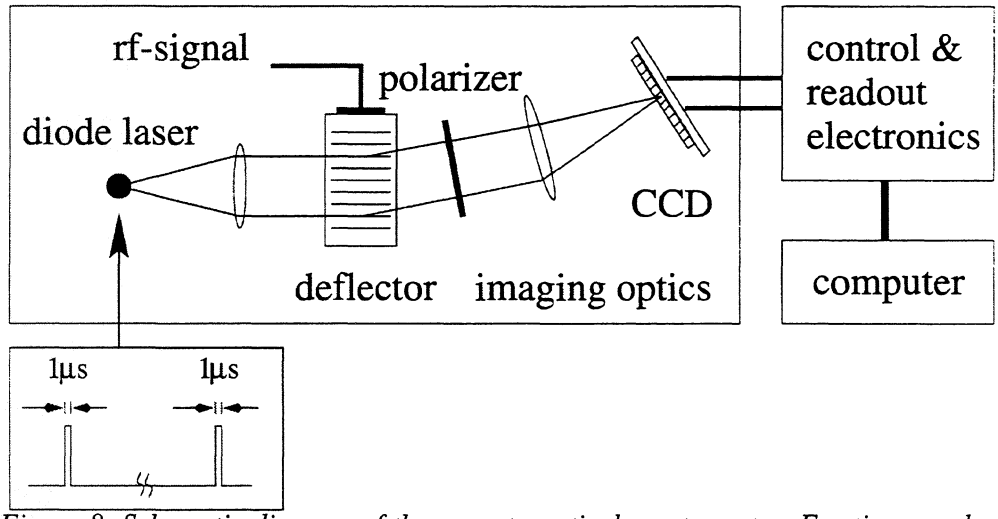

Figure 8: Schematic diagram of the acousto-optical spectrometer. For time resolved measurements the laser diode is pulsed within 1µs to 13.5µs [9].

diode array (CCD) in the focal plane. The angular dispersion of the diffracted light represents the true image of the IF-spectrum.

The resolution of the spectrometer depends on the aperture of the Bragg cell (i.e. dimensions of crystal), the crystal material and the imaging optics. For these measurements the KOSMA Low Resolution Spectrometer (LRS) has been available. The AOS-bandwidth of 1000MHz distributed over the 1450 pixels of the CCD result in a channel spacing of 688kHz.

In contrast to the working principle of a spectrum analyzer, the integration of a spectrum with an AOS happens for all channels simultaneously. In standard mode the laser is operated continuously. The default integration time of 10ms is given by the control electronics. The spectrum analyzer on the other hand sweeps sequentially through the frequency range and averages for a given time at every frequency point. The typical sweep time for a spectrum is 50ms to 100ms.

For time resolved measurements the laser diode of the acousto-optical spectrometer is pulsed by an external function generator with a pulse width in the range of 1µs to 13.5µs [9]. The rising edge of the pulse is synchronized with the system-intrinsic integration time of 10ms. The width of the laser pulse determines the integration time of the spectrometer in time resolved operation mode.

The transient time of the signal in the crystal limits the useful reduction of the integration time. For a measurement the phase grating has to be established in the complete Bragg cell, for which the signal has to cross the crystal. For the LRS the transient time is about 1µs. Higher frequency resolution demands a larger crystal and results in an increased transient time of the acoustic wave, about 20µs for the KOSMA High Resolution Spectrometer with its resolution-bandwidth of 30kHz.

VI. Time Resolved Spectroscopy of FFO-Linewidth

Time resolved measurements of FFO-lineshape were taken with the modified KOSMA Acousto-Optical Low Resolution Spectrometer.

Fig. 9 shows an schematic overview of the measurement setup. The FFO-signal is superimposed with the PLL stabilized Gunn-LO-radiation and detected in the SIS-mixer. The IF-band from 1-2GHz is amplified by 20dB at the cold-stage (HEMT) and by another 40dB outside the dewar. For time resolved measurements, the laser diode of the AOS was pulsed in the range from 1μs to 13.5μs by means of a function generator. The signal is displayed simultaneously on a spectrum analyzer and the acousto-optical spectrometer. This allows direct comparison between „standard" and time resolved spectra.

Figure 10 presents a time resolved FFO-spectrum at 350GHz taken with the modified KOSMA AOS. The integration time was 1.0μs. The FFO was biased in a region with extremely low R_d. The linewidth of the Flux-Flow Oscillator signal is smaller than 1MHz. In this measurement the frequency-resolution is limited by the AOS channel width of 688kHz. The inset of figure 10 shows the simultaneously recorded spectrum analyzer trace (sweep time 40ms) with an FFO-linewidth of more than 20MHz.

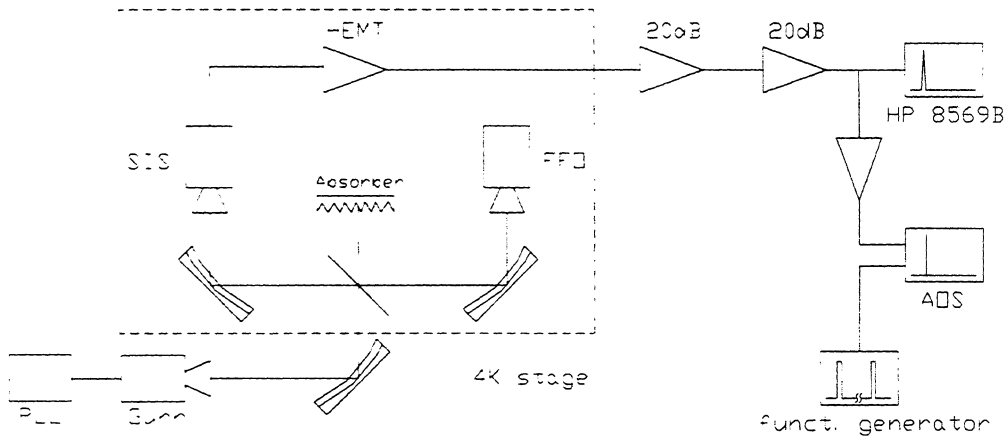

Figure 9: Systematic setup for time resolved measurements. The FFO-signal is displayed simultaneously on a spectrum analyzer (HP 8569B) and the KOSMA AOS. The laser diode of the acousto-optical spectrometer has been pulsed by the function generator in the range from 1μs to 13.5μs.

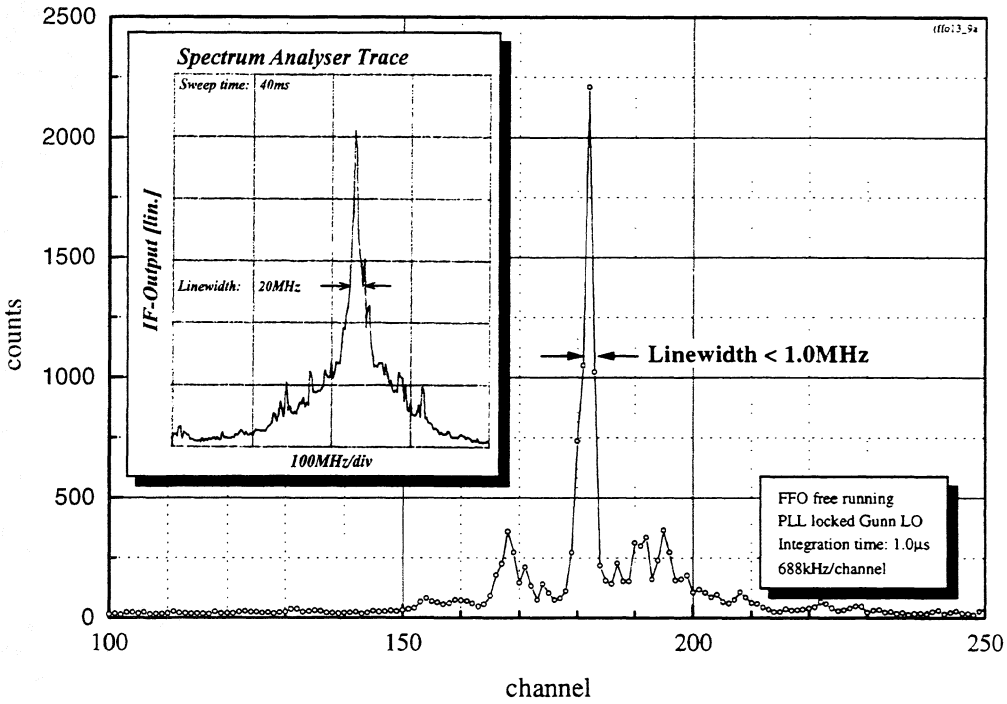

Figure 10: Time resolved AOS-spectrum of FFO-Signal at 350GHz (1µs integration time) with a linewidth smaller than 1MHz. The inset presents a simultaneously recorded spectrum analyzer trace with a FFO-linewidth of about 20MHz (sweep time 40ms).

The evolution of FFO lineshape with time is visible in figure 11. The spectra a)-c) have been taken in intervals of a few seconds with an integration time of 1µs each. While for the spectra a) and b) several maxima can be recognized, in spectrum c) the entire oscillator power is concentrated in a narrow peak with $\Delta f<1MHz$. The integrated intensity of the spectra varies less than 7% around the average of *8832* AOS counts. This means that the FFO-power has been constant over the period of measurement but experienced a frequency modulation on scale of the 1µs integration time. Figure 11d) illustrates the sum of spectra a)-c). The Gauss-profile fitted to the common curve has a 3dB-linewidth of 18MHz. This is in good agreement with the spectrum analyzer trace of the Flux-Flow Oscillator signal displayed in the inset of figure 11d) that shows a linewidth of 25MHz. A larger number of summarized time resolved AOS spectra should result in a further approach of the fitted linewidth to the value seen on spectrum analyzer.

The influence of the integration time on the linewidth of the measured signal can be seen in figure 12. The integration time of the acousto-optical spectrometer has been varied between 1.0µs and 13.5µs by choosing the appropriate pulse-width for operating the laser diode. The function generator limited the maximum pulse-length to

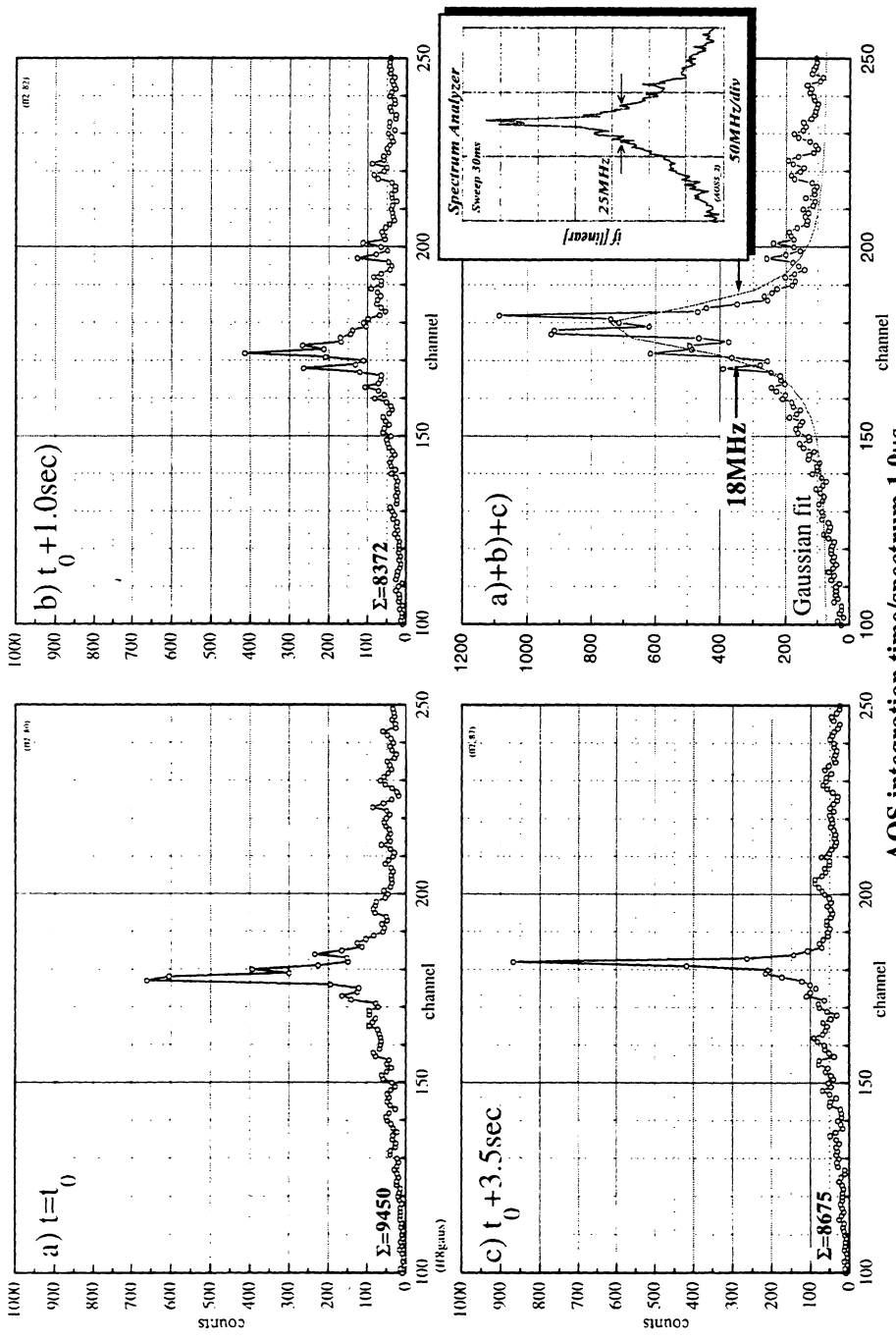

Figure 11: Evolution of FFO-lineshape with time. a) - c) Time resolved AOS-spectra of FFO-signal with 1µs integration time taken in intervals of a few seconds. d) Sum of spectra a)-c) and fitted Gauss-profile with Δf=18MHz. The inset displays the spectrum analyzer trace taken at the same time, which shows a FFO-linewidth of Δf=25MHz.

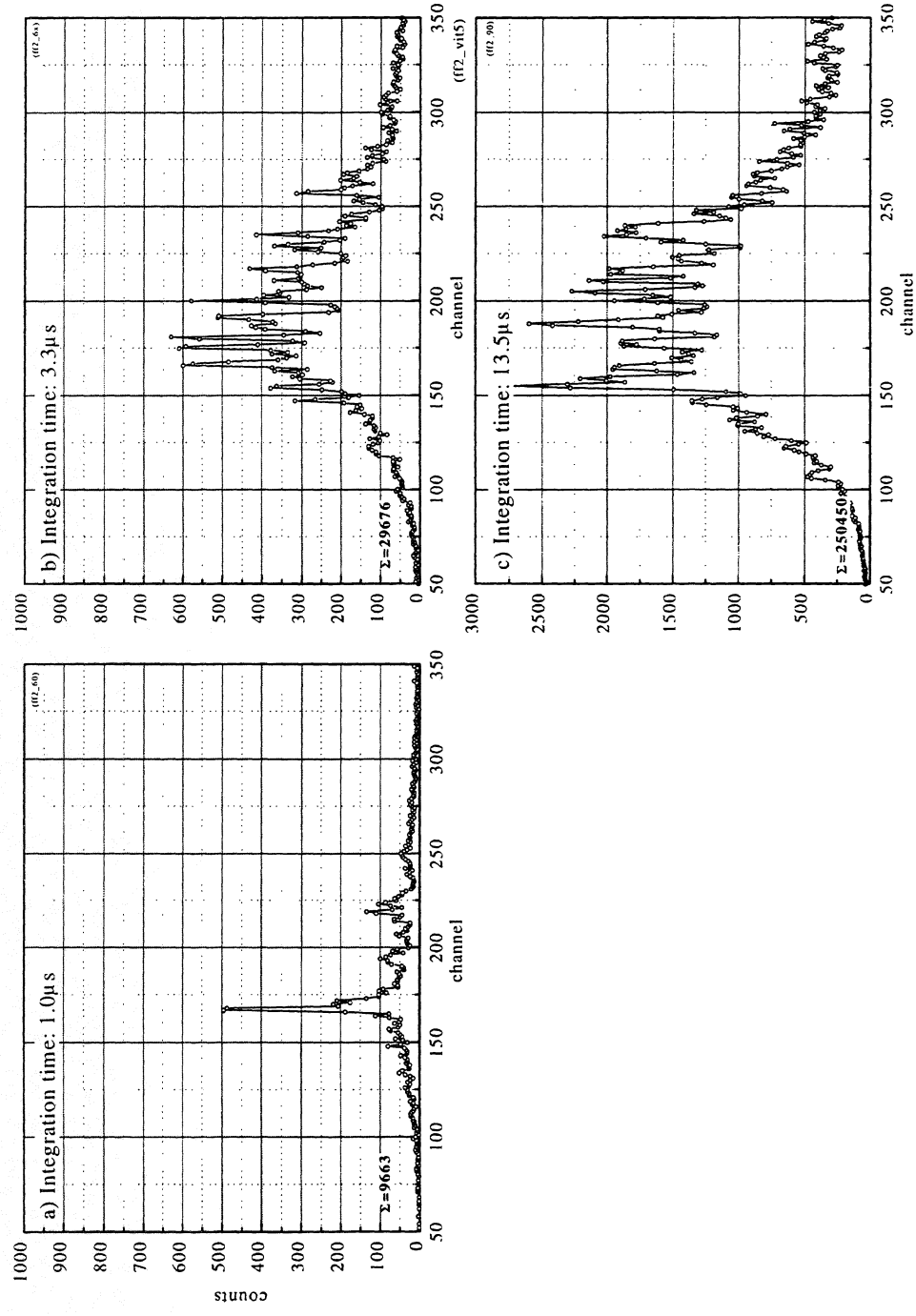

Figure 12: AOS-spectra of FFO-signal taken with an integration time of a) 1.0µs, b) 3.3µs and c) 13.5µs respectively. Already for the integration time of 3.3µs the detected FFO-linewidth approaches the value seen on the spectrum analyzer.

13.5μs (50kHz). The 1μs-snapshot in figure 12a) resolves a narrow FFO-signal. For the longer 3.3μs integration time (figure 12b) a significant smearing of the FFO-lineshape can be observed. The linewidth in this case corresponds to the value measured with the spectrum analyzer. A following increase of the integration time up to 13.5μs results in no further change in the detected FFO-linewidth, as can be seen in figure 12d).

As mentioned in chapter II the Flux-Flow Oscillator linewidth Δf_{FFO} for a high differential resistance R_d at its bias point is mainly given by a combination of shot noise and thermal noise, with $\Delta f_{FFO} \sim R_d^2$. Figure 13 displays a spectrum analyzer trace and a simultaneously taken AOS-spectrum of an FFO operated in that regime. A large linewidth of $\Delta f_{FFO} = 120MHz$ can be seen. The AOS integration time was 1.0μs. An improved signal/noise-ratio has been obtained by averaging over nine spectra. The linewidth at half maximum of the fitted curve is identical with the one of the spectrum analyzer trace (sweep time 40ms) in the inset of figure 13. The good agreement of measurements with short and long integration time gives evidence that the FFO-linewidth is probably determined by inherent noise processes which cannot even be resolved on the 1μs time scale.

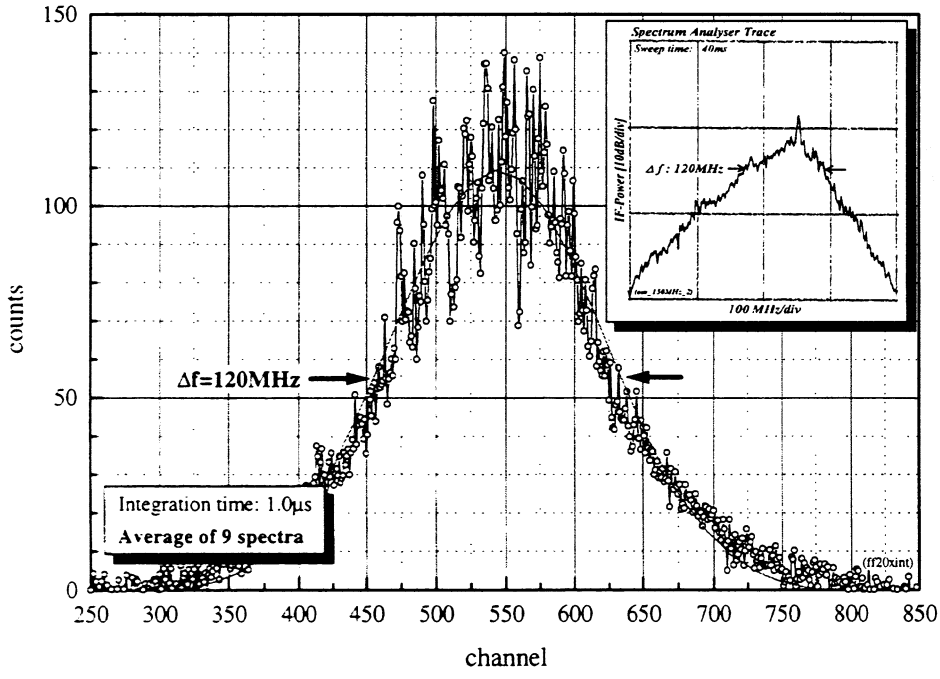

Figure 13: Time resolved measurement (1μs integration time, average of 9 spectra) of FFO-signal: Δf=120MHz. The inset shows the spectrum analyzer trace with identical FFO-linewidth (sweep time 40ms) taken at the same time.

VII. Discussion of Measurements

Time resolved measurements with the modified KOSMA AOS can distinguish between the instant (intrinsic) FFO-linewidth and additional broadening due to external contributions. Low frequency interferences up to the order of the AOS-integration time can be resolved.
AOS-measurements with an integration time of 1.0μs result in a FFO-linewidth of less than 1MHz at 350GHz (figure 10). The narrow FFO-signal is modulated by external disturbances (low frequency pickup on bias feeds, hum etc.) which result in an effective signal broadening. Due to its long sweep time of 40ms the spectrum analyzer trace taken at the same time with the AOS-spectrum shows a time averaged FFO-linewidth of 20MHz.
The evolution of FFO-lineshape with time - as can be seen in the AOS-spectra in figure 11 - gives a detailed impression of the modulation of the intrinsic FFO-signal. The lineshape visible on the spectrum analyzer arises from a superposition of these time resolved spectra (figure 11d). The smeared FFO-signal for the integration time of 1μs in figure 11 and the equidistant side-peaks visible in figure 10 suggests a modulation frequency in the MHz-region.
An increase of the AOS integration time from 1.0μs up to 13.5μs leads to an increased signal-averaging. Already for a 3.3μs integration time the FFO-linewidth approaches the value seen in the spectrum analyzer measurements. This also is an indication for a pick-up frequency in the MHz-region.

Conclusion

The determined intrinsic FFO-linewidth of less than 1MHz in principle qualifies the Flux-Flow Oscillator for use as a local oscillator in integrated radio astronomical heterodyne SIS-receivers.
An optimized RF-filtering of the bias-feeds of the Flux-Flow Oscillator and a more sophisticated magnetic shielding will result in a reduction of the effective (time averaged) FFO-linewidth and an enhanced long-term frequency stability of the oscillator signal.

For a practical integrated radio astronomical receiver it probably will be necessary to control the Flux-Flow Oscillator by a fast (>>1MHz) PLL circuit. This will further improve FFO-linewidth and -stability [1].

ACKNOWLEDGMENTS

KOSMA Superconducting Devices and Mixer developments are supported by BMBF Verbundforschung Astronomie, grants 052KV134-(6) and 053KU234-(0) and the Deutsche Forschungsgemeinschaft (DFG), grant SFB 301.

REFERENCES

[1] Valery P. Koshelets, Sergey V. Shitov, Alexey V. Shchukin, Lyudmila V. Filippenko, Pavel N. Dmitriev, Vladimir L. Vaks, Jesper Mygind, Andrey M Baryshev, Willem Luinge, Hans Goldstein, „Flux Flow Oscillators for Sub-mm Wave Integrated Receivers", Appl. Supercond. Conf. 1998, Report EQB-04, 1998

[2] V. P. Koshelets, S. V. Shitov, A. V. Shchukin, L. V. Filippenko, J. Mygind, A. V. Ustinov, „Self-pumping effects and radiation linewidth of FFO", Phys. Rev. B., Vol. 56, pp. 5572-5577, 1997

[3] S. Haas, „Low noise fixed-tuned SIS mixer for astronomical observations in the submm wave region", Ph.D. thesis, University of Cologne, 1998

[4] C. E. Tong, R. Blundell, „ Sub-millimeter distributed quasiparticle receiver employing a non-linear transmission line", 7th Int. Symp. on Space Terahertz Tech., Charlotteville, 1996

[5] G. Yassin, S. Withington, R. Padman, „Electromagnetic Analysis of Finline Mixers", University of Cambridge, Department of Physics, internal report No. 2018, 1997

[6] T. Nagatsuma, K. Enpuku, K. Sueoka, K. Yoshida, F. Irie, „Flux-flow-type Josephson oscillator for millimeter and submillimeter wave region III. Oscillation Stability", J. Appl. Phys., Vol. 58, No. 1, 1985

[7] U. Müller, „Charakterisierung supraleitender Flux-Flow Oszillatoren für den Einsatz als Lokaloszillatoren in SIS-Heterodynempfängern", Ph.D. thesis, University of Cologne, in preparation

[8] R. Schieder, V. Tolls, G. Winnewisser, „The Cologne Acousto Optical Spectrometers", Exp. Astron., Vol. 1, 1989

[9] O. Siebertz, University of Cologne, 1998

damage threshold, the increase of the laser power reflects directly the THz output power. The increase of the laser power density may also contribute to the output power improvement, because the output saturation effect could be reduced by increasing the laser power density, as described above. This can be done by shortening the active area length (laser spot size), and it contribute to reduce the stripline loss, too. Another way is increasing the photoconductivity by narrowing the stripline gap. If the 1-μm gap device is used, the output power increases by a factor of 4, though the ohmic loss would increase and cancel the power gain a little. In addition, the radiation loss can be reduced by narrowing the total stripline width, and the substrate absorption can be eliminated by employing a silicon substrate. The silicon based photomixer offers additional benefit of high power handling capability.[5] By combining these power gain factors, one order of magnitude output power improvement would be achieved.

Acknowledgment

The authors would like to thank T. E. Turner in the Microelectronics Device Laboratory at JPL for device fabrication. This research was sponsored by the Jet Propulsion Laboratory, California Institute of Technology, and the National Aeronautics and Space Administration. The work performed at UCSB was supported by the Center for Nonstoichiometric III-V Semiconductors.

References

[1] E. R. Brown, F. W. Smith, and K. A. McIntosh, *J. Appl. Phys.*, **73**, 1480 (1993).

[2] E. R. Brown, K. A. McIntosh, F. W. Smith, K. B. Nichols, M. J. Manfra, C. L. Dennis, and J. P. Mattia, *Appl. Phys. Lett.*, **64**, 3311 (1994).

[3] K. A. McIntosh, E. R. Brown, K. B. Nichols, O. B. McMahon, W. F. DiNatale, and T. M. Lyszczarz, *Appl. Phys. Lett.*, **67**, 3844 (1995).

[4] S. Matsuura, M. Tani, and K. Sakai, *Appl. Phys. Lett.*, **70**, 559, (1997).

[5] S. Verghese, K.A. McIntosh, and E.R. Brown, *IEEE Trans. Microwave Theory and Tech.*, **45**, 1301 (1997).

[6] P. Chen, G. A. Blake, M. C. Gaidis, E. R. Brown, K. A. McIntosh, S. Y. Chou, M. I. Nathan, and F. Williamson, *Appl. Phys. Lett.* **71**, 1601 (1997).

[7] S. Matsuura, P. Chen, G. A. Blake, J. C. Pearson, and H. M. Pickett, , *IEEE Trans. Microwave Theory and Tech.*, (1999), in press.

[8] L. Y. Lin, M. C. Wu, T. Itoh, T. A. Vang, R. E. Muller, D. L. Sivco, and A. Y. Cho, *IEEE Phton. Technol. Lett.*, **8**, 1376 (1996).

[9] Y. -J. Chiu, S. B. Fleischer, and J. E. Bowers, *IEEE Phton. Technol. Lett.*, **10**, 1021 (1998).

[10] S. Matsuura, P. Chen, G. A. Blake, J. C. Pearson, and H. M. Pickett, Int. *J. of Infrared and Millimeter Waves*, **19**, 849 (1998).

[11] S. Verghese, private communication.

[12] K. C. Gupta, R. Garg, and R. Chadha, *Computer-aided Design of Microwave Circuits*, (Artech House, Norwood, MA, 1981), p. 72.

[13] D. B. Rutledge, D. P. Neikirk, and D. P. Kasilingam, in *Infrared and Millimeter Waves*, edited by K. J. Button (Academic Press, New York 1983), Vol. 10, p. 1.

DESIGN OF A DISTRIBUTED TERAHERTZ PHOTOMIXER

E. K. Duerr[1], K. A. McIntosh, and S. Verghese
Lincoln Laboratory, Massachusetts Institute of Technology
Lexington, MA 02420

Abstract

Photomixers generate coherent radiation at the difference frequency of two lasers by performing optical heterodyne conversion in low-temperature-grown (LTG) GaAs. Antenna coupled photomixers have been demonstrated as local oscillators (LO) up to 630 GHz [1] and have produced power up to 5 THz [2]. Using a distributed photomixer structure may increase output power at high frequencies. The distributed photomixer consists of coplanar strips (CPS) fabricated on top of a dielectric ridge waveguide that guides the combined output of two diode lasers. The conductance of a thin layer of LTG-GaAs between the CPS and optical guide is modulated by the evanescently coupled optical beat signal. To collect the photocurrent and to velocity match the THz and optical waves, the CPS are periodically loaded with thin electrodes. The CPS are terminated in a planar antenna that efficiently radiates the THz wave guided by the CPS.

1 Introduction

Photomixers generate coherent radiation at the difference frequency of two lasers by performing optical heterodyne conversion in low-temperature-grown (LTG) GaAs. LTG-GaAs is an ultrafast photoconductor with carrier lifetime measured to be less than 200 fs [3], which gives the photomixer an extremely high intrinsic bandwidth. In previously demonstrated photomixers, a dc-biased LTG-GaAs switch is modulated by the optical beat signal of the beam-combined output of two lasers operating at slightly different frequencies [4, 5]. The metal lines which provide the dc-bias also act as the RF structure which couples the THz radiation out of the LTG-GaAs switch [6]. In addition to being demonstrated as an LO, photomixers have been used for time-domain [7] and frequency-domain [8, 9, 10] THz spectroscopy.

Using a distributed photomixer structure may increase the output power at high frequencies and provide a broader bandwidth than current "lumped-element" designs. Current designs exhibit a frequency roll-off component from the antenna resistance and capacitance of the LTG-GaAs switch. A distributed photomixer based on an active transmission line can

[1]electronic mail: duerr@alum.mit.edu

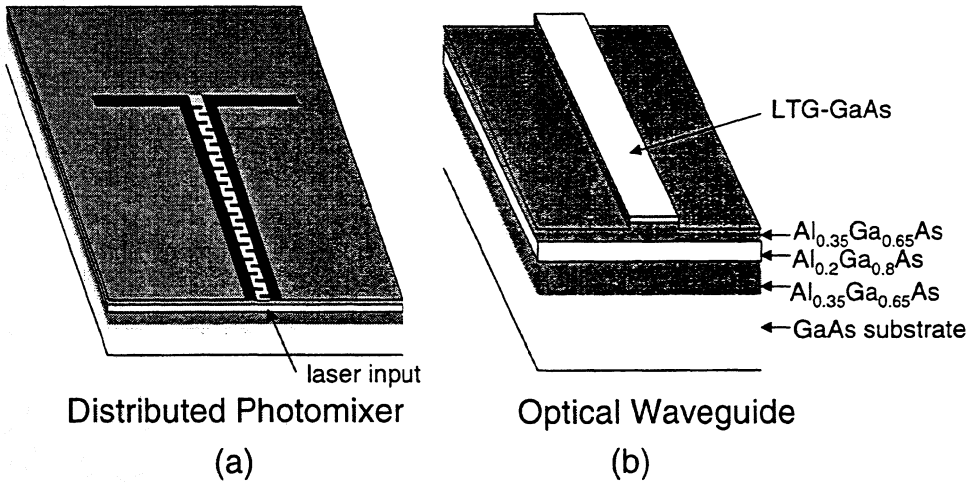

Figure 1: (a) Schematic of the distributed photomixer showing the periodically loaded cps waveguide, dipole antenna and optical waveguide. (b) Detail of optical waveguide showing LTG-GaAs absorber layer.

eliminate this roll-off. A second frequency-roll-off component is due to the finite photocarrier lifetime and is intrinsic to the material. Additionally, because the primary failure mode of photomixers is through excess thermal heating of the photomixer by the pump lasers [11], a distributed structure would mitigate this problem by causing the laser power to be absorbed in a much larger area.

2 Distributed Photomixer Design

The distributed photomixer shown in Figure 1 (a) consists of coplanar strips (CPS) fabricated on top of a dielectric ridge waveguide that guides the combined output of two diode lasers. The conductance of a thin layer of LTG-GaAs between the CPS and optical guide is modulated by the evanescently coupled optical beat signal. The THz conductance wave between the dc-biased CPS creates a THz electromagnetic wave which propagates along the CPS. To velocity match the THz and optical waves, the coplanar strips are periodically loaded with thin electrodes that add a small shunt capacitance to the line. The CPS are terminated in a planar antenna that efficiently radiates the THz wave.

2.1 Dielectric Waveguide Design

The dielectric waveguide must be designed so that the optical signal is weakly coupled to the absorbing LTG-GaAs layer. Weak coupling ensures that optical power is absorbed over a long distance ($\sim 150\,\mu$m) and that the thermal load is distributed. Weak coupling also allows the optical guide and THz guide to be analyzed separately. Confinement of the optical mode in the plane of the wafer is provided by layers of $Al_xGa_{1-x}As$ with different Al and Ga fractions. Lateral confinement is provided by a strip etched from the upper cladding layer of the waveguide as shown in Figure 1 (b). The strip-loaded waveguide provides the weak lateral confinement necessary to guide a single optical mode.

The dielectric ridge waveguide was analyzed with the effective index method to yield mode propagation constants. With these values, the mode profile was calculated and the fraction of power in each part of the waveguide was calculated. This information leads to an estimate of the absorption coefficient and, therefore, the extinction length of the optical mode—the length at which the remaining optical power is 37% (e^{-1}) of the incident power.

For the first generation of devices, the dielectric stack consists of a 5000-Å-thick $Al_{0.2}Ga_{0.8}As$ core ($n = 3.38$) grown on top of 3.5 μm of $Al_{0.35}Ga_{0.65}As$ ($n = 3.33$). The upper cladding is formed by 2500Å of $Al_{0.35}Ga_{0.65}As$ followed by 1000Å of LTG-GaAs of absorber. A ridge height of 2500Å produces a mode which is approximately 1μm by 3μm and has 0.15% of the mode in the LTG-GaAs absorbing layer. The predicted extinction length for this geometry is 90μm. The effective index seen by the optical mode is $n_{eff} = 3.35$.

2.2 THz Waveguide Design

Coplanar strips (CPS) fabricated on top of the ridge waveguide perform the dual function of providing the dc-bias for the LTG-GaAs photoconductor and guiding the THz signal. Because the velocity of the THz signal (0.38c) is higher than the group velocity of the optical signal (0.3c), the CPS must be periodically loaded with thin electrodes to slow the THz signal and velocity match it to the optical signal for optimum power transfer [12].

Quasi-static electromagnetic models provided an initial estimate for the CPS dimensions required for a particular impedance [13]. Because the LTG-GaAs is very high impedance under constant wave (cw) illumination, the photoconductor can be considered a current source. Therefore, assuming a matched antenna impedance, the output power is linearly related to the CPS impedance. However, for high values of CPS impedance the lines become very narrow and thus excessively lossy. For our first generation of devices, the CPS consist of 3.2-μm-wide strips separated by a 3 μm gap. The calculated impedance of the line was 90 Ω before being

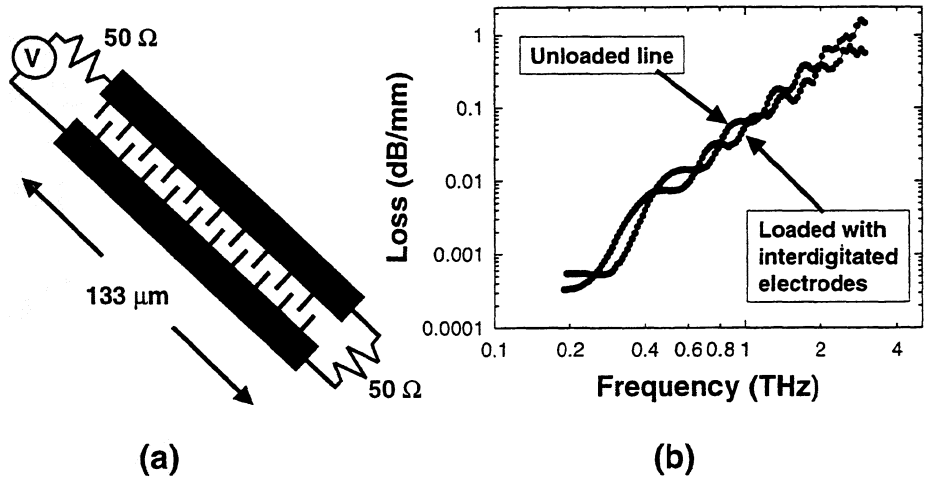

Figure 2: (a) The circuit used to determine radiation loss from a method-of-moments calculation. (b) Calculated radiation loss for CPS with and without interdigitated electrodes.

loaded with interdigitated electrodes.

The spacing and dimensions of the thin electrodes periodically loading the CPS are critical for determining the velocity of the THz wave. Quasi-static models [14] are useful for initial estimates for electrode dimensions, but a more accurate model is desirable. More precise dimensions were calculated using Hewlett Packard's electromagnetic field solver for planar circuits, Momentum [15]. Perfect metal conductors were assumed in all the calculations. Quasi-static calculations predicted that 2.1-μm-long electrodes spaced by 0.6 μm provide optimal velocity matching. Momentum calculations revised those dimensions to 2.0-μm-long electrodes spaced by 0.8 μm. The impedance of the line at 1.5 THz as modified by the presence of the electrodes is 76 Ω according to Momentum and 72 Ω according to quasi-static calculations. The loaded CPS impedance varies from 78 Ω at 170 GHz to 72 Ω at 2.4 THz.

The variation in impedance with frequency can be attributed to radiation loss, which describes attenuation of the THz wave through unwanted radiation into the substrate. To calculate the radiation loss, the S-parameters of the two-port network shown in Figure 2(a) were calculated using the method-of-moments code, Momentum. By comparing the power transmitted from the source to the power absorbed in the load, the power loss due to radiation was calculated. The results for an unloaded CPS line and for a CPS line loaded with electrodes for optimal velocity matching are shown in Figure 2(b). The radiation loss remains less than

Table 1: *Planar Antenna Designs*

Frequency [THz]	Length prediction from [17] [λ_o]	Momentum length prediction [λ_o]	Width [μm]	Z_{ant} [Ω]
0.85	0.18	0.20	2	37
1.6	0.18	0.22	1.5	41
2.5	0.17	0.24	1.5	44

2 dB/mm up to 3 THz and is cubic with frequency as expected from closed-form approximations [16]. The interdigitated electrodes do not introduce significant loss below 3 THz. Oscillations in the data can be attributed to standing wave effects that are significant in the short length of line used in the calculations.

In order to test the CPS modeling, three different electrode geometries were designed: 1) no electrodes, 2) theoretically optimal electrode dimensions which add the correct capacitance $\left(0.06\frac{\text{fF}}{\mu\text{m}}\right)$, and 3) electrodes with a 0.4μm gap and 2.3μm length which add $0.1\frac{\text{fF}}{\mu\text{m}}$. The first fabrication run of distributed photomixers included these three designs for CPS.

2.3 Antenna Design

A planar antenna at the end of the active area of the CPS radiates the THz wave. Two types of antennas were designed and fabricated, bowtie antennas and resonant half-wave dipoles. The bandwidth of the transmission line structure will be measured by terminating the CPS in a broadband bowtie antenna structure. Resonant half-wave dipoles have superior radiation patterns and better polarization performance than bowtie antennas. Therefore, dipoles were designed for 850 GHz, 1.6 THz, and 2.5 THz. Initial estimates for dipole dimensions were obtained from [17] and were revised using Momentum. Table 1 lists dimensions for the dipole antennas. Lengths deviate more from the calculations in [17] as frequency increases, because the 3μm gap between the CPS feeding the dipole becomes a larger fraction of the free-space wavelength λ_0.

2.4 Performance Estimates

By combining the data from these analyses with experimentally obtained data for photoconductance and carrier lifetime in a SPICE circuit model, photomixer performance is quantitatively predicted. An approximate model of the distributed photomixer is formed by cascading one hundred segments of the discrete circuit shown in Figure 3, where each segment represents an incremental length of the optical or THz guides. Each segment of the THz CPS model

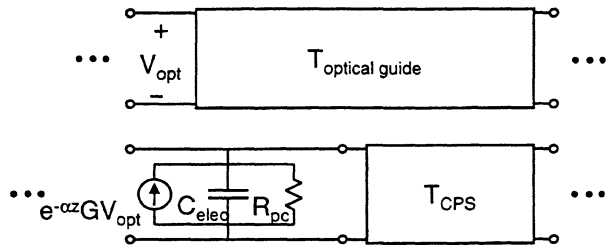

Figure 3: One segment of a SPICE circuit model for the distributed photomixer. The upper section is the optical guide model. The lower section is the THz CPS model.

Table 2: *Distributed Photomixer Performance. Values indicate fraction of power available compared to optimal velocity match* ($C_{added} = 0.06\frac{fF}{\mu m}$).

C_{added} [fF/μm]	Frac. P_{opt} at 1 THz	Frac. P_{opt} at 1.5 THz	Frac. P_{opt} at 2 THz	Frac. P_{opt} at 2.5 THz
0	1.0	0.67	0.33	0.17
0.048	1.0	1.0	0.95	0.90
0.072	0.90	0.87	0.87	0.83
0.10	0.70	0.57	0.50	0.33

consists of a transmission line segment to model the CPS, a lumped capacitor to model the thin electrodes, a resistor to model losses in the photoconductor, and a voltage-dependent current source to model the current generated by the biased photoconductor. The voltage upon which the current source depends is the voltage at the corresponding segment along the optical guide circuit model. This voltage represents the optical intensity at the corresponding point along the real optical guide. The scaling factors are the experimentally determined photoconductance and an attenuation factor to model diminishing optical power in the optical guide. The simulations predict output power of 8μW at 1.7 THz and 4μW at 2.4 THz.

To demonstrate the dependence of power on velocity matching, the distributed photomixer was simulated with different values of distributed capacitance added by the periodic thin electrodes. Table 2 shows the fraction of power available for 4 cases: 1) no electrodes, 2) $0.8C_{optimal}$, 3) $1.2C_{optimal}$, and 4) added capacitance corresponding to a gap of 0.4μm and length of 2.3μm. A power bandwidth plot for cases 1 and 4 as well as the optimal velocity matched design are shown in Figure 4. These three designs were normalized to have the same overall dc photoconductance.

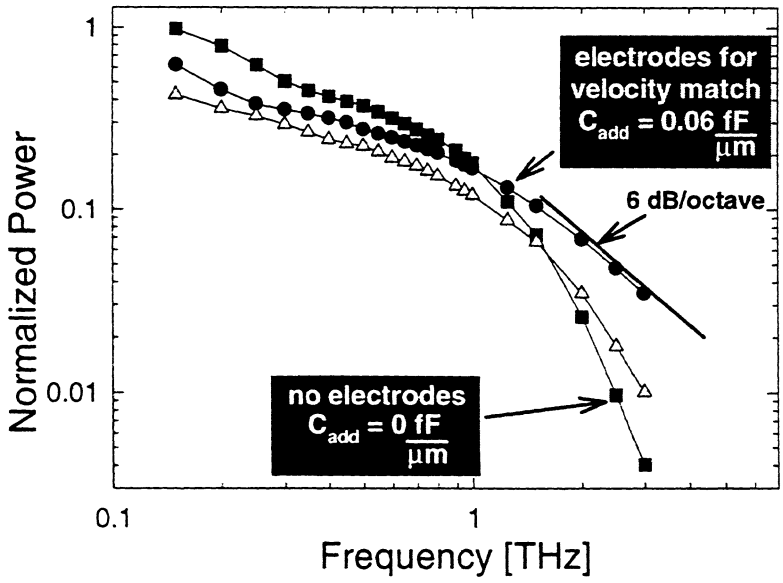

Figure 4: Power bandwidth plot for the distributed photomixer structure comparing the performance the an optimal velocity-matched structure to a structure with no electrodes and a structure with dense electrodes (case 4 in Table 2).

3 Conclusions

Distributed photomixers have been designed to overcome the limitations of current photomixer designs and provide higher power over a larger bandwidth. Through a combination of analytical and numerical techniques, the performance of distributed structures has been modeled as a function of several design parameters.

References

[1] E. K. Duerr, K. A. McIntosh, S. M. Duffy, S. D. Calawa, S. Verghese, C.-Y. E. Tong, R. Kimberk, R. Blundell, *to appear in Proc. 1999 IEEE MTT Intl. Micro. Symp.* (1999).

[2] K. A. McIntosh, E. R. Brown, K. B. Nichols, O. B. McMahon, W. F. DiNatale, and T. M. Lyszczarz, *Appl. Phys. Lett.* **67**, 3844 (1995).

[3] K. A. McIntosh, K. B. Nichols, S. Verghese, E. R. Brown, *Appl. Phys. Lett.* **70**, 354 (1997).

[4] S. Matsuura, G. Blake, P. Chen, J. C. Pearson, H. M. Pickett, *Proc. 9th Intl. Symp. on Space THz Tech.* 445 (1998).

[5] S. Verghese, K. A. McIntosh, and E. R. Brown, *IEEE Trans. Micro. Theory Tech.* **45**, 1301 (1997).

[6] K. A. McIntosh, E. R. Brown, K. B. Nichols, O. B. McMahon, W. F. Dinatale, and T. M. Lyszczarz, *Appl. Phys. Lett.* **69**, 3632 (1996).

[7] M. Tani, S. Matsuura, K. Sakai, *J. Comm. Res. Lab.* **43** 151 (1996).

[8] S. Verghese, K. A. McIntosh, S. Calawa, W. F. Dinatale, E. K. Duerr, K. A. Molvar, *Appl. Phys. Lett.* **73**, 3824 (1998).

[9] P. Chen, G. A. Blake, M. C. Gaidis, E. R. Brown, K. A. McIntosh, S. Y. Chou, M. I. Nahan, and F. Williamson, *Appl. Phys. Lett.* **71**, 1601 (1997).

[10] A. S. Pine, R. D. Suenram, E. R. Brown, K. A. McIntosh, *J. of Molec. Spect.* **175**, 37 (1996).

[11] S. Verghese, K. A. McIntosh, and E. R. Brown, *Appl. Phys. Lett.* **71**, 2743 (1997).

[12] L. Y. Lin, M. C. Wu, T. Itoh, T. A. Vang, R. E. Muller, D. L. Sivco, and A. Y. Cho, *IEEE Trans. Micro. Theory Tech.* **45**, 1320 (1997).

[13] K. C. Gupta, R. Garg, I. Bahl, P. Bhartia, *Microstrip Lines and Slotlines*, Boston: Artech House, Ch. 7, 1996.

[14] Y. C. Lim and R. A. Moore, *IEEE Trans. Elec. Dev.* **ED-15**, 173 (1968).

[15] MOMENTUM, method-of-moments solver for planar conductors. Hewlett-Packard EEsof division, 5301 Stevens Creek Blvd., Santa Clara, CA 95052-8059.

[16] M. Y. Frankel, S. Gupta, J. A. Valdmanis, G. A. Mourou. *IEEE Trans. Micro. Theory Tech.* **39**, 910 (1991).

[17] M. Kominami, D. M. Pozar, and D. H. Schaubert, *IEEE Trans. Ant. and Prop.* **33**, 600 (1985).

TRAVELING-WAVE PHOTOMIXERS BASED ON NONCOLLINEAR OPTICAL/TERAHERTZ PHASE-MATCHING

Shuji Matsuura and Geoffrey A. Blake
Division of Geological and Planetary Sciences, California Institute of Technology, Pasadena, CA 91125

Rolf A. Wyss and J. C. Pearson
Jet Propulsion Laboratory, California Institute of Technology, Pasadena, CA 91109

Christoph Kadow, Andrew W. Jackson and Arthur C. Gossard
Materials Department, University of California, Santa Barbara, CA 93106

Abstract

Traveling-wave THz photomixers based on angle-tuned optical/THz phase-matching are experimentally demonstrated. A dc-biased coplanar stripline terminated by a planar antenna is fabricated on low-temperature-grown GaAs. A distributed area between the striplines is illuminated by two noncollinear laser beams which generate interference fringes accompanied by THz waves. The velocity of the optical fringe is matched to the THz-wave velocity in the stripline by tuning the incident angle of the laser beams. The device can handle the laser power over 300 mW and provides the THz output of ~0.1 μW with the 3-dB bandwidth of 2 THz. The experimental results show that traveling-wave photomixers have the potential to surpass conventional small area designs.

1. Introduction

The difference frequency generation of THz waves by optical-heterodyne (photo) mixing in low-temperature-grown (LTG) GaAs has been investigated as a highly tunable, compact, solid-state THz source for high-resolution molecular spectroscopy and as a local oscillator for heterodyne receivers in remote-sensing applications.[1-5] The spectral purity and frequency stability of the THz output is basically determined by the pump laser source, and sufficiently high performance has now been achieved.[6,7] However, the THz output power has been limited to less than 1 μW above 1 THz, which is insufficient for many applications.

According to a photomixer theory,[1] the photomixer output power is proportional to the square of the photocurrent, which is proportional to both the pump laser power and the photoconductance. On the other hand, for conventional photomixers, the bandwidth is limited by the carrier lifetime and the electrode capacitance.[1] Since both the photoconductance and the capacitance are inversely proportional to the electrode gap width, photomixers have been designed to have small active areas ($\leq 10^2$ μm^2). However, such designs have limited power handling capabilities,[5] thus restricting the THz output power. The thermal damage threshold of typical LTG-GaAs film is <2 mW/μm^2, and the maximum laser power has been limited to ≤100 mW.

In order to overcome this difficulty, we propose a large area traveling-wave photomixer design. The device consists of a dc-biased coplanar stripline terminated by an antenna

fabricated on the LTG-GaAs. The ~10^3 μm^2 area in the stripline gap is illuminated by noncollinear two laser beams. The photocarrier density traveling-waves induced by the optical interference fringes are generated in the stripline and accompanied by the THz waves. The THz waves are transmitted to the antenna through the stripline. Owing to large active area, the laser power handling capability of the order of 1 W is expected. The traveling-wave photomixer not only has high power handling capability, but its bandwidth is also not limited by the electrode capacitance because of the nature of stripline. As high power laser sources are improved, the traveling-wave photomixer can provide good THz output with wide bandwidths, and should ultimately be superior to conventional small area photomixers.

For traveling-wave photomixers, the velocity (phase) matching between the optical interference fringes and the THz waves is essential for efficient THz wave generation. Under the phase-matching condition, the THz waves from the distributed active area are superposed in phase in the stripline. Several authors have achieved phase-matching between optical waves and microwaves in traveling-wave optical waveguide photodetectors, which slow down the microwave velocity with periodic capacitance loading of the microwave transmission line.[8,9] Such a phase-matched waveguide photomixer requires careful design and fabrication because of its fixed structure, and these devices have not yet been extended to the THz range. We propose the noncollinear optical/THz phase-matching scheme for the free space traveling-wave photomixer, which does not require such complicated waveguide structure. In this method, the velocity of the optical wave is tuned by changing the incident angle of the two laser beams.

In this paper, the phase-matching scheme is briefly described and experimentally demonstrated. The device properties and future direction for the output power improvement are discussed.

2. Optical/THz phase-matching

As described above, the phase-matching is achieved by tuning the incident angle of the two laser beams. In order to formulate the phase-matching condition, we consider a simple picture as shown in Fig. 1. When the photomixer surface is illuminated by two plane waves of

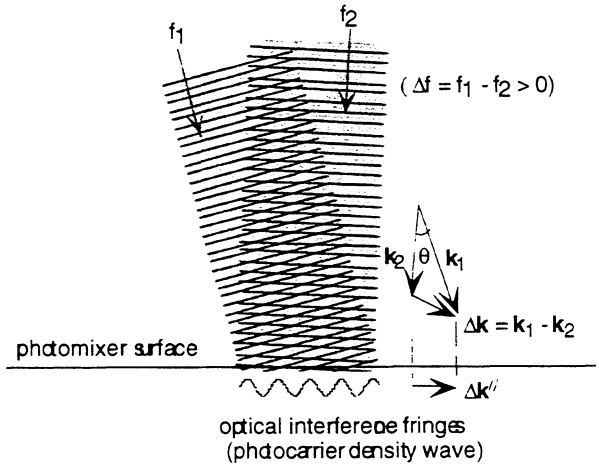

Fig. 1: Optical/THz phase-matching scheme.

frequency f_1 and f_2, and the wave vector of $\boldsymbol{k}_1$ and $\boldsymbol{k}_2$, respectively, the propagation constant of the interference fringe oscillating at the difference frequency, $\Delta f = f_1 - f_2$, is given by the parallel (//) component of the difference of the two wave vectors, $\Delta \boldsymbol{k} = \boldsymbol{k}_1 - \boldsymbol{k}_2$. Since absorption occurs in a thin surface layer (penetration depth ~1 μm), the photocarriers have the same spatial distribution as the optical interference fringes. The velocity of the interference fringes along the surface is given by

$$v_{op} = 2\pi \frac{\Delta f}{\Delta k^{//}} \ . \tag{1}$$

It is clear that the velocity can be tuned by changing the incident angles of the optical beams. In a simple case that $\boldsymbol{k}_2$ is perpendicular to the photomixer surface, Eq. 1 can be written as

$$v_{op} = \frac{c}{\sin\theta}\left(1 - \frac{f_2}{f_1}\right) , \tag{1'}$$

where c is the speed of light in the free space and θ is the incident angle of the f_1 laser beam. If it is assumed that the stripline has no dispersion, the velocity of the THz wave is approximated by

$$v_{THz} \approx \frac{c}{\sqrt{(1+\varepsilon_r)/2}} \ , \tag{2}$$

where ε_r is dielectric constant of the substrate material (ε_r = 12.8 for GaAs). The phase-matching condition is $v_{op} = v_{THz}$.

3. Photomixer

The photomixer used in the present experiment is a 1-μm thick LTG-GaAs film grown on semi-insulating GaAs substrates by molecular beam epitaxy (MBE) at a temperature of 225° C. Diffuse Reflectance Spectroscopy (DRS) was used to maintain the substrate temperature within 5° C of the setpoint through the growth. The material was annealed ex situ by rapid thermal annealing (RTA) for 30 s at 600° C in a forming gas environment. The photocarrier lifetime of the material measured by time resolved reflectance was 0.28 ps. The device structure is shown in Fig. 2. The Ti/Pt/Au metal electrodes (0.02/0.02/0.2 μm thickness) fabricated on the LTG-GaAs consist of a 2-μm gap and 4-μm wide coplanar stripline. The stripline is terminated by a 47-μm long and 5-μm wide dipole antenna or a log-periodic antenna. The other side of the stripline is terminated by wire bonding pads for the dc bias,

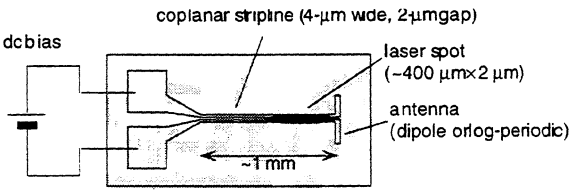

Fig. 2: LTG-GaAs traveling-wave photomixer.

which has tapered shape to reduce the reflection. Most of the THz output power from the antenna goes into the substrate and is emitted to the free space through a hyper-hemispherical high-resistivity silicon lens attached to the back side of the substrate.

4. Experimental setup

The experimental setup for the device characterization is shown in Fig. 3. The optical source is a two-frequency master oscillator power amplifier (MOPA) 850 nm semiconductor laser system. A tapered semiconductor optical amplifier is simultaneously injection-seeded by a tunable external cavity laser (λ_1 = 848-853 nm) and a cavity-locked fixed frequency laser (λ_2 = 854 nm), and provides a maximum two-frequency power of 500 mW.[10] The output from the MOPA is split into two beams by a 2000-groove/mm diffraction grating. The advantage of the split collinear beam over two individual lasers is the nearly identical spatial mode quality of the two colors, which is essential for efficient THz wave generation.

For a grating incidence angle of $\alpha = 50^\circ$, the 1st order diffraction angle and its dispersion is $\beta = 70^\circ$ and $d\beta/df = 0.8^\circ$ THz^{-1}, respectively. At this configuration the diffraction efficiency is about 80%. The diffracted beams are reflected by two plane mirrors and focused onto the photomixer by a 6-mm-focal-length cylindrical lens. The ~2-mm diameter circular MOPA beam is compressed to a ~0.4 mm × 2 mm elliptical beam by the grating. The maximum available laser power after the grating is ~300 mW.

In the present implementation, the incident angle of the fixed frequency laser beam is set to zero (perpendicular to the photomixer surface). For the GaAs substrate, the phase-matching condition is fulfilled when the angle separation between the two laser beams, θ, is approximately half the dispersion angle of the two beams, or $\theta \cong 0.5\Delta\beta$. The angle and position of the mirror M_1 is adjusted to overlap the two laser beams at the photomixer surface. The THz output power was measured with a silicon composite bolometer placed ~3 cm from

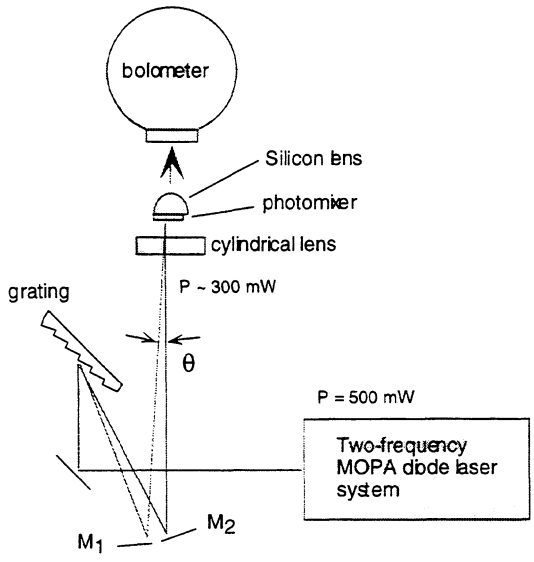

Fig. 3: Experimental setup.

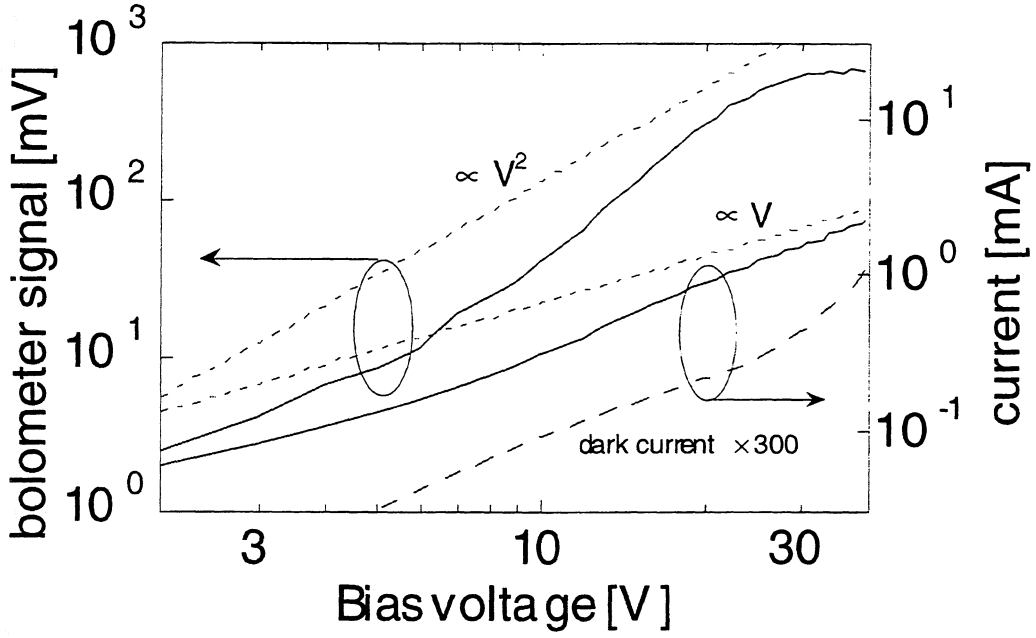

Fig. 4: The bias voltage dependence of the dc-photocurrent, dark current, and the THz output at f = 1 THz.

the photomixer by chopping the laser beams at 100 Hz. Thermal emission caused by the laser and electrical power was estimated from the bolometer signal when one laser beam was blocked.

5. Results and discussions

5-1. *Bias dependence*

Shown in Fig. 4 is the bias voltage dependence of the dc-photocurrent of the log-periodic antenna photomixer and the THz output measured at 1 THz under the phase-matching condition. The pump laser power is 280 mW at the photomixer surface. The dc-photocurrent shows a super-linear dependence, whereas linear (ohmic) dependence is expected, for the bias voltage greater than 5 V which corresponds to $E > 2.5\times10^4$ V/cm . The quadratic or super-linear dependence of the photocurrent has been seen in LTG-GaAs photomixers with sub-μm electrodes at high bias fields ($E > 10^5$ V/cm), where the space-charge-limited currents take place.[2,5] The data shows a super-linear dependence even at low bias voltage, which might arise here, because the photon or photocarrier density in the active area is ~5 times lower than that for small area photomixers. The space-charge-limited current is basically slow phenomenon and increases the dc current greatly but does not contribute to the ac current, which generates the THz wave. However, the THz output shows a super-quadratic dependence and it obeys the photocurrent square law[1] below 20 V, as seen in Fig. 4. The super-linear dependence of the photocurrent might be caused by the other effects such as

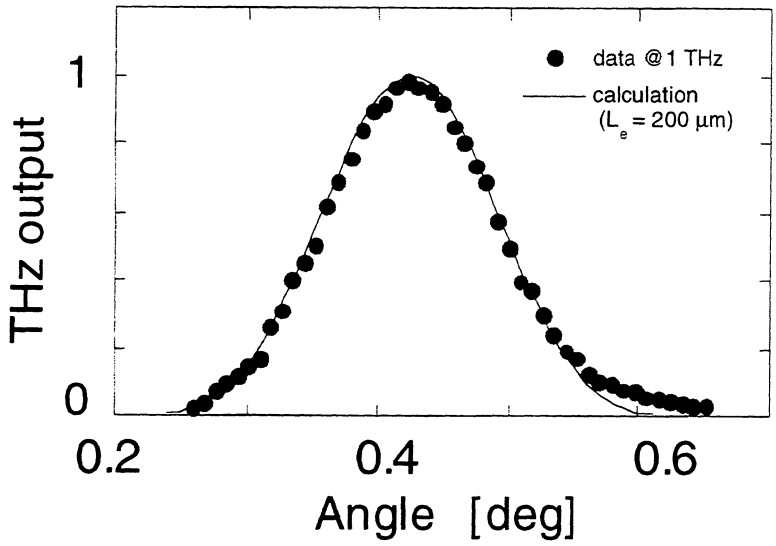

Fig. 5: The phase mismatch curve at f = 1 THz.

potential barrier at the metal contact. The THz output shows the saturation above 20 V, and the 'knee' voltage agrees with the breakdown voltage seen in the dark current curve. However, the dark current could not smooth out the photocarrier density waves directly, because it is the order of 10^{-3} of the photocurrent. Such saturation effect has been seen for small area photomixers and practically eliminated or reduced by increasing the laser power.[11] In order to clarify the saturation mechanism and improve the output power, more detailed theoretical consideration and further measurements under much higher photon density condition are required.

5-2. *Phase-matching*

For traveling-wave photomixers, the THz output power decreases with increasing the phase mismatch. Fig. 5 presents the THz output dependence on the incident angle of the f_1 laser, measured at 1 THz for the dipole device. The data show a maximum at $\theta = 0.42°$, which is close to that expected from Eq. 1 and 2. If it is assumed that the laser power density is uniform over the whole active area of the photomixer, the ac photocurrent integrated over the active area is expressed as a *sinc* function, and the THz output power is then given by

$$P_{THz} = A\left(\frac{\sin^2(\Delta kL/2)}{(\Delta kL/2)^2}\right)^2, \tag{3a}$$

where Δk is the phase mismatch,

$$\Delta k = 2\pi f\left(\frac{1}{v_{THz}} - \frac{1}{v_{op}}\right), \tag{3b}$$

A is a constant, and L is the length of active area of the photomixer. The calculated profile for L = 200 μm, shown by the solid curve in Fig. 5, shows good agreement with the data. The

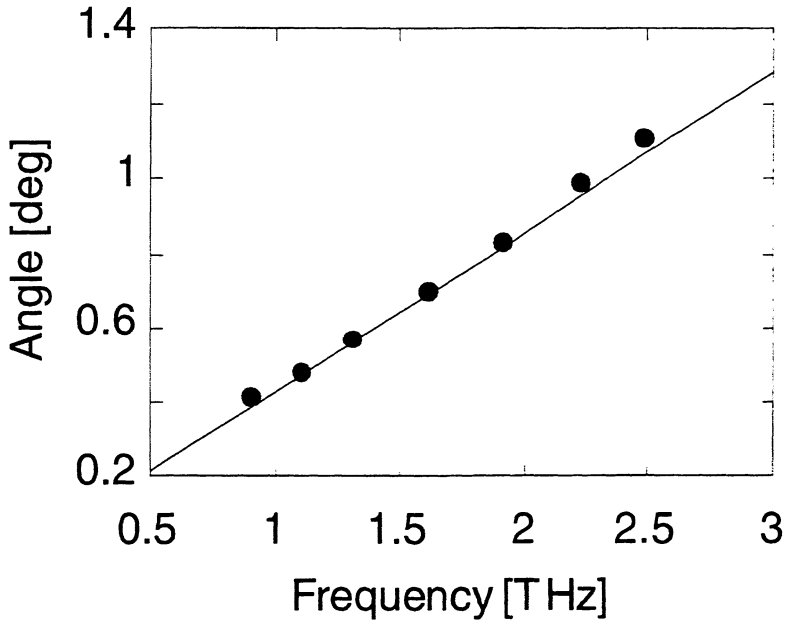

Fig. 6: The phase-matching angle vs the THz-wave frequency. The solid line is calculated from Eq. 1 and 2.

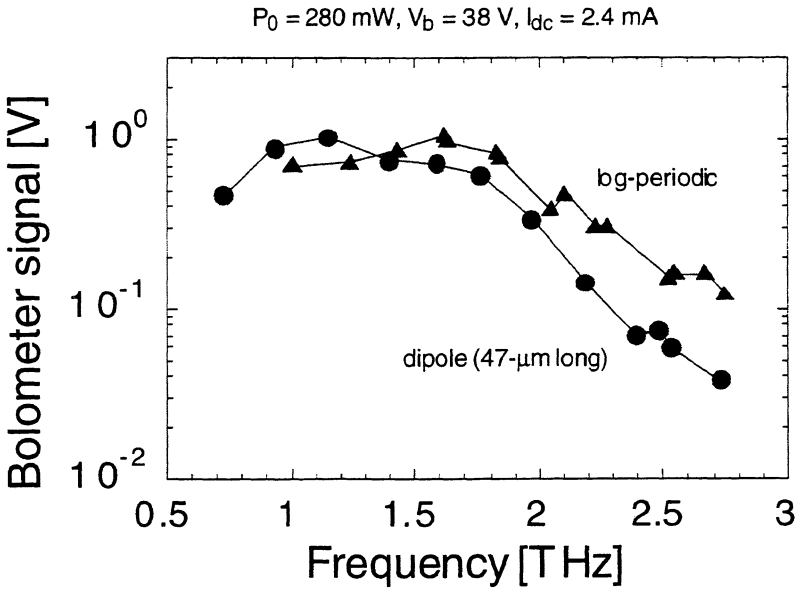

Fig. 7: The THz output spectrum of the dipole antenna device (circles) and the log-periodic antenna device (triangles).

effective active area would be smaller than the estimated laser spot size of ~400 μm, because the laser beam has a gaussian distribution rather than uniform distribution.

According to Eq. 1 for small θ, the angle mismatch curve, shown in Fig. 5, is independent on the THz-wave frequency. In fact, the measured mismatch curve was almost frequency independent. In Fig. 6 the phase-matching angle is plotted against the frequency. The data show good agreement with the tuning coefficient of 0.42° THz^{-1} predicted from Eq. 1 and 2, indicated by the solid line. Small scatter of the data from the predicted line might be due to the dispersion of the stripline. These results shown in Fig. 5 and 6 demonstrate that the present device works as a (phase-matched) distributed device.

5-3. *THz output spectrum*

The THz output spectra for both the dipole device and the log-periodic device are shown in Fig. 7. As noted above, the bandwidth of the ideal traveling-wave photomixer should be determined mainly by the LTG-GaAs carrier lifetime, which rolls-off as 6 dB/Oct. However, the data show a 3-dB bandwidth of 1.8 THz for the dipole and 2 THz for the log-periodic, which exceed the carrier-lifetime-limited bandwidth of 600 GHz, and a roll-off of ≥10 dB/Oct, similar to that of small area photomixers.[1] The spectral difference between the two devices is mainly due to the antenna impedance difference. The impedance of the log-periodic

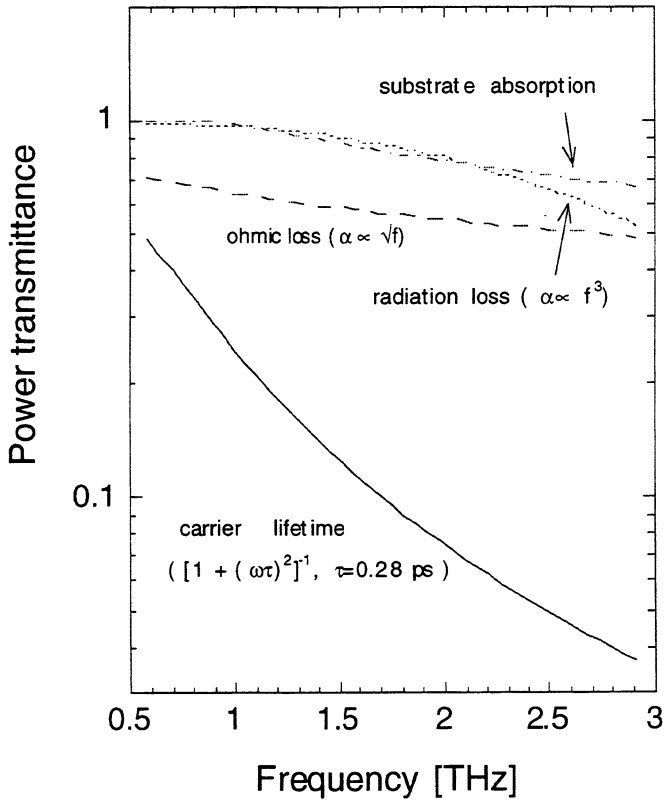

Fig. 8: The calculation of various losses; the carrier lifetime roll-off, conductor (ohmic) loss of the stripline metal, the radiation loss, and the substrate loss (the dielectric loss and the substrate transmittance).

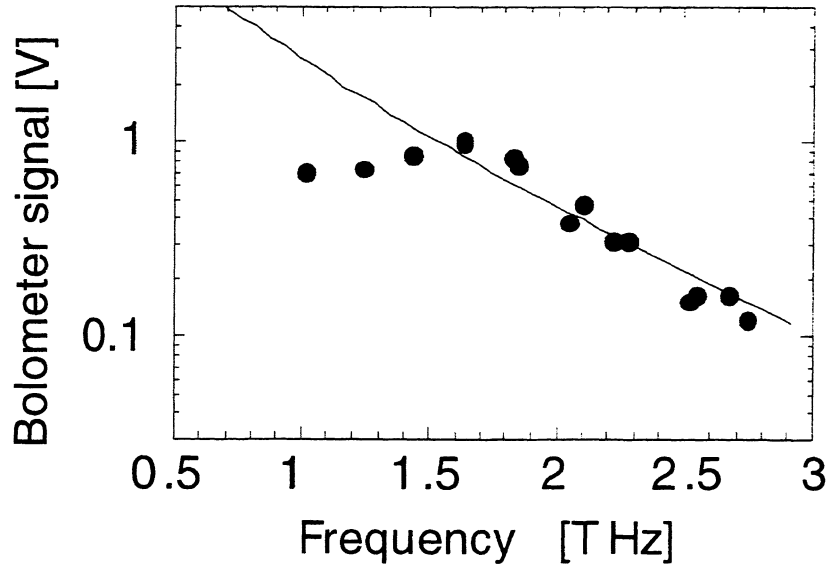

Fig. 9: The comparison between the data for the log-periodic device (circles) and the calculation (solid curve).

of 72 Ω is well-matched to the stripline impedance of 76Ω, while the dipole impedance is frequency dependent and matched to the stripline impedance only at restricted frequencies.

The additional roll-off can be interpreted as that arising from the conductor (ohmic) loss and radiation loss in the transmission line, and the substrate absorption. The conductor loss[12] calculated from the skin-effect resistance is $10\sqrt{f}$ dB/mm, where f is the frequency in THz. The radiation loss[13] is calculated to be $0.6f^3$ dB/mm. The substrate absorption measured with the FT-IR spectrometer is less than 2 dB/mm at ≤3 THz. Fig. 8 presents the THz power transmittance for the 400-μm long stripline calculated from these losses, assuming the THz-waves are uniformly generated in the active area. The total loss other than the carrier lifetime roll-off is less than 8 dB at ≤3 THz.

Fig. 9 presents the calculated spectrum for the log-periodic device, taking into account the carrier lifetime and the losses described above. The calculation shows rough agreement with the data, but the measured bandwidth is much wider than the calculation, due to the presence of a flat region at 1-2 THz. In order to clarify the details of the device property, further measurements for the devices with various electrode structures and detailed analysis are required. The bolometer signal of 1 V in Fig. 9 corresponds to ~0.1 μW, while the output power is predicted to be >4 μW at 1.5 THz for a dc-photocurrent of 2.4 mA. At present, the cause of this large discrepancy is not clear. It might be due to a shallow depth of the optical interference fringes and a effect which causes the output saturation at high bias end as described in 5-1.

6. Future direction

There are several practical ways to increase the THz output power. One is the increase of the laser power. Since the laser power density per unit area is presently ~1/5 of the thermal

damage threshold, the increase of the laser power reflects directly the THz output power. The increase of the laser power density may also contribute to the output power improvement, because the output saturation effect could be reduced by increasing the laser power density, as described above. This can be done by shortening the active area length (laser spot size), and it contribute to reduce the stripline loss, too. Another way is increasing the photoconductivity by narrowing the stripline gap. If the 1-μm gap device is used, the output power increases by a factor of 4, though the ohmic loss would increase and cancel the power gain a little. In addition, the radiation loss can be reduced by narrowing the total stripline width, and the substrate absorption can be eliminated by employing a silicon substrate. The silicon based photomixer offers additional benefit of high power handling capability.[5] By combining these power gain factors, one order of magnitude output power improvement would be achieved.

Acknowledgment

The authors would like to thank T. E. Turner in the Microelectronics Device Laboratory at JPL for device fabrication. This research was sponsored by the Jet Propulsion Laboratory, California Institute of Technology, and the National Aeronautics and Space Administration. The work performed at UCSB was supported by the Center for Nonstoichiometric III-V Semiconductors.

References

[1] E. R. Brown, F. W. Smith, and K. A. McIntosh, *J. Appl. Phys.*, **73**, 1480 (1993).

[2] E. R. Brown, K. A. McIntosh, F. W. Smith, K. B. Nichols, M. J. Manfra, C. L. Dennis, and J. P. Mattia, *Appl. Phys. Lett.*, **64**, 3311 (1994).

[3] K. A. McIntosh, E. R. Brown, K. B. Nichols, O. B. McMahon, W. F. DiNatale, and T. M. Lyszczarz, *Appl. Phys. Lett.*, **67**, 3844 (1995).

[4] S. Matsuura, M. Tani, and K. Sakai, *Appl. Phys. Lett.*, **70**, 559, (1997).

[5] S. Verghese, K.A. McIntosh, and E.R. Brown, *IEEE Trans. Microwave Theory and Tech.*, **45**, 1301 (1997).

[6] P. Chen, G. A. Blake, M. C. Gaidis, E. R. Brown, K. A. McIntosh, S. Y. Chou, M. I. Nathan, and F. Williamson, *Appl. Phys. Lett.* **71**, 1601 (1997).

[7] S. Matsuura, P. Chen, G. A. Blake, J. C. Pearson, and H. M. Pickett, , *IEEE Trans. Microwave Theory and Tech.*, (1999), in press.

[8] L. Y. Lin, M. C. Wu, T. Itoh, T. A. Vang, R. E. Muller, D. L. Sivco, and A. Y. Cho, *IEEE Phton. Technol. Lett.*, **8**, 1376 (1996).

[9] Y. -J. Chiu, S. B. Fleischer, and J. E. Bowers, *IEEE Phton. Technol. Lett.*, **10**, 1021 (1998).

[10] S. Matsuura, P. Chen, G. A. Blake, J. C. Pearson, and H. M. Pickett, Int. *J. of Infrared and Millimeter Waves*, **19**, 849 (1998).

[11] S. Verghese, private communication.

[12] K. C. Gupta, R. Garg, and R. Chadha, *Computer-aided Design of Microwave Circuits*, (Artech House, Norwood, MA, 1981), p. 72.

[13] D. B. Rutledge, D. P. Neikirk, and D. P. Kasilingam, in *Infrared and Millimeter Waves*, edited by K. J. Button (Academic Press, New York 1983), Vol. 10, p. 1.

Heterostructure Barrier Varactors on Copper Substrate for Generation of Millimeter- and Submillimeter-Waves

[1]Lars Dillner, [1]Jan Stake, [1]Stein Hollung [2]Chris Mann and [1]Erik Kollberg

[1]*Microwave Electronics Laboratory, Chalmers University of Technology, SE-412 96 Göteborg, Sweden.*
[2]*Rutherford Appleton Laboratory, Chilton, Oxon, UK.*
Email: dillner@ep.chalmers.se

Abstract:: We demonstrate a fabrication process where heterostructure barrier varactors are fabricated on a copper substrate which offers reduced parasitic losses and improved thermal conductivity. This have been done without degrading the electrical characteristics.

I. INTRODUCTION

The heterostructure barrier varactor (HBV) has received considerable attention as a promising symmetric varactor element for frequency multiplier applications at millimeter and submillimeter wave frequencies [1]. Compared with a Schottky barrier varactor, an HBV simplifies frequency tripler and frequency quintupler circuits and has the ability of epitaxial stacking, which increases its power handling capacity considerably [2]. However, parasitic resistance and limited thermal conductivity decrease the efficiency and the power handling capability of an HBV multiplier [3]. This paper describes a fabrication process which reduces the spreading resistance (part of the series resistance, R_s) and improves the heat sink by replacing the InP substrate with a copper substrate. The benefits of a copper substrate are excellent thermal and electrical conductivities.

II. DEVICE FABRICATION

The structure shown in Table 1 was grown by MBE. A Ti/Pt/Au ohmic contact is e-beam evaporated on the InAs top layer. The chip is then annealed at 200°C to improve the adhesion of the contact. Copper is then plated from a solution based on $CuSO_4$ and H_2SO_4 for 1 hour to a thickness of about 50 μm. For chemical protection, a gold layer is plated on the copper. The InP substrate is etched away in a $HCl:H_3PO_4$ 3:1 solution for about 2 hours (the epitaxial lift-off process (ELO) [4, 5]). The InGaAs buffer layer serves as etch stop layer. The buffer layer is reduced to about 0.5 μm using a wet etch ($H_3PO_4:H_2O_2:H_2O$). Notice that the epitaxial layers now are stacked on copper in reversed order compared with the growth order on the original InP substrate.

Table 1: The material structure. (The structure was originally designed for planar diodes.)

	Material	Doping (cm^{-2})	Thickness (Å)
Contact	InAs	$>10^{19}$	100
Contact	$In_{53}Ga_{47-0}As$	$>10^{19}$	300
Contact	$In_{53}Ga_{47}As$	$>10^{19}$	3000
Modulation layer	$In_{53}Ga_{47}As$	10^{17}	2500
Spacer layer	$In_{53}Ga_{47}As$	Undoped	50
Barrier layer	$In_{52}Al_{48}As$	Undoped	90
Barrier layer	AlAs	Undoped	20
Barrier layer	$In_{52}Al_{48}As$	Undoped	90
Spacer layer	$In_{53}Ga_{47}As$	Undoped	50
Modulation layer	$In_{53}Ga_{47}As$	10^{17}	2500
Spacer layer	$In_{53}Ga_{47}As$	Undoped	50
Barrier layer	$In_{52}Al_{48}As$	Undoped	90
Barrier layer	AlAs	Undoped	20
Barrier layer	$In_{52}Al_{48}As$	Undoped	90
Spacer layer	$In_{53}Ga_{47}As$	Undoped	50
Modulation layer	$In_{53}Ga_{47}As$	10^{17}	2500
Spacer layer	$In_{53}Ga_{47}As$	Undoped	50
Barrier layer	$In_{52}Al_{48}As$	Undoped	90
Barrier layer	AlAs	Undoped	20
Barrier layer	$In_{52}Al_{48}As$	Undoped	90
Spacer layer	$In_{53}Ga_{47}As$	Undoped	50
Modulation layer	$In_{53}Ga_{47}As$	10^{17}	2500
Buffer layer	$In_{53}Ga_{47}As$	$>10^{19}$	30000
Substrate	InP	S.I.	

After the ELO process, diode mesas of 3, 4.5, 7, 10, 15 and 30 μm diameter are fabricated using standard photo lithographic methods and e-beam evaporation of Au/Ge/Au/Ni/Au/Ti. The titanium serves as etch mask. After anealing at 370°C, diode mesas are etched using a chlorine based Reactive Ion Beam Etching (RIBE) and a wet etch.

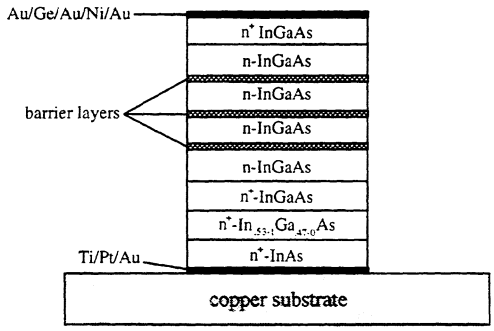

Figure 1: Schematic cross-section through HBV diode fabricated on copper substrate.

To prevent the whisker wire from sliding off the mesa, gold cups were fabricated on top of the mesas using photo lithography, sputtering of titanium and gold, and lift-off. Figure 1 shows the schematic cross-section of an HBV diode fabricated on copper, and figure 2 shows a SEM picture of HBV diodes fabricated on a copper substrate. For comparison, diodes have also been fabricated on the original InP substrate.

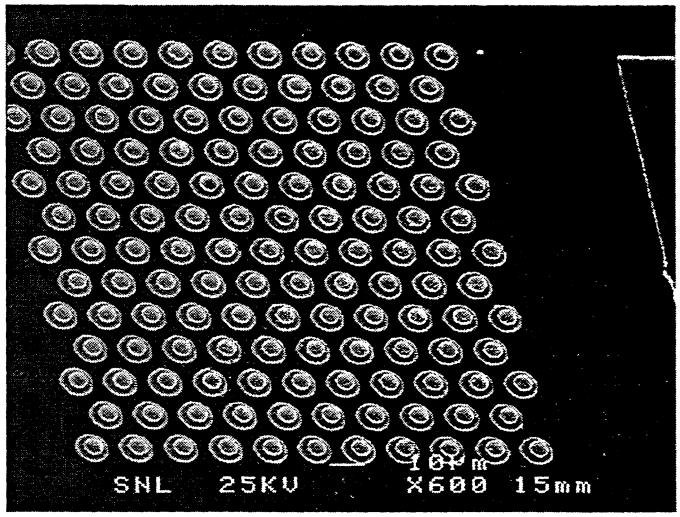

Figure 2: An array of 10 μm HBV diodes fabricated on a copper substrate

I-V and C-V characterization

The conduction current and the capacitance-voltage characteristics of HBVs on copper and InP are shown in figures 3-4. A very small difference in the electrical characteristics of the HBVs on copper and InP can be seen from the figures. This verifies that the

fabrication process does not degrade the epitaxial layers. The measured C-V characteristics are displayed with a C(V) generated by the quasi-static HBV model

$$V(Q) = N\left(\frac{bQ}{\varepsilon_b A} + 2\frac{sQ}{\varepsilon_d A} + Sign(Q)\left(\frac{Q^2}{2qN_d\varepsilon_d A^2} + \frac{4kT}{q}\left(1 - e^{-\frac{|Q|}{2L_D AqN_d}}\right)\right)\right) \quad (1a)$$

$$L_D = \sqrt{\frac{kT\varepsilon_d}{q^2 N_d}} \quad (1b)$$

where N is the number of barriers, b is the barrier thickness, s is the undoped spacer layer thickness, A is the device area, N_d is the doping concentration in the modulation layer, ε_b and ε_d are the dielectric constant in the barrier material and modulation layer respectively, T is the device temperature, q is the elementary charge, and Q is the charge stored in the HBV[3, 6]. With b=200, s=50 Å, N_d=1.15 10^{17} cm^{-3} and N=3, the model agrees excellent with the measured C-V. The measured conduction current density was fitted to the simple empirical expression

$$J_{cond.} = a * \sinh(b * V) \quad (2)$$

with the constants a= 50.3 and b=1.13.

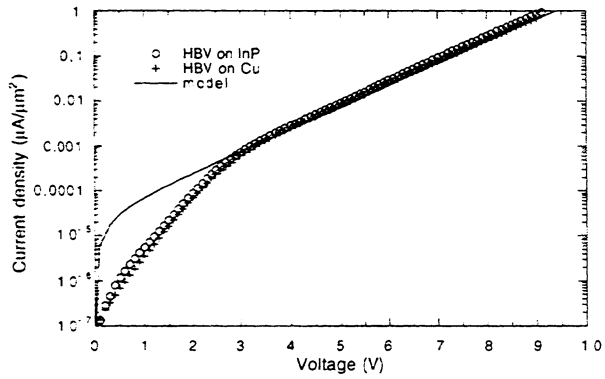

Figure 3: Measured and modeled conduction current density through an HBV fabricated on InP and copper respectively.

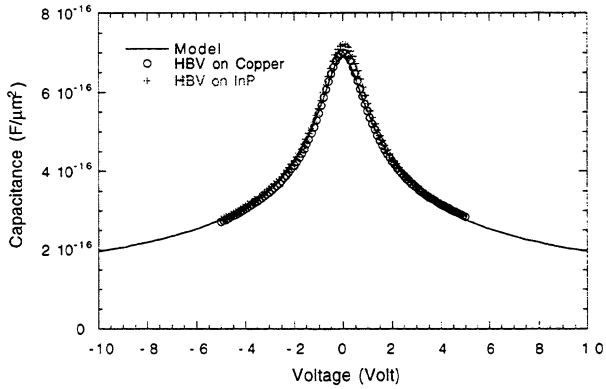

Figure 4: Measured and modeled capacitance-voltage characteristics for HBVs on InP and copper respectively. The C-V characteristic was measured with a LCR-meter (HP4285) at 1 MHz.

Thermal resistance of the heat sink

For heat flow from the diode into a semi infinite heat sink, the thermal resistance can be estimated by

$$R_{T,heat\ sink} = \frac{1}{2d\kappa} \tag{3}$$

where d is the diode diameter and κ is the thermal conductivity of the heat sink material. The thermal conductivity of copper is $\kappa \approx 400\ Wm^{-1}K^{-1}$, to be compared with $\kappa \approx 70\ Wm^{-1}K^{-1}$ for InP and $\kappa \approx 45\ Wm^{-1}K^{-1}$ for GaAs.

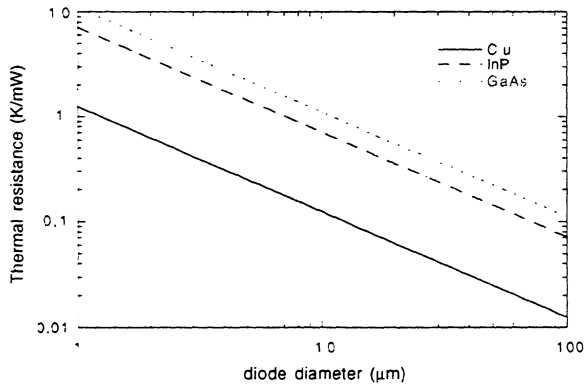

Figure 5: The thermal resistance of copper, InP and GaAs heat sinks as a funktion of diode diameter.

For a complete thermal analysis, the diode mesa and the whisker wire must be included in the calculations [7].

The series resistance

The series resistance is the sum of the resistance of the diode mesa, the spreading resistance, and the ohmic contact resistance. The resistance of the modulation layers, which dominates the mesa resistance, can be estimated by

$$R_{smesa} = \frac{(N+1)t}{\mu N_d q A} \tag{4}$$

were N is the number of barriers, t is the thickness of the modulation layers, μ is the electron mobility, N_d is the doping concentration in the modulation layers, q is the elementary charge, and A is the area of the diode. We have assumed the electron mobility to be 6500 $cm^2/(Vs)$. The specific contact resistance have been measured using TLM patterns to 40 $\Omega\mu m^2$ for the Ti/Pt/Au on InAs contact and 60 $\Omega\mu m^2$ for the Au/Ge/Au/Ni/Au on InGaAs contact. Figure 6 shows the specific contact resistance of the latter contact as a function of temperature. Notice that copper can be anealed at temperatures above 400°C were InP is unstable.

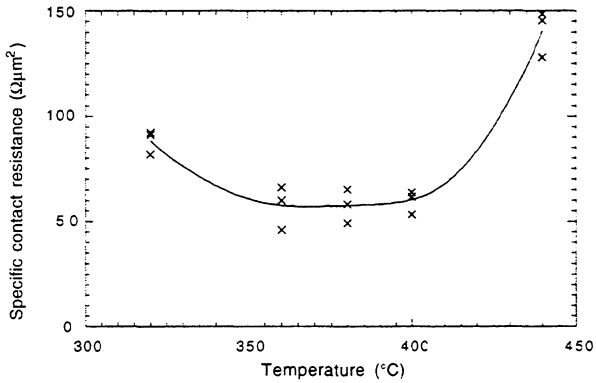

Figure 6 The specific contact resistance of the Au/Ge/Au/Ni/Au on $In_{0.53}Ga_{0.47}As$ contact as a function of temperature.

The spreading resistance at high frequencies can be estimated by:

$$R_{sp} = \frac{\ln(\frac{D}{d})}{2\pi\sigma\delta} \tag{5}$$

were D is the diode chip diameter, σ is the conductivity at the surface of the substrate, and δ is the skin depth. In our case, the substrate surface is covered by gold, platinum and titanium which makes the calculations more complicated. However, for frequencies below 1 THz the skin depth of platinum and titanium is larger then the film thickness (500 Å of titanium and 500 Å of platinum was evaporated). Therefore, the losses in the gold layer and the copper substrate dominates. We have used the conductivity of gold, 4.3 10^7 S/m, in our calculations. The chip diameter, D, have been assumed to be 200 μm. To include effects of surface roughness etc, we have multiplied the resistance from (5) by a factor 2. Table II shows estimated series resistances at DC and 1 THz. If the capacitance is extrapolated to the break down voltage, 9 Volt, and the DC series resistance is assumed, the dynamic cut-off frequency

$$f_c = \frac{1}{2\pi Rs}\left(\frac{1}{C_{\min}} - \frac{1}{C_{\max}}\right) \tag{6}$$

can be estimated to be 2.7 THz.

Table II: Estimated series resistances.

diode diameter (μm)	R_s at DC (Ω)	R_s at 1 THz (Ω)
3	28	29
4.5	13	13
7	5.2	5.5
10	2.5	2.8
15	1.1	1.4
30	0.28	0.46

IV. SIMULATIONS

We have made harmonic balance calculations for frequency multipliers with the described HBV diodes. In the simulations the series resistance, conduction current and capacitance voltage models described above were used. Circuit losses are not included in the simulation and optimum embedding impedances are assumed.

For our harmonic balance simulations to be valid, the velocity for the electrons in the modulation layers may not exceed the saturation velocity, ≈2.5 10^5 m/s for $In_{0.53}Ga_{0.47}As$. If an abrupt depletion region is assumed, the current density is given by:

$$J = N_d q v \tag{7}$$

where v is the velocity of the electrons in the modulation layers. Consequently, it is possible to estimate the maximum electron velocity from the current waveform. Table III shows results from simulations of a 250 GHz tripler and a 750 GHz quintupler. The simulations predict 44 % efficiency for the 250 GHz tripler and 10 % efficiency for the 750 GHz quintupler.

Table III: Multiplier simulations of a 250 GHz tripler and a 750 GHz quintupler for HBVs on copper substrate.

Output frequency	250 GHz	750 GHz
Input frequency	83.3 GHz	150 GHz
Diode diameter	10 μm	4.5 μm
Estimated series resistance	2.7 Ω	12.8 Ω
Input power	40 mW	18 mW
Output power	17.5 mW	1.9 mW
Efficiency	44 %	10.4 %
Input impedance	6.0-62j Ω	26-165j Ω
Optimum load impedance	10.5+26j Ω	20+40j Ω
Optimum idler impedance	--	73j Ω
Maximum voltage	8.9 V	9.0 V
Maximum electron velocity	$1.1 \cdot 10^5$ m/s	$2.5 \cdot 10^5$ m/s

V. CONCLUSION

We have demonstrated that HBV diodes can be fabricated on copper substrate without degrading the electrical characteristics. This fabrication process should decrease the spreading resistance and improve the heat sink significantly. Simulations predict very competitive efficiencies for HBV diodes on copper. Another advantage with this fabrication process is that HBV material grown on semi-insulating substrate can be used for whisker diodes, enabling the same material to be used for whisker contacted diodes and planar diodes.

VI. ACKNOWELEDGEMENT

This work was supported by SSF High Speed Electronics program. The authors would like to thank Emmanuil Choumas and Byron Alderman for fruitful discussions.

VII. REFERENCES

[1] A. Rydberg, H. Grönqvist, and E. L. Kollberg, "Millimeter- and Submillimeter-Wave Multipliers Using Quantum-Barrier-Varactor (QBV) Diodes," *Transactions on Electron Devices*, vol. 11, pp. 373-375, 1990.

[2] K. Krishnamurthi, R. G. Harrison, C. Rogers, J. Ovey, S. M. Nilsen, and M. Missous, "Stacked Heterostructure Barrier Varactors on InP for Millimeter Wave Triplers," presented at Fifth International Symposium on Space Terahertz Technology, 1994.

[3] J. Stake, L. Dillner, S. H. Jones, C. Mann, J. Thornton, J. R. Jones, W. L. Bishop, and E. Kollberg, "Effects of Self-Heating on Planar Heterostructure Barrier Varactor Diodes," *Transactions on Electron Devices*, vol. 45, pp. 2298-2303, 1998.

[4] W. K. Chan, A. Yi-Yan, and T. Gmitter, "Grafted Semiconductor Optoelectronics," *IEEE Journal of quantum electronics*, vol. 27, pp. 717-725, 1991.

[5] G. Augustine, N. M. Jokerst, and A. Rohatgi, "Single-crystal thin film InP: Fabrication and absorption measurements," *Appl. Phys. Lett.*, vol. 61, pp. 1429-1431, 1992.

[6] L. Dillner, J. Stake, and E. Kollberg, "Modeling of the Heterostructure Barrier Varactor Diode," presented at International Semiconductor Device Research Symposium, Charlottesville, 1997.

[7] J. R. Jones, "CAD of Millimeter Wave Frequency Multipliers: An Experimental and Theoretical Investigation of the Heterostructure Barrier Varactor," in *School of Engineering and Applied Science*: University of Virginia, 1997.

THE COMPLETE ANALYTICAL SIMULATION OF HETEROSTRUCTURE BARRIER VARACTOR FREQUENCY MULTIPLIERS

L Dillner[1], M L Oldfield[2], C M Mann[2], B E J Alderman[3]

[1]Chalmers University of Technology, SE-412 96 Göteborg, Sweden

[2]Rutherford Appleton Laboratory, Chilton, Didcot, Oxon, OX11 0QX

[3]University of Nottingham, UK

Abstract

Planar Heterostructure Barrier Varactor[1] (HBV) frequency multipliers are now demonstrating levels of performance that are better than the best planar Schottky varactor multipliers[2,3] . For high powered, narrow band HBV triplers, the circuit design is dramatically simplified as the need for both second harmonic idler and bias are removed. For a waveguide tripler the inclusion of movable shorts can ensure that the HBV is optimally matched at both the input and output. However, for fixed tuned broad band HBV triplers this is not the case. For specific applications where pump power is limited it becomes necessary to carefully consider both the HBV and waveguide mount together. The HBV has the advantage that unlike the Schottky varactor there are two design parameters that can be adjusted, allowing the device to be tailored for a specific application. By adjusting the number of barriers and its size, a HBV's capacitance can be kept more or less constant whilst its power handling capability can be adjusted over at least an order of magnitude. Thus it becomes necessary to consider a multiplier's application and the HBV used, hand in hand, if the optimum performance is to be attained over the frequency range required.

This paper describes the analytical simulation of a HBV frequency multiplier. An analytical model for the HBV is incorporated with a fast harmonic balance code allowing

pump power and device parameters to be varied at will. All code is integrated with *Mathematica* and so allows flexible graphical output along with parametric variation of both circuit and HBV. A quick HBV design code[4] is used to determine the initial starting point for the HBV design. This approach has been taken as it allows fast optimisation of circuit and device parameters. The simulation incorporates movable backshorts and easy adjustment of both waveguide and microstrip filter circuit. It therefore becomes possible to perform animations of the complete multiplier's frequency response as a function of input and output backshort position, number of barriers, device area, pump power, etc. Higher harmonics are also taken into account so quintuplers and septuplers can also be studied. On a 300MHz Macintosh a frequency sweep from 240-360GHz in 6GHz increments takes ≈ 30 seconds for the complete multiplier.

Introduction

Planar HBV triplers are now producing higher efficiencies and output powers than conventional planar Schottky varactors. When this is combined with their automatic cancellation of even harmonics and ability to be engineered for specific applications right the way up to terahertz frequencies it appears that the days for the Schottky are numbered. Because the HBV has more variable parameters other than size and doping level, as is the case with a Schottky, the design of a HBV multiplier can be rather more complex. This is particularly true for broadband fixed tuned devices or higher order multipliers such as quintuplers or septuplers. Starting a custom design from scratch can therefore be a time consuming affair when using a full field simulator such as HFSS etc., even after taking into account the recent improvements in computational speed. In order to quickly examine a particular circuit or HBV's suitability for a specific application we have developed an extremely fast analytical simulator for the complete multiplier. The circuit medium is waveguide and is based on a very simple waveguide geometry which has been chosen for its suitability for simulation using a proven analytical model and its

fabrication via micromachining techniques. With the use of micromachining standard waveguide sizes need not be used, thus to be able to quickly analyse custom waveguide mounts is an advantage. By combining analytical models for the complete RF circuit and the HBV itself a very fast modelling tool is produced

This approach, however, does not take all circuit effects into account, it is therefore intended that it should be used in conjunction with full field simulation, providing a sound starting point for the final design.

Simulation Procedure

The simulation is carried out in the following way:-

1.Determine frequency and power specification of the multiplier to be designed.

2.Design the HBV for the power level and impedance level required.

3.Run the HBV optimisation code (either Harmonic Balance or HBVQuic k Design, see below) to determine the embedding impedances required over the frequency range desired.

4.Model waveguide multiplier circuit , using visual comparison, adjust for best match at the input and output.

5.Run full model to determine performance of the complete device.

6.Verify circuit design using HFSS, etc.

(HBVQuick design is available at the website;- http:04/08/99/devicesim.ee.virginia.edu)

For this paper we examine a real specification required for astronomy, a fixed tuned HBV tripler. The device is to have a nominally flat frequency response, provide 50μW of power for an input power level of 10mW and operate fixed tuned from 250-350GHz.

HBVQuick Design shows that a single barrier GaAs HBV will provide sufficient efficiency and output power.

Target circuit impedances across the band of interest are now provided by an optimisation routine in the *Mathematica* frontend which .

The harmonic balance used is a modified version of the splitting method [5] to suit HBV frequency multipliers. In most harmonic balance algorithms the non-linear device is excited with a voltage. However, we model the HBV by a voltage-charge model, V(Q), which makes it rather complicated to calculate the current from the voltage. Therefore, we have chosen to excite the diode with a current. Our algorithm can briefly be described as follows.

1: An initial displacement current, $\mathbf{I}_0$, at the pump frequency is estimated.

2: The current is integrated to a charge, and the voltage over the non-linear subcircuit is calculated using a voltage-charge model.

3: The leakage current, $\mathbf{I}_{L0}$, is calculated from the voltage using a non-linear current-voltage model.

4: The voltage over the linear subcircuit is assumed to be equal to the voltage over the non-linear elements.

5: The current through the linear subcircuit, $\mathbf{I}_0'$, is calculated from the voltage over the linear subcircuit.

6: A new displacement current $\mathbf{I}_1$ is estimated between $\mathbf{I}_0$ and $\mathbf{I}_0'-\mathbf{I}_{L0}$ as

$$\mathbf{I}_1=\mathbf{I}_0+s(\mathbf{I}_0'-\mathbf{I}_{L0}-\mathbf{I}_0)$$

where the variable s is the two-dimensional splitting factor. A two-dimensional splitting factor is used to make it possible to deal with both the amplitude and the phase of the current.

7: Steps 2-6 are repeated until convergence is reached.

8:The input power is calculated and steps 2-7 are repeated with new current estimations until the set value of the input power is reached

The harmonic balance routine has been turned into a *Mathematica* function 'HBVreflect'. This can then be used in the same way that the functions Cos[x] and Sin[x] are used. This allows the *Mathematica* kermel to invisibly link the HBV code with the analytical simulation code. *Mathematica* is used as it can generate excellent graphics including animation. The function 'HBVreflect' is shown below.

?HBVreflect

"HBVreflect[F,Pavail,Is,Rsdc,{Zo1, Zo2, ...}] calculates the performance of \

a HBV multiplier at a frequency F (Hz) with available power Pavail (W), \

Initial current Is (A), DC series resistance of Rsdc (Ohms) with odd \

harmonic embedding impedances of Zoi (Ohms)."

?SetHBVParam

SetHBVParam[T, A, \[Epsilon]b, \[Epsilon]d, b, s, Nd, N, \[Phi]b, a, E0] sets

the listed HBV device parameters.

In the code the diode is pumped with 10mW across a range of frequencies and the optimum impedance is returned for the fundamental and output harmonics.

The structure that is modelled in the Eisenhart and Khan analysis is shown below in figure 1. More information can be found in [6]

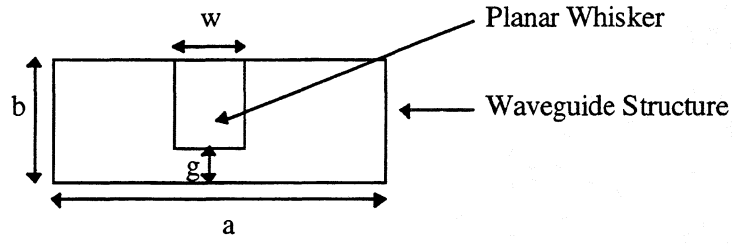

Figure 1: *The basic Eisenhart and Khan waveguide coupling structure.*

The circuit used in the simulation is shown below in figure 2 along with the parameters which can be varied within the code.

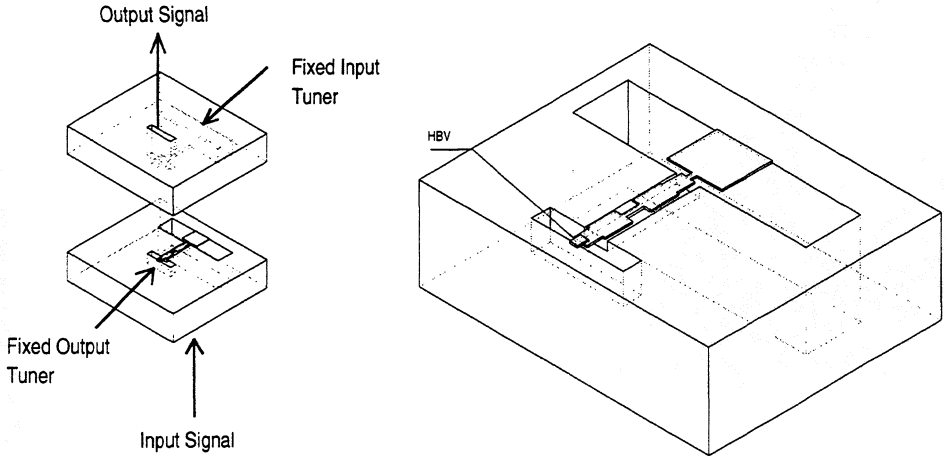

Figure 2: *A schematic of the multiplier geometry modelled.*

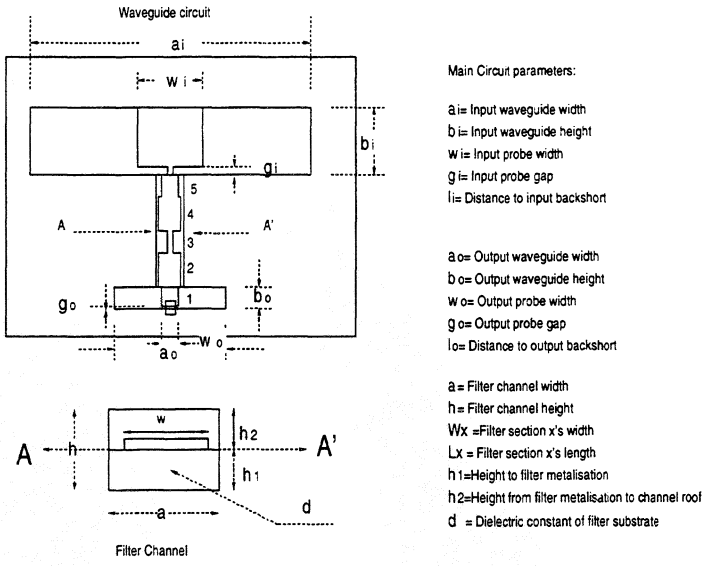

Figure 2(cont'd): *The simulated circuit and parameters.*

The simulation is carried out as follows:-

1.The ideal input diode embedding impedances are transformed through the filter circuit to provide a goal for the input circuit to meet. (figure 3)

2. The filters dimensions are adjusted and its response confirmed.(figure 4)

3.The input circuit and filter are modified to provide the best matching conditions across the band (figure 5)

3.The output circuit is modified to provide the most optimum impedance match across the band (figure 6)

4.The impedances relating to the best solution is used in the harmonic balance code to determine the complete device's performance (figure 7)

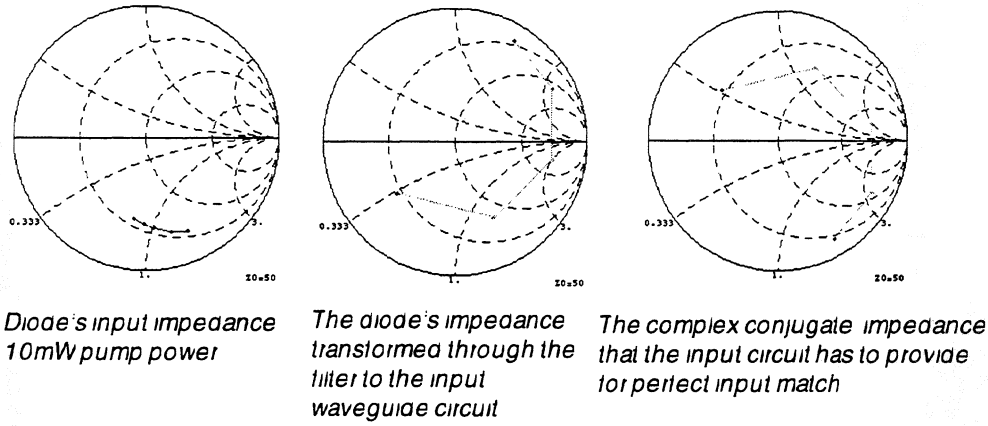

Figure 3: *The diodes impedance as a function of input frequency.*

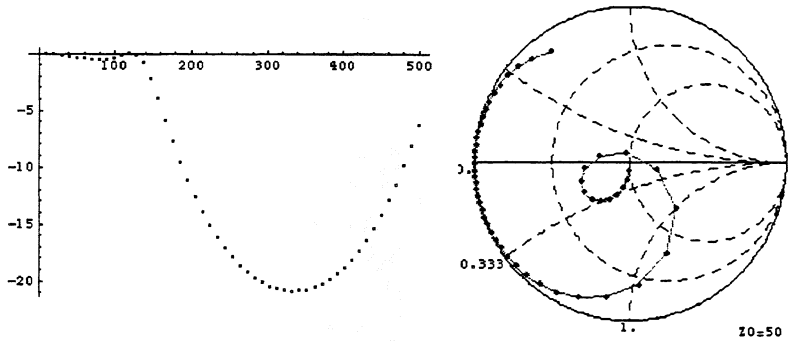

S21 for the four section filter, note less than 1dB insertion loss to 140GHz and better than 10dB rejection from 200-450GHz, more than adequate for the specification

S11 for the same filter showing the centring of the band required around the short circuit position, a requirement for accurate use of the E&K analysis

Figure 4: *The filter response.*

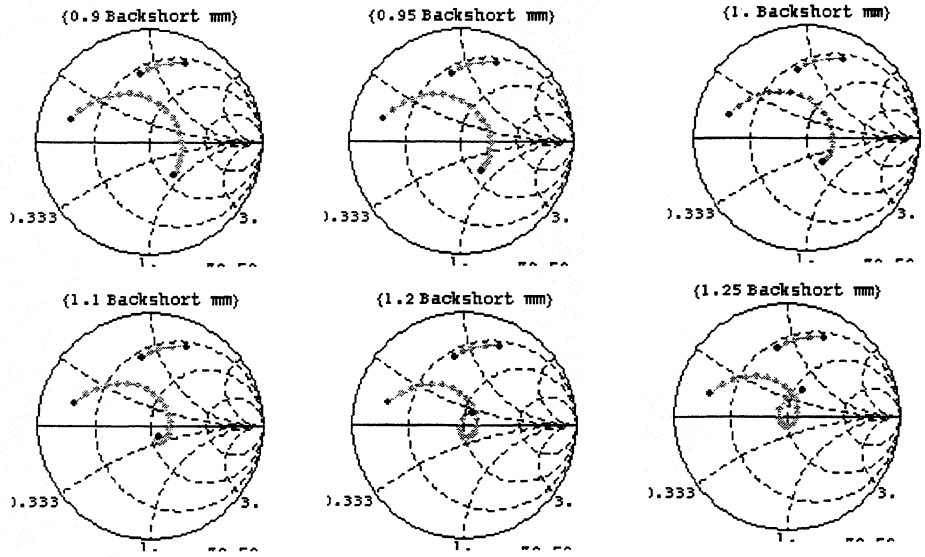

Figure 5: *Impedance presented to the diode by the input circuit /filter compared with the ideal impedance required by the diode.*

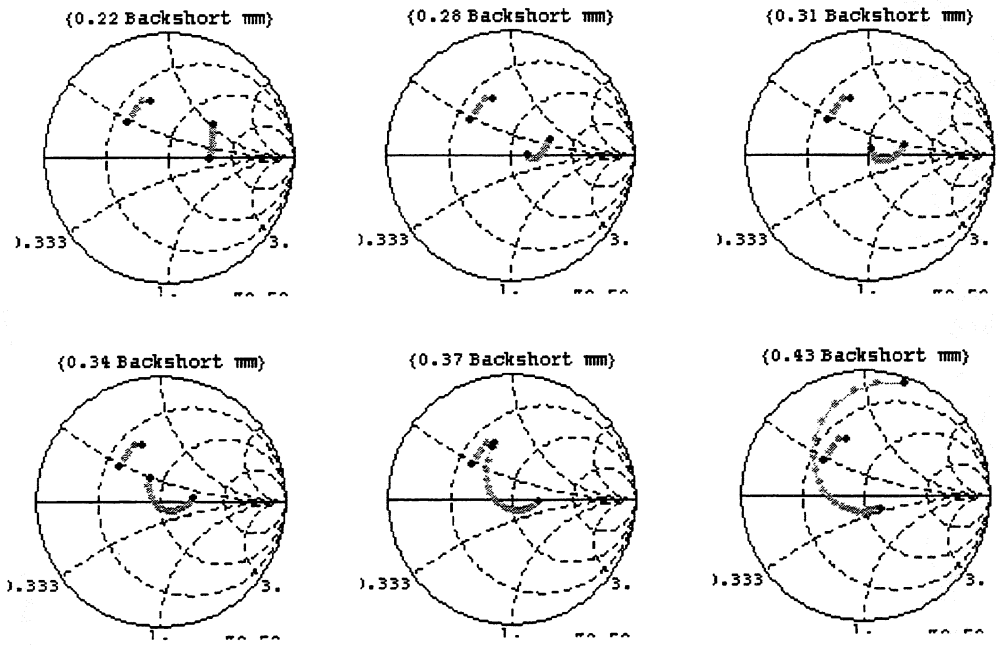

Figure 6 *Impedance presented to the diode by the output circuit compared with the ideal impedance required by the diode*

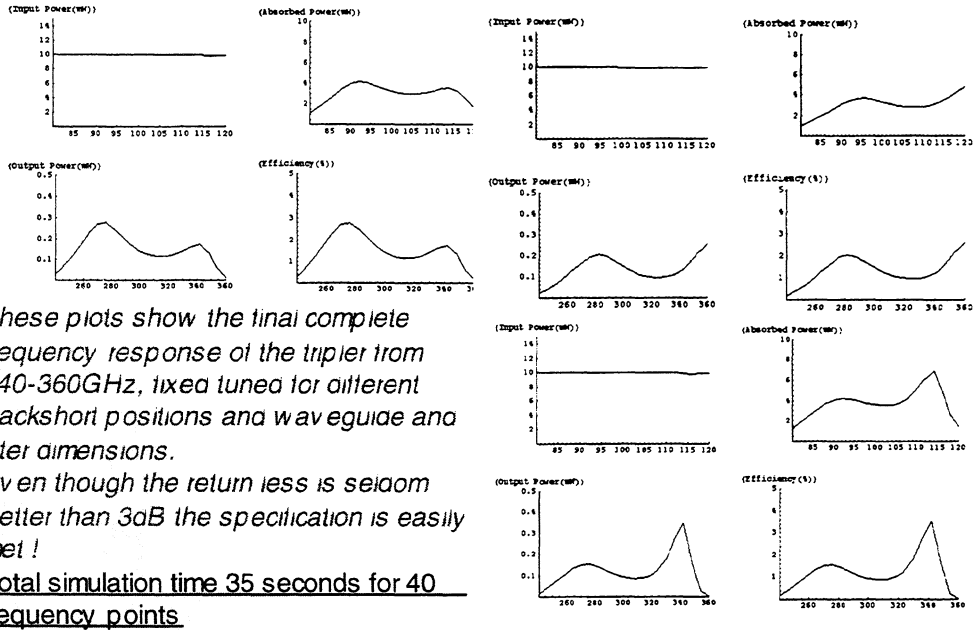

These plots show the final complete frequency response of the tripler from 240-360GHz, fixed tuned for different backshort positions and waveguide and filter dimensions.
Even though the return less is seldom better than 3dB the specification is easily met !
Total simulation time 35 seconds for 40 frequency points

Figure 7: *The complete fixed tuned frequency response of the tripler for varying backshort positions.*

Discussion

The use of a complete analytical model for a HBV tripler gives valuable insight into its behaviour as a function of frequency. It has shown that very broadband devices (>30% bandwidth) can be realised and also has shown that the input circuit is presently the limiting factor for low powered devices. Analytical models for different waveguide coupling structures are available and could easily be incorporated into the *Mathematica* front-end as importable packages.

Conclusions

A complete analytical model for HBV multipliers has been developed and has been applied to the design of a fixed tuned very broadband HBV tripler. This approach is very fast and adaptable.

Experimental verification as to its accuracy is now underway.

Acknowledgements

The authors wish to thank Professor Stephen Jones for his helpful discussions and for making HBVQuick design generally available.

---

[1] 'Quantum Barrier Varactor Diodes for High Efficiency Millimetre Wave Multipliers', E. Kollberg, A. Rydberg, Electron. Lett.., VOL. 25, no. 25, pp. 1696-1698, Dec. 1989.

[2] '5-mW and 5% Efficiency 216GHz InP-Based Heterostructure Barrier Varactor Tripler' X.Melique, C. Mann, P. Mounaix, J. Thornton, O. Vanbesien, F. Mollot, and D. Lippens, IEEE Microwave and Guided Wave Lett., Vol. 8, NO. 11, November, 1998

[3] 'Effects of Self-Heating on Planar Heterostructure Barrier Varactor Diodes', J.Stake, L.Dilner,S.H.Jones, C.M.Mann, J.Thornton, J.R.Jones, W.L.Bishop, E.Kollberg, IEEE Transactions on Electron Devices, VOL. 45, NO.11, November 1998

[4] 'Design of 100-900 GHz AlGaAs/GaAs Planar Heterostructure Barrier Varactor Frequency Triplers',J.Stake, L.Dillner, S.H.Jones, C.M.Mann, and E.Kollberg, 9th International Conference on Space THz Technology, Pasadena, CA, March 1998

[5] S. A. Maas, *Nonlinear Microwave Circuits*: Artech House, 1988.

[6] 'Optimisation of a 250 GHz Schottky Tripler Using Novel Fabrication and Design Techniques', J.Thornton, C.M.Mann, P. de Maagt, IEEE Transactions on Microwave Theory and Techniques, VOL. 46 NO. 8, August 1998.

177-207 GHz Radiometer Front End, Single-Side-Band Measurements

I. Galin[1], C. A. Schnitzer[1], R. J. Dengler[2], and O. Quintero[2]
[1]Aerojet, P.O. Box 296 Azusa, CA 91702
[2]Jet Propulsion Laboratory, 4800 Oak Dr. Pasadena, CA 91009

ABSTRACT: *Twenty years of progress in 200 GHz receivers for spaceborne remote sensing has yielded a 180-220 GHz technology with maturing characteristics. The maturing characteristics are evident by increasing hardware availability —supply side—that parallels further refinement in receiver front-end (RFE) performance requirements—demand side—at this important spectrum band. The 177-207 GHz super-heterodyne receiver, for the Earth observing system (EOS) microwave limb sounder (MLS), effectively illustrates such technology developments. This MLS receiver simultaneously detects six different signals, located at side-bands below and above its 191.95 GHz local-oscillator (LO) frequency.*

The paper describes the MLS 177-207 GHz RFE, and provides measured data for its lower and upper side bands. Side-band ratio data is provided as a function of intermediate frequency (IF), at different LO power drive, and for variation in the ambient temperature.

INTRODUCTION

The 191.95±15 GHz receiver of the MLS employs a sub-harmonic (x2) mixer simultaneously producing (Table 1) six IF outputs, three of which originate at the lower RF side-band (191.95-15 GHz) and the other three at the upper RF side-band (191.95+15 GHz).

RF [GHz]		LO [GHz]	IM [GHz]		IF [GHz]
LOWER	177.265	191.95	206.635	@	14.685
[RF_-]	181.599		202.301	RF_+	10.351
BAND	183.314		200.586	BAND	8.636
UPPER	200.980	191.95	182.920	@	9.030
[RF_+]	204.357		179.543	RF_-	12.407
BAND	206.137		177.763	BAND	14.187

Table 1. MLS 191.95 GHz Receiver Spectrum Characteristics

As Table 1 illustrates, each one of the 191.95 GHz MLS side bands contain RF inputs and image (IM) inputs; therefore, IM rejection with a filter is not a practical option. In effect, this MLS receiver relies on the availability of a double-side-band (DSB) mixer with superior single-side-band (SSB) sensitivity—i.e., mixers

yielding extremely low-noise-temperature and a side-band ratio, which approximates unity, over an RF band spanning 30 GHz.

A mixer is the prime determinant of the RF side-band characteristics of a super-heterodyne receiver—especially at high millimeter-wave (MMW) frequencies, where a low-noise MMW amplifier is not available to precede the mixer. The DSB inputs, i.e., upper/lower RF_+/RF_- side band respectively, down converts simultaneously to the same output IF band, following the relation $f_{IF} = |f_{LO}-f_{RF\pm}|$. Mixers employing non-linear resistive devices exhibit theoretically identical RF-to-IF power conversion loss [1], for $f_{RF\pm}$ inputs symmetrically paired $2xf_{IF}$ apart relative to the frequency f_{LO} of the local-oscillator.

Practically, DSB mixer operation is spectrum bounded: high-end bound, by the bandwidth of the mixer's circuit and the parasitic elements associated with a non-linear resistive device; and low-end bound, by the frequency stability of the LO.

Progress at Aerojet in subharmonic (x2) mixer's RF and IF circuit design [2] and improvements at University of Virginia in mixer Schottky diode technology [3] are the prime facilitators of the MLS 191.95±15 GHz RF side band's characteristics reported in this paper.

SINGLE-SIDE-BAND TESTS SET-UP

Single-side-band (SSB) measurements have been performed at JPL, on this MLS RFE, in the 177-207 GHz input RF band and 8-15 GHz output IF band. The test set-up is based on a parallel two-grid Fabry-Perot interferometer (FPI) configuration previously described [4]. This test set-up was originally constructed for measuring RFE conversion-loss at each side-band, for IF frequencies up to about 12 GHz. A minimum grid spacing of about 2900 μm accommodated such test capabilities, and also determined the orders of resonance of the parallel grid.

The MLS higher IF frequency requires an FPI with reduced grid spacing and lower orders of resonance, to ensure avoidance of aliasing of the lower and upper side-bands between consecutive resonance orders of the grids. Reduction in grid spacing—modified FPI achieves a minimum grid spacing of less than 1000 μm—required installing a shim on the step micrometer shaft driving the slide assembly holding one of the grids. The variable differential transformer reference was then readjusted to indicate positions to the controlling computer, consistent with the modified minimum grid spacing.

This test set-up facilitates relative measurements of RFE conversion-loss at the lower side-band (L_-) and the upper side-band (L_+), for which the mixer is assumed the sole determinant. The specific spectrum of a SSB application determines the relations between RF_-; RF_+, and RF; IM respectively, to yield a side-band ratio L_{RF}/L_{IM}. This ratio enables the calculation of the receiver's SSB noise-temperature (T_R(SSB)) from measured receiver DSB noise-temperature (T_R(DSB)).

The relation between SSB and DSB receiver noise-temperature
$T_R(SSB) = T_R(DSB)x(1+(L_{RF}/L_{IM}))$
$T_R(DSB)$ is measured by the Y-factor ("Hot" and "Cold" loads) method
$T_R(DSB) = (T(RF_{Hot})-YxT(RF_{Cold}))/(Y-1)$

SINGLE-SIDE-BAND MIXER MEASURED PERFORMANCE

The MLS 191.95 GHz RFE is designed to exhibit $T_R(DSB)\approx1000$ K over an IF of 8-15 GHz, yielding $T_R(SSB)\leq3000$ K (side-bands imbalance (≤2) is accommodated) over the 177-207 GHz RF band. Figure 1 summarizes MLS receiver DSB and SSB measurements at nominal operation conditions of base temperature 22.5°C, and an optimum 91.95 GHz LO power drive (+5 dBm). Figure 1 shows measured $T_R(SSB)$ data in comparison with measured $T_R(DSB)$ data. The measured DSB data is converted in the figure to a SSB receiver yielding "ideal" side-band balanced $\langle T_R(SSB)\rangle = 2xT_R(DSB)$. Hence, the difference between $T_R(SSB)$ and $\langle T_R(SSB)\rangle$ in the figure illustrates L_{RF}/L_{IM} deviation from perfect balance.

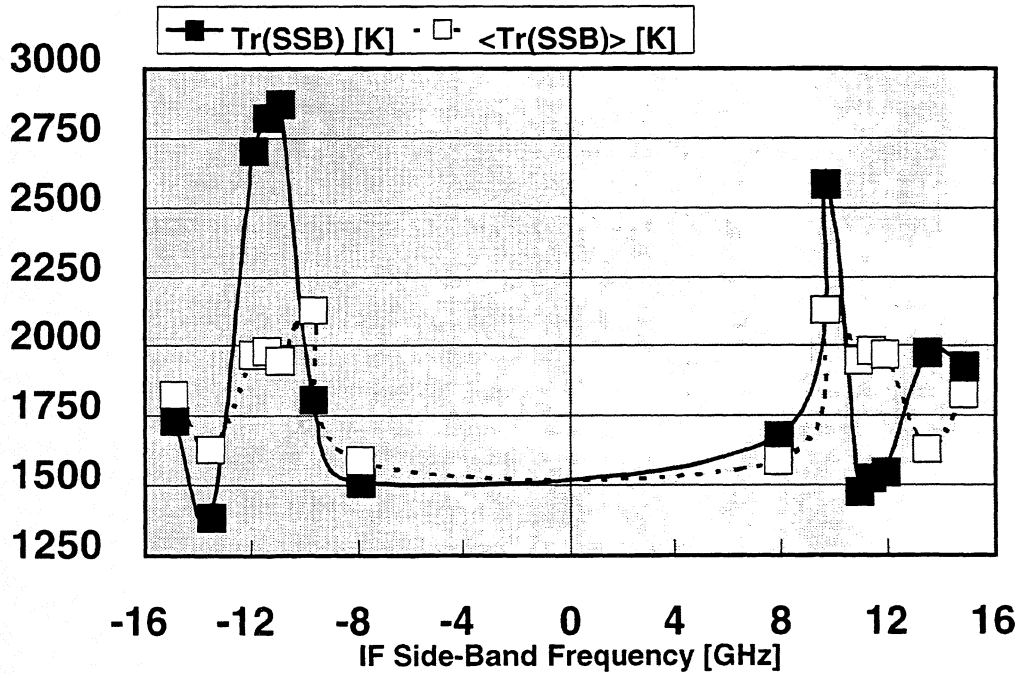

Figure 1. Measured $T_R(SSB)$ Data Compared to Measured $T_R(DSB)$.
($\langle T_R(SSB)\rangle$ is for an "Ideal" Mixer with Balanced Side bands).

Table 2 depicts the percent variation in side-band balance, relative to the nominal operation conditions, for changes in the receiver's ambient temperature (22.5°C±17.5°C) and variation in LO power drive (+5dBm±1.5dBm).

	SIDE-BAND-RATIO % CHANGE (Relative to:LO=+5dBm; $T_{AMBIENT}$=22.5°C)		
IF [GHz]	**7.9**	**11.4**	**14.9**
LO=+5dBm $T_{AMBIENT}$=40°C	**+6%**	**-8%**	**0%**
LO=+6.5dBm $T_{AMBIENT}$=22.5°C	**+17%**	**-11%**	**-11%**
LO=+5dBm $T_{AMBIENT}$=22.5°C	**Side-Band-Ratio 0.90**	**Side-Band-Ratio 1.85**	**Side-Band-Ratio 0.90**
LO=+3.5dBm $T_{AMBIENT}$=22.5°C	**0%**	**+3%**	**0%**
LO=+5dBm $T_{AMBIENT}$=4°C	**-11%**	**0%**	**0%**

Table 2. The Percentage Variation in Side-Band Balance for Different Ambient Temperatures and LO Power Drives, Within The MLS IF Band.

REFERENCES

[1] C. H. Page, "Frequency Conversion With Positive Nonlinear Resistors", Journal Research National Bureau Standards, Volume 56, April 1956.

[2] I. Galin, "A Mixer Up To 300 GHz With Whiskerless Schottky Diodes For Spaceborne Radiometers", The 7th International Symposium on Space Terahertz Technology, Charlottesville VA, 1996.

[3] P. H. Ostdiek, et al, "Integration Of An Anti-Parallel Pair Of Schottky Barrier Diodes In MMW Mixers", The 15th International Conference on IR and MM-Waves, December 1990.

[4] R. J. Dengler, A. Hanpachern, P. H. Siegel, "A Fully Automated High Accuracy RF/IF Test System for Millimeter- and Submillimeter-Wave Mixers", 1998 IEEE MTT-S International Microwave Symposium Digest, pp. 1719-1722.

PROGRESS IN SUBMILLIMETER WAVELENGTH INTEGRATED MIXER TECHNOLOGY

Steven M. Marazita, Kai Hui, Jeffrey L. Hesler,
William L. Bishop, and Thomas W. Crowe

Applied Electrophysics Laboratories
Department of Electrical Engineering
University of Virginia
Charlottesville, VA 22903

Abstract

Higher levels of device and circuit integration lead to vast improvements in millimeter and submillimeter wave Schottky mixer performance. Monolithic technologies exhibit wider operating bandwidth, reduced noise temperature, and lower LO power consumption than flip-chip methods. In addition integrated technologies offer a simplified design process, easier assembly, and drastically improved repeatability. These characteristics make planar integrated Schottky mixers the most promising technology for radiometers when cryogenic cooling is not acceptable.

This discussion focuses on the development of 585 GHz and 1 THz integrated mixers. The devices are fabricated using the MASTER wafer bonding technique on a hybrid GaAs/quartz substrate. At 585 GHz the integrated mixer's DSB performance has been measured to be T_{sys}=1608 K, T_{mix}=1184 K, L_{mix}=6.5 dB at P_{LO}=1.6 mW. If the LO power is reduced to P_{LO}=300 μW, DSB T_{sys} is only 1890 K. This is the best room temperature mixer ever reported above 500 GHz for either planar or whisker-contacted technologies.

I. Introduction

Detection of submillimeter-wave radiation is of great interest to scientists studying interstellar chemistry, star formation, and galactic structure. Research has also been driven by the need to observe radiation emitted from a number of molecules in the Earth's atmosphere such as O_3, ClO, and OH at 206 GHz, 640 GHz, and 2.5 THz, respectively. The military is also interested in analyzing submillimeter wavelength radiation. For example, compact range radar uses heterodyne detectors to measure the radar signatures of objects in a laboratory environment.

These applications require mixers with sufficient spectral sensitivity, bandwidth, and minimal LO power consumption. Although SIS junctions and hot electron bolometers now offer the best sensitivity in the THz frequency range, for many applications

cryogenic cooling is not acceptable. Also, this level of sensitivity is often not required. In these instances, GaAs Schottky diodes are the preferred mixer technology. State-of-the-art receivers in the THz regime have used quarter-micron diameter whisker-contacted Schottky diodes [1]. These mixers have achieved record sensitivity [2][3], but they are difficult to space qualify due to the fragility of the whisker contact.

Several groups have developed planar Schottky diode technologies with an integrated finger replacing the whisker [4][5][6]. The UVA surface channel diode is depicted in Figure 1. This device is more easily space-qualified due to the integrated contact between finger and anode. Several research groups have successfully used discrete planar diodes in millimeter and submillimeter wave applications in both waveguide and quasi-optical implementations [7][8][9].

Jeffrey Hesler's work at UVA on a 585 GHz fundamental, fixed-tuned waveguide mixer deserves a special note. This mixer was completely designed using Hewlett Packard's HFSS and MDS and demonstrated one of the best-reported receiver and mixer noise temperatures at 585 and 690 GHz [10]. Hesler used a traditional flip-chip soldering technique to mount a discrete planar mixer diode onto his quartz circuit. Although this scheme was successful around 585 GHz, the mixer was challenging to assemble and would be difficult to scale to the THz regime.

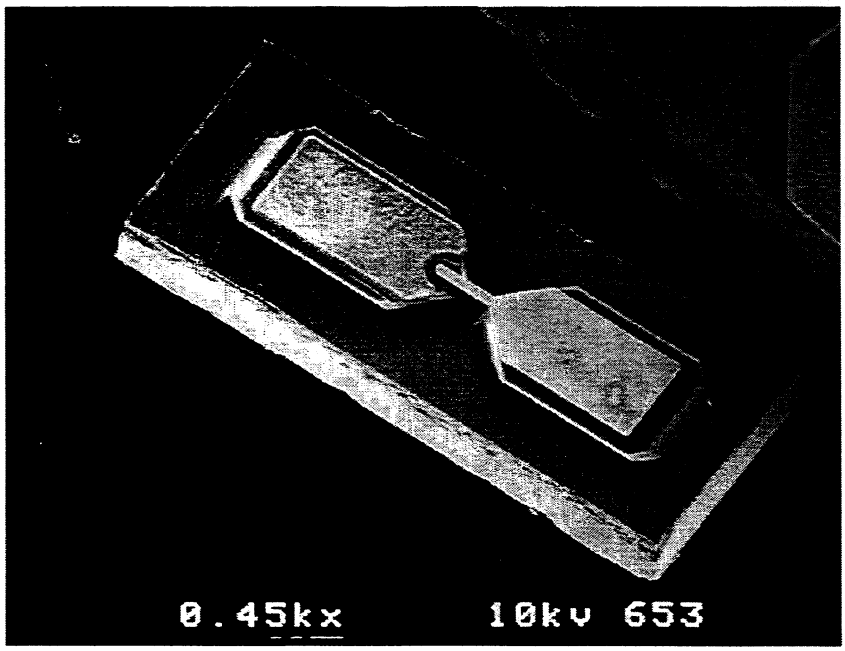

Fig. 1: UVA surface channel planar diode

II. Integrated Planar Mixers on Quartz

As operating frequencies are pushed higher, there are several issues which limit discrete planar mixer performance. The bulky, high dielectric GaAs substrate increases pad to pad capacitance, dielectrically loads the waveguide, adds extra losses to the mixer circuitry, and makes fitting discrete diodes into higher frequency blocks difficult or impossible. In addition, the imprecise alignment of the diode to the surrounding circuitry and the non-repeatable nature of the flip-chip mounting process negatively impacts RF performance, test repeatability, and computer simulation predictability.

One method of eliminating these problems is to integrate the GaAs diode with a low dielectric substrate. Removing the GaAs substrate and replacing it with quartz, for example, significantly reduces the pad to pad capacitance by leaving only a small, thin GaAs active area around the device anodes. UVA successfully has fabricated discrete planar diodes on quartz [11] and RF results at 215 GHz indicate improved performance over GaAs substrate devices [12]. Figure 2 shows a mixer diode with a quartz substrate [11]. Further integration is possible by incorporating the mixer circuitry. This achieves perfect alignment between the diode and filters without soldering or handling a discrete diode chip. The potential benefits of this configuration include better noise performance, wider bandwidth, better LO coupling, higher maximum operating frequency, better modeling predictability, and easier, more repeatable mixer assembly [13].

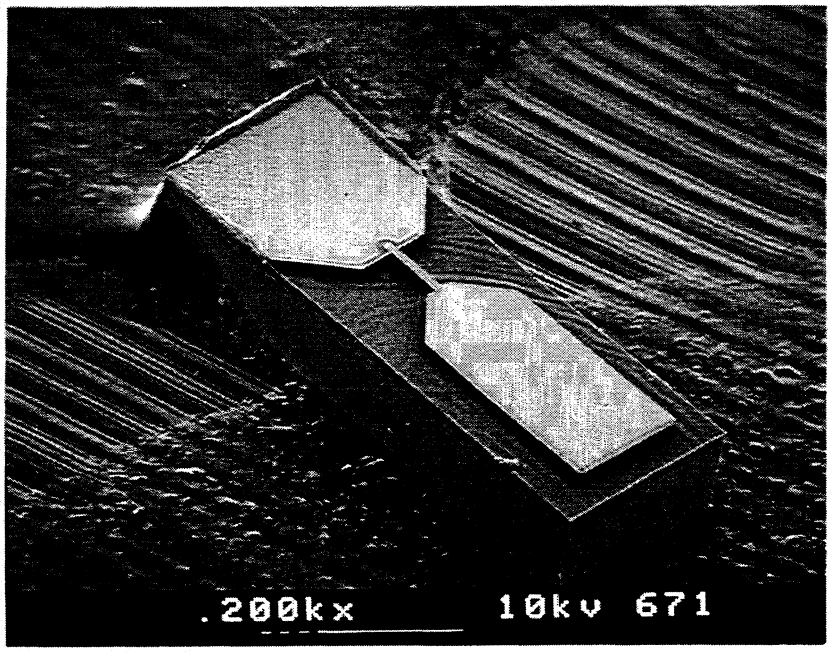

Fig. 2: Planar mixer diode with quartz substrate

In 1993 NASA's Jet Propulsion Laboratory (JPL) developed an integrated mixer on quartz using a heat-cured epoxy to hold the mixer diode and filters down to the substrate [14]. This device structure, named QUID, was an excellent first step. At first the epoxy that filled in the surface channel was causing problems with coupling radiation into the diode. An epoxy etch technique developed at UVA helped improve the mixer performance by 20-30% [15][16]. QUID devices exhibit good subharmonic performance at 640 GHz with DSB T_{mix}=2500 K and L_{mix}≈9 dB [17]. The DSB T_{mix} remains less than 3500 K over a 1.5 to 14 GHz IF band. However, the presence of the epoxy is worrisome. Even after etching it from the surface channel area, this lossy material still sits beneath the diode pads and filters. This impacts RF performance and also has reliability issues in terms of out-gassing and long-term robustness.

III. MASTER Integrated Mixer Technology

To avoid the concerns associated with epoxy bonding, an integrated mixer technology has been developed at UVA. The Method of Adhesion by Spin-on-dielectric Temperature Enhanced Reflow (MASTER) uses a patent pending semiconductor to substrate bonding process to attach the thin GaAs active areas of the mixer diode to a quartz substrate in a rightside-up orientation [13][18]. In addition, the filter circuitry is fabricated in perfect alignment with the diode using a raised diode mesa structure. Using this technique, 585 GHz and 1 THz integrated, fundamental mixers have been fabricated.

The fabrication process begins by forming the anode and ohmic contacts on a full thickness GaAs wafer covered with an SiO_2 passivation layer. The wafer is mounted face-down to a carrier, and wet etchants are used to remove the bulk GaAs substrate and AlGaAs etch stop layer. The remaining 4-5 μm of GaAs are the active layers of the mixer diode and are bonded rightside-up to a quartz wafer using the MASTER technique. A mesa etch then removes the GaAs from outside the device areas, and the spin-on-dielectric (SOD) bonding material is plasma etched in those regions to reveal the surface of the quartz substrate. A layer of Ti/Au is e-beam deposited over the entire wafer to form the Schottky anode contact. This seed layer is also used to electroplate the diode finger contacts and microstrip filter circuitry. After plating the seed layer is removed with a RIE process. Figure 3 shows an array of MASTER devices after this step. Note the microstrip filters are formed directly on quartz outside of the device mesa. The surface channel etch step is performed next to form a low parasitic air bridge underneath the finger contact. The SOD is then plasma etched to remove it from the surface channel area. In the final devices, the SOD only remains underneath the small device pads. Figures 4 and 5 show MASTER devices after the surface channel air bridge is formed. The device wafer is then mounted face down to a carrier and the quartz substrate is thinned to the proper thickness. For the 585 GHz and 1 THz mixers fabricated for this work, the quartz substrate thicknesses were 37.6±0.9 μm and 25.0±0.7μm, respectively. Dicing is performed to separate the wafer into individual circuits. The overall dimensions

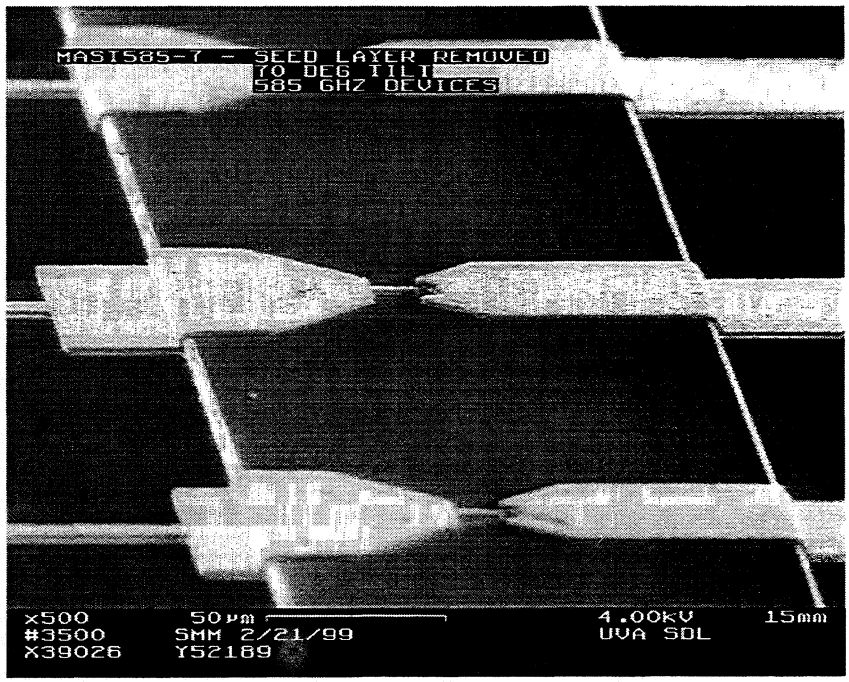

Fig. 3: MASTER devices after seed layer removal step

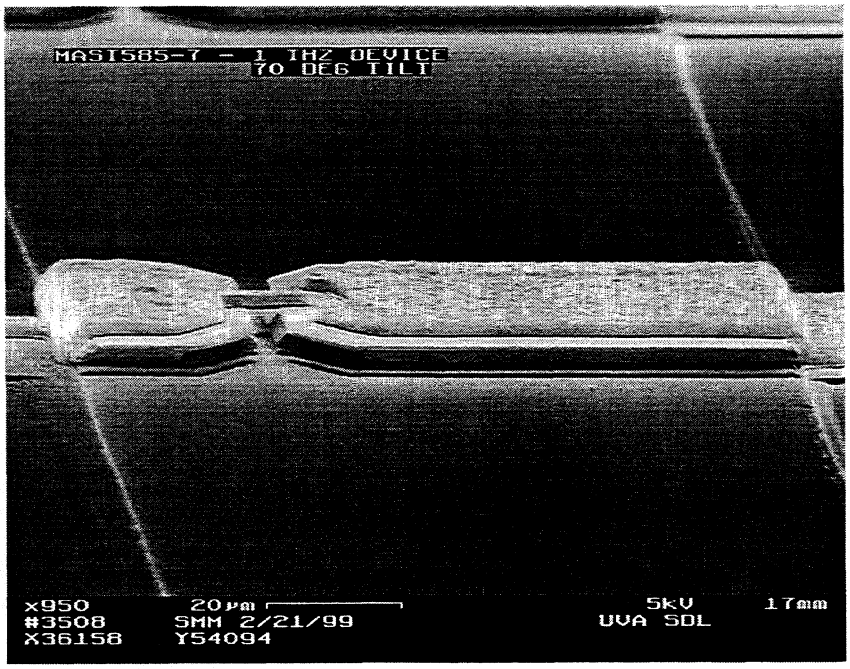

Fig. 4: MASTER device after surface channel etch

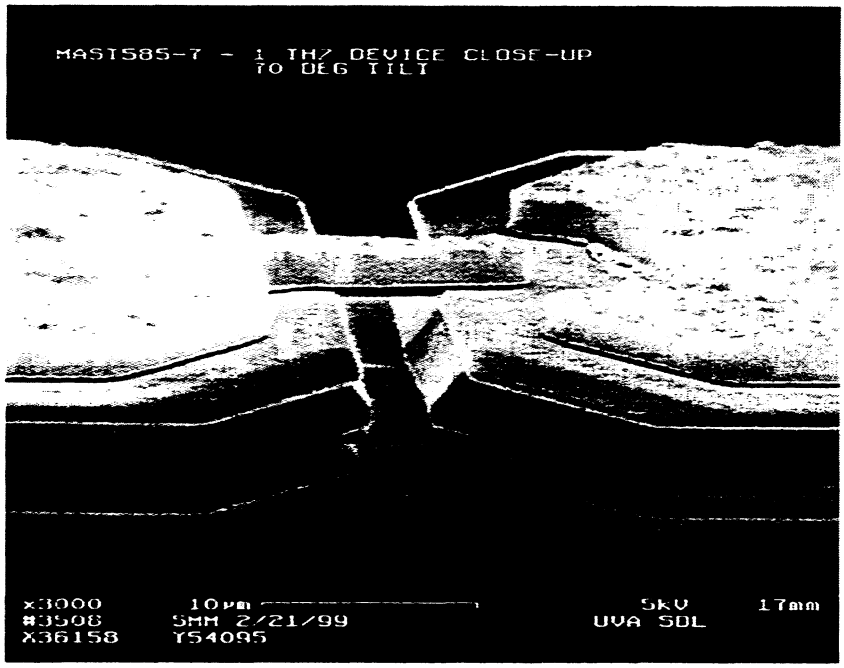

Fig. 5: Close-up of MASTER device after surface channel etch

for 585 GHz and 1 THz mixers were 1850 x 92 µm and 1065 x 59 µm. At this point, the diode's I-V characteristics are measured. Table 1 summarizes typical DC I-V and capacitance parameters for these devices. The uniformity from chip to chip was excellent.

IV. RF Design and Test Results for MASTER Mixers

The designs for the 585 GHz and 1 THz integrated mixers were based upon Hesler's previous 585 and 690 GHz fundamental fixed-tuned waveguide mixers [19]. The computer modeling was done in Sonnet and Hewlett Packard's HFSS and MDS. Figures 6 and 7 show the 585 GHz and 1 THz designs that were fabricated in each wafer batch.

RF testing of the 585 GHz MASTER mixers was performed in UVA's FIR lab. The waveguide block, mounting techniques, and RF test setup are explained in Hesler's dissertation [19]. However, with integrated devices the mounting now only requires placing the mixer in the block, butting the LO waveguide probe up against the input waveguide, and attaching two bond wires. Figure 8 shows a MASTER mixer mounted in a metal 585 GHz waveguide block. The LO source was a CO_2 pumped FIR laser. Only preliminary RF data has been taken thus far. The best performance at 585 GHz is DSB T_{sys}=1608 K, T_{rx}=1184 K, L_{rx}=6.5 dB consuming P_{LO}=1.6 mW. T_{sys} increases only 18% when the LO power is reduced to 0.3 mW. Table 2 summarizes these results and includes

Diode Parameter		**Measured Value**	
N_d		$4x10^{17}$ cm^{-3} n-type	
d_{anode}		0.9 μm nominal	
R_s		10-12 Ω	
V_{knee} (I=1μA)		490-510 mV	
ΔV (I=10-100 μA)	η	77-78 mV	1.31-1.33
C_{j0} @ f=1 MHz		1.5 fF (calculated)	
C_{total} @ f=1 MHz		5-7 fF	

Table 1: I-V parameters for 585 GHz and 1 THz MASTER mixers

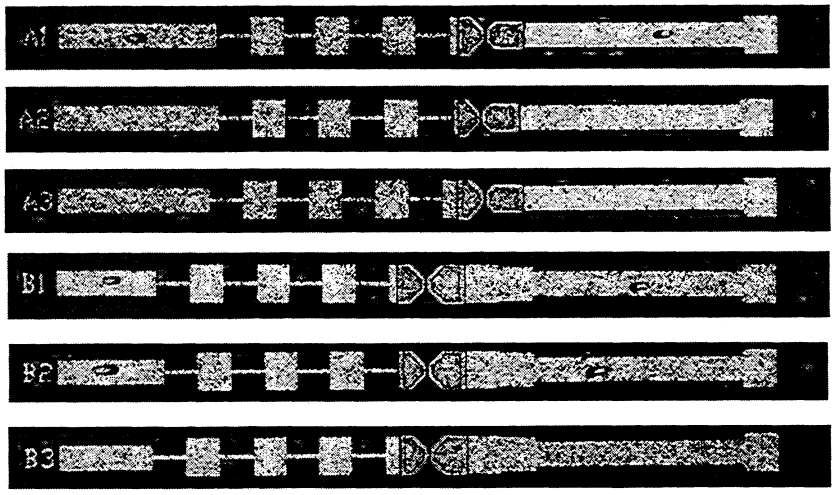

Fig. 6: 585 GHz MASTER mixer circuit variations

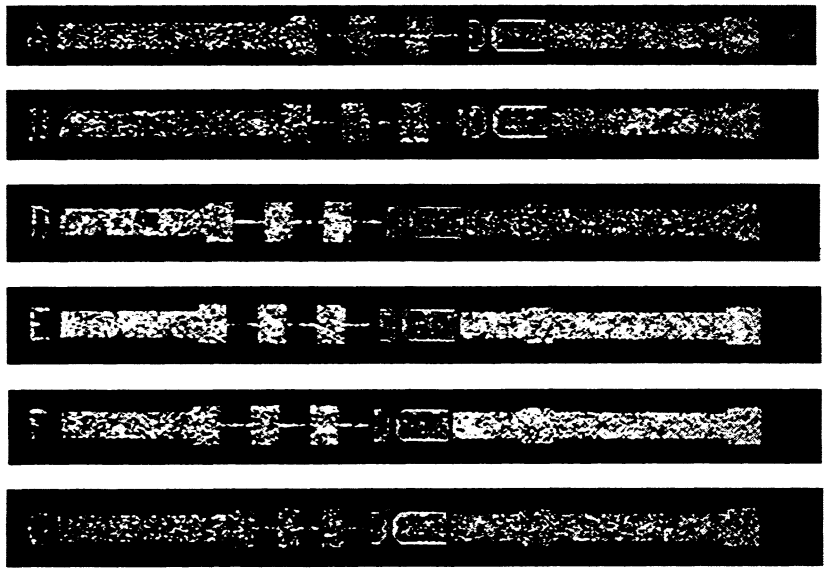

Fig. 7: 1 THz MASTER mixer circuit variations

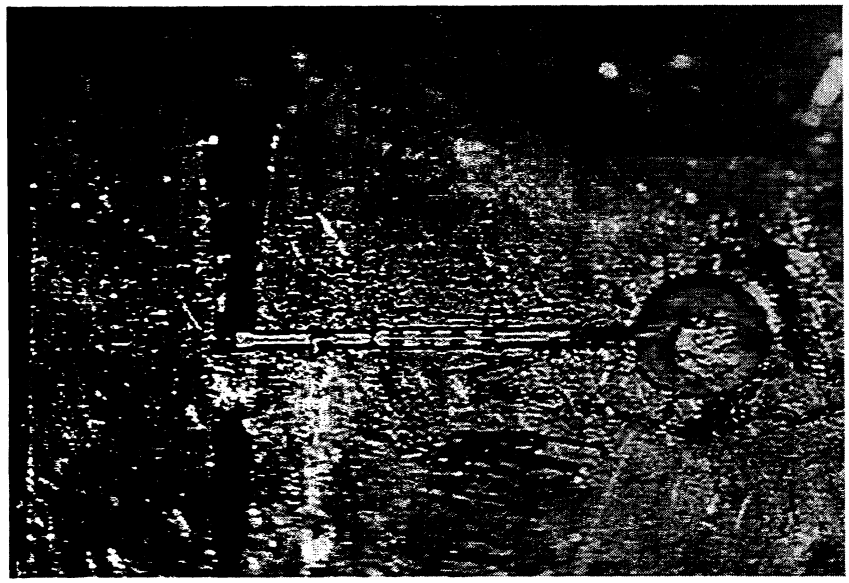

Fig. 8: 585 GHz MASTER mixer mounted in block RAL

Freq. (GHz)	Device Technology Description	T_{sys} (K)	T_{mix} (K)	L_{mix} (dB)	P_{LO} (mW)	Refer.
557	Whisker-contacted, waveguide, mech. tuners, metal block	1600	1200	8.0	not known	[21]
585	**MASTER A1 integ. planar, fixed-tuned, RAL block**	**1608**	**1184**	**6.5**	**1.60**	**this work**
585	**MASTER A1 integ. planar, fixed-tuned, RAL block**	**1890**	**—**	**—**	**0.30**	**this work**
585	SC1T5-S10 discrete planar, fixed-tuned, RAL block	2380	1800	7.6	1.16	[10]
640	QUID integ. fund. planar, mech. tuners, Metal block	2720	1636	7.93	0.35	[20]
640	QUID integ. subharm. planar, mech. tuners, Metal Block	—	2500	9.0	3.5-3.8	[17]
640	MASTER integ. subharm. planar, mech. tuners Metal Block	—	2396	10.98	4.7	[13]
690	SC1T5-S5 discrete planar, fixed-tuned, RAL Block	2970	2240	8.8	1.04	[10]

Table 2: Summary of Schottky Mixer Performance in the 500-700 GHz range

current state-of-the-art RF measurements from the literature as a comparison [20][21]. All data quoted is room temperature. From this table it is deduced that this research has produced the best room temperature mixer results above 500 GHz. This is the first time a planar Schottky mixer has achieved better performance than the best whisker-contacted mixers [21] in this frequency range.

Currently, the 1 THz MASTER mixers have been designed, fabricated, and fully characterized at DC. They are awaiting a waveguide block before RF testing is begun. The small dimensions of the waveguides at terahertz frequencies are a major difficulty for fabricating high quality blocks.

V. Summary

Waveguide mixers based on planar Schottky diodes have promised to match the performance of whisker-contacted mixers while producing more repeatable and predictable behavior. However, the increased parasitics associated with the planar structure and the imprecision of mounting discrete diodes into surrounding mixer circuitry have kept the planar mixer from achieving this goal. The QUID technology developed at JPL was a good first step. The integration of the diode and filter circuitry improved planar mixer performance, but the presence of the epoxy adhesive limited its ability to supercede whisker-contacted devices. The MASTER device technology has overcome these shortcomings through the conception and full development of a novel integrated Schottky mixer. By forming the mixer diode rightside up and the microstrip filters directly on the quartz substrate, parasitic capacitance and dielectric losses have been minimized. These mixers have demonstrated the lowest room temperature noise temperature above 500 GHz, outdoing even the best whisker-contacted mixers. They also maintain good performance at significantly reduced LO power levels. This has been accomplished without any mechanical tuning in an easy to assemble package which requires no soldering or diode alignment. The mixers are easy to design and model, and their performance is predictable from device to device.

This work has extended the usability of monolithic device technologies far into the submillimeter wavelength regime. MASTER integrated devices have set new levels of achievement for Schottky mixers in terms of noise performance, LO power consumption, and conversion efficiency in a robust, space-qualifiable structure. This technology is readily extended to other devices such as varactors and amplifiers. With the use of a low parasitic hybrid device technology such as MASTER, the possibility of submillimeter wavelength MMIC chips integrating not only passive but active devices has become a reality.

VI. Acknowledgments

This work was supported by NASA and JPL contracts NASA-NGT-51396 and JPL-960017, the Army Research Laboratory under ARL/UMD-Z847301, and the U.S. Army NGIC contract number DAHC90-96-C-0010.

VII. References

[1] W.C.B. Peatman, P.A.D. Wood, D. Porterfield, T.W. Crowe and M.J. Rooks, "A Quarter-Micron GaAs Schottky Barrier Diode with High Video Responsivity at 118 μm," Appl. Phys. Lett. 61 (3), pp. 294-296, 20 July 1992.

[2] H.-W. Hübers, W.C.B. Peatman, T.W. Crowe, G. Lundershausen and H.P. Röser, "Noise Temperature and Conversion Losses of Submicron GaAs Schottky-Barrier Diodes," Presented at the Fourth Intl. Symp. Space THz Tech., Los Angeles, CA, March 1993.

[3] W.L. Bishop, S.M. Marazita, P.A.D. Wood, and T.W. Crowe, "A Novel Structure and Fabrication Process for Sub-Quarter-Micron THz Diodes", Proceedings of the 7th International Symposium on Space Terahertz Technology, Charlottesville, VA, March 1996, p. 511-524.

[4] W.L. Bishop, R.J. Mattauch, T.W. Crowe and L. Poli, "A Planar Schottky Diode for Submillimeter Wavelengths," 15th Int. Conf. on Infrared and Millimeter Waves, Orlando, FL, Dec. 1990.

[5] I. Medhi, P. Siegel, M. Mazed, "Fabrication and Characterization of Planar Integrated Schottky Devices for Very High Frequency Mixers", in Proceedings of the IEEE Cornell Conf. on Advanced Concepts in High Speed Semiconductor Devices and Circuits, August 2-4, 1993.

[6] A. Simon, A. Grub, V. Krozer, K. Beilenhoff, H.L. Hartnagel, "Planar THz quasi-vertical diode structure," Proc. of 4th Intl. Symp. on Space THz Tech., March 30-Apr. 1, 1993, pp.392-403.

[7] I. Galin, "A Mixer up to 300 GHz with Whiskerless Schottky Diodes for Spaceborne Radiometers," 7th Intl. Symp. Space THz Tech., Charlottesville, VA, pp. 474-476, March 1996.

[8] S.S. Gearhart and G.M. Rebeiz, "A Monolithic 250 GHz Schottky Diode Receiver," IEEE Trans. Microwave Theory and Tech., Vol. 42, No. 12, pp.2504-2511, Dec. 1994.

[9] N.R. Erickson, "Wideband High Efficiency Planar Diode Doublers", Proc. Ninth Intl. Symp. Space THz Techn., pp. 473-480, Pasadena, CA, March 1998.

[10] J.L. Hesler, W.R. Hall, T.W. Crowe, R.M. Weikle II, B.S. Deaver Jr., R.F. Bradley, S.K. Pan, "Fixed-Tuned Submillimeter Wavelength Waveguide Mixers Using Planar Schottky-Barrier Diodes," IEEE Trans. on Microwave Theory and Tech., Vol. 45, No. 5, May 1997.

[11] W.L. Bishop, E.R. Meiburg, R.J. Mattauch, and T.W. Crowe, "A Micron Thickness, Planar Schottky Barrier Diode Chip for Terahertz Applications with Theoretical Minimum Parasitic Capacitance", 1990 IEEE MTT-S Int. Microwave Symp., Dallas, TX, pp. 1305-1308, May 1990.

[12] P.H. Siegel, R.J. Dengler, I. Medhi, J.E. Oswald, W.L. Bishop, T.W. Crowe, R.J. Mattauch, "Measurements on a 215 GHz Subharmonically Pumped Waveguide Mixer Using Planar Back-to-Back Air-Bridge Schottky Diodes," IEEE Trans. Microwave Theory and Tech., Vol. 41, No. 11, pp. 1913-1921, Nov. 1993.

[13] S.M. Marazita, J.L. Hesler, R. Feinäugle, W.L. Bishop, and T.W. Crowe, "Planar Schottky Mixer Development to 1 THz and Beyond", Proceedings of the 9th International Symposium on Space Terahertz Technology, Pasadena, CA, March 1998.

[14] I. Medhi, P. Siegel, M. Mazed, "Fabrication and Characterization of Planar Integrated Schottky Devices for Very High Frequency Mixers", in Proceedings of the IEEE/Cornell Conference on Advanced Concepts in High Speed Semiconductor Devices and Circuits, August 2-4, 1993.

[15] S.M. Marazita, W.L. Bishop, T.M. Cunningham, P.J. Koh, T.W. Crowe, and R.M. Weikle II, "Planar GaAs Schottky Barrier Diodes", presented at 8th Intl. Symp. on Space THz Tech., Boston, March, 1997.

[16] I. Medhi, S. Marazita, D. Humphrey, T. Lee, R. Dengler, J. Oswald, A. Pease, S. Martin, W. Bishop, T. Crowe, and P.H. Siegel, "Improved 240 GHz Subharmonically Pumped Planar Schottky Diode Mixers for Space-Borne Applications", November, 1997, to be submitted to IEEE Transactions on MTT,

[17] I. Medhi, P.H. Siegel, D.A. Humphrey, T.H. Lee, R.J. Dengler, J.E. Oswald, A. Pease, R. Lin, H. Eisele, R. Zimmerman, and N. Erickson, "An All Solid-State 640 GHz Subharmonic Mixer", submitted to International Microwave Symposium, Baltimore, June, 1998.

[18] S.M. Marazita, W.L. Bishop, T.W. Crowe, "An Improved Method of Integrating Semiconductor Device Structures with Alternative Substrates using Spin-on-Dielectric Bonding", Patent Disclosure submitted to University of Virginia Patent Foundation, Patent Pending.

[19] J.L. Hesler, "Planar Schottky Diodes in Submillimeter-Wavelength Waveguide Receivers", Dissertation, University of Virginia, January 1996.

[20] P.H. Siegel, I. Medhi, R.J. Dengler, T.H. Lee, D.A. Humphrey, A. Pease, "A 640 GHz Planar-Diode Fundamental Mixer/Receiver", IEEE MTT-S International Microwave Symposium Digest, Vol. 2, Baltimore, June 7-12, 1998, p. 407-410.

[21] R. Zimmerman, Ra. Zimmerman, P. Zimmerman, "All Solid-State Radiometer at 557 GHz", 21st European Microwave Conference, Stuttgart, 1991.

ANTI-PARALLEL PLANAR SCHOTTKY DIODES FOR SUBHARMONICALLY-PUMPED 220 GHZ MIXER.

C.-I. Lin[1], M. Rodríguez-Gironés[1], A. Simon[1], J. Zhang[2], P.V. Piironen[2], V.S. Möttönen[2], J.T. Louhi[2], H.L. Hartnagel[1], A.V. Räisänen[2]

[1]Institut für Hochfrequenztechnik, TU Darmstadt, Merckstrasse 25, D-64283 Darmstadt. Germany
Fax:+49-6151-164367, e-mail: hfmwe009@hrz2.hrz.tu-darmstadt.de
[2]Helsinki University of Technology, PL 3000, FIN-02015 HUT, Finland

Abstract

Anti-parallel planar Schottky diodes using the Quasi-Vertical Schottky Diode (QVD) geometry, developed by TU Darmstadt, have been fabricated and mounted on subharmonically-pumped waveguide mixers at 220 GHz. The design of the waveguide mixers was done at Helsinki University of Technology. The diode's geometry, an evolution of the substrateless Schottky diode [1] for integration in planar circuits [2], assures intrinsically-vertical current flow and minimizes the volume of the semiconductor diode mesa. This improves heat sink capability and simultaneously reduces diode parasitics, in particular high-frequency series-resistance increase due to skin effect. Furthermore, gold pillars grown on the contact pads confer the diode higher physical strength and protect anode air-bridge contacts, both facilitating soldering to the microstrip filters and allowing a safe flip-chip mounting technique. The QVD shows DC parameters comparable to those of whisker-contacted substrateless diodes. Measured forward I-V characteristics are identical, which contributes to minimize mixer conversion loss. The technology and the electrical characteristics of the Anti-Parallel Quasi-Vertical Schottky Diodes (APQVSD) are presented, as well as the first measurement results obtained with the 220 GHz subharmonic mixer.

Introduction

GaAs-Schottky diodes are used as the non-linear mixer element (varistor) in heterodyne receivers for THz applications because of their high cut-off frequency and low parasitics as compared with other semiconductor devices.

The Quasi-Vertical planar Schottky Diode (QVD), developed by TU Darmstadt, is based on the substrateless, whisker-contacted, Schottky-diode concept. It inherits its extremely reduced diode chip and the correspondingly increased heat-sink capabilities and combines them with the advantages of planar designs, which offer a reliable anode contact and open the door for full integration in MMIC's.

Recently, the Anti-Parallel Quasi-Vertical Schottky Diodes (APQVD) have been developed, fabricated and mounted on 220 GHz subharmonically-pumped waveguide mixers. Figure 1 shows the sketch of the mixer block having two tuners.

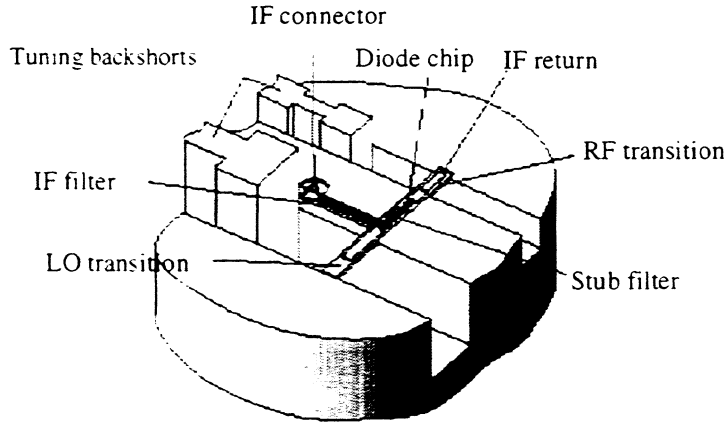

Figure 1: Sketch of the 220 GHz mixer block.

Like the whisker-contacted substrateless diode and the QVD, the APQVD present vertical current flow and low parasitics. The scheme developed to model their predecessors can be applied to them without further modifications [3].

Diode Design and Modeling

The APQVD have a structure similar to that of the single QVD. The complete geometry is presented in Figure 2, which shows some of its advantages with respect to other planar-diode concepts.

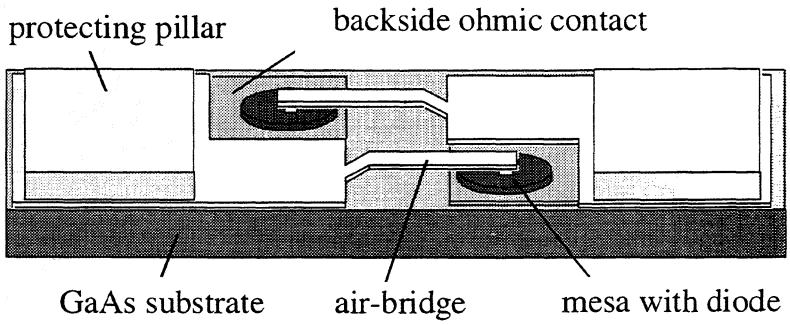

Figure 2: Geometrical structure of an APQVD chip.

The diode mesas, about 2-μm thick, lye directly on top of a gold platform. This improves the diodes' heat-sink capabilities, which in other planar structures is limited to the anode finger and in normal whisker-contacted diodes to the anode whisker. Additionally, dramatically-reduced mesa size eliminates the influence of skin effect on high-frequency series resistance.

Compared with whisker-contacted devices, a general drawback of planar diodes is the pad-to-pad stray capacitance. The need to keep air-bridges short in order to reduce their parasitic inductance sets a limitation to the minimum pad-to-pad capacitance achievable. The APQVD show two major improvements in this respect.

Firstly, a reduced substrate thickness of 10 μm is achieved by means of a novel etch-separation technique in which the diodes are photo-lithographically protected on their front side and the rest of the wafer is etched away. Reduced substrate thickness reduces in turn pad-to-pad stray capacitance. Secondly, high air-bridges have been successfully fabricated. Bridge height above the mesa is about 2 μm, whereas the backside ohmic contact lies 4 μm below the bridges. This reduces their parasitic capacitance to negligible values, which allows bridge widening without significant capacitance increase. This in turn reduces the inductive effect of the air-bridge, and in this way the necessary compromise between bridge inductance and pad-to-pad stray capacitance can be shifted to more convenient values of both.

A further geometrical improvement of the APQVD is the fabrication of gold pillars about 6 μm in height in order to facilitate flip-chip techniques. The pillars, grown on the contact pads, confer the diodes greater physical strength and protect the air-bridge anode contact during device handling. This facilitates soldering to the microstrip filters and allows a safer flip-chip mounting techniques.

According to previous experiences, a doping level of 3 x 10^{17} cm^{-3} and a thickness of 100 nm is chosen for the active n-layer, while anode diameter is set to be 0.8 μm. The thickness of the n^+-layer is 2 μm, which approximately equals the skin depth of n^+-doped GaAs at 220 GHz, eliminating the high-frequency increase of series resistance due to skin effect.

At millimeter wave lengths, diode dimensions become comparable to the wavelength and, thus, the distributed effects of the passive structure are remarkable. Also, parasitics are introduced due to the associated mounting structure and a microstrip channel surrounding the diode in the mixer block. Therefore, an accurate modeling of the APQVD is crucial for a reliable design of the mixer circuitry.

The diode model has been constructed from the active and passive diode parts. The active part includes the nonlinear junction resistance, nonlinear junction capacitance, series resistance and a series inductance. The passive part including the parasitics due to the diode structure, microstrip channel, and a quartz microstrip

substrate has been modeled with help of an electromagnetic high frequency simulator (HFSS) based on the finite element method (FEM) [4]. After the construction of a diode equivalent circuit, the results of the FEM simulations have been fitted into the equivalent circuit. The equivalent circuit of the diode chip is shown in Figure 4. The theoretical modeling work is to be further supported by vector network analyzer (VNA) measurements using CPW on-wafer test structures of single and anti-parallel diodes. The VNA measurements with coplanar probes will take place at the frequency range from 50 MHz possibly up to 110 GHz.

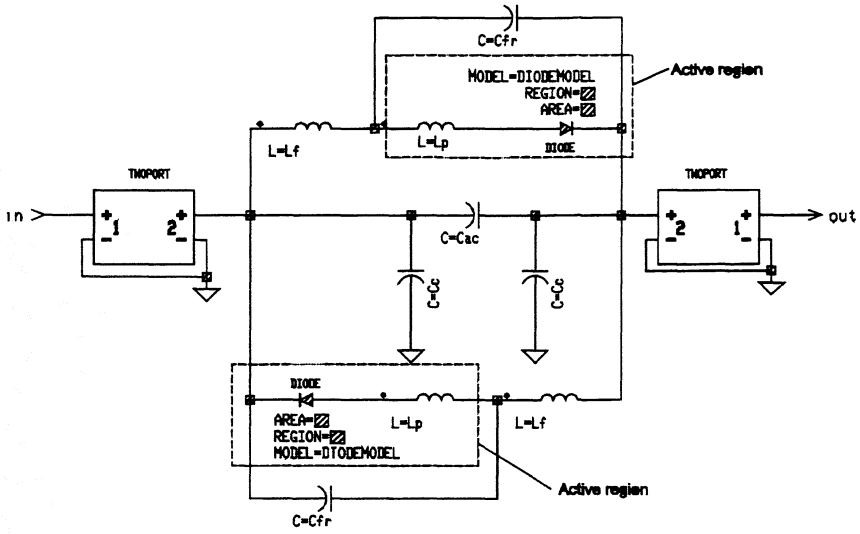

Figure 4: Equivalent circuit of diode chip. Twoports are for soldering pads.

Diode Fabrication and Characterization.

The fabrication process is based on the technologies of single QVD which were developed in the last years. Figure 5 shows a SEM picture of an APQVD chip, where the 4-μm height of the air-bridges as well as the protection gold pillars can be appreciated.

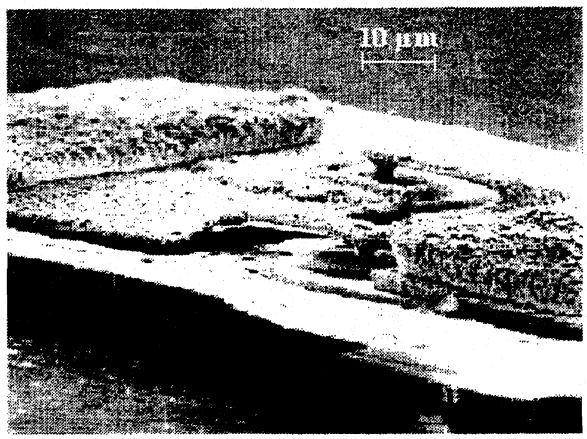

Figure 5: Side view of an APQVD chip (SEM micrograph).

Figure 6 shows an APQVD chip soldered on a quartz-substrate microstrip circuit using a flip-chip technology. The effective protection of the lateral gold pillars can be seen.

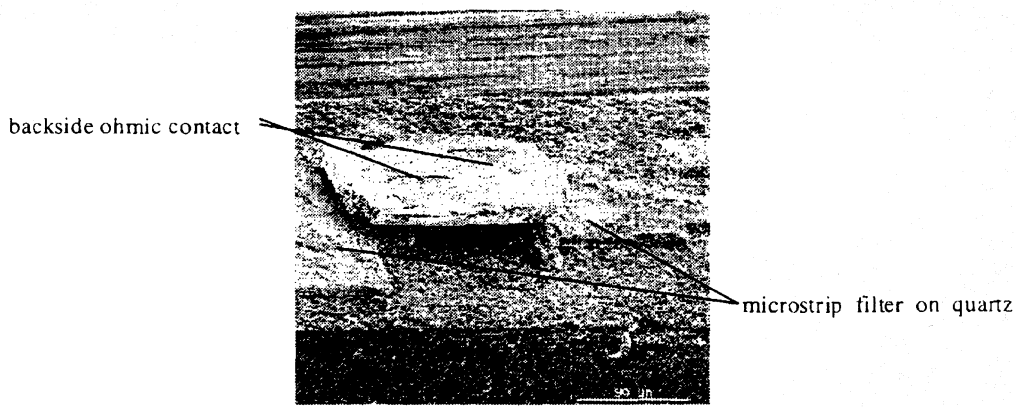

Figure 6: Anti-parallel quasi-vertical Schottky diode after soldering onto a microstrip filter on quartz substrate (SEM micrograph)

Figure ?? shows measured I/V curves of two APQVD. The diodes show an inverse saturation current of 6 x 10^{-16} A, a series resistance of 25 Ω, an ideality factor of 1.14 and a total capacitance (junction capacitance at zero bias plus parasitic capacitance) of 21 fF. The simultaneous and identical processing of both diodes in an

integrated pair achieves practically identical I/V characteristics for all current values above 10 nA. This contributes to reduce mixer conversion loss. Noise temperature measurements at 1.4 GHz have been performed on the diode pairs for different bias currents. At a typical bias of 500 μA, a noise temperature of 350 K is achieved which is comparable to values obtained with whisker-contacted diodes.

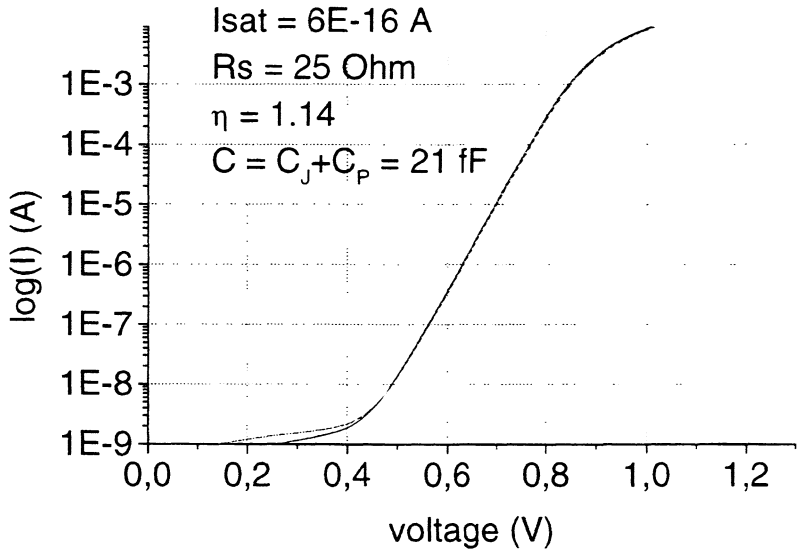

Figure ??: I/V characteristics of two APQVD

Performance of 220 GHz Subharmonic Mixers

The anti-parallel pair of Schottky diodes has been employed in two 220 GHz subharmonic mixers. These mixers are used as scaled models for a 650 GHz mixer. One of the mixers is based on a two-tuner block [5] (Figure 1) and the other one is quite similar but employs four backshort tuners [6] for better tuning possibility. So far, some diode chips have been tested. A 10.5 dB SSB conversion loss has been achieved with The two-tuner mixer design. The measured noise figures are much higher than expected. We believe that this is due to the deterioration of the diode chip during the

measurements. The best results have been obtained by using the four-tuner block. The SSB results are a 9.2 dB mixer conversion loss and a 3520 K mixer noise temperature. These figures were obtained at 215 GHz and 107 GHz RF and LO frequencies, respectively. The used LO power was 3.5 mW. The series resistances of the two diodes in the applied chip are 11 Ω and 12.5 Ω and the ideality factors are 1.29 and 1.28, respectively.

The measured conversion loss value is comparable to those of the best published subharmonic planar Schottky diode mixers at this frequency range. On the other hand, the noise temperature is somewhat higher. It should be emphasized that the diode parameters are not optimized for 220 GHz but for 650 GHz. The same diode chip will be used in the 650 subharmonic mixer.

Conclusions

Anti-parallel planar Schottky diodes using quasi-vertical structure have been developed, fabricated and mounted on different 220 GHz sub-harmonic waveguide mixers. To reduce parasitic capacitance of the contact pads, reduced chip thickness of 10 microns and high air-bridges are realized. For a reliable handling of this thin device two flip-chip pillars have been introduced in the fabrication. Several batches of APQVD have been reliably processed.. A wide-band equivalent model has been theoretically developed which includes the passive and active regions of the diode. This model will be further improved by comparison with measured values.

DC characteristics of APQVD prove to be similar to those of whisker-contacted diodes and show that the variation between two diodes of the same pair is negligible. Noise measurements performed on flip-chip-mounted structures show diode noise temperature to be 350 K at a bias current of 500 μA.

The best performance obtained to date with subharmonic mixers using these diodes is 9.2 dB of SSB conversion loss and a corresponding mixer noise temperature

of 3520 K. These values were measured at 215 GHz and 107 GHz RF and LO frequencies, respectively, for an LO Power of 3.5 mW.

Acknowledgement

The authors would like to express their acknowledgement to Dr. H. Grothe and Dr. J. Freyer from the Technical University of Munich, Germany, for supplying the high-quality epitaxial materials.

The present work was carried out under ESTEC's contract number 11806/96/NL/CN.

REFERENCES

[1] A. Simon, A. Grüb, M. Rodríguez-Gironés and H.L. Hartnagel, "A Novel Micron-Thick Whisker Contacted Schottky Diode Chip", Proc. 6th Int'l Symposium on Space Terahertz Technology, pp 5-12. 1995

[2] C.-I. Lin, A. Simon, M. Rodríguez-Gironés, H.L. Hartnagel, P. Zimmermann, R. Zimmermann, and R. Henneberger, "Planar Schottky Diodes for Submillimeter Wave Applications", *Proc. IEEE 6th Int'l. Conference on Terahertz Electronics*, Leeds, UK 1998, pp 135-138.

[3] J. Zhang, P. Piironen, V. Möttönen, J. Louhi, A. Lehto, A. Simon, C.-I. Lin, A. V. Räisänen, "Wide-Band Equivalent Circuit of Quasi-Vertical Planar Schottky Diode for 650 GHz Subharmonic Mixers," *Proc. Fifth International Workshop on Terahertz Electronics*, Grenoble, France, 1997.

[4] J. Zhang, P.V. Piironen, V.S. Möttönen, J.T. Louhi, A.O. Lehto, A. Simon, C.-I. Lin, and A.V. Räisänen, "Model of quasi-vertical planar anti-parallel Schottky diode," *Proc. of 1998 International Conference on Microwave and Millimeter Wave Technology*, China, 1998, pp. 130–133.

[5] V.S. Möttönen, P.V. Piironen, J. Zhang, J.T. Louhi, and A.V. Räisänen, "Development of millimeter and submillimeter wave quasi-vertical Schottky diode mixers," *Proc. of 2nd ESA Workshop on Millimetre Wave Technology and Applications*, Finland, 1998, pp. 254–259.

[6] A.V. Räisänen, D. Choudhury, R.J. Dengler, J.E. Oswald, and P.H. Siegel, "A novel split-waveguide mount design for millimeter- and submillimeter-wave frequency multipliers and harmonic mixers," *IEEE Microwave and Guided Wave Letters*, vol. 3, no. 10, 1993, pp. 369–371.

A FIXED-TUNED 400 GHz SUBHARMONIC MIXER USING PLANAR SCHOTTKY DIODES

Jeffrey L. Hesler*, Kai Hui, Song He, and Thomas W. Crowe

Department of Electrical Engineering
University of Virginia
Charlottesville, VA 22903

Abstract

The design and testing of a 400 GHz fixed-tuned subharmonic mixer using anti-parallel planar Schottky barrier diodes is presented. Fixed-tuned, two-sided waveguide-to-microstrip transitions are used to couple power into a microstrip channel, in which the diode is mounted. A low-pass filter is used to block the RF signal, and a short-circuited half-wave stub is used to terminate the LO. The first tests of the mixer yielded a double-sideband mixer noise temperature of 1120 K and a mixer conversion loss of 8.0 dB at 420 GHz using 5 mW of local oscillator power.

Introduction

This paper describes the design and testing of a 400 GHz anti-parallel planar-diode subharmonic mixer. The main goal of this research is the development of robust solid-state room-temperature mixers at 380 GHz and 425 GHz with broad IF bandwidth for space-based microwave sounding. In addition to this goal, we desire to develop a sensitive fixed-tuned room-temperature mixer with broad RF and IF bandwidths that is rugged and uses a relatively simple block geometry, in particular one that is compatible with molding and micromachining block fabrication techniques [1]. The use of an E-plane split block design, with the RF and LO guides machined in the same plane of the block makes this design amenable to these inexpensive block fabrication techniques. The mixing element used for this mixer will be a planar Schottky diode [2], which is mechanically robust and can give excellent sensitivity without the need for cooling. Subharmonically pumped anti-parallel diodes will be used because this configuration suppresses LO noise and eliminates the need for an external diplexer since the RF and LO signals are coupled through different ports [3]. Finally, the use of the anti-parallel diode configuration tends to reduce the diode's IF impedance, thus simplifying broadband IF matching.

---

* e-mail address: hesler@virginia.edu

Mixer Block Configuration

The mixer block is split in the E-plane of the RF and LO waveguides, which simplifies mixer assembly and reduces the losses in the waveguides. The planar diode is mounted on a 35 μm thick fused-quartz substrate and then placed in a shielded microstrip channel which runs perpendicular to the RF and LO waveguides. A schematic of the mixer block circuit configuration is shown in Fig. 1. Fixed-tuned waveguide-to-microstrip transitions, with the microstrip running through the waveguide, are used to couple power into the microstrip channel, where the diode is mounted. The use of two-sided waveguide-to-microstrip transitions required the use of reduced height RF and LO waveguides to achieve reasonable bandwidths. For this mixer, half height waveguide was used for the RF, and third height guide was used for the LO.

A low-pass microstrip filter is used to prevent the RF signal from coupling to the LO guide, and a short-circuited half-wave stub is used to provide the LO termination. The RF embedding circuit is conceptually similar to that of a successful 700 GHz fundamental planar-diode mixer [4], indicating that this design can be readily scaled to higher frequencies using existing flip-chip type planar diodes.

Block Design

The mixer was designed using Ansoft's Maxwell finite-element simulator to model the waveguides, planar diode chip, and quartz circuit. Coaxial probes were artificially introduced at the two diode junctions during the finite element modeling to allow the direct prediction of the diode embedding impedance. The circuit was designed to present an LO embedding impedance of 70+j130Ω, and an RF impedance of 65+j40Ω. Harmonic balance simulations were performed for the University of Virginia SD1T7-D20 planar diode (η=1.26, $I_{sat}=2\cdot10^{-16}$ A, R_s=18 Ω, and C_{j0}=1.3 fF), and for the above embedding impedances the simulation predicted a mixer conversion loss of 5.0 dB (DSB) and noise temperature of 250 K (DSB) using 1 mW of LO power. The total conductor and dielectric loss for the horn, waveguide, microstrip, and diode was estimated to be about 2 dB. Using this loss, the predicted performance is a mixer conversion loss of 7 dB (DSB) and mixer noise temperature of 600 K (DSB). Fig. 2 shows a plot of the RF embedding impedance as a function of frequency. It is seen that the fixed-tuned RF bandwidth of the mixer is predicted to be about 70 GHz, or about 18%. The fixed-tuned LO bandwidth is expected to be only about about 5%, with the smaller bandwidth caused by the presence of the half-wave stub terminating the LO circuit.

Mixer Testing

The sensitivity of the mixer was measured at room temperature, yielding an overall system noise temperature of 2930 K (DSB) using 5 mW of LO power. The local oscillator power for this mixer was provided by a 105 GHz Gunn oscillator with about 75 mW output power driving a planar balanced doubler [5]. A variable attenuator was used to vary the IF noise temperature from 100 K to 440 K, thus allowing the measurement of the mixer parameters T_{mix}=2130 K (DSB) and L_{mix}=9.8 dB (DSB). Correction of the IF standing-wave-ratio of 4:1 will improve the performance to

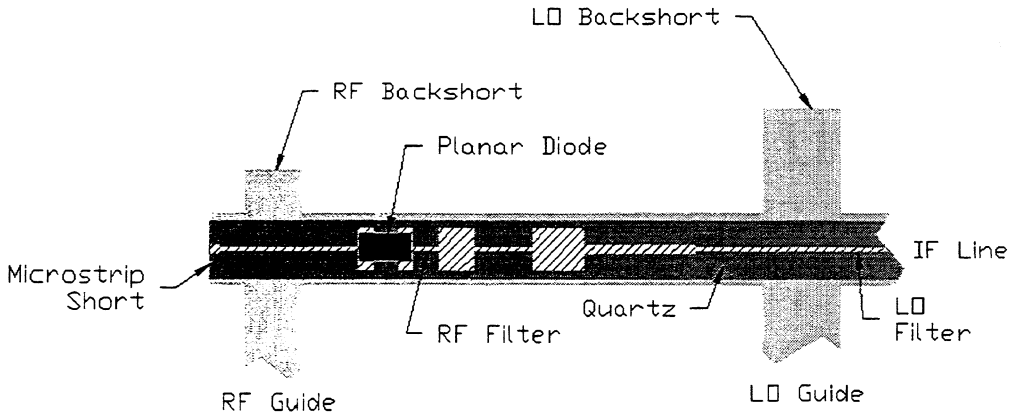

Fig. 1. Schematic of subharmonic mixer block circuit configuration.

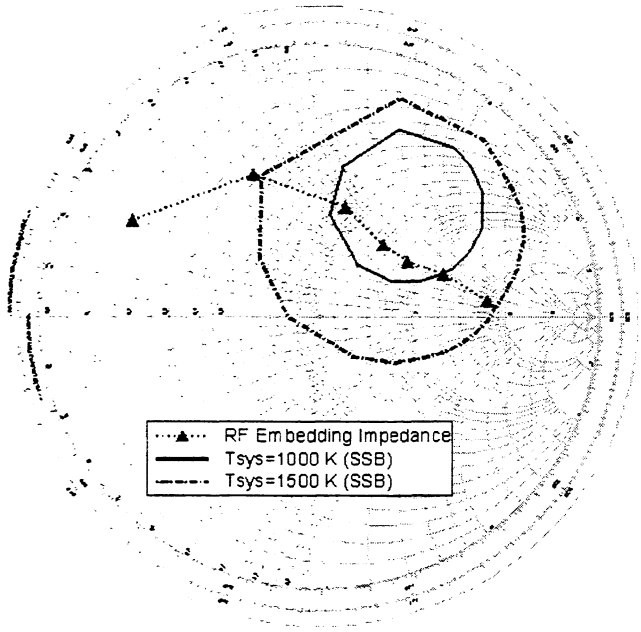

Fig. 2. RF embedding impedance from 360 GHz to 440 GHz (13.3 GHz steps) and computed noise temperature contours (contours calculated with 1.5 mW LO power, 100 Ω IF impedance, and with no transmission line losses).

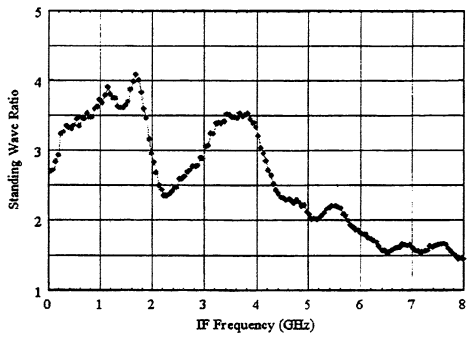

Fig. 3. Measured IF standing-wave-ratio for mixer at 420 GHz with 5 mW of LO pump power.

$T_{mix,c}$=1120 K (DSB) and $L_{mix,c}$=8.0 dB (DSB) (note that a room temperarature circulator was used at the input of the IF amplifier chain). A plot of the IF mismatch versus frequency is shown in Fig. 3.

Conclusions

We have developed an a robust 400 GHz planar-diode mixer with excellent sensitivity which can use an all-solid-state LO source. This mixer block is compatible with micromaching and molding techniques, thus allowing for the possibility of reduced component cost for submillimeter-wavelength mixers. Future testing will examine the experimental RF and IF bandwidths for this mixer. Based of previous results with fundamental mixers, it is expected that this mixer can be scaled to at least 700 GHz using existing planar flip-chip diodes, and can be scaled to THz frequencies by integrating the diode with the mixer circuitry [6].

Acknowledgments

This research was supported by NASA-GSFC Grant No. NAG5-6507 and the U.S. Army N.G.I.C. contract DAHC90-96-C-0010.

References

1. T.W. Crowe, P.J. Koh, W.L. Bishop, C.M. Mann, J.L. Hesler, R.M. Weikle II, P.A.D. Wood, D. Matheson, "Inexpensive Receiver Components for Millimeter and Submillimeter Wavelengths," *Proc. of Eighth Int. Symp. on Space THz Tech.*, Cambridge, MA, March 25-27 1997.

2. W.L. Bishop, E. Meiburg, R.J. Mattauch, T.W. Crowe and L. Poli, "A μm-thickness, planar Schottky diode chip for terahertz applications with theoretical minimum parasitic capacitance," *IEEE-MTT-S Int. Microwave Symp. Dig.*, 1990, pp. 1305-1308.

3. A.R. Kerr, "Noise and Loss in Balanced and Subharmonically Pumped Mixers: Part I - Theory," *IEEE Trans. Microwave Theory Tech.*, vol. MTT-27, pp. 938-943, Dec. 1979.

4. J.L. Hesler, W.R. Hall, T.W. Crowe, R.M. Weikle, II, B.S. Deaver, Jr., R.F. Bradley, and S.-K. Pan, "Fixed-Tuned Submillimeter Wavelength Waveguide Mixers Using Planar Schottky Barrier Diodes," *IEEE Trans. Microwave Theory Tech.*, Vol. 45, pp. 653-658, May 1997.

5. D.W. Porterfield, "A 200 GHz Broadband, Fixed-Tuned, Planar Doubler," *Proc. of Tenth Int. Symp. on Space THz Tech.*, Charlottesville, VA, March 16-18 1999.

6. S.M. Marazita, J.L. Hesler, R.Feinäugle, W.L. Bishop, and T.W. Crowe, "Planar Schottky Mixer Development to 1 THz And Beyond," Proc. 1998 Int. Symp. On Space THz Tech., Jan. 1998.

REGARDING THE IF OUTPUT CONDUCTANCE OF SIS TUNNEL JUNCTIONS AND THE INTEGRATION WITH CYROGENIC InP MMIC AMPLIFIERS

J. W. Kooi [1], F. Rice [1], G. Chattopadhyay [1], S. Sundarum [2], S. Weinreb [3] and T.G Phillips [1]

[1]MS 320-47, Caltech, Pasadena, CA 91125
[2]University of Massachusetts, Amherst, MA 01035
[3]Jet Propulsion Laboratory, Pasadena CA 91108

Abstract

There is a strong interest in the Submillimeter community to increase the IF bandwidth of SIS receivers in order to facilitate extra-galactic astronomy. However, increasing the IF bandwidth generally also means increasing the IF operating frequency of the mixer, because it is very difficult to achieve a good IF impedance match to a low noise amplifier (LNA) for more than an octave bandwidth.
Complicating the matter is that most cryogenic amplifiers do not have a very good input match, which nearly always results in severe standing waves between the mixer and amplifier, especially since the amplifier is connected to the mixer via a finite (10 cm) length of coaxial line. The use of a cryogenic isolator would eliminate the standing wave issue, however all of the currently available cryogenic isolators have less than an octave of bandwidth. The second approach would be to integrated an low noise amplifier into the mixer block, minimizing the distance between the junction and LNA.

In this paper we investigate the SIS junction's IF output conductance and the possible integration of SIS mixers with InP MMIC low noise amplifiers, as an alternative to the traditional matching network/isolator approach. In particular we look into the use of a grounded Gate and grounded Source configured low noise InP amplifier, and the performance one is likely to achieve.

I. Introduction.

From literature the IF output impedance of a Superconducting-Insulator-superconducting (SIS) junction is typically 10 times the normal state resistance of the junction [1-3]. The junction's IF output is shunted by the parasitic capacitance of the junction (A SIS junction is made of two closely spaced superconductors) and RF matching network. The resulting capacitance of a AlO_x tunnel junction with 10kA/cm^2 current density is on the order of 80fF/ μm^2. The matching network required to match the SIS junction's RF impedance to the waveguide embedding impedance is commonly implemented in micro-strip mode, and fabricated with either SiO or SiO_2 as the dielectric between the wire layer and ground-plane. For example, the JPL process uses

450- and 200 nm thick SiO (εr=5.6) dielectric layers. The relatively high dielectric constant of the dielectric guaranties that any type of RF matching network implemented in micro-strip mode introduces a significant parasitic capacitance, hence significantly limiting the obtainable IF bandwidth of the mixer.

Consider the ωR_nC product of a SIS junction. For a niobium SIS junction using an AlO_x barrier with current density equal to 7-10kA/cm ^{2}, the ωR_nC product is unity at about 100 GHz. It can be seen that the combined junction and RF matching network geometric capacitance is nearly the same for all micro-strip tuned SIS devices. This is especially the case if one considers that the fabrication process for SIS devices is universal, i.e. similar world-wide. We are justified therefore to do a case study of the popular and widely used "End-Loaded stub" RF matching network, without loosing too much generality [4-10].

For the wave-guide devices currently in use at the CSO, the RF matching network has a parallel plate capacitance of approximately 220 fF, and a junction capacitance of 40 fF giving a combined parasitic capacitance of 260 fF at the IF Port of the mixer (Fig. 1). Superconducting mixer computer simulations using Supermix, a recently developed software tool [11], have been performed in order to better understand the IF output conductance, optimum IF load impedance and IF frequency limitations of the SIS mixer. Using the results of these simulations, we investigate what happens when one of these devices is interfaced directly with an ultra-wide bandwidth InP MMIC device.

II. IF Output Conductance

The outline of the computer simulations is shown in Figure 2. We use a program called "Supermix" [11] which is developed at Caltech. The antenna impedance is taken to be 40-i20 Ohm. For clarity we show the RF choke with the SIS junction situated at the center of the bowtie antenna. To the left of the junction the RF matching network is visible. Also shown are two bond-wires, ordinarily one of the bond-wires is connected to ground, the other to a IF matching/bias network [12]. The IF output in the computer model is taken through the RF matching network and terminated into a 50 Ohm load via a transformer. This technique enables us to calculate both the mixer gain and IF output impedance.

In Figure 3 we plot the junction's IF output admittance as a function of bias voltage. For reference sake we show the pumped and unpumped IV curves as well. The IF frequency is 6 GHz, and 3 harmonics were used in the harmonic balance part of the program. The Junction's IF output impedance consists of a real part (10Rn) shunted by a capacitive component of 307 fF. This includes the quantum susceptance and is a more accurate value than the estimated 260 fF mentioned earlier. To see how the junction's IF admittance varies as a function of IF frequency we ran the mixer simulation from 0.5 to 12 GHz. The results is shown in figure 4. Clearly the IF admittance is made up out of a parallel RC, whose values are 10Rn, and 307 fF.

III. RF Port Reflection Coefficient

Intuitively one may think that it is best to conjugate match the above mentioned IF output conductance. This does indeed provide maximum mixer gain (Fig. 5), but also gives a reflection gain at the RF input of the mixer! This likely results in significant standing waves (VSWR) between the mixer and the telescope and consequently an unstable baseline for the back-end spectrometer. A more suitable value for S11(RF) is perhaps -3 to -5 dB, which results in a slightly lower mixer gain but more stable receiver.

We used the optimizer in Supermix [11] to calculate the required IF load impedance from 0.5 to 12 GHz that provides a particular RF reflection coefficient. When we do this, the mixer gain (Gmix) happens to be nice and flat as well. The required IF load impedance is complex and is plotted against IF frequency in figure 6.

Traditionally the IF port of a SIS junction has often been terminated by a real impedance, simply because it turns out to be very complicated to precisely calculate the required load impedance needed to achieve both an acceptable RF reflection Coefficient and mixer gain. For comparison's sake, we plot Gmix and S11(RF) for two distinct real load impedance's, 2Rn and 5Rn. In the case of a 1-2 GHz IF frequency, a IF load impedance of 5Rn is quite acceptable. It provides a near optimum mixer gain and a RF reflection coefficient of about -1 to -3 dB. The disadvantage is of course that the mixer gain is very much IF frequency dependent (10dB from 1-12 GHz)! For higher IF frequencies then 2 GHz, an IF load of 2Rn is not a bad choice. However the mixer gain is still a slight function of IF frequency and 2-3 dB in mixer gain is sacrificed as compared to an optimal design.

The real and imaginary components of the calculated IF load admittance are presented in Figure 6. Note that the real part of Yif varies from 10Rn for a conjugate match (maximum Gmix and S11(RF)) to 2.3 Rn for a RF reflection coefficient of -10dB. The imaginary part is essentially constant at -296 fF, the conjugate of the combined junction capacitance, junction quantum susceptance and RF matching network parasitic capacitance. In general, the required IF load impedance will be on the order of (2.8-3.7) * Rn shunted with a negative capacitor whose magnitude is the total combined junction capacitance.

IV. IF Matching Network

Since nature does not provide us with a negative capacitance, we need to come up with some kind of compromise to obtain the required IF load impedance. An inductance will do at a single frequency, with a 3dB bandwidth related to the Q of the circuit. A wider bandwidth (octave) is achieved with a more complicated circuit. As an example we use a 7 pole Chebyshev impedance transformer, implemented in micro-strip mode (Fig 7) and centered from 4-8 GHz. The conditions are S11(RF) = -3dB with a flat/optimal mixer gain. On the Smith chart we show the simulated IF load impedance and actual obtained IF impedance as measured at the junction (Match[S22]). If we replace the junction with the required IF load, and look into the 50 Ohm output of the matching network we see a return loss of -14 dB (4% reflected power).

Now that we have designed a complete IF matching network, we calculate the combined IF matching network/RF choke impedance from 0.5 - 12 GHz and present this to the IF port of the mixer. Re-running the superconducting mixer software (Supermix) with this new load impedance gives us the final mixer performance (Fig. 8). Note that Gmix is nice a flat at -1.4 dB, while the RF reflection coefficient is -5dB. This is slightly different from the design goal of -3dB, because we were not able to perfectly match the required IF load for a RF reflection coefficient of -3db (Figures 6, 7). It should also be noted that at the LO frequency (0 GHz) the RF reflection coefficient goes positive. In practice this problem can be prevented by including a termination resistor in series with a small inductance.

V. Reality check

To compare our superconducting mixer simulations against actual measurements, we plot the IV and Total Power curves of both the simulation and measurement in Fig. 9. The difference in the total power curve shape is primarily due to a difference in Antenna impedance. From the simulations we get a 345 GHz mixer noise temperature of 12 K and a mixer gain of -1.4 dB (IF frequency = 6 GHz). The optics loss at the RF frequency is measured to be about -0.5 dB using a Fourier Transform Spectrometer. Using the intersecting line technique[13, 14] we calculate an actual optics temperature of 25K.

The 352 GHz measured result uses a SIS receiver with a 1-2 GHz GaAs balanced low noise amplifier (noise temperature equals 5-6 K) as opposed to the 6 GHz intermediate frequency in our computer simulations. Finally, if in our simulations we use an InP Hemt amplifier centered at 6 GHz with a noise temperature of 7K, we calculate a receiver temperature of about 53K DSB. This compares very well with the measured receiver temperature of about 52K (different IF frequency). From this discussion it is clear that the noise in the receiver is very much dominated by the optics loss in front of the mixer!

VI. InP MMIC's

A promising technology for wide IF bandwidth applications are InP MMIC's. In figure 10 we show the characteristics of three of such devices. The simulations cover 1-20 GHz and show very good gain and noise performance, especially for the grounded gate devices. The input impedance for a grounded gate device is about 20 Ohm, with the optimum noise impedance close to 50 Ω. The models were obtained from Professor Sander Weinreb [15]. At the present time, none of the MMIC's have been measured. Nevertheless it is very instructional to connect the MMIC models to the SIS junction under discussion ("End-Loaded stub" RF matching network) and re-run the Supermix mixer simulations.

The result is shown in Figure 11. The MMIC is wire-bonded directly to the RF choke without a matching network. Because the MMIC's and SIS device are not matched to one another, the mixer gain and RF reflection coefficient are quite erratic. This experiment clearly demonstrates two important points.
First, if a MMIC is to be used with a existing SIS junction then an IF matching network is inevitable. This of course will restrict the IF bandwidth that can be achieved.
Secondly, to obtain a wide IF bandwidth system the junction has to have very low parasitic capacitance[16] an be designed to properly match the MMIC. In other words, both MMIC and SIS devices need to be very well characterized and understood.

VII. Conclusion

SIS devices employing highly capacitive RF matching networks such as the popular "End-Loaded" stub can be used up to IF frequencies of at least 8 GHz. The parasitic capacitance from the actual SIS device, RF matching network, and junction's quantum susceptance is significant for most mixers in operation at the present time. Increasing the IF bandwidth to 8 GHz, or higher, requires a knowledge of the proper IF load impedance if one is to obtain an optimally flat mixer gain and acceptable RF reflection coefficient. As a rule of thumb, the IF load impedance will be on the order of (2.8-3.7) * Rn shunted with a negative capacitor whose magnitude is the total combined junction capacitance. Presenting a real load impedance to the IF port will limit the mixer performance at the higher IF frequencies. Another important observation is that the RF choke will resonate with the junction parasitic capacitance at about 9-10 GHz for most SIS devices currently in use. This sets a practical upper limit to IF frequency, unless the junction is redesigned of course.

Low noise InP MMIC technology is very promising indeed. If one is to take full advantage of the MMIC's bandwidth however, the Junction/RF matching network combination needs to be carefully re-designed and characterized. Current SIS devices

can of course be used with MMIC's, but will need to use some sort of IF matching network, which will limit the available IF bandwidth.
Last, we have demonstrated Supermix as being a very useful tool for superconducting mixer analyses.

VIII. References

1. A.R. Kerr, S.-K. Pan, and S. Withington "Embedding Impedance Approximations in the Analysis of SIS Mixers" *IEEE Trans. Microwave Theory and Techniques*, Vol. MTT-41, No. 4, pp. 590-594, April 1992.
2. Q. Ke and M. J. Feldman "Optimum Source Conductance for high Frequency Superconducting Quasiparticle Receivers" *IEEE Trans. Microwave Theory and Techniques*, Vol. MTT-41, No. 4, pp.600-604, April 1992.
3. A.R. Kerr "Some fundamental and practical limits on broadband matching to capacitive devices and the implications for SIS mixer design", *IEEE Trans. Microwaves Theory and Techniques*, Vol. 43, No. 1, pp. 1-13, January 1995.
4. J. W. Kooi, M. Chan, B. Bumble, T. G. Phillips, "A low noise 345 GHz waveguide receiver employing a tuned 0.50 μm^2 Nb/AlO_x/Nb tunnel junction," *Int. J. IR and MM Waves*, Vol. 15, No. 5, May 1994.
5. J. W. Kooi, M. Chan, B. Bumble, H. G. Leduc, P.L. Schaffer, and T. G. Phillips, "230 and 492 GHz Low-Noise SIS Waveguide Receivers employing tuned Nb/AlOx/Nb tunnel junctions," *Int. J. IR and MM Waves*, vol. 16, No. 12, pp. 2049-2068, Dec. 1995
6. C.E. Honigh, S. Haas, D. Hottgenroth, K. Jacobs, J. Stutzki, "Low-noise broadband fixed tuned waveguide mixers at 660 and 800 GHz", *IEEE-Applied Physics*, Vol. 7(2), Part 3, pp2582-2586, June 1997.
7. R. Blundell, C.-Y E. Tong, D.C Papa, R.L. Leombruno, X. Zhang, S. Paine, J.A. Stern, H.G. LeDuc, and B. Bumble, "A wideband fixed-tuned SIS receiver for 200 GHz Operation," *IEEE Trans. Microwave Theory and Techniques*, Vol. MTT-43, April 95, pp.933-937, 1995.
8. C.-Y E. Tong, R. Blundell, S. Paine, D.C Papa, J. Kawamura, X. Zhang, J.A. Stern, and H.G. LeDuc, "Design and Characterization of a 250-350 GHz Fixed Tuned Superconductor-Insulator-Superconductor Receiver", *IEEE Trans. Microwave Theory and Techniques*, Vol. 44, No.9, September 1996, pp.1548-1556
9. G. de Lange, C.E. Honingh, M.M.T.M. Dierichs, H.H.A. Schaeffer, H. Kuipers, R.A. Panhuyzen, T.M. Klapwijk, H. van de Stadt, M.W.M. de Graauw, and E. Armandillo, "Quantum limited responsivity of a Nb/Al_2O_3/Nb SIS waveguide mixer at 460 GHz", *Proc. 4th Int'l Symp. Space THz Technology*, Los Angeles, pp. 41-49, 1993
10. K. Jacob's, U. Kotthaus, and B Vowinkel, "Simulated performance and model measurements of an SIS waveguide mixer using integrated tuning structures", *Int. J. IR and MM Waves*, Vol 13, No. 1, pp. 15-26, 1992
11. J. Ward, F. Rice and J. Zmuidzinas "Supermix: a flexible software library for high-frequency circuit simulation, including SIS mixers and superconducting components", Tenth International Symposium on Space Terahertz Technology, University of Virginia, Charlottesville, VA, March 1999.
12. J. W Kooi, M. Chan, T.G. Phillips, B. Bumble, and H.G. Leduc, "A low noise 230 GHz heterodyne receiver employing 0.25 μm^2 area Nb/AlO_x/Nb tunnel junctions," *IEEE Trans. Microwaves Theory and Techniques*, Vol. 40, pp. 812-815, May 1992.
13. R Blundell, R.E. Miller and K H Gundlach, "Understanding noise in SIS Receivers," *Int. J. IR and MM Waves*, Vol 13, No. 1,1992

14. Q. Ke and M.J. Feldman, "A technique for accurate noise temperature measurements for the superconducting quasiparticle receiver," Proceedings of the Fourth International Symposium on Space Terahertz Technology, UCLA, March, 1993
15. Prof. Sander Weinreb, Jet Propulsion Laboratory, Pasadena CA 91108, 72164.560@compuserve.com
16. A.R. Kerr, S.-K. Pan, A.W. Lichtenberger and H.H. Huang "A tunerless SIS mixer for 200-280 GHz with low output capacitance and inductance "Proceedings of the Ninth International Symposium on Space Terahertz Technology, 17-19 March, 1998

Motivation

SIS mixers employing an "End-loaded Stub" RF matching network are currently in use at many institutions, such as the CSO, CFA, JCMT, KOSMA, MPIfr and SMT.
We investigate if the this type of RF matching network lends itself to IF bandwidth's as high as 12 GHz.

Questions:

- What is the best possible mixer performance achievable given a 4-8 GHz IF frequency.
- What is the mixer performance when InP MMIC's are integrated with this kind of RF matching network.

Basic Issue:

- What is the IF Load Admitance required to obtain near unity mixer gain and at the same time an acceptable RF reflection Coefficient ($S11_{RF}$).

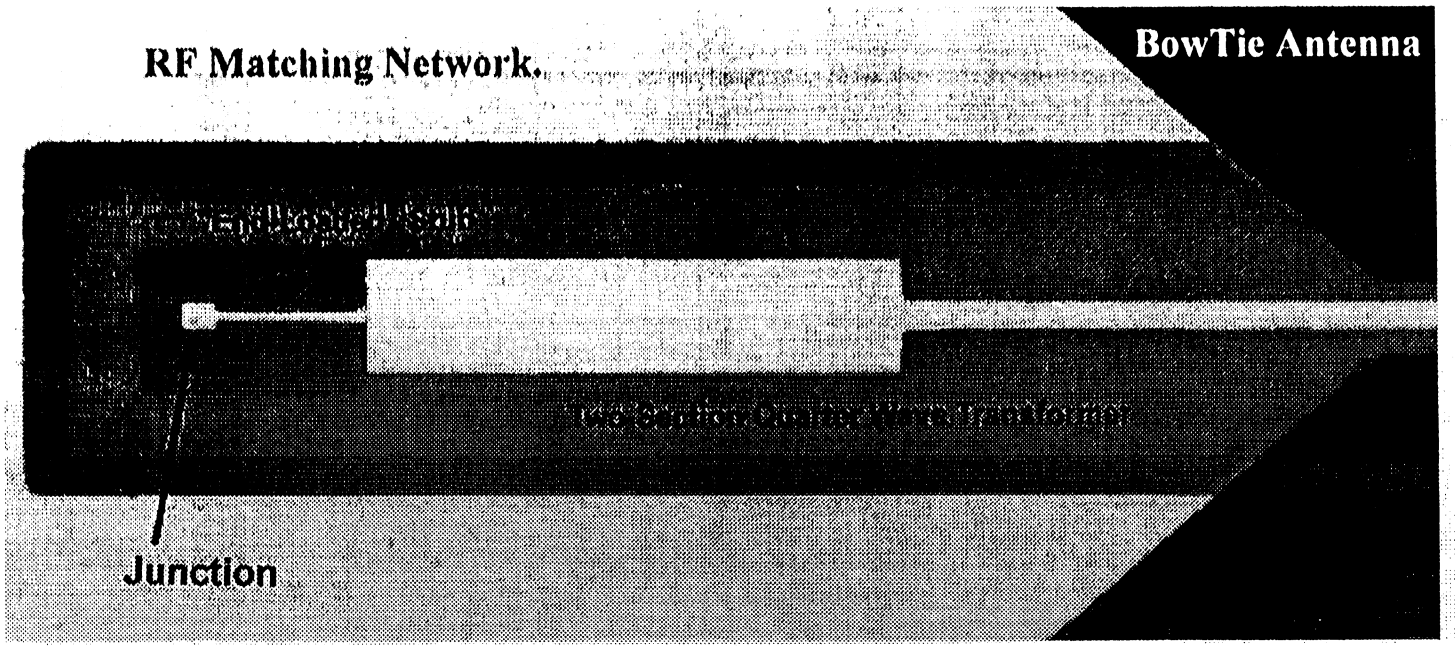

Fig. 1 End Loaded Stub RF matching Network and motivation for the work

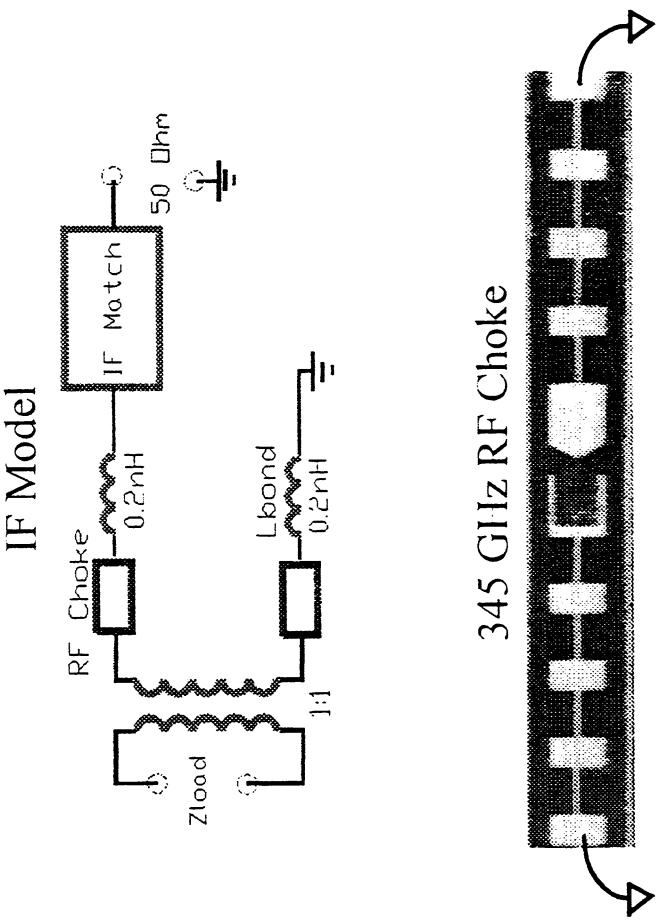

Fig. 2 Outline of the Computer Simulations. The Supermix mixer model assumes 3 harmonics for the harmonic balance. The Antenna impedance is taken to be 40-i20 Ohm. The IF model includes the RF choke and bond wires. A ideal transformer is used to obtain the load impedance at the junction/RF matching network, situated in the center of the Bowtie antenna.

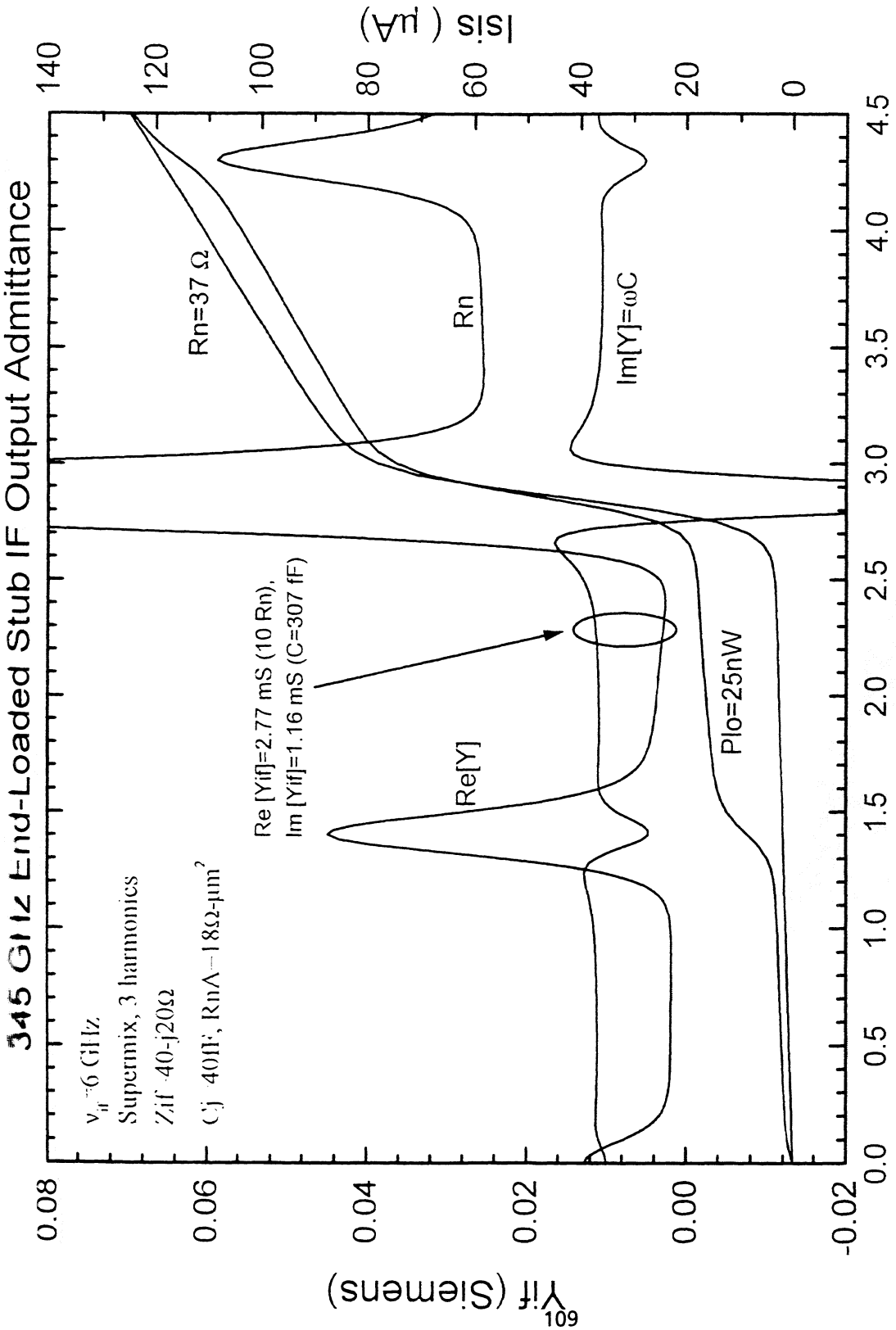

Fig. 3 345 GHz End-loaded stub IF output admittance. The real part of the IF impedance is close to 10Rn, while the imaginary part corresponds to a 307 fF capacitance. This capacitance is a combination of junction, RF choke and quantum susceptance.

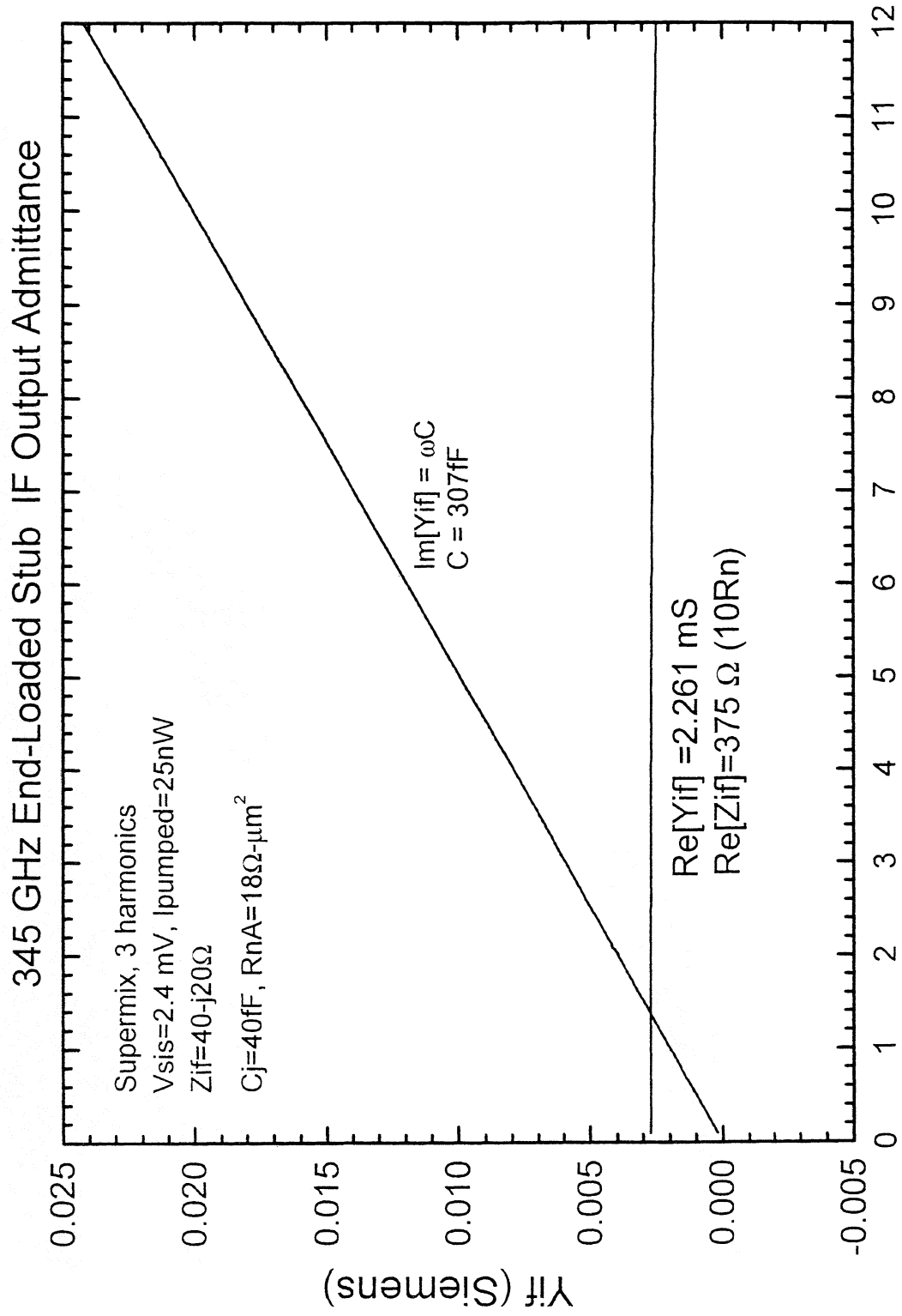

Fig. 4 End loaded Stub IF output admittance as a function of IF frequency.

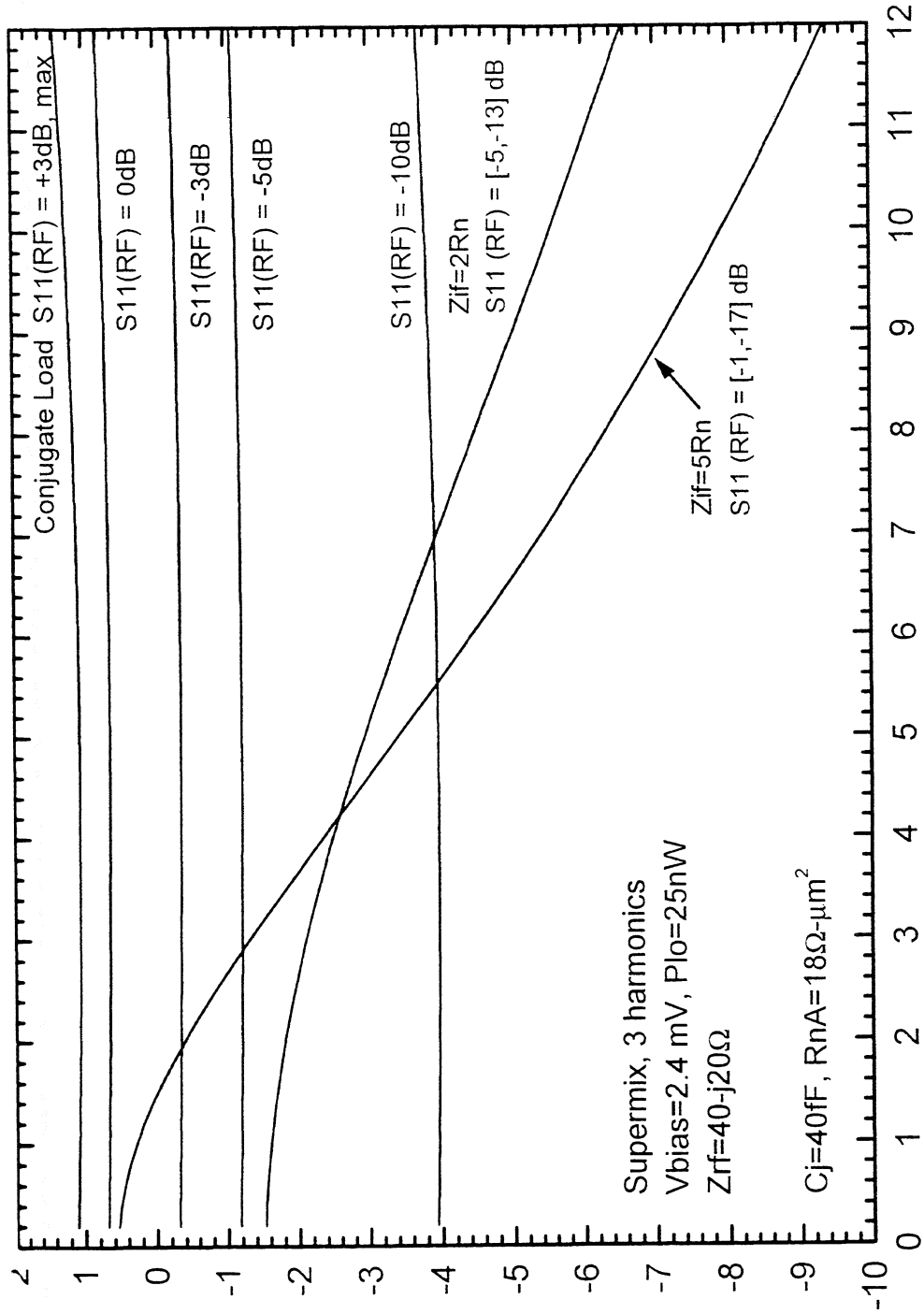

Fig. 5 Mixer gain and RF reflection, S11(RF), as a function of IF frequency for different IF loads. Presenting a conjugate load results in a mixer gain, but also a large RF reflection gain (+3dB)! Presenting a real load such as 2Rn or 5Rn is adequate at the lower IF frequencies, but results in a large loss in mixer performance at the higher IF frequencies.

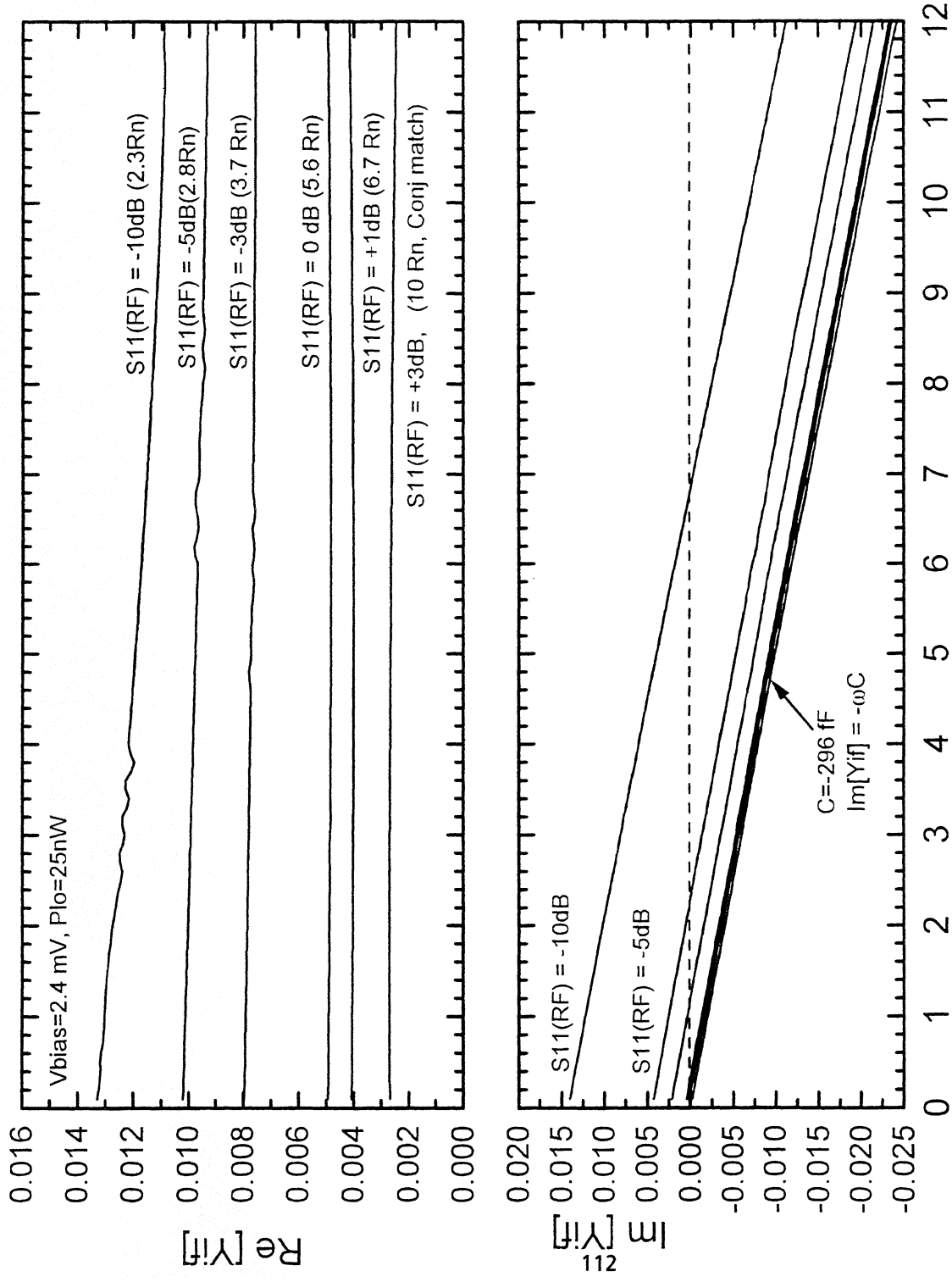

Fig. 6 IF load impedance required to obtain a fixed RF reflection Coefficient, S11(RF), and flat mixer gain. Note that a negative capacitance is required to achieve a good match over the whole IF frequency range.

4-8 GHz IF Matching Network

Conditions:
- S[rf][rf]=-3dB
- Flat/Optimal Gmix.

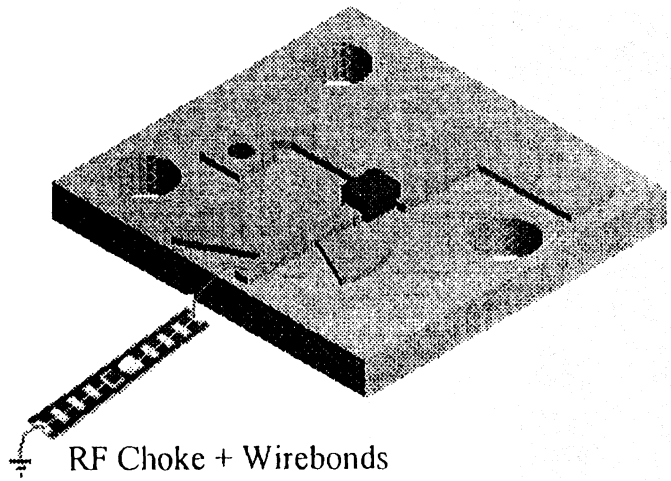

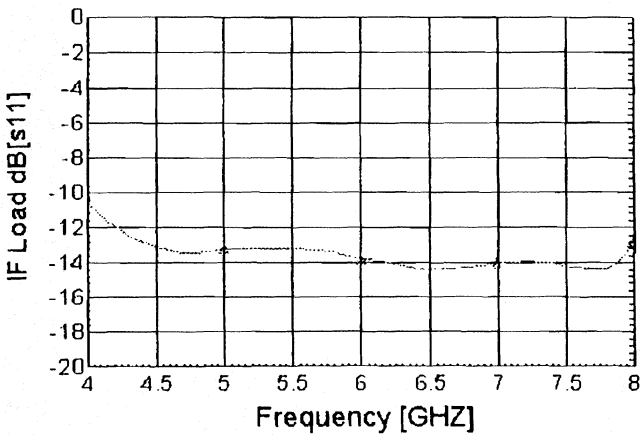

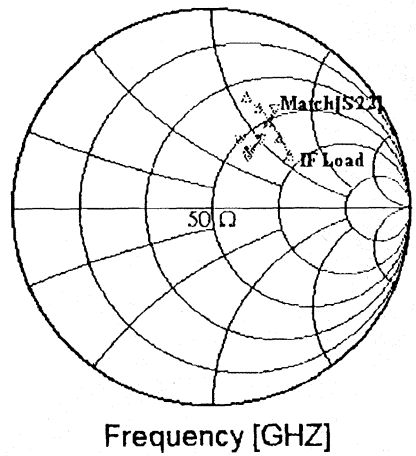

Fig. 7 A 4-8 GHz IF matching network which transforms a 50 Ohm input impedance to the required IF load impedance given the condition, S11(RF) = -3dB.
Since it is physically impossible to provide a negative capacitance, a good impedance match can only be provided over a limited (octave) of bandwidth.

Tenth International Symposium on Space Terahertz Technology, Charlottesville, March 1999

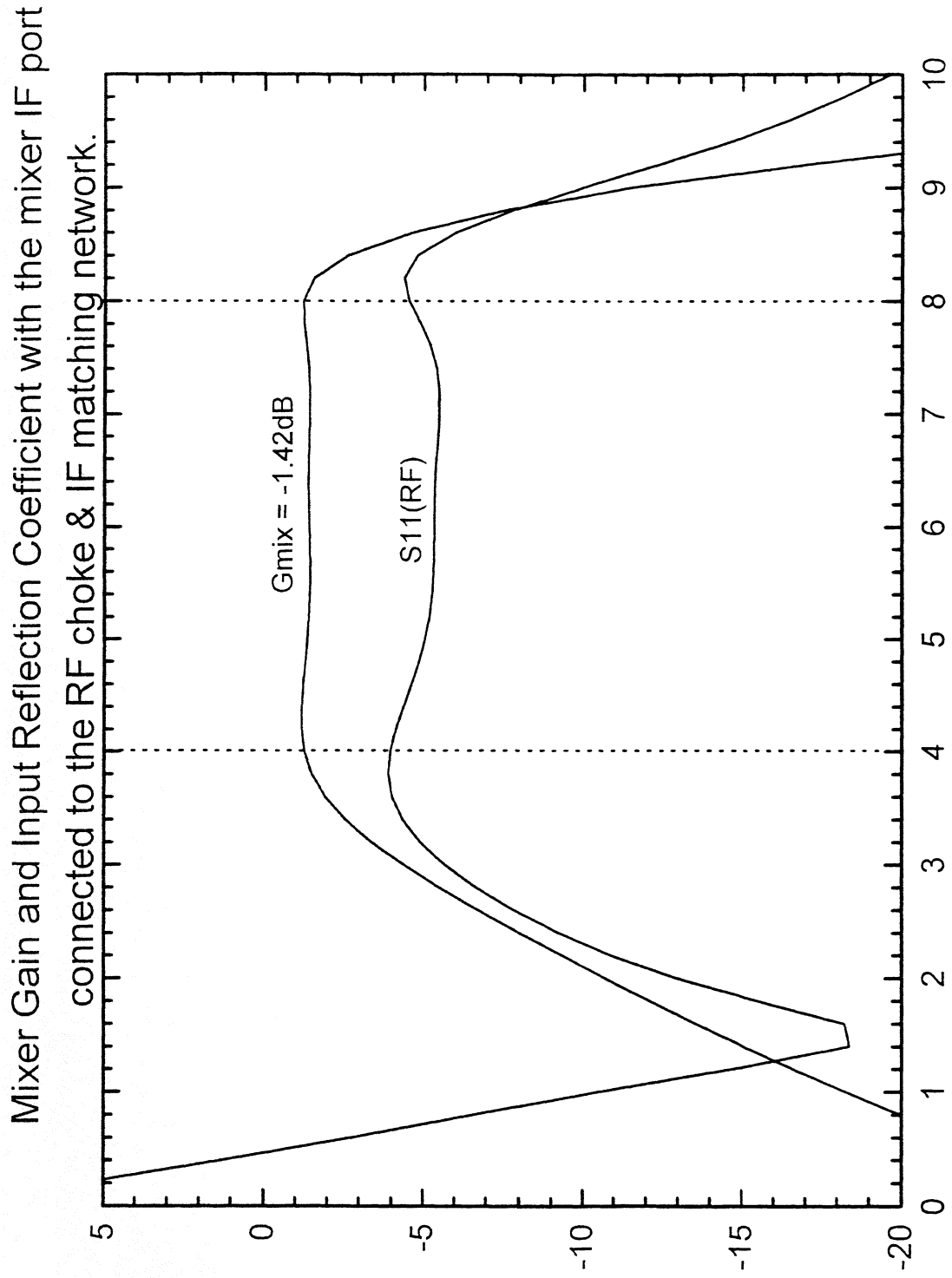

Fig. 8 The calculated IF load presented by the IF matching network and RF choke is now used to terminate the IF port of the mixer model. Supermix computer simulations are re-run, and the result for Gmix and S11(RF) plotted.

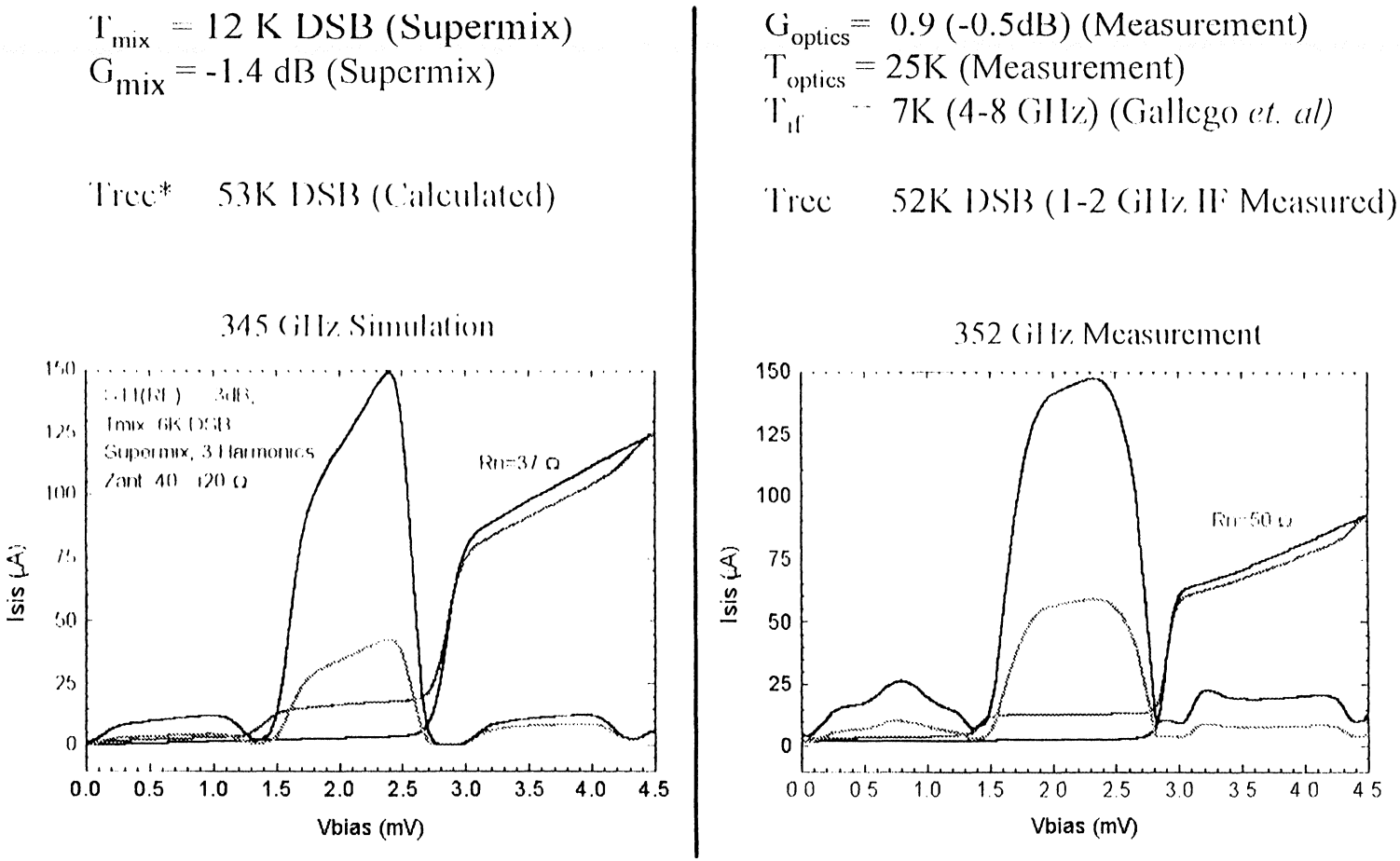

Fig. 9 To show that the simulations fit closely to actual measurements, we show this graph. The 352 GHz data was taken with a 1-2 GHz IF. The noise temperature of the LNA is about 5-6 K. The simulations assume a IF frequency of 6 GHz, but with similar IF noise characteristics. Material loss is measured in the lab and verified by the intersecting line technique (Blundell, Feldman *et al).*

InP MMIC MODELS

DC Power: 10mW, primarily due to resistive drain loading for low frequency operation

Tnoise: 5-8K

Gain: 20-25 dB

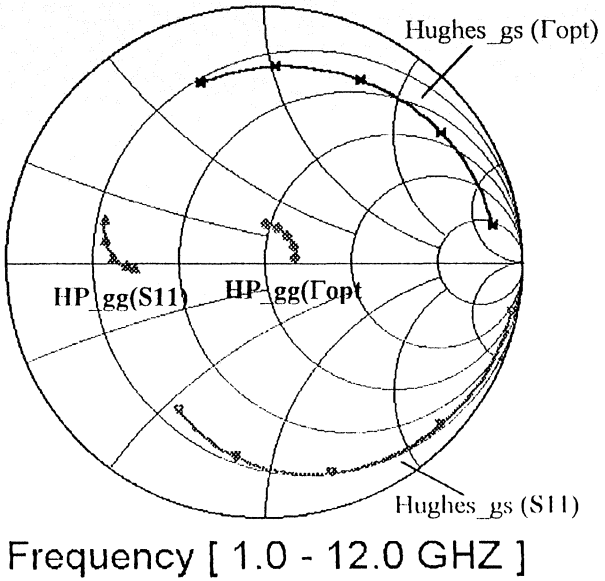

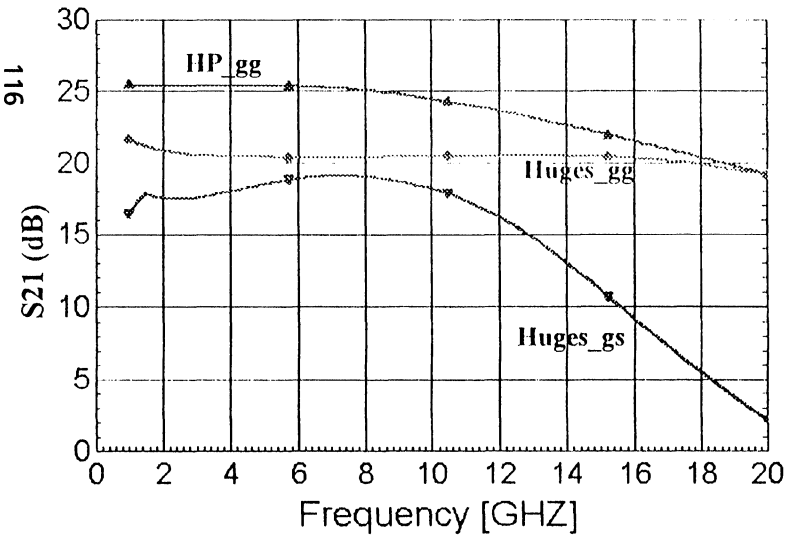

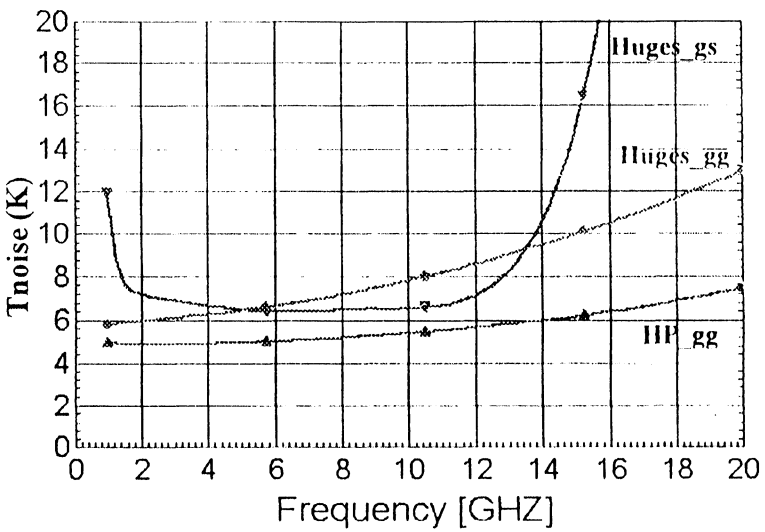

Fig. 10 InP MMIC computer simulations. Models obtained from Sander Weinreb. These simulations assume a fixed 50 Ohm input/output termination.

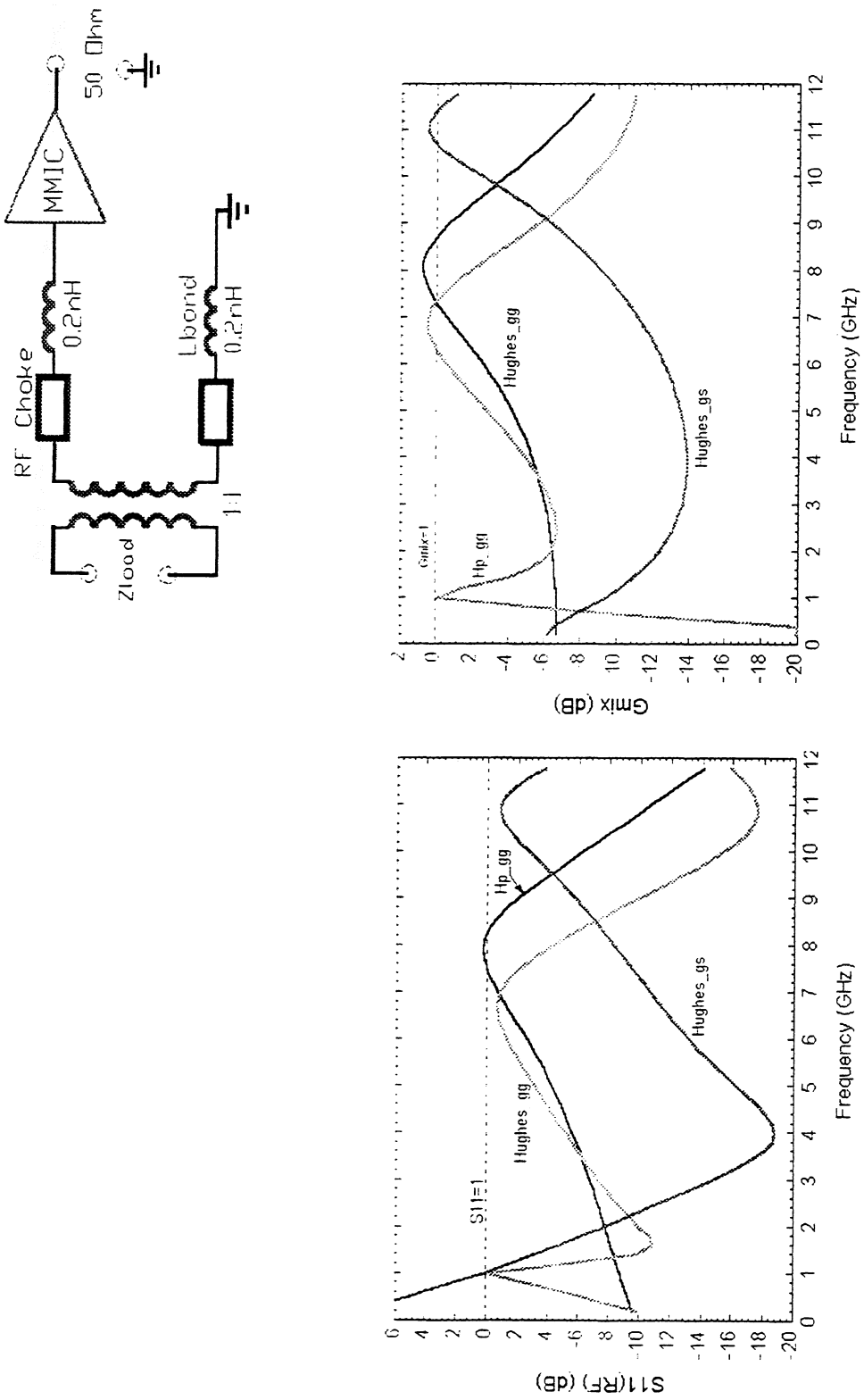

Fig. 11 Supermix computer simulations with the InP MMIC's connected to mixer IF port via a RF choke. That the IF load impedance presented by the MMIC to the mixer is far from ideal, is evident by the mixer gain and RF reflection, S11(RF). To take full advantage of the MMIC's very large IF bandwidth, the mixer will have to be redesigned so that the MMIC amplifier/RF choke combination provides an adequate termination to the mixer IF port (less capacitive RF matching network).

E-BEAM SIS JUNCTION FABRICATION USING CMP AND E-BEAM DEFINED WIRING LAYER

Patrick Puetz*, Karl Jacobs

KOSMA, I. Physikalisches Institut, University of Cologne
Zuelpicher Str. 77, 50937 Koeln, Germany

ABSTRACT

High frequency (> 0.5 THz) circuit design of SIS mixer elements used in radioastronomical heterodyne receivers demand tightly controlled junction areas with sizes smaller than 0.5 μm^2, suggesting the use of electron beam lithography (EBL). The thin PMMA electron beam resist, however, cannot be used for the usual self-aligned liftoff of the insulating dielectric. We implemented a new processing scheme similar to the PARTS (Planarized All-Refractory Technology for Superconducting electronics [1]) fabrication process developed at IBM. In this process a chemical mechanical polishing (CMP) step is used to planarize the dielectric (SiO_2). CMP of the circuits on fused quartz substrates was performed on a standard lapping machine with a simple motorized polishing head. Dielectric thickness variations across the active chip diameter (∅ 20 mm) of only ± 20 nm were achieved. In order to test the quality of our junction fabrication, square and rectangular junctions with areas ranging from 0.02 μm^2 to 25 μm^2 were fabricated and DC-tested. We further investigated EBL for the wiring layer, thus extending the process to a precise definition and positioning accuracy of all critical circuit geometries. This is especially interesting for tuning circuits at 1 THz and beyond, with typical lengths and widths in the order of a few microns. First results indicate that junctions with EBL defined wiring layers can have the same quality as those with UV defined wiring.

I. INTRODUCTION

Junction area is a crucial design factor for the integrated tuning circuits of SIS junctions. With the development of SIS mixers for frequencies at or above 1 THz, e. g. for use in the receivers of the Far Infrared Space Telescope (FIRST), junction areas have to become smaller (< 0.5 μm^2) and more precisely defined ($\Delta A_J/A_J < 10$ %) in order to ensure optimum performance of the integrated tuning circuits. At lower frequencies, ongoing developments of multi-junction circuit designs and array

* puetz@ph1.uni-koeln.de

applications make tightly controlled junction areas necessary. Junction designs employing rectangular submicron areas or distributed junctions are very demanding for junction definition.

Standard UV300 contact mask-aligner lithography has its limits with linear dimensions approaching 0.8 μm and thus needs to be replaced by a more powerful technology. Two commonly employed solutions are deep UV stepper technology or EBL. In this paper we will focus on latter, as EBL technology has already been developed at KOSMA for fabrication of hot electron bolometers [2].

In the conventional self-aligned liftoff process for the fabrication of SIS junctions, a thick ($\geq$ 1.2 μm) photoresist is used both for the definition of the top electrode and for the following self-aligned liftoff of the evaporated insulating dielectric. The electron beam resist PMMA used for high resolution EBL is too thin (190 nm) to be used for these purposes (Figure 1, first column). Therefore a different fabrication scheme has to be implemented.

One possibility for pattern transfer is the use of a relatively thick polyimide underlayer beneath the EBL resist as described in [3] shown in Figure 1, second column. A disadvantage of this process is the rather difficult processing of the polyimide films and the fact that the critical liftoff step still has to be used.

A completely different approach is the use of a chemical mechanical polishing (CMP) step for planarization of the dielectric, first used in the PARTS (Planarized All-Refractory Technology for Superconducting electronics) process [1]. Here a self-aligned process step is not necessary, thus eliminating the need for a thick EBL resist. After junction top electrode RIE the dielectric is deposited onto the whole wafer without any patterning and then the dielectric is locally and globally planarized in a polishing step. Polishing is terminated when the junction top electrodes emerge at the dielectric surface (Figure 1, third column).

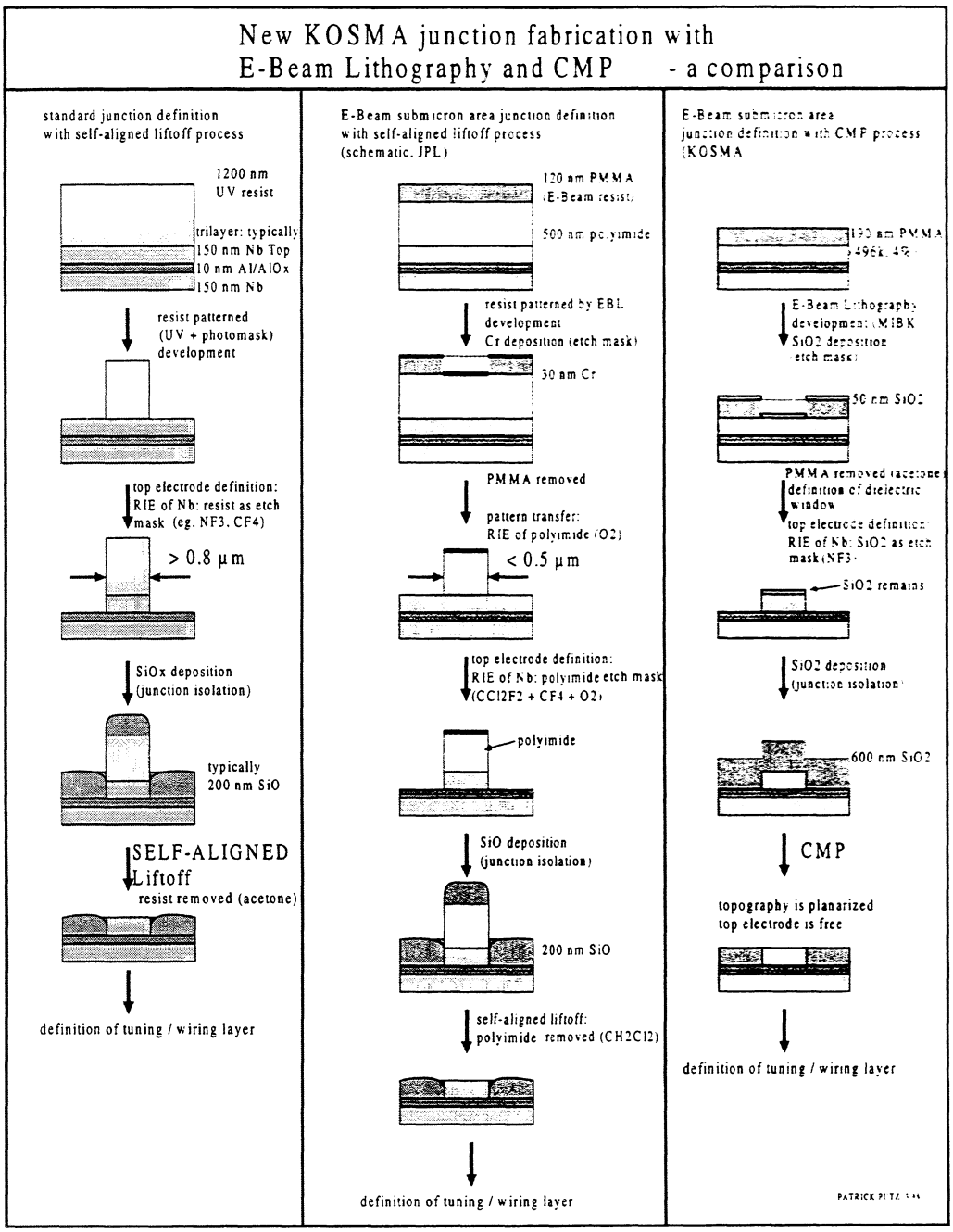

Figure 1 Comparison of junction definition with CMP to standard self-aligned liftoff and JPL processing schemes

II. CHEMICAL MECHANICAL PLANARIZATION OF INTERLAYER DIELECTRICS

CMP for planarization of interlayer dielectrics (ILD) was developed at IBM in the mid 80's for multilevel VLSI chip developments out of the need to cope with increased topography generation (also referred to as oxide CMP).

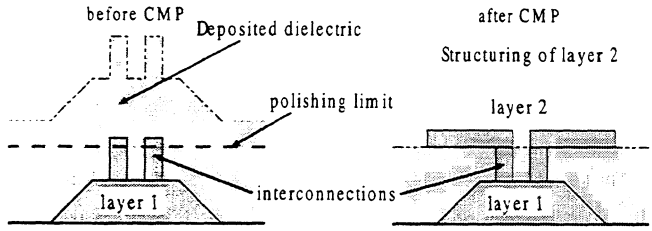

Figure 2 Illustration of ILD planarization through CMP

In a typical application the ILD, SiO_2 is deposited onto underlying circuits and is planarized through CMP and thinned until interconnections can be used for further contacting (Figure 2). During CMP the wafer is pressed onto a polishing surface (a polyurethane polishing pad) with both the wafer and the pad being rotated. A caustic aqueous polishing slurry, containing small abrasives (typically silica particles of approx. 100 nm diameter) is dispensed onto the pad. The SiO_2 surfaces of the ILD on the wafer and the silica particles become hydroxylated, and hydrogen bonding in combination with the mechanical induced slurry flow then carries away material from the ILD [5].

Because of the complex hydromechanical interactions at the ILD surface, an empirical approach for establishing the proper set of parameters for an optimal planarization yield and process stability has to be chosen. In order to establish a high planarization rate (i. e. the time it takes to reduce ILD topography to a desired level) and global uniformity of the ILD thickness, the wafer has to be in partial contact with the polishing pad. This is achieved by empirically influencing the slurry fluid film thickness through pad velocity, pad properties, wafer applied load and the wafer mounting, with the latter determining how much the wafer is recessed into its carrier. As shown in [6] for 2″ wafers, this semi-direct contact mode is achieved when the wafer sticks out less than a few mils above the carrier surface. Another important effect is the feature size dependency of the planarization rate. Structures with larger linewidths planarize slower than smaller structures due to the finite deformability of the polishing pad [6–9]. This can be a problem for

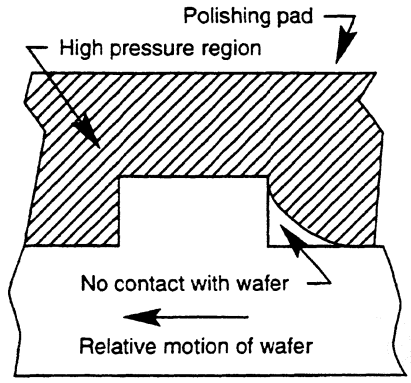

Figure 3 Deformation of polishing pad leads to greater pressure on high features and thus their planarization (from [7])

establishing interconnection of all circuits on a chip. This must be solved by the appropriate chip design.

III. KOSMA E-BEAM SIS JUNCTION FABRICATION SCHEME

The trilayer structure for the waveguide junctions is sputter-deposited onto fused quartz substrates (INFRASIL, ∅ 25 mm, 250 µm thickness) into UV lithographically patterned bilayer AZ 7212 photoresist windows [10]. The trilayer film thicknesses are 150 nm niobium for the bottom electrode, 10 nm aluminum, which is oxidized in-situ to form the AlO_x tunnel barrier with critical current densities around 17 kA/cm^2, and 230 nm niobium for the junction counter electrode. After liftoff, alignment marks are defined onto the chip through sputter-deposition of aluminum and gold, also as a liftoff process. These marks are needed for pattern alignment during EBL. Then the chip is spin-coated with a monolayer 190 nm PMMA (4 %, 496 k) and covered with 10 nm aluminum for charge dissipation during EBL.

Our EBL system, based on a CAMBRIDGE S240 SEM, is controlled by a PC running customized AutoCAD software in which the structures are defined using AutoCAD trace elements. Patterns are written into the PMMA with a beam current of 14.0 pA and doses ranging from 100 to 150 µC/cm^2 (structures are not proximity effect corrected, but larger structures receive less dose for compensation). After removing the aluminum in an acidic solution and PMMA development, 50 nm SiO_2 as the etch mask for RIE is electron beam evaporated into the PMMA patterns. A thorough O_2 plasma clean to remove H_2O from the chips' surface prior to deposition has proven to be necessary for proper SiO_2 film adhesion. After junction etch mask liftoff, a secondary etch mask, patterned with UV lithography, defines the junction isolation window. Now the top electrode is etched with RIE using NF_3 at 40 µbar, -55 V, 0.13 W/cm^2 for 48 sec.

600 nm SiO_2 as dielectric for the integrated tuning structures is electron beam evaporated (after plasma cleaning) onto the whole chip in agreement to the PARTS processing scheme (a minimal dielectric thickness according to the feature step height to be planarized, in our case 390 nm, is needed for planarization). CMP is terminated after 3–4 polishing passes when the mean dielectric thickness in the junction isolation windows is measured to be 200 nm. After CMP and post-CMP cleaning procedures – which are discussed in following chapters – the integrated tuning circuits are sputter deposited into UV-lithographically (or EBL – discussed later) patterned photoresist windows, again as a liftoff process. The wiring layer consists of 350 nm niobium covered with 30 nm gold for wire bonding. Prior to deposition the chip is argon plasma cleaned (4 min, 3.0 Pa, -450 V, 0.4 W/cm^2) in order to remove any residue from CMP (in particular the modified niobium layer on the junction tops). The chip is then diced into several parts, ultrasonically wire bonded and DC tested.

IV. Experimental Assembly for CMP

CMP was developed on a standard lapping machine [11]. This machine is equipped with a 12″ plate drive with continuously variable speeds from 0–70 rpm and a semi-circle roller sweep arm, with variable sweep amplitude and frequency, to guide the lapping / polishing head (Figure 4). Because this machine is also used for lapping fused quartz substrates it was placed in our clean room facilities or in an individual flow box environment.

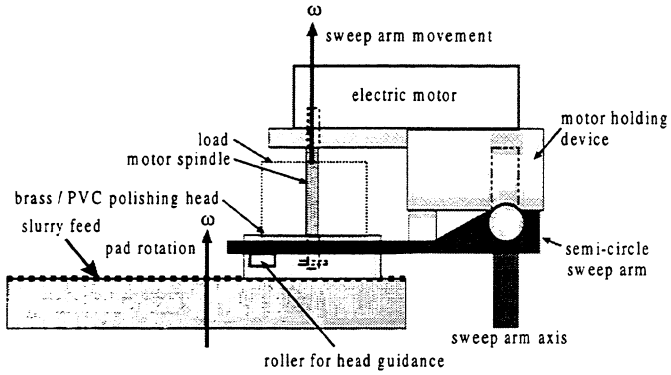

Figure 4 Schematic side-view of CMP assembly

A machined DELRIN (PVC) disc containing the wafer pocket on the bottom is mounted to the polishing head. The disc is grooved to improve slurry flow towards the wafer pocket. The applied load on the wafer is controlled by adding a specific weight on top of the polishing head. Because we use delicate 250 µm thick fused quartz substrates they are wax mounted onto a 2″ silicon wafer. A thin (2–3 µm) wax films ensure the necessary planarity of the configuration. The wafer/substrate pocket depth is designed to project the chips' surface 4 mil above the polishing head underside (Figure 5).

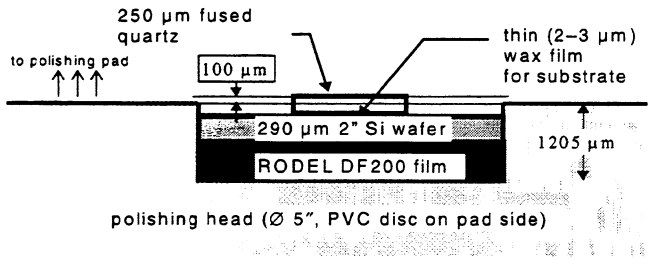

Figure 5 Schematic view of wafer pocket with wax mounting of substrate

The wafer pocket is backed by a soft buffed poromeric self-adhesive film [12] for reasons of reducing pocket surface roughness and therefore unifying load distribution onto the wafer / substrate combination. The polishing head is driven by an electric motor, its speed is adjusted according to the polishing pad speed to ensure constant relative velocity for all points of the wafer [7].

We chose a similar configuration as investigated in [6] for pocket geometry, polishing pad and slurry [12]. The IC-1000 is a hard polishing pad and exhibits greater

planarization capabilities than softer pads [6]. Slurry feed is automated by a membrane dose pump. All CMP relevant process data can be found in Table 1.

polishing head		polishing pad		slurry	
size	Ø 5″	brand	RODEL IC-1000	brand	RODEL ILD-1200
pocket size	Ø 2″	material	perforated polyurethane with soft backing	pH	11.0
wafer projection	4 mil			specific gravity	1.08
rotation speed	60 rpm	pad velocity	0.96 m/sec (60 rpm)	abrasive	silica
position	center of pad radius	size	Ø 12″	mean particle size	Ø 140 nm
sweep arm	frequency 0.1 Hz amplitude ± 2 cm	compressibility	5 %	flow rate	6 ml/min
		specific gravity	0.6–0.8	silica concentration (dilution with H_2O)	3 % weight
applied load	55 N	surface roughness	12 µm rms		
wafer backing	RODEL DF200 film	removal rate	12 nm/min		

Table 1 Summary of current CMP process data

V. CMP RESULTS

We observed no negative influence of the non-cleanroom surrounding of our CMP assembly. This can partly be explained by careful cleaning procedures, which include the storage of polishing pad and head in containers and thorough H_2O rinsing of all parts prior to CMP. We believe that the conditioning of pad surface with H_2O and the slurry also has a cleaning effect. The very small number (< 10) of microscopical scratches result from broken away material at edge of the fused quartz substrates. As a result only a few devices (of 248) on the chip actually become useless through scratching, because most of the scratches only extend 2–3 mm from the edge.

This area of the chip cannot be used anyway, because in this edge region the removal rate of the dielectric is much higher than the remainder of the chip. This effect is actually common to CMP and is described in [6]. In order to compensate for loss of chip area through this edge exclusion zone, we increased the diameter of our fused quartz substrates from 22 to 25 mm.

The IC-1000 is conditioned after every polishing pass with a diamond conditioning head to ensure constant surface roughness, which is essential for constant planarization results.

Figure 6 shows the progress of planarization on trilayer-generated SiO_2 topography, and a typical planarization result is shown in Figure 7.

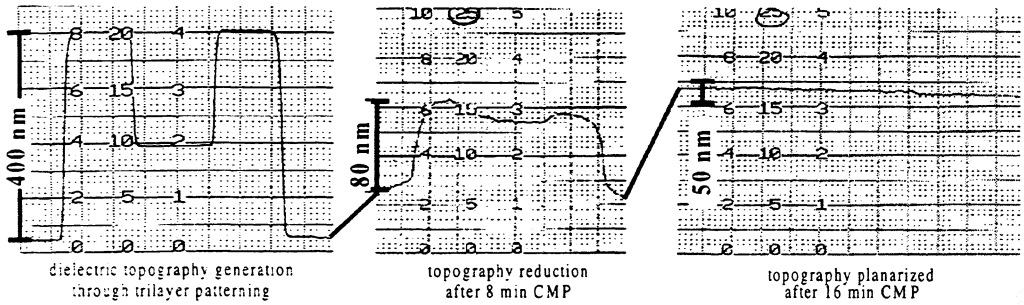

Figure 6 Profilometer scans of planarization progress (note: ordinate scale changes and is not absolute)

Another important observation we made is effect of planarization feature size dependency: The geometry of the individual waveguide mixer devices in our chip layout result to a higher SiO_2 planarization rate at the junction area (the tapered waveguide probes) than on the larger bondpads at the end of each device (Figure 7). Contact problems arising from this situation were solved by patterning windows into the dielectric on the bondpads.

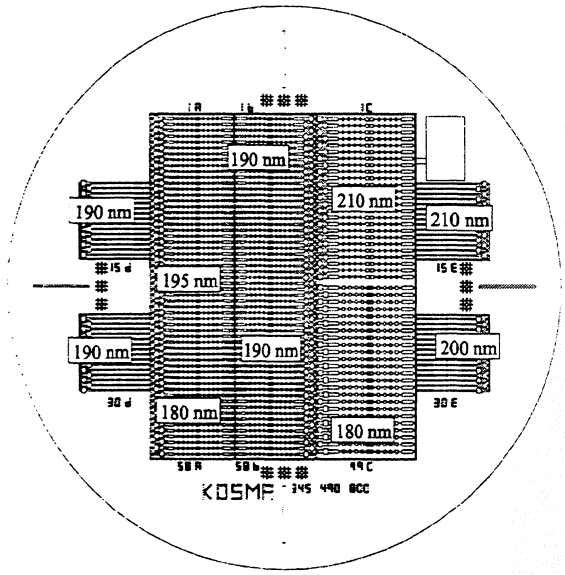

Figure 7 Typical global planarity result of CMP process on dielectric: ± 20 nm

Post-CMP cleaning is made by extending the CMP pass for another two minutes, with stopped slurry flow but generous H_2O rinsing of the polishing pad. The wafer/substrate combination is kept wet for transport into the cleanroom and then swabbed with H_2O and dried with IPA on a photoresist spinner.

VI. Investigation of EBL Defined Wiring Layer

Terahertz mixer circuits react very sensitive to misalignment of the integrated tuning structures relative to the SIS junctions. Typical tolerances of 1–2 μm in wiring positioning by optical mask-aligner tolerances are not tolerable for circuits working at these high frequencies. We therefore investigated EBL definition of the integrated

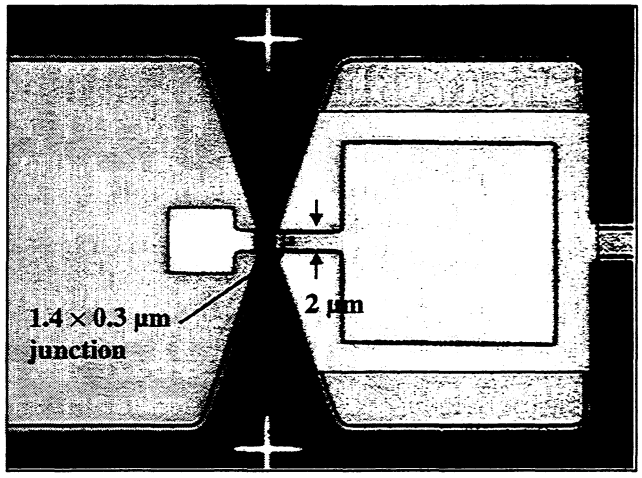

Figure 8 Photograph of a 800 GHz shorted stub tuning structure EBL patterned in photoresist prior to wiring layer deposition

tuning circuits, which allows a relative positioning accuracy of about 100 nm. This precision makes it possible to use tuning circuit designs which are even more critical in adjustment, such as rectangular junctions embedded in narrow tuning lines (Figure 8).

Another large advantage of EBL of tuning circuits is its flexibility. Changes in tuning designs can easily and fast be incorporated into the fabrication process, as there is no need to fabricate chrome masks for UV lithography.

EBL defined tuning structures could easily be integrated into our new EBL/CMP junction process scheme described earlier: After CMP the wafer is spin-coated with a 600 nm thick UV photoresist (AZ 5206, resolution 0.3 µm) and 10 nm copper is deposited on top for charge dissipation during EBL. The tuning structures are written with a beam current of 14.0 pA and a dose of 15 $\mu C/cm^2$ without any proximity effect corrections. After removal of the copper layer through an $FeCl_3$ solution etch, the photoresist is developed with AZ 400K (diluted 1:3 with H_2O).

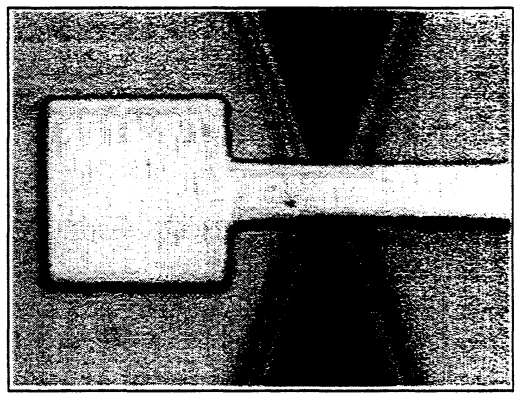

Figure 9 Close-up on waveguide feed of the same tuning structure depicted in Figure 8 after liftoff of 380 nm thick wiring layer

The wiring layers are then sputtered into these photoresist windows as a liftoff structure in the same manner as described previously for UV definition. Pattern alignment during wiring EBL is made with the same alignment marks as used for junction EBL.

Liftoff of the 380 nm thick wiring in the 600 nm thick photoresist produces very smooth edges (Figure 9). We attribute this to the fact that EBL intrinsically produces undercut photoresist sidewall profiles, because a large exposure contribution is made by backscattered secondary electrons from underneath.

VII. DC I/V ANALYSIS

Junction areas of square and rectangular shape ranging from 0.02 to 25 μm^2 were defined and their subgap leakage characteristics examined. The tuning structures were UV-lithographically and EBL defined for different parts of the chips in order to investigate possible adverse effects of wiring EBL on junction quality.

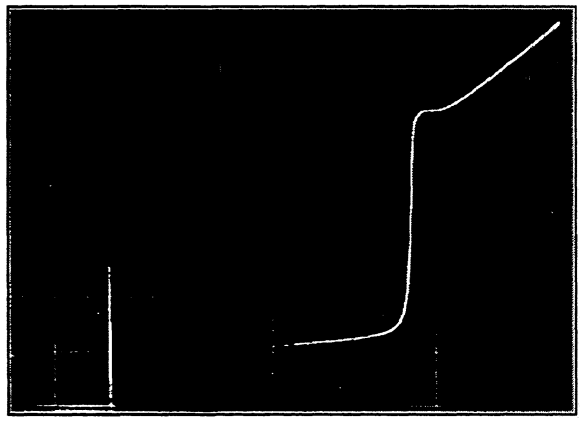

Figure 10 I/V-curve (0.5 mV/div, 5 μA/div) of a 0.1 μm^2 Nb/AlO_x/Nb SIS junction (J_c = 17 kA/cm^2, R_{subgap}/R_N = 18) with E-Beam defined wiring layer

To present date our I/V analysis data does not give clear indication that the junction barrier quality is deteriorated due to charge buildup during wiring EBL

All junctions, with areas from 0.1 μm to 0.6 μm analyzed, were fabricated with EBL wiring.

share of junctions with $R_{subgap}/R_N > 10$	share of junctions with $R_{subgap}/R_N > 15$	variation of junction area < 0.6 μm^2
84 %	**38 %**	**7 %**
80 junctions measured		20 junctions measured

Table 2 Junction process yield of one chip (all junctions measured have EBL wiring, J_c = 13 kA/cm^2)

The precision of area definition was calculated from the junction normal resistance variance, as it is not easy to measure such small area deviations in an optical microscope. The junction area variations are below 10 %.

CONCLUSION

It has been shown that a CMP process step in combination with EBL defined SIS junctions on thin fused quartz substrates for use in radioastronomical heterodyne waveguide mixers is feasible with off-the-shelf equipment. The approach of using an existing lapping machine with a simple polishing head and the "piggyback" mounting of fused quartz substrates on 2″ Si wafers delivers very promising first results. We are convinced that further evaluation of the process and more detailed investigation of all input variables will improve the global planarization results.

With R_{subgap}/R_N ratios well above 10 our new fabrication process delivers $Nb/AlO_x/Nb$ junctions with the same quality as with the present standard self-aligned liftoff junction fabrication, with highly reproducible junction areas as small as 0.2 μm^2.

EBL definition of the wiring layer does not noticeably deteriorate junction quality and will lead to an increased precision in alignment and definition of the integrated tuning circuits.

ACKNOWLEDGMENT

KOSMA Superconducting Devices and Mixer developments are supported by the Deutsche Forschungsgemeinschaft (DFG), grant SFB 301 and by the BMBF Verbundforschung Astronomie, grant 053KU3348.

We are grateful for Stephan Wulffs' assistance in all fabrication issues.

REFERENCES

[1] M. B. Ketchen, D. Pearson, A. W. Kleinsasser, C.-K. Hu, M. Smyth, J. Logan, K. Stawiasz, E. Baran, M. Jaso, T. Ross, K. Petrillo, M. Manny, S. Basavaiah, S. Brodsky, S. B. Kaplan, W. J. Gallagher, M. Bushan, "Sub-μm, planarized, Nb-AlO_x-Nb Josephson process for 125 mm wafers developed in partnership with Si technology", Appl. Phys. Lett., **59**, No. 20, pp. 2609–2611, 1991

[2] K. Fiegle, D. Diehl, and K. Jacobs, "Diffusion-cooled superconducting hot electron bolometer heterodyne mixer between 630 and 820 GHz", IEEE Trans. Appl. Superconductivity, pp. 3552–3555, 1997

[3] H. G. LeDuc, B. Bumble, S. R. Cypher, A. J. Judas, and J. A. Stern, "Sub Micron Area $Nb/AlO_x/Nb$ Tunnel Junctions for Submm Mixer Applications", Proc. 3rd Int. Symp. On Space THz Tech., Ann Arbor, 1992

[4] J. A. Stern, B. Bumble and H. G. LeDuc, "Fabrication and DC-Characterization of NbTiN based SIS Mixers for use between 600 and 1200 GHZ", Proc. 9th Int. Symp. On Space THz Tech., Pasadena, 1998

[5] Joseph M. Steigerwald, Shyam P. Murarka, Ronald J. Gutmann, *"Chemical Mechanical Planarization of Microelectronic Materials"*, John Wiley & Sons, Inc.: New York, 1996

[6] M. Bushan, R. Rouse, J. E. Lukens, "Chemical Mechanical Polishing in Semi-direct Contact Mode", J. Electrochem. Soc., to be released

[7] W. J. Patrick, W. L. Guthrie, C. L. Stanley, P. M. Schiable, "Application of Chemical Mechanical Polishing to the Fabrication of VLSI Circuit Interconnections", J. Electrochem. Soc., Vol. 138, No. 6, pp. 1778–1784, 1991

[8] J. Warnock, "A two-dimensional process model for chemimechanical polish planarization", J. Electrochem. Soc., Vol. 138, No. 8, 1991

[9] Z. Bao, M. Bushan, S. Han, J. E. Lukens, "Fabrication of High Quality, Deep-Submicron Nb/AlO_x/Nb Josephson Junctions Using Chemical Mechanical Polishing", Proc. Applied Superconductivity Electronics Conference, Boston, 1994

[10] CLARIANT GMBH, BUSINESS UNIT ELECTRONIC MATERIALS, Wiesbaden, Germany: AZ Series Photoresists and Developers

[11] LOGITECH, Glasgow, Scotland: PM4 Precision Lapping Machine

[12] RODEL CORP., Newark, Delaware: DF200 Films, IC-1000 polishing pads, ILD-1200 polishing slurry

[13] S. Wulff, private communication

A 550-GHZ DUAL POLARIZED QUASI-OPTICAL SIS MIXER

Goutam Chattopadhyay, David Miller, and Jonas Zmuidzinas

California Institute of Technology, 320-47, Pasadena, CA 91125, USA.

Henry G. LeDuc

Jet Propulsion Laboratory, 320-231, Pasadena, CA 91125, USA.

Abstract

We describe the design, fabrication, and the performance of a low-noise dual-polarized quasi-optical superconductor insulator superconductor (SIS) mixer at 550 GHz. The mixer utilizes a novel cross-slot antenna on a hyperhemispherical substrate lens, two junction tuning circuits, niobium trilayer junctions, and an IF circuit containing a lumped element 180° hybrid. The antenna consists of an orthogonal pair of twin-slot antennas, and has four feed points, two for each polarization. Each feed point is coupled to a two-junction SIS mixer, and therefore, for each polarization there are two IF outputs and four junctions, for a total of eight junctions on the chip. Due to the mixer structure and the use of series bias of the junction pairs, it turns out that the two IF outputs for a given polarization are 180° out of phase, requiring a 180° hybrid to combine the IF outputs. The hybrid is implemented using a combination of lumped element/microstrip circuit located inside the mixer block. Fourier transform spectrometer (FTS) measurements of the mixer frequency response show good agreement with computer simulations. The measured co-polarized and cross-polarized patterns for both polarizations also agree well with the theoretical predictions. The noise performance of the dual polarized mixer is excellent, giving uncorrected receiver noise temperature of better than 115K (DSB) at 528 GHz for both the polarizations.

I. Introduction

Dramatic advances in millimeter and submillimeter wave receivers in recent years have resulted from the development of sensitive superconductor insulator superconductor (SIS) mixers, which now offer unsurpassed performance from 70 GHz to 1 THz. In principle, the sensitivity of SIS mixers is limited only by the zero-point quantum fluctuations of the electro-magnetic field. In terms of the single-sideband (SSB) noise temperature, this limit is $h\nu/k_B \approx 0.05$ K/GHz. In practice, the SSB noise temperatures of the best SIS receivers now fall below 0.5 K/GHz over the 100-700 GHz band, dropping as low as 0.2 K/GHz in some cases. One should note that 0.5 K/GHz is about the level of performance of HEMT amplifiers in the 30 GHz band. SIS mixers have improved to the point that optical elements such as the cryostat vacuum window and the LO injection beamsplitter often contribute a significant fraction of the receiver noise.

One way to increase the sensitivity of SIS receivers further is to use a dual polarized receiver. When both polarizations are received simultaneously, there is a $\sqrt{2}$ improvement in signal to noise (S/N) or a factor of two reduction in observing time. Dual polarization operation can be achieved by using a wire grid polarizer to split the telescope beam into two polarizations. The local oscillator (LO) can be injected using a beamsplitter, either

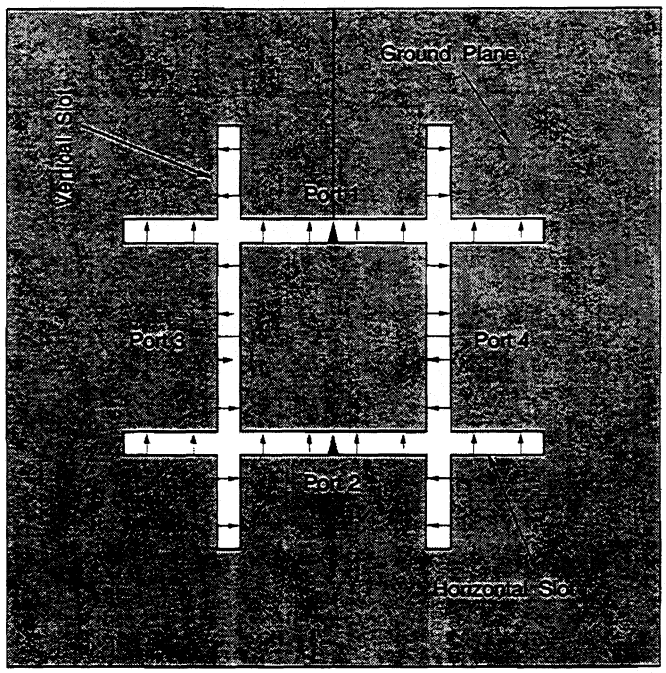

Fig. 1. Cross-slot antenna structure showing the field distribution in the slots when the two horizontal slots are excited symmetrically.

after the polarizer, in which case two beamsplitters are necessary; or before the polarizer, necessitating a single, correctly oriented beamsplitter. Either approach tends to lead to fairly complicated optical designs, especially for receivers with multiple bands. A much more elegant and compact solution is to directly construct a dual-polarization mixer. This is reasonably straightforward for quasi-optical designs, since the receiving antenna is lithographically fabricated, and can be designed to receive both polarizations simultaneously. The slot-ring mixer is one such example where a single annular (circular or square-shaped) slot is used, which is fed at two points which are 90° apart, and which has been shown to provide good results at 94 GHz [1]. A slot-ring antenna could easily be adapted for use in a SIS mixer. One drawback for this antenna is that it has a broader radiation pattern (in angle) than the twin-slot antenna [2]. This is simply due to the fact that at any given frequency, the transverse dimensions of a slot-ring are smaller than those of a twin-slot. This broader pattern of the slot-ring will be somewhat more difficult to couple to, so the efficiency will be a bit lower than for a twin-slot.

However, we adapted the twin-slot antenna for dual-polarization simply by crossing two sets of slots at 90°, as shown in Fig. 1. In this case, there are four feed points as can be seen in the figure. The field distribution in the slots can be intuitively obtained from symmetry considerations. In particular, the field distributions in the vertical slots must be antisymmetric and, therefore, the voltage at the orthogonal ports (3,4) must vanish. The characteristics of the cross-slot antenna have been calculated using the method of moments

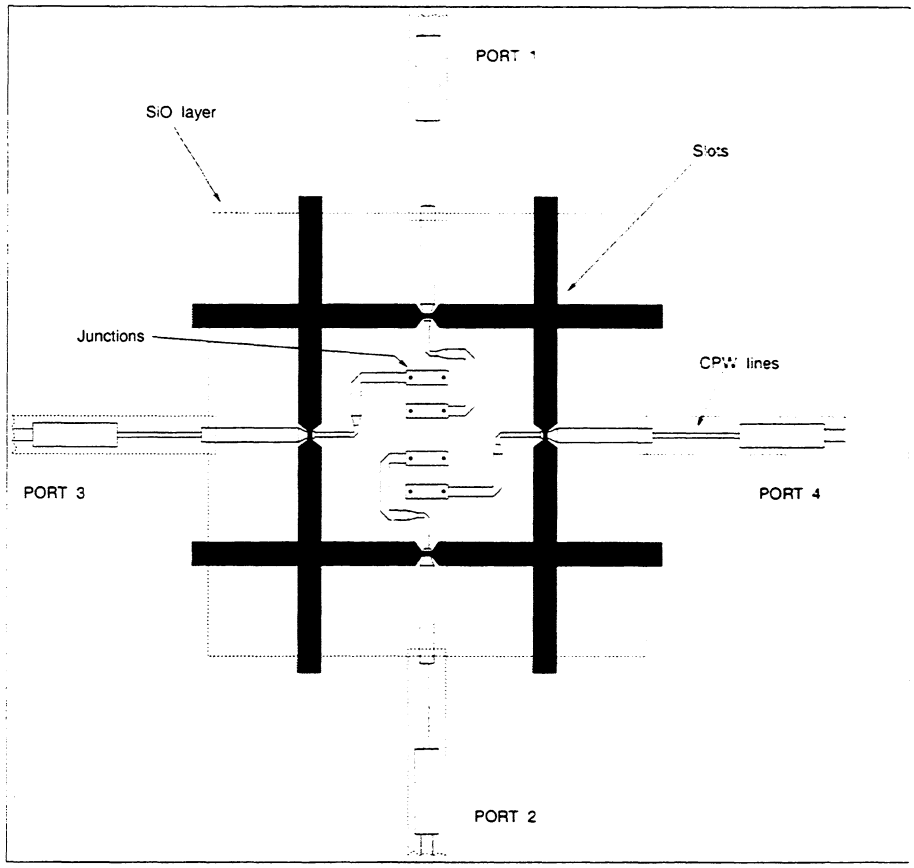

Fig. 2. Details of the mixer layout. CPW lines carry the IF output to the 180° hybrid. The junctions are placed as shown to allow suppression of the Josephson effect with a single magnet.

(MoM), and this design was found to have an excellent radiation pattern with fairly symmetric E-plane and H-plane beams, low impedance, wide bandwidth, low cross polarization, and high coupling efficiency [3].

II. Mixer Design and Fabrication

To design an SIS mixer using the crossed-slot antenna, the easiest method would be to couple a separate tuned SIS circuit to each of the four ports. One possible concern in this approach would be that the resonant frequencies of the four SIS circuits might not all be the same, which would lead to degraded cross-polarization, and inferior performance overall. To minimize this effect, we decided to use tuning circuits in which the junction *separation* dictates the tuning inductance. The four SIS circuits are combined into the two horizontal and vertical polarization outputs simply by biasing in series from IF port 1 to 2, and from 3 to 4. This also eliminates the necessity of attaching an electrical connection to the isolated

ground plane in the center of the cross-slot. Fig. 2 shows the details of the mixer layout. The mixer tuning circuit design is quite similar to twin-slot mixer described by Zmuidzinas *et al.* [5]. The two section microstrip transformer, shown in Fig. 2, allows a good impedance match between the antenna ($\approx 30\ \Omega$) and the tunnel junctions ($\approx 7\ \Omega$). The relatively low antenna impedance promotes good matching to even low resistance tunnel junctions. We used a simulation program, developed in house [6], to simulate and optimize the RF device performance. We used JPL's all optical-lithography junction fabrication process to fabricate junctions with three different junction areas $1.44\,\mu m^2$, $1.69\,\mu m^2$, and $1.96\,\mu m^2$. Though the design was optimized for $1.69\,\mu m^2$ area junctions, we decided to fabricate three different junction area devices to allow for process variations. We used a three mask level Nb/Al-Oxide/Nb junction fabrication with a 2000 Å thick niobium ground plane, 2500 Å thick niobium wiring layer and a single layer of 2000 Å thick SiO which is used as the dielectric for the superconducting microstrip line. The SIS mixer chip is placed on a hyperhemispherical silicon substrate lens. It can be seen from Fig. 2 that for each polarization there are two IF outputs and four SIS junctions, for a total of eight junctions on the chip. In principle, single junction mixers could also be used, which would require only four junctions per chip.

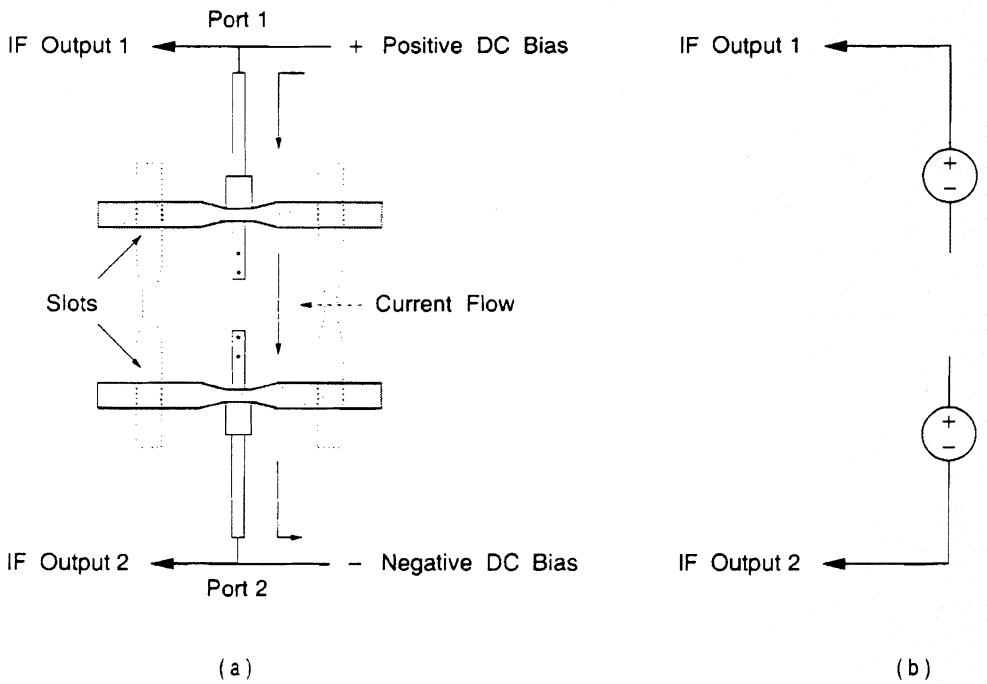

Fig. 3. Schematic showing how the two IF outputs for a given polarization are 180° out of phase : (a) shows the current flow for biasing the junctions in series and (b) shows the equivalent circuit.

Due to the mixer structure and the series bias of the junction pairs, it turns out that the two IF outputs for a given polarization are 180° out of phase. This can be easily explained. For a given polarization (let's assume for the horizontal pair of slots), the LO and RF will

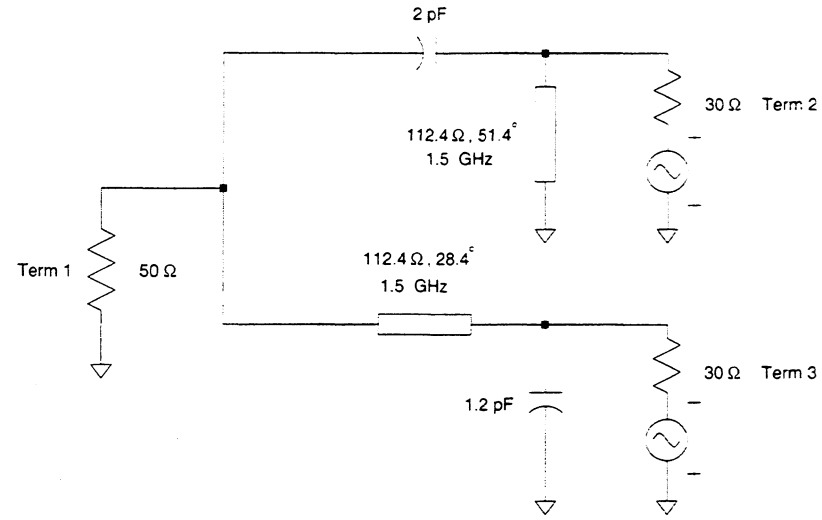

Fig. 4. Circuit diagram for the 180° hybrid.

have the same relative phase at either port (1 or 2), so we would expect the IF currents to be in phase. However, due to the series biasing of the junctions one junction pair is "forward" biased while the other is "reverse" biased. As shown in the equivalent circuit in Fig. 3(b), the two IF outputs are 180° out of phase and hence, a 180° hybrid is necessary to combine the IF outputs. The hybrid circuit is designed using a first order lowpass-highpass filter combination, whose bandwidth at 1.5 GHz center frequency is wide enough for our 500 MHz bandwidth HEMT amplifier. The hybrid is implemented using a combination of lumped element/microstrip circuit as shown in Fig. 4, and is located inside the mixer block. The circuit was optimized using Hewlett Packard's microwave design system (MDS) [7] to deliver maximum power to a 50 Ω load at terminal 1 (the LNA input impedance) from two 180° out of phase 30 Ω generators at terminals 2 and 3 (the SIS IF output impedance). We have measured the input reflection coefficient (S_{11}) of the lumped hybrid IF circuit at cryogenic temperatures to evaluate its performance and to verify the design.

III. Receiver Configuration

A general view of the receiver configuration is shown in Fig. 5, specific modifications for single and dual-polarization measurements will follow in the next section. The LO used is a tunable Gunn oscillator with a varactor multiplier [8], [9]. The RF signal and the LO inputs pass through a 10 μm thick mylar beamsplitter and the combined signal travel into the cryostat through a 3.8 mm thick crystal quartz pressure window at room temperature, followed by a 0.1 mm thick Zitex [10] IR filter at 77 K. Inside the cryostat the well-collimated ($\approx F/17$) beam is matched to the broad beam pattern of the cross-slot antenna with a polyethylene lens and a silicon hyperhemisphere lens with anti-reflection (AR) coating of alumina-loaded epoxy [5], [11]. The quartz pressure window is AR coated with Teflon.

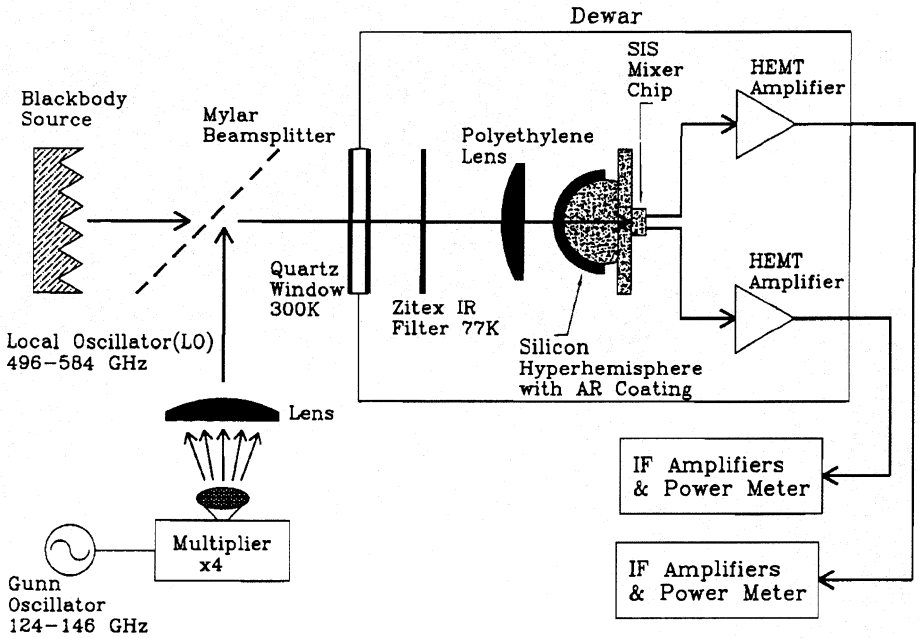

Fig. 5. Simplified receiver layout. The elements within the dewar are mounted on a 4.2 K cold plate.

For the dual-polarization mixer, we used our existing single polarization mixer block, described in detail by Gaidis *et al.* [12], with some minor modifications, such as another SMA connector to bring out two IF outputs for the two polarizations. Fig. 6 presents a detailed view of the mixer block and the associated circuitry. Fig. 6(a) shows a disassembled block with the mixer chip at the center. Fig. 6(b) shows the hardware details for the mixer block and Fig. 6(c) shows the bias and IF circuitry. The back side of the SIS mixer chip is glued [13] to one side of a silicon support disk, and the silicon hyperhemisphere is glued [13] to the opposite side of the disk. The SIS devices are fabricated on a 0.25 mm thick, 50 mm diameter silicon wafer, which is then diced into 2.0 x 2.0 mm individual chips. The high resistivity ($> 1000\ \Omega$-cm) silicon support disk is 2.5 cm in diameter and 1.0 mm thick. The silicon hyperhemisphere is similar to the one described by Gaidis *et al.* [12].

The silicon disk is clamped in the mixer block by a printed circuit board, which itself is held in place by metal clamps and screws as shown in Fig. 6(a). The circuit board is 0.64 mm thick TMM6 temperature stable microwave laminate from Rogers corporation [14], with room temperature dielectric constant 6.0.

DC bias supply and readout leads enter from the multi-pin connector on the right, and the mixer outputs, after being combined by the 180° hybrids, are carried on two different microstrip lines to SMA connectors on the left. The schematic in Fig. 6(c) details the circuitry on the printed circuit board. The dc bias source resistance is adjustable by feedback to present the mixer with either a current source or a voltage source. Resistor R_{neg} is chosen at approximately 100 Ω to prevent unstable biasing due to regions of negative dynamic resis-

tance in the SIS I-V curve. The current-sensing resistor R_{sense} is 10 Ω. and the IF-blocking spiral inductors (17 nH) at liquid helium temperature (4.2 K) add $\ll 1$ Ω series resistance. The 150 pF dc blocking capacitors in Fig. 6(c) are attached to the IF output microstrips with silver-loaded epoxy. The chip inductors are wire-bonded to the top electrodes of the 150 pF bypass capacitors. The SIS mixer chip sits within a through hole at the center of the board, allowing straight forward wire-bonding of the mixer chip to the biasing network and to the 180° hybrid circuits. The remaining chip resistors. chip capacitors. and connector pins are attached to the circuit board traces with either solder or silver-loaded epoxy.

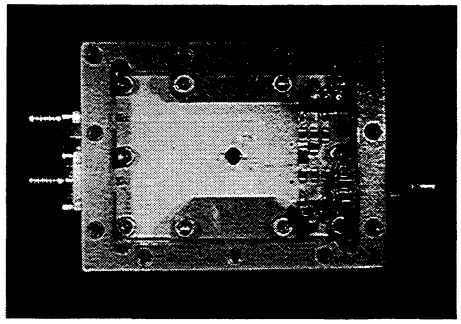

(a)

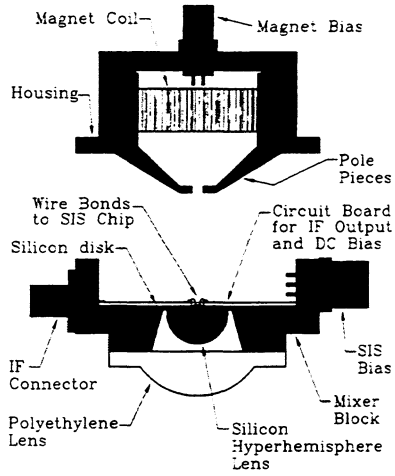

(b)

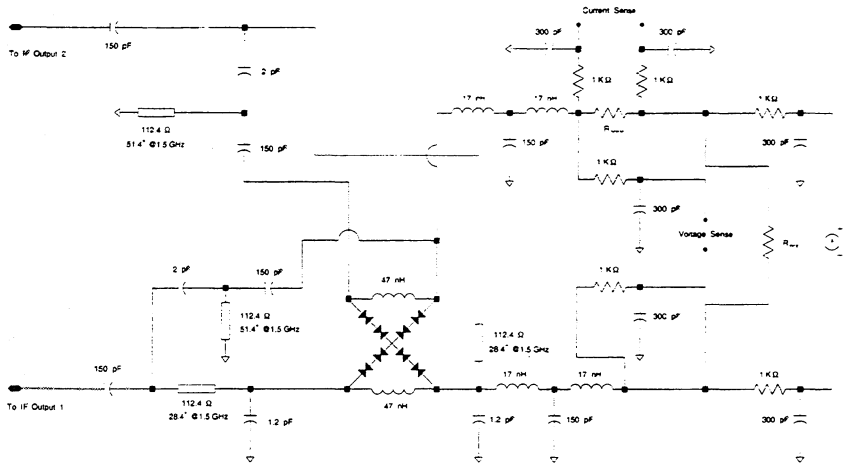

(c)

Fig. 6. Details of the mixer block and associated circuitry : (a) shows the block revealing the internal components, (b) provides a key to the hardware used within the block. (c) shows the details of biasing circuit along with the components on the printed circuit board.

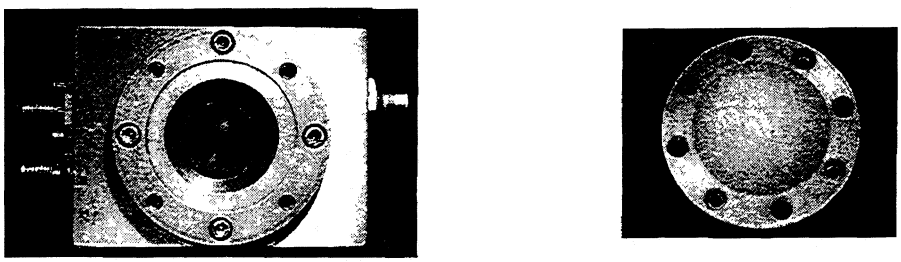

Fig. 7. Actual picture of an assembled block, with the polyethylene lens removed to show the AR coated silicon hyperhemisphere.

The picture in Fig. 7 shows the assembled mixer block. with the polyethylene lens removed to reveal the silicon hyperhemispherical lens. Semi-rigid coaxial cables connect the SMA ports with HEMT low noise amplifiers (LNAs). The measurements presented below were obtained using a 1.0-2.0 GHz LNA with measured noise temperatures of 5 K [15]. The LNA outputs are sent to room temperature amplifiers and diode detectors which measure the total power in 500 MHz IF bandwidth.

IV. Measurement and Results

A. Antenna Beam Pattern Measurements

The beam pattern of the dual polarized antenna was measured with an antenna measurement system built in-house [16]. The test setup consists of an aperture limited chopped hot-cold load on a x-z linear stage, stepper motors to drive the linear stage, a lock-in amplifier, and a data acquisition system. The IF output of the mixer is detected and amplified in a total power box and is fed in to the lock-in amplifier. The hot-cold load linear stage was placed at 24 cm away from the cryostat vacuum window for our beam pattern measurement. The hot-cold load aperture was set at 3.2 mm and the lock-in amplifier time constant was set at 3 seconds, giving signal to noise of about 18 dB for the measurement set-up. The mixer was pumped with a 528 GHz LO source. The hot-cold RF signal and the LO were coupled to the junction through a 10 μm thick beamsplitter. Fig. 8 shows the co-polarized beam pattern along with E-plane and H-plane cuts for the horizontal pair of slots and Fig. 9 shows the same for the vertical pair of slots. The E-plane beam is wider than the H-plane beam (as is expected) for both the polarizations. For the horizontal slots, the E-plane and H-plane FWHM was found to be 18.5 mm and 14 mm respectively, giving E/H ratio of 1.3, which is higher than our theoretical prediction of 1.1. The discrepancy between the measured and the calculated beam asymmetry may be a result of distortion of the shape of the plastic lens at liquid helium temperature (4.2 K). We are currently investigating this possibility. Similarly, for the vertical slots, the E-plane and H-plane FWHM was found to be 18 mm and 13 mm respectively. For cross polarization measurement we used a wire grid polarizer in front of the cryostat window. The hot-cold load aperture was set at 6.4 mm and the lock-in amplifier time constant was set at 10 seconds, which improved the signal to noise to about 28 dB. The cross polarization beam pattern is shown in Fig. 10. It can be seen from the cross polarization beam pattern that the cross polarization is indeed low as predicted by MoM calculations [3].

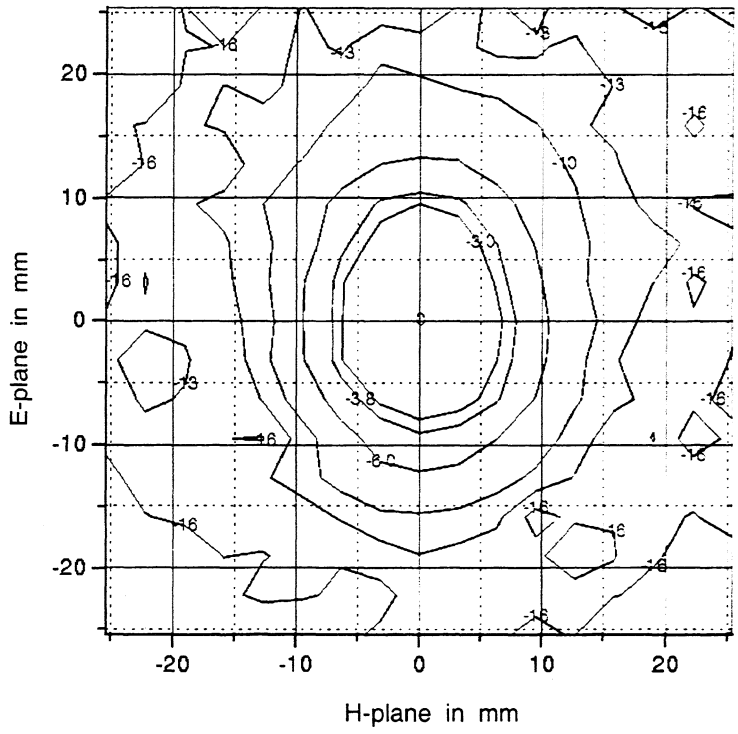

(a)

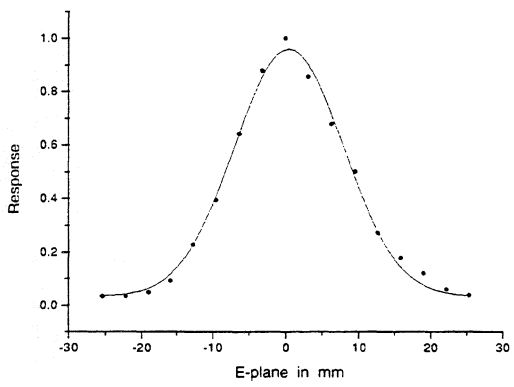

(b)

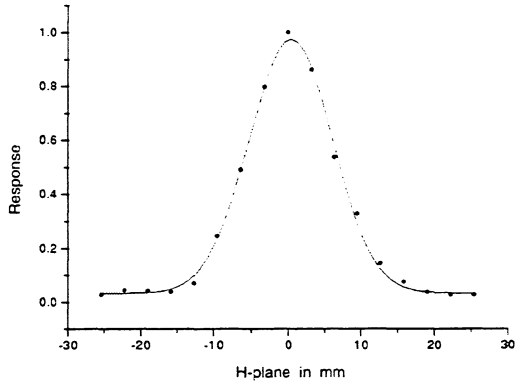

(c)

Fig. 8. Antenna beam pattern for the horizontal pair of slots : (a) shows the contour plot, (b) and (c) are the E-plane and H-plane cuts for the beam. The LO frequency for the beam pattern measurement was set at 528 GHz.

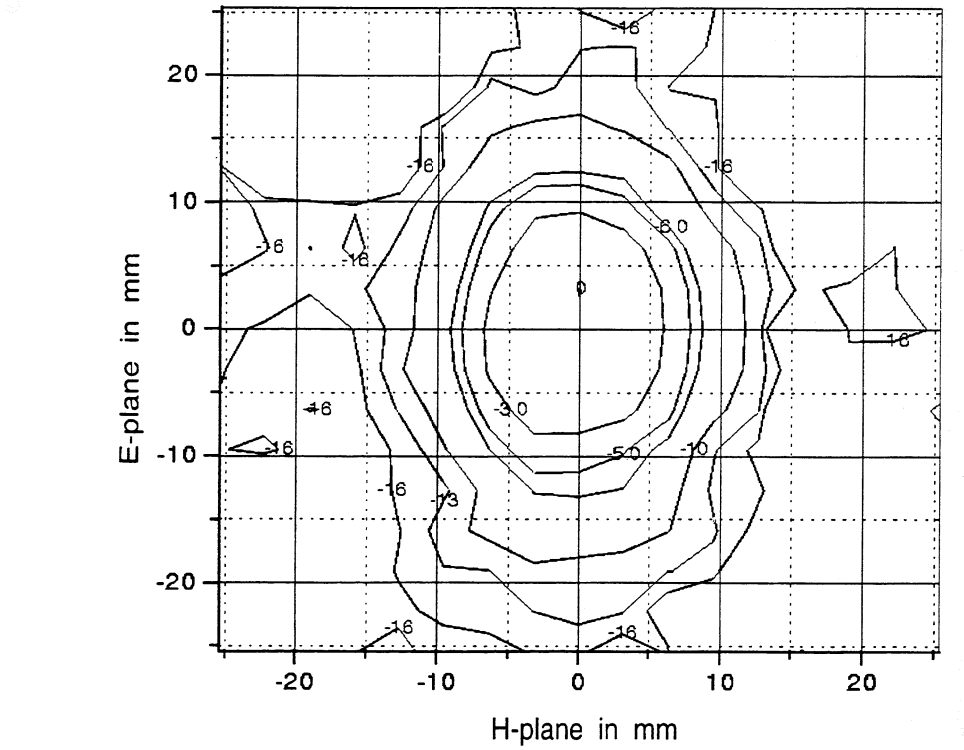

(a)

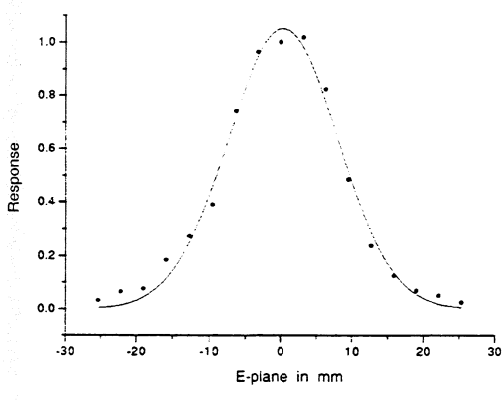

(b)

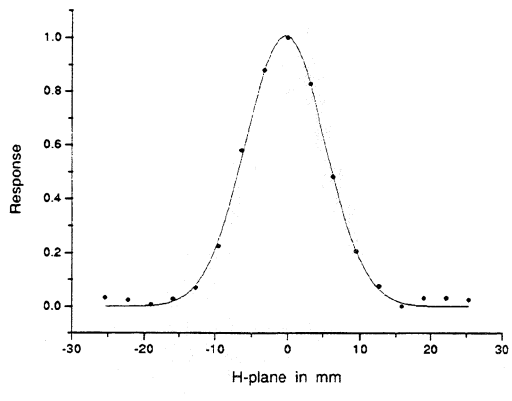

(c)

Fig. 9. Antenna beam pattern for the vertical pair of slots : (a) shows the contour plot, (b) and (c) are the E-plane and H-plane cuts for the beam. The LO frequency for the beam pattern measurement was set at 528 GHz.

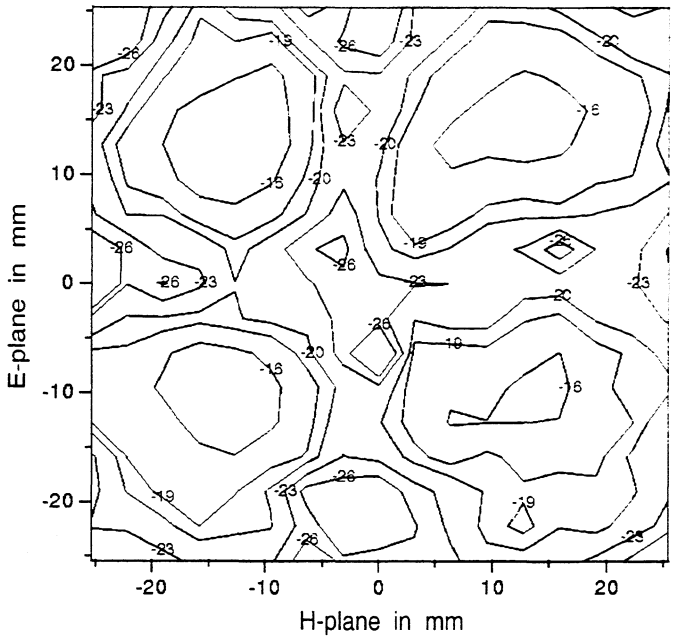

Fig. 10. Cross-polarization beam pattern in dB relative to peak co-polarized power. The LO frequency for the beam pattern measurement was set at 528 GHz.

B. Fourier Transform Spectroscopy

The receiver response as a function of frequency was measured with an FTS system built in-house using the mixer as a direct detector [17]. Although we can not measure the *absolute* response using the FTS, the *shape* of the relative response as a function of frequency is quite reliable and useful. Fig. 11 shows the FTS response for each polarization of the receiver. The device we used for this measurement was a $1.69\,\mu m^2$ area junction optimized for 550 GHz frequency band. The FTS response agrees well with our simulation results, as can be seen from Fig. 11. The dip around 550 GHz is due to the water absorption line, shown by the transmission graph. The FTS response is very similar for both the polarizations, and the peak response was found at 528 GHz, which means that the best noise temperature should be around that frequency.

C. Heterodyne Measurements

We measured the noise temperature of the receiver, for both the polarizations, first with one polarization active at a time, and then with both polarizations simultaneously active, using the Y-factor method. The cryostat temperature was 4.2 K for all the measurements. The noise temperatures reported here are referred to the input of the beamsplitter; *no corrections have been made for beamsplitter or any other optical losses.*

For measuring one polarization at a time, we mounted the device in such a way that the active pair of slots was horizontal with respect to Fig. 6(a) and biased only two of the ports

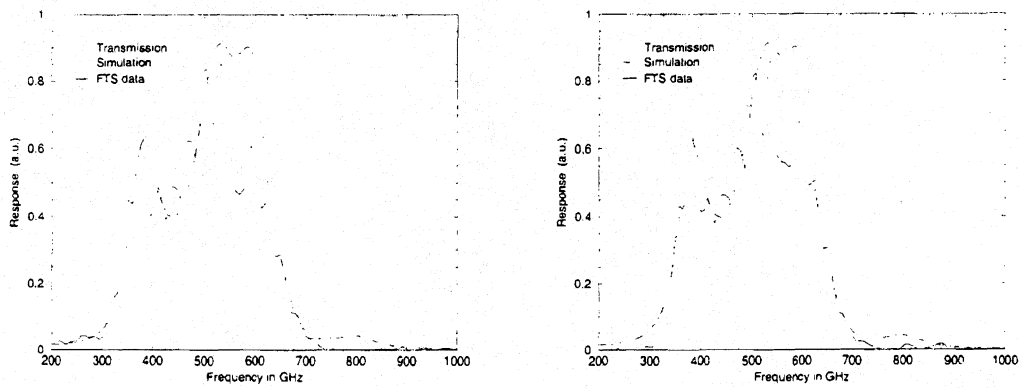

Fig. 11. FTS measured response (solid lines) versus mixer simulation (dashed lines) : (a) for the horizontal slots and (b) for the vertical slots. The dotted lines show the transmission for the instrument.

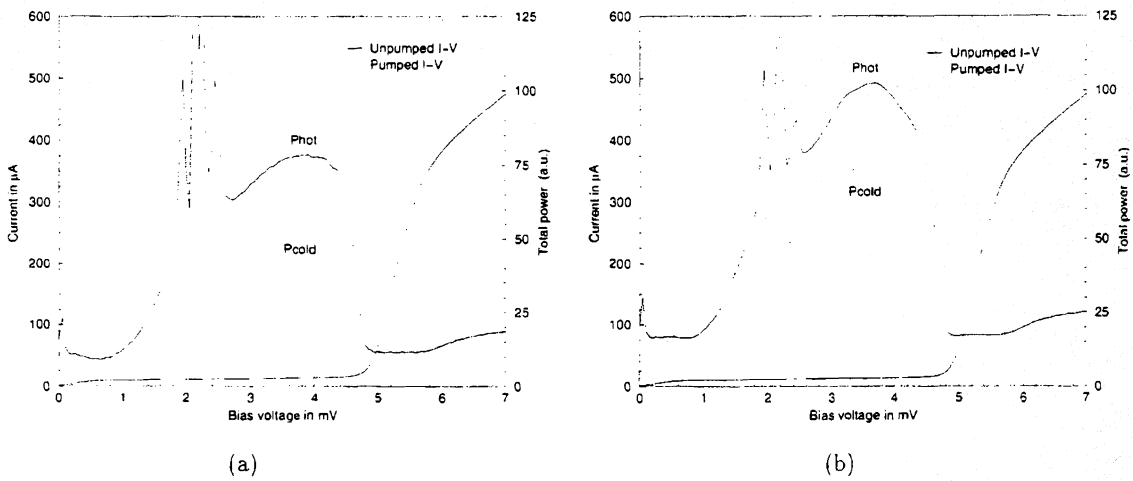

Fig. 12. Current and IF power versus bias voltage at 4.2 K : (a) for the horizontal polarization and (b) for the vertical polarization. The LO frequency for both of them is 528 GHz and the measured DSB receiver noise temperatures are 145 K.

at a time (1,2 or 3,4) in series. The correctly polarized LO pumped only four junctions for the active polarization. Fig. 12 shows the d-c current voltage characteristics for the "horizontal" and the "vertical" pair of slots. The pumped and unpumped I-V curves clearly show the photon step around $V \approx 1.4$ mV, as expected from a 528 GHz LO source ($h\nu/e \approx 2.2$ mV, since the junctions are in series, the gap voltage is at 5.8 mV and the photon step will appear at 5.8 mV - 2 x 2.2 mV = 1.4 mV). Also shown in Fig. 12 are the total IF output power in a 500 MHz bandwidth when hot and cold loads (absorber at room temperature and at 80 K respectively) are placed at the receiver input. The curves for both the polarizations are relatively smooth, in spite of the fact that four junctions were under a single magnet,

indicating good suppression of Josephson noise. At 528 GHz the best DSB noise temperature was measured to be 145 K for both the polarizations. We also measured noise temperatures at frequencies from 512 GHz to 580 GHz, and found that the results closely follow the FTS response, giving close to the best noise temperature near 528 GHz, getting worse near the water absorption line and getting better again towards the 570 GHz range.

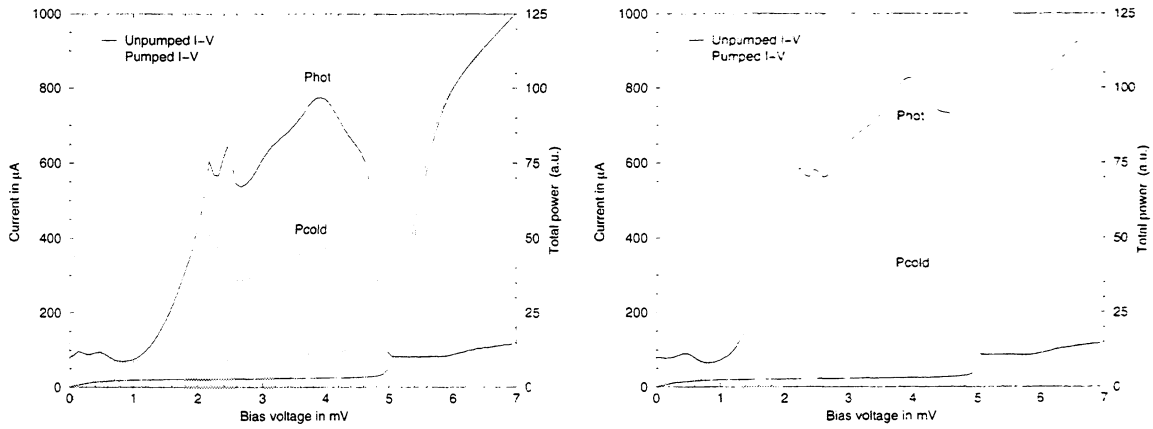

Fig. 13. Current and IF power versus bias voltage at 4.2 K when we measured both the polarizations simultaneously : (a) for the "horizontal" polarization and (b) for the "vertical" polarization. The LO frequency for both of them is 528 GHz and the measured DSB receiver noise temperatures are 115 K.

For measuring noise temperature for both the polarizations at once, we mounted the device at 45° angle with respect to the horizontal microstrip line shown in Fig. 6(a). The junctions are biased as shown in Fig. 6(c), where the IF outputs of the two different polarizations are isolated from each other by two 45 nH spiral inductors. A single LO source pumped the junctions for both the polarizations simultaneously. We confirmed that we indeed were measuring two orthogonal polarizations at the same time by using a wire grid polarizer in between a cold load (80 K) and the beamsplitter input. As we rotated the wire-grid, the cold load became visible to one polarization and its IF output power went down while the IF output power for the other polarization went up as it could not see the cold load, confirming dual-polarization operation. We adjusted the LO and the magnet current to get a smooth IF output for both the polarizations and then measured the noise temperature. Fig. 13 shows the pumped and the unpumped I-V curves along with the IF outputs for hot and cold loads at 528 GHz. We measured DSB noise temperature of 115 K for both the polarizations at 528 GHz. The receiver noise temperature was also measured from 512 GHz to 580 GHz range and was found to be similar to the single polarization measurement.

V. Conclusion

We have designed, fabricated and measured a dual-polarized quasi-optical SIS receiver at 550 GHz using a cross-slot antenna structure on a anti-reflection coated hyperhemispherical silicon lens which gives excellent noise temperature performance (115 K DSB) for both the polarizations. The measured antenna radiation patterns agree reasonably well with theoretical predictions. We have shown that this receiver has almost identical performance for both the polarizations, and could be very effectively used for submillimeter radio astronomy observations. We think the improvement in the performance of the receiver would be possible if we integrate the 180° hybrid with the SIS chip. It is also possible to use this device as a balanced mixer and we will look into that in future.

Acknowledgments

This work was supported in part by NASA/JPL and its Center for Space Microelectronics Technology, by NASA grants NAG5–4890, NAGW–107, and NAG2–1068, by the NASA/USRA SOFIA instrument development program, and by the Caltech Submillimeter Observatory (NSF grant AST–9615025).

References

[1] S. Raman, and G. M. Rebeiz, "Single- and dual-polarized millimeter-wave slot-ring antennas," *IEEE Trans. Antennas Propagat.*, vol. AP-44, no. 11, pp. 1438-1444, November 1996.

[2] J. Zmuidzinas, and H. G. LeDuc, "Quasi-optical slot antenna SIS mixers," *IEEE Trans. Microwave Theory Tech.*, vol. MTT-40, no. 9, pp. 1797-1804, September 1992.

[3] G. Chattopadhyay, J. Zmuidzinas, "A dual-polarized slot antenna for millimeter waves," *IEEE Trans. Antennas Propagat.*, vol. AP-46, no. 5, pp. 736-737, May 1998.

[4] J. Zmuidzinas, H. G. LeDuc, J. A. Stern, and S. R. Cypher, "Two-junction tuning circuits for submillimeter SIS mixers," *IEEE Trans. Microwave Theory Tech.*, vol. MTT-42, no. 4, pp. 698-706, April 1994.

[5] J. Zmuidzinas, N. G. Ugras, D. Miller, M. C. Gaidis, H. G. LeDuc, and J. A. Stern, "Low-noise slot antenna SIS mixers," *IEEE Trans. Appl. Superconduct.*, vol. 5, pp. 3053-3056, 1995.

[6] M. Bin, "Low-noise THz Niobium SIS mixers," PhD Dissertation, California Institute of Technology, Pasadena, October 1996.

[7] Microwave Design Systems (MDS) version mds.07.10, Hewlett Packard Company, Test and Measurement Organization, Palo Alto, CA.

[8] J. E. Carlstrom, R. L. Plembeck, and D. D. Thornton, "A continuously tunable 65-115 GHz Gunn oscillator," *IEEE Trans. Microwave Theory Tech.*, vol. MTT-33, no. 7, pp. 610-619, July 1985.

[9] N. R. Erickson, "High efficiency submillimeter frequency multipliers," *1990 IEEE MTT-S Int'l Microwave Symp.*, pp. 1301, June 1990.

[10] *Zitex* - Norton Co. Wayne, NJ 201696-4700.

[11] Janos Technology, Inc., HCR #33, Box 25, Route 35, Townshend, VT 05353-7702.

[12] M. C. Gaidis, H. G. LeDuc, M. Bin, D. Miller, J. A. Stern, and J. Zmuidzinas, "Characterization of low-noise quasi-optical SIS mixers for the submillimeter band," *IEEE Trans. Microwave Theory Tech.*, vol. MTT-44, no. 7, pp. 1130-1139, July 1996.

[13] Litetak 3761 UV-curing adhesive, by Loctite Corp., Hartford, CT 06106.

[14] Rogers Corporation, Microwave Circuit Materials Division, 100 S. Roosevelt Ave., Chandler, AZ 85226.

[15] J. W. Kooi, California Institute of Technology, Pasadena, CA, *private communications.*

[16] David A. Miller, "Comparison between theory and measurement of beam patterns for double-slot quasi-optical SIS mixers," MSEE Dissertation, California State Polytechnic University, Pomona, May 1998.

[17] Q. Hu, C. A. Mears, P. L. Richards, and F. L. Lloyd, "Measurement of integrated tuning elements for SIS mixers," *Int. J. IR and MM Waves.*, vol. 9, pp. 303-320, 1988.

DC AND TERAHERTZ RESPONSE IN Nb SIS MIXERS WITH NbTiN STRIPLINES

B.D. Jackson[1,2], N.N. Iosad[1], B. Leone[1], J.R. Gao[2], T.M. Klapwijk[3]

W.M. Laauwen[2], G. de Lange[2], H. van de Stadt[2]

[1] *University of Groningen, Department of Applied Physics and Materials Science Centre, Nijenborgh 4.13, 9747 AG Groningen, The Netherlands*

[2] *Space Research Organization of the Netherlands, PO Box 800, 9700 AV Groningen, The Netherlands*

[3] *Delft University of Technology, Department of Applied Physics (DIMES) Lorentzweg 1, 2628 CJ Delft, The Netherlands*

Abstract

It is expected that the integration of NbTiN striplines with Nb-based SIS junctions will extend the range of operation of sensitive SIS mixers up to the energy gap of NbTiN (~ 1.2-1.25 THz) to meet the requirements of the HIFI instrument for the Far-Infrared Space Telescope (FIRST). We have fabricated prototype SIS waveguide mixers in which Nb/Al-AlO_x/Nb SIS junctions are integrated with NbTiN and Al wiring layers. DC current-voltage measurements of these devices show that the voltage gap is somewhat lower and the sub-gap current is somewhat higher for devices with two NbTiN wiring layers in comparison with those in which the top wiring layer is Al (V_{gap} = 2.7 mV vs. 2.8 mV, and $R_{2.0}/R_N$ ~ 32 vs. 35). Additionally, the gap voltage of the NbTiN stripline devices is further suppressed by the application of 890-1040 GHz local oscillator power during heterodyne measurements. These effects are attributed to the trapping of heat in the Nb junction electrodes due primarily to quasi-particle trapping at the Nb/NbTiN interface. FTS measurements result in what is believed to be the first reported observation of direct detection response in a NbTiN stripline device above 1.1 THz. From an analysis of the resonance frequencies of several devices, it appears that the frequency response of the NbTiN striplines is predicted reasonably well by the Mattis-Bardeen theory for the conductivity of a superconductor in the extreme anomalous limit. Furthermore, we present what is believed to be the first reported heterodyne measurements of NbTiN stripline devices in the 0.9-1 THz range. These measurements yield a receiver sensitivity of T_N = 830 K at 930 GHz at a bath temperature of 3.3 K, after correction for beamsplitter losses.

1. Introduction

The development of the Heterodyne Instrument for the Far-Infrared Space Telescope (HIFI) requires the development of SIS mixers with noise temperatures below 200 K (DSB) at 1 THz. According to Mattis-Bardeen theory [1], Nb striplines become lossy at frequencies above the Nb gap frequency (~ 680 GHz). Thus, the development of sensitive THz SIS mixers requires the use of novel stripline materials such as Al [2,3], NbN [4], or NbTiN [5,6,7]. To-date, the best results in this frequency range have been obtained with Nb SIS junctions in combination with Al striplines, with the best-reported sensitivity being $T_{N,\ uncorrected}$ = 840 K at 1042 GHz [3]. Although it has been predicted that this sensitivity could be enhanced by the use of junctions with a smaller sub-gap current [8], losses in the Al striplines are expected to limit the optimum noise temperature of this device geometry to T_N ~ 500-600 K [8,9]. A significant improvement upon these results likely requires the use of a low-loss superconducting stripline material with a frequency gap larger than 1.1-1.2 THz. In particular, it is hoped that the integration of NbTiN strip-lines with Nb-based SIS junctions will enable the development of low noise SIS receivers in the 0.8-1.2 THz frequency range. With this in mind, NbTiN films, which have been used for thin-film coated RF cavities for high-energy accelerators [5], have recently been introduced as a stripline material for SIS mixers [6,7,10].

In this paper we discuss the DC and RF properties of SIS mixers in which Nb junctions are integrated with either NbTiN striplines or a combination of NbTiN and Al striplines. First, an examination of their DC current-voltage characteristics allows us to evaluate the degree to which the trapping of heat in the Nb junction electrodes is a problem in these devices. Next, we present a comparison of the measured and predicted spectral response of several devices as one means of evaluating the behaviour of NbTiN as a stripline material at high frequencies. Additionally, we present what we believe to be the first reported high frequency (0.9-1 THz) heterodyne measurements of NbTiN stripline devices. Finally, we discuss the significance of these results in view of the ongoing work to develop sensitive SIS mixers for the 0.8-1.2 THz range.

2. Device Fabrication

As described in [10], Nb/Al-AlO_x/Nb junctions are integrated with NbTiN and Al striplines following a process similar to that previously developed for the fabrication of Al stripline devices [11]. Figure 1 shows the layer structure and the stripline geometry of the devices discussed in this paper. The devices are fabricated using a mask set that was originally designed for Nb and Al stripline devices in the 400-1200 GHz range. In this mask layout, the mixers are equally split between the end-loaded stripline geometry shown in Figure 1b and the ¼-λ stripline geometry shown in Figure 1c. Table 1 summarizes the layer parameters for the three fabrication runs from which devices are taken.

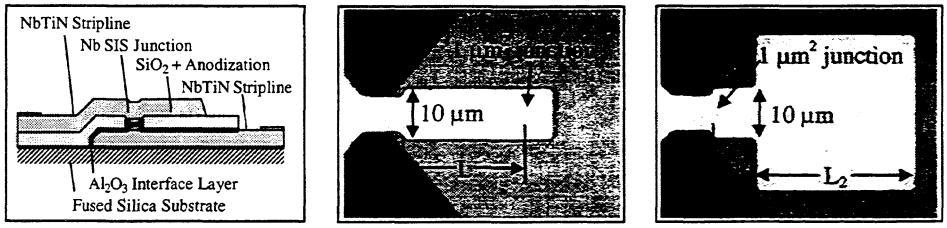

Figure 1 - a) device cross-section, b) optical microscope image of an end-loaded stripline device, where the stripline length is varied to obtain a range of resonant frequencies (L = 15-120 μm), c) optical microscope image of a ¼-λ stripline device, where L_1 and L_2 are varied to obtain a range of resonant frequencies (L_1 = 3-50 μm and L_2 = 20-75 μm).

Past work has shown that there is a strong inverse correlation between compressive stress and resistivity in NbTiN films deposited at room temperature [5,6,10]. Although films can be obtained with resistivities of ~ 80 μΩ·cm, their high compressive stress (> 2.5 GPa) precludes their integration with Nb SIS junctions. For this reason, the NbTiN films used here have a nominal resistivity of ~ 110 μΩ·cm, ~ 0.5 GPa of compressive stress, and a transition temperature of 14.4 K [10].

Table 1 - Layer parameters for the three fabrication runs

Batch	Bottom Wiring	Trilayer (*)	Dielectric	Top Wiring
A	260 nm NbTiN	23' x 10 mTorr O_2	250 nm SiO_2	400 nm NbTiN
B	300 nm NbTiN	23' x 10 mTorr O_2	250 nm SiO_2	250 nm Al + 100 nm Nb
C	280 nm NbTiN	20' x 6 mTorr O_2	250 nm SiO_2	400 nm NbTiN

*oxidation parameters only, trilayer = 90 nm Nb + 6 nm Al + oxidation + 90 nm Nb

3. Measurement Configuration

DC current-voltage characteristics are obtained at 4.2 K by 4-point dipstick measurements in a magnetic field for cancellation of the Josephson effect. Tuning the magnetic field allows the identification of resonant features in the sub-gap current at voltages corresponding to the resonant frequency of the junction plus microstrip tuning structure, according to the Josephson relation (484 GHz/mV).

After DC testing, the substrate is polished to 40-μm thickness for testing in a 1-THz waveguide mixer block with a 120 by 240 μm^2 waveguide and a 90 by 75 μm^2 substrate channel [2]. A 15 μm mylar beamsplitter is used to couple the local oscillator and blackbody signal power through a Teflon lens, a 100 μm Mylar window and a 200 μm quartz heat filter at 77 K. A diagonal horn is used to couple radiation into the waveguide and a contacting backshort is used as a mechanical tuning element. A Fourier transform spectrometer is used to measure the mixer bandwidth and centre frequency

with the junction operated as a direct detector. The heterodyne sensitivity of the receiver is measured using a standard 293-K / 77-K hot-cold measurement with a Carcinotron plus tripler as a local oscillator in the 840-930 GHz range and a BWO local oscillator in the 900-1100 GHz range.

4. Heating Effects in DC Current-Voltage Characteristics

Current-voltage characteristics of four "1-μm^2" junctions are shown in Figure 2 a-d, with the average device parameters for each batch summarized in Table 2. As can be seen in Figures 2a and 2b, the lower current-density devices (6.3-6.5 kA/cm^2) have a relatively small amount of sub-gap leakage current, with a sharp current rise at the gap voltage. Due to the higher current-density of devices from batch C (12 kA/cm^2), a significant amount of sub-gap leakage current is seen in the current-voltage characteristic in Figure 2c. The marked features in the sub-gap currents of the devices seen in Figures 2a-c are due to resonances of the junctions' AC Josephson radiation (484 GHz/mV) with

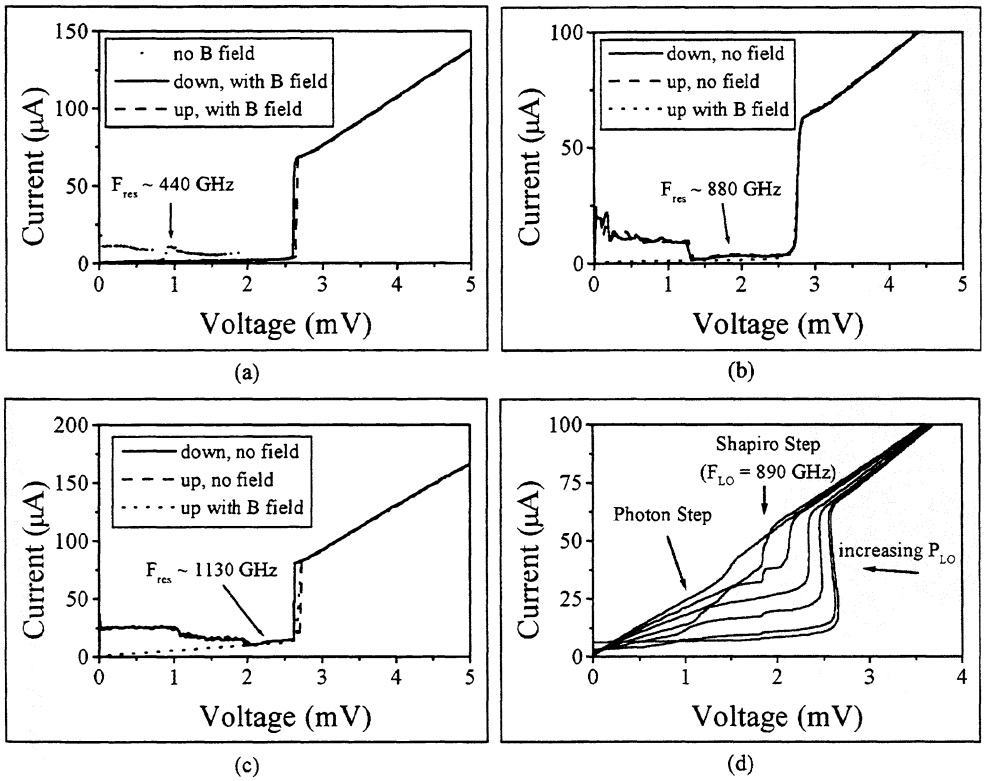

Figure 2 - sample I-V characteristics of four junctions (a-c in voltage-bias mode, d in current-bias mode): a) a 6.5 kA/cm^2, ¼-λ stripline device with two NbTiN wires, b) a 6.3 kA/cm^2 end-loaded stripline device with one NbTiN and one Al wire, c) a 12 kA/cm^2, end-loaded stripline device with two NbTiN wires, d) a 12 kA/cm^2, end-loaded device with NbTiN striplines mounted in the 1-THz mixer block: unpumped and with 6 increasing levels of 890 GHz local oscillator power. Note the decrease in V_{gap} and increase in $V_{photon\ step}$ with increasing LO power.

Table 2 - DC current-voltage characteristic summary

Batch	Wiring	V_{gap} (mV)	$R_n \cdot A$ ($\Omega \cdot \mu m^2$)	J_c (kA/cm^2)	A (μm^2)	$R_{2.0\,mV}/R_n$
A	NbTiN	2.65-2.72	32	6.5	0.9-1.0	~ 32
B	NbTiN - Al	2.68-2.81	35	6.3	0.6-0.9	~ 35
C	NbTiN	2.63-2.72	18	12	0.5-0.8	~ 10

the RF stripline structure. The correlation between the measured and predicted resonant frequencies will be discussed in more detail in section 5 of this paper.

From the data in Table 2, it is seen that the gap voltage and resistance ratio, $R_{2.0\,mV}/R_n$, are somewhat lower for devices with two NbTiN striplines, as compared with devices with one NbTiN and one Al stripline. Additionally, a significant amount of hysteresis can be seen at the gap voltage in devices with two NbTiN striplines (Figures 2a and 2c). These effects can be attributed to Joule heating of the junction electrodes, enhanced primarily by quasi-particle trapping at the Nb/NbTiN interfaces [12]. Further evidence of heating in junctions with two NbTiN wires is seen in Figure 2d, in which the current-voltage characteristics of a device mounted in the 1-THz mixer block are compared for a range of 890 GHz pumping powers. From this figure, it can be seen that the gap voltage decreases and the first photon step moves to higher voltages with increasing pump power.

Using the gap voltage to estimate the effective electron temperature in the Nb electrodes, it is possible to estimate the relationship between the junction temperature and the dissipated Joule power at the gap voltage for the unpumped and pumped current-voltage curves in Figure 2d. The calculated relationship between junction temperature and DC power is seen in Figure 3a. The observed back-bending in the unpumped curve is used to estimate the dependence of junction temperature on heating power by assuming that $V \sim V_{gap}(T)$ in the back-bending region. For each of the six pumped curves, a temperature is estimated from either the maximum voltage at the bottom of the gap (for the three curves in which back-bending is observed) or the point of maximum slope (for the remaining three curves). Comparing the estimated electron temperature versus DC power for the pumped and unpumped curves, it is clearly seen that the observed junction temperature can not be explained by Joule heating alone — RF power must also be dissipated in the junction. If the temperature is assumed to follow the approximately linear dependence on total power observed for the unpumped junction, it is possible to estimate the amount of dissipated RF power. In particular, for the third pumped curve in Figure 2d, it is estimated that, in addition to Joule heating, ~ 200 nW of RF power must be dissipated in the junction to raise the effective electron temperature to 6.5 K.

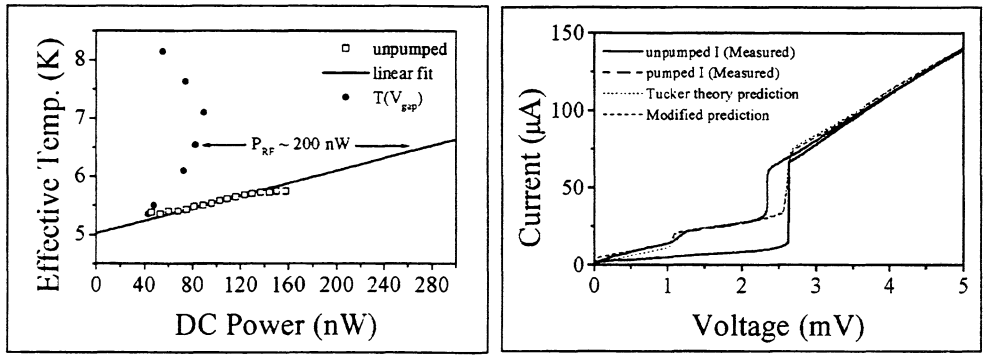

(a) (b)

Figure 3 - (a) Effective electron temperature versus DC power calculated from the pumped current-voltage curves in Figure 2d, using V_{gap} as a measure of temperature. The set of points for the unpumped curve is generated from the back-bending at the gap voltage by assuming that $V \sim V_{gap}(T)$ in this region. The temperatures of the pumped junctions are estimated using either the maximum voltage at the bottom of the gap (for curves with back-bending) or the point of maximum slope. (b) Results of a Tucker theory calculation to estimate the LO power needed to generate the measured pumped curve (third pumped curve from Figure 2d chosen due to the absence of a Shapiro step).

The estimated RF dissipation in the junction can be compared with the RF power needed to generate the measured photon-assisted tunneling current, using the RF voltage-match method [13] to determine the junction's embedding impedance and the Tucker theory [14] to calculate the pumped current-voltage curves. Figure 3b presents the measured and calculated pumped current-voltage curves for the third pumping level in Figure 2d (the only curve in which the Shapiro step is negligibly small). From this calculation, it is estimated that 180 nW of RF power is needed to generate the observed photon-assisted tunneling current. However, due to heating of the junction by the absorption of RF power, the observed current increase due to pumping is actually a sum of photon-assisted tunneling and an increase in the thermally generated quasi-particle current. This may explain why the calculated pumped curve under-estimates the current in the region below the photon step, as seen in Figure 3b. The correlation between the calculated and measured curves below the photon step is improved if 5 μA is added to the unpumped sub-gap current (6.5% of the current at the gap). In this case, the pumping power needed to match the measured and calculated curves is estimated as 150 nW. Thus, it can be said that the RF power contributing to the observed photon-assisted tunneling is ~ 150-180 nW, which is comparable to the estimated RF dissipation in the junction, 200 nW.

5. Measured and Predicted Spectral Response

Figures 4a-c present the measured FTS spectra for three NbTiN stripline devices operated in a direct detection mode. Also seen in these figures are the calculated spectral response and a description of the stripline geometry for each device. From Figures 4a and 4b it can be seen that the high-frequency end-loaded devices have broad tuned

bandwidths, with central frequencies of ~ 900 and 1000 GHz, fixed-tuned bandwidths as high as 100-120 GHz (Figure 4a), and significant responses up to 1150-1200 GHz (Figure 4b). To the best of our knowledge, this is the highest frequency at which a direct detection response has been reported in NbTiN stripline devices. As seen in Figure 4c,

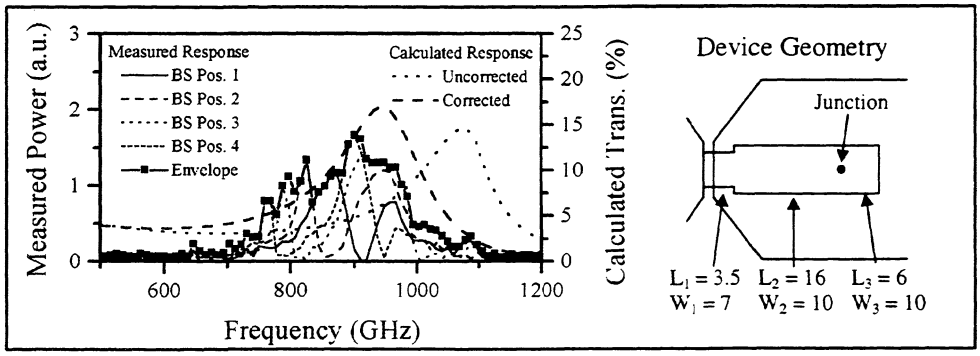

(a)

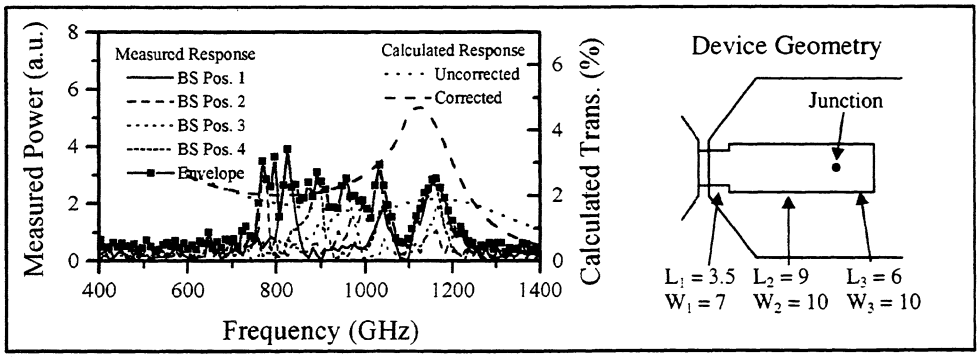

(b)

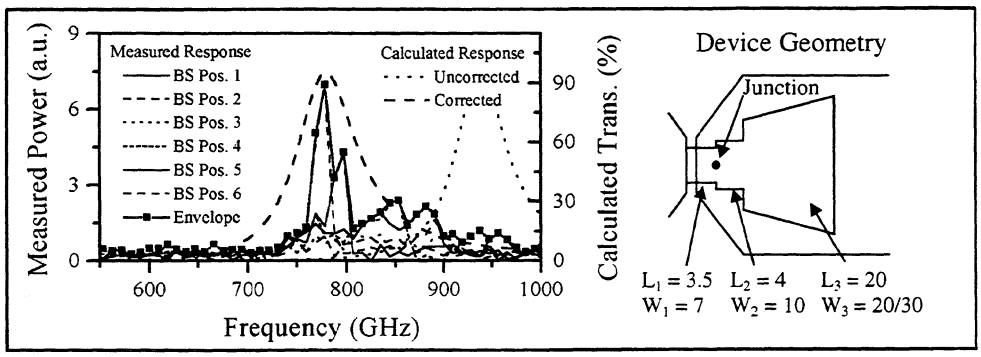

(c)

Figure 3 - Spectral response of three Nb SIS junctions integrated with NbTiN striplines. Seen here for each device are measured FTS spectra for a range of backshort positions, calculated resonance spectra for a match to a 50 Ω source impedance, and a sketch of the corresponding device geometry (all dimensions in μm). (a) response of an end-loaded stripline with a 0.6 μm^2, 6.5 kA/cm^2 junction, (b) response of an end-loaded stripline with a 0.6 μm^2, 6.5 kA/cm^2 junction, and (c) response of a ¼-λ stripline device with a 0.6 μm^2, 12 kA/cm^2 junction.

the ¼-λ stripline device has a much sharper spectral response than the measured end-loaded devices, with a peak frequency of 775 GHz and a fixed-tuned bandwidth of < 50 GHz. The cause of the dip observed at ~ 1100 GHz in Figure 4b is not known (the measurement is performed in a vacuum FTS to minimize absorption by water vapour). However, it may be a waveguide effect, possibly related to the fact that the substrate thickness is ~ ¼-λ at 1100 GHz.

Included in each of Figures 4a-c are two calculations of the predicted transmission of power to the junction from a 50 Ω source located at the input of the stripline. In all cases, the surface impedance of the NbTiN wiring layers is calculated using the local limit approximation for the surface impedance as a function of the frequency-dependent conductivity, σ_s. This conductivity is determined from the Mattis-Bardeen formulation for $\sigma_s = \sigma_1 - j\cdot\sigma_2$ in the extreme anomalous limit [1], using the previously measured parameters for our films ($\rho_{n.DC}$ ~ 110 μΩ·cm, T_c = 14.4 K [10]). The uncorrected transmission curve is calculated from the actual device geometry, and can be seen to predict, in each case, a resonance frequency significantly higher than the measured central frequency. The correlation between the measured and predicted spectra is significantly improved if an extra length of 3.7 μm is added to the stripline on each side of the junction, as seen from the "corrected" calculations in Figures 4a-c. This effect is seen to be particularly significant for the ¼-λ stripline device in Figure 4c, due to the low length-to-width ratio of the striplines in this structure. An examination of the sub-gap current resonances for a number of end-loaded and ¼-λ devices finds a similar correlation between the measured voltages and the resonant frequency predicted by the corrected calculation (for resonances from 350 GHz to 1100 GHz).

6. Heterodyne Response

Figure 5 shows the results of a hot/cold measurement of a NbTiN stripline device pumped at 930 GHz at a mixer block temperature of 4.5 K. To the best of our knowledge, this is the highest frequency at which heterodyne sensitivity in an SIS mixer with NbTiN striplines has been reported to-date. Figure 5a presents the pumped and unpumped current-voltage characteristics, together with the hot and cold IF output powers as a function of bias voltage. Figure 5b presents the corresponding Y-factor and uncorrected noise temperatures as a function of bias voltage. The measured device is a 0.6 μm^2, 12 kA/cm^2 junction with the same end-loaded stripline geometry as that seen in Figure 4a.

From Figure 5b, it is seen that the minimum receiver noise temperature calculated from the measured IF output powers is ~ 1000 K DSB. Correcting for loss in the 15-μm Mylar beamsplitter yields a corrected receiver noise temperature of ~ 900 K. However, because this sensitivity is calculated at 2.1-2.2 mV, in the region of the small side-peak in the IF output power, it is sensitive to averaging and small offsets between the hot and cold curves. A manually chopped hot-cold measurement at an optimum bias point

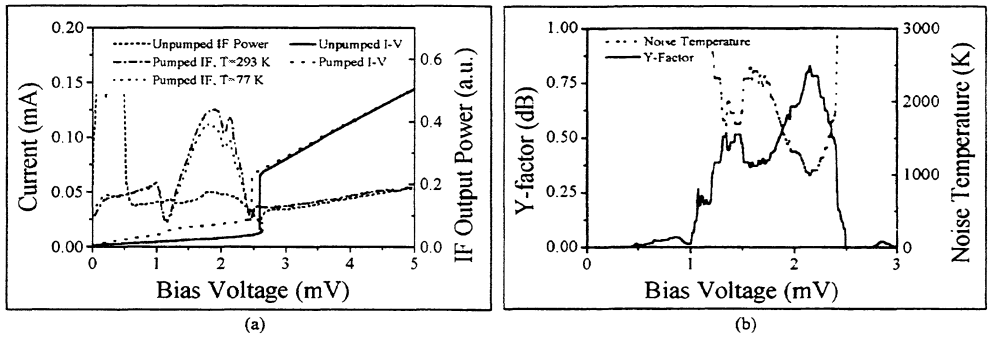

Figure 5 - Noise temperature measurements of a 12 kA/cm^2, end-loaded stripline device at 930 GHz and a mixer block temperature of 4.5 K. (a) unpumped and pumped current-voltage curves and IF output powers for a hot (293 K) and a cold (77 K) blackbody load. Note that the dip at 2-2.1 mV is too high in voltage to be due to a Shapiro step. (b) calculated Y-factor and noise temperature within the sub-gap region..

produces a Y-factor of 0.51 dB, which corresponds to a corrected noise temperature of 1540 K. Pumping on the helium bath is seen to improve the corrected noise temperature to 830 K at a mixer block temperature of 3.3 K, also for a manually chopped hot/cold measurement at a fixed bias point.

These receiver measurements are complicated by the already mentioned suppression of the gap voltage by Joule heating and the absorption of RF power. This effectively reduces the bias range available for high frequency measurements. Furthermore, an observed instability in the magnetic field needed to suppress the Josephson effect adds an additional degree of complication — at these frequencies the Shapiro step (at 2.07 mV/THz) lies in the centre of the already reduced bias range. As a result of these effects, it is not possible to produce reliable heterodyne measurement results at 1040 GHz for the device whose spectral response is seen in Figure 4b.

7. Discussion and Conclusions

It has been seen that the gap voltage of Nb junctions integrated with NbTiN striplines is suppressed by the trapping of Joule heat and absorbed local oscillator power. For a junction with a current density of 12 kA/cm^2, the unpumped gap voltage is 2.7 mV, while the application of 890 GHz local oscillator power further reduces the gap voltage to 2.3-2.4 mV for pumping levels typically used in a heterodyne experiment. This corresponds to effective electron temperatures of 5.2 K for the unpumped junction and ~ 6.5 K for the pumped junction. This large temperature difference can only be explained if ~ 200 nW of local oscillator power is dissipated in the pumped junction. Furthermore, from Tucker theory, it is estimated that 150-180 nW of local oscillator power are needed to generate the observed photon-assisted tunnelling. Although these estimates are not accurate enough to draw firm conclusions, the excess dissipated power could represent RF loss in the Nb electrodes due to the incident radiation being higher in frequency than

the Nb gap frequency. In a heterodyne measurement, such a loss would result in a reduction in device sensitivity for frequencies above ~ 700 GHz.

Heating of the Nb junctions by a combination of DC and RF power will affect mixer performance in at least three ways:

1. an increase in mixer noise due to an increase in the thermally generated sub-gap leakage current
2. a reduction in the maximum frequency which can be efficiently detected by the junction ($F_{max} \sim V_{gap} \cdot 484$ GHz/mV)
3. a reduction in the bias range available during receiver measurements due to the reduced gap voltage and increase in the voltage of the the first photon step from the negative branch of the I-V curve

The observed trapping of heat in the junction electrodes can be attributed primarily to quasi-particle trapping at the Nb/NbTiN interface. Because of this effect, heat may not escape the Nb electrodes through electron diffusion. Rather, heat must be transferred to the phonons in the Nb electrodes through the electron-phonon interaction. Heat may then be transferred to the NbTiN, and eventually the substrate, through phonon-phonon interactions. Further study is needed to identify the rate-limiting step(s) in this process, in order that the device geometry can be modified to reduce the observed heating effects. For example:

1. Replacing one NbTiN wire with Al will eliminate one trapping interface, at the cost of increased stripline losses.
2. The use of the recently introduced Nb/Al-AlN_x/NbTiN junction structure [15] will also eliminate one trapping interface.
3. If the barrier to heat transfer from NbTiN to the substrate (the Kapitza resistance) is high, an Al layer between the NbTiN and the substrate may enhance the cooling of phonons in the NbTiN.
4. The effect of THz radiation being absorbed in the Nb electrodes may be reduced by a change in the junction geometry to shorten the current path within the Nb.

As mentioned previously, the reduction of the available bias range is further complicated by the apparent instability of these devices with respect to the magnetic field needed to suppress the Josephson effect. This instability means that it is desirable to bias the device well away from the Shapiro step (at 2.08 mV/THz). However, this is difficult because in the frequency range of interest, around 1 THz, this voltage lies within the already reduced bias range. Although the cause of the observed instability has not been examined, it is thought that flux trapping within the NbTiN wires may be responsible.

The frequency response of Nb SIS junctions integrated with NbTiN striplines has been compared with model calculations to evaluate the high frequency behaviour of NbTiN. These measurements include the first reported measurements of direct detection response above 1.1 THz in devices with NbTiN striplines. The qualitative agreement between the measured and calculated central frequency for the end-loaded devices is generally good. This qualitative agreement is seen to break down for the higher frequency ¼-λ stripline devices, likely due to the small length-to-width ratios in the striplines in these devices. However, relatively good quantitative agreement for all devices can be obtained by the addition of an extra stripline length of 3.7 μm on each side of the junction. This extra length may approximate the effect of the discontinuity in width between the 1-μm junction and the 10-μm stripline. Thus, absolute confirmation of the high frequency properties of NbTiN striplines will require either the calculation of the two-dimensional current distribution in the stripline geometries used here, or the testing of new devices with geometries which are much less sensitive to the effects of discontinuities. In general, though, the results presented here, together with those of previous studies [6,7] indicate that the frequency response of NbTiN striplines can be reasonably well predicted by the Mattis-Bardeen theory for a superconductor in the extreme anomalous limit.

The receiver sensitivity measurement reported here is, to the best of our knowledge, the first heterodyne measurement above 900 GHz of a Nb SIS junction integrated with NbTiN striplines. It has been shown that an end-loaded device with a high current-density junction yields a sensitivity of $T_{N,\ corrected}$ ~ 830 K DSB at 930 GHz, at a mixer block temperature of 3.3 K. Although this sensitivity remains 4-5 times higher than required for HIFI, it approaches the best sensitivity reported for Al stripline devices in this frequency range — $T_{N,\ uncorrected}$ = 840 K at 1040 GHz and a bath temperature of 2.5 K [3].

Unfortunately, the DC and RF heating of the junction complicate the use of the standard Tucker theory to determine the contributions of individual elements to the measured receiver noise. Thus, it is difficult to draw further conclusions from these heterodyne results at this time. However, three general comments can be made. First, it is noted that, due to the effects of Andreev reflection enhanced shot noise [9,16], it should be possible to improve upon these results by the use of a junction with a lower current-density than that used here (12 kA/cm^2). Furthermore, the dewar window and the 77 K heat filter are found to have significant losses at 930 GHz (~ 19 % and 35%, respectively), and thus, are likely responsible for a significant contribution to the receiver noise. Finally, FTS measurements show this device to have relatively broad fixed-tuned bandwidths (up to 140 GHz, similar to Figure 4a), which may be the result of poor matching of the incoming radiation to the junction impedance. Indeed, calculations of the coupling of radiation from a 50 Ω source to the junction predict only ~ 25% coupling for this geometry, although the use of a tunable backshort makes it difficult to know what the junction's real embedding impedance is. In general, these calculations indicate that other stripline geometries, such as the ¼-λ stripline, may give much better coupling at these

high frequencies. Thus, although these initial results are promising, further measurements of a range of devices with different resonant frequencies and stripline geometries are needed before the benefits of using NbTiN as a stripline material can be fully quantified.

8. Acknowledgements

The authors would like to thank S. Bakker, B. Wolfs, D. Nguyen, and H. Schaeffer for their technical assistance and A. Baryshev, P. Dieleman, W. Ganzevles, N. Whyborn, and D. Wilms Floet for numerous discussions. The authors would also like to thank H. LeDuc, J. Stern, and B. Bumble of the Jet Propulsion Laboratory's Center for Space Microelectronics Technology and J. Zmuidzinas of the California Institute of Technology, for exchanging information regarding the integration of NbTiN in Nb-based SIS mixers. This work is supported in part by the Stichting voor Technische Wetenschappen (STW), the Nederlandse Organisatie voor Wettenschappelijk Onderzoek (NWO), and the research program of the European TMR network for Terahertz electronics (INTERACT).

9. References

[1] D.C. Mattis and J. Bardeen, "Theory of the anomalous skin effect in normal and superconducting metals", *Phys. Rev.*, vol. 111, p. 412, July 1958.

[2] H. van de Stadt, A. Baryshev, P. Dieleman, Th. de Graauw, T. M. Klapwijk, S. Kovtonyuk, G. de Lange, I. Lapitskaya, J. Mees, R.A. Panhuyzen, G. Prokopenko, and H. Schaeffer, "A 1 THz Nb SIS heterodyne mixer with normal metal tuning structure", *Proc. 6th Internat. Symp. On Space Terahertz Technology*, CIT, PC, p. 66, March 1995.

[3] M. Bin, M.C. Gaidis, J. Zmuidzinas, T.G. Phillips, and H.G. LeDuc, "Low-noise 1 THz niobium superconducting tunnel junction mixer with a normal metal tuning circuit", *Appl. Phys. Lett.*, vol. 68 (12), p. 1714, March 1996.

[4] Y. Uzawa, Z. Wang, A. Kawakami "Terahertz NbN/AlN/NbN mixers with Al/SiO/NbN micostrip tuning circuits", *Proc. 9th Internat. Symp. on Space Terahertz Technology, CIT, PC*, p. 273, March 1998.

[5] R. Di Leo, A. Nigro, G. Nobile, R. Vaglio, "Niobium-titanium nitride thin films for superconducting rf accelerator cavities", *J. Low Temp. Phys.*, vol. 78, p. 41, November 1990.

[6] J.A. Stern, B. Bumble, H.G. LeDuc, W. J. Kooi, J. Zmuidzinas, "Fabrication and dc-characterization of NbTiN based SIS mixers for use between 600 and 1200 GHz", *Proc. 9th Internat. Symp. on Space Terahertz Technology, CIT, PC*, p. 305, March 1997.

[7] J.W. Kooi, J.A. Stern, G. Chattopadhyay, H.G. LeDuc, B. Bumble, and J. Zmuidzinas, "Low-loss NbTiN films for THz SIS mixer tuning circuits", *Int. J. of IR and MM Waves*, vol. 19, 1998.

[8] P. Dieleman, T.M. Klapwijk, J.R. Gao, and H. van de Stadt, "Analysis of Nb superconducting-insulator-superconducting tunnel junctions with Al striplines for THz radiation detection", *IEEE Transactions on Applied Superconductivity*, vol. 7, p. 2566, 1997.

[9] P. Dieleman, J.R. Gao, and T.M. Klapwijk, "Doubled shot noise in niobium SIS mixers", *Proc. 9th Internat. Symp. on Space Terahertz Technology, CIT, PC*, p. 235, March 1998.

[10] N.N. Iosad, B.D. Jackson, T.M. Klapwijk, S.N. Polyakov, P.N. Dmitriev, and J.R. Gao, "Optimization of rf- and dc-sputtered NbTiN films for integration with Nb-based SIS Junctions", to be published in *IEEE Transactions on Applied Superconductivity*, June 1999.

[11] J.R. Gao, S. Kovtonyuk, J.B.M. Jegers, P. Dieleman, T.M. Klapwijk, and H. van de Stadt, "Fabrication of Nb-SIS mixers with UHV evaporated Al striplines", *Proc. 7th Internat. Symp. on Space Terahertz Technology, CIT, PC*, p. 538, March 1996.

[12] N.E. Booth, "Quasiparticle trapping and the quasiparticle multiplier", *Appl. Phys. Lett.*, vol. 50, p. 293, Feb. 1987.

[13] A. Skalare, *International Journal of Infrared and Millimeter Waves*, vol. 10, p. 1339, 1989.

[14] J.R. Tucker and M.J. Feldman, "Quantum detection at millimeter wavelengths", *Reviews of Modern Physics*, Vol. 57, No. 4, p. 1055, Oct. 1985.

[15] B. Bumble, H.G. LeDuc, and J.A. Stern, "Fabrication of Nb/Al-Nx/NbTiN junctions for SIS mixer applications above 1 THz", *Proc. 9th Internat. Symp. on Space Terahertz Technology, CIT, PC*, p. 295, March 1998.

[16] P. Dieleman, H.G. Bukkems, T.M. Klapwijk, M. Schicke, and K.H. Gundlach, "Observation of Andreev reflection enhanced shot noise", *Appl. Phys. Lett.*, vol. 79, p. 3486, 1997.

A WIDE BAND RING SLOT ANTENNA INTEGRATED RECEIVER.

Andrey Baryshev

Groningen Space Research Laboratory and Material Science Center,
P.O. Box 800,
9700 AV Groningen,
The Netherlands.

Sergey Shitov, Andrey Ermakov, Lyudmila Fillipenko, Pavel Dmitriev,

Institute of Radio Engineering and Electronics Russian academy of Science,
Mokhovaya 11,
103907 Moscow,
Russia.

ABSTRACT

A wide band 500 GHz integrated receiver has been designed fabricated and tested. The receiver combines a ring slot antenna SIS mixer with a twin junction type tuning circuit and a Josephson Flux-Flow oscillator as LO. The receiver layout has been made using Nb technology. The receiver chip is glued on the silicon elliptical lens with antireflection coating. According to calculations a 30% 3-dB bandwidth can be achieved with this design. Measured SIS mixer pumping level is sufficient for SIS mixer operation in the band 400-570 GHz. We present the antenna beam pattern of a ring slot antenna on a silicon elliptical lens, a DSB noise temperature of the receiver and a FTS spectrum. The measured receiver DSB noise temperature is analyzed.

Introduction

A single chip heterodyne receiver comprising a Superconductor-Insulator Superconductor (SIS) junction as sensitive element and a long Josephson junction Flux-Flow Oscillator (FFO) as a local oscillator (LO) is very attractive as imaging array in space and airborne applications because of its low weight and power consumption. A double dipole integrated receiver has recently demonstrated a 100 K DSB noise temperature at 500 GHz [1]; which is on the level of state of the art receivers in this frequency band. This receiver had an internal LO (FFO) and had a bandwidth of about 10 %. A possibility to phase lock a FFO to an external reference source in 300-430 GHz frequency band has been shown [2]. This makes it more attractive to design a wide band integrated receiver to utilize a wide tuning range of FFO. The increasing complexity of integrated receivers demands a more accurate analysis of receiver parameters.

In this report a layout of a wide band quasioptical integrated receiver utilizing a one port annular slot antenna is described. The preliminary measurements of receiver DSB noise temperature, receiver beam and integrated control parameters are presented. A receiver DSB noise temperature is analyzed in detail in one frequency

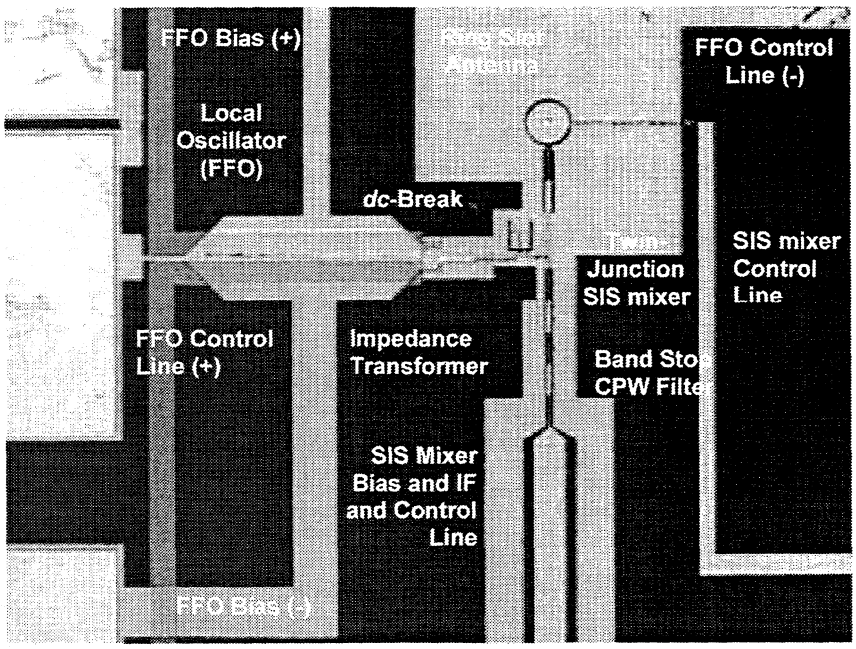

Fig. 1 Photograph of the central part of receiver chip

point.

Receiver layout

The photograph of the central part of the receiver chip is shown in fig. 1.

Quasioptical configuration.

The receiver uses an annular slot line antenna on a silicon substrate. The receiver chip (3 x 4.2x 0.5 mm) is mounted on the flat surface of a (synthesized) elliptical lens such that the center of the antenna is the focal point. An antireflection layer with center frequency 500 GHz covers the front surface of the lens. No additional optical elements are used to form the receiver beam.

Ring slot antenna.

The ring slot antenna is known to have a symmetrical linear polarized antenna beam pattern [3], [4]. It is a compact antenna surrounded by a ground plane. This gives more flexibility to place all strip line elements very close to antenna itself. This antenna doesn't need a blocking capacitor if the central part is made in the wiring layer. The antenna with a circumference of one wavelength for 500 GHz has been chosen. The input impedance of the antenna has been calculated using the momentum method in the Momentum ™ software package as a part of a HP ADS design system. The calculated impedance is shown in fig. 2 and it is in agreement with values used in [3], [4].

LO chain.

A FFO junction has a size of 500 x 4 μm. The three stage tapered strip line impedance transformer is used to convert the low (0.5 Ohm) source impedance to the

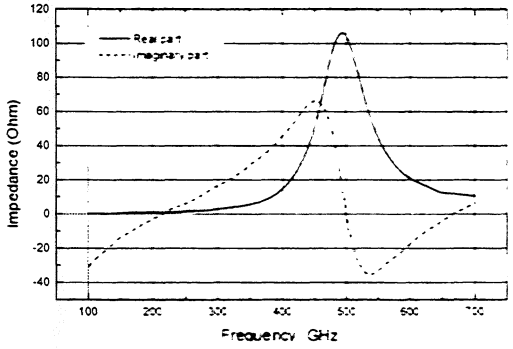

Fig. 2 Impedance of ring slot antenna

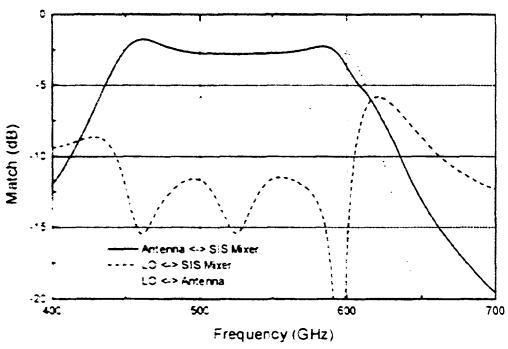

Fig. 3 Calculated layout parameters

level appropriate to combine it with the DC-break. The single insulator layer is used for in first transformer section to decrease its characteristic impedance. The pi-shape DC break is used in order to disconnect the SIS junction bias current and the FFO bias current path. A common ground plane is used throughout the design. The additional micro strip line tuner is used to transform the resulting impedance of LO path to create a required mismatch between LO and detector. This mismatch is needed to avoid leak of a *rf* signal from antenna towards the local oscillator.

The magnetic field for FFO operation is applied by passing current through the bottom electrode along the junction.

Signal chain and SIS tuning elements.

A twin junction tuning circuit [5], [6] is used to compensate the SIS junction geometrical capacitance in wide frequency range. A two stage CPW transformer followed by a one stage strip line transformer is used to match the rather high ring slot line antenna impedance (100 Ohm) to the input impedance of twin junction circuit.

An integrated control line supplies the magnetic field required for suppression of Josephson effect during SIS mixer operation. The control line is placed in the top electrode. Possible leak of *IF* signal should be blocked outside the chip. The return path of SIS junction magnetic field control current is located across the cross-polarized port of the ring slot antenna to avoid the influence to the antenna properties by the other port. A CPW choke filter is used to prevent the leak of *rf* signal towards the bias leads.

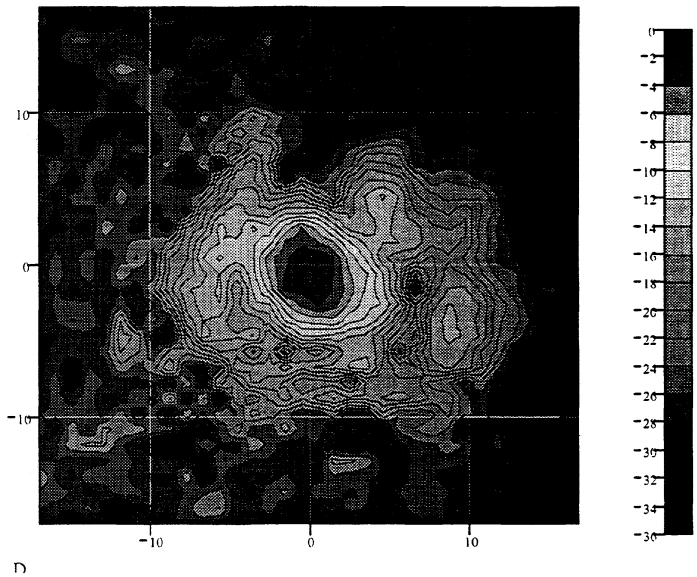

Fig. 4 2D antenna beam pattern of integrated receiver. X-Y axis units: degrees. X-axis corresponds to E-plain. The contour levels are in log scale.

The result of layout calculation for 1.1 x 1.1 μm junction size, 8 kA/cm^2 critical current density and two 135 nm thick insulator layers made of SiO_2 is presented in fig. 3. The mismatch between antenna and twin junction circuit is stable across 30 % bandwidth and is about 1.5 dB. The mismatch between FFO and SIS mixer has been chosen to be 12.5 dB. This level still allows to get sufficient LO power.

Fabrication and Measurement

The first batch of integrated receiver has been fabricated using Nb-AlOx-Nb technology. The SIS junctions size in tuning circuit was estimated to be 1.6 times larger than expected and critical current density was 2 times smaller than required. The only preliminary experimental results can thus be presented.

Antenna Beam Pattern

The antenna beam pattern of antenna lens combination has been measured by scanning a point source in the far field of the lens. A Thomson carcinotron with an horn output blocked by a 1 mm diameter diaphragm has been used as a point source. It allows measuring the antenna parameters within +/- 15 degrees at 500 GHz. The result of the X-Y scan at 475 GHz is presented in fig. 4. It shows the rotationally symmetrical beam with sidelobe level at about −10 dB. The F-ratio of the beam is about #5. Asymmetric excitation of CPW transformer or influence of the edge of ground plane can explain measured sidelobes level.

FFO Test

The pumping level of SIS mixer was measured while scanning the FFO I-V

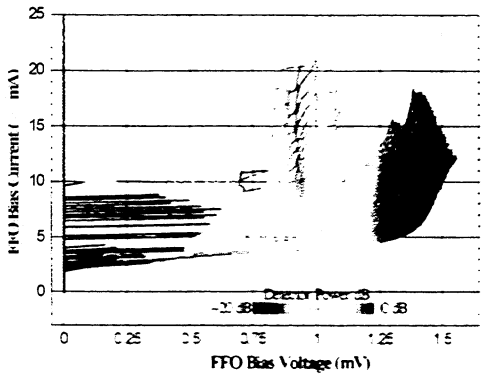

Fig. 5 FFO I-V characteristics. Pumping level is indicated in gray scale. Magnetic field is a parameter.

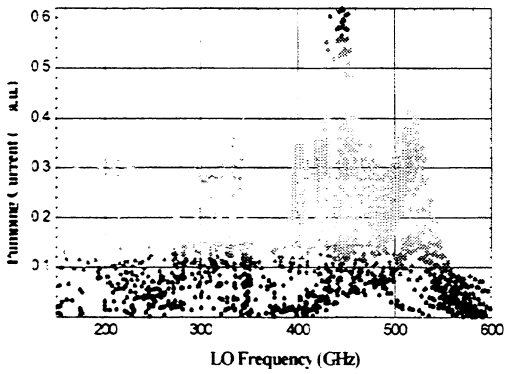

Fig. 6 SIS mixer pumping level vs. FFO frequency.

curve. The recorded set of FFO I-V curves is presented in Fig. 5. Figure 6 shows the measured frequency dependence of the LO level of SIS mixer. The pumping level is sufficient for SIS mixer operation in frequency region 250-550 GHz. It was possible to operate the FFO with magnetic field control line current in the range –30...30 mA and bias current in the range 0...40 mA.

SIS junction magnetic field control line test

The SIS mixer I-V curve has been scanned to determine a critical current while the SIS mixer control line current was changed as a parameter. It was possible to obtain up to third minimum of the critical current without switching the control line in a normal state. The dependence of critical current from the control line current in fig. 7 shows also the SQUID like behavior structure. This is because a twin junction tuning circuit forms SQUID interferometer. The experiment showed that for efficient Josephson effect *IF* noise suppression the first minimum determined by the junction's area rather than the area of SQUID loop is required.

Noise Temperature Measurement

For the noise temperature measurement the receiver has been mounted on the cold plate of LHe cryostat. The input window was made of 10 mkm thick kapton. The 100 mkm thick quartz plate was used as 78 K far infrared radiation filer. The Zitex ™ plate was used as 4.5 K level radiation filter. A circulator and a low noise HEMT amplifier were used in *IF* chain. A directional coupler has been installed between circulator and receiver chip for reflection measurements of SIS junction dynamic resistance at IF frequency. This measurement is required for an accurate estimation of

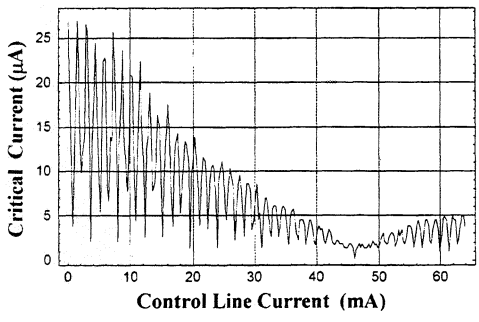

Fig 7 SIS junction critical current vs. magnetic field control line current.

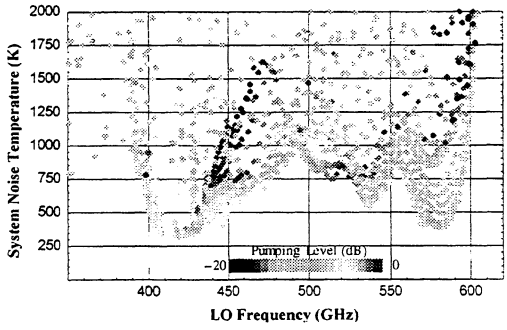

Fig 8 System DSB noise temperature vs. LO frequency. Pumping level is indicated in gray scale.

receiver parameters. The Y-factor has been measured by using two switchable black bodies (78 K/300 K). The IF output power was detected and a calibrated logarithmic amplifier was used to record the Y-factor automatically while scanning the FFO I-V curve. The resulting DSB noise temperature graph is presented in fig. 8. The lowest noise temperature was 300 K for a given production parameters.

Noise Temperature Analysis

The receiver consists of several linear elements connected in series. Each element has its own gain G_i and equivalent input noise power P_i^n. The output power from such an element can be written as $P_{out} = (P_{in} + P_i^n) \cdot G_i$. It is convenient to express all powers in equivalent noise temperatures, because a wide band calibration noise source is used for the measurement. The corresponding noise temperature can be expressed as $P^n = k_b T^n \Delta f$, where Δf is a bandwidth of the intermediate frequency detector. The output power of a linear element can be redefined as $T_{out} = (T_{in} - T_i^n) \cdot G_i$. The receiver gain G_{sys} and the receiver noise temperature T_{sys} can be calculated:

$$G_{sys} = G_1 \cdot G_2 \cdot \ldots \cdot G_k, \; T_{sys} = T_1^n + T_2^n / G_1 + T_3^n / (G_1 \cdot G_2) + \ldots + T_k^n / (G_1 \cdot \ldots \cdot G_{k-1}). \quad (1)$$

The overall receiver performance can be measured using the Y-factor technique. A calibrated black body source can be used to measure G_{sys} and T_{sys}. The properties of all receiver elements can be measured independently except for the *rf* loss in the tuning elements and the lens. This unknown loss of tuning elements and lens can be found by solving (1) when G_{sys} and all other G_k is known. The same is true for the

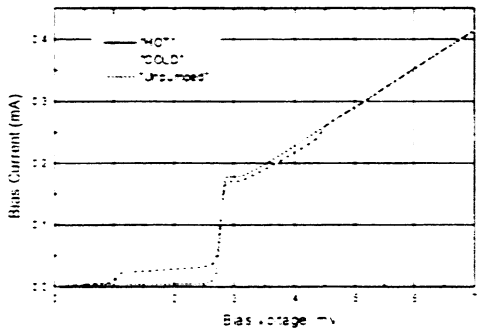

Fig. 9 SIS junction I-V curves.

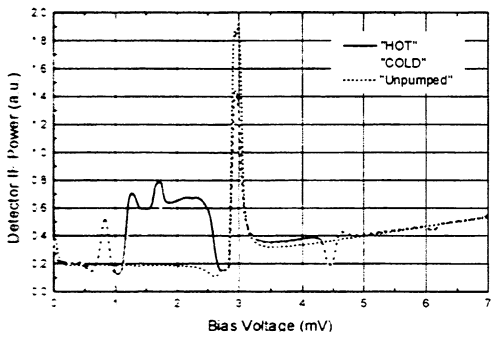

Fig. 10 SIS junction IF output power.

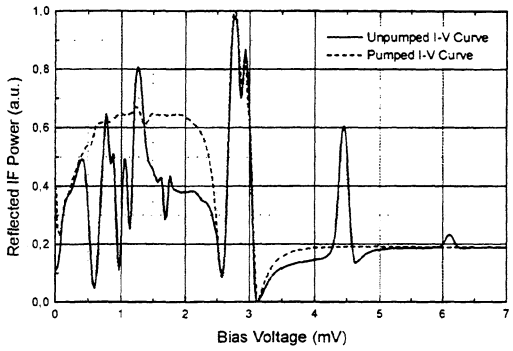

Fig. 11 *IF* port test tone reflected signal for pumped and unpumped I-V curves

noise of this 'element'.

The parameters for the dewar window and all radiation filters can be determined separately by measuring the film transmission with a Micelson FTS spectrometer.

The parameters of the *IF* low noise amplifier chain and detector can be calibrated using the unpumped SIS junction as a calibrated noise source [7]. The noise temperature of the *IF* chain as well as the impedance as seen by the junction at the *IF* port can be determined by fitting the unpumped SIS junction *IF* output power calculated from the measured I-V curve and dynamic resistance to the measured data.

The SIS mixer can be analyzed with the Tucker theory [8]. The information about mixer gain and noise can be obtained from the pumped and unpumped I-V curves and the independently measured dynamic resistance of the junction. Using the measured dynamic resistance allows us to avoid the numerically unstable calculation of the junction's embedding impedance at the *rf* port. A DSB operation of the mixer with equal lower and higher side band parameters is assumed. *Rf* loss due to mismatch in the tuning circuits or non optimal receiver beam efficiency and the associated noise are found using measured receiver parameters. Details of this method will be published elsewhere.

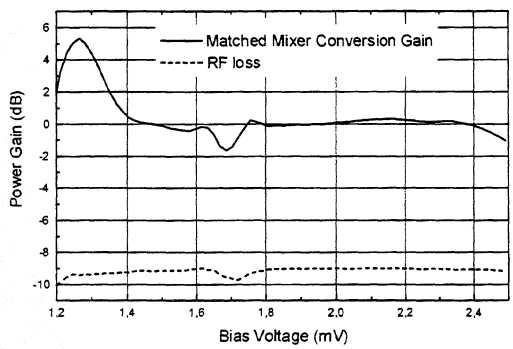

Fig. 12 Calculated *rf* loss and matched mixer conversion gain.

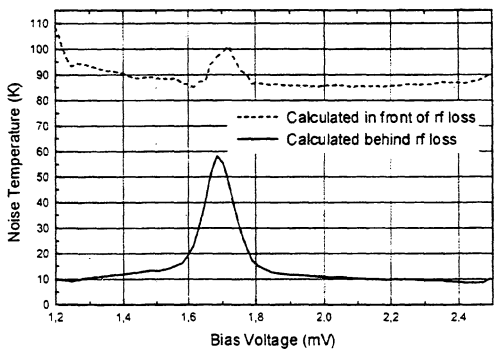

Fig. 13 Noise temperature associated with *rf* loss.

Element	T_I (K)	G (dB)
Dewar Window (10 μm capton)	6	-0.09
IR Filter at 78 K (Quartz Plate)	8	-0.1
IR Filter at 4.3 K (Zitex)	0.3	-0.13
rf Mismatch	73	-9
Mixer Gain Element (Tucker theory)	86	0.16
if Mismatch	38	-1.9
if Amplifier and Detector	91	0
Receiver	302.3	-10.93

Table 1. Receiver elements noise temperature (recalculated to the front of receiver) and gain for bias point of 2 mV and *LO* frequency 410 GHz.

Noise Temperature Analysis Result and Discussion.

Experimental data needed for the receiver analysis is shown in fig. 9-11. The analysis is made for a *LO* frequency of 410 GHz. Based on these curves one can calculate the noise budget for all receiver components. The matched mixer conversion gain along with the calculated *rf* loss is shown in fig. 12. The value of the *rf* loss should not depend on the bias voltage across the first photon step. This is seen from the measurement despite the varying mixer gain. The noise temperature associated with *rf* loss is shown in fig. 13. It corresponds to a level of approximately 85 K referred to the front of the receiver and 10 K if it is attributed after this element. The value of 10 K is the zero-point fluctuations level at this frequency. The ripple near bias voltage of 1.7 mV corresponds to the position of second Shapiro step and reflects the additional noise due to Josephson effect. A noise temperature and gain budget for the receiver is shown in table 1. Noise temperature is referred to the input of the receiver, so the receiver noise temperature can be obtained by adding all contributions. From the table follows that the main contribution to the system noise temperature arises from *rf* loss. This loss is due to increased junction area.

Acknowledgements

Authors would like to thank Teun Klapwijk, Willem Luinge, Herman van de Stadt and Valery Koshelets for stimulating discussions. The work was supported in parts by the Russian Program for Basic Research, the Russian SSP "Superconductivity", ESA TRP contract 11653/95/NL/PB.

Conclusion

A wide band integrated receiver layout with a ring slot line antenna and a twin junction tuning circuit has been developed. Calculation showed 30% instantaneous bandwidth. The preliminary experiments showed that this design could be used as a wide band integrated receiver for frequencies of 400...550 GHz. The receiver noise temperature analysis demonstrated stable receiver parameters across first photon step of SIS junction and shows the most critical parts of the measurement setup.

References

[1] S.V. Shitov, A. B. Ermakov, L. V. Filippenko, V. P. Koshelets, A.M. Baryshev, W. Luinge, Jian-Rong Gao, *Superconducting Chip Receiver for Imaging Applications*,. Was presented at ASC-98, Palm Desert, CA, USA, Report EMA-09, (1998), to be published in IEEE Trans. on Appl. Supercond. (1999).

V.P. Koshelets, S.V. Shitov, L.V. Filippenko, A.M. Baryshev, H. Golstein, T. de Graauw, W. Luinge, H. Schaeffer, H. van de Stadt, *First Implementation of a Superconducting Integrated Receiver at 450 GHz*, Appl. Phys. Lett., Vol. 68, No. 9, pp. 1273-1275, 1996.

[2] V. P. Koshelets, S. V. Shitov, A. V. Shchukin, L. V. Filippenko, P. N. Dmitriev, V. L. Vaks, J. Mygind, A. M. Baryshev, W. Luinge, H. Golstein, *Flux Flow Oscillators for Sub-mm Wave Integrated Receivers.* Was presented at ASC-98, Palm Desert, CA, USA, Report EQB-04, (1998), to be published in IEEE Trans. on Appl. Supercond. 1999.

[3] C.E. Tong, R. Blundell, *An Annular Slot Antenna on a Dielectric Half-Space*, IEEE Trans. On Ant. and Propagation, vol. 42, No 7, pp. 967-974, July 1994

[4] S. Raman, G.M. Rebeiz, Single – and Dual-polarized Millimeter-Wave Slot-Ring Antennas, IEEE Trans. On antennas and propagation, vol 44, no. 11, pp. 1438-1444, Nov 1996

[5] Belitsky V.Yu., Jacobsson S.W., Filippenko L.V., Kovtonjuk S.A., Koshelets V.P., Kollberg E.L., *0.5 THz SIS Receiver with Twin Junctions Tuning Circuit.*, Proc. 4th Space Terahertz Technology Conference, p.538, March 30 - April 1, Los Angeles, USA.,1993

Belitsky V. Yu., Tarasov M.A., "SIS Junction Reactance Complete Compensation", IEEE Trans. on Magnetic, MAG- 27, v. 2, pt. 4, pp. 2638-2641., 1991

[6] M.C. Gaidis, H.G. Leduc, Mei Bin, D. Miller, J.A. Stern, and J. Zmuidzinas, *Characterization of Low Noise Quasi-Optical SIS Mixers for the Submillimeter Band*, IEEE Transactions of Microwave Theory and Techniques, p. 1130-1139, 1996

[7] Belitsky V.Yu, Serpuchenko I.L., Tarasov M.A., *Shot Noise In Superconducting Single Junction And Arrays*, 5th Conf. on WEAK

SUPERCONDUCTIVITY, Smolenice, Czechoslovakia. May 29 - 2 June 1989, Nova Science Publisher, ISBN 0-941743-78-0 Conf. Proc. pp. 191-195, 1990

D.P. Woody, *Measurement of the Noise Contributions to SIS Heterodyne Receivers*, ASC'94 Proceedings, 1995

[8] R. Tucker, M.J. Feldman, *Quantum Detection at millimeter wavelengths*, P.1055-1112, Reviews of Modern Physics, Vol. 57, No. 4, October 1985

A.R. Kerr, M.J. Feldman, S.-K. Pan *Receiver Noise Temperature, the Quantum Noise Limit, and the Role of the Zero-Point Fluctuations*, Eight Int. Symp. on Space Terahertz Technology proceedings, p. 101-111, 1997.

GAIN AND NOISE SPECTRA FOR $YBa_2Cu_3O_7$ HOT-ELECTRON BOLOMETER MIXERS

C. -T. Li, G. Schoenthal, B. S. Deaver, Jr., R. M. Weikle II, and Mark Lee
University of Virginia, Charlottesville, VA 22903

R. A. Rao and C. B. Eom
Duke University, Durham, NC 27708

The conversion gain and output noise spectra for YBCO hot-electron bolometer (HEB) mixers will be presented. Devices were formed from a small area of YBCO thin film, with nominal physical dimensions of 1 μm (wide) × 2 μm (long) × 1000 Å (thick), coupled to planar log-periodic antennas. Two tunable Gunn oscillators, providing several mW radiation from 75 to 106 GHz, were used. One acted as the LO, the other one as the RF. Both signals were combined first with a 3 dB directional coupler before emerging from a corrugated feedhorn. Measurements were performed quasi-optically, with the devices mounted on the back of a Si extended hemispherical lens, and coupling losses estimated 12 dB. Within the IF range (2-18 GHz, set by the amplifiers we were using), single Lorentzian roll-off bandwidths were observed for mixer conversion gain, with conversion efficiency close to -18 dB around 2 GHz, and 3 dB bandwidth ~ 6 GHz.

A broadband amplifier chain, connected with a tunable band-pass filter and microwave power detector, was used to measure the output noise up to 12 GHz. To cancel Johnson noise contributions from the HEB, circulator matched load, and lossy transmission lines, we also measured the noise using a 50 Ω thin-film resistor in place of HEB. The mixer input noise temperature, not taking into account the coupling loss, was estimated of the order of 10,000 K. A tungsten lamp with 3200 K color temperature will be used as the hot load to implement the hot/cold load experiment.

MICROWAVE MIXING AND IF BANDWIDTH IN SUB-MICRON LONG HIGH-T_c HOT-ELECTRON BOLOMETERS

Oliver Harnack[1], Boris Karasik, William McGrath, Alan Kleinsasser, Jeff Barner

Center for Space Microelectronics Technology, Jet Propulsion Laboratory, California Institute of Technology, Pasadena, CA 91109, USA

[1] *On leave from Institute of Thin Film and Ion Technology, Research Center Juelich, 52425 Juelich, Germany*

Abstract

We have systematically measured both the length and temperature dependence of the intermediate frequency (IF) bandwidth of hot-electron bolometer (HEB) mixer made from a high-T_c superconductor (HTS). Mixer devices with lengths (L) between 50 nm and 1 μm were fabricated from 25 - 35 nm thick YBCO films on $YAlO_3$ (YAO), MgO, and sapphire substrates. Bandwidth measurements were done using signal and local oscillator (LO) frequencies in the range 1 - 300 GHz. At low operation temperatures where self-heating effects occured, the IF bandwidths were about 30 MHz, 100 MHz, and several 100 MHz for devices on YAO, MgO, and sapphire, respectively. The theoretically predicted L^{-2}-dependence of the IF bandwidths was not observed. At higher operation temperatures, where self-heating disappeared and flux-flow effects define the shape of the IV characteristic (IVC), the measured IF bandwidth increased significantly, while the overall conversion efficiency at low IF's decreases by several dB. Our data indicate that the temperature dependence of the HEB mixer performance may be influenced by vortex dynamics effects in HTS materials.

I. Introduction

The hot-electron bolometer (HEB) mixer made from a high-T_c superconductor (HTS) was introduced recently as a competing alternative to a Schottky-diode mixer. The HEB mixer would require 100-times less LO power and thus would be a desirable candidate for long-term atmospheric remote-sensing and planetary missions. The required operating temperatures between 65 K and 75 K can be achieved with available space-qualified coolers or even with passive radiative coolers.

The HEB mixer consists of a microbridge of HTS material between normal metal contacts (Fig. 1). Electrons in the microbridge can be heated by absorbed RF radiation and dc transport current. Nonequilibrium "hot" electrons (e*) transfer their energy to the

lattice (ph*) during a very short electron-phonon relaxation time $\tau_{e\text{-}ph}$, which is about 1-2 ps at 80-90 K in $YBa_2Cu_3O_7$ (YBCO) [1-3]. The performance of the mixer depends strongly on the total thermal conductance for heat removal from the phonon sub-system. As shown in Fig. 1, this heat can be removed by escape of the phonons to the substrate (τ_{es}) or by diffusion of phonons to the normal metal contacts (τ_{diff}). In the case of the phonon diffusion, the mixer IF response would depend strongly on the microbridge length. In contrast, the heat removal through the film-substrate boundary is determined by the thermal boundary resistance and the heat diffusion in the substrate. Two substrates with good dielectric properties and high thermal conductivity on which high quality HTS films can be grown are magnesium oxide (MgO) and sapphire (Al_2O_3). MgO provides a low boundary resistance of about $5.3 \cdot 10^{-4}$ Kcm^2/W, while Al_2O_3 gives $1.1 \cdot 10^{-3}$ Kcm^2/W [4].

Modelling of the performance of HTS HEB mixers was done by some of us and the results showed that single sideband mixer noise temperatures around 2000 K, optimum LO power levels in the range of a few μW, and IF bandwidths of several GHz could be possible [5]. However, this approach assumes that phonon diffusion into the normal metal contacts takes place and dominates for the heat removal out of the microbridge. Based on the calculations in [5], phonon diffusion could be a dominat thermal process, only if the length of the bolometer is less than a few hundred nanometer.

The aim of our experimental work was to fabricate sub-μm long HTS HEB mixer on MgO and sapphire substrates and to determine their intrinsic thermal relaxation times as inferred from the - 3dB IF bandwidth. Available HEB mixers on YAO substrates were also measured in order to compare our results with the performance of devices on a perovskite substrate that has a good lattice match to YBCO but less favorable thermal properties [6].

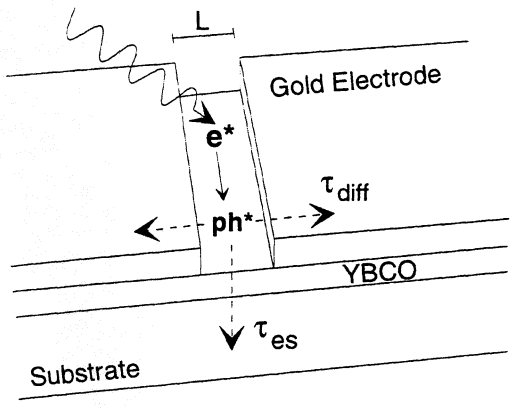

Fig. 1: Schematic of a HTS hot-electron bolometer mixer and possible energy-relaxation mechanisms for the heat removal (see text for details)

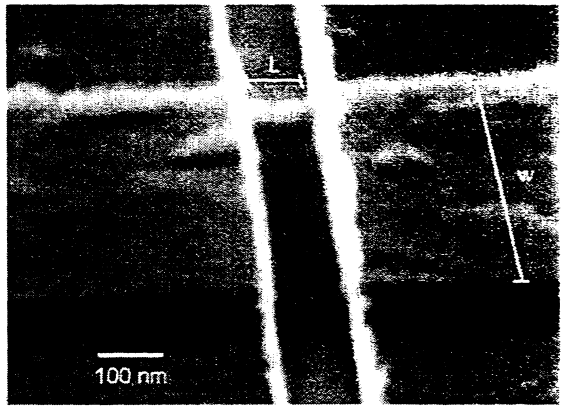

Fig. 2: Sub-μm YBCO HEB on MgO. The gold/YBCO sandwich electrodes are visible on the left and right. The YBCO strip which forms the microbridge is located in the center, L=100 nm, w=1μm.

II. **Sample fabrication**

For the fabrication of HEB mixers, YBCO films with thickness of about 20-40 nm were grown on MgO and sapphire substrates using the laser deposition method. In the case of sapphire we used a 30 nm thin CeO_2 buffer layer between the substrate and the YBCO film. The thin YBCO films were protected by an in-situ sputtered gold layer. Inductive T_c-measurements showed critical temperatures of 89-90 K for YBCO films on sapphire substrates and 84-86 K for films on MgO substrates. The transition widths were in the range between 0.5 and 1 K. After patterning the microbridges (width of the bridge $w \approx 1\mu m$), with integrated bow-tie antennas, a small-area window (50 nm to 500 nm length and 1 μm width) was defined across the bridge by using electron beam lithography. After removing the gold layer from the window using ion beam etching (IBE), a SiOx protection layer was deposited by thermal evaporation. HEB mixers on YAO substrates were fabricated using a similar growth technique. However, for the lithographic steps a self-alignment process was used and for the gold removal a selective Cl_2 etch was applied (see ref. [7] for details). A finished HEB device on MgO is shown in Fig. 2.

III. **IF bandwidth measurements at low operation frequencies**

IF bandwidth measurements were done using two monochromatic signals in the frequency ranges 1-20 GHz, 100 GHz, and 300 GHz. The lowest frequency range was choosen due to the simplicity of the microwave circuits and readily available RF equipment. If the mixer relaxation properties are determined by the thermal properties of the HEB device only, one could assume that the IF bandwidth measured at low operation frequencies would be comparable with that at submillimeter waves. Low-frequency effects (e.g., because of possible Josepshon weak links in the bridge) can certainly give a misleading picture of the HEB performance. Therefore, similar measurements at 100 GHz and 300 GHz are a necessary test for operation frequency dependent effects. In this way we expect to be able to get more data on the real HEB performance in the submillimeter wave range, rather than from mixer measurements at optical frequencies done earlier [8].

1. Setup for 1-20 GHz signal frequencies

As shown in figure 3, two sweep oscillators feed the LO signal (OSC 2) and a second, weaker signal (OSC 1) into a 12.4 GHz-broadband directional coupler (I d. c.). The output port was connected to a 18 GHz-broadband directional coupler (II d.c.) in order to use the same coaxial cable for the LO/signal input and the IF signal output. The coaxial

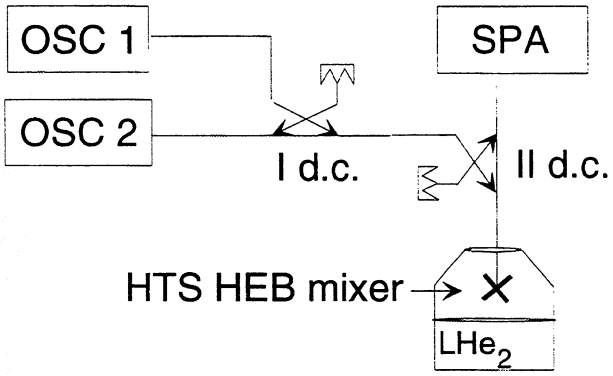

Fig. 3: Setup for IF bandwidth measurements, LO range 1-20 GHz, d.c. = directional coupler, SPA = spectrum analyzer

cable, the bias-tee, the voltage bias source and the mixer mount were assembled inside a dipstick in order to make measurements in a transport helium dewar at different temperatures. The IF bandwidth was measured by maintaining the signal frequency constant and sweeping the LO frequency. The LO level was adjusted for each data point in order to keep the amount of LO power coupled to the device constant. The whole measuring process was computer-controlled. The biaspoint and LO level were adjusted in order to get stable mixing conditions. Oscillations which occur in the region of negative differential resistance in the IVC were avoided by biasing the mixer in the resistive branch close to the drop-back voltage. (Self-heating, i.e. the formation of a hot-spot across the microbridge, is the reason for the hysteric device behaviour. Inside the hot-spot, the electron temperature is higher than T_c).

We have to point out that we never adjusted the mixer for best conversion efficiency, since this would require a bias point very close to the hysteretic region where the device output noise becomes very large. Therefore, the absolute level of the low-IF conversion efficiency does not necessarily represent the best mixer performance. More important in our investigation was to get a measure of the IF dependence of the conversion efficiency.

2.a. HEB device on MgO substrates

Fig. 4 shows a set of IVCs of a 50 nm long YBCO HEB on MgO taken at different temperatures. Self-heating was observed in most of our devices below 70 K, flux-flow like IVCs were observed at temperatures above 70 K. The normal-state resistance of this device was about 50 Ω. Fig. 5 shows the result of measurements of the conversion efficiency at different temperatures. The data clearly show a temperature dependence of the IF bandwidth. At 50 K we measured a bandwidth of about 100 MHz. At the highest temperature (83 K) the bandwidth increased to about 2 GHz. Additional measurements with devices with lengths of 200 nm and 300 nm gave very similar results. This is a first indication that the length dependence of the IF bandwidth does not exist or reveal itself in our type of device (As a caveat, it should be noted that the resistance of our devices did

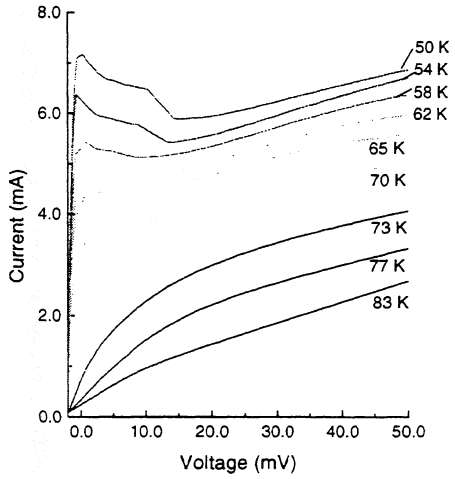

Fig. 4: IVCs at different temperatures of a 50 nm long HTS HEB on MgO, pumped at 1 GHz for optimum conversion

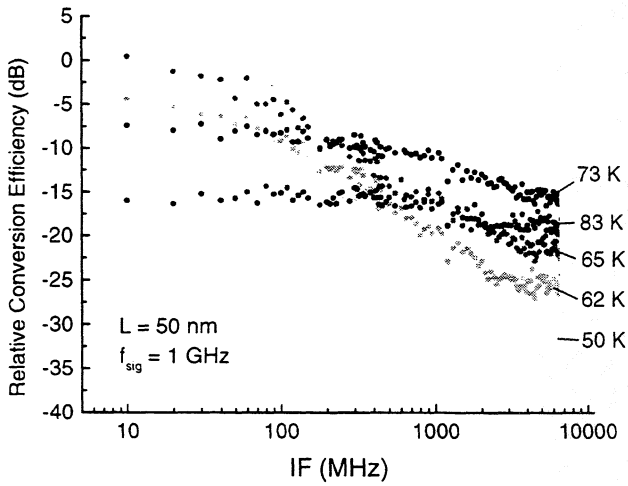

Fig. 5: IF bandwidth measurement at different temperatures using a 50 nm long HTS HEB on MgO

not scale as expected with length, and this may effect the results). Additionally, at temperatures below 60 K, the hot-electron plateau was clearly seen starting around 2 - 3 GHz. This indicates that the relaxation mechanisms can be explained by the two-temperature model in this temperature range, similar to results reported earlier [8]. At temperatures above 70 K, where the measured IF bandwidth increased significantly, self-heating disappeared and we speculate that flux-flow effects began to dominate.

2.b. Temperature dependence of conversion efficiency

In order to get a better measure of the variation of the optimum conversion efficiency with temperature in the low-frequency limit, we biased the mixer very close to the hysteresis (but avoided any biaspoints at negative-differential resistance to keep the noise low) and adjusted the LO level for optimum output signal. As shown in Fig. 4 the shape of the IVC changes completely with temperature. At temperatures higher than 73 K we cound not obtain a hysteresis any longer. In this regime it was possible to find an optimum biaspoint on the IVC without a large increase of the output noise. We attribute this regime to a vortex-flow mechanism inside the bridge. A similar shape of the IVC can be obtained also at lower temperatures by appling enough LO power. However, physical reasons for that could be different and in latter case a smooth IVC under strong pumping can be explained by the heating processes only.

Fig. 6 shows the optimum conversion efficiency versus operation temperature (same device as in section 2.a.). The IF was 10 MHz, the LO frequency was 1010 MHz and the

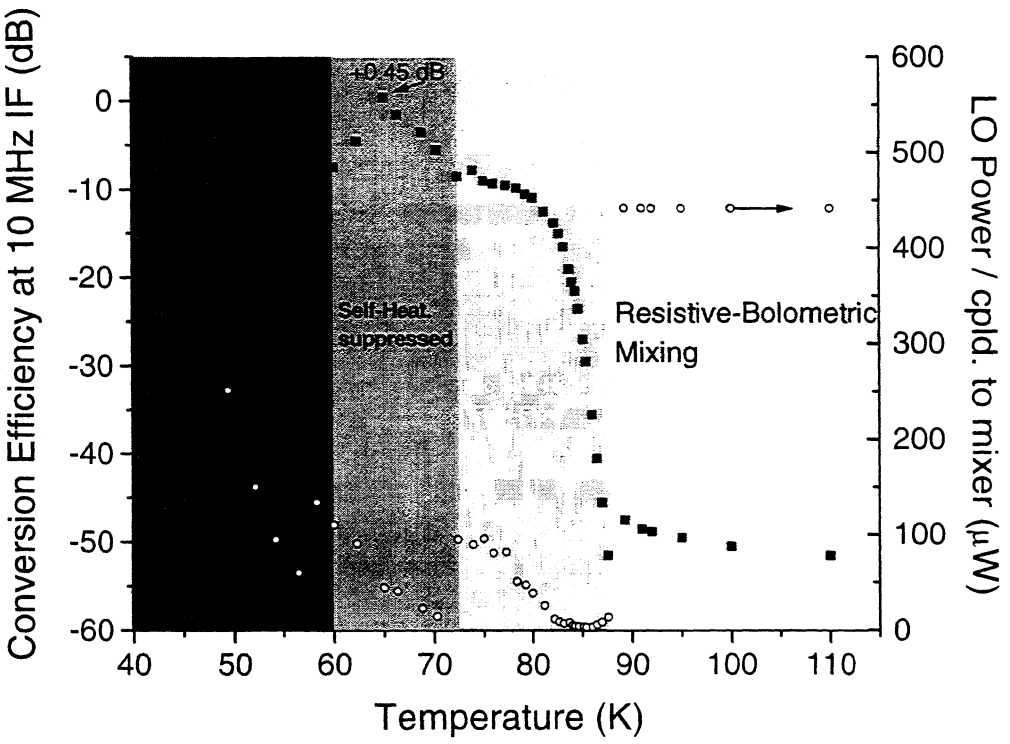

Fig. 6: Temperature dependence of maximum conversion efficiency of a 50 nm long HTS HEB on MgO

signal frequency was 1000 MHz. We can clearly separate the temperature range by different shapes of the IVC. At temperatures below 60 K, the self-heating was still present the at optimum LO level. At temperatures between 60 K and 73 K the hysteresis was still present without LO, but suppressed by the LO at optimum pumping. As mentioned before, at higher temperatures no self-heating was present.

The data show that the maximum conversion efficiency (≈ 0dB !, corrected for coupling) can be found at 65 K in the range where self-heating can be suppressed by the LO. By increasing the temperature, the conversion efficiency starts to drop and reaches a plateau about 10 dB below the maxium value. At the same time the self-heating disappears and flux-flow type rounding starts to dominate the shape of the IVC. A further increase of the temperature results in a decrease of the conversion efficiency. A $T>T_c$ we obtained pure resistive-bolometric mixing, due to the temperature dependence of normal-conducting YBCO. Fig. 6 also displays the coupled LO power. In the range of maxium conversion

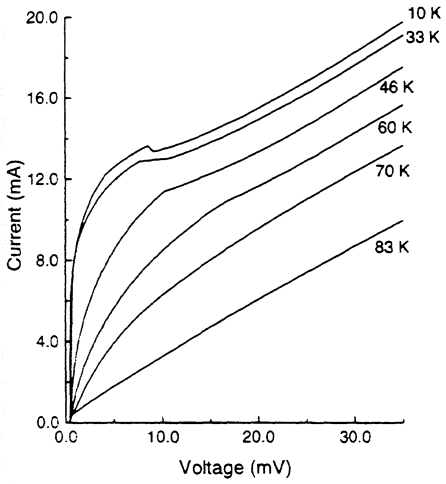

Fig. 7: IVCs at different temperatures of a 50 nm long HTS HEB on sapphire, pumped at 1 GHz

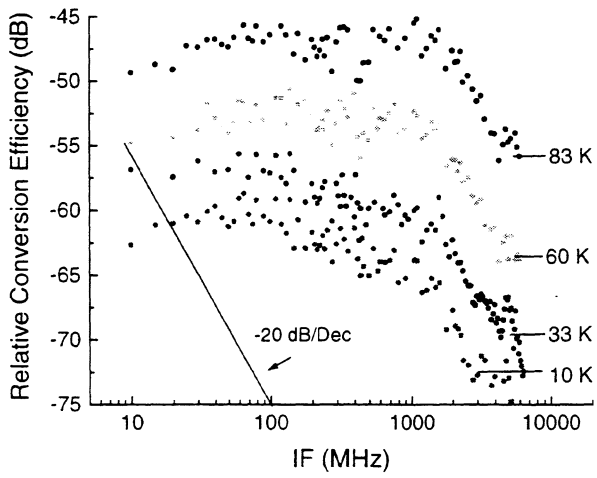

Fig. 8: IF bandwidth measurement at different temperatures using a 50 nm long HTS HEB on sapphire

efficiency, about 50 μW of LO power is needed to pump the mixer. In the flux-flow regime starting at 73 K, the optimum LO level increases by a factor of 10 reaching of about 100 μW. This in fact indicates that the mechanism of mixing could have changed at this point. Also the unexpected high bandwidths would confirm this suggestion.

3. HEB on CeO_2/sapphire substrates

Fig. 8 shows the results of IF bandwidth measurements done by using a 50 nm long mixer on CeO_2/sapphire at different temperatures. The normal resistance of this device was about 5 Ω, which is consistent with its length and film sheet resistance. All curves show a clear roll-off with a -20 dB/Dec slope starting at about 2 GHz, as expected in the two-temperature model [5]. This slope does not change with temperature. In contrast to the data on MgO devices, we could not clearly obtain a comparable hot-electron plateau over our IF measurement range up to 8 GHz. Measurements at higher IF may be needed. At temperatures below 50 K the conversion at low IFs slightly increases due to self-heating, which leads to effectively lower IF bandwidths (≈ 460 MHz at 10 K).
However, as the set of IVCs in Fig.7 shows, the self-heating at low temperatures is much weaker than was seen for a similar device device on MgO. This indeed suggests that the heat removal on CeO_2/sapphire substrates is more effective than on MgO, due to a lower thermal boundary resistance and/or higher thermal conductivity of CeO_2/sapphire. Also, a longer device (80 nm) on CeO_2/sapphire gave very similar bandwidth data.

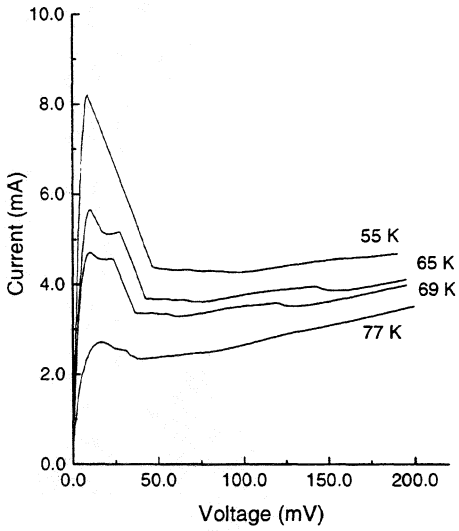

Fig. 9: Weakly pumped IVCs of a 1 μm long HTS HEB on YAO at different temperatures

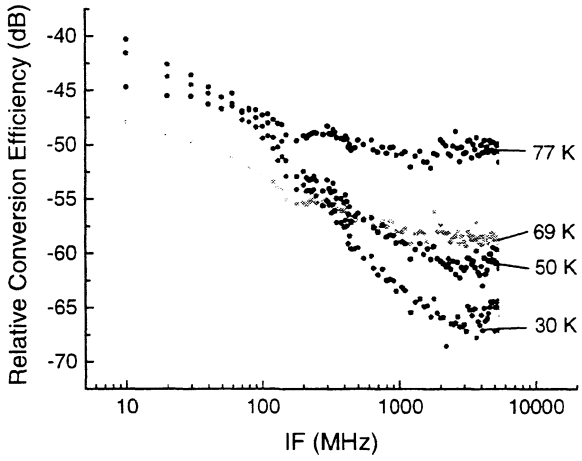

Fig. 10: IF bandwidth measurement at differentatures using a 1 μm long HTS HEB on YAO

4. HEB on YAO substrates

Fig. 9 displays a set of IV curves for a 1 μm long HTS HEB on YAO. Note that self-heating effects are evident at temperatures up to 77 K, indicating that heat removal from the device is less efficient with this substrate than with MgO or sapphire. Fig. 10 shows the results of the IF bandwidth measurements. In contrast to the MgO and sapphire data, these IF characteristics show no low-frequency plateau, but instead a continuous drop of the conversion efficiency starting at the lowest frequency point of 10 MHz. This in general indicates that the heat diffusion into the substrate is a dominant heat removal process. This behaviour also was earlier reported for very large-area devices [8].

According to [5], the thermal resistance due to the diffusion in the substrate becomes important if the device area is large and/or the substrate has a poor thermal conductivity. Our devices were small enough to eliminate this effect for MgO and sapphire substrates but the thermal resistance was still significant for YAO substrates. Due to this fact, the IF bandwidth is in the range of a few 10 MHz in the low-temperature limit. At 77 K it is still around 100 MHz, however, the high-frequency (hot-electron-like) plateau which we also see in this device, moved up by about 16 dB. A similar dependence was measured on MgO, but not on CeO_2/sapphire.

IV. IF bandwidth measurements at 100 GHz and 300 GHz

1. Setup

IF bandwidth measurements at 100 GHz and 300 GHz were performed inside a vacuum cryostat with optical windows. The mixer was a 50 nm long HEB device an MgO. The signals were generated by multiplied solid-state sources (100 GHz, 300 GHz) and by a backward wave oscillator (300 GHz). The mixer chip was glued with the backside to an elliptical lense made from high-resistivity silicon and the IF signal was coupled to a coaxial cable and directly monitored with a spectrum analyzer.

2. IF bandwidths

Fig. 11 shows a set of IF characteristics taken at 100 GHz and 300 GHz in the low and high-temperature limit. The most important result is that the IF bandwidth in the high-temperature limit (≈ 450 MHz at 77 K) is not as large as it was at operation frequencies in the 1-20 GHz range (≈ 1.4 GHz at 78 K). The bandwidth of about 200 MHz is even lower at a signal frequency of 300 GHz.
This indicates that the mixing mechanism responsible for the large IF bandwidth does not continue to operate well or at least does not couple to the radiation well at high RF. Of course flat response with RF would be expected in the case of bolometric mixing. In contrast to this, in the low-temperature limit the IF bandwidth seems to increase slightly

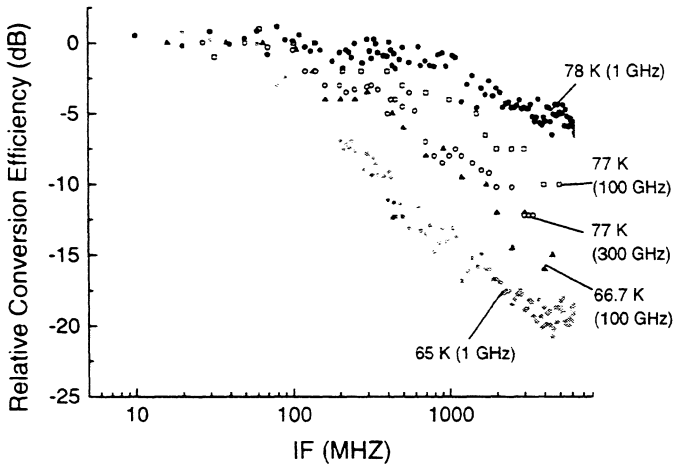

Fig. 11: IF bandwidth measurements at different operation frequencies using a 50 nm long HTS HEB on MgO in the low-temperature limit (around 65 K) and high-temperature limit (around 77 K)

with increasing operation frequency. However, the absolute conversion efficiency could not be estimated from these experiments, as the RF coupling efficiency is both poor and unknown.

VI. Discussion and Conclusion

For practical mixer applications, IF bandwidths larger than 1 GHz are desired. Our data show that HTS HEB mixers can meet this requirement. The measured bandwidths are lower than expected and a dependence on the device length was not found in a first set of devices. These facts suggests that phonon diffusion may not effectively decrease the energy relaxation times in our mixers. The reason for this and whether it depends on the specific device geometry is still under investigation.

However, the bandwidth performance of the HTS HEB even without heat diffusion into the contact is already encouraging. Thinner films may make the phonon escape into the substrate faster and enhance the bandwidth. Devices on CeO_2/sapphire have shown the best bandwidth performance. Mixer noise measurements have to be done in order to get a direct measure of the device performance. In fact, first noise measurements (to be discussed in a later publication) already indicate that the HTS HEB mixer performance agrees well with a model which does not include phonon diffusion.

Whether mixing in the high-temperature limit gives any advantage also depends on the device noise in this regime. The corresponding experimental data and analysis will be published soon [9]. The discovered temperature dependence of the IF bandwidth can probably account for previously reported unexpectedly high bandwidth of HTS mixers [10]. The origin of mixing in the flux-flow regime at high-temperatures, which obviously give larger IF bandwidths - but lower conversion efficiency, needs to be studied.

Acknowledgments

This research was partly funded by NASA through the JPL Director's Research and Development Fund. Funding for O.H. was provided by a HSP III Graduate Student Stipend of the German Academic Exchange Service (DAAD).

References

[1] M. Lindgren, V. Trifonov, M. Zorin, M. Danerud, D. Winkler, B. S. Karasik, G. N. Gol'tsman, and E. M. Gershenzon, *Appl. Phys. Lett.* 64, 3036 (1994)

[2] M. Danerud, D. Winkler, M. Lindgren, M. Zorin, V. Trifonov, B. S. Karasik, G. N. Gol'tsman, and E. M. Gershenzon, *J. Appl. Phys.*, 76, 1902 (1994)

[3] A. D. Semenov, R. S. Nebosis, Yu. P. Gousev, M. A. Heisinger, and K. F. Renk, *Phys. Rev. B* 52, 581 (1995)

[4] A. V. Sergeev, A. D. Semenov, P. Kouminov, V. Trifonov, I. G. Goghidze, B. S. Karasik, G. N. Gol'tsman, and E. M. Gershenzon, Phys. Rev. B 49, 9091 (1994)

[5] B.S. Karasik, W. R. McGrath, and M. C. Gaidis, *J. Appl. Phys.*, 81 (3), 1997

[6] For data of the thermal conductivity of YAO see: B. S. Karasik, W. R. McGrath, M.C. Gaidis, M. J. Burns, A. W. Kleinsasser, K. A. Delin, R. P. Vasquez, Proc. of *7. Int. Symp. on Space THz Technology*, p.571, March 1996

[7] A. W. Kleinsasser, J.B. Barner, M. J. Burns, B. S. Karasik, W. R. McGrath, accepted for *IEEE Trans. on Appl. Supercond.*, *Proc. of Applied Superconductivity Conference,* 1999

[8] M. Lindgren, M. A. Zorin, Trifonov, M. Danerud, D. Winkler, B. S. Karasik, G. N. Gol'tsman, E. M. Gershenzon, , *Appl. Phys. Lett.* 65 (26), 1994

[9] O. Harnack, B. S. Karasik, W. R. McGrath, A. W. Kleinsasser, J. Barner, in preparation for *7.th Int. Superconductive. Electronics Conference*, June 1999

[10] C.-T. Lee, Li, B. S. Deaver, Jr., Mark Lee, R. M. Weikle II, R. A. Rao and C. B. Eom, *Appl. Phys. Lett.,* 73, 1727 (1998)

DEVELOPMENT OF HIGH-T_c DETECTORS FOR SUB-MM RADIATION

G. de Lange, P. de Korte

Space Research Organization of the Netherlands, Postbus 800, 9700 AV Groningen, The Netherlands. e-mail:gert@sron.rug.nl

O. Harnack, M. Darula

Institute for Thin Film and Ion Technology, Research Center Juelich, 52425 Juelich, Germany

We investigate heterodyne detectors based on high-T_c superconducting materials, for the frequency range of 500-2500 GHz. Our current research includes detectors based on the Josephson effect and on the hot-electron bolometric effect. These devices are predicted to outperform Schottky-diode type mixers, with respect to sensitivity and LO-requirements. This, together with a required operating temperature which can be easily reached by space-qualified cryo-coolers, makes the high-T_c detector a promising candidate for long lasting space missions for atmospheric research.

Hot-electron bolometer devices made of 1x1x0.2 um YBCO on sapphire have been fabricated. 30 nm thick ceriumoxide buffer layers and YBCO films were grown by using pulsed laser deposition technique and optical lithography was used to define the microbridge and gold electrodes. These detectors are mounted in a 500 GHz waveguide system. We will present data on the RF and IF behavior of these devices. For higher frequencies, we designed a quasi-optical RF-coupling scheme consisting of a double-slot antenna mounted on a Si-lens. Devices for this set-up are currently fabricated.

$YBa_2Cu_3O_{7-\delta}$ HOT-ELECTRON BOLOMETER WITH SUBMICRON DIMENSIONS

S.Cherednichenko[1,2], F.Rönnung[1], G.Gol'tsman[2], E.Gershenzon[2] and D.Winkler[1]
[1] Department of Physics, Chalmers University of Technology and Göteborg University, Göteborg S-412 96, Sweden
[2] Department of Physics, Moscow State Pedagogical University, Moscow 119435, Russia

Photoresponse of $YBa_2Cu_3O_{7-\delta}$ hot-electron bolometers to modulated near-infrared radiation was studied at a modulation frequency varying from 0.2 MHz to 2 GHz. Bolometers were fabricated from a 50 nm thick film and had in-plane areas of 10×10 μm^2, 2×0.2 μm^2, 1×0.2 μm^2, and 0.5×0.2 μm^2. We found that nonequilibrium phonons cool down more effectively for the bolometers with smaller area. For the smallest bolometer the bolometric component in the response is 10 dB less than for the largest one.

Recently there has been increasing progress [1-7] in the development of bolometric mixers which utilize electron heating in thin Nb and NbN superconducting films. Regimes of both phonon cooling [1-4] and diffusion cooling [5-7] of hot electrons have been studied. These results prove that hot-electron bolometric (HEB) devices can successfully be used in terahertz heterodyne receivers [4]. Implementation of high-T_c superconducting materials may allow one to operate the mixer at liquid nitrogen temperature and also to increase the intermediate frequency bandwidth up to at least 20 GHz [8] while the fundamental limitation suggests 140 GHz.

The major obstacle to the realization of superconducting electronics on the basis of nonequilibrium effects is the presence of the bolometric component in the resistive response of high-T_c films. For mixers this component significantly increases the conversion loss and noise temperature. Since the bolometric response relates to phonon heating in the film, it may be diminished by improving the heat exchange through the film/substrate interface. There are two approaches in doing that: decreasing acoustic mismatch between the film and the substrate or making use of thinner films. Another phenomenon which delays the phonon cooling is the heating of the substrate underneath the film. Such an effect substantially contributes to the total thermal resistance between phonons and substrate [9]. Minimization of the substrate heating can be achieved by making use of a smaller bolometer fabricated on a substrate with larger

heat conductivity. Finally, there is a possibility for phonons to be cooled down via their diffusion from the bolometer to contacts [10]. The contribution of this channel to the total cooling rate should also increase with a decrease of the bolometer dimensions.

In this work we studied how the cooling rate of phonons in a $YBa_2Cu_3O_{7-\delta}$ (YBCO) HEB evolved with a decrease of the bolometer size.

We manufactured bolometers with different in-plane area (see Table I), which were integrated into planar bow-tie antennas. YBCO films with a thickness of 50 nm were deposited onto $LaAlO_3$ substrates by pulsed laser deposition in an oxygen atmosphere. Details of the deposition technique are described elsewhere [11]. After deposition, the films had a superconducting transition temperature of ≈88 K. X-ray diffraction showed that the films were predominantly c-axis oriented. Bolometer and antenna structures were patterned using electron-beam lithography and argon ion milling. After processing, the devices had a transition temperature of ≈87 K. A scanning electron microscope (SEM) image of device #4 with the antenna is shown in Fig.1.

Table I. Length (l), width (w), critical temperature (T_c) and critical current density (j_c) at T=77 K for samples #1 through 4.

Sample number	l [μm]	w [μm]	T_c [K]	$j_c \times 10^6$ [A/cm^2]
1	10	10	87	5.2
2	0.2	2	87	6.7
3	0.2	1	87	4.8
4	0.2	0.5	87	2.0

The experimental setup is shown in Fig.2. A semiconductor laser (1.56 μm wavelength) coupled to a single-mode fiber was used as a radiation source. The radiation power in the fiber was 1.4 mW. An optical isolator added 3 dB loss. The intensity of the laser radiation was modulated by a high-frequency signal generator. The modulated part of the total radiation intensity was about 10%. The bolometer was

driven into resistive state by a dc bias current. The bolometer response was measured with a Tektronix 494AP spectrum analyzer for modulation frequency from 0.2 MHz to 2000 MHz. For frequencies higher than 300 MHz additional amplifiers with a total gain of 30 dB were used. The magnitude of the photoresponse and, thus, responsivity depended on the bias current (see Fig.3). Measurements were performed at 77 K using the bias current that corresponded to the largest responsivity.

The photoresponse of different bolometers versus modulation frequency is shown in Fig.4. The curves are made to cross each other at frequency 300 MHz for comparison.

For sample #1 in the frequency range from 1 MHz to 10 MHz there is a gradual decrease of the response according to $f^{-0.3}$, where f is the modulation frequency. At frequencies larger than 40 MHz this dependence changes to f^{-1}, which characterizes a roll-off process with a single relaxation time. Such an evolution of the response agrees well with the observation made earlier [12] for bolometers of the same size. Samples #1 and #2 demonstrate practically the same dependence of the response on the modulation frequency. The response of the sample #3 shows a 5 dB smaller decrease in the low frequency bolometric range. For this sample the response remains constant for f<1 MHz, decreases according to $f^{-0.3}$ at larger frequencies, and follows a f^{-1} law at f>40 MHz. For sample #4 that has the smallest bolometer area the magnitude of the response remains constant until 60 MHz (within 3 dB) and then rolls off according to f^{-1}.

Several studies of hot-electron detectors from thin YBCO films have been made in the optical and millimeter wavelength ranges [11-16]. Both bolometric and nonbolometric components have been identified in the resistive response. The nonbolometric component controls the early stage of relaxation after pulse excitation or, in the case of modulated continuous wave excitation, the frequency dependence of the response at high modulation frequency (above 2 GHz) [11, 17]. The nonbolometric component corresponds to the heating up and cooling down of quasiparticles. The quasiparticle cooling rate is controlled by the reciprocal electron-phonon interaction time $(\tau_{e\text{-}ph})^{-1}$ in the resistive state of the superconductor. Recent direct measurements have shown that in thin YBCO films at 80 K this time equals 1.1 ps [17], i.e. the electron temperature can be modulated with a frequency as large as 140 GHz.

The bolometric component of the response is related to the heating of both the phonons and electrons in the film. If the film thickness d is smaller than $l_{ph,f}/\alpha_{f-s}$ ≈500 nm [9], where $l_{ph,f}$ is the phonon mean free path in the YBCO film and α_{f-s} is the transparency of the film/substrate interface for thermal phonons, thermal diffusion in the film towards the substrate can be neglected. Hence, the rate of phonon cooling is determined by the heat exchange rate through the film/substrate interface. It has been shown [9] that the total heat exchange rate depends not only on the rate of phonon escape $(\tau_{esc})^{-1}$ from the film into the substrate but also on the rate of reverse flow $(\tau_R)^{-1}$ of phonons back from the substrate to the film. Depending on the substrate material, for a 50 nm thick film the phonon escape time varies from 2 ns to 5 ns [9, 11], which corresponds to roll-off frequencies from 80 MHz to 30 MHz. The reverse phonon flow slows down the cooling of phonons in the film and results in the gradual decrease of the bolometric component of the response at small modulation frequencies according to f^{-m}, where m is between 1/2 and 1/3. The characteristic time of the phonon return to the film can be estimated as $\tau_R \approx \tau_{ph,s}/(\alpha_{s-f})^2$ where $\tau_{ph,s}$ is the phonon scattering time in the substrate and α_{s-f} is the transparency of the interface for phonons in the direction from the substrate to the film. Corresponding characteristic length is $l_R=(D_s\tau_R)^{1/2}=l_{ph,s}/\alpha_{s-f}$ where D_s is the phonon diffusivity in the substrate and $l_{ph,s}$ is the phonon mean free path in the substrate. The length l_R is the mean distance over which a phonon travels in the substrate until it returns to the film. The reverse flow of phonons can be minimized making use of substrates with larger heat conductivity, i.e. larger $\tau_{ph,s}$ and $l_{ph,s}$, and also by decreasing the in-plane sizes of the bolometer down to a magnitude less than l_R. Using $\tau_{ph,s} \approx 42$ ps and $\alpha_{s-f} \approx 0.059$ [9] we estimate $l_R \approx 0.4$ μm for our samples. Our estimate corresponds well to the area (0.5×0.2 μm^2) of the bolometer #4 that demonstrates a flat response in the frequency range from 2 to 60 MHz.

In the absence of the reverse flow of phonons from the substrate to the film, the response of HEB follows predictions of the two-temperature model [18] even at lowest modulation frequencies used in our experiment (see the solid line in Fig.4). The frequency dependence of the conversion loss in the heterodyne regime is controlled

by the frequency dependence of the responsivity [19]. Therefore the conversion loss in the hot-electron mode scales with the magnitude of the bolometric component. This suggests that at frequencies larger than 30 MHz and, consequently, in the hot-electron mode the conversion loss for a submicron YBCO HEB mixer should be ≈5 dB and ≈10 dB less, than for a 1 μm and 2 μm wide HEB mixer, respectively.

Further decrease of the conversion loss can be achieved due to additional improvement of the heat removal from the bolometer. One possibility is to decrease the film thickness and, consequently, shorten the phonon escape time. Another direction is to utilize the diffusion of nonequilibrium phonons from the bolometer to contacts. This mechanism of phonon cooling has been discussed in [10]. Authors theoretically estimated out-diffusion time τ_{diff} for a 0.2 μm long bolometer. They found τ_{diff}=260 ps that is an order of magnitude less than τ_{esc} for a 50 nm thick film. The effective cooling time due to both cooling mechanisms can be estimated as $(\tau_{esc}^{-1}+\tau_{diff}^{-1})^{-1}$ which results in a 240 ps overall cooling time and a corresponding roll-off frequency of 650 MHz. In comparing modulation frequency dependence of the response we did not find a noticeable difference between roll-off frequencies of bolometers with the length 10 μm and 0.2 μm (devices #1 and #3). The absence of the diffusion contribution to the phonon cooling rate in our samples can be attributed to defects and impurities that are not considered in [10] but may decrease the diffusivity of phonons.

In conclusion, we studied the response of YBCO hot-electron bolometers of different sizes to modulated laser radiation. We found that the decrease of the in-plane size of the bolometer below 1 μm resulted in the disappearance of the $f^{-0.5}$ dependence of the bolometric component in the response. It means that for a bolometer with such a small area the bolometric response is flat at frequencies smaller than the roll-off frequency corresponding to the phonon escape time, and above this frequency drops according to the two-temperature model. The obtained results suggest that the use of the submicron bolometer as mixer in the hot-electron mode should result in an increase of the conversion efficiency of the order 10 dB compared to larger bolometers.

Acknowledgments

The authors are grateful to Dr. A.Semenov for helpful discussions and detailed review of the manuscript. The project was in part funded by Swedish Foundation for Strategic Research and Russian Program on Condensed Matter (Superconductivity Division) under Grant No. 3.4. The samples were fabricated at the Swedish Nanometer Laboratory.

---

1 J. Kawamura, R. Blundell, C.-Y.E. Tong, G. Gol'tsman, E. Gershenzon, B. Voronov, and S. Cherednichenko, *Appl. Phys. Lett.* **70**, 12, 1619-1621, 1997.

2 J. Kawamura, R. Blundell, C.-Y.E. Tong, G. Gol'tsman, E. Gershenzon, B. Voronov, and S. Cherednichenko, "Phonon-cooled NbN HEB mixers for submillimeter wavelengths", Proc. of the 8th Int. Symp. on Space Terahertz Tech., Boston, MA, 23-26, 1997.

3 P. Yagoubov, M. Kroug, H. Merkel, E. Kollberg, G. Gol'tsman, A. Lipatov, S. Svechnikov, and E. Gershenzon, , "Quasioptical NbN phonon-cooled hot electron bolometric mixers with low optimal local oscillator power", Presented at the 9th Int. Symp. on Space Terahertz Tech., Pasadena, USA, 1998, in press.

4 J. Kawamura, R. Blundell, C.-Y. E. Tong, D. Cosmo Papa, T. R.Hunter, G. Gol'tsman, S. Cherednichenko, B. Voronov, and E. Gershenzon, "First light with an 800 GHz phonon-cooled HEB mixer receiver", Presented at the 9th Int. Symp. on Space Terahertz Tech., Pasadena , USA, 1998, in press.

5 A.Scalare, W.R.McGrath, B.Bumble, H.G.LeDuc, P.J.Burke, A.A.Verheijen, R.J.Schoelkopf, and D.E.Prober, "Large bandwidth and low noise in a diffusion-cooled hot-electron bolometer mixer", Appl. Phys. Lett. **68**, 11, 1558, (1996).

6 A.Scalare, W.R.McGrath, B.Bumble, H.G.LeDuc, IEEE Trans. Appl. Supercond. **7**, 2, 3568-3571,1997.

7 B.S.Karasik, M.C.Gaidis, W.R.McGrath, B.Bumble, H.G.LeDuc, Aappl.Phys.Lett. **71**, 1567,1997.

8 M.Lindgren, M.A.Zorin, V.Trofonov, M.Danerud, D.Winkler, B.S.Karasik, G.N.Gol'tsman, E.M.Gershenzon, "Optical mixing in patterned $YBa_2Cu_3O_{7-\delta}$ thin film", Appl.Phys.Lett., **65** (26), 1994.

9 A.V.Sergeev et al, "Transparency of YB $_2$C $_3$O $_7$-film/substrate interface for thermal phonons measured by means of voltage response to radiation", Phys.Rev.B, **49**(13), pp.9091, 1994.

10 B.S.Karasik, W.R.McGrath, and M.C.Gaidis, " Analysis of a high-T_c hot-electron superconducting mixer for terahertz applications", J.Appl.Phys. **81** (3), pp.1581-1589, 1997.

11 M.Danerud, D.Winkler, M.Lindgren, M.A.Zorin, V.Trifonov, B.S.Karasik, G.N.Gol'tsman, E.M.Gershenzon, J.Appl.Phys. **76** (3), 1994.

12 M.Lindgren, V.Trifonov, M.A.Zorin, M.Danerud, D.Winkler, B.S.Karasik, G.N.Gol'tsman, E.M.Gershenzon, "Transient resistive photoresponse of $YBa_2Cu_3O_{7-\delta}$ films using low power 0.8 and 10.6 μm laser radiation", Appl.Phys.Lett., **64**(22), 1994.

13 Yu.P.Gousev, A.D.Semenov, E.V.Pechen, A.V.Varlashkin, R.S.Nebosis, and K.F.Renk, "Coupling of terahertz radiation to a high-T_c superconbducting hot electron bolometer mixer", Appl.Phys.Lett. **69**(5), 1996.

14 M.J.Burns, A.W.Kleinsasser, B.Karasik, M.Gaidis, and W.R.McGrath, Pros. of the 8th Int. Symp. on Space Terahertz Tech., Pasadena . USA, 1997.

15 V.Trifonov, B.S.Karasik, M.A.Zorin, G.N.Gol'tsman, E.M.Gershenzon, M.Lindgren, M.Danerud, D.Winkler, Appl. Phys. Lett. **68**, 1418 (1996).

16 C.-T.Li, Mark Lee, B.S.Deaver, Jr, R.M.Weikle II, "High-Tc superconducting hot electron bolometer mixers", Presented at the 9th Int. Symp. on Space Terahertz Tech., Pasadena , USA, 1998, in press.

17 M.Lindgren, M.Currie, C.Williams, T.Y.Hsiang, P.M.Fauchet, R.Sobolewsky, S.H.Moffat, R.A.Hughes, J.S.Preston, F.A.Hegmann, "Intrinsic picosecond response times of Y-Ba-Cu-O superconducting photoresponse", subm.Appl.Phys.Lett. Sept.1998.

18 N.Perrin and C.Vanneste, "Response of superconducting films to periodic optical irradiation", Phys. Rev. B**28**, 5150 (1983).

19 E.M.Gershenzon, G.N.Gol'tsman, I.G.Gogidze, Yu.P.Gousev, A.I.Elant'ev, B.S.Karasik,and A.D.Semenov, Sov. J.Superconductivity 3, 1582 (1990).

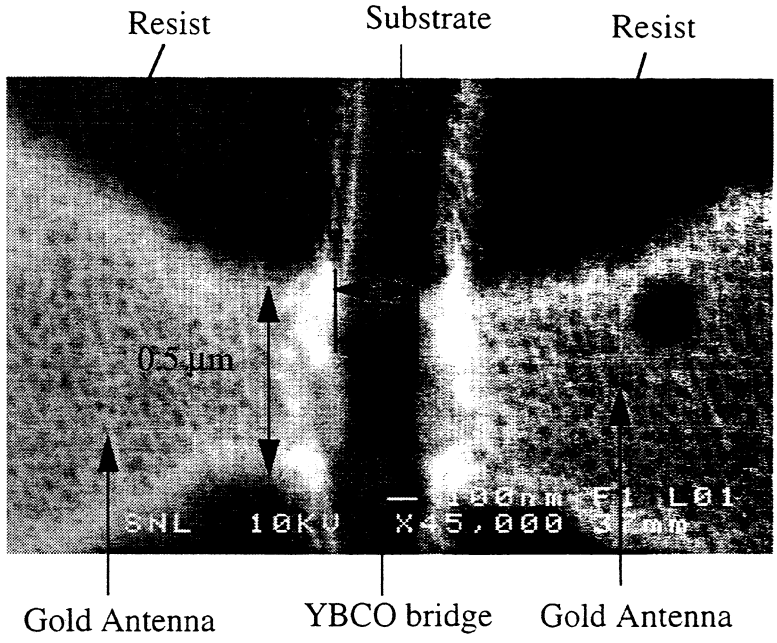

Fig.1. Scanning electron microscope image of sample #4.

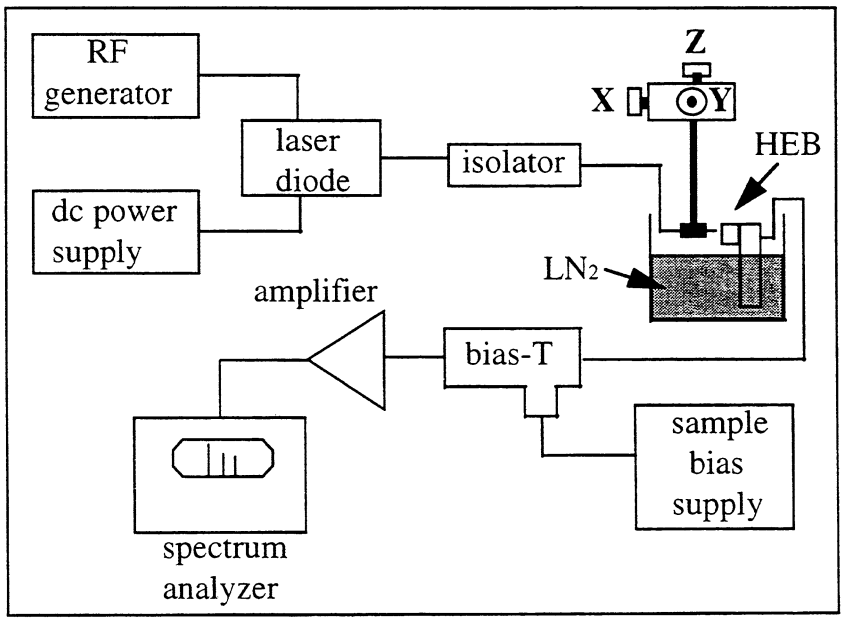

Fig 2. Experimental set-up.

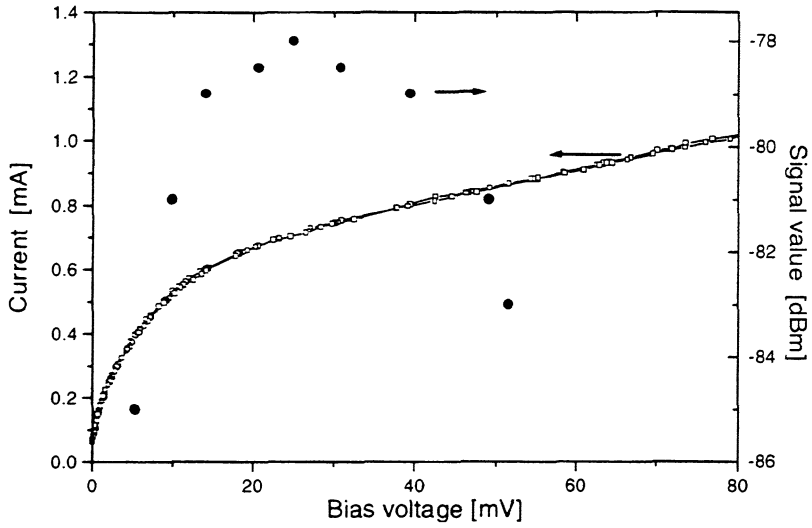

Fig.3. Current-voltage and detected signal vs. bias voltage characteristics of sample #4 (0.5×0.2 μm^2).

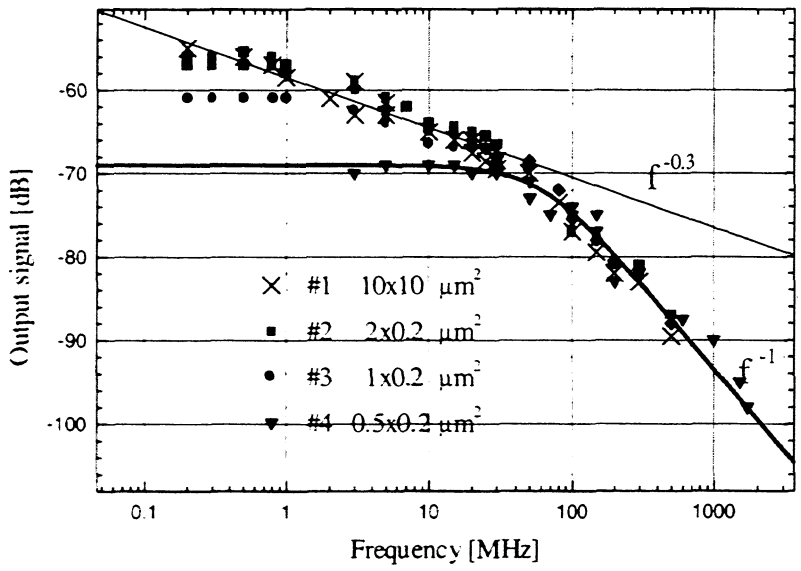

Fig.4. The photoresponse of samples #1 through 4 vs. modulation frequency. The solid line corresponds to the two-temperature model calculation.

NOISE TEMPERATURE AND SENSITIVITY OF A NbN HOT-ELECTRON MIXER AT FREQUENCIES FROM 0.7 THz TO 5.2 THz

J. Schubert[1], A. Semenov[2], G. Gol'tsman[2], H.-W. Hübers[1], G. Schwaab[3], B. Voronov[2], E. Gershenzon[2],

[1] DLR Institute of Space Sensor Technology, Rudower Chaussee 5, 12489 Berlin, Germany
[2] Physical Department, State Pedagogical University, 119435 Moscow, Russia
[3] Physical Chemistry Department II, Ruhr University Bochum, 44801 Bochum, Germany

Abstract

We report on noise temperature measurements of a NbN phonon-cooled hot-electron bolometric mixer at different bias regimes. The device was a 3 nm thick bridge with in-plane dimensions of 1.7 x 0.2 μm^2 integrated in a complementary logarithmic spiral antenna. Measurements were performed at frequencies ranging from 0.7 THz up to 5.2 THz. The measured DSB noise temperatures are 1500 K (0.7 THz), 2200 K (1.4 THz), 2600 K (1.6 THz), 2900 K (2.5 THz), 4000 K (3.1 THz) 5600 K (4.3 THz) and 8800 K (5.2 THz). Two bias regimes are possible in order to achieve low noise temperatures. But only one of them yields sensitivity fluctuations close to the theoretical limit.

1. Introduction

High resolution heterodyne spectroscopy in the frequency range from 1 to 6 THz yields important information on astronomical objects as well as on the chemical composition of the atmosphere of the earth. Some prominent examples are the CII fine structure line at 1.6 THz and the OI fine structure line at 4.75 THz which are major coolant lines of the interstellar medium. The OH rotational transitions at 2.5 THz and 3.5 THz allow for the determination of the OH volume mixing ratio in the stratosphere and gives important information on the catalytic cycles which are responsible for the destruction of stratospheric ozone. A number of on-going astrophysical and atmospheric research programs are aimed at these goals.

So far Schottky diodes have commonly been used as mixers in heterodyne receivers at frequencies above 1.2 THz. The achieved double sideband (DSB) receiver noise temperatures range from 2500 K at 1 THz to about 70000 K at 4.75 THz [1,2]. These numbers are far above the quantum noise limit. However, many research and observation goals require a receiver noise temperature close to the quantum limit. Superconducting hot-electron bolometric (HEB) mixers are prominent devices in order to satisfy this requirement. In the following we report on the results of noise temperature measurements performed with the same phonon-cooled NbN HEB mixer at seven frequencies from 0.7 THz to 5.2 THz.

2. Mixer Design

The investigated HEB was made from a 3 nm thick superconducting NbN film. The film was deposited by dc reactive magnetron sputtering onto a 350 μm thick high resistivity Si substrate (5 kΩ cm). The details of the process are described elsewhere [3]. The bolometer itself is a 1.7 μm wide and 0.2 μm long bridge; it has a transition temperature of 9.3 K and a 870 μΩ cm resistivity at room temperature.

A planar two-arm logarithmic-spiral antenna is used to couple both the signal and the local oscillator (LO) radiation with the bolometer (fig. 1). The central part of the antenna was patterned using electron beam lithography while the outer part was defined by conventional UV photolithography (for details see Ref. [4]). The circle, inside which the antenna arms formed inner terminals and seized to represent a spiral, has 2.6 μm diameter. The diameter of the circle that circumscribes the spiral structure is 130 μm. Between these circles, the antenna arms make two full turns. A radial line from the origin of the antenna intersects a spiral arm at an angle of 70°. The spiral structure terminates a coplanar line that has an impedance of 50 Ω and was lithographed on the same substrate. According to estimates [5], such an antenna should have rf impedance of about 75 Ω when suspended in free space. We expect an even smaller value for our antenna since it is supported by the semi-infinite dielectric half-space simulated by the substrate with the thickness much larger than the wavelength.

The substrate supporting the HEB with the planar antenna was glued onto the flat side of an extended hyperhemispheric lens. The lens was cut off from an optically polished 6 mm diameter sphere that was made from high resistivity (>10 kΩ cm) silicon. No antireflection coating was used. The extension of the lens together with the substrate yields a total extension length of 1.2 mm. This is very close to the optimal extension length for which the beam pattern of the hybrid antenna is diffraction limited, i.e. the pattern is rather determined by the diameter of the lens than by the beam properties of the planar feed antenna. In this case the side-lobes are still low. It is worth mentioning that in the range of the diameter to wavelength ratios,

which we covered in the experiment, the optimal extension length is almost independent on the wavelength [6].

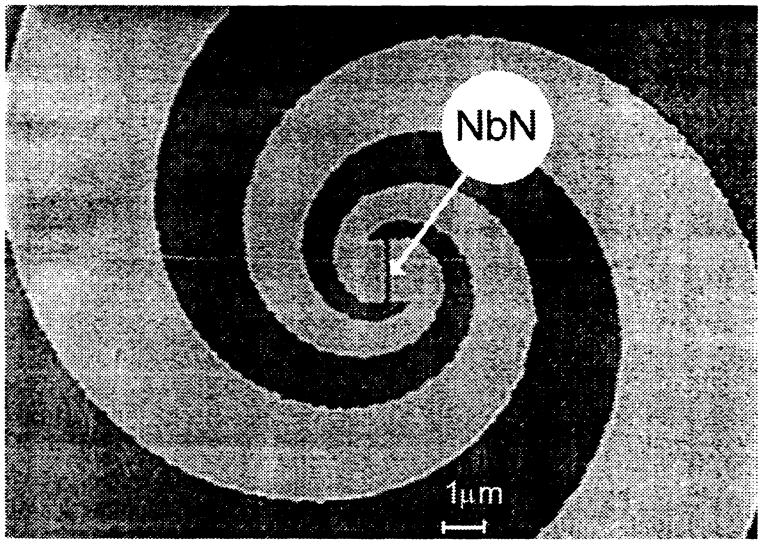

Fig. 1: SEM picture of the inner part of the spiral antenna with the NbN HEB.

3. Experimental Setup

The lens and the HEB were mounted in a copper holder which in turn was directly screwed to the 4.2 K cold plate of an Infrared Labs HD-3 LHe cryostat. The cryostat has a wedged 1.5 mm thick TPX pressure window. A 1.2 mm thick quartz window with an antireflection coating was mounted on the 77 K shield. This filter has a cut-off frequency exceeding 6 THz. The intermediate frequency (IF) signal was guided out of the HEB via a 50 Ω coplanar line, which was soldered to SMA connector. A bias tee followed by an isolator was used to feed the bias to the mixer and to transmit the IF signal to a low noise (< 3 K) 1.2 - 1.8 GHz HEMT amplifier (36 dB gain at 1.5 GHz). Bias tee, isolator and amplifier were also mounted on the cold plate of the cryostat. The output of the amplifier was filtered at 1.5 GHz with a bandwidth of 75 MHz, further amplified and finally detected with a crystal detector.

The device was investigated at seven different frequencies ranging from 0.7 THz up to 5.2 THz. Two FIR gas laser systems were used to cover this frequency region. The measurements from 0.7 THz to 2.5 THz were performed using an optically pumped FIR ring laser [7]. The ring laser design prevents back-reflection of CO_2 pump radiation from the FIR cavity into the CO_2 laser cavity resulting in a stable output power of the FIR laser. Out-coupling of FIR radiation was performed through a 3 mm

diameter hole in one of the laser mirrors. For the measurements between 2.5 THz and 5.2 THz a transversely excited FIR laser was used. As it is the case for the ring laser this design inhibits the back-reflection of CO_2 radiation into the pump laser. For this laser a 45° moveable mirror was used for the output coupling of the FIR radiation. This mirror can be moved transversely to the optical axis of the FIR laser and allows for optimization of the output power for each laser line separately [8]. It should be mentioned that the noise temperature measured at 2.52 THz was the same independently on which laser system was used for the measurements.

Freq. [THz]	0.6929	1.3971	1.6266	2.5228	3.1059	4.2517	5.2456
Lasing medium	HCOOH	CH_2F_2	CH_2F_2	CH_3OH	CH_3OH	CH_3OH	CH_3OD
CO_2 pump line	9R20	9R34	9R32	9P36	9R10	9P34	9R8

Table 1: The laser lines used for the investigations.

The output radiation of the ring laser (see fig. 2) was focussed onto the HEB mixer by two high-density polyethylene lenses (one lens for the setup with the transversely excited FIR laser). In order to monitor the LO output power a wire grid in the LO beam path deflected a minor fraction of the LO radiation onto a pyroelectric detector. A second, rotatable wire grid served for attenuation of the LO power delivered to the HEB. The signal and the LO beam were superimposed by a 6 μm thick Mylar beamsplitter.

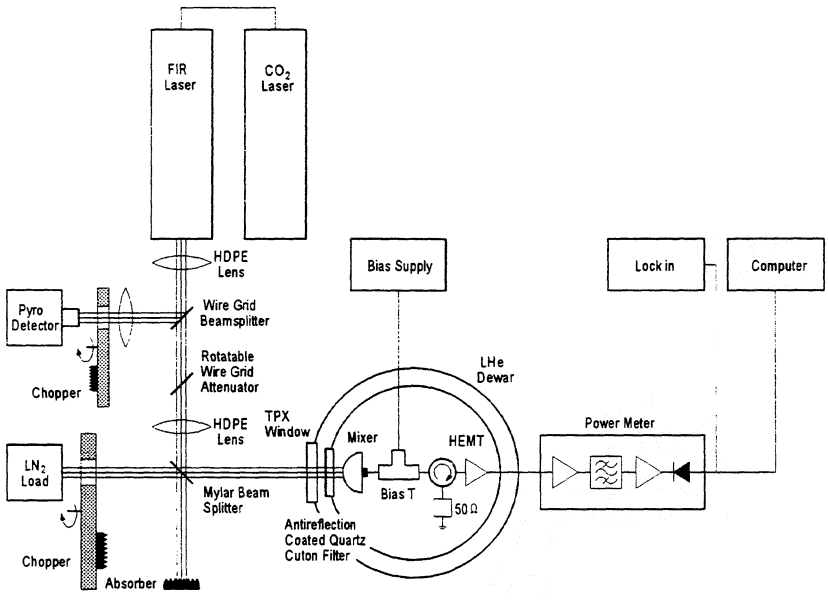

Fig. 2: Experimental setup.

Double sideband (DSB) receiver noise temperatures were determined by the Y-factor method. Ecosorb was used as the hot and cold load. The temperature of the hot and cold load was 293 K and 77 K, respectively. The stability of the laser systems was good enough to measure the noise temperature by putting alternately the hot load and the cold load for about ten seconds in the signal path behind the beamsplitter. The not evacuated optical path from the load to the pressure window of the cryostat was about 25 cm long. The hot and cold reading were averaged by a computer and the Y-factor as well as the noise temeperature were calculated. Due to the relatively weak laser line and the narrow line profile the noise temperature at 5.2 THz was measured by chopping (frequency: 15 Hz) between the hot and cold load using lock-in technique. It was verified at the other frequencies that the direct technique and the chopping technique yield the same result At frequencies above 1 THz the Rayleigh-Jeans approximation does no longer closely describe the power radiated by a black body into a single mode. Therefore, we used the general form of the dissipation-fluctuation theorem (Callen and Welton, [9]) for deriving the receiver noise temperature from the measured Y-factor.

4. Noise Temperature Measurements

All noise temperatures reported in this paper were measured with the same NbN HEB mixer. Compared to previously published results with this device [10] we were able to improve its performance mainly by improving the accuracy of the mounting of the HEB with respect to the center of the Si lens and by using a lower loss beamsplitter. It is worth mentioning that the device has shown no degradation in either the dc characteristics or the noise performance, although it has been already eight months under test.

In Fig. 3 the unpumped and pumped I-V curves of the HEB mixer at a temperature of 4.2 K are shown. The series resistance in the superconducting state is about 3 Ω. There is a first plateau in the IV-characteristic at a current of 45 μA that is followed by a second linear increase corresponding to a resistance of 40 Ω. Another plateau develops at a current of 55 μA. After the third almost linear increase, which corresponds to a resistance of 80 Ω, the maximum critical current of 90 μA is reached. The normal resistance of the HEB at the operation temperature was almost the same as at room temperature. This behavior is likely to be due to the existence of three patches in the superconducting film each with a different critical current. We speculate that two of them are situated under the contact pads. The critical current in those parts is reduced due to the proximity effect between NbN and gold. A tail seen in the resistive transition of the device below the critical temperature likely supports this tentative explanation.

We have measured the receiver noise temperature for different bias conditions and different LO powers. Low noise temperatures were usually found at a moderate bias voltage (around 1.8 mV and 22 μA) corresponding to an almost linear part of the IV-characteristic (region 1 in fig. 3). However, at smaller bias voltages (around 0.05 mV and 24 μA) corresponding to the nonlinear regime the noise temperature was usually somewhat lower (region 2 in fig. 3). At 2.5 THz we measured a lowest noise temperature of 2900 K in region 1 while in region 2 the lowest noise temperature was 2200 K. At 1.4 THz it was 2200 K (region 1) and 1600 K (region 2). The values for region 2 are corrected for the direct detection contribution which is significant while insignificant in region 1. The region 2 is very close to the unstable region of the IF signal (fig. 3). In the following part of this section we will discuss only the results for the region 1 which is better suited for radiometric applications (see section 5).

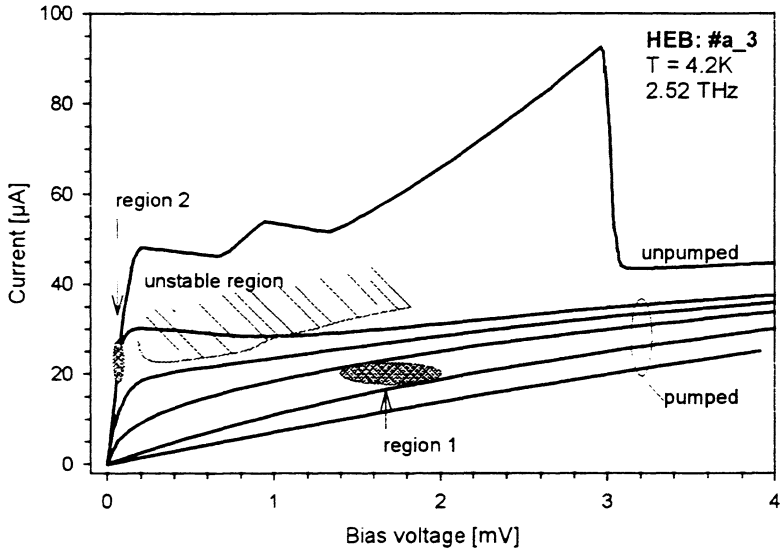

Fig. 3: Unpumped and pumped (at 2.5 THz) IV characteristics of the investigated HEB mixer. Also shown are the different regions with low noise temperatures and the unstable region (explanation see text).

In table 2 and fig. 4 the DSB receiver noise temperature is shown as a function of the LO frequency between 0.7 THz and 5.2 THz. Also shown in Fig. 4 is the DSB receiver noise temperature when corrected for the losses in the optical elements as given in table 3. In this case the increase is linear and follows closely the 10 hν/k line. This result suggests that the hybrid antenna of the mixer is frequency independent from 0.7 THz up to 5.2 THz.

Freq. [THz]	0.6929	1.3971	1.6266	2.5228	3.1059	4.2517	5.2456
T_{rec} DSB [K]	1500	2200	2600	2900	4000	5600	8800

Tab. 2: Measured DSB receiver noise temperatures at different frequencies.

We use the criterion $\lambda/2 \leq D$ (D =.130 μm) [5] for the cut-off at the low frequency side. For our antenna this yields the free space wavelength outside the silicon of 884 μm (0.34 THz). The shortest wavelength for which the spiral antenna is still working properly is about 10 times the inner radius at which the spiral deviates from the ideal shape [11]. In our case this is 1.3 μm yielding a lower wavelength limit of 44 μm (6.8 THz).

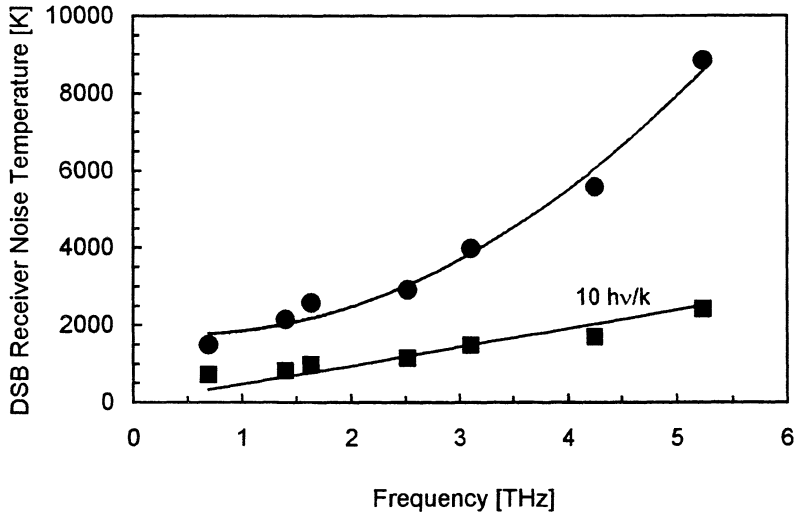

Fig.: 4: DSB receiver noise temperature as a function of frequency. The circles indicate the measured noise temperature while the squares correspond to the noise temperature corrected for losses in the optics.

According to table 2 the quartz filter and the Si lens give the major contributions to the total losses. Using a Zitex filter instead of the quartz filter could reduce the noise temperature by about 0.6– 1.4 dB in the frequency range from 0.7 THz to 2.5 THz. This for example would yield a DSB noise temperature of about 2400 K at 2.5 THz (loss of Zitex filter ≤0.5 dB [12]). This is comparable with other phonon cooled HEB mixers [13,14] as well as with Nb diffusion cooled HEB mixers [15]. However Zitex has a roll-off slightly above 2.5 THz [12]. Above this frequency a quartz filter has an

advantage. For the reduction of the loss in the Si lens no straightforward solution is available. One possibility to reduce the reflection could be the use of grooves and separation of a certain shape on the surface of the Si lens. This approach is discussed in Ref. 16.

	Loss [dB]						
Frequency	0.7 THz	1.4 THz	1.6 THz	2.5 THz	3.1 THz	4.3 THz	5.2 THz
Beamsplitter	0.1	0.2	0.3	0.6	0.7	1.2	1.2
TPX window	0.4	0.4	0.5	0.6	0.6	0.8	0.9
Quartz filter	1.1	1.8	1.9	1.2	1.3	1.5	1.9
Si lens (refl.)	1.5	1.5	1.5	1.5	1.5	1.5	1.5
Si lens (absorp.)	0.1	0.1	0.1	0.1	0.1	0.1	0.1
Sum	3.2	4.0	4.3	4.0	4.2	5.1	5.6

Table 2: Losses in the optics (data for the beamsplitter are calculated, data for the TPX window and the quartz filter are from the transmission curves as given by the manufacturer, data for the Si lens are estimated).

The LO power absorbed in the HEB was evaluated from the pumped and unpumped IV characteristics. We used the isothermal method described elsewhere [12]. An absorbed LO power around 100 nW was determined at all frequencies.

5. Sensitivity Fluctuation

It is instructive to determine not only the noise temperature but also the sensitivity fluctuation ΔT of a receiver. Fig. 5 shows the sensitivity fluctuation for the optimum bias (region 1 in fig. 2) at 1.4 THz. The first half of the scan is with the cold load in the signal path while the second half is with the hot load in the signal path. This scan documents the good stability of the laser LO. The temperature ΔT_{min} that corresponds to fluctuations of the total output power of the receiver is given by $\Delta T_{min} = T_{sys} / (\Delta\nu\ \tau_{int})^{1/2}$ [17] (bandwidth $\Delta\nu$ = 75 MHz, integration time τ_{int} = 2 ms). From the scan in fig. 5 we estimate a rms sensitivity fluctuation of 7.4 K, that is in a good agreement with the calculated value of 6.2 K. In comparison, the rms fluctuation sensitivity is about 30 K in region 2, for which the best noise temperature was measured (1600 K). The situation at 2.5 THz is similar. While in region 1 the sensitivity fluctuation is close to the theoretical limit it is up to 100 K in region 2. We attribute this dramatic increase of sensitivity fluctuations to an enhanced magnitude of rms noise at the device output. The region 2 corresponds to the strongly nonlinear operation regime when the impedance of HEB is very sensitive against small variations of the bias

voltage, LO power, and operation temperature. This was also experimentally found and is indicated in fig 2 by the much smaller area of region 2 compared to region 1. Instabilities of any of the operation parameters effect the operating point of the HEB and, consequently, the matching of the HEB to the IF network. This results in additional noise. Besides that there could be intrinsic reasons caused by physics of the detection and mixing process, e.g. switching of the bias current between different paths in a non-uniform film driven in the resistive state. However, at this stage a definite answer to the question about the origin of excess rms noise is not possible. Results of our measurements make clear that, although region 2 yields the better noise temperature, it is not readily suitable for radiometric applications.

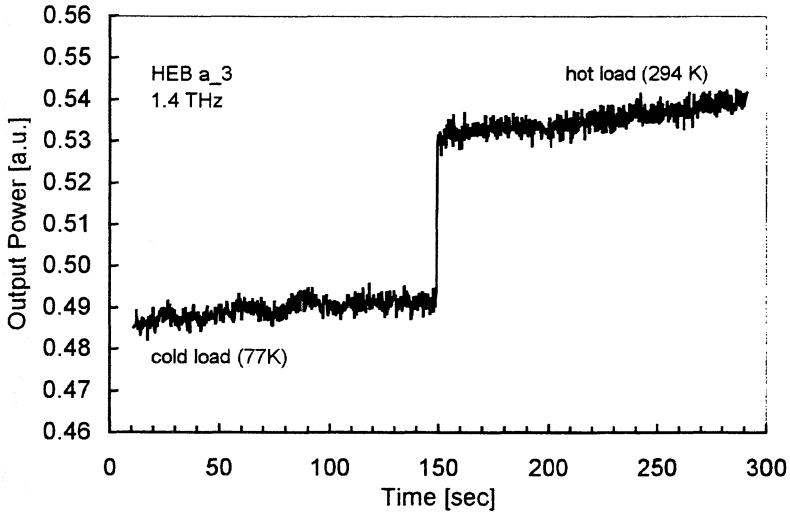

Fig. 5: Output noise of the HEB mixer as a function of time.

6. Conclusions

We have measured the noise temperature and fluctuation sensitivity of a phonon-cooled hot-electron bolometric mixer operated in different bias regimes in the frequency range from 0.7 THz to 5.2 THz. We demonstrated that the superlinear increase of the DSB noise temperature with frequency resulted from frequency dependent losses in coupling optics. When corrected for losses, the noise temperature of the mixer increased linearly with frequency with the slope 10 hv/k, thus suggesting that the hybrid antenna was frequency independent in the specified frequency range. We found two distinctive bias regimes resulting in fairly low noise temperature, of which only one provided fluctuation sensitivity corresponding to theoretical estimates. Our results show that it is possible to build a broadband HEB mixer with lowest noise temperatures.

Acknowledgment

We would like to thank U. Bartels for assistance with the mounting of the HEB and for assistance during the measurements.

References

[1] H. P. Röser, H.-W. Hübers, T. W. Crowe, W. C. B. Peatman, Infrared Phys. Technol. **35**, 451 (1994).
[2] A. L. Betz, R. T. Boreiko, Proc. of the 7th Int. Symp. on Space Terahertz Technology, 503 (1996).
[3] S. Cherednichenko, P Yagoubov, K. Il'in, G. Gol'tsman, E. Gershenzon, Proc. of the 8th Int. Symp. on Space Terahertz Technology, 245 (1997).
[4] S. Svechnikov, A. Verevkin, B. Voronov, E. Menschikov, E. Gershenzon, G. Gol'tsman, Proc. of the 9th Int. Symp. on Space Terahertz Technology, 45 (1998).
[5] J. D. Kraus, *Antennas*, McGraw-Hill, Inc., (1988).
[6] T. H. Büttgenbach, IEEE Trans. Microwave Theory Tech. **41**, 1750 (1993).
[7] H.-W. Hübers, G. W. Schwaab, H. P. Röser, Proc. 30th ESLAB Symp. „Submillimetre and Far-Infrared Space Instrumentation", ESA SP-388, 159 (1996).
[8] H.-W. Hübers, L. Töben, H. P. Röser, Rev. Sci. Instr. **69**, 290 (1998).
[9] A. R. Kerr, M. J. Feldman, S. K. Pan, Proc. of the 8th Int. Symp. on Space Terahertz Technology, 101 (1997).
[10] G. W. Schwaab, G. Sirmain, J. Schubert, H.-W. Hübers, G. Gol'tsman, S. Cherednichenko, A. Verevkin, E. Gershenzon, to appear in IEEE Trans. on Appl. Superconductivity (1999)
[11] T. H. Büttgenbach, R. E. Miller, M. J. Wengler, D. M. Watson, T. G. Phillips, IEEE Trans. On Microwave Theory Tech. **36**, 1720 (1988).
[12] B. Karasik, M. Gaidis, W. R. McGrath, B. Bumble, H. G. LeDuc, Proc. of the 8th Int. Symp. on Space Terahertz Technology, 55 (1997).
[13] P. Yagoubov, M. Kroug, H. Merkel, E. Kollberg, H.-W. Hübers, J. Schubert, G. Gol'tsman, E. Gershenzon, G. Schwaab, this volume (1999).
[14] P. Yagoubov, M. Kroug, H. Merkel, E. Kollberg, J. Schubert, H.-W. Hübers, G. Schwaab, G. Gol'tsman, E. Gershenzon, to appear in IEEE Trans. on Appl. Superconductivity (1999).
[15] B. Karasik, M. Gaidis, W. R. McGrath, B. Bumble, H. G. LeDuc, Appl. Phys. Lett. **71**, 1567 (1997).
[16] G. Schwaab, H.-W. Hübers, J. Schubert, G. Gol'tsman, A. Semenov, A. Verevkin, S. Cherednichenko, E. Gershenzon, this volume (1999)
[17] J. D. Kraus, *Radio Astronomy*, 2nd ed., Powell (1986).

IMPROVED CHARACTERISTICS OF NbN HEB MIXERS INTEGRATED WITH LOG-PERIODIC ANTENNAS

E. Gerecht

Department of Physics and Astronomy, University of Massachusetts at Amherst, Amherst, MA 01003

C.F. Musante, H. Jian, Y. Zhuang, and K.S. Yngvesson

Department of Electrical and Computer Engineering, University of Massachusetts, Amherst, MA 01003

J. Dickinson, T. Goyette, and J. Waldman

Submillimeter Technology Laboratory, University of Massachusetts at Lowell, Research Foundation, Lowell, MA 01854

P.A. Yagoubov

Department of Microelectronics, Chalmers University of Technology, S-41296 Gothenburg, Sweden

G.N. Gol'tsman, B.M. Voronov, and E.M. Gershenzon

Department of Physics, Moscow State Pedagogical University, Moscow, Russia

I. INTRODUCTION

Hot Electron Bolometric (HEB) mixers have recently demonstrated the lowest receiver noise temperatures ever measured in the THz frequency region. HEB receivers have become the most promising approach for applications such as high-resolution heterodyne spectral measurements of astronomical objects from airborne or space-based platforms at frequencies above 1 THz. At most frequencies the lowest noise temperatures attained so far have used NbN Phonon-cooled HEB (PHEB) mixers. We have developed NbN PHEB devices and have improved their characteristics very substantially since our paper at the Ninth STT Symposium. We report total DSB receiver noise temperatures of 485 K at 620 GHz (440 K when the device was cooled to 3 K), 1,000 K at 1.56 THz, and 2,200 K at 2.24 THz. NbN HEB mixers have been shown to have sufficient bandwidths for the anticipated applications such as future receiver frontends for THz astronomical observation from space. We have measured a conversion gain bandwidth of 3 GHz at 620 GHz for one of our devices and calculated the receiver noise bandwidth to be 6.5 GHz with a sufficiently wideband IF amplifier. The lowest LO power required is 500 nW which makes NbN PHEB mixers suitable for use with future solid state tunable THz sources. However, the LO power is not at such a low level that its operating point is affected by input thermal noise power. This paper describes the development of our NbN PHEB mixers and discusses device fabrication and optical coupling issues as well as our measurement setup and results.

II. DEVICE DESIGN AND FABRICATION

NbN Films

The NbN films were fabricated on silicon substrates at Moscow State Pedagogical University (MSPU) by magnetron reactive sputtering in an argon/nitrogen gas mixture. For this work we have primarily used films of thickness 3.5-4 nm in order to maximize the conversion gain bandwidth. The production of such thin films is still an evolving technology but recent films on both sapphire and silicon substrates have shown much improved properties [Cherednichenko et al., 1997]. The optimum thickness, based on the sapphire work, appears to be close to 3.5-4 nm. The surface resistance of the films is from 300 Ω/square to 600 Ω/square. The devices fabricated during the last year have shown an improvement of T_c from 7.5-9 K to 10-10.5 K (11 K for the 5 nm device). The transition width is still about 1 K and the critical current density can be as high as 3 x 10^6 to 4 x 10^6 A/cm^2 for the 3.5 to 4 nm devices.

Optical Design

Optical design considerations are crucial for efficiently coupling LO and signal power into the device. Quasi-optical coupling to the device is most common for frequencies above 1 THz. We still use an extended hemispherical silicon lens coupled to a self-complementary log-periodic toothed antenna (see Figure 1), as successfully demonstrated and analyzed at 250 GHz and 500 GHz by [Filipovic et al, 1993]. The log-periodic toothed antenna is convenient since it can be used over a very wide frequency range; later versions will employ other antennas tuned to smaller frequency bands, which may possibly have higher efficiency. For our original design, we scaled the dimensions of the lens and the antenna used in the 250 GHz setup by a factor of ten, resulting in a lens diameter of 1.3 mm. We chose an extension length, beyond the hemispherical lens, of 0.33 times the lens radius. We can predict the amount of beam-scan which would be

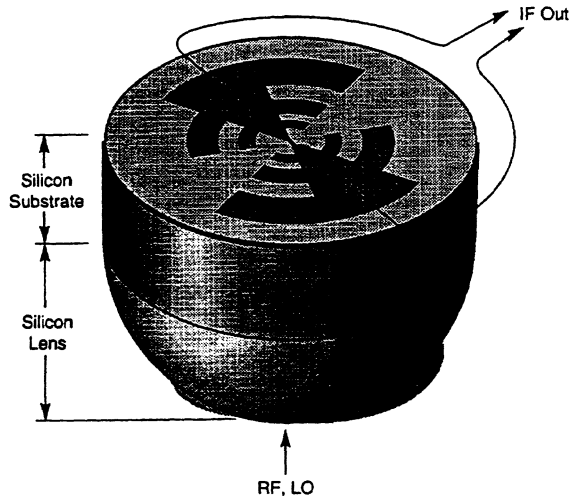

Figure 1: Log-periodic antenna fabricated on an extended hemispherical lens.

caused by misalignment of the center of the antenna with respect to the center of the lens: a 20 micrometer misalignment results in a 5 degree beam scan. This makes it imperative to use an accurate alignment procedure, which will be described below. We are not employing a matching layer at this stage. The beamwidth of this lens at 1.56 THz is 8 degrees, which is sufficiently narrow for the beam to clear the dewar window. Recently, we have also used an elliptical lens with a base diameter of 4 mm. The elliptical lens is less critical in terms of alignment and does not require the substrate thickness to be adjusted. The device is then mounted at the foci of the lens.

Device Fabrication

Devices were fabricated at UMASS/Amherst. The gold log-periodic antenna is fabricated using liftoff. After the pattern has been defined in the photoresist, 20 nm of Ti and 100 nm of Au are deposited by E-beam evaporation and the lift-off is performed. The NbN strips (strip) are then defined and etched using Reactive Ion Etching (RIE). In the most recent fabrication run, we tested wet etching of the NbN as an alternative technique with excellent results. All devices fabricated since the beginning of 1998 have had a configuration of a single wide strip which results in the lowest normal resistance and thus the best match to the antenna. For the device used with the 1.3 mm lens, the substrate is thinned by lapping to a thickness equal to the lens extension length. The position of a square alignment window for the lens is defined in a photoresist layer on the opposite side of the substrate from the antenna and device using an infrared mask aligner, whereupon the alignment window is etched by RIE to a depth of 100nm. The lens is attached to the silicon substrate using purified bees wax. The final dimensions of the device strips for the original design are about 0.6 μm long by 1.0 μm wide. The single strips have the same length and are either 5 μm or 10 μm wide. Two different sizes of antennas with maximum frequencies of 1.2 THz (Antenna A) and 2.4 THz (Antenna B), respectively, were employed. Figure 2 shows an SEM picture of a device of the older type with four strips.

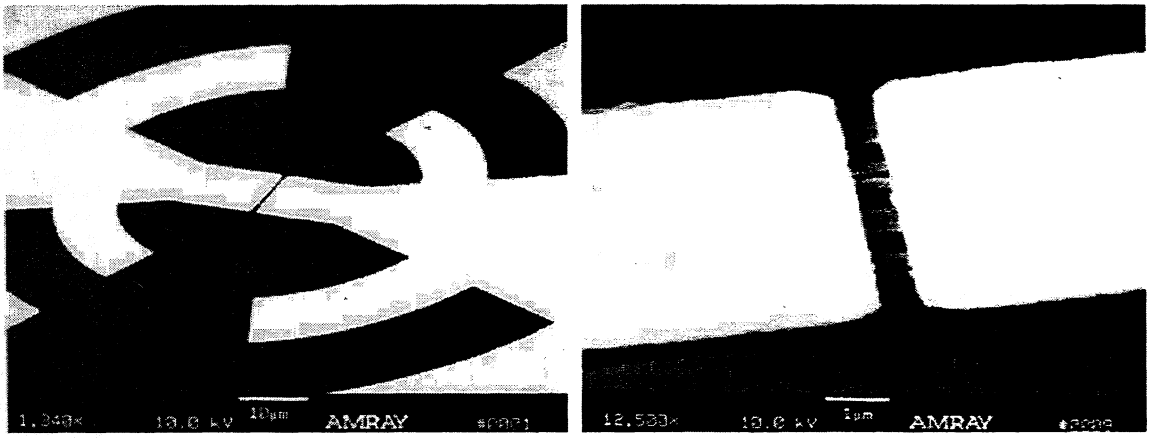

Figure 2: SEM photographs of the NbN device.

III. EXPERIMENTAL SETUP

Receiver Configuration

The integrated antenna/HEB device and lens are attached to a copper post, which is thermally anchored at the other end to the liquid helium reservoir of an IRLAB dewar (see Figure 3). The antenna is connected to the IF and bias system via a microstrip/semirigid coax line and bias tee. A cooled HEMT amplifier with isolator input is also used inside the dewar. This IF amplifier has a bandwidth from 1250 to 1750 GHz with a noise temperature of about 13K except for in the most recent experiment in which we used an amplifier with 7 K noise temperature.

Figure 3: Top view of the IRLAB dewar showing the *dc* and *IF* connections.

Optical Setup

The optical coupling loss as well as the receiver noise temperature are measured with a CO_2 laser pumped FIR gas laser as the LO source. The laser setup is illustrated in Figure 4. Mylar beam splitters with a thickness of 6 μm act as diplexer between the LO and a chopped hot/cold noise source. The LO radiation is focused by a TPX lens. The active medium of the FIR laser is difluoromethane and two output frequencies of 1.56 THz (wavelength 191 μm) and 2.24 THz (wavelength 134 μm), respectively, are available. The gain bandwidth of NbN HEB devices at the IF cannot be easily measured at THz frequencies. At present, we measure the mixer gain bandwidth at 94 GHz instead. Noise temperature and bandwidth measurements at 0.6 THz to 0.75 THz were also performed at Chalmers University in a setup which used a BWO as LO source and a 12.5 μm beam splitter . The experimental arrangement was as described in [Ekström et al., 1997].

FTS Spectra of the Device Response

Fourier Transform Spectra were obtained at Chalmers University by employing the device as a detector at a temperature close to T_c.

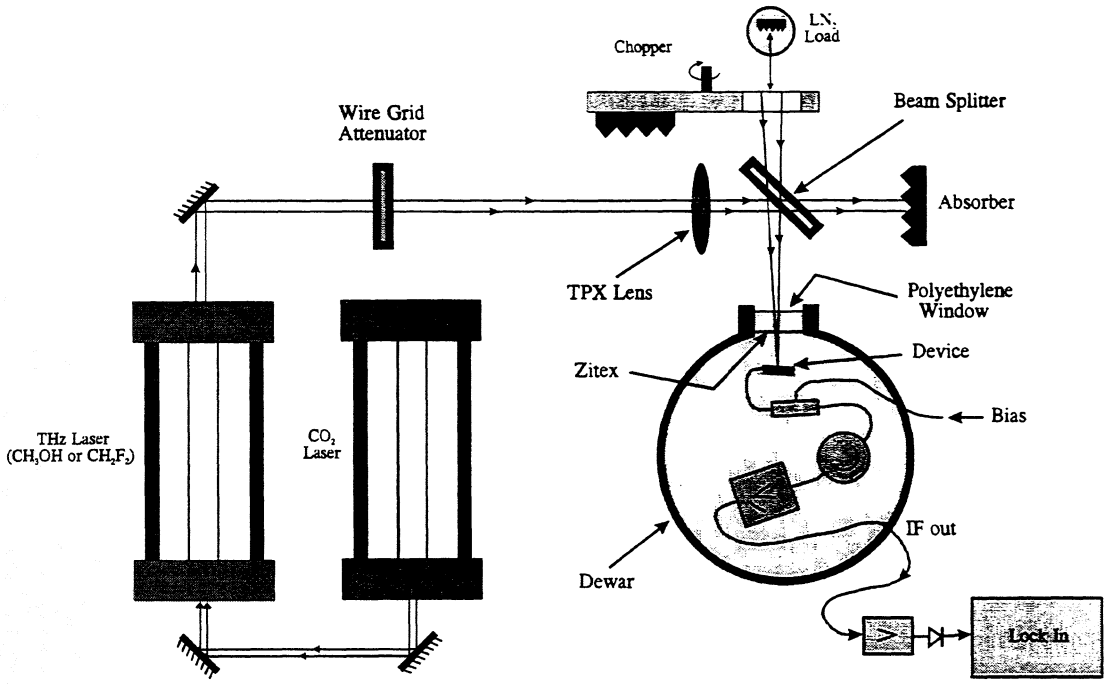

Figure 4: Optical setup for measurement of optical coupling loss and receiver noise temperature.

IV. RESULTS AND DISCUSSION

FTS Spectra of the Device Response

Figure 5 shows the spectra obtained for a NbN device integrated with the larger version of the log-periodic antenna described above. The device was mounted in two perpendicular orientations in order to elucidate the frequency-dependence of its optimum polarization. [Kormanyos et al., 1993] showed that the polarization for optimum response varies periodically with frequency at an amplitude of ±22.5°. This is consistent with the spectra we observed in which dips in the response occur at frequencies which are one octave apart. As the orientation of the device was changed by 90 degrees, peaks appear where dips occur for the perpendicular orientation. The highest frequency peak corresponds to when the second smallest tooth is one quarter wavelength long when considering the effective dielectric permittivity of the silicon medium. When utilizing self-complementary log-periodic antennas, one has to be aware of their sensitivity to the incident polarization. The power available, when lasers are used as the LO sources, is generally sufficiently large such that a polarization rotater can be used to produce the optimum polarization. This was confirmed in our experiments at both 1.56 THz and at 2.24 THz.

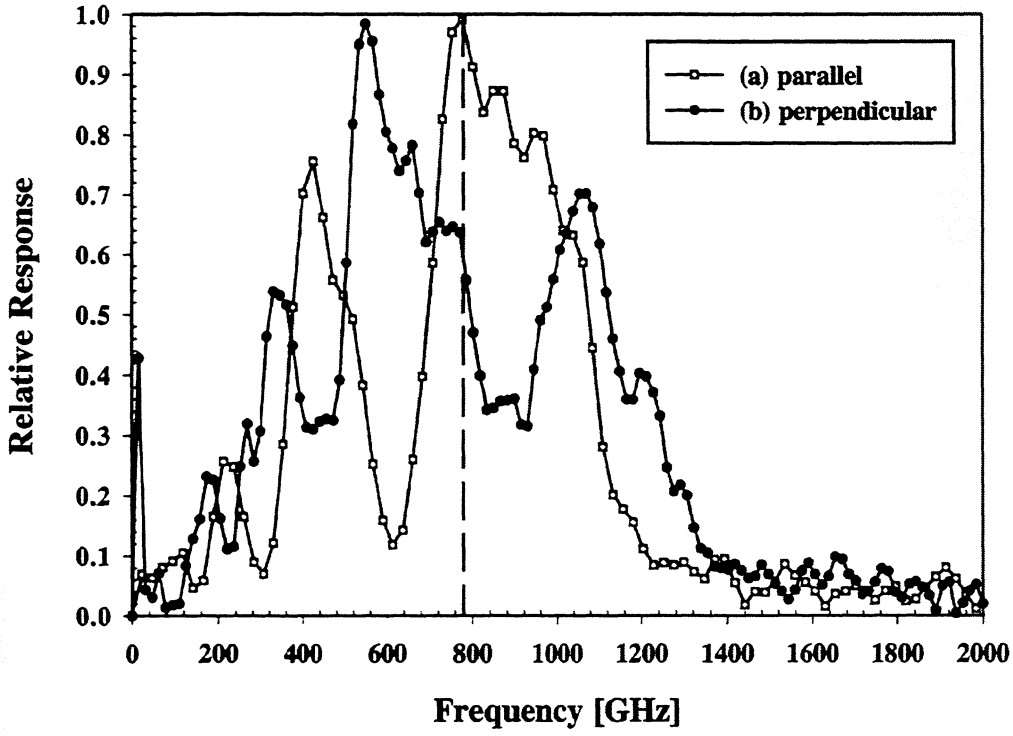

Figure 5: FTS spectra of the device for (a) device orientation parallel to the FTS polarization, and (b) perpendicular to the FTS polarization.

Noise Temperature Measurements

Our results from the noise temperature and conversion loss measurements at different frequencies are summarized in TABLE I below.

TABLE I: Noise Temperature and Conversion Loss Summary

f [THz]	Dev.# / Ant.	T_{out} [K]	T_{DSB} [K]	$L_{c,tot}$ [dB]	L_{opt} [dB]	$L_{c,i}$ [dB]
0.62	#1/A	82	485[a]	12.5	4	8.5
1.56	#2/B	10	5,800	27	8	19
1.56	#3/B	44	2,800	20	8	12
1.56	#4/B	43	2,700	20	8	12
1.56	#5/B	70	1,000	14.5	6	8.5
2.24	#5/B	70	2,200	18	9.5	8.5

[a] **440 K at a device temperature of 2 K.**

The Y-factor was measured by inserting a liquid nitrogen cooled absorber by hand into the path of the beam several times. In the 1.56 THz experiment, the IF output power was recorded on a chart recorder and the results of several individual Y-factor measurements were averaged. The fact that it was possible to perform the Y-factor measurement at this noise temperature level without the use of a rotating chopper is a tribute to the excellent amplitude stability of the UMass/Lowell laser used for this experiment. The stability is also evident in the I-V curves recorded by our fast (about 1 ms) computerized recording system. In a separate test we measured the amplitude stability of the FIR laser at 1.56 THz with a relatively fast (0.1 sec) integration time over a period of several minutes. We found that the amplitude stability was ±0.3 %. The optimum operating point for the devices reported here is not very sensitive to variations in LO power or bias voltage. This is a distinct advantage compared to the DHEB Nb mixers which must be adjusted to a bias voltage very close to an unstable region of the IV-curve in order to optimize the receiver noise temperature. The antenna/lens combination clearly performed well at 1.56 THz as evidenced by the fact that during a chopped noise measurement on the system, it was possible to blank out essentially the entire signal by blocking the cold source with a piece of absorber of a size equal to the predicted beamwidth (about 8 degrees with the 1.3 mm diameter lens and 2.5 degrees with the 4 mm diameter lens). The LO power absorbed by the device with the lowest noise temperature at 1.56 THz was 500 nW. TABLE I shows the estimated break-down of the total conversion loss into components. We assume that the optical coupling loss is essentially given by the losses of the different components, such as the window, the Zitex thermal radiation filter, the reflection loss of the lens, etc.. The remaining loss is attributed to the mixer itself. **The intrinsic conversion loss, including IF output mismatch, is about 8.5 dB at all three frequencies (620 GHz, 1.56 THz, and 2.24 THz)** within the accuracy of the measurement and the error in our estimate of the optical losses is about ±2 dB. **This shows that the intrinsic receiver noise temperature does not depend on the frequency, up to 2.24 THz.** We measured both the receiver noise temperature and the output noise temperature for several de-

vices. The intrinsic receiver noise temperature, the intrinsic conversion loss, and the output noise temperature were analyzed and compared with predictions of the standard model in a different separate paper at this symposium [Yngvesson and Kollberg]. The measured data agrees well with the theory. Both conversion loss and output noise temperature are relevant in establishing the receiver noise temperature. It should be clear, however, that receiver noise temperatures of NbN HEB mixers at THz frequencies are likely to progressively get lower. Specifically, we expect to be able to lower the optical coupling loss substantially in the future. We note that so far none of the HEB mixers above 1 THz have employed a matching layer for the lens.

V. CONCLUSIONS

We have demonstrated receiver noise temperatures of 485 K at 620 GHz, 1,000 K at 1.56 THz, and 2,200 K at 2.24 THz for a NbN HEB device, coupled through a silicon lens and a log-periodic toothed antenna. The very small LO power required by such devices when optimally matched (presently 500 nW) has been verified. We expect that measured receiver noise temperatures of NbN HEB mixers will continue their downward trend at frequencies above 1 THz in the future.

VI. ACKNOWLEDGMENTS

This work was supported by the Russian Program on Condensed Matter (Superconductivity Division) under Grant No.98062, as well as grants from the National Science Foundation (ECS-96128), the National Research Council, and NASA (NAG5-7651). We would also like to thank Prof. Erik Kollberg for making resources available for measurements at Chalmers University of Technology as well as for lending us a low-noise IF amplifier.

VII. REFERENCES

S. Cherednichenko et al., "Large Bandwidth of NbN Phonon Cooled Hot Electron Bolometer Mixers on Sapphire Substrates," *8th Intern.Symp.Space THz Technol.*, Cambridge, MA, March 1997.

H. Ekstrom, E. Kollberg, P. Yagoubov, G. Gol'tsman, E. Gershenzon, and K.S. Yngvesson, "Gain and Noise Bandwidth of NbN Hot Electron Bolometric Mixers," *Appl. Phys. Lett.*, **70**, 3296, 1997.

D.F. Filipovic et al., "Double-Slot Antennas on Extended Hemispherical and Elliptical Dielectric Lenses," *IEEE Trans.Microwave Theory Techniques*, **MTT-41**, 1738, 1993.

B.K. Kormanyos et al., "A Planar Wideband 80-200 GHz Subharmonic Receiver," *IEEE Trans. Microw.Theory Techniques*, MTT-41, 1730 (1993).

M. Kroug, P. Yagoubov, G. Gol'tsman and E. Kollberg, "NbN Quasioptical Phonon Cooled Hot Electron Bolometric Mixer at THz Frequencies," *EUCAS'97*, Eindhoven, The Netherlands, June 29-July 3, 1997.

NBN PHONON-COOLED HOT ELECTRON BOLOMETER MIXER DEVELOPMENT AT IRAM

C. Rösch, F. Mattiocco,
K.H. Gundlach, K.-F. Schuster

IRAM, Institut de Radio Astronomie Millimetrique
300, Rue de la Piscine, 38406 St. Martin d'Heres, France

Introduction :

NbN phonon cooled bolometric mixers offer very competitive performance up to the highest frequencies. Processing of NbN HEB's is relatively easy and reliable and due to microstructuring by Ebeam lithography LO power could be reduced to a level where pumping is possible with solid state sources and simple beam splitters up to around 1 THz. The typical sheet resistance for very thin NbN films is relatively well adapted to a variety of antennas or waveguide coupling structures. All these points make the NbN bolometric mixers very attractive for radio astronomical applications in the THz regime [8]. The main problem with the NbN devices however stays the limitation in IF bandwidth and contrary to predictions bandwidths beyond 2-3 GHz are hardly reached for NbN films on substrates which are suitable for high frequency applications. After establishing a reliable process [10], we have focused on the characterisation of the devices and improvements of antenna device coupling.

Bandwidth characterisation :

A variety of IF bandwidth characterisations for HEB's have been proposed in the past [1,2,3,4]. The IF bandwidth of a HEB mixer generally depends on the bias point which itself strongly influences noise and gain of the mixer. At heterodyne operation a global optimisation of all parameters is therefore required which is time consuming and often not straight forward.
For optimisation of film processing parameters, impedance measurements offer a more direct way to access the intrinsic characteristic time scales of the NbN films.
After having measured the bandwidth of a device with a 5 nm thick NbN film by a direct signal injection method [4], we investigated the possibilities of characterisation by an impedance measurement similar to the procedure, which was described by Karasik et al. [1].
In order to allow for rapid measurements we installed the set-up in a dipstick, which could be immersed in liquid He. The measurement was done with a HP8510 network analyser. The DC bias was directly fed over the internal bias input of the HP8510. The measurements were

performed with a sweep between 200MHz and 5GHz and a power level of –60 dBm at the device. Using the available signal averaging option, we did not find any particular need for an additional cryogenic wide band amplifier. With a similar calibration scheme as described by [1] we obtained the complex impedance as plotted in Fig. 1. The solid lines show the results of a simultaneous fit to the real and imaginary part of the measured impedance to a theoretical model [9] :

$$Z(\omega) = R \cdot \frac{1+C}{1-C} \cdot \frac{1+i\omega\dfrac{\tau_T}{1+C}}{1-i\omega\dfrac{\tau_T}{1-C}}$$

Where R is the device resistance and τ_T (intrinsic electron temperature relaxation time) and C (self heating parameter) were the free fitting parameters. The fit is good for the real part of the impedance but only just acceptable for the imaginary part, a phenomenon that has been observed by other groups. The resulting IF bandwidth is 1.7 GHz, which is in reasonably good agreement with the bandwidth of 2GHz measured by the direct injection method.

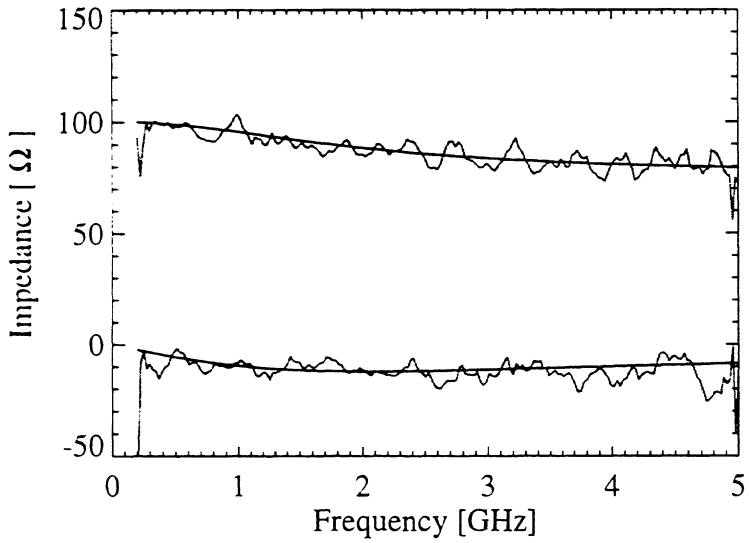

Fig. 1: Measured complex impedance for a HEB with a 5nm NbN film.

New Antenna Detector Structure for very high Frequencies :

Our first results on NbN HEB mixers were obtained with single lean bowtie dipoles in combination with elliptical or hyperhemispherical quartz lenses [4]. Such an antenna is largely sufficient to pass most of the radiation pattern through a dewar window of reasonable size and therefore allows for simple mixer tests. However the resulting beam is not well suited for coupling to practical antennas for radio astronomy. A variety of planar antenna structures have been proposed for HEB Mixers [1,4,5,6]. Here we investigated a double dipole structure with two different integration schemes of the HEB mixer elements.
In a first structure one central bolometric element is fed symmetrically over coplanar striplines (Fig 2). IF output and DC bias are connected over coplanar rf blocking filters on either side. Other groups [5] have successfully used the described double dipole structure with a central detector element with slight modifications. The structure was designed for a working frequency around 800 GHz assuming a fused quartz substrate.

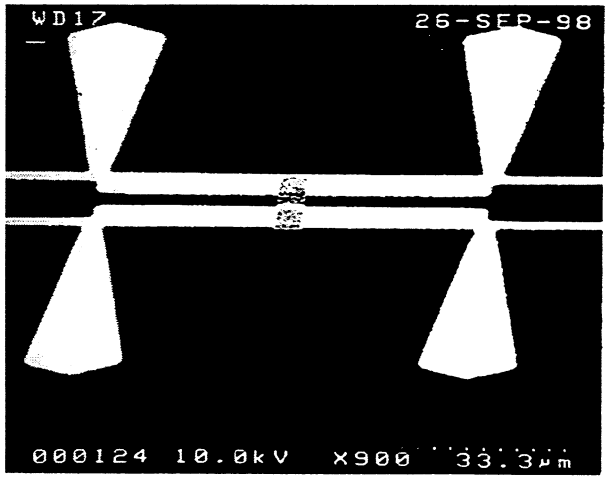

Fig 2 Double dipole with single central HEB element.

To control the frequency dependent response of this antenna detector structure we performed FTS measurements using the bolometer element in the direct detection mode. The FTS spectrometer consisted of a computer controlled Martin-Puplett Interferometer with a chopped liquid nitrogen cold load and a phaselock amplifier which is read out automatically. The response is plotted in Fig 3. The measured response is very wide band and shows that the structure is reasonably well tuned to 800 GHz. It should however be mentioned that the atmospheric absorption which is clearly present in our current set-up (typical pathlength is 1.5 m) does not allow to exclude a coupling maximum at higher frequencies. In this sense the measurement should be considered preliminary until we have installed a dry nitrogen container for the spectrometer.

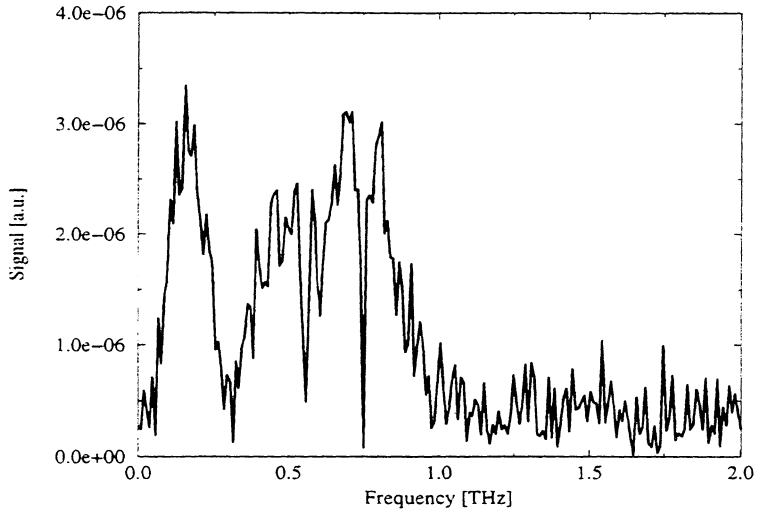

Fig.3: FTS measurement of a double dipole structure with central HEB element designed for 800 GHz .

The result for heterodyne mixing is given in figure Fig.4. The heterodyne mixing results for this structure are comparable to the results which were obtained with a simple dipole. Yet future beam measurements still have to show the desired improvement in the beam shape.

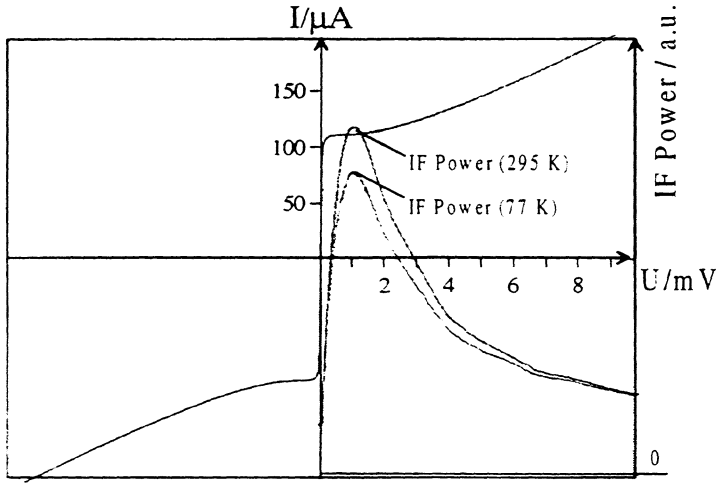

Fig. 4: Heterodyne measurement of a double dipole structure with central HEB element for 800 GHz . The best DSB receiver noise temperature is 1250 Kelvin (IF 1.5 GHz).

A disadvantage of the described double dipole is that the coplanar connections to the central detector element perturb the antenna pattern and at very high frequencies cause also undesired ohmic losses. Furthermore control over the characteristic impedance of the connecting transmission lines becomes increasingly difficult for frequencies above 1 THz.
The wide range of achievable device impedance for NbN HEBs did suggest another antenna coupling solution for the double dipole. We propose a structure where each dipole is equipped with its own HEB element and the signals of both dipoles are combined in the IF path Fig. 5. With such a structure the losses in the connections to a central mixing element are avoided. This makes the structure especially interesting for the very high frequency region where ohmic losses are important.

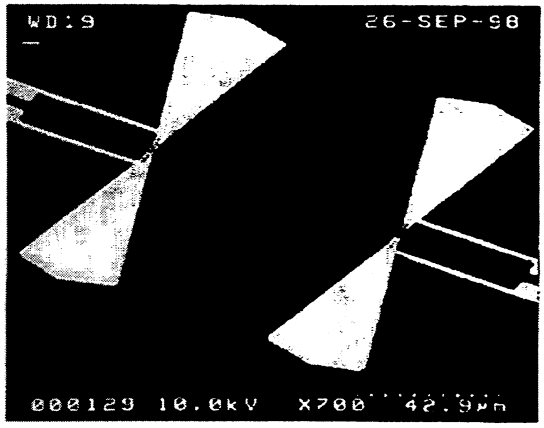

Fig 5 Double dipole with individual HEB elements for each dipole.

In a sense such a structure represents a miniature interferometer where the phase reference is given by the common local oscillator radiation field. Obviously such a structure requires identical mixer elements in order to conserve the symmetry of the antenna and therefore challenges processing of the devices. Gain imbalance would cause an increased sidelobe level and phase imbalance would lead to a beam deflection.
It should be mentioned that a simple FTS measurement does not anymore represent very well the frequency behaviour of the heterodyne mode because in the direct detection mode used for the FFT measurements one measures the incoherent sum of the response of the individual dipoles rather than the phased response.

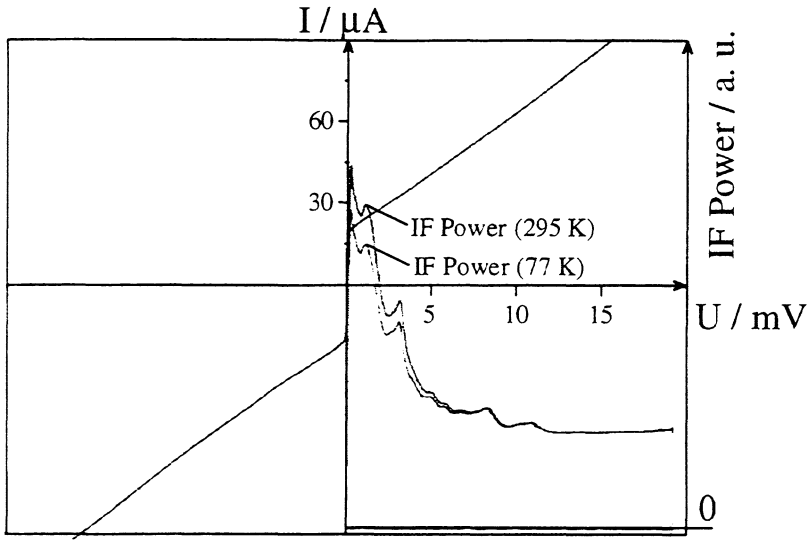

Fig. 6: First heterodyne measurement of a double dipole structure with individual HEB elements for each dipole. The best DSB receiver noise temperature is 1800 Kelvin at 810 GHz (IF 1.5 GHz).

First heterodyne results with the distributed mixing element structure at 800 GHz yielded receiver noise temperatures which were higher than our best results. However the conversion curve is cut off at the most sensitive area and we were clearly LO power starved in these measurements (Fig.6).

We do not yet really understand the particular structure of the conversion curves. As both of the HEB elements are connected with a common superconducting Nb film on either side of the elements we investigated possible SQUID effects but could not find any sensitivity to magnetic field. We suspect that the observed effect does origin from an instability which is due to the in parallel bias of the two elements.

Possible improvement of this problem could be obtained by completely separated IF branches for the two antenna elements with individual DC bias and cryogenic amplifiers. Although the effort seems high, such a solution would have other very interesting features as for example the possibility of very fast beam switching by a phase switch in the IF line.

The described antenna detector coupling scheme is not restricted to double dipoles but can also be applied for double slot antennas if the impedance level of the HEB elements can be made reasonable close to the feed point impedance of the slots.

References :

[1] B.S. Karasik, M.C. Gaidis, W.R.McGrath, B.Bumble, and H.G. LeDuc in 8th Int. Symp. on Space Terahertz Technology, Harvard University, March 1997

[2] P.J. Burke, R.J. Schoelkopf, D.E.Prober, A.Skalare, B.S. Karasik, M.C. Gaidis, W.R. McGrath, B.Bumble, H.G. LeDuc in JAP 1999, Vol. 85, Nr. 3, p 1644.

[3] S, Cherednichenko, P. Yagoubov, K. Il'in, G. Gol'tsman, and E. Gershenzon in 8th Int. Symp. on Space Terahertz Technology, Harvard University, March 1997

[4] C. Rösch, T. Lehnert, C. Schwoerer, M. Schicke, K.H. Gundlach, K.F. Schuster in 9th Int. Symp. on Space Terahertz Technology, Pasadena, March 1998

[5] A. Skalare, W.R. McGrath, B.Bumble, H.G. LeDuc in 8th Int. Symp. on Space Terahertz Technology, Harvard University, March 1997

[6] P. Yagoubov, M.Kroug, H.Merkel, E.Kollberg, G.Gol'tsman, A.Lipatov, S.Svechnikov, E. Gershenzon in 9th Int. Symp. on Space Terahertz Technology, Pasadena, March 1998

[7] E. Gerecht, C.F. Musante, Z.Wang, K.S.Yngvesson, J. Waldman, G.N. Golts'man, P.A. Yagoubov, S.I. Svenchnikov, B.M. Voronov, S.I. Cherednichenko, E.M. Gershenzon, in 8th Int. Symp. on Space Terahertz Technology, Harvard University, March 1997

[8] Kawamura, R. Blundell, C.-Y. E. Tong, D.C. Papa, T.R. Hunter, G. Gol'tsman, S. Cherendichenko, B. Voronov, E. Gershenzon in 9th Int. Symp. on Space Terahertz Technology, Pasadena, March 1998

[9] B.S. Karasik and A.I.Elantiev in APL 1996, Vol 68, p 853.

[10] T. Lehnert, H. Rothermel, K.H. Gundlach, JAP 1998, Vol 83, No 7, p 3892.

NOISE AND BANDWIDTH MEASUREMENTS OF DIFFUSION-COOLED Nb HOT-ELECTRON BOLOMETER MIXERS AT FREQUENCIES ABOVE THE SUPERCONDUCTIVE ENERGY GAP

R.A. Wyss, B.S. Karasik, W.R. McGrath, B. Bumble and H. LeDuc

Center for Space Microelectronics Technology,
Jet Propulsion Laboratory, California Institute of Technology,
Pasadena, CA 91109

ABSTRACT

Diffusion-cooled Nb hot-electron bolometer (HEB) mixers have the potential to simultaneously achieve high intermediate frequency (IF) bandwidths and low mixer noise temperatures for operation at THz frequencies (above the superconductive gap energy). We have measured the IF signal bandwidth at 630 GHz of Nb devices with lengths L = 0.3, 0.2, and 0.1 μm in a quasioptical mixer configuration employing twin-slot antennas. The 3-dB IF bandwidth increased from 1.2 GHz for the 0.3 μm long device to 9.2 GHz for the 0.1 μm long device. These results demonstrate the expected $1/L^2$ dependence of the IF bandwidth at submillimeter wave frequencies for the first time, as well as the largest IF bandwidth obtained to date. For the 0.1 μm device, which had the largest bandwidth, the double sideband (DSB) noise temperature of the receiver was 320-470 K at 630 GHz with an absorbed LO power of 35 nW, estimated using the isothermal method. A version of this mixer with the antenna length scaled for operation at 2.5 THz has also been tested. A DSB receiver noise temperature of 1800 ± 100 K was achieved, which is about 1,000 K lower than our previously reported results. These results demonstrate that large IF bandwidth and low-noise operation of a diffusion-cooled HEB mixer is possible at THz frequencies with the same device geometry.

I. INTRODUCTION

To date, diffusion-cooled hot electron bolometer (HEB) mixers have achieved low receiver noise temperatures at 1,100 GHz[1] and 2.5 THz[2] and large intermediate frequency (IF) bandwidths[3]. Phonon-cooled HEB mixers have also shown very good performance[4-6], though the IF bandwidth is ultimately limited by the electron-phonon energy relaxation time. The combination of low-noise and high IF is both desirable and critical for applications in radioastronomy. Unlike the SIS mixer, the HEB mixer works well above the superconductive energy gap frequency ($f_g \approx 750$ GHz for Nb) which makes it the detector of choice for observational science applications at THz frequencies.

In fact, the HIFI Instrument planned for ESA's Far-IR and Sub-millimeter-wave Telescope (FIRST) will employ HEB-based receivers for its two highest THz bands.

We will present recent measurements of the small area Nb HEB mixers, which have been measured at frequencies above the superconductive energy gap. The purpose of this work is to verify theoretical predictions of large IF bandwidth in the diffusion-cooled regime and ascertain that low receiver noise temperatures are maintained for the same device geometry for operation at THz frequencies. First, IF bandwidth measurements at 630 GHz are discussed, followed by mixer noise temperature measurements at 2.5 THz and 630 GHz. Comparison with other published works shows that these results are among the best reported to date.

II. HEB MIXER DESIGN AND EXPERIMENTAL CONSIDERATIONS

The dimensions of the Nb devices tested are designed to have bridge lengths of 0.3, 0.2, and 0.1 μm, and a width of 0.1 μm. The thickness of the bridge is nominally 12 nm, however, the actual thickness may vary because it is inferred by monitoring the deposition time. A detailed account of the self-aligned fabrication process, DC electrical characterization and mask layout are given by Bumble *et al.*[7]. Good thermal and electrical contact between the Nb microbridge and the gold contact pads is assured because the evaporation of the two films is done consecutively without breaking the vacuum. Figure 1 depicts the mixer design showing the layout of the twin-slot antenna, the CPW transformer connecting the antenna to the HEB device located at the center, and the CPW rf filter structure used for DC bias of the bolometer and coupling the IF signal out of the mixer.

For our quasioptical mixer design, the silicon chips containing the HEB device, antenna, and embedding circuit are glued to the backside of an elliptical Si-lens with an cyanoacrylate adhesive. Using a microscope and micropositioners, the device center is placed at the second focus of this lens. The alignment accuracy of this procedure has been verified to be better than 25 μm (see discussion of beam pattern measurements below). The Si-lens is then clamped into the mixer mount and aligned with the optical axis of an Infrared Labs dewar.

The IF signal bandwidth was measured using two monochromatic sources. A fixed frequency signal source at 630 GHz signal is provided by a Gunn oscillator pumping a frequency doubler followed by a frequency tripler (×2×3). The tunable local oscillator (LO) source is a backward-wave oscillator (BWO), which is easily tuned over a 20 GHz span by varying the anode voltage. Since the spatial mode pattern of the emitted radiation from the over-moded BWO varies with voltage, a polyethylene lens is used to redirect the beam into the dewar. The radiation from the BWO and from the multiplier is combined

using a 2 mil Mylar beamsplitter. At each frequency point the LO radiation is re-aligned as necessary to maintain a constant pump power level and hence a fixed bias point of the HEB. Since the objective is to observe a large signal bandwidth, narrow-band cooled amplifiers were not used for this measurement. The frequency dependent loss of the microstrip line connecting the HEB chip to the K-connector, the semi-rigid cable used to bring the signal from the 4.2 K stage to the outside of the dewar, the two 30-dB room-temperature Miteq amplifiers, and the input of the spectrum analyzer, were all carefully measured. The product of these losses was used to calibrate the data before extracting the intrinsic frequency dependence of the HEB mixer. The receiver noise temperature was also measured at 630 GHz by the Y-factor method using a similar setup. The monochromatic signal source was replaced with a hot or cold load. These loads are made of a cone-shaped eccosorb foam which was either at room temperature or LN_2 temperature. A 4.2 K cooled HEMT amplifier was used as the first stage for the IF system to amplify the signal from the HEB mixer by ~40 dB, and a bandpass filter with center frequency of 2.180 GHz and bandwidth of 300 MHz was inserted before the two Miteq amplifiers. A power meter was used to measure the IF output.

The receiver performance at THz frequencies is measured using an experimental setup similar to that described Karasik *et al.*[2], and briefly discussed here. The local oscillator source is a CO_2-pumped far-infrared laser operating on the 118.8 μm (i.e. 2.5 THz) lasing line of methanol gas. The radiation is steered towards the input window of the dewar using two mirrors and a 1 mil thick Mylar beamsplitter. The power level and polarization is controlled using two metal grids which can be rotated relative to each other. The Y-factor is determined by switching between a hot (295 K) and cold load (~95 K). Atmospheric absorption is eliminated in the signal path and part of the LO path by placing the beamsplitter and the temperature loads in a vacuum box mounted to the dewar. The need for a vacuum window on the dewar is hence eliminated and only a Zitex filter[8] is mounted on the LN_2-shield to prevent room-temperature infrared radiation from reaching the mixer block. This minimizes the loss between the hot/cold load and the HEB mixer, and reduces superfluous noise temperature contributions. Thus our system accurately measures the receiver noise temperature without any corrections for atmospheric absorption or windows. The mixer IF output is amplified using a LHe-cooled HEMT amplifier having a gain of ~40 dB with a noise temperature <4.0 K in the frequency band of interest, 1.9 to 2.4 GHz. The IF signal is bandpass limited to 300 MHz, with center frequency of 2.18 GHz and is further amplified using two room-temperature 30-dB amplifiers. A 3-dB attenuator is inserted between the amplifiers to avoid standing-waves and reflections. A DC voltage proportional to the signal intensity is obtained using a fast rectifier diode after the amplifier chain. The Y-factor is derived from measuring the AC and DC component from the voltage of the diode as a chopper periodically switches between the hot and cold load. The AC voltage component is measured using a lock-in which measures the rms value of the waveform. Since the waveform created by the chopper is approximately sinusoidal, the Y-factor is calculated

as follows: $Y = (\mathrm{DC} + \sqrt{2}\mathrm{AC})/(\mathrm{DC} - \sqrt{2}\mathrm{AC})$. Due to power fluctuations in the FIR-laser power it is currently necessary to use this technique. A more stable LO source would make a lock-in measurement technique unnecessary.

III. RESULTS AND DISCUSSION

A. DC Measurements

In Fig. 2 a representative I-V characteristic of an Nb HEB device is shown at 4.2 K (upper trace). This curve was measured during the initial DC tests of the device, using a dipstick setup. The nominal device dimensions are L×W×H=0.1×0.1×0.012 μm^3. The critical current of 186 μA implies a critical current density of this device is 1.6×10^7 A/cm^2. The normal state resistance is 15.4 Ω. The lower three traces are of the same device, measured at 2.2, 3.1 and 4.2 K, after mounting it into the mixer block several times. The critical current density is noticeably reduced, 75 μA at 4.2 K, but is almost fully recovered when the bath temperature is lowered to 2.2 K. This change to the microbridge effectively lowers the T_c of the superconductor and results in a small kink in the I-V when the critical current density is reached. This kink typically occurs with a reduction of the critical current. All receiver noise measurements at 2.5 THz were performed using this device after this small change occured. Excellent mixer performance was obtained as discussed below, and other devices showing similar small changes have also given good performance.

B. Twin-slot Antenna Beam Pattern

The proper alignment of the HEB mixer was verified by measuring the beam pattern of the receiver, as shown in Fig. 3. The HEB was operated as a direct detector for this measurement by heating it to just below the transition temperature of the superconducting film and biasing it in a constant current mode. The dewar is placed in the far-field (>10× Rayleigh length) of the beam from an FIR-laser operating at 2.5 THz. The magnitude of the AC response to the chopped far-infrared radiation is recorded as a function of the E-plane rotation around the axis of the bolometer. The main beam full-width-half-maximum, θ_{HP}, is 0.87° degrees with the first sidelobe intensity down 10 dB. The calculated effective Gaussian beam waist of the exiting beam from the Si-lens is $\omega_0 = 2\lambda/\pi\theta_{HP} = 5$ mm which agrees well with published findings at lower frequencies[9]. The highly collimated receiver beam pattern, having an f-number ≈ 66, is due to this large beam waist which is directly related to the diameter of the Si-lens. The slight asymmetry of the receiver beam is believed to be due to displacement of the HEB from the lens center. For the Si-lens used in the experiment, the thickness along the central axis is 8.153 mm. A displacement of the HEB along in the E-plane, δx, can be related to the off-axis angle, θ, of the exiting beam: $\delta x = 40\cdot\theta$ μm/degree. Hence the displacement seen in

Fig. 3 of <0.1 degrees translates to less than 5 μm in the E-plane. The resulting displacement of the beam away from the central axis in the E-plane is, in this case, only a very small fraction of a degree. A displacement might also exist in the orthogonal direction, the H-plane, but currently we have no method of adjusting the dewar pitch angle in a controlled manner.

C. RF Spectral Response

Prior to characterizing HEB mixer performance the RF spectral response has been checked using a Bruker IFS120HR Fourier-transform spectrometer. The center frequencies and bandwidths (≈50%) in general agreed with that expected for twin-slot antennas, indicating that the mixer RF spectral response is dominated by the planar antenna. The center frequency found experimentally for a twin-slot design at 600 GHz matches well with theory, however, a shift to lower frequencies of 20% is observed for designs at 2.5 THz[2]. A new twin-slot design, with a 10% reduction in the slot length was therefore fabricated to obtain a more desirable center frequency for the 2.5 THz measurements. The HEB was used as a direct detector for the spectral response measurements. In order to increase the HEB voltage responsivity, the device was operated at 6.9 K. Since, based on the design, the peak response was expected to occur around 2.5 THz, the spectra were measured using a 23 μm Mylar beamsplitter which was judged to be ideal for the required frequency band: 1,200 GHz to 3,450 GHz (the Fabry-Perot resonances of the beamsplitter were outside of this band). The spectral response for antenna/RF-filter Type I (our first design), shown in Fig. 4, peaked at 2.0 THz having a somewhat asymmetric shape. The 10% shorter version, Type II (new design), not only displays the desired shift upwards in frequency, centered on 2.2 THz, but it's shape is also more symmetric. At an LO frequency of 2.5 THz, Type II offers an increase of 1 dB in responsivity relative to Type I. Hence, the device geometry we have investigated has an slot length of $0.28\lambda_0$ (λ_0 is the free-space wavelength) and a RF-filter Type II. The large ringing present in the spectra, especially pronounced for the shorter slot antenna device, is due to standing waves in the device substrate. From the 164 GHz period of the undulations, the predicted substrate thickness is 267 μm which is close to the nominal 254 μm thickness specified by the wafer supplier. The 5 to 10% amplitude variations are due to the finite thickness of the cyanoacrylate adhesive that is used to glue the devices to the Si-lens. This adhesive is currently used since it readily dissolves in Acetone. If a less viscous adhesive, such as UV-curable optical glues, is substituted, this thickness would decrease and the standing wave pattern would be negligible.

D. Intermediate Frequency Bandwidth Measurements at 630 GHz

A systematic study of the mixer 3-dB IF bandwidth on the HEB device length has been performed. The objective is to confirm that the $1/L^2$ dependence, measured at low microwave frequencies[5], holds as expected at submillimeter wave frequencies (where

these mixers will find practical applications). The IF bandwidths of HEB devices with lengths of 0.3, 0.2, and 0.1 μm were measured. Figure 5 shows the results of two devices with dimensions L×W=0.1×0.1 μm^2, which had a normal state resistance of 17 Ω and critical currents of 160 and 130 μA. The data exhibits some scatter and periodic dips which we attribute to the interplay between the frequency sources, and also to reflections in the microstrip section. Since the two sources are not frequency locked together, the BWO displays a frequency drift on the order of 10 to 15 MHz. Although the IF spectrum is averaged during the measurement, the IF-power can vary by as much as ±1 dBm over the 15 MHz span. The data points in the graph represent the average power throughout this band. Reflections are caused by impedance mismatch at the bonding wire transition from the device chip to the microstrip line and the solder joint between the microstrip line and the K-connector. From a 1-pole fit to the data, the 3-dB points are found to be 8.1 GHz and 9.2 GHz. The difference in the IF bandwidth could be caused by the choice of the bias point and physically different bridge lengths. The IF bandwidth of a 0.08×0.08 μm^2 device has also been measured. The results showed no clear roll-off for frequencies up to 15 GHz. Due to the large scatter in the data, about 4 dB, this measurement result has not been included in the analysis of the length dependence.

In order to compare the experimental findings to theoretical predictions, the length and width of selected devices have been inspected using an SEM. The measured and "designed" sizes[10] are plotted together in Fig. 6. A trend is apparent that the length is about 20% longer and the width is about 20% narrower for the very smallest devices. Taking account of this correction the IF bandwidth has been plotted versus the actual bridge length in Fig. 7. The plot also includes our previous microwave results[3] for comparison. Using a electron diffusion-cooling limited model, the frequency roll-off is predicted to depend on the bridge length as: $f_{3dB} = \pi D / 2L^2$, where D is the diffusion coefficient and L is the device length. As seen in Fig. 7, the 630 GHz results fit the expected length dependence well. From the fit we find the diffusion coefficient to be 0.95 cm^2/s, which is a reasonable result for a 120 Å thick Nb film[11].

E. Receiver Noise Temperature Measurements at 2.5 THz

In Fig. 8(a), a series of pumped I-V curves are shown when systematically varying the LO power of the 2.5 THz FIR-laser. For each of the curves, the optimal bias point resulting in the lowest receiver noise temperature, is indicated with a square marker. The position of the marker is consistently coincident with the knee in the I-V curve separating the normal state domain from the large differential resistance domain. The corresponding receiver noise temperature as function of the bias voltage is also shown - a characteristic parabolic shape is apparent.

Figure 8(b) shows the receiver noise as a function of LO power at 2.5 THz. The absorbed LO power is estimated using the "iso-thermal" method[12]. This method

assumes the HEB mixer element can be treated as a lumped element with a single electron temperature. The best result of 1,800±100 K was obtained for an absorbed LO power of 22 nW, at a bath temperature of 4.2 K. The large error bar for the noise temperature is due to laser power fluctuation during the measurement. These power fluctuations are due to oscillations between several transverse modes in the FIR laser, only one of which couples to the HEB mixer[13,14]. Efforts are underway to improve the stability of the FIR laser. This result is an improvement over our previous results[15] and is attributed primarily to the improved antenna design.

F. Receiver Noise Temperature Measurements at 630 GHz

The lowest stable receiver noise temperature achieved at 630 GHz was 470 K, as shown in Fig. 8(b), with an estimated absorbed LO power of 35 nW. Because of the stability of the local oscillator source (a BWO was used to pump the HEB mixer) chopping techniques were not needed during the measurement. For some LO power levels a lower receiver noise temperature (minimum was 320 K) was observed when biasing the device at a point of large or slightly negative differential resistance. However, biasing at a point of negative differential resistance should not be considered a viable operating point because of stability problems and fluctuations.

Figure 9 summarizes the DSB receiver noise temperatures available in the published literature to date. In this work we have been able to achieve the lowest receiver noise temperature for diffusion-cooled Nb HEB mixers at two frequencies: 630 GHz and 2.5 THz.

IV. SUMMARY

This paper presents recent experimental results obtained with Nb HEB mixers having geometrical dimensions which makes diffusion the dominant cooling mechanism. A systematic study of the 3-dB IF bandwidth with length has shown the expected $1/L^2$ dependence for the first time at submillimeter wave frequencies. In fact, a 0.1 μm long device has given an IF bandwidth of 9 GHz, a receiver noise temperature of about 470 K, and an absorbed LO power of only 35 nW at 630 GHz. This is the largest IF bandwidth reported to date with extremely low receiver noise. In addition, by improving the mixer antenna and RF filter circuit, a receiver noise temperature of 1800±100 K has been achieved at 2.5 THz. This is the lowest noise to date obtained at this high frequency, and represents a significant improvement in the state-of-the-art for THz heterodyne mixers.

ACKNOWLEDGEMENT

The authors are thankful to M.C. Gaidis for valuable contributions to the device design and acknowledge T. Crawford for the assistance with the use of the FTS for the antenna spectral response measurement. The research described in this paper was performed by the Center for Space Microelectronics Technology, Jet Propulsion Laboratory, California Institute of Technology, and was sponsored by the National Aeronautics and Space Administration, Office of Space Science.

REFERENCES

[1] A. Skalare, W.R. McGrath, B. Bumble, and H.G. LeDuc, "Measurements with a diffusion-cooled Nb hot-electron bolometer mixer at 1100 GHz," *Proc. of the 9th Int. Symp. on Space THz Tech.*, pp. 115-120, Jet Propulsion Laboratory, Pasadena, CA (1998).

[2] B.S. Karasik, M.C. Gaidis, W.R. McGrath, B. Bumble, and H.G. LeDuc, "A low-noise 2.5 THz superconductive Nb hot-electron mixer," *IEEE Trans. Appl. Supercond.* **7** (2), 3580 (1997).

[3] P.J. Burke, R.J. Schoelkopf, D.E. Prober, A. Skalare, W.R. McGrath, B. Bumble, and H.G. LeDuc, "Length scaling of bandwidth and noise in hot-electron superconducting mixers," *Appl. Phys. Lett.* **68** (23), 3344 (1996).

[4] J. Schubert, A. Semenov, G.N. Gol'tsman, H.-W. Hübers, G. Schwaab, B. Voronov, and E. Gershenzon, "Noise temperature and sensitivity of a NbN hot-electron mixer at 2.5 THz," *Proc. of the 10th Int. Symp. on Space THz Tech.*, University of Virginia, Charlottesville, VA (1999).

[5] E. Gerecht, C.F. Musante, H. Jian, Y. Zhuang, K.S. Yngvesson, J. Dickinson, T. Goyette, J. Waldman, P. Yagoubov, G.N. Gol'tsman, B.M. Voronov, and E.M. Gershenzon, "Improved characteristics of NbN HEB mixers integrated with log-periodic antennas," *Proc. of the 10th Int. Symp. on Space THz Tech.*, University of Virginia, Charlottesville, VA (1999).

[6] P. Yagoubov, M. Kroug, H. Merkel, E. Kollberg, J. Schubert, H.-W. Hübers, G. Schwaab, G.N. Gol'tsman, and E.M. Gershenzon, "NbN hot electron bolometric mixers at frequencies between 0.7 and 3.1 THz," *Proc. of the 10th Int. Symp. on Space THz Tech.*, University of Virginia, Charlottesville, VA (1999).

[7] B. Bumble and H.G. LeDuc, "Fabrication of a diffusion cooled superconducting hot electron bolometer for THz mixing applications," *IEEE Trans. Appl. Supercond.* **7** (2), 3560 (1997).

[8] Zitex A-135, Norton Performance Plastics Corp., Wayne, NJ.

[9] D.F. Filipovic, S.S. Gearhart, and G.M. Rebeiz, "Double-slot antennas on extended hemispherical and elliptical silicon dielectric lenses," *IEEE Trans. on Microwave Theory Tech.* **41** (10), 1738 (1993).

[10] P.M. Echternach, H.G. LeDuc, A. Skalare, and W.R. McGrath, "Fabrication of an Aluminum based hot electron mixer for terahertz applications," *Proc. of the 10th Int. Symp. on Space THz Tech.*, University of Virginia, Charlottesville, VA (1999).

[11] B.S. Karasik, K.S. Il'in, E.V. Pechen, and S.I. Krasnosvobodtsev, "Diffusion cooling mechanism in a hot-electron NbN microbolometer," *Appl. Phys. Lett.* **68** (16), 2285 (1996); and references therein.

[12] H. Ekström, B.S. Karasik, and E. Kollberg, "Conversion gain and noise of Niobium superconducting hot electron mixers," *IEEE Trans. Microwave Tech.* **45** (4), 938 (1995); for a more precise method see H. Merkel, P. Yagoubov, P. Khosropanah, and E. Kollberg, "An accurate calculation method of the absorbed LO power in hot electron bolometric mixers," *IEEE 6th Int. Conf. On THz Elec. Proc.*, Leeds, UK, September 1998, pp. 145-148.

[13] H.P. Röser, M. Yamanaka, R. Wattenbach, and G.V. Schultz, "Investigation of optically pumped submillimeter wave laser modes," *Int. J. Infrared and Millimeter Waves* **3** (6), 839 (1982).

[14] R. Wattenbach, H.P. Röser, and G.V. Schultz, "A microprocessor stabilized submillimeter laser system," *Int. J. Infrared and Millimeter Waves* **3** (5), 753 (1982).

[15] B.S. Karasik, M.C. Gaidis, W.R. McGrath, B. Bumble, and H.G. LeDuc, "Low noise in a diffusion-cooled hot-electron mixer at 2.5 THz," *Appl. Phys. Lett.* **71** (11), 1567 (1997).

[16] A. Skalare, W. R. McGrath, B. Bumble, H. G. LeDuc, P. J. Burke, A. A. Verheijen, R. J. Schoelkopf, D. E. Prober, "Large bandwidth and low noise in a diffusion-cooled hot electron bolometer mixer," *Appl. Phys. Lett.* **68**, 1558 (1996).

FIGURES

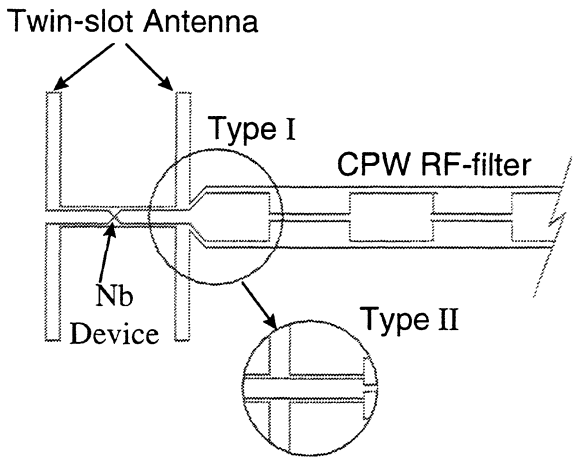

FIG. 1. Layout of HEB mixer circuit. Two slot lengths, $0.31\lambda_o$ and a 10% reduced version measuring $0.28\lambda_o$ (where λ_o is the free space wavelength), together with two variations of the first section of the rf bandstop filter, Type I and Type II, have been implemented.

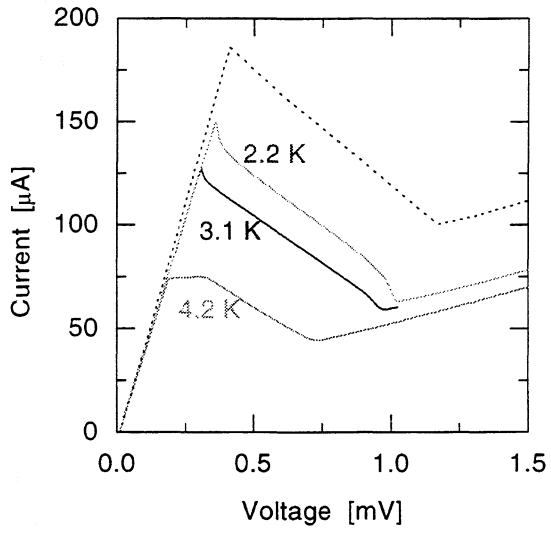

FIG. 2. DC I-V characteristics of a Nb HEB device measured during the initial dipstick test into LHe (dashed line) and three months later after multiple mountings in the mixer block (solid line). Note the decrease of the critical current from 186 μA to 74 μA at 4.2 K, which is partially recovered when lowering the bath temperature to 2.2 K (150 μA).

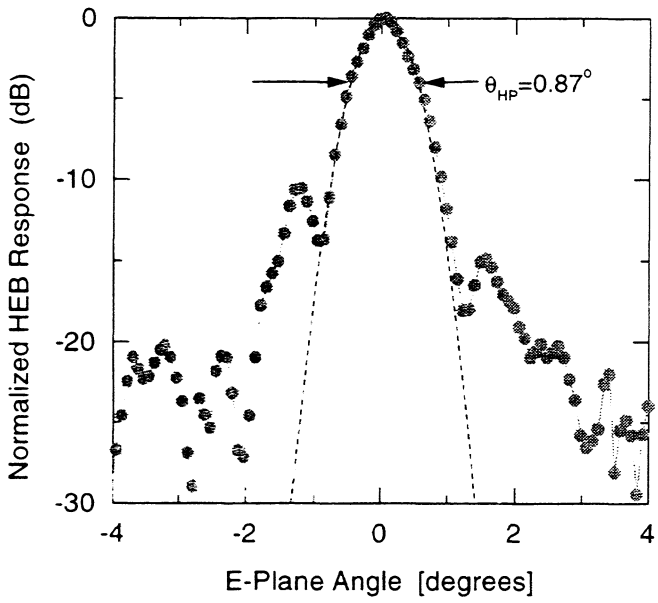

FIG. 3. Measured E-plane beam pattern at 2.5 THz receiver with HEB operated as a direct detector.

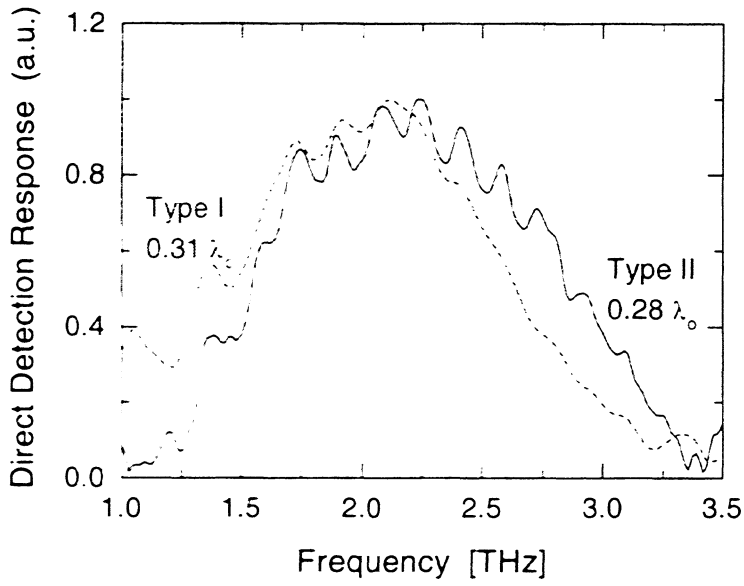

FIG. 4. RF-response of HEB mixer. A spectral resolution of 1 cm^{-1} was used during the measurement with the Fourier-transform spectrometer.

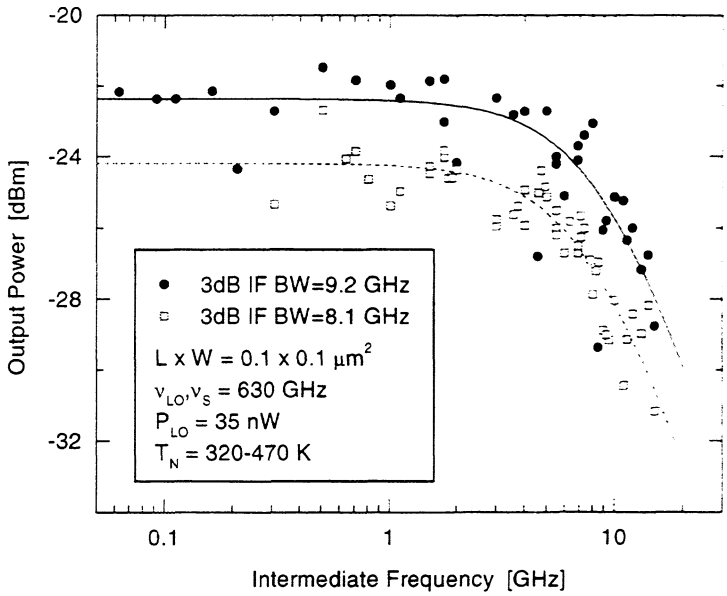

FIG. 5. Relative SSB conversion efficiency vs. intermediate frequency for two different HEB devices with 600 GHz twin-slot antennas.

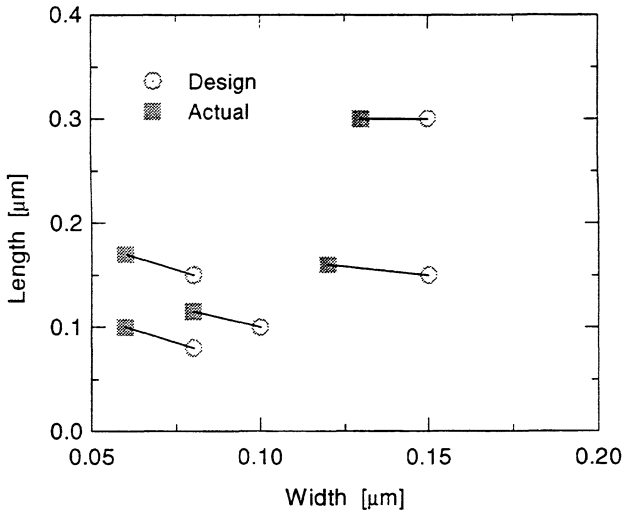

FIG. 6. Design and actual dimensions of Nb microbridge. The actual dimensions are found by visual inspection of SEM photographs.

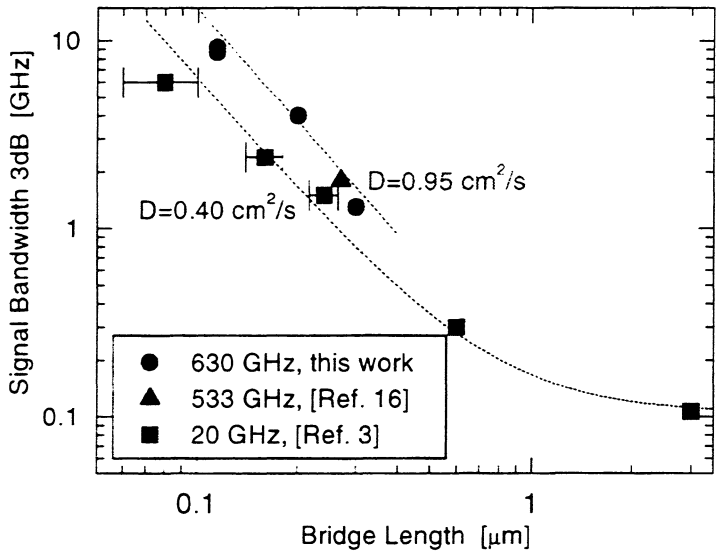

FIG. 7. Scaling of signal bandwidth with device length.

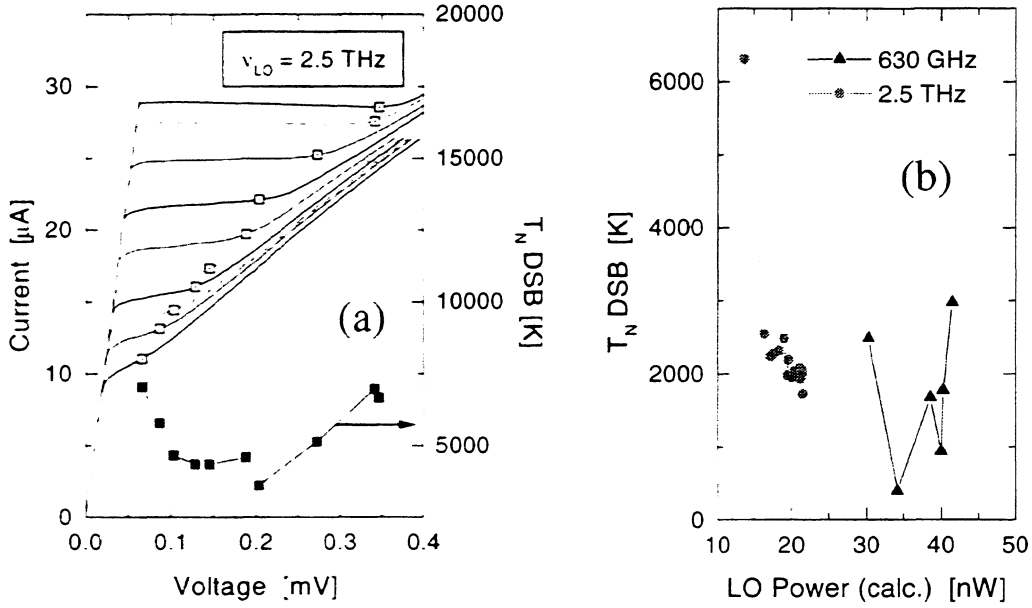

FIG. 8. (a) Pumped DC I-V of HEB mixer for increasing LO power levels at 2.5 THz. The square symbol indicates the optimal bias point to achieve the lowest DSB noise temperature. (b) DSB noise temperature of HEB mixer vs. the estimated absorbed LO power.

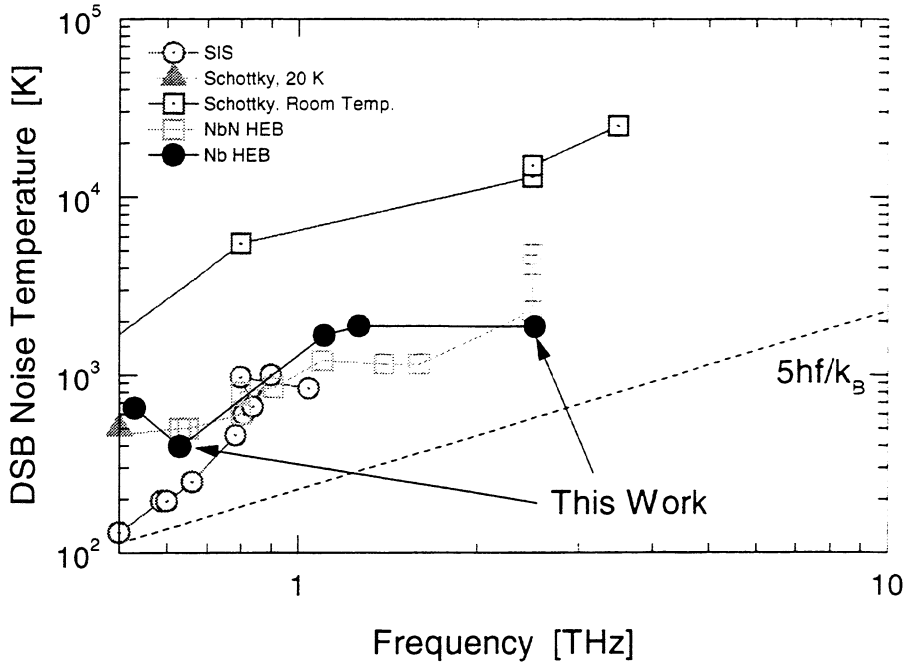

FIG. 9. The graph gives a summary of the currently reported DSB noise temperatures of competing heterodyne receiver technologies. In the graph, the most recent results, 320-470 K at 630 GHz and 1800±100 K have been included.

Receiver Measurements at 700 GHz with a Niobium Diffusion-Cooled Hot-Electron Bolometer Mixer

D. Wilms Floet[1ab], J.R. Gao[2], W.F.M. Ganzevles[1], T. M. Klapwijk[1]
G. de Lange[2], and P.A.J. de Korte[2]

[1]*Department of Applied Physics, Delft University of Technology, Lorentzweg 1, 2628 CJ Delft, The Netherlands*

[2]*Space Research Organization of the Netherlands (SRON), PO Box 800, 9700 AV Groningen, The Netherlands*

Abstract

We report on heterodyne measurements with a Nb diffusion-cooled hot-electron bolometer in a fixed tuned waveguide mixer at 700 GHz. The device is a 300 nm long and 12 nm thick Nb microbridge, with a normal state resistance of 31 Ω. We have measured the DSB receiver noise temperature using a standard Y-factor method with a 300 K and 77 K blackbody load. At 700 GHz, a bath temperature of 4.3 K, and an intermediate frequency of 1.25 GHz, the receiver noise temperature $T_{rec,DSB}$ is 1690 K after correction for the losses in the beamsplitter. Reducing the bath temperature to 3.3 K decreases $T_{rec,DSB}$ to 1100 K. Careful inspection of the pumped differential I(V) characteristics does not reveal any influence due to direct detection. From the data we extract a maximum value of −17.8 dB for the conversion gain of the mixer at 4.3 K. The minimum mixer noise is determined to be 1170 K by applying a noise breakdown calculation. We expect significant improvement of the receiver noise performance upon further reduction of the bath temperature.

I. Introduction

Since the suggestion of using superconducting HEBs as mixer elements in heterodyne receivers [1], there has been a wealth of experimental results using these devices. An HEB mixer roughly consists of a superconducting microbridge, which is operated in a resistive state by dc biasing and irradiation with THz radiation generated by a local oscillator (LO) power. Heterodyne mixing occurs when a small RF signal is applied, leading to a modulation of the dissipated radiation in the microbridge at the intermediate frequency (IF). This leads to a length variation of the resistive region, called a hotspot, and consequently to a modulation of the resistance [2]. Based on the way in which the thermal energy of the hot electrons is removed, they can be divided into two classes.

The first class uses outdiffusion of the hot electrons as a cooling mechanism [3]. Nb based diffusion-cooled hot-electron bolometers have been tested successfully in heterodyne experiments and the results have clearly confirmed the

[a] Corresponding address: University of Groningen. Department of Applied Physics, Nijenborgh 4, 9747 AG Groningen. The Netherlands
[b] Electronic mail: wilms@phys.rug.nl

expected advantages of HEBs at frequencies between 533 GHz and 2.5 THz [4-6]. They have shown a low-noise, low LO power consumption, and a reasonable IF bandwidth. Further improvement of diffusion-cooled HEBs is expected by using Al instead of Nb for the microbridge [7]. A disadvantage of using Al, however, is the need of cooling the mixer well below a bath temperature of 1 K.

The second class uses electron-phonon coupling as a cooling mechanism for the hot-electrons. Commonly, the superconducting material in phonon-cooled devices is NbN. In order to achieve a very fast phonon escape time, the film is made very thin, ~ 3 nm. Experiments with NbN HEB mixers have been performed up to 3.12 THz [8-11].

In this paper we report on heterodyne receiver measurements with a Nb diffusion-cooled HEB at 700 GHz in a *fixed-tuned* waveguide. In section II we give a short overview of the technology used to fabricate the devices. In section III we describe the RF experiments, consisting of a FTS measurement and heterodyne measurements with hot and cold loads.

II. Device fabrication

The essential part of the fabrication process of Nb HEBs is the definition of the Nb microbridge and cooling pads. In order to let diffusion-cooling dominate over electron-phonon cooling, the length of the bridge should be shorter than ~ 400 nm. Also, to achieve a reasonable match between mixer and the IF load, the resistance should be about 50 Ω. This can be achieved by making the film thin (~ 12 nm) to get a high sheet resistance (± 20-30 Ω) and by choosing a proper length-width ratio. Thus, to define the microbridge, electron-beam lithography (EBL) is required.

The process starts off with the deposition of a 12 nm thick Nb film by dc sputtering over the whole area of a 300 μm thick fused quartz wafer. Then the Au cooling pads are defined by EBL using a standard lift-off process with PMMA. The RF choke structure and electrical contacts are defined by optical lithography and lift-off. In the last step, the etch-mask to pattern the microbridge via reactive ion etching (RIE) is defined using a combination of deep-UV photolithography and EBL. Before heterodyne measurements, devices are diced and polished so that the substrate has a width of 90 μm and a thickness of 50 μm. A more detailed description of the process can be found in [12]. Note that the devices used for the measurements in this paper have been fabricated in June 1997 and have not shown any significant degradation upon storage in ambient atmosphere.

III. Experimental results

III.A FTS measurement

Before mounting a HEB in the mixerblock, the devices are characterized by a dc I(V) measurement on a dipstick and by inspection under the scanning electron microscope (SEM). A SEM picture of the device that has been used for the measurements described in this paper is shown in Fig. 1. Typically, the microbridges

have a critical temperature of 5.9 K and a critical current density of ~ $4x10^{10}$ A/m^2. The device that has been used for the measurements described in this paper has a normal state resistance R_n of 31 Ω. The device is mounted in a fixed-tuned (tunerless) waveguide[1] which is designed for frequencies around 700 GHz. Photographs of the complete mixermount and the substrate channel are shown in Fig. 2a and Fig. 2b. The mixer is placed in a dewar and cooled down with liquid helium to a temperature of 4.3 K.

The frequency response of the HEB mixer with the waveguide is measured by operating the device as a direct detector in a Fourrier Transform Spectrometer (FTS) using a broadband source. Fig. 3 shows the measured spectra with and without a vacuum between the source and dewar. During the measurement the device is biased in a resistive state close to the dropback point in the I(V) characteristic (see inset). The peak response is of the waveguide is at 690 GHz, and the bandwidth is 120 GHz. The dip around 560 GHz in the measurement without vacuum is due to water absorption. The exact shape of the spectrum is not well understood at this moment and is still under investigation.

III.B Measurement of the receiver noise temperature

We have measured the receiver noise temperature using a standard Y-factor method. LO power is provided by a carcinotron-doubler combination, with a frequency range from 660 GHz to 760 GHz. All experiments described here are performed at exactly 700 GHz. To couple enough LO power to the device, we used a thick beamsplitter (55 μm mylar), because, due to a technical problem, the LO source did not allow to pump the device with a thinner beamsplitter. This causes an extra 2.3 dB loss in the RF path. The IF chain consists of a Berkshire HEMT cryo-amplifier and two room temperature amplifiers with a total gain of 68.7 dB, a center frequency of 1.4 GHz, and a gain bandwidth of 0.6 GHz. The intermediate frequency is tuned with a narrow bandpass filter. The measurements described here are performed at an IF of 1.25 GHz in a 65 MHz band. The IF output power was measured with a HP power meter. A schematic picture of the experimental set-up is given in Fig. 4.

The maximum measured Y-factor by manual switching between the hot (300 K) and cold load (77 K) is 0.29 dB, which corresponds to a DSB receiver noise temperature of 1690 K, after correction for the beamsplitter loss. Fig. 5a shows the IF output power of the pumped mixer with hot and cold load. The corresponding pumped I(V) curves are shown in Fig. 5b, together with the unpumped I(V). In order to exclude contributions of direct detection to the receiver noise temperature, we have performed a careful inspection of the pumped I(V) curves with hot and cold close to the optimum operating point (inset Fig. 5a), as well as a calculation the differential resistance of the I(V) curves (Fig. 5b). Both do not show any significant differences upon switching between the blackbody loads, indicating that the measured signal is truly heterodyne. The observed peaks in the dV/dI curves are not well understood at this moment. They are device specific and usually not observed. Possibly they are related to (electronic) inhomogeneities in the microbridge.

The noise of the receiver decreased to 1100 K upon reducing the bath temperature to 3.3 K. A further reduction of the bath temperature was not possible

[1] waveguide and mixermount developed at SRON by H. van de Stadt and H. Schaeffer

due to the limited capacity of the pump for the helium bath. However, it is reasonable to expect a receiver noise well below 1000 K at about 2 K.

IV. Calculation of the mixer gain and mixer noise temperature

We have extracted the mixer gain G_{mix} and mixer noise T_{mix} of the bolometer at 4.3 K from the measured IF output powers with hot and cold load. The gain is calculated according to

$$G_{mix} = \frac{\Delta P_{out}}{\Delta P_{in} G_{IF}} = \frac{\Delta P_{out}}{2k_B (T_{eff,h} - T_{eff,c}) G_{IF}}. \quad [1]$$

Here, ΔP_{in} and ΔP_{out} are the RF input power from the blackbody loads (USB and LSB) and IF output power of the HEB mixer, respectively. G_{IF} is the gain of the IF chain. $T_{eff,h}$ and $T_{eff,c}$ are the effective input and output temperatures of the hot and cold load at the mixer input, corrected for the loss in the RF optics. Here, the waveguide is assumed to couple the radiation without loss to the bolometer.

Calibration of gain (and noise temperature) the IF chain is performed by using a SIS tunnel junction as a calibrated shotnoise source. The values for $T_{eff,h}$ and $T_{eff,c}$ are calculated using the known transmission coefficients and physical temperatures of the beamsplitter (55 μm mylar, 300 K), dewar window (125 μm mylar, 300 K), and heatfilter (115 μm black poly-ethyleen, 77 K). The values for the gain and noise temperature of the RF optics and IF chain are summarized in table 1. The high noise contribution of the RF optics is mainly due to the high loss in the 55 μm beamsplitter. Once the gain of the mixer is calculated, the mixer noise follows from

$$T_{rec} = T_{RF} + \frac{T_{mix}}{G_{RF}} + \frac{T_{IF}}{G_{RF} G_{MIX}} \quad [2]$$

Figure 6 shows the calculated gain and noise of the HEB mixer as a function bias voltage, together with the pumped I(V) curve. Close to the dropback point of the I(V) characteristic, a gain of –17.8 dB is observed, whereas the corresponding mixer noise is 1170 K. It was not possible to do the same calculation for the Y-factor measurements at 3.3 K, because the IF chain is not calibrated at this temperature. Therefore, on the basis of our measurements, we cannot conclude whether the strong decrease in receiver noise temperature on decreasing the bath temperature is due to an increase of the mixer gain, a decreased mixer noise, or a combination of both. In the near future, we hope to answer this question by performing a systematic measurement of the mixer gain and noise as a function of the bath temperature.

Table 1 : *Gain and noise contribution of the IF chain and RF optics.*

	IF chain	*RF optics*
Gain (dB)	68.7	-2.5
Noise Temperature (K)	7.1	214

V. Conclusions

In summary, we have presented receiver measurements with a Nb diffusion-cooled HEB mixer in a fixed-tuned waveguide. At an IF of 1.25 GHz and a bath temperature of 4.3 K, the DSB receiver noise temperature is 1690 K. This value decreases to 1100 K upon reduction of the bath temperature to 3.3 K. The maximum mixer gain at 4.3 K was −17.8 dB and the corresponding mixer noise is 1170 K. On the basis of our measurements, we cannot resolve what the origin is of the strong decrease in receiver noise temperature after reducing the bath temperature.

Acknowledgements

Assistance and helpful discussions of H. Schaeffer, W. M. Laauwen, A. Baryshev, H. Nijland, and D. Nguyen are acknowledged. A. van Langen is acknowledged for assistance in e-beam lithography. This work is supported by the European Space Agency (ESA) under Contract No. 11738/95/NL/PB and by the Nederlandse Organisatie voor Wetenschappelijk Onderzoek (NWO) through the Stichting voor Technische Wetenschappen (STW).

References

[1] E. M. Gershenzon, G. N. Gol'tsman, I. G. Gogidze, Y. P. Gusev, A. I. Elant'ev, B. S. Karasik, and A.D. Semenov, Sov. Phys. Superconductivity 3, 1582 (1990).

[2] D. Wilms Floet, E. Miedema, T. M. Klapwijk, and J. R. Gao, Appl. Phys. Lett. 74, 433 (1999).

[3] D. E. Prober Appl. Phys. Lett. 62, 2119 (1993).

[4] A. Skalare, W.R. McGrath, B. Bumble, H.G. LeDuc, P.J. Burke, A.A. Verheijen, R.J. Schoelkopf, and D.E. Prober Appl. Phys. Lett. 68, 1558 (1996).

[5] A. Skalare, W. R. McGrath, B. Bumble, and H. LeDuc, Proc. 9th Int. Symp. Space THz Technology, 115 (1998).

[6] B.S. Karasik, M.C. Gaidis, W.R. McGrath, B. Bumble, and H.G. LeDuc, Appl. Phys. Lett. 71, 1567 (1997).

[7] B.S. Karasik, W.R. McGrath, and R. Wyss, submitted to the 1998 Applied Superconductivity Conference, Palm Desert, USA (1998).

[8] H. Ekström, E. Kollberg, P. Yagoubov, G. Gol'tsman, E. Gershenzon, and S. Yngvesson Appl. Phys. Lett. 70, 3296 (1997).

[9] P. Yagoubov, M. Kroug, H. Merkel, E. Kollberg, G. Gol'tsman, S. Svechnikov, and E. Gershenzon, Appl. Phys. Lett. 73, 2814 (1998).

[10] E. Gerecht, C. F. Musante, H. Jian, K.S. Yngvesson, J. Dickinson, J. Waldman, P. Yagoubov, G. N. Gol'tsman, B.M. Voronov, and E.M. Gershenzon, submitted to the 1998 Applied Superconductivity Conference, Palm Desert, USA (1998).

[11] P. Yagoubov, M. Kroug, H. Merkel, E. Kollberg, J. Schubert, H. W. Hübers, G. Schwaab, G. N. Gol'tsman, E. Gershenzon, submitted to the 1998 Applied Superconductivity Conference, Palm Desert, USA (1998).

[12] D. Wilms Floet, J. R. Gao, W. Hulshoff, H. van de Stadt, T. M. Klapwijk, and A. K. Suurling, IOP Conf. Series No. 158, edited by H. Rogolla and D. H. A. Blank, 401 (1997).

Figures

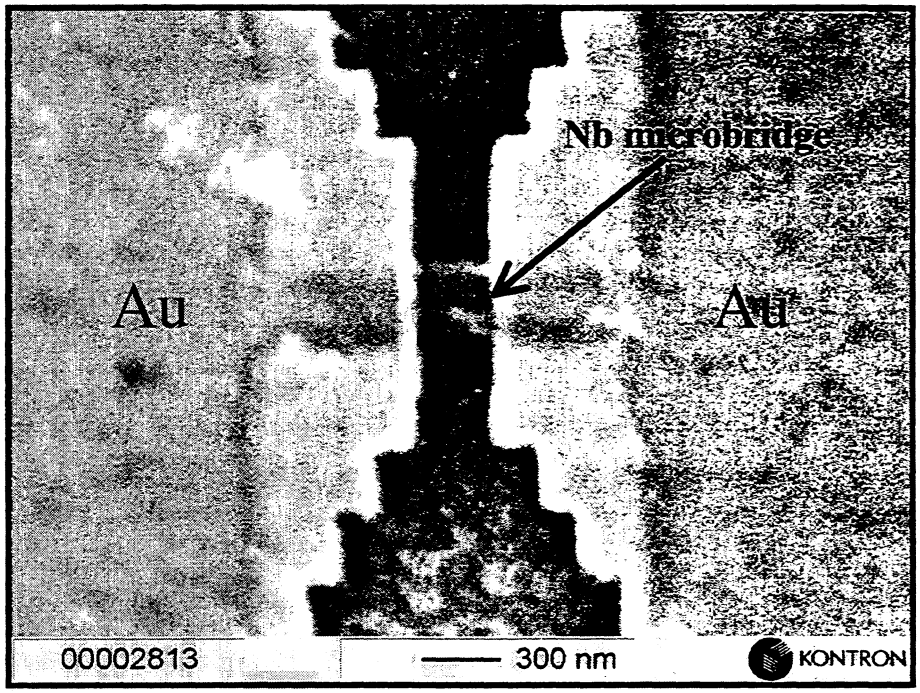

Fig.1 : SEM picture of the device that has been used for the measurements described in this paper. The length and width of the device are approximately 300 nm.

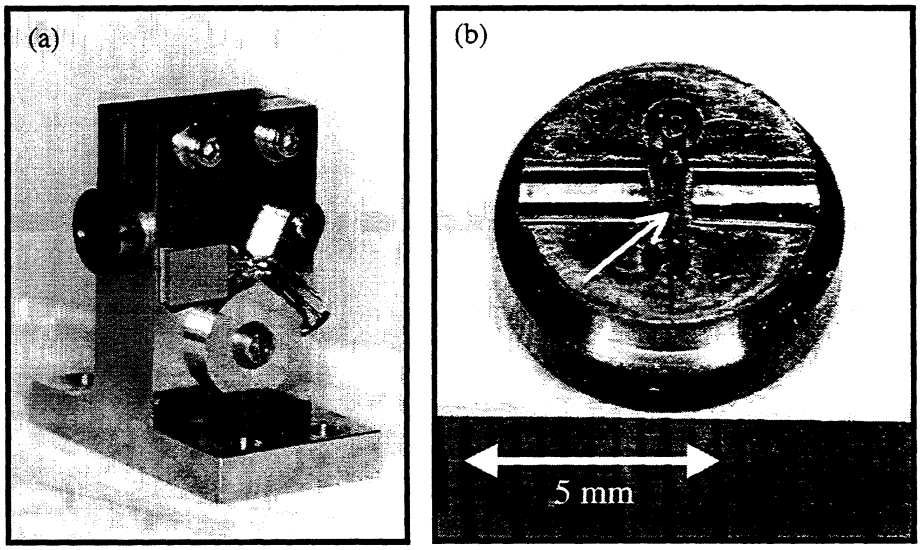

Fig.2 : (a) Photograph of the mount of the fixed-tuned mixer in combination with a diagonal horn.
(b) Part of the mixerblock where the device is mounted. The arrow indicates the substrate channel.

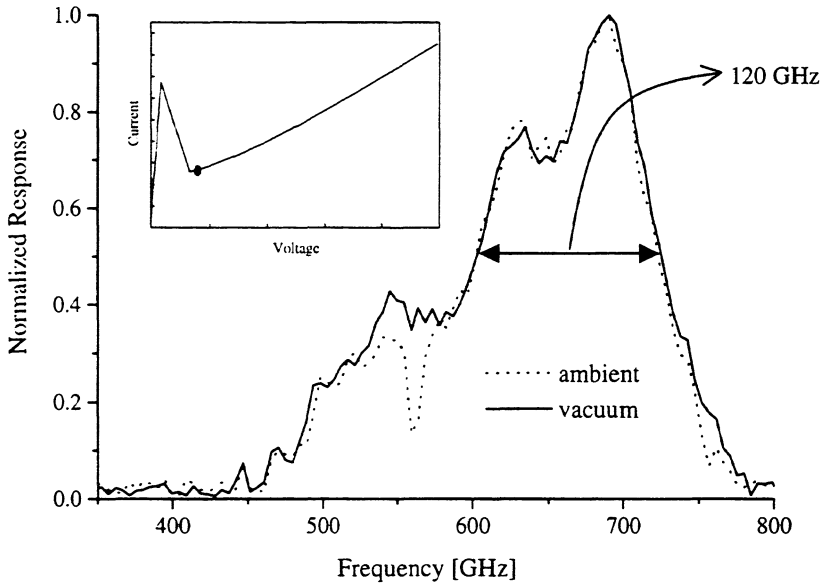

Fig.3 : FTS response of the HEB-waveguide combination. The measurement is performed with (solid line) and without (dotted line) vacuum between dewar and source. The inset shows the I(V) characteristic of the device. The dot indicates the bias point during the measurement of the spectra.

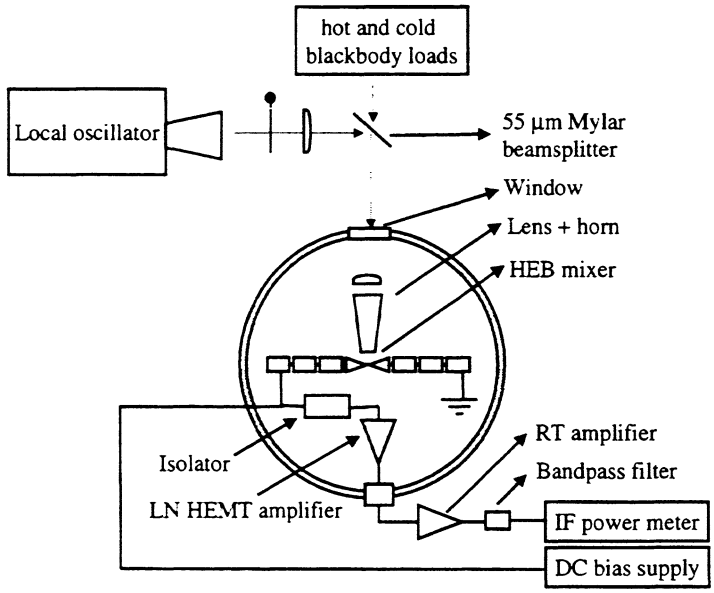

Fig.4 : Schematic representation of the experimental set-up used for the receiver noise measurements.

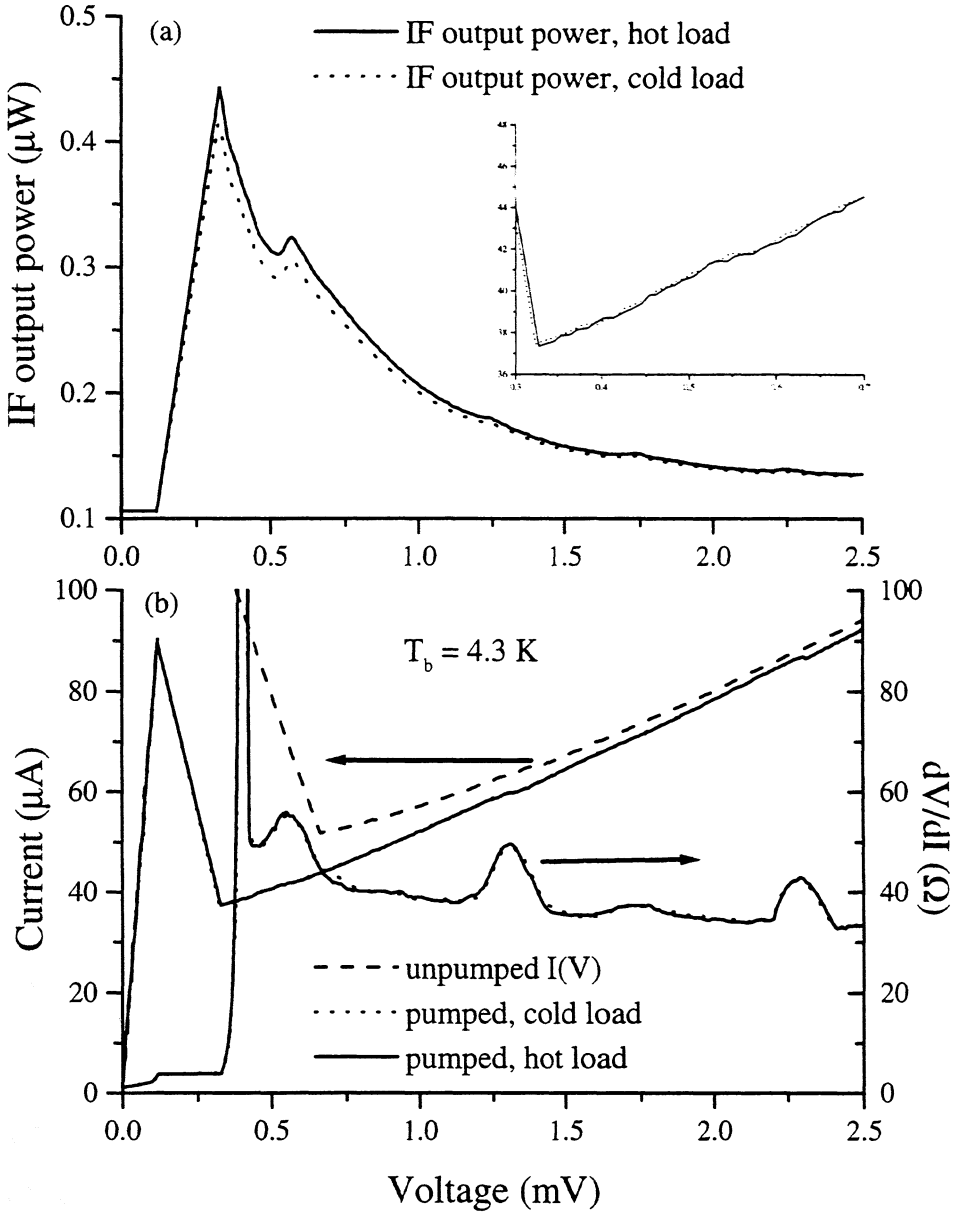

Fig.5 : (a) IF output power of the mixer with hot and cold load as a function of bias voltage. The inset shows the pumped I(V) with hot and cold load close to the optimal operation point.
(b) Measured pumped and unpumped I(V) curves together with the calculated differential resistance as a function of bias voltage.

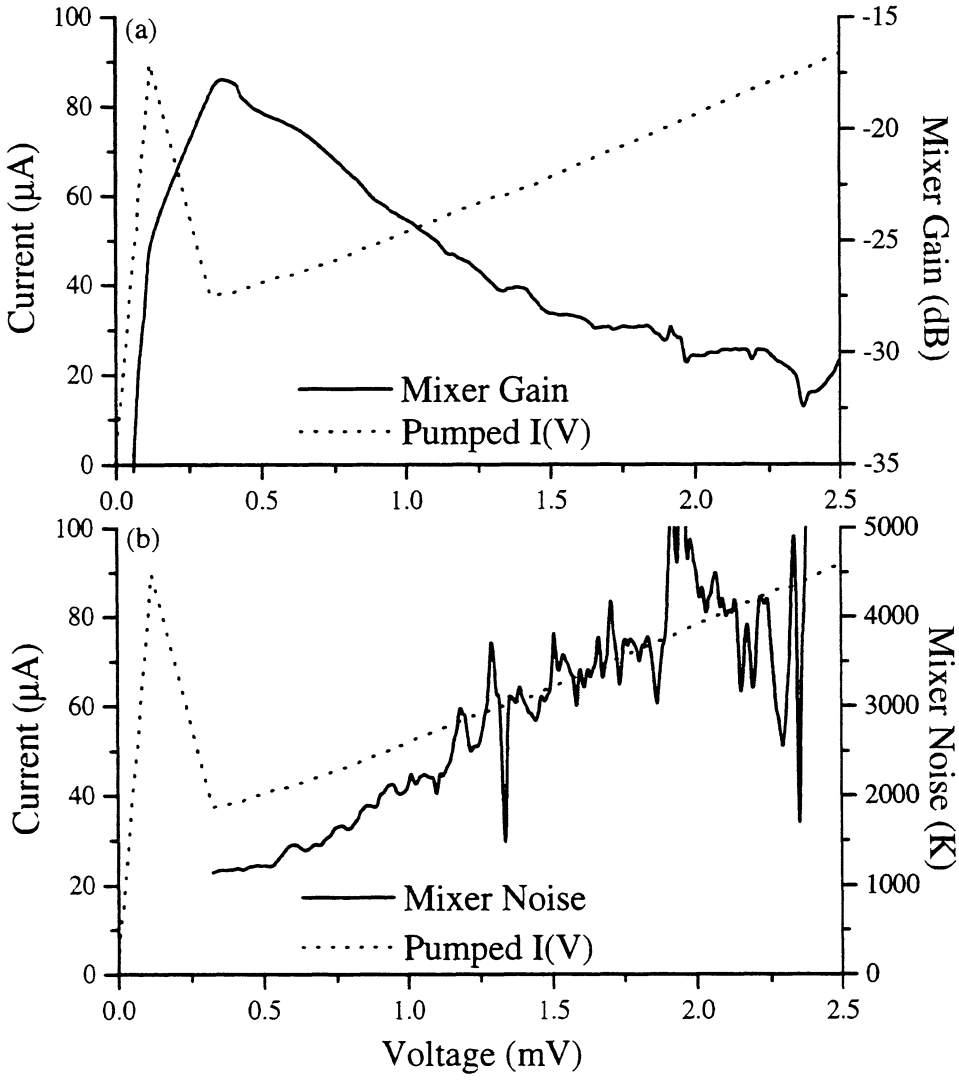

Fig.6 : Calculated mixer gain (Fig. 6a) and mixer noise (Fig. 6b) as a function of bias voltage at a bath temperature of 4.3 K. Also shown in each graph is the pumped I(V) characteristic.

NbN HOT ELECTRON BOLOMETRIC MIXERS AT FREQUENCIES BETWEEN 0.7 AND 3.1 THz

P. Yagoubov*, M. Kroug, H. Merkel, E. Kollberg

Department of Microelectronics
Chalmers University of Technology
S-412 96 Gothenburg, Sweden
*E-mail: yagoubov@ep.chalmers.se

H. -W. Hübers, J. Schubert, G. Schwaab

DLR Institute of Space Sensor Technology
D-12489 Berlin, Germany

G. Gol'tsman, E. Gershenzon

Department of Physics
Moscow State Pedagogical University
119435 Moscow, Russia

Abstract

The performance of NbN based phonon-cooled Hot Electron Bolometric (HEB) quasioptical mixers is investigated in the 0.7-3.1 THz frequency range. The devices are made from a 3.5-4 nm thick NbN film on high resistivity Si and integrated with a planar spiral antenna on the same substrate. The length of the bolometer microbridge is 0.1-0.2 μm, the width is 1-2 μm. The best results of the DSB receiver noise temperature measured at 1.5 GHz intermediate frequency are: 800 K at 0.7 THz, 1100 K at 1.6 THz, 2000 K at 2.5 THz and 4200 K at 3.1 THz. The measurements were performed with a far infrared laser as the local oscillator (LO) source. The estimated LO power required is less than 500 nW at the receiver input. First results on the spiral antenna polarization measurements are reported.

Introduction

In the past years, several research groups have been working on the development of low noise broadband receivers for detection of THz radiation. They are needed in particular for atmospheric observation and radio astronomical applications. Only Schottky diode mixers are used now as receivers at frequencies beyond 1 THz. The prime advantage of this mixer technology is the possibility to operate at room temperature. However, Schottky diodes have rather poor sensitivity which makes it difficult to detect weak signals. In addition, the local oscillator (LO) power requirement for these mixers is very high. Due to the few available powerful laser lines in the THz frequency range, this is a very important issue.

The concept of superconducting HEB mixers has been suggested for receivers at submillimeter wavelengths in [1]. They have already been shown to be competitive with SIS mixers at frequencies around 1 THz [2-4] and represent a very attractive candidate at higher frequencies [5-7]. The development has now reached a stage where they are

successfully used for astronomical observations [8]. HEB mixers can in principle operate up to at least 30 THz without degradation in performance. Optical losses, however, increase with frequency. Therefore, careful design and choice of materials for the optical components in the receiver is needed.

An intermediate frequency (IF) bandwidth of several GHz has been achieved for both phonon-cooled [9-11] and diffusion-cooled [12,13] HEB mixers in experiments below 1 THz. Another attractive feature of HEB mixer technology is a very low power required from the LO source. In our experiments the measured power absorbed in the bolometer element is about 100 nW. Taking into account the estimated optical losses of 3-5 dB we end up with less than 500 nW needed from the LO source at the input of the receiver. This is 3-4 orders of magnitude lower than that of Schottky diode mixers.

At the previous Symposium we reported the measurements of NbN HEB mixers in the 0.65-1.1 THz frequency range [2]. Since that time we went up towards higher frequencies and in this paper we present results of heterodyne mixing between 0.7 and 3.1 THz.

Mixer fabrication and design

The devices are made from a 3.5-4 nm NbN film sputtered on a high resistivity, double side polished, silicon substrate. The film is patterned by e-beam lithography to form a 0.1-0.2 μm long and 1-2 μm wide strip across the center gap of an Au spiral antenna. A SEM micrograph of the bolometer integrated with the antenna is shown in Fig. 1. Details of the fabrication process can be found in [14]. The normal state resistance of the bolometer measured at 20 K ambient temperature is 250-450 Ohm depending on the bolometer strip geometry and film thickness. The critical current density at 4.5 K is about $4x10^6$ A/cm^2. The antenna is an equiangular spiral with a 90° arm width yielding a self-complementary design. This implies that the antenna impedance is purely real and equal to 75 Ohm for the antenna on a Si substrate. Three different antenna designs have been used: spiral "A", "B" and "C". The spiral structure of all antennas extends 1.5 turns and the spiral expansion rate is 3.2 per turn. The spiral "A" antenna is the largest one with an outer radius of 100 μm and inner radius of about 10 μm. Spirals "B" and "C" are the products of scaling down spiral "A" by a factor of 2 and 4, respectively.

Measurement setup and technique

The setup for heterodyne measurements at frequencies between 0.7 THz and 3.1 THz is shown in Fig. 2. The local oscillator source is a far infrared (FIR) laser which is optically pumped by a CO_2 laser. To prevent back-coupling between the FIR and CO_2 laser cavities the FIR laser cavity uses a ring laser design. The FIR laser power is coupled out via a 3 mm diameter hole coupler. To be able to monitor its output power, part of the FIR laser beam is coupled onto a pyro detector via a wire grid. For measurements at 3.1 THz a different laser system is used. Here, the FIR laser consists of a high-Q FIR cavity that is transversally excited by the CO_2 laser. Outcoupling is done by a movable mirror.

A photograph of the mixer block is shown in Fig. 3. The mixer chip and the 12 mm diameter elliptical lens are mounted from opposite sides on a Si substrate which is clamped on the copper mixer block. The mixer block is placed in a liquid helium vacuum cryostat (Fig. 4) equipped with a high-density polyethylene window. IR radiation is blocked by a

380 μm Zitex G115 filter. The device output is connected through a bias-T to a 1.3-1.7 GHz cooled HEMT amplifier with a noise temperature of ≈5 K. The output of the HEMT amplifier is filtered with a 1.5±0.02 GHz bandpass filter, further amplified and detected with a power meter.

The LO and the signal are combined by a thin dielectric beamsplitter. Earlier we used a Martin Puplett diplexer based on 10 μm thick wire grids but it introduces losses of about 1-2 dB in the signal path. Since the FIR laser is powerful enough it is possible to pump the mixer by reflection from a 6 μm Mylar beamsplitter with almost no transmission losses for the signal. The LO power is adjusted by a rotatable wire grid in the LO path before the beamsplitter.

The receiver noise temperature is measured using the traditional Y-factor technique by alternatively placing a hot/cold (295/77) load in the signal path of the receiver which is normally done without chopping. Using a chopper was necessary only at 3.1 THz because of the poor stability of the laser system at this frequency.

For polarization measurements we used one more rotatable grid in the LO path as shown in Fig. 2. The Mylar beamsplitter is replaced by a metal mirror in order to avoid the polarization modification by reflection from the dielectric film. By changing the orientation of both grids (polarizer and analyzer) and measuring the coupling efficiency one can determine the polarization of the receiver antenna. The radiation coupling to the bolometer is obtained from the pump level of the IV curve which is a measure of the power absorbed in the bolometer. Details of the absorbed power measurement technique can be found elsewhere [3].

Device dc parameters

The results presented here are obtained with 5 devices from two different batches, named "V" and "W". The full information about the devices' geometry, dc parameters and noise temperature data are summarized in Table 1. The device dc parameters (resistance and critical current) scale very well with the geometry of the bolometer element. This fact indicates the spatial uniformity of the film and the reproducibility of the fabrication process. The normal state resistance, however, is about factor of 2-3 higher than that derived from the sheet resistance of the non-patterned film, which is 600-800 Ohm/sq for a 3.5 nm NbN film. A possible reason for this discrepancy is a poor dc contact between the film and antenna arms. The actual length of the bolometer is thus longer and the NbN film covered by Au contact pads also contributes to the device dc resistance. Another indication of this fact is the "multiple tooth" structure of the IV curve for some devices, where several critical currents are observed, see the I_c for devices V24 and V33. The first two critical currents in the IV curve can be thus attributed to the critical currents of the superconducting film under the contact pads and the third one to the critical current of the microbridge in between. We are trying to improve the electrical contact between the NbN film and Au contact pads by using an in-situ cleaning of the film before depositing Au. This could decrease the dc resistance of the bolometer. In addition, it might improve the performance of the mixer because absorption of rf radiation in the film with suppressed superconductivity (under the contact pads) most probably deteriorates the conversion gain.

Noise temperature

The noise temperature data shown in the table is the total DSB receiver noise temperature, not corrected to any losses. It is derived from the measured Y-factor with 77/295 K loads at the input of the receiver. At terahertz frequencies and low temperatures the radiated power temperature of a black body is not equal to its physical temperature. The value of the load noise temperature has been calculated using the Callen & Welton formula which is the Planck formula plus half a photon. The difference between receiver noise temperatures calculated using the "standard" Rayleigh-Jeans and Callen & Welton laws is perceptible at frequencies beyond 2 THz. Details can be found in [15].

All devices measured in this work show very similar performance. The best results of the DSB receiver noise temperature obtained at 4.2 K ambient temperature are: 800 K at 0.7 THz, 1100 K at 1.6 THz, 2200 K at 2.5 THz and 4200 K at 3.1 THz. Lowering the device ambient temperature gives slight improvement of the noise temperature. For instance, 2200 K at 2.5 THz measured for device W24 at 4.2 K drops to 2000 K at 3 K. The reason for the strong rise in the noise temperature to 4200 K at 3.1 THz is not clear yet. We believe that it could be due to increase of optical losses in the mixer (cryostat window, Zitex filter, etc.) and the strong water absorption in the atmosphere at this frequency.

The degradation of the sensitivity of the devices V33 and W47 at 0.7 THz is because this frequency is well below the lower cutoff frequency of antenna "C", see next chapter for details.

Antenna polarization

As mentioned before we have used three antenna designs, spiral "A", "B", and "C". Spiral "A" has inner and outer radii of 10 and 100 μm, respectively. The spirals "B" and "C" are just downscaled versions (factors of 2 and 4) of spiral "A".

The total antenna arm length of spiral "A", calculated from its radii and the expansion rate of 3.2 per turn, is about 300 μm. Setting this equal to a maximum effective wavelength yields a lower cutoff frequency of the antenna of 300 GHz in free space. The cutoff of spiral "B" and "C" is 600 GHz and 1.2 THz. This explains the deterioration of the noise temperature performance of the mixers V33 and W47 (utilizing spiral "C") at 700 GHz.

The higher cutoff frequency of the antenna is defined [16] as the frequency at which the antenna polarization becomes elliptical with an axial ratio of 2 to 1. This frequency depends on the construction precision of the antenna feed. Since the spiral arms naturally converge to a point, one has to terminate the center in a tapered section, see Fig.1. According to [16] the cutoff frequency occurs when the total length of the tapered section becomes effectively a half-wavelength. This length is roughly 20 μm, 10 μm, and 5 μm for spirals "A", "B", and "C" setting the upper frequency limit to 2.2 THz, 4.4 THz, and 8.8 THz, respectively.

The axial ratio of elliptical polarization increases towards higher frequencies. Notice, however, that since there are no distinctive changes in pattern shape of the antenna at these frequencies [16], the antenna can still work efficiently although the polarization might not be circular.

The antenna polarization measurements have been performed at 2.5 THz with a device based on spiral "C". The polarization is elliptical with the ellipse axial ratio of about 3 to 1. The last number is within ± 50% error due to the uncertainty of the absorbed power measurement technique. This technique is based on the assumption that the resistance of the bolometer is equally affected by dc and rf power. The limited accuracy of this technique causes an error for determining the coupling efficiency and hence the ellipse axial ratio. The long axis of the ellipse coincides with the direction of the tapered section in the antenna center, Fig. 1.

The obtained result on the antenna polarization does not agree well with that reported in [16]. In that paper the change of polarization from circular to elliptical with 2 to 1 ratio happens at a frequency such that the tapered section is equal to the effective half-wavelength. At higher frequencies the ellipse axial ratio increases further. In our case the length of the tapered portion is only 1/7 of the effective wavelength but the axial ratio is already larger than 2 to 1. One possible reason is that not only the length but also the shape of the tapered section is important. The design of the antenna terminal region used in ref. [16] is quite different from our one and may be more advantageous in terms of the polarization property. Another explanation could be that by some reasons (high resistivity of the Au, impedance mismatch, etc) the field decays faster along the antenna arms making the influence of the antenna center larger. To understand this better, further investigation (testing different antenna designs at different frequencies) is needed.

Acknowledgments

This work has been supported by ESA (ESTEC/No.11738/95/NL/MV), Swedish Research Council for Engineering Sciences, Swedish National Space Board and Russian program on Condensed matter Grant # 96128. The authors are thankful to S.Yngvesson for many useful discussions and B. Voronov for fabrication of NbN films.

References

[1] E. M. Gershenzon, G. N. Gol'tsman, I. G. Gogidze, Y.P. Gusev, A. I. Elant'ev, B. S. Karasik and A. D. Semenov, "Millimeter and submillimeter range mixer based on electronic heating of superconducting films in the resistive state", *Sov. Phys. Superconductivity*, 3, 1582, 1990.

[2] P. Yagoubov, M. Kroug, H. Merkel, E. Kollberg, G. Gol'tsman, A. Lipatov, S. Svechnikov and E. Gershenzon, "Quasioptical NbN phonon cooled hot electron bolometric mixers with low optimal local oscillator power", *Proc. 9th Int. Symp. on Space Terahertz Technology*, Pasadena, CA, 131, 1998.

[3] P. Yagoubov, M. Kroug, H. Merkel, E. Kollberg, G. Gol'tsman, S. Svechnikov and E. Gershenzon, "Noise temperature and local oscillator power requirement of NbN phonon-cooled hot electron bolometric mixers at Terahertz frequencies", *Appl. Phys. Lett.*, 73, 2814, 1998.

[4] A. Skalare, W.R. McGrath, B. Bumble and H. G. LeDuc, "Noise and RF bandwidth measurements of a 1.2 THz HEB heterodyne receiver", *Proc. 8th Int. Symp. on Space Terahertz Technology*, Cambrige, MA, 47, 1997.

[5] B. S. Karasik, M. Gaidis, W.R. McGrath, B. Bumble and H. G. LeDuc, "Low noise in a diffusion-cooled hot-electron mixer at 2.5 THz", *Appl. Phys. Lett.* 71, 1567, 1997.

[6] E. Gerecht, C.F. Musante, H. Jian, K.S. Yngvesson, J. Dickinson, J. Waldman, P.A. Yagoubov, G.N. Gol'tsman, B.M. Voronov, and E.M. Gershenzon, "New results for NbN Phonon-Cooled Hot Electron Bolometric Mixers Above 1 THz", Presented at the *Applied Superconductivity Conference*, Palm Springs, 13-18 September, 1998.

[7] P. Yagoubov, M. Kroug, H. Merkel, E. Kollberg, J. Schubert, H.-W. Hübers, G. Schwaab, G. Gol'tsman, and E. Gershenzon, "Heterodyne Measurements of a NbN Superconducting Hot Electron Mixer at Terahertz Frequencies", Presented at the *Applied Superconductivity Conference*, Palm Springs, 13-18 September, 1998.

[8] J. Kawamura, C.Y.E. Tong, R. Blundell, G. Gol'tsman, S. Cherednichenko, B. Voronov, G. Gershenzon, "NbN Phonon-cooled Hot-electron Mixer Receivers at 800 GHz", Presented at the *Applied Superconductivity Conference*, Palm Springs, 13-18 September, 1998.

[9] P. Yagoubov, G. Gol'tsman, B. Voronov, L. Seidman, V. Siomash, S. Cherednichenko, and E. Gershenzon. "The Bandwidth of HEB Mixers Employing Ultrathin NbN films on Sapphire Substrate", *Proc. 7th Int. Symp. on Space Terahertz Technology*, Charlottesville, VA, 290, 1996.

[10] S. Cherednichenko, P. Yagoubov, K. Il'in, G. Gol'tsman and E. Gershenzon, "Large bandwidth of NbN phonon cooled hot-electron bolometer mixers on supphire substrates", *Proc. 8th Int. Symp. on Space Terahertz Technology*, Cambrige, MA, 245, 1997.

[11] H. Ekström, E. Kollberg, P. Yagoubov, G. Gol'tsman, E. Gershenzon and S. Yngvesson, "Gain and noise bandwidth of NbN hot-electron bolometric mixers", *Appl. Phys. Lett.* 70, 3296, 1997.

[12] D.Prober. "Superconducting Terahertz Mixer using a Transion Edge microbolometer", *Appl. Phys. Lett.* 62(17), 2119, 26 April, 1993.

[13] B.S. Karasik, A. Skalare, W.R. McGrath, B. Bumble, H.G. LeDuc, J.B. Barner, A.W. Kleinsasser, P.J. Burke, R.J. Schoelkopf and D. Prober, "Low noise and wide band hot-electron superconductive mixer for THz frequencies", Presented at the *4th Int. Conf. On MM & CMM Waves and Applications*, San Diego, 20-23 July, 1998.

[14] M. Kroug, P. Yagoubov, G. Gol'tsman and E. Kollberg, "NbN quasioptical phonon cooled hot electron bolometric mixers at THz frequencies", *Proc. the 3rd. European Conference on Applied Superconductivity*, Veldhoven, Netherlands, 1997, (Inst. Phys. Conf. Ser. No 158, p.405).

[15] A. R. Kerr, M.J. Feldman, and S.-K. Pan, "Receiver Noise Temperature, the Quantum Noise Limit, and the Role of the Zero-Point Fluctuations", *Proc. 8th Int. Symp. on Space Terahertz Technology*, Cambrige, MA, 101, 1997.

[16] J. D. Dyson, IRE Trans. Ant. Prop. AP-7, 181, 1959.

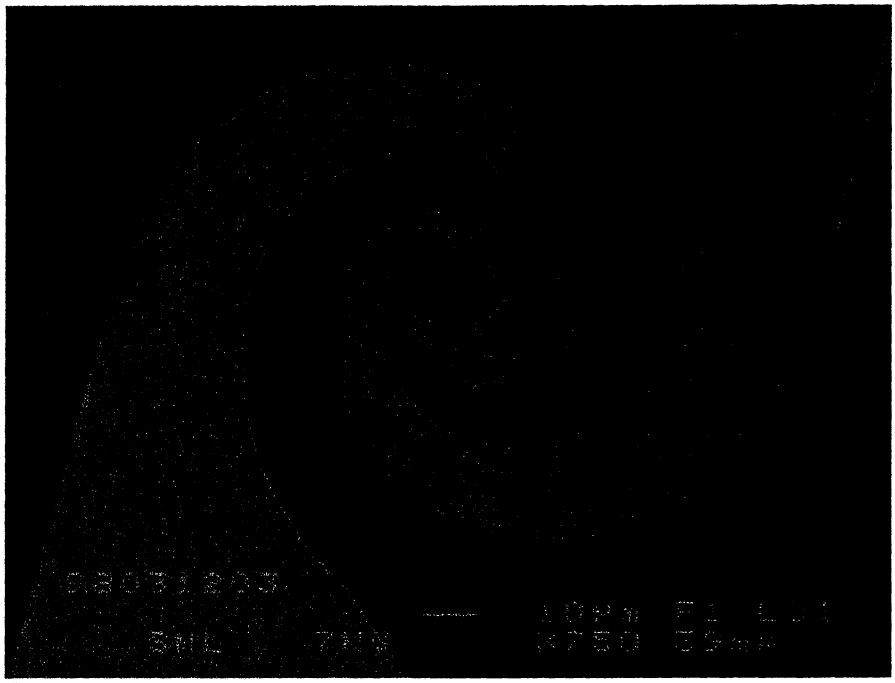

Fig.1. SEM micrograph of the spiral antenna integrated HEB mixer. The antenna design is spiral "B".

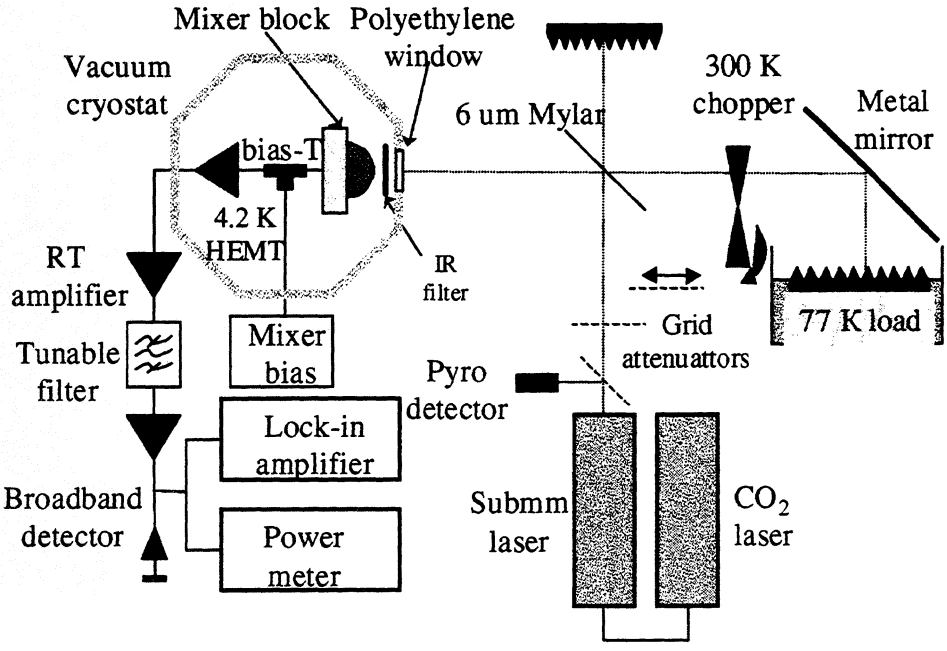

Fig.2. Setup for noise temperature measurements.

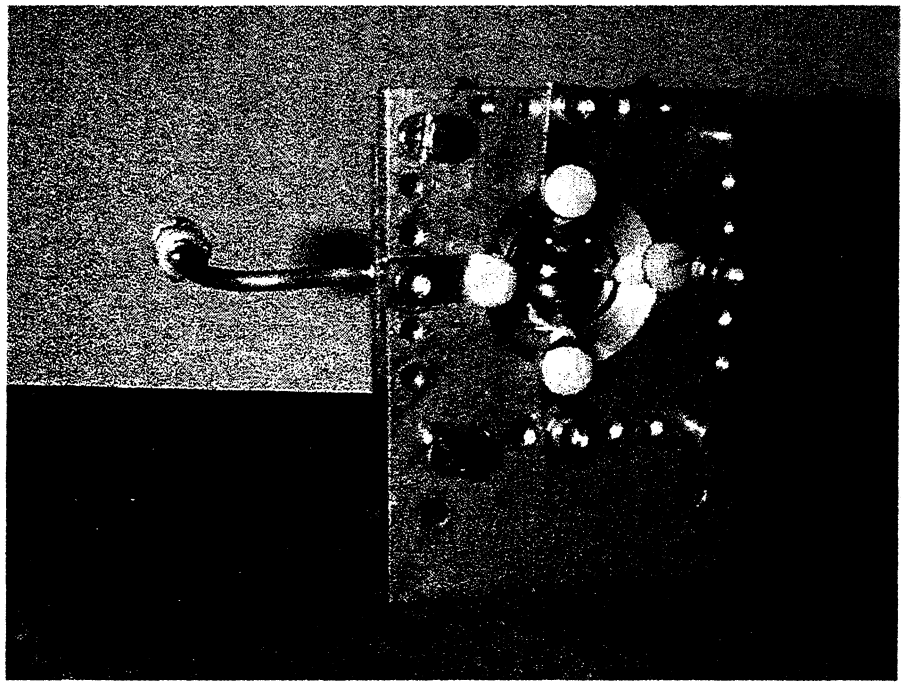

Fig.3. Photograph of the mixer block. The 12 mm diameter Si lens is clamped with springs and four plastic screws against the Si substrate.

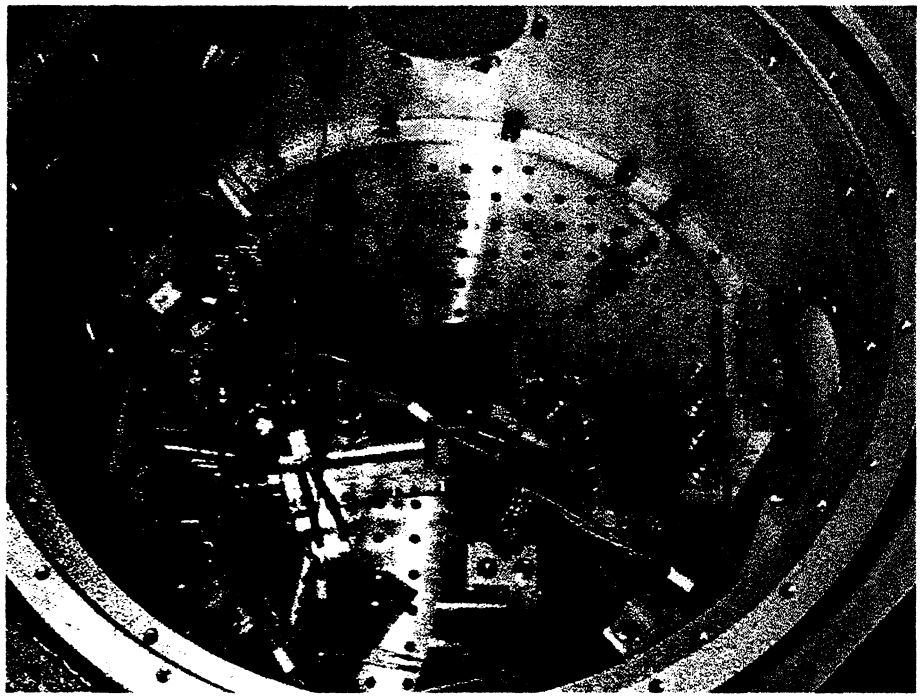

Fig.4. The interior of the LHe vacuum cryostat. The HEMT amplifier is in the center of the cold plate.

Device number	**V14**	**V24**	**V43**	**V24**	**V47**
R_{300K}, Ohm	160	160	230	100	190
R_{20K}, Ohm	350	320	410	230	430
Antenna design	A	B	C	B	C
Bolometer length, μm	0.2	0.15	0.15	≤0.1	≤0.1
width, μm	2	2	1	2	1
I_c, μA (at 4.2 K)	290	180,215,285	110,120,130	280	145
Bias current, μA	45	45	30	60	30
voltage, mV	1.2	0.8	1.2	1.1	1.0
Absorbed LO power, nW	100	100	50	nm	nm
DSB NT, K					
0.7 THz	800	800	1750	1100	1900
1.4 THz	1500	1100	1500	1300	1700
1.6 THz	1300	1100	1300	1300	1700
2.5 THz	2300	2100	2300	2300	2200(2000*)
3.1 THz	nm	nm	nm	4200	4200

nm = not measured

*measured at 3 K ambient temperature

Table 1. Device parameters and results of noise temperature measurements.

TWIN-SLOT ANTENNA COUPLED NB HOT ELECTRON BOLOMETER MIXERS AT 1 THZ AND 2.5 THZ

W.F.M. Ganzevles[†1], J.R. Gao[‡], D. Wilms Floet[†], G. de Lange[‡], A.K. van Langen[†], L.R. Swart[§], T.M. Klapwijk[†] and P.A.J. de Korte[‡]

[†]Department of Applied Physics
Delft University of Technology
Lorentzweg 1, 2628 CJ Delft, The Netherlands

[‡]Space Research Organization of the Netherlands
PO Box 800, 9700 AV Groningen, The Netherlands

[§]Department of Applied Physics
University of Groningen
Nijenborgh 4, 9747 AG Groningen, The Netherlands

Abstract

We have designed quasi-optically coupled Nb diffusion-cooled Hot Electron Bolometer Mixers (DC HEBMs) using a twin-slot antenna and Co-Planar Waveguide (CPW) transmission lines for 1.0 and 2.5 THz. The devices have been realized using two-step e-beam lithography and deep UV lithography. DC measurements give a critical temperature of the bridge of 6.1 K and a critical current density of $7 \times 10^{10} \mathrm{Am}^{-2}$. Typical normal state values for R_{square} are in the order of 30Ω. At 1 THz, we obtain, in contrast to results at 2.5 THz, excellent agreement between design and the response as measured in a Fourier Transform Spectrometer. For the 2.5 THz devices the peak response is shifted to 1.5 THz, similar to results reported in literature[1]. Heterodyne measurements on a 1 THz mixer have shown a corrected receiver noise temperature $T_{N,corr}$ of 3600 K at $T_{bath} = 3.3K$. The Y-factor measurements at different IF suggest an IF bandwidth of at least 1.7 GHz.

[1]Corresponding address:
Department of Applied Physics
University of Groningen
Nijenborgh 4, 9747 AG Groningen, The Netherlands
electronic mail: W.F.M.Ganzevles@phys.rug.nl

1 Introduction

The recent interest in the investigation of the universe through one of the last major windows of the electromagnetic spectrum has given large impetus to research and development of sub-millimeter detectors.

Up to about 1 THz, Nb superconductor-insulator-superconductor (SIS) mixers have proven to be very suitable. Above this frequency, superconducting Hot Electron Bolometer Mixers (HEBMs) are promising candidates to fulfill the need for low-noise, high frequency detectors.

In order to study diffusion-cooled Nb HEBMs at high frequencies, we develop an RF setup using Quasi-Optical (QO) techniques to couple radiation to the microbridge. Our design includes lens, holder, on-chip RF and IF structures and the connection to the IF chain.

In this contribution, we will describe our on-chip RF design and the device fabrication process. DC measurements are reported and we will describe the design of some major components used in our receiver. Predicted RF response is then compared to the measured response around both 1 THz and 2.5 THz as considerable disagreement exists between calculation and measurements of the response. This is observed by both Karasik et al.[1] and the authors. Lastly, we report heterodyne measurements at 0.93 THz.

2 RF design and characterization

Out of a number of possible antenna geometries such as log periodic, log spiral and double dipole, we have chosen the twin slot antenna because it has properties suitable to possible applications. Among these, there are reasonably small bandwidth, linear polarization, circular beam pattern, good Gaussian coupling and low sidelobe levels.

The antenna geometry we use has length $l = 0.32\lambda_0$, separation $s = 0.16\lambda_0$ and width $w = 0.05 \cdot l$, where λ_0 is the free-space wavelength. Several antennas close to this geometry have been investigated. We have chosen this particular geometry because it has almost zero imaginary part at the center frequency f_{center} and a reasonably symmetric beam pattern.

To feed the signal to the heart of the detector, a superconducting Nb bridge with a length, width and thickness of typically 200 nm $\times$ 200 nm $\times$ 12 nm, we use a Co-Planar Waveguide (CPW) transmission line. This line has nominal dimensions slot width $a = 0.5\mu$m and center line width $b = 2\mu$m.

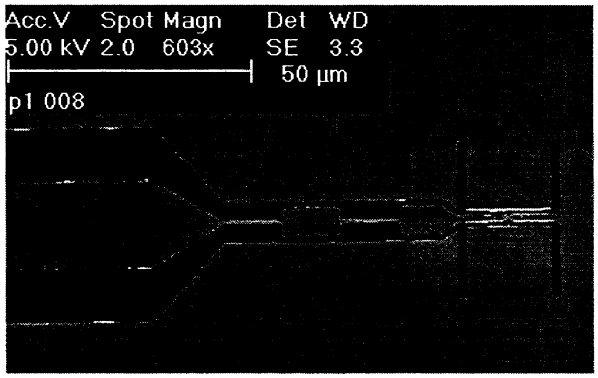

Figure 1: *Lay out of a 2.5 THz device. The antenna and filter are clearly visible, as is the IF CPW on the left. The CPW transmission lines connect the antenna to the bridge.*

A $\frac{1}{4}\lambda$ RF filter is used to prevent signal from entering the IF chain. The filter consists of high impedance sections with a width of 1.5 μm and low impedance sections having a width of 8 μm. At 2.5 THz, the length of the sections is 12 μm. A CPW transmission line is connected to the filter. This acts as the connection to both the DC bias supply and the IF amplifier. Fig. 1 shows an SEM micrograph of a 2.5 THz device. A similar design is reported in literature at various frequencies[1],[2].

To design the RF structure to be used in the QO HEBMs, we use a method in which we separate the antenna, filter and CPW transmission line to obtain the coupling efficiency of the antenna-bridge combination. The impedance of each of these elements is calculated separately, using analytical formulas from [3]. The antenna impedance however is calculated using a computer program by Zmuidzinas and Chattopadhyay[4], based on a model by Kominami et al.[5]. We only include geometry and ε_r of the structure.

For small CPW-structures, we find that the models from[3] yield results that are doubtfull[6]. Therefore, we use several commercially available software programs ([7],[8]), yielding $Z_{0,CPW} = 39\,\Omega$. This value then is linearly extrapolated using the CPW geometry as measured after device fabrication. The impedance of each filter section is calculated using a model from [3], as the filter is relatively large and both [3] and [7],[8] yield similar results. In this paper, we will call this approach the analytical approach, although not fully justified.

For the HEB impedance Z_{HEB}, we assume the normal state resistance of

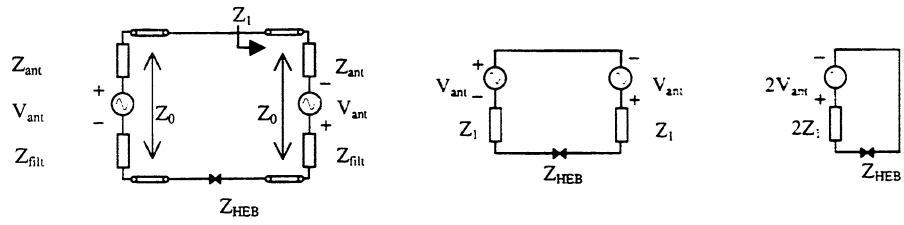

Figure 2: *Equivalent circuit used in the analytical RF modeling.*

the device R_N. Using the equivalent circuit shown in Fig. 2 (which is similar to the one in [2]), we then calculate the coupling efficiency η between the HEB and the antenna-filter-loaded CPW, having total impedance Z_1, using the relation

$$\eta = \frac{4Re\,(Z_{HEB})\,Re\,(Z_1)}{|Z_{HEB} + Z_1|^2}, \tag{1}$$

where Z_1 is the effective impedance seen by the bolometer. Results will be presented in section 5.2. Note that in this approach, the disturbing influence of the filter on the antenna geometry is not taken into account. Only reflection losses are taken into account.

3 Device Fabrication

A fabrication process for Nb HEBMs has been developed using two-step electron beam lithography (EBL) to define both bridge length and width. Deep UV lithography is used to define the RF structure. In this section, we shortly sketch the fabrication process of the device. DC measurements will be shown in section 4, indicating that this process is suitable for production of diffusion cooled QO HEBMs.

In the first step, 75 nm thick Au squares are DC-magnetron sputtered on the high-resistivity Si substrate (double-sided polished). These are used as alignment markers in subsequent optical and e-beam lithography steps.

Then we deposit 12 nm Nb using magnetron sputtering. Using a lift-off mask, only patches 12 μm $\times$12 μm are covered. This decreases the amount of Nb to be opened up for etching, thus reducing the writing area in the EBL machine. Also, only a small fraction of RF current has to run in –lossy– Nb. Au coolpads (100 nm thick) are defined using EBL in a double layer

PMMA system. RF cleaning of the Nb in an Ar-plasma is used to remove the native Nb oxide, in order to achieve a high interface transparency. In situ, ~ 10 nm Au is sputtered. Then, 90 nm Au is e-beam evaporated at a pressure of 2×10^{-6}mbar.

After lift-off, 5 nm Al plus 10 nm Au is sputtered, using a lift-off mask in Shipley DUV III-resist. This layer requires the use of DUV lithography because of the 0.5 μm slots in the CPW structure. 160 nm Au is evaporated under similar conditions as the cooling pads. As a last optical step, we deposit 100 nm Nb on the IF CPW-transmission line.

In the last production step, we define the bridge width. Using EBL, we define a PMMA bridge in the double layer resist system as before. Only the Nb parts that have to be etched are opened up, see Fig. 3. In a mixture of CF_4+3%O_2, the Nb is reactive ion etched. We monitor the process by measuring the optical reflectivity of the Nb on the Si substrate by using a laser endpoint detection system. Using this process we are able to produce Nb bridges as small as 60 nm, as shown in Fig. 3.

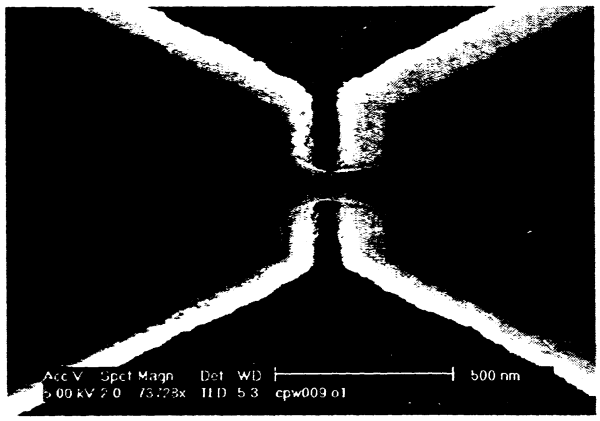

Figure 3: *The microbridge after etching. The PMMA etch mask is still present. Bridge dimensions: $l \times w \sim 60$ nm$\times 80$ nm. The tapered structures are the Au cooling pads.*

During processing, all devices are electrically shorted. After dicing these shorts are opened. Therefore, all further handling must be done with extreme care to prevent damage due to electrostatic discharge. After wire bonding, DC measurements are performed at 4.2 K in a metal vacuum can.

4 DC Measurements

Suitable devices for RF measurements are selected based on IV-curves. Also the R-T curve is used for quality assessment. Several devices show IV-curves that are suitable for use in RF experiments.

Measurements on a large structure yield for 12 nm Nb a residual resistance ratio (RRR) of 1.65 and a square resistance of about $R_{square} = 33\Omega$. The gold, 175 nm thick, that is used for the RF structure has an RRR of around 3.5 and $R_{square} = 0.1\Omega$.

As can be seen in Fig. 4, the critical temperature of the Nb bridge $T_{c,bridge}$ is 6.1 K. The Nb under the cooling pads $T_{c,pads}$ is 5.2 K. Both values are close to what is found in literature[1],[9],[10].

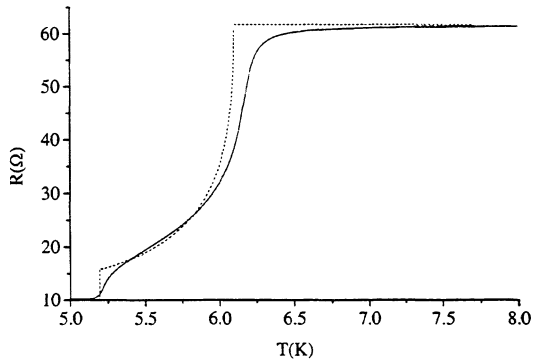

Figure 4: *RT-curve of 1 THz device. The simulation (dashed) is done assuming* $T_{c,bridge} = 6.1$ K; $R_{square} = 33\Omega$.

The RT-curve is modelled according to [11] (dashed line in Fig. 4), taking into account the superconducting proximity effect, Andreev reflection and charge imbalance. The measured curve can be modelled reasonably well. This indicates that our devices show RT-behavior as one would expect.

An unpumped IV-curve of a bridge (nominally 200 nm long, 200 nm wide, 12 nm thick) is shown in Fig. 8 (dashed line). We observe a critical current density of 7×10^{10} Am^{-2}. This agrees to values found in literature[1],[9],[12] within a factor of 2.

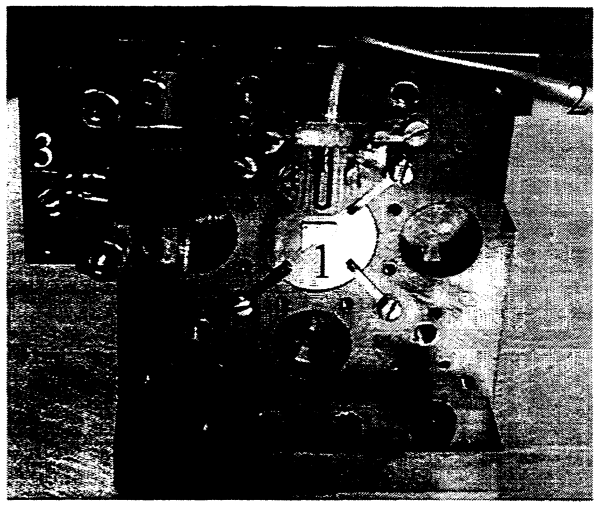

Figure 5: *Photograph of the mixer block. The lens and (h.l. broken) chip (1) and IF cable (2) can be clearly seen. Upper left is the thermometer (3). The connecting IF board (4) is also visible.*

5 RF Measurements

5.1 Receiver Setup

The on-chip HEB is placed in the second focus of a synthesized elliptical high-resistivity Si lens by gluing it to the lens. Instead of using beeswax we now use superglue. This is done to avoid damaging the bridge by heating it to melt the wax ($\sim 80°C$).

Before applying glue, we align the antenna to the optical axis (accuracy better than 5 μm) by moving the die with micrometers to the center of the lens. Using a microscope with XY-table, this center is found relative to the lens' outer edge, which is accurately machined.

The lens itself is held in a copper block as can be seen in Fig. 5. To obtain good thermal contact, 4 springs press the lens softly into the In foil between the flange of the lens and the Cu block.

We find the temperature of the lens to be 4.7 K, not pumping the He-bath. The block is bolted to the cold plate, applying a small amount of Apiezon N vacuum grease for thermal contact. Connection to a standard

IF-chain[1] (centered at 1.4 GHz) is made by wire bonding to a microstrip line on a printed circuit board (Duroid^{TM}, 0.5mm thick, $\varepsilon_r = 4.7$), having $<$ -10 dB reflection over a bandwidth of 4.7 GHz. A standard SMA-connector is soldered to its end to connect to the IF chain.

The window of our dewar is made of 195μm Mylar. Behind that, a black polyethylene IR-filter (105μm)is placed.

Y-factor measurements are done using a carcinotron or, in the near future, an FIR laser as a Local Oscillator (LO) source. A standard hot/cold setup (300 K/77 K) is used as a calibrated source, the signals of both being combined by a Mylar beam splitter (15μm).

5.2 RF Response Measurements

To characterize the RF response of the HEBMs, we use a Fourier Transform Spectrometer (FTS) to measure the relative coupling efficiency as a function of frequency. In doing these measurements, the device is kept at a temperature of about 4.8 K. A bias point slightly above the drop-back point is chosen to have optimal signal. In this paper, we show results for devices designed for both 1 THz and 2.5 THz. The data we show are obtained from 1 specific device, although similar data are measured on several devices.

Relative coupling efficiency for 1 THz devices shows good agreement with the predictions by the model sketched in section 2. The vertical scale of the FTS data is adjusted to give the best match to the simulation. As can be seen in Fig. 6 (solid line), a downward shift of about 12% from design value (1 THz) is observed. This can be well accounted for by taking actual device parameters into account (dashed line): the 500 nm line widths needed in the CPW turn out slightly wider (800 nm) in the fabrication process and R_{HEB} is 50% higher than designed.

The fact that we do not observe the increase in the measurements (starting around 1.3 THz) is due to the decrease of the main beam efficiency when off-center. Radiation is coupled into this main beam, so the observed efficiency goes down with respect to calculation. Optimization is done for the first peak only.

The 2.5 THz device on the contrary, shows its peak response over a wide band around 1.5 THz (solid line), a decrease of $\sim$ 30% with respect to the

[1]The IF chain consists of a Berkshire cryo-amplifier (44dB), an isolator, room temperature amplifier (44dB), band pass filter (80 MHz at 1.4 GHz) and a Hewlett Packard power meter. The total gain is 76dB.

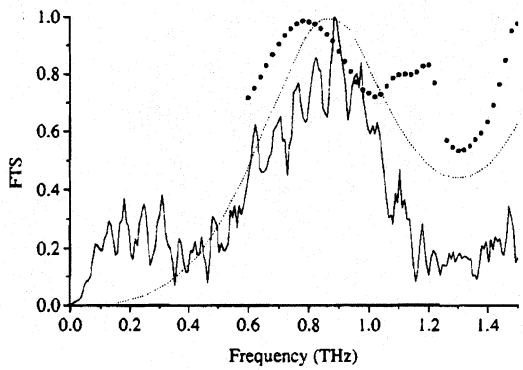

Figure 6: *FTS results and simulations on 1 THz-device. The solid curve is the measurement, the dotted curve is the analytical simulation. The solid dots are the distributed calculation with* $R_{HEB} = 51\Omega$. *See the text of section 6.*

curve that is simulated based on actual device geometry (Fig. 7, dotted). A similar, though not as severe, shift is observed by Karasik et al.[1]. Calculating the expected response based on actual device parameters results in a center frequency of 2.1 THz (dashed line). The observed and calculated bandwidth are in reasonable agreement.

5.3 Heterodyne measurements

Using a standard hot/cold technique we performed heterodyne measurements on a 1 THz bolometer. We determine the corrected receiver noise temperature to be 3600 K at an estimated bath temperature of 3.3 K and an IF-bandwidth of 1.25 GHz. The correction is for the beam splitter only.

Using the isothermal technique at relatively high V_{bias}, we find that about 40 nW of LO power is needed to obtain the highest Y-factor.

Fig. 8 shows the IV-curve of the pumped and unpumped device. The Y-factor does not change noticeably with varying LO frequency in the range of 0.90-0.94 THz. The IF bandwidth of the mixer is limited by the IF chain used (1.7 GHz).

The IV-curve of the device is fit using the hot spot model by Wilms Floet et al.[13]. This model describes the mixing in terms of a hot spot oscillating at IF. The IV-curves can be predicted using this model. Our experimental

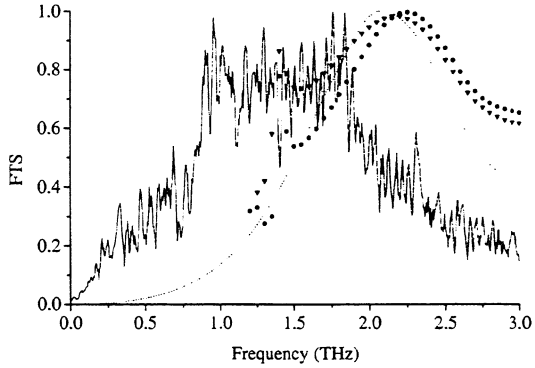

Figure 7: *FTS results and simulations on 2.5 THz-device. For* Z_{HEB} *the measured value* $R_{HEB} = 51\Omega$ *is taken. The solid curve is the measurement, the dotted curve is the analytical simulation. The solid dots are the distributed calculation with infinite* $\sigma_{groundplane}$*, the open dots assume* $\sigma_{groundplane} = 4.1 \times 10^7 \Omega m^{-1}$.

data can be well described by this model using realistic values for the relevant parameters in the model. For the LO power needed, we find 55 nW. This value agrees with the 40 nW obtained in the isotherm method, where it is assumed that absorption of DC power is uniform over the microbridge and hence, less RF power is needed to sustain the same hot spot length.

6 Discussion

Heterodyne measurements done on a similar system[14], although using a doube dipole, yield $T_N = 1880$ K at 1.267 THz, measurements on a twin slot by [1] at 2.5 THz yield 2750 K. Waveguide devices[15] have shown a best noise temperature of 1100K at 0.70THz. We expect to be able to decrease the noise temperature by cooling the device to 2.2K. Based on the decrease seen by[15], we expect a value in the order of 2500 K. A full noise breakdown has to be done in order to identify the major noise contributions.

As shown in the section on RF response measurements, devices designed for 1 THz have an RF response that can be well accounted for. Because the reason for the large difference between these devices and those designed for 2.5 THz is not clear, we investigate the origin of the additional shift in our

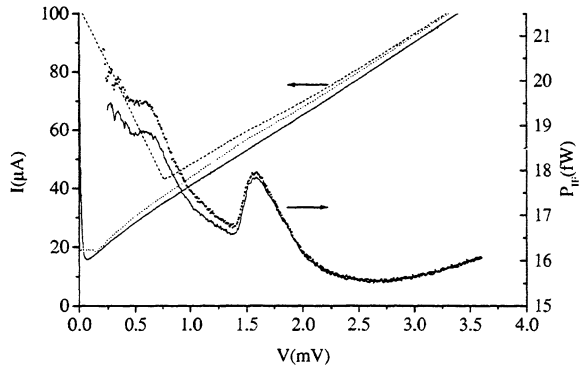

Figure 8: *Pumped (dotted) and unpumped (dashed) IV-curve of 1 THz device J1. The solid line is a simulation by the hot spot model. Hot (dots) and cold (line) IF output are also shown.*

2.5 THz geometry.

We do this by simulating the structure in a distributed element approach, in which we take into account the finite conductivity ($\sigma_{\text{groundplane}} = 4.1 \times 10^7\ \Omega^{-1}\text{m}^{-1}$) of the gold groundplane and the geometrical effect of the filter on the antenna. These calculations are done for both 1 THz and 2.5 THz.

The antenna-CPW-filter combination is drawn in Momentum[7]. At the position of the microbridge, a slot is assumed, keeping both CPW signal lines unconnected. To define a good plane of reference, a microstrip line with a via to the end of one CPW signal line is included. At the end of this microstrip line the reference plane is defined. It is checked that this microstrip line/via combination has little or no effect on the actual device. After calculation of the impedance at the position of the bolometer, the coupling of both impedances is calculated using equation 1 and the measured value for R_{HEB}.

Fig. 7 includes the results of a distributed element simulation on the designed structure compared to both measurement and an analytical simulation. It can be seen that the distributed element approach predicts the peak response frequency to be 10% lower than the original design (2.5 THz).

When the actual device geometry is put into the analytical simulations, peak response is expected at 2.1 THz. This is still 30% higher than the observed value.

To identify a possible cause for the shift, the influence of $\sigma_{\text{groundplane}}$ is looked at. It can be seen that including a finite groundplane conductivity ($\sigma_{\text{groundplane}} = 4.1 \times 10^7 \Omega^{-1}\text{m}^{-1}$, a reasonable value for our films) yields a small shift and also increases the band width. Including a finite groundplane conductivity still does not explain the large shift in response frequency.

We performed a similar analysis for the 1 THz device using the distributed element approach. Fig. 6 includes the results of a distributed element simulation on the designed structure compared to both measurement and an analytical simulation. The lumped (dotted) and distributed (solid dots) element-approach differ less than 10% in peak position, both their bandwidths agree with the measured bandwidth. Considering the fact that the actual CPW impedance, which is an important factor in the lumped-element peak position, is only roughly known, agree reasonably well in all three curves. The shoulder around 1.2THz is believed to be caused by structures present in the ground plane, e.g. the filter or filter-IF line transition.

To get rid of the structures in the CPW groundplane (i.e. filter, CPW transmission line) that may influence the antenna performance, we designed and produced a microstrip line design[16]. In that design, filter and antenna-bridge transmission line are included in the top layer of an $Al/SiO_2/Al$ microstrip line.

There are various reasons why we prefer the microstrip line design to the CPW. First, in a CPW-design, there is the already mentioned influence on the antenna properties. This is absent in the microstrip line design. Second, the microstrip transmission line has proven to work very well in an SIS-mixer up to 1 THz[17],[18]. Third, it allows us a much larger variation in characteristic impedance of the transmission line, making it easy to match a diffusion cooled HEB, which usually has a low impedance. Lastly, with respect to the fabrication, the microstrip line design is easier than that of the CPW transmission line because the structures can be defined by conventional optical lithography without the need of a high-resolution lithography such as e-beam lithography[1].

7 Conclusions

We report the design and fabrication of our quasi-optically coupled HEBMs for use at 1 and 2.5 THz. A twin slot antenna is used, in which the signal is transferred to the microbridge using CPW transmission lines.

The fabrication process for these devices is shown to work well. FTS measurements show the relative coupling efficiency to be in good agreement with the expected curve for 1 THz devices. For devices designed for 2.5 THz, a considerable down shift in peak response is observed. This shift cannot be accounted for in a more sophisticated approach based on the field distribution in the structure.

Our preliminary heterodyne measurements show a noise temperature of 3600 K at 0.93 THz. The IF bandwidth of the receiver is limited by the IF chain used.

8 Acknowledgment

Useful discussions with B. Jackson, H. Golstein, D. Van Nguyen, W. Laauwen and A. Baryshev and their support are acknowledged. This work is financially supported by the Stichting voor Technische Wetenschappen, which is part of the Nederlandse Organisatie voor Wetenschappelijk Onderzoek and partly by ESA under contract no. 11738/95/NL/PB.

References

[1] B.S. Karasik, M.C. Gaidis, W.R. McGrath, B. Bumble, and H.G. LeDuc. *IEEE Transactions on Applied Superconductivity*, 7:3580, 1997.

[2] S.S. Gearhart and G.M. Rebeiz. *IEEE Transactions on Microwave Theory and Techniques*, 42:2504-2511, 1994.

[3] Brian C. Wadell. *Transmission Line Design Handbook.* Artech House, Inc., 685 Canton Street Norwood, MA 02062, 1991.

[4] J. Zmuidzinas and H.G. LeDuc. *IEEE Transactions on Microwave Theory and Techniques*, 40:1797, 1992.

[5] M. Kominami, D.M. Pozar, and D.H. Schaubert. *IEEE Transactions on Antennas and Propagation*, 33:600, 1985.

[6] R. van der Laan. Master's thesis, University of Groningen, 1997.

[7] Hewlett Packard Advanced Design Software, Momentum planar solver.

[8] Sonnet EM software.

[9] D. Wilms Floet, J.J.A. Baselmans, J.R. Gao, and T.M. Klapwijk. Proceedings of the 9^{th} International Symposium on Space Terahertz Technology, Pasadena, CA. 1998.

[10] P.J. Burke, R.J. Schoelkopf, D.E. Prober, A. Skalare, M.C. Karasik, B.S. Gaidis, W.R. McGrath, B. Bumble, and H.G. LeDuc. *Journal of Applied Physics*, 85(3):1644, 1653 1999.

[11] D. Wilms Floet, J.J.A. Baselmans, T.M. Klapwijk, and J.R. Gao. *Applied Physics Letters*, 73(19):2826–2828, 1998.

[12] A. Skalare, W.R. McGrath, B. Bumble, H.G. LeDuc, P.J. Burke, A.A. Verheijen, R.J. Schoelkopf, and D.E. Prober. *Applied Physics Letters*, 68(11):1558–1560, 1996.

[13] D. Wilms Floet, E. Miedema, T.M. Klapwijk, and J.R. Gao. *Applied Physics Letters*, 74(3):433–435, 1999.

[14] A. Skalare, W.R. McGrath, B. Bumble, and H.G. LeDuc. *IEEE Transactions on Applied Superconductivity*, 7:3296, 1997.

[15] D. Wilms Floet, J.R. Gao, W.F.M. Ganzevles, T.M. Klapwijk, G. de Lange, and P.A.J. de Korte. Proceedings of the 10^{th} International Symposium on Space Terahertz Technology, Charlottesville, VA. 1999.

[16] W.F.M. Ganzevles, J.R. Gao, N.D. Whyborn, P.A.J. de Korte, and T.M. Klapwijk. page 504, 1998.

[17] M. Bin, M.C. Gaidis, J. Zmuidzinas, T.G. Phillips, and H.G. LeDuc. *Applied Physics Letters*, 68:1714, 1996.

[18] P. Dieleman, T.M. Klapwijk, J.R. Gao, and H. van de Stadt. *IEEE Transactions on Applied Superconductivity*, 7:2566, 1997.

FABRICATION OF AN ALUMINUM BASED HOT ELECTRON MIXER FOR TERAHERTZ APPLICATIONS

P. M. Echternach, H.G. LeDuc, A. Skalare and W.R. McGrath
Center for Space Microelectronics Technology, Jet Propulsion Laboratory,
California Institute of Technology, Pasadena, CA, 91109-8099

ABSTRACT

Aluminum based diffusion cooled hot electron bolometers (HEB) mixers, predicted to have a broader bandwidth, to require less LO power, and perhaps even have lower noise than Nb based diffusion cooled HEBs, have been fabricated. Preliminary DC tests were performed. The bolometer elements consisted of short (0.18 to 0.53 μm), narrow (0.08 to 0.15 μm) and thin (11 nm) aluminum microbridges connected to large contact pads consisting of a novel trilayer Al/Ti/Au. The patterns were defined by electron beam lithography and the metal deposition involved a double angle process, with the aluminum microbridges being deposited at –degree (i.e. straight on) and the pads being deposited at a 45 degree angle without breaking vacuum. The Al/Ti/Au trilayer was developed to provide a way of making contact between the aluminum microbridge and the gold antenna without degrading the properties of the microbridge. The titanium layer acts as a diffusion barrier to avoid damage of the aluminum contact and bolometer microbridge and to lower the transition temperature of the pads to below that of the bolometer microbridge. The Au layer avoids the formation of an oxide on the Ti layer and provides good electrical contact to mixer rf embedding circuit and planar antenna. The resistance of the bolometers as a function of temperature was measured. It appears that below the transition temperature of the microbridge (1.8K) but above the transition temperature of the contact pads (0.6K), the proximity effect drives much of the bolometer microbridge normal, which gives the apperance of a very broad transition. This however should not affect the performance of the bolometers since they will be operated at a temperature below the Tc of the pads, and hence no proximity effect will be present. This is evident from the IV characteristics measured at 0.3K. RF characterization tests will begin shortly.

INTRODUCTION

Hot electron bolometric mixers , both phonon[1,2] or diffusion[3,4] cooled have become a very attractive choice for heterodyne detection above 1 THz, in terms of temperature noise and LO power. However, requirements and constraints of future missions and applications will benefit from even lower LO power, higher bandwidth, and lower noise temperatures. It has been predicted that aluminum-based diffusion cooled bolometers might have better performance in all counts. Absorbed LO power, which is proportional to the square of the transition temperature and inversely proportional to the device resistance, could be a factor of at least5 to 10 times lower than either Nb or NbN for optimized devices.[5] In terms of IF bandwidth, aluminum should also be better due to its higher diffusion constant, having the potential to yield bandwidths of several tens of GHz.

We have now fabricated and performed DC characterization on Al-based hot electron bolometers. The DC characterization reveals that the devices are well within the design parameter space for optimal performance.[5] RF characterization will start shortly.

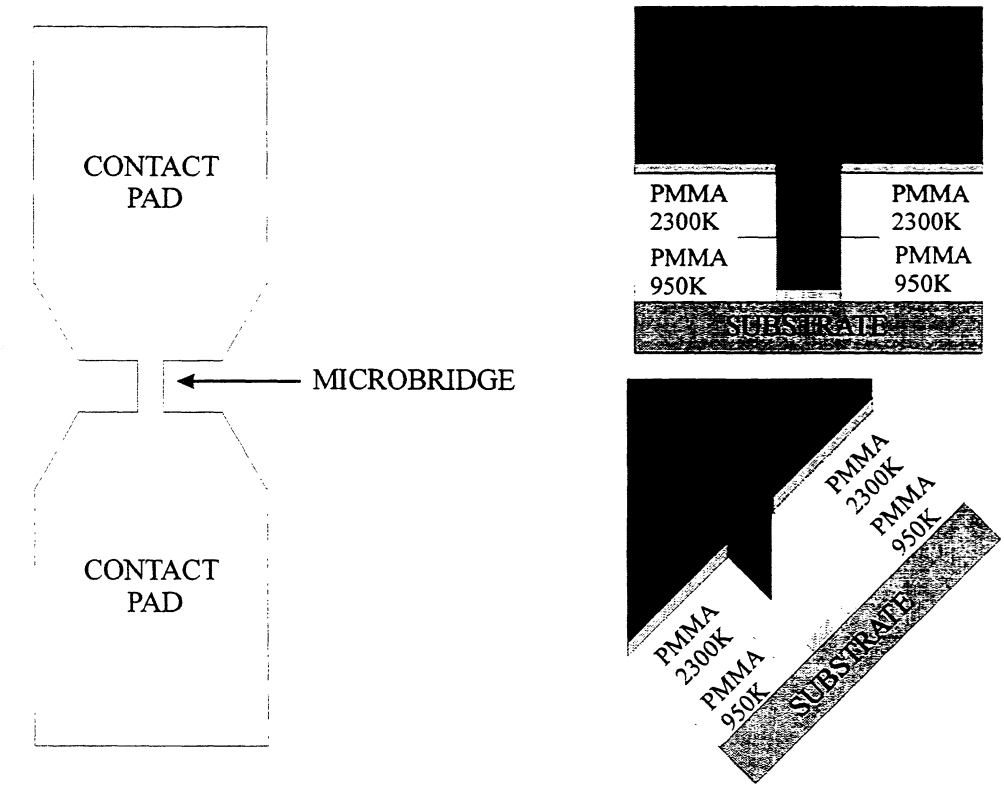

Figure 1. *Schematic drawing of microbridge and its cross section. The microbridge materal is deposited straight on and the pads at a 45 degree angle.*

FABRICATION PROCESS

The devices were fabricated on 3 inch silicon wafers with a 20 nm thermally grown silicon oxide layer. The microbridge and contact pad patterns were defined by electron beam lithography on a double layer PMMA structure. Since the bottom layer (140 nm thick 950K PMMA) is more sensitive than the top (120nm 2300K PMMA) an undercut profile is achieved upon developing in a MIBK:IPA 1:3 solution for 90 seconds. The microbridge width varied from 80nm to 140 nm. Metal depositions are performed in an electron beam evaporator with a base pressure of $3x10^{-6}$ Pa equipped with a tilt stage that allows evaporations at two angles. The microbridge material (11 nm Al) is evaporated with the substrate perpendicular to the material flux. The contact pad material (63nm Al/28nm Ti/28nm Au) is evaporated at a 45 degree angle. This ensures that the contact pad material hits the PMMA vertical wall in the microbridge region as depicted in Figure 1. Lift off in acetone is performed next. Note that this process results in a 0.25μm inconsequential misalignment between the contact pads and the microbridge.
The twin slot antennas and RF filter circuits are defined next using a process developed for Nb HEB devices[6]. The layer composition is 500nm Polyimide/40nm Nb/130 nm PMMA9500K/ 120nm PMMA 2300K. Electron beam lithography followed by chromium

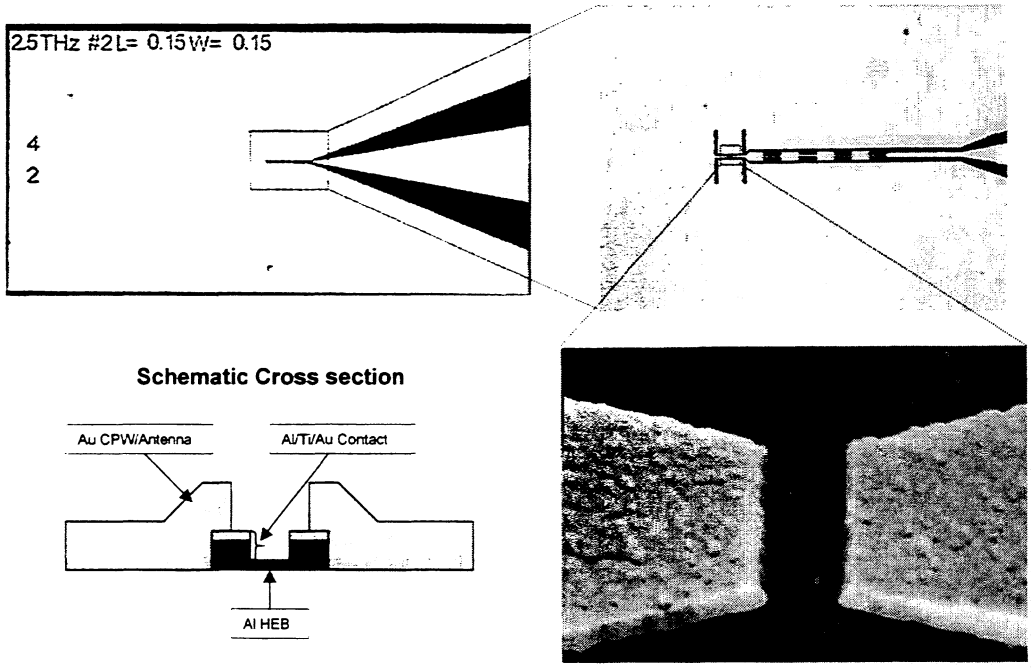

Figure 2. *Pictures of finished Al based hot electron bolometer and schematic representation of layer structure.*

deposition and lift off in acetone is used to define an etch mask for the high resolution portion of the twin slot antennas and RF filter circuit. A matching photoresist mask for the low resolution portion is defined by standard photolithography using AZ5214 photo-resist. With chromium and photoresist as a composite mask, the Nb in exposed areas is etched with CF4 +10%O_2 and the polyimide with pure 0_2. This is followed by deposition of 2.5 nm Ti and 300 nm Au. The last step is lift-off in methylene Chloride. Figure 2 shows a finished device and its layer composition.

ELECTRICAL CHARACTERIZATION

Resistance versus temperature and I-V characteristics of a number of devices were measured. The table shows a summary of resistance measurements at room temperature and at 2K. The actual dimensions were measured from SEM micrographs. The difference between design and actual dimensions is due to an over-compensation for the over-sizing inherent to the electron beam lithography process and will be corrected for the next iteration. The uncertainty in each dimension measurement is 10% yielding a 20% uncertainty in the R values. The average value is roughly 51 Ω, which would provide a good match for the IF amplifier for a microbridge containing one or two squares. This should yield a diffusion constant D□10 cm^2 and is well within the desired range of the design parameters.[7]

Device	Antenna	Design dim.		Actual dim.		R_{300K} (Ω)	R_{2K} (Ω)	R_{2K} (Ω)
		L(μm)	W(μm)	L(μm)	W(μm)			
1	1.9THz	0.3	0.15	0.35	0.14	128	90	36±7
2	1.9Thz	0.2	0.1	0.25	0.08	149	108	35±7
3	1.9THz	0.15	0.15	0.25	0.14	159	120	67±14
4	4.25THz	0.2	0.1	0.27	0.08	175	133	40±8
5	1.9THz	0.2	0.1	0.27	0.08	251	190	56±11
6	2.5THz	0.1	0.1	0.18	0.08	204	162	72±14
7	1.9THz	0.3	0.15	0.35	0.14	195	135	54±10

The resistance of the devices was measured as a function of temperature down to 0.3K. Figure 3 shows the results for three devices with different lengths. The curves were normalized to the resistance at 2K of the shortest sample. The curves feature a broad transition starting at 1.8K(which would be roughly the transition temperature of the microbridge film) and a second sharper transition at 0.6K, which is the transition temperature of the contact pads. Since the second transition features a large drop in resistance, it can not be due to the resistance of the contact pads. It must be that a large portion of the link undergoes a superconducting transition at that temperature. The contact pads while in the normal state are driving a significant portion of the microbridge normal through the proximity effect. As the temperature is lowered, gradually larger

portions of the microbridge become superconducting, lowering the overall resistance. This explains the broad transition. Note that the shortest sample features the largest fractional drop in resistance at 0.6K and the longest shows the smallest effect. This is consistent with our explanation and provides a rough measurement of the normal metal coherence length ξ_N. For the sake of simplicity, we assume that the center of the microbridge is superconducting at 0.6K, and divide it in two halves. The coherence length would be roughly equal to the normal length of a half bridge, if we assume that the proximity effect acts up to a distance roughly equal to the coherence length. For the 180 nm bridge this would be roughly 90 nm, since the resistance drop at 0.6K is about equal to the total normal resistance, i.e. ξ_N =90nm. For the 270 nm it would be $\xi_N \approx \frac{55\Omega}{90\Omega}\frac{270nm}{2} = 83nm$. For the 350 nm bridge it would be $\xi_N \approx \frac{40\Omega}{90\Omega}\frac{350nm}{2} = 78nm$. Using the average value, we would have ξ_N= 84 nm,

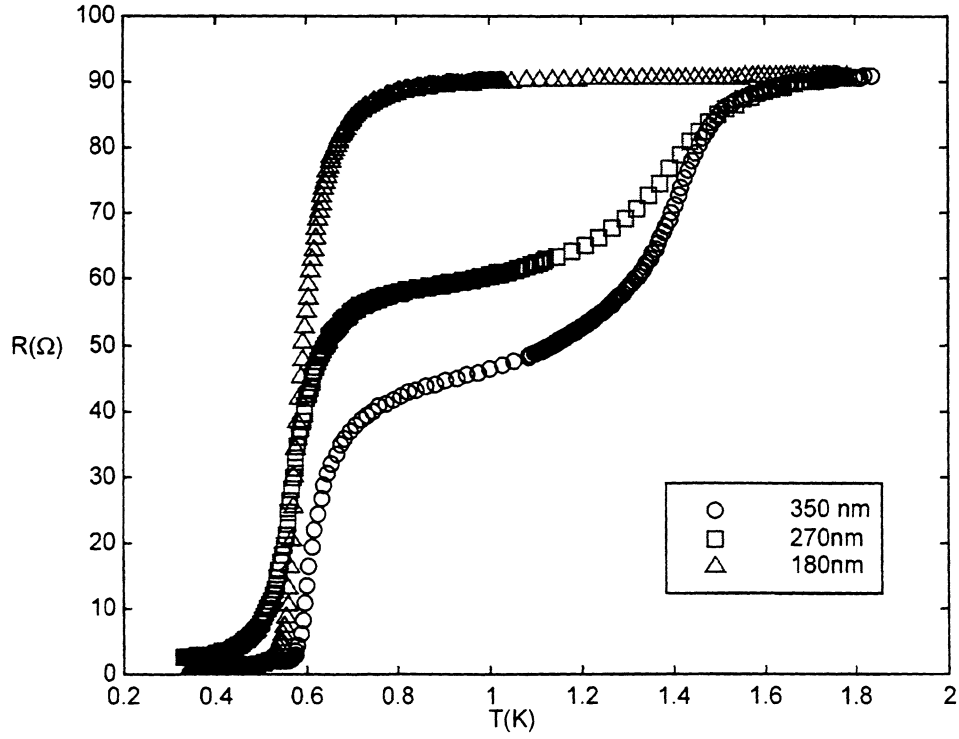

Figure 3. *Resistance vs temperature of selected devices. All values were normalized to the values of the shortest microbridge at 2K.*

yielding a diffusion constant $D = \frac{k_B T}{\hbar} \xi_N^2 \cong 6\text{cm}^2/\text{s}$, which is consistent with the value of D estimated from the resistance. Attempts to model the data using results for the proximity effect in bulk materials provide qualitative but not quantitative agreement, which is not surprising since all the dimensions in this case are smaller than or comparable to the normal metal coherence length. We have tried to fit our data using the charge imbalance and Andreev reflection model developed for Nb devices[8], which could be viewed as a microscopic picture of the proximity effect. Again, the agreement was qualitative, at best.

Even though the resistance vs temperature characteristics of the bolometers has such broad features that at first glance would be undesirable, in actual operation the mixers would be kept below the transition temperature of the pads. At those temperatures the pads are superconducting and the signal would "see" just the superconducting microbridge. This is corroborated by IV characteristics measured at 0.3K. One such IV characteristic is shown in figure 4.

To check that the transition temperature of the pads was at 0.6K we fabricated macroscopic samples with the same layer composition and measured its transition temperature obtaining a value of 0.67 K. The agreement is reasonable, since in additional

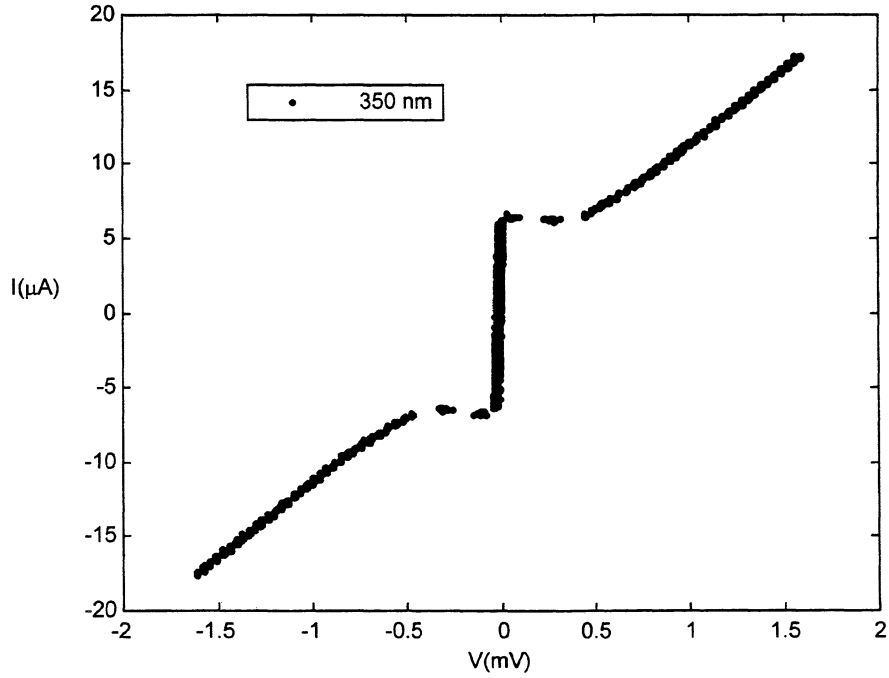

Figure 4. *I-V characteristic of 350nm long Al based HEB*

to the precision of the layer thickness measurement (10%) there is an additional uncertainty due to the evaporation at an angle. Not only the angle has an uncertainty but also the thickness should vary across the wafer, since the distance to the evaporation source varies. We fabricated and measured the transition temperatures of samples with thicknesses of Al ranging from 100 to 630 Å for fixed thicknesses of Ti (280Å) and Au (280Å). Figure 5 shows the results, indicating that we can tailor the Tc of this trilayer from 350 mK up making it very useful for applications such as transition edge sensors. We have also fabricated one sample without an Au layer to demonstrate that the Au layer has an influence on the Tc and is not just acting as a normal metal layer on top of the Al/Ti proximity layer. This confirmation is important for applications in which this normal layer would be undesirable. We have also heated some of the samples up to 170C for 10 minutes and measured their characteristics afterwards with no discernible changes. This makes the Al/TiAg superior to Al/Ag bilayers, which are extremely sensitive to heating, making them unsuitable for applications in which processing is necessary after the deposition of the film.

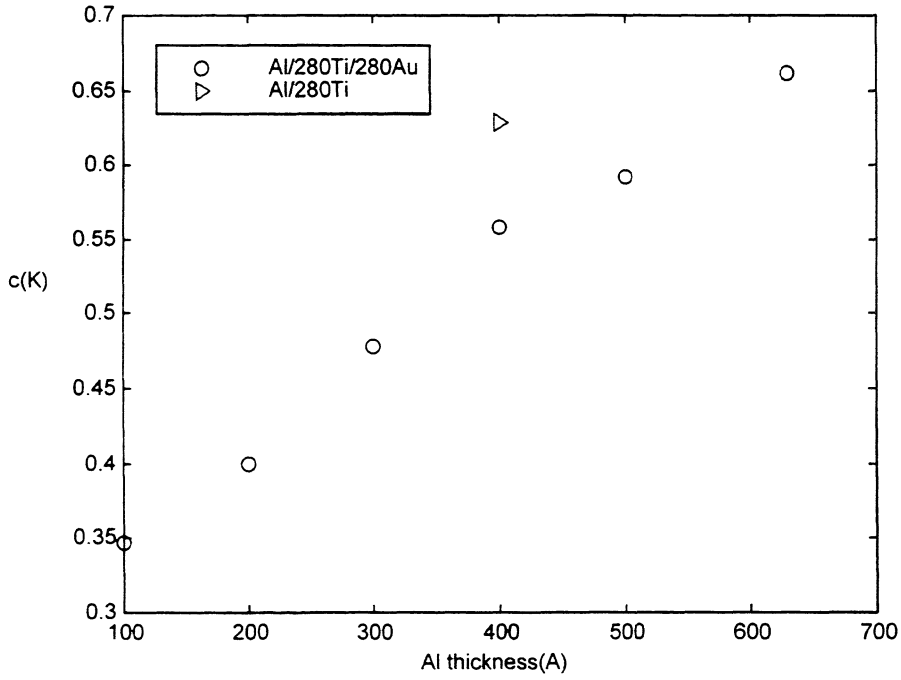

Figure 5. *Transition temperatures of Al/Ti/Au trilayers as a function of Al thickness.*

CONCLUSION

We have fabricated aluminum based hot electron bolometers to be used as mixers at 1.9 and 2.5THz. DC electrical characterization shows that the devices are within the design parameters. A novel trilayer Al/Ti/Au was developed to provide contact between the microbridge and the antenna structures. This trilayer is superior to Al/Ag bilayers due to its insensitivity to heating.

This research is supported by the Center for Space Microelectronic Technology, Jet Propulsion Laboratory under contract to the National Aeronautics and Space Administration, Office of Space Science.

---

[1] E. Gerecht, C.F. Musante, H. Jian, K.S. Yngvesson, J. Dickinson, J. Waldman, G.N. Gol'tsman, P.A. Yagoubov, B.M. Voronov, E.M. Gershenzon, , Proceedings of the Ninth International Symposium on Space Terahertz Technology, pp 105-114 (1998) and references therein.

[2] Y.P. Gousev, H.K. Olson, G.N. Gol'tsman, B.M. Voronov, E.M. Gershenzon, Proceedings of the Ninth International Symposium on Space Terahertz Technology, pp 121-130 (1998), and references therein.

[3] P.J. Burke, R.J. Schoelkopf, I. Siddiqi, D.E. Prober, A. Skalare, B.S. Karasik, M.C. Gaidis, W.R. McGrath, B.Bumble, H.G. LeDuc, Proceedings of the Ninth International Symposium on Space Terahertz Technology, pp 17-34 (1998), and references therein.

[4] A.Skalare, W.R. McGrath, B. Bumble, H.G. LeDuc, Proceedings of the Ninth International Symposium on Space Terahertz Technology, pp 115-120 (1998), and references therein.

[5] B.S. Karasik and W.R. McGrath, Proceedings of the Ninth International Symposium on Space Terahertz Technology, pp 73-80 (1998).

[6] B.Bumble and H.G. LeDuc, IEEE Transaction on Applied Superconductivity 7, 105 (1997)

[7] Estimate of D from figure 4 in reference 5.

[8] D.W. Floet , J.J. Baselmans, J.R. Gao T.M. Klapwijk, Proceedings of the Ninth International Symposium on Space Terahertz Technology, pp 63-72 (1998).

Tenth International Symposium on Space Terahertz Technology, Charlottesville, March 1999

SuperMix: A Flexible Software Library for High-Frequency Circuit Simulation, Including SIS Mixers and Superconducting Elements

John Ward, Frank Rice, Goutam Chattopadhyay, and Jonas Zmuidzinas

California Institute of Technology, 320-47, Pasadena, CA 91125, USA.

Abstract

"SuperMix" is a software library written to aid in the calculation and optimization of the signal and noise performance of high-frequency circuits, especially those including superconductors and superconducting tunnel junctions. Using this library, C++ programs can be written to simulate circuits of arbitrary size, complexity, and topology. The library includes an optimizer which can minimize an arbitrary error function by varying chosen circuit parameters. Using SuperMix, it is now possible to directly optimize an SIS receiver design to minimize the average noise temperature across the desired RF frequency band, including a full harmonic balance analysis at every frequency point together with a full analysis of the IF amplifier circuit and its noise contribution.

I. Introduction

A. Motivation: designing and simulating SIS receivers

Although there are many excellent software packages available to aid in the design of microwave circuits, none provide the specialized elements needed for the design of complete superconducting tunnel junction (SIS) receivers. For instance, thin film microstrip lines, which are widely used in SIS mixers for impedance matching circuits, have characteristics which depend on the surface impedance of the normal or superconducting metal films. Surface impedance calculations usually involve nontrivial numerical computations, such as numerical integration or the solution of integral equations [1], [2], [3], and are not available in commercial microwave software packages. Furthermore, the calculation of the signal and noise properties of SIS mixers requires the use of Tucker's theory [4] combined with a nonlinear harmonic–balance calculation [5], [6] of the local oscillator waveform. Again, the required calculations are numerically intensive and are not available in commercial packages.

It is clear that a complete simulation of an SIS mixer is a substantial computational task. Because of this, SIS mixer design is usually performed using simplifying approximations. For instance, the RF circuit is usually designed and optimized by treating the problem as an impedance matching exercise. Once a circuit is designed in this way, the embedding admittances it presents to the SIS junction can be calculated, and these can be used in a Tucker theory calculation to determine the conversion loss and noise temperature of the mixer. The results of such a calculation could then be imported into a standard microwave program to explore the effect of the HEMT IF amplifier and its matching circuit. This was the approach followed by Padin et al. [7] for the design of an integrated HEMT IF amplifier for an SIS mixer.

However, to our knowledge, no one has ever designed an SIS receiver by directly calculating the noise temperature across some desired RF band, including the harmonic effects and the IF amplifier contribution, and optimizing this total receiver noise temperature as a function of the circuit parameters. Even though this sounds like the most obvious and straightforward approach to the design, the software to do this has simply been unavailable until now. Furthermore, with the exception of a few special cases involving two junction circuits [8], [9], parallel arrays [10], and distributed junctions [11], most of the Tucker-theory programs that have been written for SIS design assume that only a single SIS junction will be used. However, now that junction fabrication processes are reliable and reproducible, there is a clear trend toward more complex mixer designs incorporating multiple junctions.

B. Alternative approaches

There are several possible solutions to our problem. Some commercial circuit simulators allow user-defined elements to be written using an interpreted "scripting" language. However, we felt that this approach would not provide the necessary level of computational performance needed for simulating and optimizing superconducting mixers. Indeed, the Tucker theory SIS mixer programs we are aware of are written in standard compiled programming languages such as FORTRAN. Alternatively, we could have attempted to work with a software vendor to have our routines for SIS mixer simulation incorporated directly into a commercial microwave package. However, our judgement was that few vendors would be interested given the very limited market. Furthermore, given that we are continually developing new materials and mixer designs, we felt that it would be extremely important to be able to rapidly add new elements and models to the code. Finally, we wanted to have software that would run on a large variety of platforms, and not be plagued by licensing restrictions. For these reasons we decided to develop our own stand-alone code.

C. SuperMix: a C++ class library

We have developed a C++ library, which we call "SuperMix", to provide a flexible tool with which to design and optimize receiver circuits, and microwave circuits in general.

SuperMix calculates circuits in the familiar wave representation, in which the behavior of a linear circuit is specified by a scattering matrix, a noise wave correlation matrix, and an outgoing source wave amplitude vector. The source wave vector represents the effects of generators inside the circuit, such as a local oscillator. Easy-to-use functions can convert the wave representation to other quantities, such as impedance or admittance matrices, gain, or noise temperature.

The C++ programming language [12] was chosen for this project to provide flexibility, ease of use, and a means to design the library with a modular approach. For this project, complex numbers, vectors, and matrices are used extensively. Although these data types are not included as part of standard C++, the language can be extended to include them in a natural and powerful way. For instance, the standard arithmetic

Basic Elements	*Transmission Lines*	*Transistors*	*Miscellaneous Elements*
Resistor	Superconducting Film	Transconductance	Mixer
Capacitor	Normal Metal Film	FET	SIS junction
Inductor	Layered Film	Fujitsu FHR02X	Transformer
Attenuator	Dielectric	Fujitsu FHX13X	180° Hybrid
Terminator	Microstrip	Kukje HEMT	90° Hybrid
	Transmission Line		Circulator
	Radial Stub		Voltage Source
	Time Delay		Current Sink
			Generator

TABLE I
CIRCUIT ELEMENTS CURRENTLY PROVIDED BY THE LIBRARY.

operations with complex numbers can be defined, as can the operation of multiplying a vector by a matrix.

As an object-oriented language, C++ provides a natural way to write modular programs. The SuperMix library was written from the ground up to be highly modular, flexible, and expandable. Circuits and circuit elements are implemented as C++ class objects. The modular approach used allows new elements to be added to the library by writing only a few lines of code (to calculate the scattering and noise matrices) without having to deal with details about how the overall library works. The modular design of the optimizer provides a straightforward means to add new optimization algorithms if needed. Almost every part of the library benefits from the flexibility provided by the C++ programming language.

Each circuit element in SuperMix inherits the properties common to all devices. This way, each element added to the library automatically includes a standard interface, for instance, a function to return scattering parameters of the circuit element. Lossy elements which generate noise can be assigned arbitrary temperatures. A list of circuit elements currently available in the library is given in table I.

II. The Wave Representation

Internally, circuits are represented using a "wave" representation based on the scattering matrix. The incoming and outgoing wave amplitudes at some port i of a linear circuit are defined in terms of the voltage V_i across the port terminals and the current I_i flowing *into* the positive terminal by the expressions

$$a_i = \frac{1}{2\sqrt{Z_0}}(V_i + Z_0 I_i) \quad \text{and} \quad b_i = \frac{1}{2\sqrt{Z_0}}(V_i - Z_0 I_i)$$

where Z_0 is some standard normalizing impedance. These definitions are motivated by transmission line theory. Note that the normalization is chosen such that power can be calculated simply by squaring the wave amplitudes. For instance, the incoming

power at port i is $P_{incident} = |a_i|^2$ and the reflected power is $P_{reflected} = |b_i|^2$. Extensive discussions of the scattering matrix and its use in circuit calculations can be found in the references [13], [14], [15].

SuperMix uses three quantities to represent a circuit: the scattering matrix $\mathcal{S}$, the noise wave correlation matrix $\mathcal{C}_\mathcal{S}$, and the wave source vector $\mathbf{b}_s$. The definition of these quantities comes from the following expression, in which the outgoing wave amplitudes $\mathbf{b}$ are considered to be dependent upon the incoming wave amplitudes $\mathbf{a}$:

$$\mathbf{b} = \mathcal{S}\mathbf{a} + \delta\mathbf{b} + \mathbf{b}_s$$

The source vector $\mathbf{b}_s$ represents the effect of *deterministic* voltage or current generators inside the circuit which cause outgoing waves with various amplitudes and phases to emanate from the circuit's ports even in the case that the incoming wave amplitudes $\mathbf{a}$ all vanish. In contrast, $\delta\mathbf{b}$ represents outgoing *noise* waves, which are the result of various noise current or noise voltage generators inside the circuit. These noise waves are characterized by the noise wave correlation matrix, whose elements are the expectation values

$$(C_S)_{ij} = \left\langle \delta b_i \, \delta b_j^* \right\rangle$$

Finally, the product $\mathcal{S}\mathbf{a}$ represents the outgoing waves that are generated when the incoming deterministic waves $\mathbf{a}$ are scattered by the N-port circuit, which has a scattering matrix $\mathcal{S}$.

III. Noise in Passive Elements

The noise correlation matrices of *passive* elements or passive circuits at a uniform temperature T are computed from their scattering matrices:

$$\mathcal{C}_\mathcal{S} = \frac{h\nu}{2k_B} \coth(h\nu/2k_BT)\,(\mathcal{I} - \mathcal{S}\mathcal{S}^\dagger)$$

where $\mathcal{S}$ is the scattering matrix, $\mathcal{I}$ is the identity matrix, and $\mathcal{C}_\mathcal{S}$ is the noise correlation matrix. These equations are derived and discussed in [16], [17], [13].

The Callen–Welton formula [18] used for the noise spectral density can be considered to be the sum of a Planck term and a zero–point quantum fluctuation term,

$$\frac{h\nu}{2k_B} \coth(h\nu/2k_BT) = \frac{h\nu/k_B}{\exp(h\nu/k_BT) - 1} + \frac{h\nu}{2k_B}$$

and reduces to T in the Rayleigh–Jeans limit, $h\nu << k_BT$. Because the zero–point term is included, the use of the Callen-Welton spectral density for passive elements ensures that the correct value of the IF output noise is calculated for a mixer whose RF input is terminated with a load [19], [20]. Thus, SuperMix automatically includes both quantum noise as well as the thermal noise produced by lossy elements (e.g. warm optics). Note that commercial microwave programs usually use the Rayleigh–Jeans approximation for thermal noise, which is inappropriate for cryogenic receiver

systems at millimeter wavelengths which have components at temperatures below $h\nu/k_B$.

The passive noise computations are carried out by a single standard function. Thus, when adding new passive elements to the library, it is usually sufficient to program only the scattering matrix calculation, and then use the standard library function to calculate the noise correlation matrix.

IV. Connecting Circuits

The SuperMix library provides an object of type `circuit` to create composite circuits. A user can assemble a circuit from the basic elements (resistors, capacitors, etc.) by calling the `connect` "member" function belonging to the `circuit` object. The `connect` function allows the user to connect ports between circuits or basic elements. For instance, the output port of an isolator might be connected to the input port of an amplifier. The circuits being connected can have arbitrary numbers of ports; hence the concept implemented by the `connect` function is much more general than a simple cascade of two-ports. Furthermore, the `connect` function allows both *interconnections*, in which the two subcircuits are distinct, as well as *intraconnections*, in which two different ports of the same circuit are being connected. Series and parallel "tee" components are available to allow series or parallel connections.

Since all elements including the composite circuits share the same "software interface" (in C++ parlance, they are derived from a single generic device class), composite circuits themselves can be used in other composite circuits. Thus, a hierarchical design is possible: large, complicated circuits can be built up from smaller, more manageable pieces. This capability is a direct benefit of the modular design described in the Introduction.

A composite circuit calculates itself by making a single connection between the ports of its elements or subcircuits at a time. The $\mathcal{S}$ and $\mathcal{C}_\mathcal{S}$ matrices for the two subcircuits are combined using equations developed by Wedge and Rutledge [13] using signal flow graphs. When a composite circuit is asked to calculate itself, it splits itself into two subcircuits and asks each for its $\mathcal{S}$ and $\mathcal{C}_\mathcal{S}$ matrices and source vector $\mathbf{b_s}$. Each of these subcircuits splits itself in two. The process continues until all subcircuits are broken down to the original basic elements. This process creates a binary tree. The desired circuit is the base, and the tips of the branches are the components of the circuit. The intermediate subcircuits form the branches. This algorithm is fast because the tree only needs to be built a single time yet can be used for an unlimited number of calculations, such as for different frequency points or in the inner loop of the optimizer.

V. Transmission Lines

The SuperMix C++ library includes a number of classes which can be used to calculate the properties of normal and superconducting transmission lines such as the characteristic impedance and propagation constant. The transmission lines can be used as elements in circuits such as SIS mixers. At present, microstrip is the only physical type of transmission line available in SuperMix, although adding new types

is straightforward. In particular, the user only needs to calculate the characteristic impedance and the propagation constant; the conversion of these quantities into the scattering and noise correlation matrices is handled by library routines.

The characteristics of thin-film transmission lines (such as microstrip) often depend heavily on the surface impedance of the metal conducting films used. At present, SuperMix can calculate the surface impedance for normal metals and superconductors [1] in the case of a *local* conductivity $\sigma(\omega)$, defined by Ohm's law $\vec{J}(\vec{r},\omega) = \sigma(\omega)\,\vec{E}(\vec{r},\omega)$. Addition of the nonlocal *anomalous* skin effect in normal metals is planned for a future release. Multilayered metal films can also be created. The simplifying assumption is that the conductivity of any given layer is not influenced by the properties of the surrounding layers. This assumption may not be valid in some circumstances – for instance, in cases where the superconducting proximity effect is important.

Transmission lines such as microstrips often use dielectric films or substrates, and the complex dielectric constant ϵ of the material must be specified. Dielectrics can be defined in SuperMix by specifying the real part of ϵ and the loss tangent, $\mathrm{Im}[\epsilon]/\mathrm{Re}[\epsilon]$. If necessary, a table of values specifying a frequency-dependent $\epsilon(\nu)$ can be read from a data file and automatically interpolated. Actually this can be done for any circuit parameter, and the interpolation can be done with respect to any other parameter (e.g. temperature), not just frequency. Metal films, layered films, and dielectrics form the building-blocks for transmission lines. After the dielectrics and conductors have been specified, transmission lines such as microstrip can be assembled from them.

VI. Mixers

Mixers are created using a combination of linear `circuits` and devices derived from a generic nonlinear device class named `junction`. The `junction` class simply provides a standard "software interface" for devices that can calculate both their large and small signal responses. At the moment, the only nonlinear devices available within SuperMix are superconducting tunnel (SIS) junctions. The SIS junction reads its current-voltage (IV) curve from a data file, which can be either experimentally measured or mathematically generated. However, other nonlinear devices (such as Schottky diodes) could be added by writing the code that simulates the device behavior, and interfacing this code to SuperMix using the `junction` class. This would allow a complicated multiple diode mixer circuit to be simulated, including a full harmonic balance solution of the LO waveform. In principle, one could even simulate a circuit containing a mixture of superconducting and semiconducting nonlinear devices.

The `mixer` device is assembled from any number of `junctions`, a radio-frequency (RF) linear circuit, and an intermediate-frequency (IF) linear circuit. These circuits can be arbitrarily complicated and can contain arbitrary numbers of ports. The local oscillator (LO) can be injected anywhere in the RF linear circuit. The `mixer` will then calculate its operating state by performing a harmonic balance; the number of harmonics used in the balance is arbitrary as well. Once the operating state is determined, the user can ask the `mixer` object to perform a small signal analysis [6]. Once the calculation is complete, which typically takes a few tens of milliseconds per frequency point, the user may examine standard quantities such as noise temperature

or conversion gain, or look into details such as the impedance, admittance, or reflection coefficient looking into each port at each sideband of each harmonic of the LO, as well as the transmission via mixing from one harmonic of the LO to another, including the IF. In other words, the entire multifrequency scattering and noise matrices are calculated and are available to the user.

VII. The Optimizer

The optimizer was designed to be a very general tool that can minimize general error functions by varying nearly any circuit parameter, real or complex. At present, SuperMix allows the standard quantities of interest such as gain, noise temperature, input or output match to be readily included in the definition of the error function. These quantities are usually calculated while sweeping the frequency over one or more bands. For instance, the design of a bandpass filter requires that the transmission across the passband be maximized while the transmission in stopbands be minimized. SuperMix supports this capability; furthermore, any parameter can be swept, not just frequency. Even multi-dimensional sweeps are allowed.

The modular design allows easy addition of new types of error function terms. In addition, the interface between the error function and the optimization algorithm is very simple and generic, and so it is easy to add new minimization algorithms. Although SuperMix allows for the possibility of multiple minimization algorithms, the only algorithm currently implemented is Powell's method. This routine is both robust and fast. In practice, it has been used to optimize 10 parameters of a 50 element linear amplifier across an octave bandwidth. On a 333 MHz Sun Ultra 10, this entire optimization and simulation runs in less than 10 seconds. One downside of Powell's method is that it can converge upon local minima, so the user must choose reasonable initial values for the parameters being optimized. This is a generic feature of aggressive optimization alogrithms that make use of gradient information. Other approaches, particularly the stochastic algorithms, are much slower but are better at finding global minima, and could easily be added to SuperMix.

VIII. Using the SuperMix Library

A circuit is simulated by writing a C++ program that uses the SuperMix library. Devices in the library are represented as C++ class objects, which can be used simply by declaring a variable of the appropriate type. For example, declaring a variable of type `resistor` will automatically provide all functionality needed for the simulation of a resistor, including parameters for resistance and physical temperature, and functions to return the scattering matrix, noise correlation matrix, noise temperature, etc. of this element. All elements are derived from a single generic device class, guaranteeing a uniform standard interface for all devices and allowing the user to add elements to the library with a minimum of effort.

A. *Simulation of a low-noise amplifier*

The code in figure 6 is a complete program to optimize and simulate the single-stage low-noise HEMT amplifier drawn in figure 1. This program demonstrates the

key features of the linear circuit library, including creating circuit elements, connecting them, and running the optimizer. Results are plotted in figure 2.

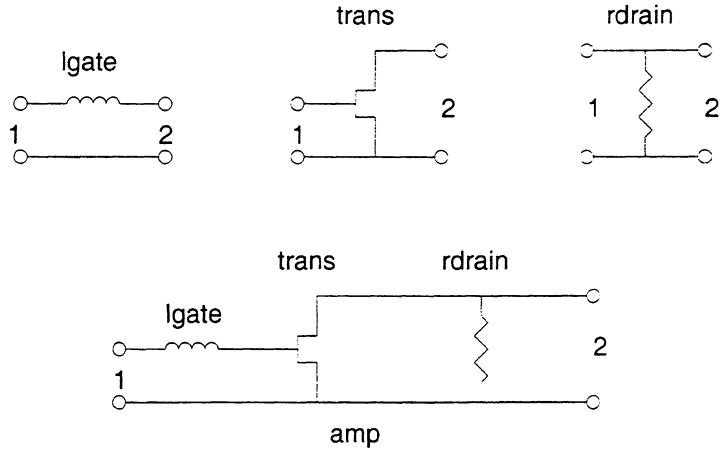

Fig. 1. Block diagram of single stage LNA.

In this example, there are only three subcircuits being connected together to produce the composite circuit `amp`: the gate inductor `lgate`, the Fujitsu FHX13X transistor `trans`, and the drain resistor `rdrain`. (The SuperMix library actually constructs a composite equivalent circuit to calculate the transistor according to the Pospieszalski model [21].) Each of the subcircuits is a two-port: the ports are labeled by integers as shown in figure 1. The C++ statement `amp.connect(lgate, 2, trans, 1)` connects port 2 of the inductor to port 1 (the gate) of the transistor. Similarly, `amp.connect(trans, 2, rdrain, 1)` connects the drain of the transistor to the resistor. The statement `amp.add_port(lgate, 1)` simply specifies that port 1 of the inductor will be used as port 1 (input) of the overall amplifier circuit. Finally, `amp.add_port(rdrain, 2)` specifies the output port of the amplifier.

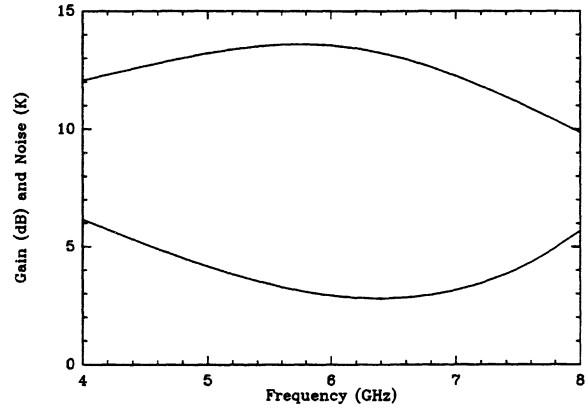

Fig. 2. Gain (top curve) and noise temperature (bottom curve) of a single stage LNA.

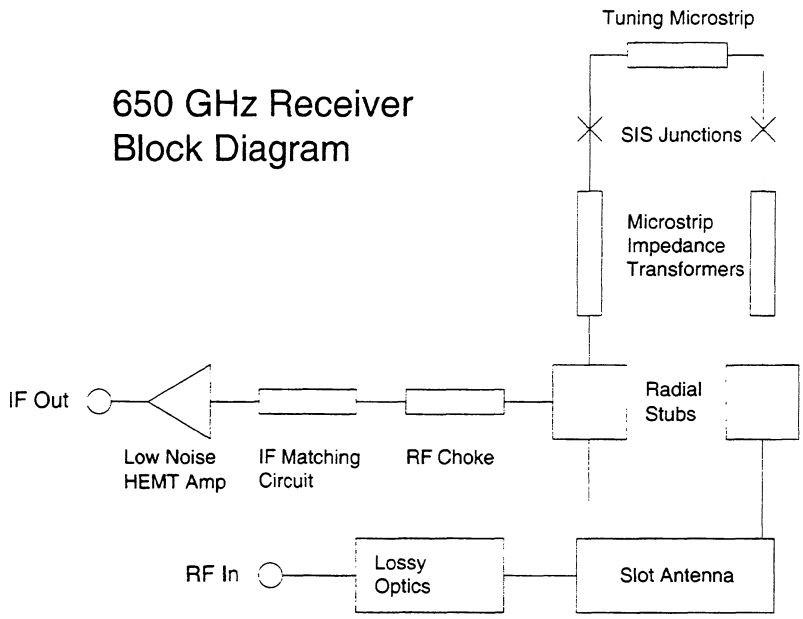

Fig. 3. Block diagram of a 650 GHz quasi-optical twin-slot double-junction SIS receiver.

B. Simulation of a section of microstrip

The code in figure 7 is a complete program to simulate a segment of superconducting microstrip. It demonstrates the ease with which a circuit can be constructed and the high level of readability of a C++ circuit file.

C. Simulation of a 650 GHz receiver

A 650 GHz quasi-optical twin-slot double-junction SIS receiver (figure 3) was simulated using the SuperMix library. The frequency-dependent impedance of the slot antenna and a measured unpumped current-voltage (IV) curve were read from data files. The losses of optical components such as the LO injection beamsplitter, the cryostat vacuum window, etc. were simulated using attenuators whose temperatures were set to the physical temperatures of the optical components. In this way, the thermal noise produced by these components was included in the simulation. In addition, a complete 3 stage HEMT amplifier was included at the IF output as part of the simulation. The complete simulation can calculate about 35 frequency points per second on a 333 MHz Sun workstation, including a full simultaneous harmonic balance calculation for the two SIS junctions at every frequency point.

The simulated pumped IV curve and IF power curves (figure 4) agree reasonably well with measured data. The measured and simulated receiver passband and noise temperatures (figure 5) are also similar. In this example, we have made no attempt to adjust the parameters of the simulation to make it agree with the measured data. However, in the future these types of simulations could be used to extract information about the performance of the receiver (e.g. the noise contribution due to optics

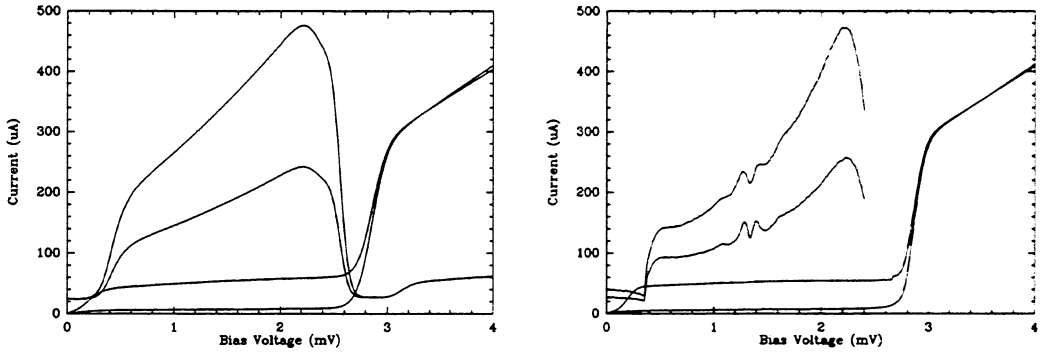

Fig. 4. Simulated pumped IV curve with 300 K and 77 K IF power curves at 638 GHz (left) compared to the measured values (right). The HEMT amplifier and IF matching circuit that were simulated are not the same as in the actual receiver: hence, the shapes of the IF power curves are not expected to be the same in detail.

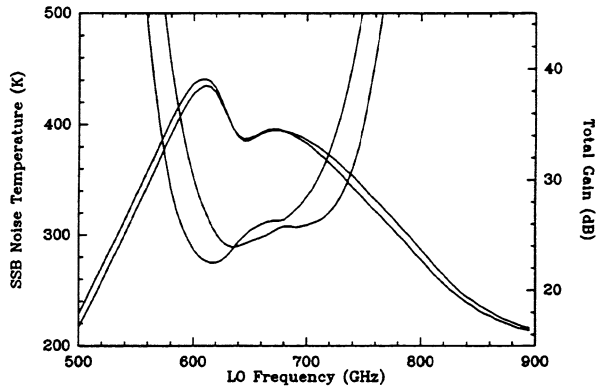

Fig. 5. Simulated passband and noise temperature of a 650 GHz receiver. The double curves are for lower and upper sidebands; the IF frequency is 6 GHz.

losses, the behavior of the tuning circuit, etc.) and to provide insight for possible optimizations.

IX. Compatibility and Availability

The software was written in standard C++ and should compile on any UNIX platform using an ANSI C++ compiler that supports the Standard Template Library (STL.) The package has been tested using the freely available GNU g++ compiler on the SPARC Solaris 2.6 and Intel Linux platforms.

The library, which is currently composed of over 28,000 lines of source code, is already nearly fully functional, and a user's manual is being prepared. Our intention is to provide this software, including the source code, free of charge to any interested users. We hope that other users will find SuperMix useful and will contribute to its

```
#include "supermix.h"

int main(void) {

  // Set the global temperature.
  device::T = 4.2 * Kelvin;

  // Declare the components we will use for the circuit.
  fhx13x trans;      // Fujitsu HEMT transistor
  inductor lgate;    // Gate tuning inductor
  resistor rdrain;   // Drain bias line

  // The inductor is series, resistor parallel.
  lgate.series();
  rdrain.parallel();

  // Construct the circuit.
  circuit amp;
  amp.add_port(lgate, 1);            // Put the gate inductor at the input.
  amp.connect(lgate, 2, trans, 1);   // Connect the inductor and transistor.
  amp.connect(trans, 2, rdrain, 1);  // Connect the transistor and resistor.
  amp.add_port(rdrain, 2);           // Make the drain resistor the output.

  // Define the optimization band.
  sweeper band1;
  band1.sweep(device::f, 4.*GHz, 8.*GHz, 0.5*GHz);

  // Declare an error function.
  err_func ef;

  // Define which parameters are optimized.
  lgate.L = ef.vary(1.*nHenry, 3.0*nHenry, 10.*nHenry);
  rdrain.R = ef.vary(30.*Ohm, 50.*Ohm, 100.*Ohm);

  // Define the error functions.
  gain_dB gain(12, 1, 2, err_term_mode::MATCH);  // Optimize for flat gain.
  ef.add_term(1.0, band1, gain, amp);
  input_tn tn(0.0, 1, 2, err_term_mode::MATCH);  // Optimize for low noise.
  ef.add_term(2.0, band1, tn, amp);

  // Use the Powell algorithm for minimizing.
  powell pow1(ef);          // Minimize the error function we created above.
  pow1.POW_TOL = 0.00001;   // Define the tolerance for the convergence test.
  pow1.minimize();          // Run the optimizer.
  ef.get_parms().show();    // Print the optimized parameters.

  cout << "\n   Freq    S21(dB)   Tn(K)" << endl;

  // Print out gain and noise temperature in our optimization band.
  for(double freq = 4.0*GHz; freq <=8.0*GHz; freq += 0.2*GHz)
  {
    device::f = freq;
    sdata sd = amp.get_data();
    cout << freq/GHz            // Print the frequency in GHz.
         << "  "
         << sd.SdB(2,1)         // Print the gain in dB.
         << "  "
         << sd.tn(2,1)/Kelvin   // Print the noise temperature in Kelvin.
         << endl;
  }
}
```

Fig. 6. Simulation and optimization of a 1 stage LNA.

```
#include "supermix.h"

main()
{
  device::T = 4.2*Kelvin ;      // Default temperature
  device::Z0 = 50.*Ohm ;        // Normalization impedance

  // Define metal film
  super_film nb1;

  // Standard parameters for Niobium
  nb1.Vgap = 2.9*mVolt ;
  nb1.Tc = 9.2*Kelvin ;

  double cm = 1.e4 * Micron;
  nb1.rho_normal = 5.*Micro*Ohm*cm ;

  // Set thickness
  nb1.Thick = 2000.*Angstrom ;

  // Define dielectrics
  const_diel sio ;
  const_diel vacuum ;

  vacuum.eps = 1.0 ;
  vacuum.tand = 0.0 ;

  sio.eps = 5.6 ;   // dielectric constant
  sio.tand = 0. ;   // loss tangent

  // Now make a microstrip line
  microstrip ms1;

  ms1.top_strip(nb1) ;              // use Nb film for top strip
  ms1.ground_plane(nb1) ;           // same for ground plane
  ms1.superstrate(vacuum) ;         // nothing above
  ms1.substrate(sio) ;              // SiO insulator
  ms1.sub_thick = 2000.*Angstrom ;  // SiO thickness

  ms1.length = 100.0*Micron ;   // microstrip length
  ms1.width = 5.0*Micron ;      // microstrip width

  // Print out S21 for this microstrip from 100 to 1000 GHz, step by 10 GHz.
  for(double freq = 100. ; freq <= 1000.; freq += 10)
  {
    device::f = freq*GHz ;
    complex S21 = ms1.S(2,1) ;        // The S(2,1) function returns S21.
    cout << freq << "   "
      << zabs(S21) << "   "           // Print |S21|
      << arg(S21)/Degree << "   "     // and arg(S21)
      << endl ;
  }
}
```

Fig. 7. Simulation of superconducting microstrip in SuperMix.

development by adding new circuit elements, optimization algorithms, etc. However, we cannot yet make SuperMix available for public download until certain copyright issues have been resolved. After these issues are resolved and the documentation is completed, the package will be available at http://www.submm.caltech.edu/supermix.html.

ACKNOWLEDGEMENTS

This work was supported in part by NASA/JPL and its Center for Space Microelectronics Technology, by NASA grants NAG5-4890, NAGW-107, and NAG2-1068, by the NASA/USRA SOFIA instrument development program, and by the Caltech Submillimeter Observatory (NSF grant AST-9615025).

REFERENCES

[1] D. C. Mattis and J. Bardeen, "Theory of the anomalous skin effect in normal and superconducting metals," *Phys. Rev.*, vol. 111, pp. 412–417, 1958.

[2] R. Pöpel, "Surface impedance and reflectivity of superconductors," *J. Appl. Phys.*, vol. 66, pp. 5950–5957, 1989.

[3] M. Bin, *Low-Noise Terahertz Niobium SIS Mixers*. PhD thesis, California Institute of Technology, 1997.

[4] J. R. Tucker and M. J. Feldman, "Quantum detection at millimeter wavelengths," *Rev. Mod. Phys.*, vol. 57, no. 4, pp. 1055–1113, 1985.

[5] S. Withington and E. L. Kollberg, "Spectral-domain analysis of harmonic effects in superconducting quasiparticle mixers," *MTT*, vol. 37, pp. 231–238, January 1989.

[6] F. Rice, "Fast harmonic balance of SIS mixers with multiple junctions and superconducting circuits," *Proceedings, Tenth International Symposium on Space Terahertz Technology*, 1999.

[7] S. Padin, D. P. Woody, J. A. Stern, H. G. LeDuc, R. Blundell, C. Y. E. Tong, and M. W. Pospieszalski, "An integrated SIS mixer and HEMT IF amplifier," *MTT*, vol. 44, pp. 987–990, June 1996.

[8] J. Zmuidzinas, H. G. Leduc, J. A. Stern, and S. R. Cypher, "Two-junction tuning circuits for submillimeter SIS mixers," *IEEE Transactions on Microwave Theory Techniques*, vol. 42, pp. 698–706, April 1994.

[9] T. Noguchi, S. C. Shi, and J. Inatani, "Parallel connected twin SIS junctions for millimeter and submillimeter-wave mixers – analysis and experimental verification," *IEICE Trans. Elect.*, vol. E78C, pp. 481–489, May 1995.

[10] S. C. Shi and T. Noguchi, "Low-noise superconducting receivers for millimeter and submillimeter wavelengths," *IEICE Trans. Elect.*, vol. E81C, pp. 1584–1594, October 1998.

[11] C. Y. E. Tong, L. Chen, and R. Blundell, "Theory of distributed mixing and amplification in a superconducting quasi-particle nonlinear transmission line," *MTT*, vol. 45, pp. 1086–1092, July 1997.

[12] B. Stroustrup, *The C++ Programming Language*. Reading: Addison-Wesley, 1997.

[13] S. Wedge, *Computer Aided Design of Low Noise Microwave Circuits*. PhD thesis, California Institute of Technology, 1991.

[14] S. W. Wedge and D. B. Rutledge, "Wave techniques for noise modeling and measurement," *IEEE Trans. Microwave Theory Tech.*, vol. MTT-40, pp. 2004–2012, 1992.

[15] J. A. Dobrowolski and W. Ostrowski, *Computer-Aided Analysis, Modeling, and Design of Microwave Networks*. Boston: Artech House, 1996.

[16] H. Bosma, "On the theory of linear noisy systems," *Phillips Res. Repts. Suppl.*, vol. 10, 1967.

[17] S. W. Wedge and D. B. Rutledge, "Noise waves and passive linear multiports," *IEEE Microwave Guided Wave Lett.*, vol. MGL-1, pp. 117–119, 1991.

[18] H. B. Callen and T. A. Welton, "Irreversibility and generalized noise," *Phys. Rev.*, vol. 83, pp. 34–40, 1951.

[19] M. J. Wengler and D. P. Woody, "Quantum noise in heterodyne detection," *IEEE J. Quantum Electronics*, vol. QE-23, pp. 613–622, 1987.

[20] I. A. Devyatov, L. S. Kuzmin, K. K. Likharev, V. V. Migulin, and A. B. Zorin, "Quantum-statistical theory of microwave detection using superconducting tunnel junctions," *J. Appl. Phys.*, vol. 60, pp. 1808–1828, 1986.

[21] M. W. Pospieszalski, "Modeling of noise parameters of MESFETs and MODFETs and their frequency and temperature dependence," *MTT*, vol. 37, pp. 1340–1350, September 1989.

Fast Harmonic Balance of SIS Mixers with Multiple Junctions and Superconducting Circuits

Frank Rice, John Ward, Jonas Zmuidzinas, and Goutam Chattopadhyay

California Institute of Technology, 320-47, Pasadena, CA 91125, USA.

Abstract

We have extended the spectral domain harmonic balance method of Withington and Kollberg [1] to handle quasiparticle mixer circuits of arbitrary complexity containing any number of superconducting tunnel junctions. Our algorithm uses a multidimensional Newton-Raphson technique to achieve rapid convergence, even when many harmonics are included in the analysis. Another improvement is to perform all linear circuit calculations using the scattering matrix representation typical of modern circuit modeling techniques. This algorithm has been implemented as part of an extensive C++ class library for modeling the signal and noise performance of superconducting heterodyne receivers (SuperMix). Using the common, free C++ compiler "g++" (Free Software Foundation), impressive results can be achieved on modern workstations of moderate capability. Such speeds will make complex nonlinear optimization calculations a routine part of SIS receiver design.

I. Introduction

As the state of the art in submillimeter wave heterodyne mixers utilizing superconductor-insulator-superconductor (SIS) devices has progressed, SIS mixers are rapidly evolving to ever more complex and wide bandwidth designs. Examples include a sideband separating mixer [2], distributed junction arrays [3], and a dual-polarization receiver [4]. Additionally, the quest for wide IF bandwidth is spurring several investigations regarding the design of integrated SIS/HEMT receiver systems. To successfully optimize the performance of such sophisticated designs, accurate and efficient software modeling is required. Correctly calculating the complex interactions of the nonlinear responses of multiple SIS junctions will be vital to the success of such modeling. Consequently such software must include a fast and accurate harmonic balance method.

The small signal response of an electronic circuit containing nonlinear elements, such as a mixer, obtains from a perturbation analysis of the operating state. The operating state is determined by the large signal voltage and current waveforms across the nonlinear elements. Clearly it is essential to accurately determine these waveforms in order to proceed with the small signal analysis. The harmonic balance technique is a well established method for determining these large-signal waveforms.

For the purposes of harmonic balance, a network involving two-terminal nonlinear devices is normally modeled as in figure 1. Each nonlinear device is connected to its own port in the linear embedding network; the network includes dc and ac sources. The goal of harmonic balance is to determine the voltage and current waveforms $v(t)$ and $i(t)$ at each nonlinear device, thereby fixing its operating state and resultant small signal behavior. Traditionally harmonic balance proceeds by analyzing the linear

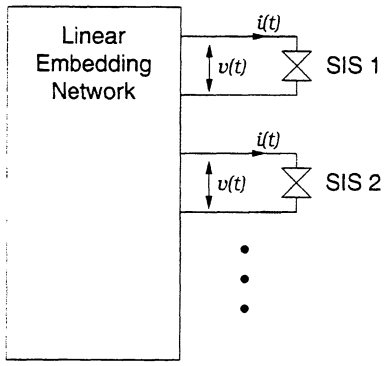

Fig. 1. SIS junctions attached to a linear network.

network in the frequency domain, constructing the Thevenin or Norton equivalent at each of the harmonic frequencies present in the network. Concurrently a time domain calculation of the response at each nonlinear element is conducted starting with some suitable initial driving function (current or voltage). The results of the two analyses are compared following suitable transformation; differences lead to adjustment of the harmonic signals present at the ports of the linear network and the time domain waveforms used for the driving functions of the nonlinear elements. The process is iterated until reaching convergence of the solutions. Hicks and Khan [5] provide a detailed analysis of this technique and its convergence properties.

In the case of mixers utilizing SIS devices as the nonlinear elements, the traditional harmonic balance approach outlined above has a very serious limitation: the time domain analysis must proceed for many cycles in order to determine the steady-state waveforms, greatly increasing the computation time for each iteration of the procedure. This limitation was overcome by Withington and Kollberg [1] who developed an algorithm for performing the nonlinear analysis of such devices purely in the frequency domain, a technique they refer to as spectral domain analysis. Starting from the mixer theory of Tucker [6], they develop the equations needed to fully analyze the frequency domain current response of a single SIS junction to the set of large-amplitude voltages induced by a dc bias and local oscillator source.

This paper extends the results of Withington and Kollberg to networks containing multiple SIS devices. The large signal solution is found using a multidimensional Newton-Raphson technique to achieve very rapid convergence, even when several harmonics and junctions are included in the analysis. The technique requires the Jacobian matrix of the nonlinear SIS response to changes in the large signal voltages. As will be shown, this matrix can be easily generated from the small signal RF conversion matrix. A final improvement is to conduct the linear circuit calculations using the scattering matrix representation rather than an impedance or admittance representation (which might not exist for certain circuit configurations).

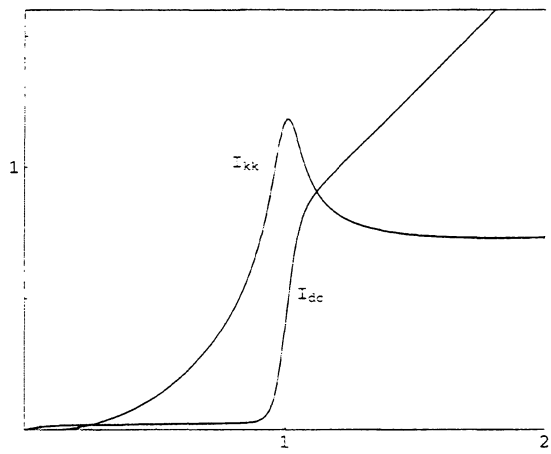

Fig. 2. Typical normalized SIS I-V characteristic curves

II. The Harmonic Balance Equations

A. Nonlinear Calculation of the Harmonic Currents

To perform the spectral domain analysis of the SIS operating state, the voltages and currents across each junction are represented as:

$$v(t) = V_0 + \mathrm{Re}\left[\sum_{m=1}^{\infty} V_m\, e^{jm\omega_0 t}\right] \quad ; \quad i(t) = I_0 + \mathrm{Re}\left[\sum_{m=1}^{\infty} I_m\, e^{jm\omega_0 t}\right] \tag{1}$$

where V_0 and I_0 are the constant (dc) components, ω_0 is the local oscillator frequency, and the V_m and I_m are complex phasors. In the case where the circuit contains a single junction, the Fourier coefficients in (1) can be represented by the single, complex valued vectors $\mathbf{v}$ and $\mathbf{i}$; if there are multiple junctions, these vectors will still be used, but the individual components will be denoted by V_m^n and I_m^n, where m is the harmonic number ($m = 0$ for the dc component) and n is the junction index, ranging from 1 to the total number of junctions in the circuit. Withington and Kollberg's adaption of Tucker's mixing theory provides an "admittance" representation of an SIS device: the junction currents $\mathbf{i}$ are calculated from the junction voltages $\mathbf{v}$, $\mathbf{i} = \mathbf{i}(\mathbf{v})$.

The currents through an SIS junction may be calculated as follows (*cf.* [1]):

$$I_0 = \mathrm{Re}\left[I_{(0)}\right] \quad : \quad I_m = I_{(m)} + I_{(-m)}^{*} \quad , \quad m > 0 \tag{2}$$

where:

$$I_{(m)} = -j \sum_{k=-\infty}^{\infty} C_k C_{k+m}^{*}\, \mathrm{I}(V_0 + kV_{ph}) \quad , \quad -\infty < m < \infty \tag{3}$$

In this equation V_0 is the junction dc bias voltage, $V_{ph} = (\hbar/e)\,\omega_0$ is the photon voltage of the local oscillator frequency, the C_k are complex phase factors defined below, and $\mathrm{I}(v)$ is the complex dc I-V characteristic function of the junction, $\mathrm{I}(v) \equiv$

$I_{kk}(v) + j\,I_{dc}(v)$. $I_{dc}(v)$ is the measured dc I-V characteristic curve of the junction; $I_{kk}(v)$ is its Kramers-Kronig transform. A typical $I_{dc}(v)$, $I_{kk}(v)$ pair is shown in figure 2, where the curves have been normalized so that the junction's gap voltage and normal resistance are both unity. Various versions of the Kramers-Kronig transform are seen in the literature; the version shown in figure 2 is that due to Tucker, which vanishes at $v = 0$:

$$I_{kk}(v) = \frac{1}{\pi} P \int_{-\infty}^{\infty} I_{dc}(v') \left(\frac{1}{v' - v} - \frac{1}{v'} \right) dv' \tag{4}$$

where the P denotes the Cauchy principle value of the integral. $I_{dc}(v)$ is an odd function and $I_{kk}(v)$ an even function of the voltage v, so that $I(-v) = I^*(v)$. The parentheses around the subscripts in (2) and (3) are used to distinguish harmonic indices of Fourier coefficients which range over negative as well as positive values; harmonic indices without the parentheses may take on nonnegative values only. This notation will be used extensively in Section III.

The complex phase factors C_k are defined by:

$$C_k = \lim_{n\to\infty} C_k^n \;\; ; \;\; C_k^0 = \delta_{0,k} \;\; ; \;\; C_k^{n>0} = \sum_{m=-\infty}^{\infty} C_{k-nm}^{n-1} A_{m,n} \tag{5}$$

where $\delta_{0,k}$ is Kronecker's delta and the complex coefficients $A_{m,n}$ are given by:

$$A_{m,n} = J_m(\alpha_n)\, e^{-jm\phi_n} \tag{6}$$

The coefficients α_n and ϕ_n are derived from the magnitude and phase of the harmonic voltage phasor V_n, where the magnitude is normalized by the photon voltage of harmonic n, which is nV_{ph}:

$$\alpha_n\, e^{j\phi_n} = V_n/(n\,V_{ph}) \tag{7}$$

Expressions (2) to (7) define the harmonic currents I_m through a junction in terms of the harmonic voltages V_n, thereby defining the vector function $\mathbf{i}(\mathbf{v})$. Note that the functions $A_{m,n}$ of the V_n (expressions (6) and (7)) are not analytic; this will be an important consideration when constructing the Jacobian matrix used by the Newton-Raphson algorithm.

B. The Junction Operating States and the Linear Network

The linear embedding network (figure 1) connecting the junctions will be represented as having a port for every junction at every harmonic frequency and dc; its behavior may be represented by a scattering matrix $\mathcal{S}$ and wave source vector $\mathbf{b_s}$. Referring to figure 3, the linear network experiences incoming waves $\mathbf{a}$ and responds by emitting waves $\mathbf{b}$. Because there are active sources embedded in the network (the dc bias and local oscillator), the network will emit waves $\mathbf{b_s}$ in the absence of any

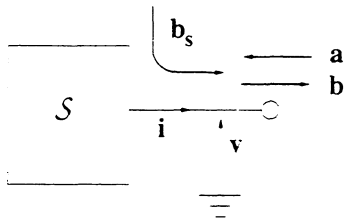

Fig. 3. The scattering matrix representation of a linear network.

incoming waves (as well as noise, which we ignore for the purposes of harmonic balance). Also indicated in figure 3 are the conventional voltages $\mathbf{v}$ and currents $\mathbf{i}$ at the ports. The various vectors are related as follows:

$$\mathbf{b} = \mathbf{b}_s + \mathcal{S}\,\mathbf{a}\,; \quad \mathbf{v} = (\mathbf{b} + \mathbf{a})\sqrt{Z_0}\,; \quad \mathbf{i} = (\mathbf{b} - \mathbf{a})/\sqrt{Z_0} \tag{8}$$

where Z_0 is the normalizing impedance of the scattering representation of the network (usually $50\,\Omega$). A major advantage of the scattering representation over the impedance and admittance representations of a linear network is that it always exists: some common networks have either no impedance representation or no admittance representation. Note that the voltages and currents in (8) are RMS, whereas the vectors of Fourier coefficients from (1) are peak amplitudes. This means that we must be careful about factors of $\sqrt{2}$ for the ac coefficients when solving the harmonic balance equations.

The relationships in (8) where $\mathbf{v}$ and $\mathbf{i}$ are the RMS harmonic voltages and currents through the SIS devices attached to the network lead to the nonlinear system of equations which must be solved by the harmonic balance routine:

$$Z_0(\mathcal{I} + \mathcal{S})\,\mathbf{i}(\mathbf{v}) + (\mathcal{I} - \mathcal{S})\,\mathbf{v} - 2\sqrt{Z_0}\,\mathbf{b}_s = 0 \tag{9}$$

where $\mathcal{I}$ is the identity matrix. One advantage of this scattering matrix formulation is that the impedance and admittance matrices are not needed; as already mentioned, one or the other of these matrices may not exist. For example, a mixer circuit containing a series array of junctions would not have an impedance representation.

C. Newton-Raphson Iteration Calculations

The Newton-Raphson method for solving a nonlinear system $\mathbf{y}(\mathbf{x}) = 0$ is to replace the estimated solution $\mathbf{x}_i$ with the improved estimate $\mathbf{x}_{i+1} = \mathbf{x}_i + \delta\mathbf{x}_i$, where $\delta\mathbf{x}_i$ is the solution to the *linear* system $(d\mathbf{y}/d\mathbf{x})_{\mathbf{x}_i}\delta\mathbf{x}_i = -\mathbf{y}(\mathbf{x}_i)$, and $(d\mathbf{y}/d\mathbf{x})_{\mathbf{x}_i}$ is the Jacobian matrix of $\mathbf{y}(\mathbf{x})$ evaluated at $\mathbf{x}_i$. This method is quadratically convergent so long as the Jacobian does not vanish at the root and the initial estimate is sufficiently close to the root.

In expression (9), $\mathcal{S}$, $\mathcal{I}$, $\mathbf{b}_s$, and Z_0 are not functions of $\mathbf{v}$ and $\mathbf{i}$, so differentiating with respect to the components of $\mathbf{v}$ results in the following equation for the correction

$\delta\mathbf{v}$ to an estimated $\mathbf{v}$:

$$\left(Z_0(\mathcal{I}+\mathcal{S})\,\frac{d\mathbf{i}}{d\mathbf{v}} + (\mathcal{I}-\mathcal{S})\right)\,\delta\mathbf{v} = 2\sqrt{Z_0}\,\mathbf{b_s} - Z_0(\mathcal{I}+\mathcal{S})\,\mathbf{i}(\mathbf{v}) - (\mathcal{I}-\mathcal{S})\,\mathbf{v} \quad (10)$$

When using (9) and (10) the elements of the source vector $\mathbf{b_s}$ representing ac signals must be multiplied by $\sqrt{2}$ to convert them to peak amplitudes from their RMS values, since these are the relevant quantities in the Tucker theory. The final values of the harmonic currents $\mathbf{i}$ and voltages $\mathbf{v}$ should be divided by $\sqrt{2}$ if their RMS values are required. One must be careful not to apply these corrections to the dc bias values.

The harmonic balance routine will seek a solution to the nonlinear system (9) by first calculating the linear network characteristics $\mathcal{S}$ and $\mathbf{b_s}$. After assuming an initial trial voltage vector $\mathbf{v}$, the routine must update $\mathbf{v}$ by finding the Jacobian matrix $d\mathbf{i}/d\mathbf{v}$ and then solving (10) for the corrections $\delta\mathbf{v}$. The process is repeated until the corrections become sufficiently small. The actual implementation of a satisfactory Newton-Raphson algorithm is somewhat more complicated; it must continually monitor the convergence behavior of the iterations and be prepared to adjust $\delta\mathbf{v}$. Potential difficulties include the algorithm's behavior near saddle points or local extrema of the right hand side of (10).

III. Generating the Jacobian Matrix

A. Basic Properties

In order to use (10) we must form the Jacobian matrix $d\mathbf{i}/d\mathbf{v}$ with elements $\partial I_m^n/\partial V_{m'}^{n'}$ ranging over all pairs of harmonics m and m' and SIS devices n and n'. Since the currents through one device n do not directly depend on the voltages across a different device n', where $n \neq n'$, we know immediately that:

$$\partial I_m^n/\partial V_{m'}^{n'} = \delta_{n,n'}\,\partial I_m^n/\partial V_{m'}^{n} \quad (11)$$

Unfortunately, because the $A_{m,n}$ defined in (6) are not analytic, it is impossible to define a single complex derivative $\partial I_m/\partial V_{m'}$. The solution chosen here is to define the Jacobian matrix in terms of separate derivatives of the real part and imaginary part of each harmonic current I_m with respect to the real part and imaginary part of each harmonic voltage $V_{m'}$ (recall that harmonic number 0 denotes the dc bias component). These four derivatives are real, not complex, and will be symbolized by:

$$\frac{\partial I_{m;r}}{\partial V_{m';r}}\;;\;\frac{\partial I_{m;i}}{\partial V_{m';r}}\;;\;\frac{\partial I_{m;r}}{\partial V_{m';i}}\;;\;\frac{\partial I_{m;i}}{\partial V_{m';i}} \quad (12)$$

where the "; r" and "; i" suffixes denote the real and imaginary parts, respectively, of the harmonic voltages or currents.

As for harmonic 0 (the dc bias) the imaginary parts I_0 and V_0 will be assumed to be identically zero. In order to keep the resulting Jacobian from becoming singular,

we set the derivatives as follows:

$$\frac{\partial I_{0;i}}{\partial V_{m;r}} = \frac{\partial I_{0;i}}{\partial V_{m;i}} = \frac{\partial I_{m;r}}{\partial V_{0;i}} = \frac{\partial I_{m;i}}{\partial V_{0;i}} = 0 \quad , \quad m > 0 \quad :$$
$$\frac{\partial I_{0;i}}{\partial V_{0;r}} = \frac{\partial I_{0;r}}{\partial V_{0;i}} = 0 \quad : \quad \frac{\partial I_{0;i}}{\partial V_{0;i}} = 1 \tag{13}$$

In the actual implementation we apply (13) not to $d\mathbf{i}/d\mathbf{v}$ in (10), but to the entire matrix multiplying $\delta\mathbf{v}$, saving a little time. Another alternative to (13), of course, would simply be to eliminate the imaginary part of the dc bias current and voltage from the equations.

B. Relation to the Small Signal Admittance Matrix

When the SIS junction is used as a heterodyne mixer, the infinitesimal signal voltage and current response can be expressed using the following Fourier expansions:

$$\delta v(t) = \mathrm{Re} \sum_{m=-\infty}^{\infty} \delta V_{(m)}\, e^{j\omega_{(m)}t} \quad ; \quad \delta i(t) = \mathrm{Re} \sum_{m=-\infty}^{\infty} \delta I_{(m)}\, e^{j\omega_{(m)}t} \tag{14}$$

where $\omega_{(m)} = m\omega_0 + \omega_{if}$, and ω_{if} is the IF output frequency. Note that parentheses are used with the harmonic index m since it takes on negative values as well as nonnegative in these expressions. The infinitesimal sideband currents and voltages are linearly related through the small signal RF conversion admittance matrix, $\mathcal{Y}_{(m,m')}$:

$$\delta I_{(m)} = \sum_{m'=-\infty}^{\infty} \mathcal{Y}_{(m,m')} \delta V_{(m')} \tag{15}$$

Clearly this is the case if and only if

$$\mathcal{Y}_{(m,m')} = \frac{\partial I_{(m)}}{\partial V_{(m')}} \tag{16}$$

In the limit of zero IF frequency, $\omega_{(m)} = m\omega_0$, and (14) becomes an alternate form of the harmonic expansions in (1). The relation expressed in (16) provides the connection between $\mathcal{Y}_{(m,m')}$ and the derivatives in (12).

Equating the expansions (1) and (14) we find the relations between the coefficients in the alternate expansions for $i(t)$:

$$I_0 = I_{(0)} \quad ; \quad I_m = I_{(m)} + I^*_{(-m)} \; , \quad m > 0 \tag{17}$$

with a similar relation for the harmonic voltages. Note that $I_{(0)}$ has been arbitrarily chosen to be real with no loss of generality in (14), since $\omega_{if} = 0$.

Consider the real and imaginary parts of I_m, for $m > 0$, using (17):

$$\begin{aligned} I_m &= I_{m;r} + jI_{m;i} \; , \quad m > 0 \\ I_{m;r} &= \left(I_{(m)} + I_{(-m)} + I^*_{(m)} + I^*_{(-m)}\right)/2 \\ I_{m;i} &= \left(I_{(m)} - I_{(-m)} - I^*_{(m)} + I^*_{(-m)}\right)/2j \end{aligned} \tag{18}$$

Using these expressions and the similar ones for the V_m, we can differentiate (1):

$$\begin{aligned}
dI_m &= dI_{m;r} + j\, dI_{m;i}\,, \quad m > 0 \\
&= \sum_{m'=0}^{\infty} \left[\left(\frac{\partial I_{m;r}}{\partial V_{m';r}} + j \frac{\partial I_{m;i}}{\partial V_{m';r}} \right) dV_{m';r} + \left(\frac{\partial I_{m;r}}{\partial V_{m';i}} + j \frac{\partial I_{m;i}}{\partial V_{m';i}} \right) dV_{m';i} \right] \\
&= \left(\frac{\partial I_{m;r}}{\partial V_{0;r}} + j \frac{\partial I_{m;i}}{\partial V_{0;r}} \right) dV_{(0)} \\
&\quad + \frac{1}{2} \sum_{m'=1}^{\infty} \left[\left(\frac{\partial I_{m;r}}{\partial V_{m';r}} + j \frac{\partial I_{m;i}}{\partial V_{m';r}} - j \frac{\partial I_{m;r}}{\partial V_{m';i}} + \frac{\partial I_{m;i}}{\partial V_{m';i}} \right) dV_{(m')} \right. \\
&\quad + \left(\frac{\partial I_{m;r}}{\partial V_{m';r}} + j \frac{\partial I_{m;i}}{\partial V_{m';r}} + j \frac{\partial I_{m;r}}{\partial V_{m';i}} - \frac{\partial I_{m;i}}{\partial V_{m';i}} \right) dV^*_{(m')} \\
&\quad + \left(\frac{\partial I_{m;r}}{\partial V_{m';r}} + j \frac{\partial I_{m;i}}{\partial V_{m';r}} + j \frac{\partial I_{m;r}}{\partial V_{m';i}} - \frac{\partial I_{m;i}}{\partial V_{m';i}} \right) dV_{(-m')} \\
&\quad \left. + \left(\frac{\partial I_{m;r}}{\partial V_{m';r}} + j \frac{\partial I_{m;i}}{\partial V_{m';r}} - j \frac{\partial I_{m;r}}{\partial V_{m';i}} + \frac{\partial I_{m;i}}{\partial V_{m';i}} \right) dV^*_{(-m')} \right] \qquad (19)
\end{aligned}$$

where we've made use of the fact that $V_0 = V_{(0)}$ is real.

Performing a similar expansion starting from (17) and using (15) and (16),

$$\begin{aligned}
dI_m &= dI_{(m)} + dI^*_{(-m)}\,, \quad m > 0 \\
&= \sum_{m'=-\infty}^{\infty} \left(\mathcal{Y}_{(m,m')}\, dV_{(m')} + \mathcal{Y}^*_{(-m,m')}\, dV^*_{(m')} \right) \\
&= \left(\mathcal{Y}_{(m,0)} + \mathcal{Y}^*_{(-m,0)} \right) dV_{(0)} \\
&\quad + \sum_{m'=1}^{\infty} \left(\mathcal{Y}_{(m,m')}\, dV_{(m')} + \mathcal{Y}^*_{(-m,m')}\, dV^*_{(m')} \right. \\
&\quad \left. + \mathcal{Y}_{(m,-m')}\, dV_{(-m')} + \mathcal{Y}^*_{(-m,-m')}\, dV^*_{(-m')} \right) \qquad (20)
\end{aligned}$$

Finally consider $I_0 = I_{(0)}$ (real), making use of (13):

$$\begin{aligned}
dI_0 &= dI_{0;r} \\
&= \frac{\partial I_{0;r}}{\partial V_{0;r}}\, dV_0 + \sum_{m'=1}^{\infty} \left(\frac{\partial I_{0;r}}{\partial V_{m';r}}\, dV_{m';r} + \frac{\partial I_{0;r}}{\partial V_{m';i}}\, dV_{m';i} \right) \\
&= \frac{\partial I_{0;r}}{\partial V_{0;r}}\, dV_{(0)} \\
&\quad + \frac{1}{2} \sum_{m'=1}^{\infty} \left[\left(\frac{\partial I_{0;r}}{\partial V_{m';r}} - j \frac{\partial I_{0;r}}{\partial V_{m';i}} \right) dV_{(m')} + \left(\frac{\partial I_{0;r}}{\partial V_{m';r}} + j \frac{\partial I_{0;r}}{\partial V_{m';i}} \right) dV^*_{(m')} \right. \\
&\quad \left. + \left(\frac{\partial I_{0;r}}{\partial V_{m';r}} + j \frac{\partial I_{0;r}}{\partial V_{m';i}} \right) dV_{(-m')} + \left(\frac{\partial I_{0;r}}{\partial V_{m';r}} - j \frac{\partial I_{0;r}}{\partial V_{m';i}} \right) dV^*_{(-m')} \right] \qquad (21)
\end{aligned}$$

and

$$\begin{aligned} dI_0 &= dI_{(0)} = dI^*_{(0)} = \left(dI_{(0)} - dI^*_{(0)}\right)/2 \\ &= \mathcal{Y}_{(0,0)} dV_{(0)} \\ &\quad + \frac{1}{2}\sum_{m'=1}^{\infty}\left(\mathcal{Y}_{(0,m')}\, dV_{(m')} + \mathcal{Y}^*_{(0,m')}\, dV^*_{(m')}\right. \\ &\quad \left. + \mathcal{Y}_{(0,-m')}\, dV_{(-m')} + \mathcal{Y}^*_{(0,-m')}\, dV^*_{(-m')}\right) \end{aligned} \tag{22}$$

Comparing (19) to (22) we find the following relations between the derivatives (12) needed for the Jacobian matrix and the small signal admittance matrix $\mathcal{Y}_{(m,m')}$ (when $\omega_{if} = 0$):

$$\mathcal{Y}_{(-m,-m')} = \mathcal{Y}^*_{(m,m')} \tag{23}$$

$$\frac{\partial I_{0;r}}{\partial V_{0;r}} = \mathcal{Y}_{(0,0)} \tag{24}$$

$$\frac{\partial I_{0;r}}{\partial V_{m';r}} = \mathrm{Re}\,\mathcal{Y}_{(0,m')} \qquad \frac{\partial I_{0;r}}{\partial V_{m';i}} = -\mathrm{Im}\,\mathcal{Y}_{(0,m')} \tag{25}$$

$$\frac{\partial I_{m;r}}{\partial V_{0;r}} = 2\,\mathrm{Re}\,\mathcal{Y}_{(m,0)} \qquad \frac{\partial I_{m;i}}{\partial V_{0;r}} = 2\,\mathrm{Im}\,\mathcal{Y}_{(m,0)} \tag{26}$$

$$\frac{\partial I_{m;r}}{\partial V_{m';r}} = \mathrm{Re}\left(\mathcal{Y}_{(m,m')} + \mathcal{Y}_{(m,-m')}\right) \qquad \frac{\partial I_{m;i}}{\partial V_{m';r}} = \mathrm{Im}\left(\mathcal{Y}_{(m,m')} + \mathcal{Y}_{(m,-m')}\right) \tag{27}$$

$$\frac{\partial I_{m;r}}{\partial V_{m';i}} = -\mathrm{Im}\left(\mathcal{Y}_{(m,m')} - \mathcal{Y}_{(m,-m')}\right) \qquad \frac{\partial I_{m;i}}{\partial V_{m';i}} = \mathrm{Re}\left(\mathcal{Y}_{(m,m')} - \mathcal{Y}_{(m,-m')}\right) \tag{28}$$

where $m > 0$ and $m' > 0$ in (25) to (28).

C. Calculating the Small Signal Admittance Matrix

The small signal admittance matrix $\mathcal{Y}_{(m,m')}$ must be calculated in order to perform the RF conversion analysis of a heterodyne receiver. Tucker's theory provides the following expressions for $\mathcal{Y}_{(m,m')}$ in the case of an SIS mixer:

$$\begin{aligned} \mathcal{Y}_{(m,m')} = & \\ & \frac{-j}{2(m'V_{ph} + V_{if})} \sum_{k=-\infty}^{\infty} C_k C^*_{k+m-m'} \left[\mathrm{I}(V_0 + kV_{ph}) - \mathrm{I}(V_0 + (k-m')V_{ph} - V_{if})\right. \\ & \left. - \mathrm{I}^*(V_0 + (k+m)V_{ph} + V_{if}) + \mathrm{I}^*(V_0 + (k+m-m')V_{ph})\right] \end{aligned} \tag{29}$$

where $V_{if} = (\hbar/e)\omega_{if}$ is the photon voltage of the IF frequency ω_{if}.

For $\omega_{if} = 0$, expression (29) becomes:

$$\mathcal{Y}_{(m,m'\neq 0)} = \frac{-j}{2m'V_{ph}} \sum_{k=-\infty}^{\infty} C_k C^*_{k+m-m'} \left[\mathrm{I}(V_0 + kV_{ph}) - \mathrm{I}(V_0 + (k-m')V_{ph}) - \mathrm{I}^*(V_0 + (k+m)V_{ph}) + \mathrm{I}^*(V_0 + (k+m-m')V_{ph}) \right] \tag{30}$$

$$\mathcal{Y}_{(m,0)} = \frac{-j}{2} \sum_{k=-\infty}^{\infty} C_k C^*_{k+m-m'} \left[\mathrm{I}'(V_0 + kV_{ph}) - \mathrm{I}'^*(V_0 + (k+m)V_{ph}) \right] \tag{31}$$

The primes (') on the currents in (31) denote derivatives of the I-V characteristic curves (figure 2) with respect to voltage. A little effort with index manipulation in (30) and (31) would suffice to show that these expressions satisfy (23). Now we have all the information needed to perform the Newton-Raphson iteration (10).

D. Final Considerations

Once routines to calculate $\mathbf{i}(\mathbf{v})$ and the $\mathcal{Y}_{(m,m')}$ have been developed, along with more traditional circuit routines to determine the linear embedding network behaviors $\mathcal{S}$ and $\mathbf{b}_s$, the harmonic balance routine may be implemented. Expressions (9) and (10) define the complex vector function of $\mathbf{v}$ and its Jacobian which are used by the Newton-Raphson solver to perform the harmonic balance. The vectors and matrices involved are potentially large, having dimension $N = n_j(m_{max}+1)$, where n_j is the number of SIS junctions in the circuit and m_{max} is the number of harmonics to be included in the analysis: each element must hold a pair of real numbers to represent the complex quantities involved.

The potentially most time-consuming calculation in these expressions is the matrix multiplication $(\mathcal{I}+\mathcal{S})(d\mathbf{i}/d\mathbf{v})$ in the formula for the Jacobian. This calculation is not as bad as it seems, however, because the matrices involved are block-diagonal. This characteristic was previously described for $d\mathbf{i}/d\mathbf{v}$ in expression (11). Consider the elements of the matrices $(\mathcal{I}-\mathcal{S})$. Since the embedding network is linear, it cannot connect signals with different frequencies: therefore the elements of $\mathcal{S}$ must look like (using the same index notation as in (11)):

$$\mathcal{S}^{n,n'}_{m,m'} = \delta_{m,m'} S^{n,n'}_{m} \tag{32}$$

The elements of the matrix product in (10) are therefore:

$$\left[(\mathcal{I}-\mathcal{S}) \frac{d\mathbf{i}}{d\mathbf{v}} \right]^{n,n'}_{m,m'} = \sum_{n'',m''} \left(\delta_{n,n''}\delta_{m,m''} + \delta_{m,m''} S^{n,n''}_{m} \right) \delta_{n'',n'} \frac{\partial I^{n'}_{m''}}{\partial V^{n'}_{m'}} = (\delta_{n,n'} - S^{n,n'}_{m}) \frac{\partial I^{n'}_{m}}{\partial V^{n'}_{m'}} \tag{33}$$

and no summing over an index is required to perform the multiplication.

IV. Implementation and Results

Routines to perform the calculations outlined above have been implemented and included in an extensive C++ class library (named "SuperMix") used to model SIS mixers and receivers. This library includes a complete complex linear algebra capability as well as a multiparameter optimizer and is described in more detail in [7]. It can perform gain and noise analyses of superconducting and conventional circuitry of arbitrary complexity, including superconducting surface impedance calculations and modeling of HEMT amplifiers. The source code of this library will be made freely available. It compiles under the Free Software Foundation's freely available compiler *g++* and has been tested on Linux (Pentium) and Sun UltraSparc platforms.

Twin-slot, two-junction mixers as described in [8] have been modeled using SuperMix. A schematic block diagram of the circuit model is illustrated in figure 4. Not shown is the dc bias circuit for the two junctions, which is modeled as an ideal voltage source (battery). Note that the entire RF superconducting circuitry is included in the model, including both SIS junctions. To illustrate some of the capabilities of the library interface, we have included figure 5, which shows the short C++ file which fully specifies the physical design parameters of the twin-slot circuitry to SuperMix. The `parameter` objects declared in the file are given initial values which may be modified by the program. Because the circuit parameters are modifiable, SuperMix's optimizer may be used to adjust them during program execution. The illustrated specification file is for a "device 63", which is a mixer designed for operation in the 600 to 700 GHz range and which is described in detail in [8]. The SIS I-V characteristics used are those shown in figure 2; SuperMix scales these normalized curves using the SIS parameter data provided in the specification file.

Figure 6 shows various dc current-voltage characteristic curves predicted by the model. The pumped curves show the effect of varying local oscillator (LO) frequency around the design frequency of 650 GHz; the LO power at the antenna was held constant at 200 nW. In this and subsequent figures the currents shown are the total bias currents obtained by summing the currents from each of the two SIS junctions. The values of these currents are found in elements of $\mathbf{i}(\mathbf{v})$ following a successful harmonic balance calculation. Even though each harmonic balance considered both junctions and three harmonic frequencies, the Newton-Raphson technique required an average of only four iterations to converge to about 0.1% or better accuracy. On average, a full harmonic balance took approximately 0.015 seconds to complete using a 333 Mhz Sun Ultra 10 workstation (6.3 seconds total execution time: 324 harmonic balances were required).

Figure 7 shows hot and cold load (RF background temperature) total IF output power into 100 MHz bandwidth centered at 6 GHz. The LO power was set to 200 nW at the antenna, with a frequency of 650 GHz. As with the other simulations shown, the LO fundamental frequency plus two harmonics were included in each harmonic balance and subsequent mixer analysis. The noise effects of the associated optics and IF stage were not included in the figure 7 analysis, although SuperMix is fully capable of including their effects as well. The curves were obtained by performing

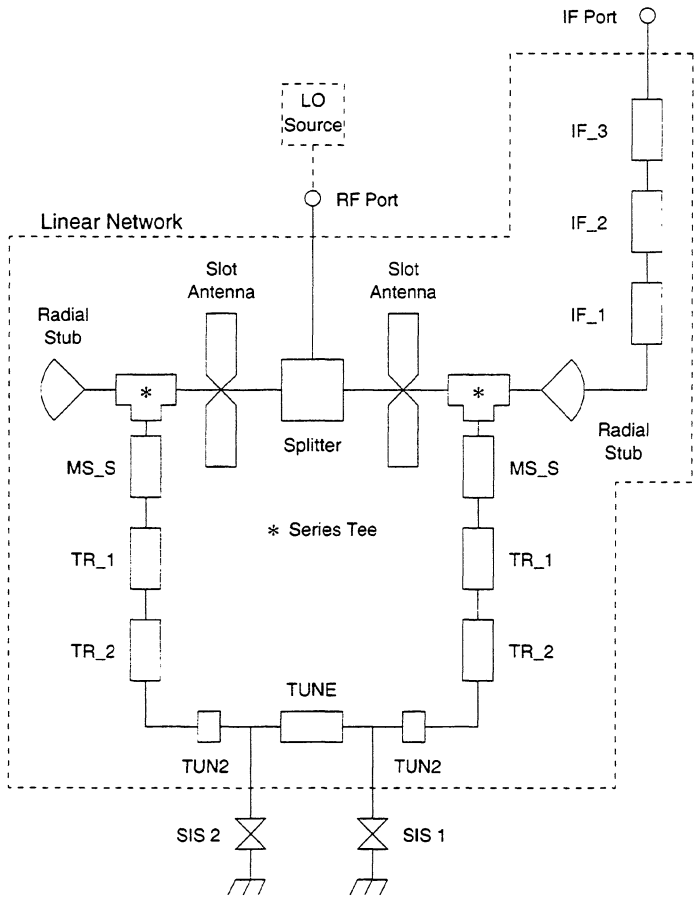

Fig. 4. Schematic block diagram of the twin-slot, two-junction mixer circuit used for the examples. Each labeled block is a circuit element. Several of the labels correspond to the names used in the SuperMix specification file shown in figure 5 and represent superconducting transmission line elements. The splitter is an ideal power splitter which is used to feed the RF and LO signals equally to the two slot antennas.

two complete harmonic balances (for the unpumped and pumped conditions) and two complete RF conversion analyses, including conversion gain and noise calculations, at each of 81 bias points. The total execution time was under 10 seconds, of which approximately 1.5 seconds were required for initialization (reading data files and building interpolation tables), again on a 333 Mhz Sun Ultra 10 workstation.

As a final example, figure 8 compares a calculated Fourier-Transform Spectrometer (FTS) response with a measured response for a device 63 twin-slot mixer. The FTS technique is described in detail in [8]. FTS "response" is defined as the change in mixer bias current in response to a large change in the RF background source temperature as a function of RF frequency, normalized to arbitrary units in which the peak response is set to approximately unity. There is no separate local oscillator source; the background RF thermal energy serves as a very weak local oscillator

```
// 63 Device specification file
// 2/1/99 FRR


// The superconductors used:
const sc_material & GP_MATERIAL  = nb;      // niobium ground plane material
const sc_material & TOP_MATERIAL = nb;      // niobium top strip material

// SIS junction parameters
parameter RNA  = 19.9*Ohm*Micron*Micron;    // normal resistance - area product
parameter SCAP = 85.0*fFarad/Micron/Micron; // specific capacitance (per area)
parameter AREA = 1.3*1.3*Micron*Micron;     // effective junction area
parameter VGAP = 2.8*mVolt;                 // SIS gap voltage
parameter VBIAS = 2.4*mVolt;                // SIS bias voltage
const char * const IDC_FILE = "72_idc.dat"; // DC IV characteristic (normalized to Vgap and Rn)
const char * const IKK_FILE = "72_ikk.dat"; // Kramers-Kronig transform of the DC IV curve

// layer thicknesses:
parameter GP_THICKNESS   = 2000.*Angstrom;  // ground plane
parameter TOP_THICKNESS  = 2000.*Angstrom;  // top strip
parameter MS_THICKNESS   = 4000.*Angstrom;  // SiO layer generally
parameter TUNE_THICKNESS = 2000.*Angstrom;  // SiO in tuning inductor

// Microstrip dimensions (width,length) (each entry is a parameter):
wl TR_1 = { 2.0*Micron, 37.7*Micron };      // transformer section 1
wl TR_2 = { 4.5*Micron, 41.1*Micron };      // transformer section 2
wl MS_S = { 2.0*Micron, 2.5*Micron };       // bit between radial stub and TR_1
wl IF_1 = { 2.0*Micron, 44.0*Micron };      // if section 1 (nearest radial stub)
wl IF_2 = { 10.0*Micron, 41.*Micron };      // if section 2
wl IF_3 = { 10.0*Micron,  1.0*Micron };     // if section 3 (nearest IF output)
wl TUNE = { 5.0*Micron, 9.8*Micron };       // full length of tuning inductor
wl TUN2 = { 5.0*Micron, 2.5*Micron };       // tuning inductor between transformer and SIS

// 90 degree radial stub dimensions:
parameter STUB_R   = 36.0*Micron;           // radial stub radius
parameter STUB_L   = 2.5*Micron;            // length of strip from antenna into stub

// Local Oscillator and IF output parameters:
parameter LO_POWER = 50*Nano*Watt;          // the LO power at the antenna
parameter LO_FREQ  = 650.0*GHz;             // the LO frequency
parameter LO_TEMP  = 0.0*Kelvin;            // thermal noise source temperature at input
parameter IF_FREQ  = 6*GHz;                 // the IF frequency
complex_parameter IF_TERM = complex(50*Ohm);// the input impedance of the IF amplifier

// The antenna impedance information (these cannot change during runtime):
const char * const ANT_FILE = "Zslot.750";  // antenna impedance file name
const double ANT_FILE_FREQ  = 750.0*GHz;    // antenna center frequency used in the file data
const double ANT_TUNE_FREQ  = 650.0*GHz;    // the actual antenna design center frequency

// Mixer calculations:
int HARMONICS = 3;

// The receiver temperature (remains constant during runtime):
const double TEMPERATURE = 4.0*Kelvin;
```

Fig. 5. SuperMix specification file for the twin-slot mixer shown in figure 4. Nearly all of the numerical values may be modified as required during program execution: this file provides initial or default values.

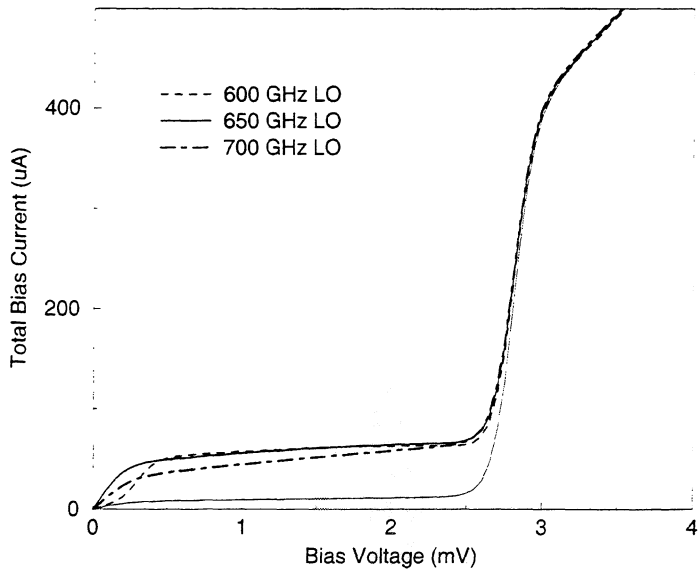

Fig. 6. Calculated pumped IV curves for a 650 GHz twin-slot, two-junction mixer. LO power 200 nW. The unpumped curve is also shown. The sum of the bias currents for the two junctions was calculated every 0.05 mV for a total of 324 points for the four curves. Each point required a full harmonic balance using 3 harmonics. The total execution time was 6.3 seconds on a 333 MHz *Sun Ultra 10.*

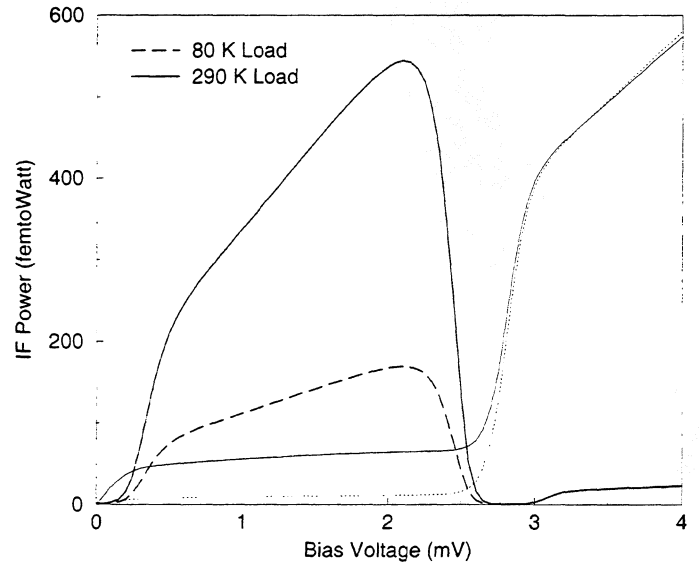

Fig. 7. Calculated hot and cold load IF power curves into a 200 MHz IF bandwidth centered at 6 GHz for a 650 GHz twin-slot mixer. LO power 200 nW. The IV curves are also shown. Only the superconducting mixer circuitry is modeled: noise contributions of the optics and IF amplifier are not included. Required 162 complete harmonic balance calculations and 162 mixer gain and noise analyses: execution time was under 10 seconds on a 333 MHz *Sun Ultra 10.*

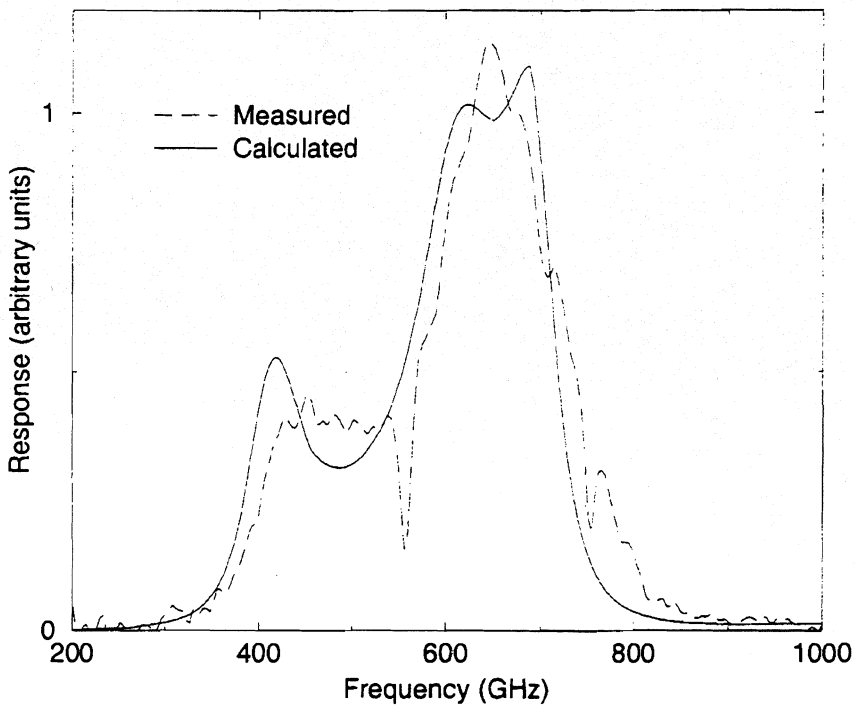

Fig. 8. Calculated and measured FTS response curves for a 650 GHz twin-slot mixer (device 63). Bias voltage was 2.0 mV. 802 harmonic balances were required to calculate the curve shown; execution time was 11.7 seconds. The text describes how the simulated response was calculated; at the peak, the calculated change in bias current is only 3 parts in 10^6.

which slightly pumps the junctions in the mixer. To model this measurement using SuperMix, the program balances the mixer for a very small LO power (0.1 picoWatt was used to generate figure 8); it then rebalances the mixer with the LO source turned off. The resultant change in the total calculated dc bias current drawn by the two junctions is then output as a function of LO frequency. The calculated current differences in the simulation are extremely small—only 31 picoAmps at the peak of the curve (3 parts in 10^6). The fidelity of the result demonstrates the precision of the harmonic balance calculations. The curve shown was calculated every 2 MHz, requiring 802 total harmonic balances. Execution time was 11.7 seconds, again giving 0.015 seconds per harmonic balance. The similarity of the calculated and measured responses is evident in the figure 8; it is important to note that no adjustment of free parameters was done to the mixer model in order to optimize the match of the curves; the parameters shown in figure 5 were the values used by the simulation, except that the bias voltage was set to 2.0 mV to match that used for the measured response. The only adjustment was to uniformly scale the calculated bias current responses (following the program run) to match the scaling used by the measured data.

ACKNOWLEDGEMENTS

This work was supported in part by NASA/JPL and its Center for Space Microelectronics Technology, by NASA grants NAG5-4890, NAGW-107, and NAG2-1068, by the NASA/USRA SOFIA instrument development program, and by the Caltech Submillimeter Observatory (NSF grant AST-9615025).

REFERENCES

[1] S. Withington and E. Kollberg, "Spectral-domain analysis of harmonic effects in superconducting quasiparticle mixers," *IEEE Trans. Microwave Theory Tech.*, vol. 37, pp. 231–238, 1989.

[2] A. Kerr, S.-K. Pan, and H. LeDuc, "An integrated sideband separating SIS mixer for 200–280 GHz," *Proc. Ninth International Symposium on Space Terahertz Tech.*, pp. 215–221, 1998.

[3] S.-C. Shi, T. Noguchi, J. Inatani, Y. Irimajiri, and T. Saito, "Experimental results of SIS mixers with distributed junction arrays," *Proc. Ninth International Symposium on Space Terahertz Tech.*, pp. 223–234, 1998.

[4] G. Chattopadhyay, D. Miller, and J. Zmuidzinas, "A 550 GHz dual polarized quasi-optical SIS mixer," *Proc. Tenth International Symposium on Space Terahertz Tech.*, 1999.

[5] R. Hicks and P. Khan, "Numerical analysis of nonlinear solid-state device excitation in microwave circuits," *IEEE Trans. Microwave Theory Tech.*, vol. 30, pp. 251–259, 1982.

[6] J. Tucker, "Quantum limited detection in tunnel junction mixers," *IEEE Jour. Quantum Electronics*, vol. 15, pp. 1234–1258, 1979.

[7] J. Ward, F. Rice, and J. Zmuidzinas, "SuperMix: a flexible software library for high-frequency circuit simulation, including SIS mixers and superconducting components," *Proc. Tenth International Symposium on Space Terahertz Tech.*, 1999.

[8] M. Gaidis, H. LeDuc, M. Bin, D. Miller, J. Stern, and J. Zmuidzinas, "Characterization of low-noise quasi-optical SIS mixers for the submillimeter band," *IEEE Trans. Microwave Theory Tech.*, vol. 44, pp. 1130–1139, 1996.

ACCURATE ELECTROMAGNETIC CHARACTERIZATION OF QUASI–OPTICAL PLANAR STRUCTURES

P. Arcioni[1], *M. Bozzi*[1], *L. Perregrini*[1], *A. R. Ruiz Laso*[2]

[1] University of Pavia, Dept. of Electronics, Via Ferrata 1, 27100, Pavia, Italy.
Phone +39 0382505200 Fax +39 0382422583 E–mail m.bozzi@ele.unipv.it

[2] University of Cantabria, Av. los Castros s/n, 39005, Santander, Spain.

ABSTRACT – Quasi–optical planar circuits include large arrays integrated with non–linear devices. Their design requires the modeling of the planar array as well as the characterization of the active devices. In this paper we present a method for the calculation of the voltages induced on the elements of a planar array by the input beam, as well as the evaluation of the array impedance matrix. These parameters, together with the active device modeling, allow for a full characterization of the quasi–optical circuit.

1. INTRODUCTION

In the recent years, a considerable attention has been devoted to the design and modeling of quasi–optical circuits [1]. They find many applications (mixers, frequency multipliers, amplifiers, *etc.*) in the microwave as well as in the millimeter–wave range. Moreover, they are relatively easy to fabricate, small and light, and represent a very attractive solution for circuits operating in the submillimeter–wave range.

In many millimeter–wave applications, quasi–optical circuits consist of a planar array of antennas on a semiconductor substrate, monolithically integrated with non–linear devices. In order to improve the system performance, it is typically required the use of external filters and of dielectric matching layers (Fig. 1) [2].

The design of a quasi–optical circuit requires, on one hand, the characterization of the active device (Schottky diode, HBV, Gunn diode, *etc.*), and, on the other hand, the electromagnetic modeling of the whole structure, including the planar array, the filters and the dielectric layers.

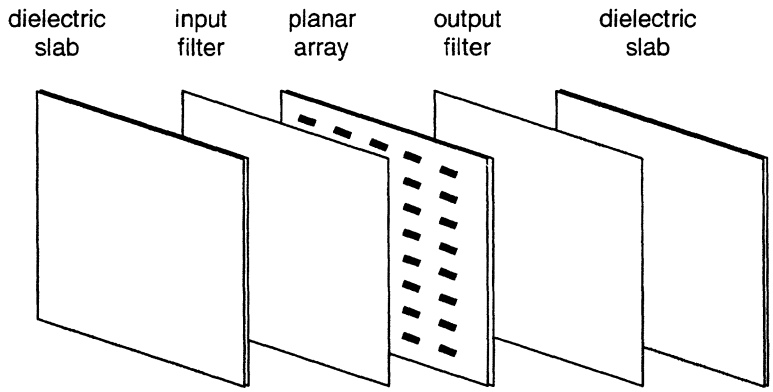

Fig. 1 – Complete setup of a quasi–optical circuit for millimeter–wave applications.

The global modeling provides a multi–port equivalent junction, each port being connected to a non–linear active device (Fig. 2).

Many research groups have been involved in the accurate modeling and characterization of active devices [3,4], achieving an excellent level in the device optimization. On the contrary, less attention has been devoted to electromagnetic issues. The use of commercial software may result not satisfactory, due to the long computation time and, consequently, to a cumbersome optimization process.

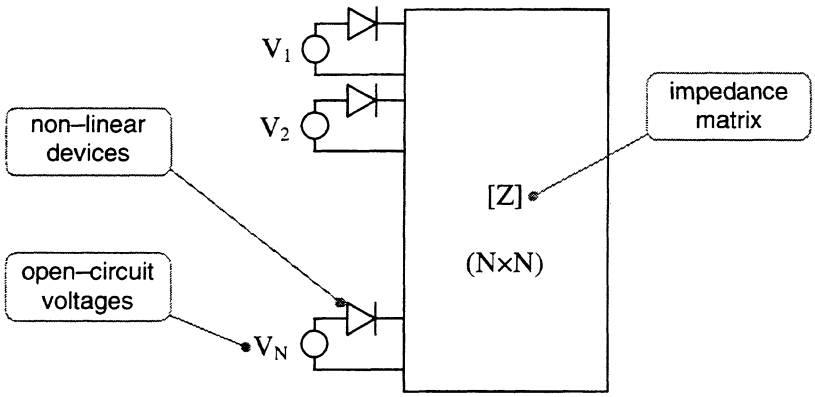

Fig. 2 – Equivalent circuit model of a quasi–optical active circuit.

In this paper, we present a fast and rigorous method for the electromagnetic characterization of the linear part of the quasi–optical circuit. This analysis provides:

i) the voltages induced at the antenna terminals of a planar array by the input beam (typically gaussian);

ii) the impedance matrix of the planar array.

This approach is very efficient from a computational point of view, since the calculation of both the voltages and the impedance matrix can be reformulated under the infinite array approximation. Moreover, the algorithm is very flexible: the array geometry, as well as the position and characteristics of filters and dielectric layers, can be given arbitrarily.

2. CALCULATION OF THE VOLTAGES

For the calculation of the voltages induced at the antenna terminals, we consider an input beam with a gaussian transverse distribution on the plane of the array (Fig. 3). This hypothesis well represents a typical setup of quasi–optical structures, where the field radiated by a horn is focused on the array by a system of mirrors.

Even if the array has a finite transverse dimension, the incident field effectively illuminates only a portion of the array: as a consequence, from an engineering point of view, the edge effects can be completely neglected and the array can be considered as an infinite array.

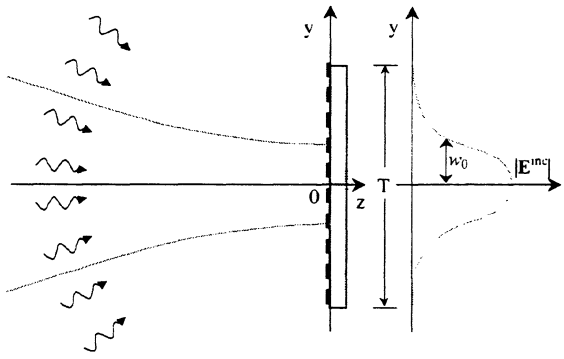

Fig. 3 – Planar array exited by a gaussian beam.

In order to calculate the voltages induced on the array elements, the incident gaussian field $\mathbf{E}^{inc}$ can be approximated by the combination of a set of uniform plane waves incident from different directions

$$\mathbf{E}^{inc}(x,y,z) = \sum_{m,n=-N}^{N} \mathbf{F}_{mn} e^{j(\kappa_{x_m} x + \kappa_{y_n} y)} e^{-\gamma_{mn} z} \tag{1}$$

where

$$\mathbf{F}_{mn} = \frac{A\pi w_0^2}{T^2} e^{-\frac{w_0^2(\kappa_{x_m}^2 + \kappa_{y_n}^2)}{4}} \left(\mathbf{u}_y + j \frac{\kappa_{y_n}}{\gamma_{mn}} \mathbf{u}_z \right) \tag{2}$$

$$\kappa_{x_m} = \frac{2\pi}{T} m = k \sin\vartheta_{mn} \cos\varphi_{mn} \tag{3}$$

$$\kappa_{y_n} = \frac{2\pi}{T} n = k \sin\vartheta_{mn} \sin\varphi_{mn} \tag{4}$$

$$\gamma_{mn} = \sqrt{(\kappa_{x_m}^2 + \kappa_{y_n}^2) - k^2} \tag{5}$$

Moreover, $k = \omega\sqrt{\varepsilon\mu}$ is the wave–number at the operation frequency, $(\vartheta_{mn}, \varphi_{mn})$ represents the direction of the (m,n)–th incident plane wave, T is the transverse dimension of the array and A and w_0 are the amplitude and the beam waist of the incident gaussian field, respectively.

Each plane wave determines a periodic excitation of the array. Therefore, due to the periodicity of the array and of the excitation field, the calculation of the voltages induced on all the array elements by each plane wave can be performed under the infinite array approximation. With this assumption, the analysis of the array reduces to the investigation of a single unit cell (Fig. 4).

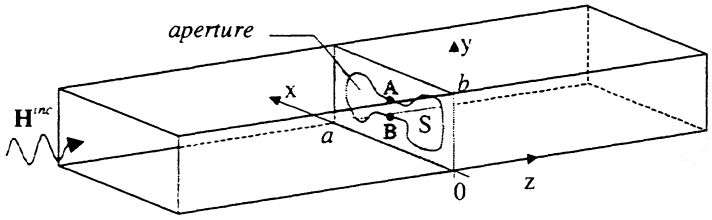

Fig. 4 – Elementary cell of the array.

The elementary cell of the array is a rectangular waveguide with periodic boundary conditions [5]. It includes a metal screen, with an arbitrarily shaped aperture, and (possibly) a layered medium stratified along with the z direction. The layered medium inside the waveguide accounts for the presence of filters and dielectric slabs.

The aim of the work becomes the calculation of the partial voltages $V_{\alpha\beta}^{mn}$, due to the single plane wave (m,n) on a generic array element (α,β). These voltages have the same amplitude on all the array elements and a periodic phase shift depending on the angle of incidence of the plane wave and on the position of the element in the array.

The analysis of the unit cell is based on the equivalence theorem and on an integral representation of the fields. The resulting integral equation is solved by the Method of the Moments [6].

Once the partial voltages induced by all the plane waves on the unit cell have been computed, the total voltages on all the array elements can be obtained using the superposition of the effects.

In such a way, we reduce the calculation of the voltages on all the array elements to the solution of a number of "small" problems (one for each plane wave used in the gaussian beam representation).

3. CALCULATION OF THE IMPEDANCE MATRIX

The method applied in the calculation of the impedance matrix is similar to the one previously presented for the evaluation of the voltages.

In the case of an array, the generic element of the impedance matrix is defined as

$$Z_{ij} = \left.\frac{V_i}{I_j}\right|_{I_k=0 \ \forall k\neq j} \tag{6}$$

where I_j is the test current applied to the terminals of the j–th element of the array—being all the other elements open circuited—and V_i is the voltage induced by the same current on the i–th element.

The test current I_j is defined on a narrow strip, connecting the terminals A–B. We observe that it is possible to represent the filament of current on a single cell as a summation of a finite number of periodic excitations

$$I_j(x,y) = \sum_{m,n=-N}^{N} I_j^{mn}(x,y) = \sum_{m,n=-N}^{N} G_j^{mn} e^{j(\kappa_{x_m} x + \kappa_{y_n} y)} \qquad (7)$$

Each current I_j^{mn} is periodic and defined on all the elements of the array. Therefore, the infinite array approximation can be applied, and the problem reduces to the investigation of a single unit cell of the array. The aim of the work, in this case, is the calculation of the voltage V_i^{mn} on the i–th element of the array, due to the impressed current I_j^{mn}. As shown in the previous section, the voltages on all the elements can be deduced from the voltages on an element taken as a reference. In fact, all these voltages have the same amplitude, and a periodic phase shift depending on the position of the element in the array.

The calculation of these voltages is based on an integral method, and is exploited using the Method of the Moments [7]. Once the voltages due to all the excitation currens have been calculated, the voltage V_i is found by the superposition of the effects.

4. CONCLUSIONS

The approach we present in this paper is very efficient, from a computation point of view. In fact, the analysis of a finite array with a non–uniform excitation is reduced to a number of "small" analyses, each performed under the infinite array approximation.

Furthermore, this method is very flexible, since the array geometry, the shape of the antennas and the characteristics of the layered medium (filters, slabs) can be given arbitrarily.

This algorithm has been implemented in a Fortran code, which represents a useful CAD–tool for the analysis and the design of quasi–optical structures, e. g. frequency multipliers [8].

5. ACKNOWLEDGEMENTS

This work is supported by the European Commission under the TMR Programme contract n. ERBFMRXCT960050 and by the University of Pavia under F.A.R. 1998 Funding.

REFERENCES

[1] Y. Qian and T. Itoh, "Progress in Active Integrated Antennas and Their Applications," *IEEE Trans. Microwave Theory Tech.*, Vol. MTT–46, No. 11, pp. 1891–1900, Nov. 1998.

[2] A. Mousessian *et al.*, "A Terahertz Grid Frequency Doubler," *IEEE Trans. Microwave Theory Tech.*, Vol. MTT–46, No. 11, pp. 1976–1981, Nov. 1998.

[3] A. V. Räisänen, "Frequency Multipliers for Millimeter and Submillimeter Wavelenghts," *Proc. IEEE*, Vol. 80, No. 11, pp. 1842–1852, Nov. 1992.

[4] J. R. Jones *et al.*, "Planar Multibarrier 80/240–GHz Heterostructure Barrier Varactor Triplers," *IEEE Trans. Microwave Theory Tech.*, Vol. MTT–45, No. 4, pp. 512–518, April 1997.

[5] N. Amitai, V. Galindo and C. P. Wu, *Theory and Analysis of Phased Array Antennas*, John Wiley and Sons, Inc., 1972.

[6] P. Arcioni *et al.*, "Accurate modelling of quasi–optical frequency multipliers excited by a gaussian beam," *Proc. of the 6th IEEE Intern. Conf. on Terahertz Electronics*, Leeds (UK), pp. 26–29, Sept. 3–4, 1998.

[7] P. Arcioni *et al.*, "Accurate Calculation of the Impedance Matrix of Planar Arrays for Quasi–Optical Applications," *Proc. of the PIERS 99*, Taipei (Taiwan), Mar. 22–26, 1999.

[8] P. Arcioni *et al.*, "A 430.5 GHz Quasi-Optical HBV Frequency Tripler," *Proc. of the 9th Intern. Symposium on Space Terahertz Technology*, Pasadena, California (USA), pp. 493–500, March 17–19, 1998.

EFFICIENT ANALYSIS OF QUASI–OPTICAL FILTERS BY THE BI–RME METHOD

P. Arcioni, M. Bozzi, D. Giani and L. Perregrini.

University of Pavia, Dept. of Electronics, Via Ferrata 1, 27100, Pavia, Italy.

Phone +39 0382505200 Fax +39 0382422583 E–mail m.bozzi@ele.unipv.it

ABSTRACT – In this paper, we present an efficient algorithm for the analysis of Frequency Selective Surfaces, which consists of a periodic array of arbitrarily shaped apertures in a conductive screen. The effectiveness of our algorithm strongly depends on the application of the Boundary Integral–Resonant Mode Expansion (BI–RME) method. The computational efficiency and the flexibility of the method are discussed through some examples.

1. INTRODUCTION

Frequency selective surfaces (FSSs) typically consist of a metal screen, perforated by periodic apertures of arbitrary shape, possibly backed by a dielectric layer (Fig. 1). FSSs find several applications as antenna sub–reflectors, quasi–optical filters and polarizer grids in the microwave and in the millimeter–wave range [1].

In this paper, we present a novel approach for the analysis of FSSs. In our analysis, the shape of the apertures can be given arbitrarily. Moreover, we consider both thin and thick metal screens.

Our approach is based on the equivalence theorem and on the representation of the fields as a modal expansion. The fields in free space are given as a summation of Floquet modes, whereas the fields on the aperture S are expanded on the modal fields of the waveguide of cross–section S.

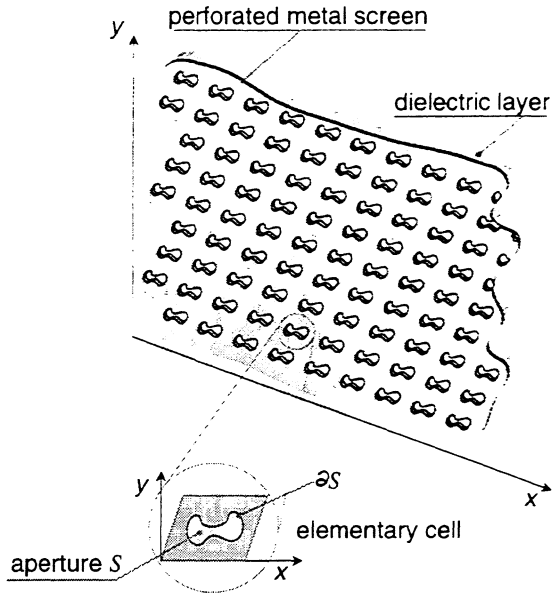

Fig. 1 – Structure of a frequency selective surface.

The analysis requires the determination of the mode spectrum of the waveguide and the calculation of the coupling integrals between the waveguide modes and the Floquet modes on the aperture *S*.

The waveguide modes are determined by the Boundary Integral–Resonant Mode Expansion (BI–RME) method [2] in a fast and reliable way. Moreover, the calculation of the coupling integrals can be obtained as a by–product of the BI–RME analysis.

This algorithm has been implemented in a computer code. An example proves the effectiveness and the accuracy of the method.

2. ANALYSIS OF THIN FSSs

An algorithm for the analysis of periodic arrays of apertures in a thin–screen metal layer is presented in [3]. Using the equivalence theorem, the problem is split in two parts (Fig. 2). The aperture *S* is closed by a metal screen and two sheets of (unknown) magnetic current densities **M** and **–M** are defined on the opposite sides of the screen.

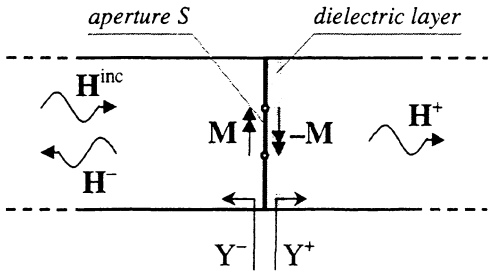

Fig. 2 – Equivalent problem for the analysis of thin frequency selective surfaces.

The continuity of the tangential component of the electric field is automatically guaranteed by the proper choice of the magnetic current densities, equal in amplitude and opposite in phase.

The value of the unknown $\mathbf{M}$ is determined by imposing the continuity of the tangential component of the magnetic field across the aperture S

$$\mathbf{H}^{inc}(\mathbf{r}) + \mathbf{H}^{-}(\mathbf{r}) = \mathbf{H}^{+}(\mathbf{r}) \quad \text{on } S \tag{1}$$

where $\mathbf{H}^{inc}$ is the (given) incident magnetic field, i.e., a plane wave incident at an arbitrary angle. Moreover, $\mathbf{H}^{+}$ and $\mathbf{H}^{-}$ are the magnetic fields which propagate in direction z and –z, respectively, due to the magnetic current densities defined on S.

Using the Floquet theorem [4], the magnetic fields in free space are expressed as a summation of Floquet modes $\mathcal{H}_m$. In particular, the fields $\mathbf{H}^{+}$ and $\mathbf{H}^{-}$ are defined as follows

$$\mathbf{H}^{-}(\mathbf{r}) = -\sum_{m} Y_m^{-} \mathcal{H}_m \int_S \mathbf{M}(\mathbf{r}) \cdot \mathcal{H}_m^{*} \, dS \tag{2}$$

$$\mathbf{H}^{+}(\mathbf{r}) = \sum_{m} Y_m^{+} \mathcal{H}_m \int_S \mathbf{M}(\mathbf{r}) \cdot \mathcal{H}_m^{*} \, dS \tag{3}$$

where Y_m^{-} is the modal admittance of the m–th Floquet mode, and Y_m^{+} is the modal admittance seen through the dielectric layer (Fig. 2).

Using (2)–(3) in (1), we obtain an integral problem, which is solved by the Method of the Moments (MoM). In the application of the MoM, the magnetic current density $\mathbf{M}$ is

expanded on a set of basis functions, corresponding to the magnetic modal fields $\mathbf{h}_q$ of the waveguide of cross–section S

$$\mathbf{M} = \sum_q x_q \, \mathbf{h}_q \tag{4}$$

As discussed in [3], the choice of entire domain basis functions, which satisfy the right boundary conditions, is very convenient, since it leads to a matrix problem of small dimension.

After expanding $\mathbf{M}$ using (4) and testing the continuity condition (1) using the same functions $\mathbf{h}_q$, the following matrix problem results

$$[\mathbf{A}][x] = [\mathbf{B}] \tag{5}$$

where

$$A_{qi} = \sum_m \left(Y_m^+ + Y_m^-\right) \int_S \mathbf{h}_q \cdot \mathcal{H}_m^* \, dS \int_S \mathbf{h}_i \cdot \mathcal{H}_m \, dS \tag{6}$$

$$B_i = 2 \int_S \mathbf{h}_i \cdot \mathbf{H}^{inc} \, dS \tag{7}$$

If $\mathbf{H}^{inc}$ is a plane wave, it can be expressed as a combination of Floquet modes. Thus, the integral appearing in (7) can be written as a combination of the integrals appearing in (6), i.e., the coupling integrals between the waveguide modes and the Floquet modes.

Therefore, this analysis requires *i*) the determination of the mode spectrum of a waveguide of cross–section S, and *ii*) the calculation of the coupling integrals between the waveguide modes and the Floquet modes.

If the aperture S has a conventional shape (rectangular or circular), both the mode spectrum and the coupling integrals are known analytically [5]. On the contrary, if the shape of S is arbitrary, a fast and reliable algorithm is required, to numerically evaluate the waveguide modes as well as the coupling integrals.

In this work, we apply the Boundary Integral–Resonant Mode Expansion (BI–RME) method [2] to perform the evaluation of the mode spectrum of the waveguide. The BI–RME method provides the cutoff frequencies and the normalized modal fields in a prescribed frequency band. This method is accurate and reliable, with no risk of either missing some modes or yielding spurious solutions.

With regards to the calculation of the coupling integrals, it can be proved that the surface integrals on S can be reduced to contour integrals on the aperture boundary ∂S

$$\int_S \mathbf{h}'_i \cdot \mathcal{H}'^*_m \, dS = \frac{k_m}{\kappa_i (k_m^2 - \kappa_i^2)} \int_{\partial S} \frac{\partial \psi_i}{\partial n} \xi^*_m \, d\ell \tag{8}$$

$$\int_S \mathbf{h}'_i \cdot \mathcal{H}''^*_m \, dS = 0 \tag{9}$$

$$\int_S \mathbf{h}'_i \cdot \mathcal{H}^{0*}_m \, dS = 0 \tag{10}$$

$$\int_S \mathbf{h}''_i \cdot \mathcal{H}'^*_m \, dS = -\frac{1}{\kappa_i} \int_{\partial S} \varphi_i \, (\mathbf{n} \cdot \mathcal{H}'^*_m) \, d\ell \tag{11}$$

$$\int_S \mathbf{h}''_i \cdot \mathcal{H}''^*_m \, dS = -\frac{\kappa_i}{(\kappa_i^2 - k_m^2)} \int_{\partial S} \varphi_i \, (\mathbf{n} \cdot \mathcal{H}''^*_m) \, d\ell \tag{12}$$

$$\int_S \mathbf{h}''_i \cdot \mathcal{H}^{0*}_m \, dS = -\frac{1}{\kappa_i} \int_{\partial S} \varphi_i \, (\mathbf{n} \cdot \mathcal{H}^{0*}_m) \, d\ell \tag{13}$$

In expressions (8)–(13), the superscripts prime, double prime and zero refer to TM, TE and TEM modes, respectively. Moreover, ψ_i and φ_i are the potentials of the TM and TE waveguide modes, and ξ_m is the potential of the Floquet modes; κ_i and k_m are the resonance wave–numbers of the waveguide and Floquet modes, respectively. Finally, $\mathbf{n}$ is the outward unit vector normal to ∂S.

Integrals (8)–(13) involve the potential φ_i of the TE waveguide modes and the normal derivative of the potential ψ_i of the TM modes, on the aperture boundary ∂S. It is worthy noting that both these quantities are provided by the BI–RME method as a by–product of the mode calculation. Moreover, the Floquet modes are known analytically. Therefore, the calculation of the coupling integrals can be efficiently performed by a numerical integration.

Occasionally, if $\kappa_i^2 = k_m^2$, relations (8) and (12) are not applicable: in these cases, the numerical integration on the surface S is required.

3. ANALYSIS OF THICK FSSs

The theory presented in the previous section can be extended to the analysis of thick–screen FSSs. The approach is very similar: using the equivalence theorem, the problem is split in three parts (Fig. 3).

The electric and magnetic fields are expressed as a summation of Floquet modes $\mathcal{H}_m$ in regions I and III, and as a summation of waveguide modal fields $\mathbf{h}_q$ in region II. The magnetic current densities $\mathbf{M}_1$ and $\mathbf{M}_2$ ensure the continuity of the fields across the apertures S_1 and S_2.

By imposing the continuity condition at the apertures S_1 and S_2 and applying the MoM, an integral problem similar to (5) is obtained.

It results that, also in this case, the only significant computational efforts are the determination of the mode spectrum of the waveguide of cross–section S and the calculation of the coupling integrals (8)–(13) between the waveguide modes and the Floquet modes.

Therefore, all the advantages deriving from the use of the BI–RME method well apply also in the case of thick–screen FSSs.

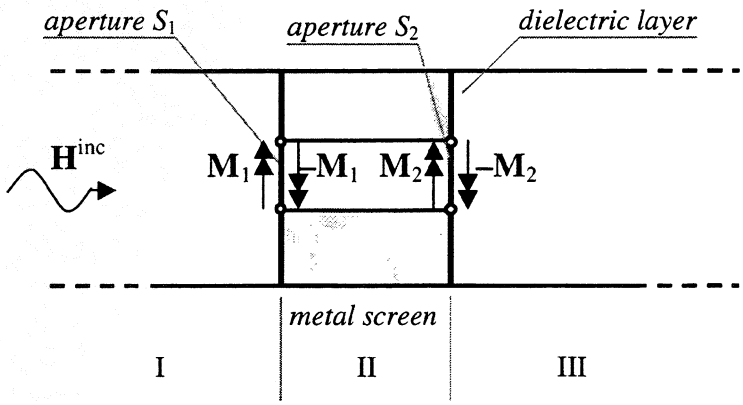

Fig. 3 – Equivalent problem for the analysis of thick–screen frequency selective surfaces.

4. VALIDATION OF THE METHOD

In order to validate the method described in this work, we report the analysis of a FSS firstly presented by Mittra [1]. The filter (Fig. 4) consists of a free–standing array of apertures in a thin metal screen. Each aperture has a Jerusalem–cross shape.

The analysis with our code on a workstation Sun Ultra 10 required only 30" for calculating 30 waveguide modes and the corresponding samples on the boundary ∂S, and 2'30" for calculating the reflection and transmission coefficients in 15 frequency points. Fig. 5 shows that our results are in good agreement with the ones reported in [1].

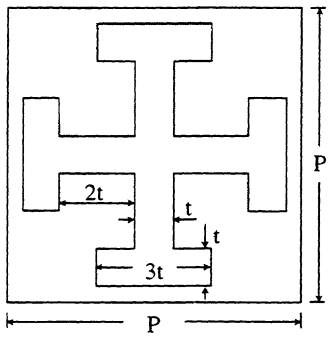

Fig. 4 – Unit cell of the FSS proposed in [1]. Dimensions: t=0.19 cm, P=1.52 cm.

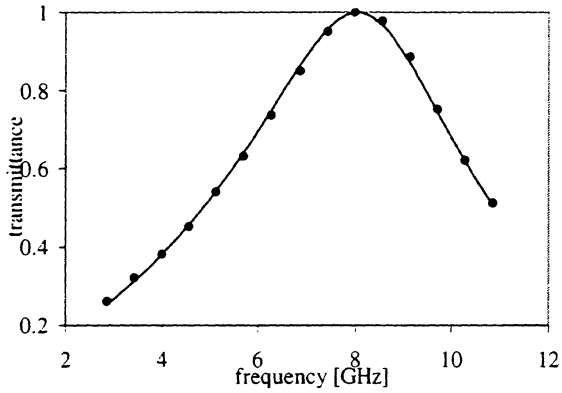

Fig. 5 – Transmittance of the Jerusalem cross FSS (solid line = our simulation, markers = from literature [1])

5. CONCLUSIONS

This paper presents an efficient algorithm for the analysis of thin and thick frequency selective surfaces.

The analysis requires the determination of the mode spectrum of an arbitrarily shaped waveguide and the calculation of the coupling integrals between the waveguide modes and the Floquet modes. We apply the BI–RME method for the determination of the mode of the waveguide, and obtain the calculation of the coupling integrals as a by–product of the BI–RME analysis.

An example demonstrates the accuracy and the rapidity of the method.

REFERENCES

[1] R. Mittra, "Techniques for Analyzing Frequency Selective Surfaces," *Proc. of the IEEE*, Vol. 76, No. 12, pp. 1593–1615, Dec. 1988.

[2] G. Conciauro *et al.*, "Waveguide Modes Via an Integral Equation Leading to a Linear Matrix Eigenvalue Problem," *IEEE Trans. on Microwave Theory Tech.*, Vol. MTT–32, No. 11, pp. 1495–1504, Nov. 1984.

[3] C. C. Chen, "Transmission Through a Conductive Screen Perforated with Apertures," *IEEE Trans. on Microwave Theory Tech.*, Vol. MTT–18, No. 9, pp. 627–632, Sept. 1970.

[4] N. Amitay, V. Galindo and C.P. Wu, *Theory and Analysis of Phased Array Antennas*, Wiley Interscience, ed., 1972.

[5] T. K. Wu, *Frequency Selective Surface and Grid Array*, John Wiley and Sons, 1995.

A MODIFIED HARMONIC-BALANCE ANALYSIS OF SCHOTTKY DIODE MULTIPLIERS BASED UPON A HYDRODYNAMIC TRANSPORT MODEL

C. C. Lee[1], B. L. Gelmont[3], D. L. Woolard[2] and C. Fazi[1]

U.S. Army Research Laboratory
[1]RF & Electronics, Adelphi, MD 20783
[2]Army Research Office, RTP, NC 27709

[3]The University of Virginia
Electrical Engineering Department
Charlottesville, VA 22903

Abstract

The accurate design and successful implementation of very high frequency nonlinear circuits requires both a detailed understanding of the physical operation of the active devices and of how these nonlinear devices interact with the linear embedding circuit. This work addresses the specific task of establishing a robust simulation tool that can be used to for the future design of GaAs Schottky diode multipliers at terahertz (~ 0.3-10.0 THz) frequencies. This paper will present an entirely new algorithm for the optimization of these combined multiplier elements. In this novel approach, the available second-harmonic power of the diode is first optimized over all allowable diode excitation voltages and harmonics.

I. INTRODUCTION

It is well known that energy-transport effects become important above approximately 300 GHz, where the oscillation period becomes comparable to the intrinsic energy relaxation time in GaAs (~ 3 picoseconds). Hence, the accurate modeling of the electron dynamics within reversed- or forward-biased GaAs Schottky diodes, even in the lower portion of the terahertz frequency band, requires the incorporation of a hydrodynamic, or energy-transport, approach. The specific focus of this paper is on energy transport effects and their influence on the harmonic multiplication within reversed-bias Schottky-barrier varactor diodes. Equally important to the characterization of diode multipliers is the optimization of the nonlinear element to the externally coupled embedding impedance. Here, the second-harmonic power (i.e., current and voltage) of the matched diode is optimized before constraints on embedding impedance, local voltage and dc bias are specified. The key of this approach is the reduction of systems variables by an efficient mathematical ordering of the optimization procedure. Specifically, this new method reduces the typical optimization problem (i.e., where device and circuit are considered simultaneously) for a doubler, where 2 harmonics are considered, from n+2 variables to n variables. As will be shown, this approach leads to a significant computational advantage for Schottky-diode multiplier design.

In this paper, a one-dimensional time-dependent simulation algorithm is presented which employs a fully hydrodynamic transport model (i.e. first three moments of the Boltzmann equation) to describe the diode physics within the depletion and bulk regions. These preliminary studies consider diode operation in the lower portion of the terahertz band (i.e. < 1 THz) where electron momentum relaxation is not a factor. These studies assume a reversed-biased situation and employ appropriate boundary conditions at the barrier interface. Specifically, boundary conditions include an energy-dependent constraint on the thermionic-emission current and an energy-dependent constraint on the energy-flow density. In addition, this work combines the physically accurate diode model with a

modified harmonic-balance algorithm to determine diode-circuit designs that maximize power generation and/or power efficiency in the second harmonic. The modified harmonic-balance method utilizes a novel two-step procedure where the available doubler-power and the second-harmonic diode-impedance is first derived as a function of first and second harmonic diode excitation. The harmonic diode-voltages and second-harmonic diode-impedance at the optimum power-point are then used define the matched embedding impedance and the optimum local-oscillator (LO) voltage. Note that the optimum values for both the direct and alternating components of the LO source are derived. The utility of this simulation tool is illustrated by comparing to prior studies, by others, that employed traditional drift-diffusion transport models, Monte Carlo transport models and a conventional harmonic-balance algorithm. Specifically, this work demonstrates a computationally efficient and accurate physical description as well as a more robust approach for circuit optimization.

II. PHYSICS-BASED DIODE MODEL

These multiplier studies utilize a physics-based Schottky-diode model accurate for both momentum and energy relaxation effects. Here, a one-dimensional time-dependent simulation algorithm is implemented that employs a fully hydrodynamic transport model (i.e. first three moments of the Boltzmann equation) to describe the diode physics within the depletion and neutral regions. The application this type of approach will be necessary for GaAs diodes operating at terahertz frequencies because energy relaxation is important above 300 GHz (i.e., since $\tau_w \approx 3.0\times10^{-12}$ seconds) and momentum relaxation is important above 1 THz (i.e. since $\tau_m \approx 0.25\times10^{-12}$ seconds). While our method is fully amenable to momentum relaxation these initial studies will consider device operation below 1 THz and the explicit time-dependence on current density (i.e., momentum) in the momentum balance equation will be suppressed for computational convenience. These studies consider the large-signal operation of a Schottky-barrier varactor frequency multiplier and will therefore consider diodes under time-dependent reverse-bias up to the breakdown voltage. Hence, these studies assume a reversed-biased situation and employ traditional boundary conditions at the barrier interface. Specifically, boundary conditions include an energy-dependent constraint on the thermionic-emission current and an energy-dependent constraint on the energy-flow density.

Hydrodynamic Transport Model

The electron-transport model equations used here are similar to that in [1]. Specifically, the time-dependent hydrodynamic model used in this study conserve electron density, n, electron charge-flux, $\bar{J}_n$, and average electron energy, w_n, according to

$$q\frac{\partial n}{\partial t} - \nabla\cdot(\bar{J}_n) = 0, \tag{1}$$

$$\bar{J}_n = qD_n\nabla n + n\mu_n(k_B\nabla T_e - q\nabla\psi). \tag{2}$$

$$\frac{\partial(nw_n)}{\partial t} + \nabla\cdot\bar{S}_n = -\bar{J}_n\cdot\nabla\psi + n(\frac{\partial w_n}{\partial t})_c, \tag{3}$$

and derives self-consistent, ψ, potentials from Poisson's equation

$$\nabla \cdot (\varepsilon \nabla \psi) = q(n - N_D). \tag{4}$$

Here, q is the free electron charge, D_n is the diffusion coefficient, μ_n is the electron mobility, k_B is the Boltzmann constant, T_e is the electron-gas temperature, $\bar{S}_n$ is the electron energy-flux density, ε is the electric permittivity and N_D is the donor concentration. The diffusion coefficient is determined from the generalized Einstein relation

$$D_n = \frac{\mu_n k_B T_e}{q} \tag{5}$$

The electron energy flow $\bar{S}_n$ is given by

$$\bar{S}_n = -\kappa_n \nabla T_e - (w_n + k_B T_e)\frac{\bar{J}_n}{q}. \tag{6}$$

The thermal conductivity κ_n is related to the mobility μ_n by the Wiedmann-Franz law

$$\kappa_n = (\frac{5}{2} + c) q n \mu_n (\frac{k_B}{q})^2 T_e, \tag{7}$$

where c is an adjustable parameter, taken here to be –1/2. The average electron energy w_n is defined using the usually thermal approximation (i.e., drift component ignored)

$$w_n = \frac{3}{2} k_B T_e. \tag{8}$$

The collision terms are modeled by the relaxation-time approximation. The energy collision term in (3) is expressed as

$$(\frac{\partial w_n}{\partial t})_c = -\frac{w_n - w_0}{\tau_w}, \tag{9}$$

where $w_o = 3k_B T_o/2$ is the equilibrium energy at the lattice temperature T_o and τ_w is the energy relaxation time. In this work, a constant relaxation time, $\tau_w = 3$ ps, has been utilized [1]. The diffusion coefficient is defined from the generalized Einstein relation (5) where a general mobility with a temperature dependence is assumed. For free particle path-lengths much less that the epitaxial layer width, the mobility dependence on electric field, $F = -\nabla \psi$. can be approximated by [1]

$$\mu_n(F) = \frac{\mu_0 + v_{sat} \cdot F^3 / F_0^4}{1 + (F / F_0)^4} \tag{10}$$

where μ_0 is the low-field, doping-dependent mobility, v_{sat} is the saturation velocity and F_0 is the critical electric field. Here, $v_{sat} = 1.5 \times 10^5$ m/s and $F_0 = 4.0 \times 10^5$ V/m has been utilized. The doping-dependent mobility is given by

$$\mu_0 = \frac{\mu_{00}}{1 + [\log(N_T) / B]^n} \tag{11}$$

where N_T is the total doping density (here total ionization is assume so $N_T = N_D$). Here, $\mu_{00} = 0.838$ m^2/V-s, $n = 23$, and $B = 23.26$ are used for GaAs. A temperature-dependent mobility may be obtained by requiring the energy transport equation in the spatially homogeneous bulk to be consistent with the empirical field dependent mobility. Specifically, the energy-balance equation for a spatially homogeneous semiconductor yields

$$q\mu_n(F)F^2 = \frac{3}{2}\frac{k_B(T_e - T_0)}{\tau_w} \tag{12}$$

which can be solved self consistently with Eq. (10) to determine mobility as a function T_e. The previous model was utilized in this work to incorporate the effects of electron energy into the time-dependent operation of a reverse-bias Schottky varactor embedded into an arbitrary tuning network. A consistent and physically accurate set of boundary conditions will now be presented.

Boundary Conditions at the Schottky and Ohmic Contacts.

The accurate implementation of the hydrodynamic model to diode operation requires that an appropriate set of boundary conditions be applied to the device. Here, we will consider the case where a reverse bias is maintained on the diode during large signal operation. It is also important to note that the boundary conditions used in the physical devices must be applied at the ohmic-contact (i.e., at $z = L$, where L is the diode epitaxial length) and on the semiconductor-side of the Schottky-contact (i.e., at $z = 0^+$). In this investigation, conditions on the electron potential, electron density and electron temperature were enforced at both contacts. Here, nonlinear, mixed boundary conditions [1] were employed at the Schottky-contact to allow for nonequilibrium variations in density and energy. These boundary conditions are physically accurate and reasonable for reverse-bias diode operation, see discussion in [2].

The potential applied to the diode is defined in terms of the shift in the Fermi-energy between the Schottky-contact and the ohmic-contact. Hence, if $\psi(L)$ is used to denote the potential energy at the conduction-band edge of the ohmic-contact then the electron potential at the semiconductor-side of the Schottky contact is given by

$$\psi(0^+) = \psi(0^-) - \phi_b = \psi(L) - \phi_b - E_{F0} + V_D \,. \tag{13}$$

where V_D is the diode applied bias, ϕ_b is the metal-semiconductor barrier height and E_{F0} is the difference between the Fermi-energy and the conduction band edge at the ohmic contact. The potential at the ohmic-contact $\psi(L)$ is used as the reference voltage and is kept constant during a simulation

The electron concentration at the ohmic-contact is assumed to be in dynamic equilibrium with the reservoir and therefore specified as

$$n(L) = N_D \tag{14}$$

The carrier concentrations at the Schottky-contact are determined from Sze's thermionic-diffusion theory [1]. The electron concentration is defined dynamically from the electron exchange between metal and semiconductor. Here, the relative recombination velocity for electrons in the semiconductor, v_S, and in the metal, v_M, are employed. Hence, the thermionic-emission current of electrons across the metal-semiconductor boundary is expressed as

$$J_{TE}(0^+) = q(v_S\, n(0^+) - v_M\, n_M) \tag{15}$$

where $n(0^+)$ is the electron concentration in the semiconductor at the interface and n_M is the electron concentration in the metal with energy enough to reach the conduction band of the semiconductor. This electron concentration is given by

$$n_M = N_C \exp(-\frac{\phi_B}{k_B T_e}) \,. \tag{16}$$

where N_C is the effective density of states. A hemi-Maxwellian distribution at the interface is use to approximate the electron recombination velocity in the semiconductor as

$$v_S = \sqrt{k_B\, T_e(0^+)/\pi\, m_n} \,, \tag{17}$$

and in the metal as

$$v_M = \sqrt{k_B\, T_0/\pi\, m_n} \,, \tag{18}$$

where, T_0 is the lattice temperature.

The electron energy, or electron temperature, at the ohmic-contact is assumed to be in dynamic equilibrium with the reservoir and therefore specified as

$$T_e(L) = T_0 \tag{19}$$

The condition on electron temperature, at the Schottky-contact, is determined such that the energy crossing the boundary, derived from a recombination velocity model, is consistent with the energy-flux terms of the physical model. Here, energy carried by electrons passing from metal-to-semiconductor is balanced against energy carried by electrons passing from semiconductor-to-metal to derive the phenomenological energy-flux boundary condition [1]

$$S_n(0^+) = v_M\, n_M\, \delta\, k_B\, T_0 - v_S\, n(0^+)\, \delta\, k_B\, T_e(0^+), \tag{20}$$

where $\delta = 2$ is used. The hydrodynamic electron transport model was solved subject to the previous boundary conditions to provide a physically accurate description for Schottky-diode varactor operation.

III. VARACTOR FREQUENCY-MULTIPLIER NUMERICAL SIMULATION

Harmonic-Balance Technique

While an accurate model for the physical diode is very important as one attempts to design varactor multipliers at very high frequencies, the ability to effectively couple the device to the proper embedding impedance is of paramount importance. In fact, the majority of the analytical and numerical effort involved in realizing efficient multipliers is expended in the matching of the nonlinear device to the embedding circuit [3]. For example, many harmonic-balance methods have been derived (e.g., accelerated fixed point [4] and multiple reflection algorithm [5]) to improve the matching of the various harmonics between nonlinear device and linear circuit. Here the difficulty lies in the large number of iterations that are required to optimize power-efficiency of a given nonlinear element over both embedding impedance and local oscillator (LO) voltage. This problem becomes compounded for optimization over the physical diode design and in circuits that contain many nonlinear device elements [6]. Of course, in some situations where multiple diodes are involved equivalent-circuits can be developed that reduce groups of diodes to a single nonlinear element.

When a conventional harmonic-balance (HB) algorithm is applied to the analysis of a varactor-doubler the problem is to optimize the second-harmonic generation. Here, embedding impedances are selected for the first- and second-harmonic circuits and short-circuit conditions are assumed at the higher harmonics. While there are many HB techniques one of the most popular is the multiple reflection algorithm [5] that seeks to smooth transients via the introduction of a loss-less transmission-line section. This relaxation method, which in some cases requires long convergence times, has been improved by Tait [4]. Regardless of the exact mathematical algorithm employed, the primary challenge in the design of a doubler is to determine the embedding impedance that will yield the maximum second-harmonic power. In the conventional approach, the physical model of the Schottky diode is used in conjunction with the HB algorithm to optimize the second-harmonic power. Specifically, the HB technique will iterate between the Fourier-domain solutions of the circuit(s) and the current/voltage harmonics derived from steady-state time-domain simulations of the diode. Since this combined Fourier-domain and time-domain analysis inevitably leads to extensive iterations and to a large computational cost, it is natural to seeks alternative methods that reduce the numerical burden of the optimization task. In the simulations presented here, a new two-step procedure has been utilized to achieve this goal. This modified HB algorithm introduces a

new optimization constraint that enables a natural separation of the device-circuit problem. Specifically, this procedure allows the current/voltage harmonics of the nonlinear device to be optimized independently of the external circuit. Subsequently, the optimum embedding circuit can then be derived from a very simple analysis.

The key to this simplified approach is to formulate the optimization-problem of the varactor-doubler in a completely different way. Specifically, to recognize that the available-power of the diode at the doubler-frequency may be optimized a priori (i.e., independent of the external circuit) and that the Fourier results can be used, subsequently, to determine the embedding impedance and LO voltage. While this technique represents, in a manner of speaking, a inverse transformation of the conventional problem, it is completely valid and offers definite computational advantages. The technique is outlined in the text that follows. Invoking the normal assumptions that the nonlinear diode-element of a doubler experiences first- and second-harmonic voltage excitation, it is possible to express the total instantaneous voltage across the diode as

$$V_D(t) = -|V_{D0}| + V_{C1}\cos(\omega t) + V_{C2}\cos(2\omega t) + V_{S2}\sin(2\omega t) \tag{21}$$

where, ω, is the fundamental angular frequency and $|V_{D0}|$, V_{C1}, V_{C2} and V_{S2} is the dc, first, and second harmonic voltages, respectively. Note, the absence of the first sine-harmonic is completely general in that one only needs a specific time-reference point. The assumption that these harmonics are *known* and presented to the diode, only require that we assume that the first- and second-harmonic embedding impedances are matched and that the higher-harmonics are subject to an short-circuit. While a traditional HB algorithm is able to treat arbitrary embedding impedances, these imposed conditions are ones that are optimal for the final design. Hence, they are completely consistent with an optimization of the varactor-doubler. The main goal of the technique now is to maximize either (1) the second harmonic power available from the diode, or (2) the overall efficiency of diode-doubler. The first-harmonic power delivered to the diode is,

$$P_1 = V_{C1}I_{C1}/2, \tag{22}$$

and the available second-harmonic power from the diode is

$$P_2 = -(V_{C2}I_{C2} + V_{S2}I_{S2})/2. \tag{23}$$

The simple relations given in Eqs. (22) and (23) can now be used to optimize multiplier operation. The first step in the problem is to maximize either P_2, or P_2/P_2, over the four-dimensional space $(V_{D0}, V_{C1}, V_{C2}, V_{S2})$. Here, the current harmonics I_{C1}, I_{C2}, and I_{S2} are supplied by Fourier transforms of time-domain simulations from the physical diode model according to

$$I_D(t) = I_{D0} + \sum_{k=1}\left\{I_{Ck}\cos(k\omega t) + I_{Sk}\sin(k\omega t)\right\}. \tag{24}$$

Note that this new approach offers an immediate reduction in problem complexity as compared to the conventional HB approach. Specifically, the traditional HB method will maximize the nonlinear diode-circuit problem over LO voltage (dc and ac) and over the real and imaginary parts of the first- and second-harmonic embedding impedance which is a six-dimensional space. It should be noted that this reduction from N to N-2 in the

double problem also occurs in the analysis of a varactor-tripler due to symmetry considerations.

Once the optimization over diode-voltages has been completed. the matching embedding impedances are easily determined from

$$R_1 = 2P_1/(I_{C1}^2 + I_{S1}^2), \tag{25}$$

$$X_1 = -R_1 I_{S1}/I_{C1}, \tag{26}$$

$$R_2 = 2P_2/(I_{C2}^2 + I_{S2}^2), \tag{27}$$

$$X_2 = (V_{S2}I_{C2} - I_{S2}V_{C2})/(I_{C2}^2 + I_{S2}^2). \tag{28}$$

The final step to the procedure is to derive the optimum LO voltage. Shifting the time reference-point again (i.e., by θ) so that the fundamental harmonic of LO voltage only depends cosine leads to

$$V_D(t) = -|V_{D0}| + V_{C1}\cos(\omega t - \theta) + V_{C2}\cos(2\omega t - 2\theta) + V_{S2}\sin(2\omega t - 2\theta) \tag{29}$$

where

$$(\cos\theta, \sin\theta) = (I_{C1}, -I_{S1})/\sqrt{I_{C1}^2 + I_{S1}^2} \tag{30}$$

The total LO voltage is now given by

$$V(t) = V_O + V_{LO}\cos(\omega t) \tag{31}$$

where

$$V_{LO} = 2R_1\sqrt{I_{C1}^2 + I_{S1}^2}, \tag{32}$$

$$V_O = I_O R_O - |V_{DO}|. \tag{33}$$

Here, the real impedance of the dc bias circuit is R_O and I_O is the dc diode current. Figure 1 summarizes the major differences between the conventional HB technique and the modified approached discussed here. As shown, the traditional HB technique requires two iterations. For each mapping over the six-dimensional LO-impedance space, one must perform convergent iteration to balance the harmonics between the embedding impedance and the nonlinear device. On the other hand, the modified method invokes allowable constraints on the available diode power and the embedding impedance(s) (i.e., are always matched to the diode impedance) to reduce the optimization space by two variables. Furthermore, the method requires a trivial calculation in the second step to derive the final impedance(s) and the LO voltage. In simplest terms reducing the degrees of freedom allows for a significant reduction in computation.

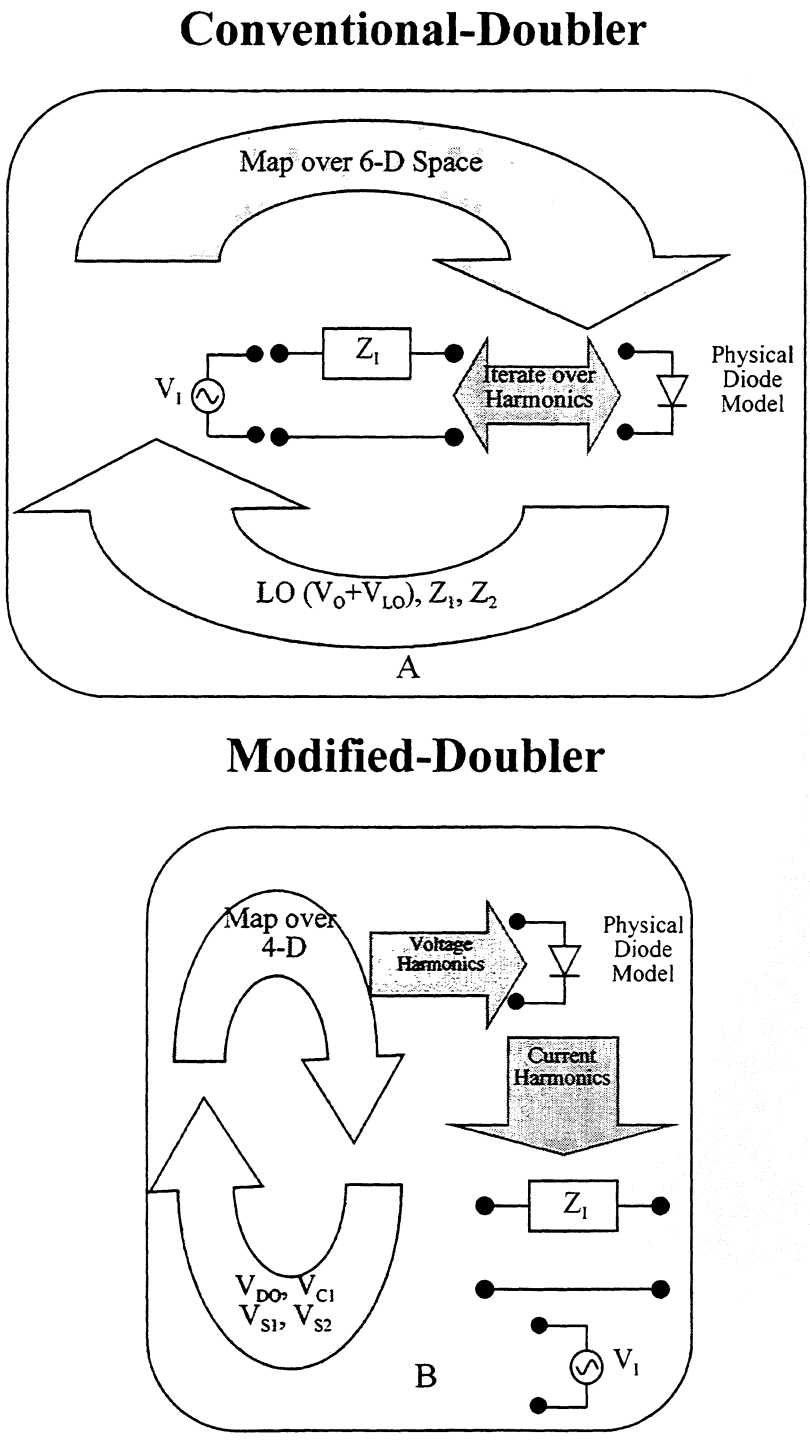

Figure 1. Comparison of harmonic-balance schemes. (A) The conventional-doubler approach requires a map over six system variables and iterations for the harmonic-balance. (B) The modified-doubler only requires a map over four system variables and no balance iterations.

Simulation Results

The modified harmonic-balance approach was utilized with the hydrodynamic diode model to study Schottky diode multiplier operation at a doubler-frequency of 200 GHz. Here, the earlier varactor diode investigations that were presented in [7] were considered for comparison purposes. The GaAs Schottky diode considered was a UVA-6P4 with an epitaxial doping density of $n_D \approx 3.5 \times 0^{16}\,\mathrm{cm}^{-3}$, epitaxial thickness of 1.0 μm, anode diameter 6.3 μm, series resistance 9.5 ohms and a breakdown voltage of 20 volts. The earlier studies in [7] were based upon a drift-diffusion diode-model. Hence, the studies presented here utilized both a simple depletion-region physical model and the hydrodynamic model presented in the last section.

The depletion-region (DR) diode model is based upon the familiar abrupt-junction approximation width depletion layer with w and neutral region width L-w. The thermionic emission current J_{TE} follows directly from Eqs. (15) and (16) and may, for the nondegenerate conditions considered here, be expressed as [8]

$$J_{TE} = q v_{rno} N_c \exp(-\frac{\phi_B}{k_B T_e})[\exp(\frac{qV_{bi}}{k_B T} - \frac{q^2 N_d w^2}{2\varepsilon k_B T}) - 1]. \tag{34}$$

The total particle and displacement current density for the diode is therefore given by

$$J_D = J_{TE} - qN_D \frac{\partial w}{\partial t}. \tag{35}$$

The system of equations resulting from application of the DR model to the diode are [9]

$$\frac{J_D L}{q\mu_o N_d} = V_D - V_{bi} + \frac{qN_d w^2}{2\varepsilon} \tag{36}$$

$$\frac{dw}{dt} + \frac{\mu_o}{L}(V_D - V_{bi} + \frac{qN_d w^2}{2\varepsilon}) - \frac{J_{TE}}{qN_d} = 0 \tag{37}$$

where ε is the permittivity, μ_0 is the low-field mobility and V_{bi} is the built-in potential. The DR model was utilized to provide an initial guess for the hydrodynamic simulator and for comparing to the final optimized results. The DR model and the modified harmonic-balance algorithm were used to estimate the optimum second-harmonic power of the Schottky-diode multiplier. The location this optimal power point in harmonic-space (i.e., V_{D0}, V_{C1}, V_{C2}, V_{S2}) was then used to define a new neighborhood for the hydrodynamic-based simulation algorithm. The hydrodynamic diode model simulator was used to generate the second-harmonic power map given in Fig. 2. Here, the second-harmonic power is mapped over the space (V_{C2},V_{S2}) at the optimal values V_{D0} = 8.6, and V_{C1} = 9.0. The results indicate the strongest dependence on V_{C2}.

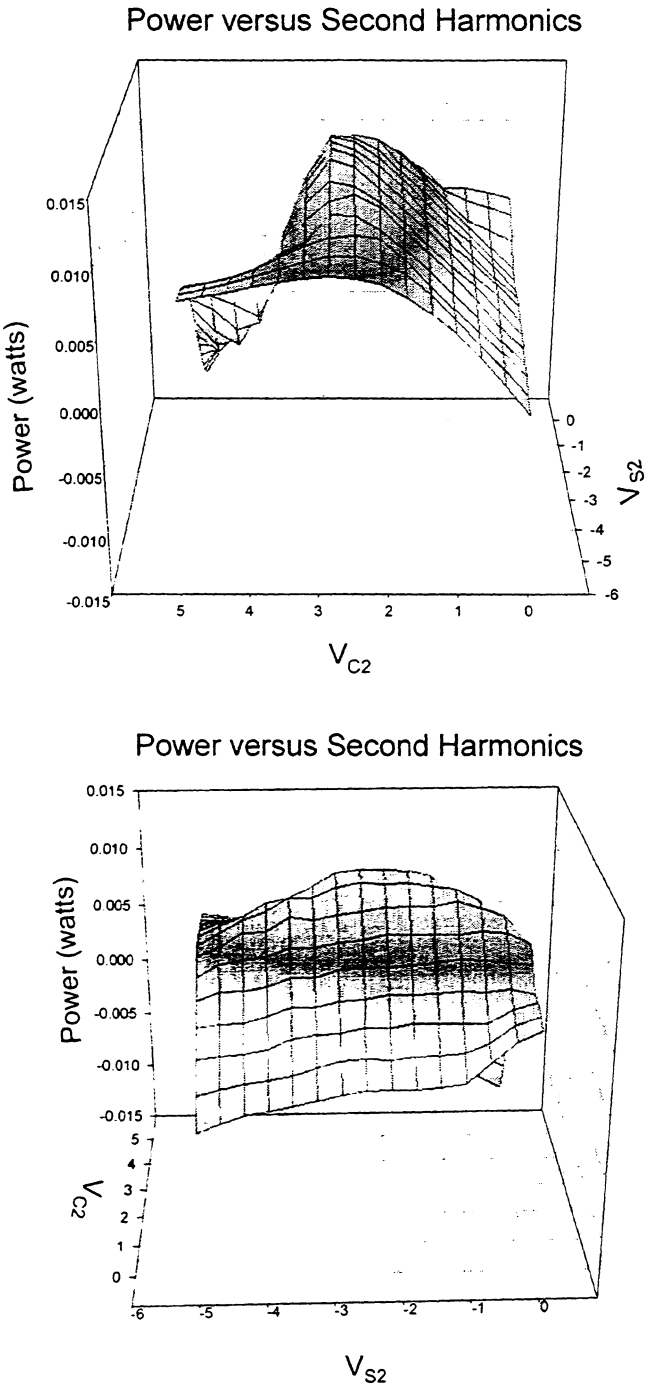

Figure 2. Second-Harmonic power versus second-harmonic voltages. Here, two perspectives are given to clearly show the variation along V_{C2} and V_{S2}.

The optimized results obtained from the hydrodynamic-based model are very close to the results from the DR model as shown in Table I-A. The very good agreement between both power and efficiency from the two models is not surprising since the frequency is much below the terahertz regime. These conclusions are further substantiated by the time-dependent results derived from the hydrodynamic model for electron charge-density and electron temperature given in Fig 3. As shown, the regular variation in the depletion-region edge (i.e., shown by the time-contour in Fig 3 (A)) and the nominal heating outside the depleted region are consistent with the assumptions of the simple DR model. The results are also in good agreement with the optimal power results, derived from the Monte Carlo transport model in reference [7]. These results are given in Table I-B. The discrepancy in the power results derived from the drift-diffusion model It is important to note that the results

Table I-A

Hydrodynamic Model with Modified HB		Depletion-Region Model with Modified HB	
Second Harmonic Power (mW)	P_{out}/P_{in} (%)	Second Harmonic Power (mW)	P_{out}/P_{in} (%)
13.03	60.34	12.57	57.06

Table I-B

MCHB simulator		DDHB simulator with weighted average a.c. mobility	
Second Harmonic Power (mW)	P_{out}/P_{in} (%)	Second Harmonic Power (mW)	P_{out}/P_{in} (%)
11.8	25.1	17.36	36.9

Table II-A

Hydrodynamic Model with Modified HB		Depletion-Region Model with Modified HB	
Z_1	Z_2	Z_1	Z_2
34+j251	41+j111	35+j253	40+j113

Table II-B

MCHB simulator		DDHB simulator with weighted average a.c. mobility	
Z_1	Z_2	Z_1	Z_2
62+j249	60+j128	39+j232	42+j117

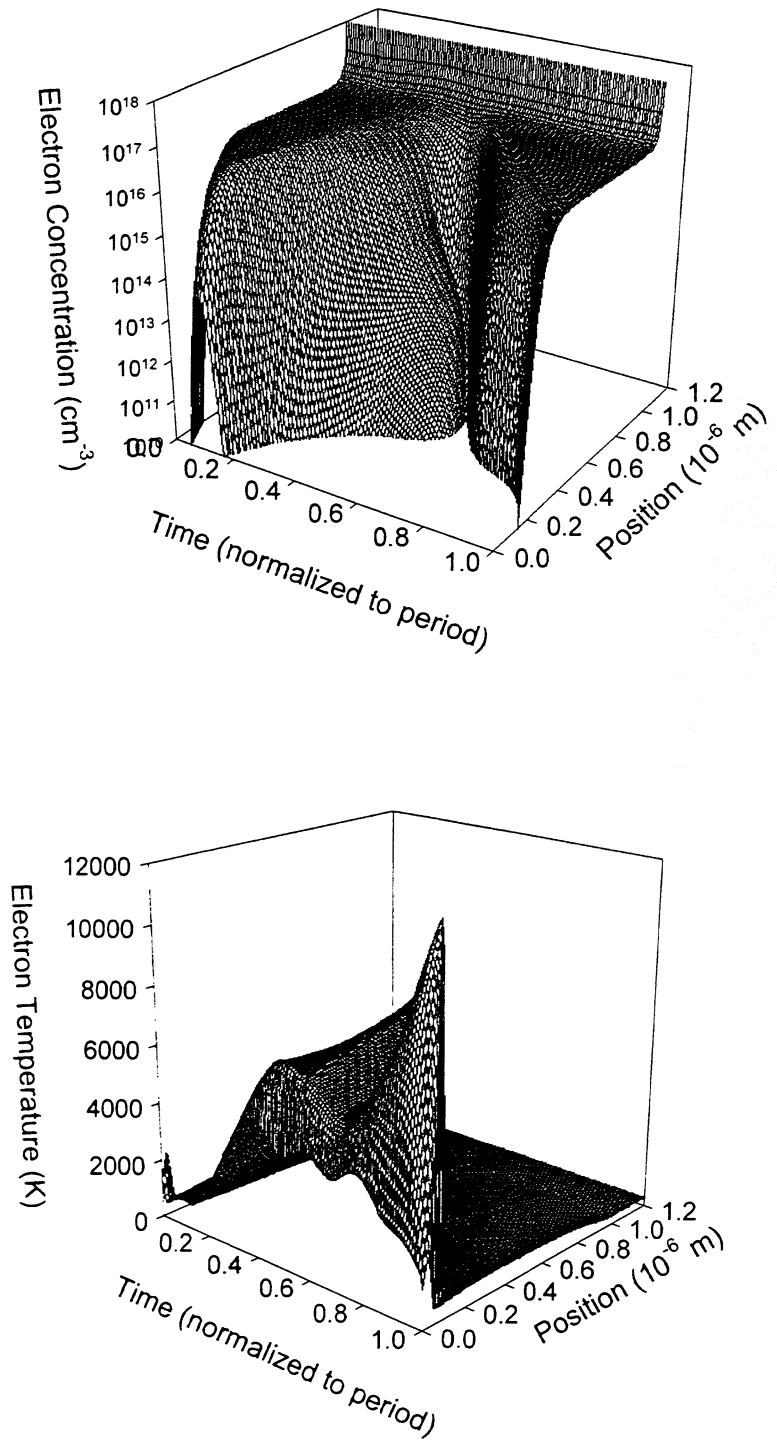

Figure 3. (A) electron density , and (B) electron temperature, versus position and time.

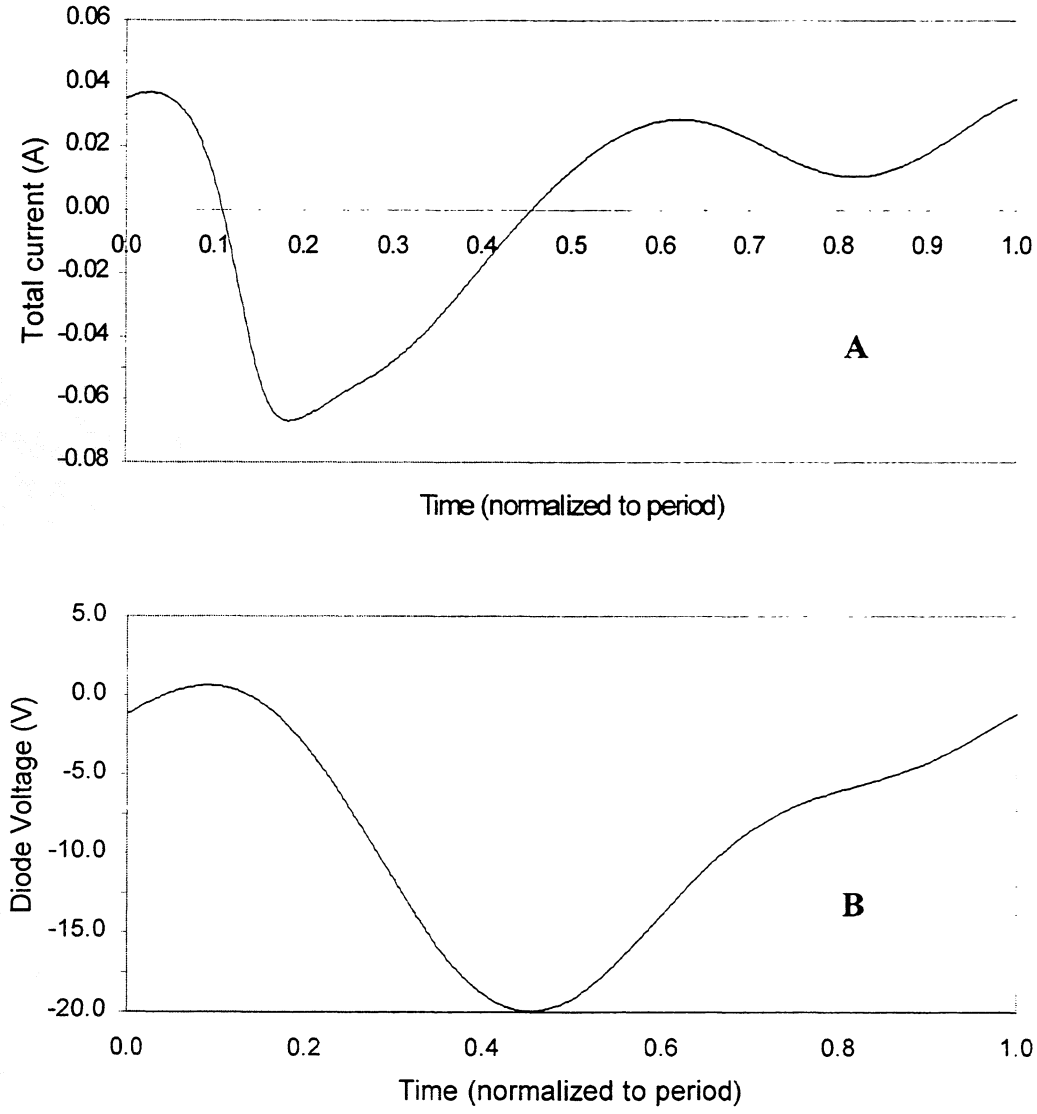

Figure 4. Large signal , (A) diode current density, (B) diode voltage derived from the hydrodynamic transport model.

for the time-dependent current and voltage waveforms of the UVA-6P4 diode, derived by the hydrodynamic model, are in very good agreement with those obtained from the Monte Carlo harmonic-balance simulator given in reference [7]. As shown in Fig. 4, the peak current density at the optimal power point was approximately *-0.06* amps. This peak value and the overall large-signal current-density characteristic are in almost exact agreement with the MCHB results from [7]. Conversely, the peak value in the large-signal voltage reported here is just below the breakdown value of *20* volts and this is significantly larger the value *~15* volts reported in [7]. It should be noted that the earlier studies in [7] used a constant dc bias voltage did not optimize over the dc bias voltage as was done here (i.e., optimal V_{D0} = *-8.6*). Hence, our preliminary conclusion is that the previous studies given in [7] did not arrive at the absolute optimal results. This is supported by the difference in embedding impedances for the two studies given in Table II-A and Table II-B. Future simulation studies are planned to resolve the issue of the absolute optimal biasing and embedding for this doubler design.

IV. CONCLUSIONS

This paper has applied a hydrodynamic transport model and a modified harmonic-balance algorithm to the problem of Schottky diode multiplier optimization. The results for a 100/200 doubler study have be compared to an earlier investigation that utilized Monte Carlo and Drift-Diffusion based harmonic-balance algorithms. These results show that this approach can be used to realize improved multiplier operation with a minimal expense of numerical computation. This model will be used in the future to optimize multiplier operation at terahertz frequencies. The physical model and optimization algorithm will be very important to integrated device design that seeks to optimize harmonic-power generation at very high frequencies.

ACKNOWLEDGEMENT

The authors wish to acknowledge the support of the MRCP Program of the Army Research Laboratory, Adelphi.

References.

[1] H. Hjelmgren , "Numerical Modeling of Hot Electrons in n-GaAs Schottky-Barrier Diodes," *IEEE Transactions on Electron Devices*, **37**, pp. 1228-1234 (1990).

[2] J. O. Nylander, F.Masszi, S. Selberherr and S. Berg , "Computer Simulations of Schottky Contacts with a Non-Constant Recombination Velocity," *Solid State Electronics*, **32**, pp. 363-367 (1989).

[3] S. A. Maas, *Nonlinear Microwave Circuits*, (Artech House, MA,1988).

[4] G. B. Tait, "Efficient Solution Method for Unified Nonlinear Microwave Circuit and Numerical Solid-State Device Simulation," *IEEE Microwave Guided Wave Letters,* **4**, pp. 420–422, December (1994).

[5] P. H. Siegel, A. R. Kerr, and W. Hwang, "Topics in the Optimization of Millimeter-Wave Mixers," *NASA Technical Papers*, no. 2287, March (1984).

[6] M. T. Faber, J. Chramies and M. E. Adamski, *Microwave and Millimeter-Wave Diode Frequency Multipliers*, (Artech House, MA, 1995).

[7] R. E. Lipsey, S. H. Jones, J. R. Jones, T. W. Crowe, L. F. Horvath, U. V. Bhapkar, and R. J. Mattauch, "Monte Carlo Harmonic-Balance and Drift-Diffusion Harmonic-Balance Analysis of 100-600 GHz Schottky Barrier Varactor Frequency Multipliers," *IEEE Transactions on Electron Devices*, **44**, pp. 1843-1850 (1997).

[8] B. L. Gelmont, D. L. Woolard, J. L. Hesler, and T. W. Crowe, "A Degenerately-Doped GaAs Schottky Diode Model Applicable to Terahertz Frequency Regime Operation," *IEEE Transactions on Electron Devices*, **45**, pp. 2521-2527, December (1998).

[9] D. L. Woolard, B. L. Gelmont, J. L. Hesler and T. W. Crowe, "Physical Aspects of GaAs Schottky Diode Operation at Terahertz Frequency," in Proceedings to 1997 International Device Research Symposium, December 10-13, The University of Virginia, Charlottesville (1997).

A 200 GHz Near Field Measurement System

C.C. Chin, S.C. Yang, Robert Hu and S.S. Shen
The Institute of Astronomy and Astrophysics,
Academia Sinica, Nankang,
Taipei, Taiwan

We have designed a near field measurement system operating at 200 GHz which has a dynamic range more than 60 dB. The system has a short term (over a period of a second) and long term phase variation (over a period of 15 to 20 minutes) less than 0.5 degree and 2 degree respectively. By turning on the averaging function of the network analyzer, each measurement point was averaged by an average number of 128, and then the short term phase variation decreases to less than 0.2 degree. The phase of the system did not vary more than 2 degrees during the measurement, which took approximately 4 hours. The contours of the near field obtained shows that the field is highly circular as expected from the theoretical predication. In our talk, we will give the details of the design of the near field measurement system and the method of data corrections. We will also demonstrate that the system can distinguish the quality of the corrugated feed horns.

THE DESIGN CONCEPT OF A TERAHERTZ IMAGER USING A Ge:Ga PHOTOCONDUCTOR 2D ARRAY

Ken-ichi Watabe, Mikio Fujiwara, and Norihisa Hiromoto
Communications Research Laboratory, Ministry of Posts and Telecommunications
4-2-1 Nukui-kita, Koganei, Tokyo 184-8795, Japan.

ABSTRACT

A terahertz (3-THz band) camera using a gallium-doped germanium (Ge:Ga) photoconductor two-dimensional (2D) direct hybrid array is proposed. We describe the design concept of the camera, which has high spatial resolution, high responsivity, and photon-noise-limited noise equivalent power (NEP).

INTRODUCTION

Terahertz imaging has applications in the spectroscopy of molecules and solids, biology, astronomy, plasma diagnostics, etc. Conventional terahertz imaging mainly uses a single detector and a scanning mechanism [1], [2]. The use of such multiple detectors as a detector array, however, eliminates the need of mechanical scanning and makes video-rate (30-Hz frame rates) imaging possible. We are developing a terahertz passive camera using a 20×3 Ge:Ga terahertz photoconductor 2D direct hybrid array [3], [4]: the camera still uses mechanical scanning but the number of scans necessary for taking a 2D image is greatly reduced as a result of using the array detector.

Ge:Ga 2D ARRAY

The Ge:Ga photoconductor [5] detector array has a format of 20×3, with a unit sensitive area of 0.5×0.5 mm^2. The pixel pitch of the detector array is 0.55 mm and the detector has high responsivity and photon-noise-limited NEP. Crosstalk between neighboring detectors is less than 5 %. The Ge:Ga photoconductor array is directly hybridized to a cryogenic Si-pMOS FET readout circuit with 20×3 format each of which is a source-follower-per-detector type circuit.

DESIGN OF TERAHERTZ CAMERA SYSTEM

A configuration of the terahertz camera is shown in Fig. 1. The optical system was designed to have a spatial resolution of 0.5 mm, a dimension of 120×120 pixels, a magnification of 1.1, and an effective F-number of 4.5. The optics has been designed by using a ray tracing method. An example of the ray trace is illustrated in Fig. 2. The

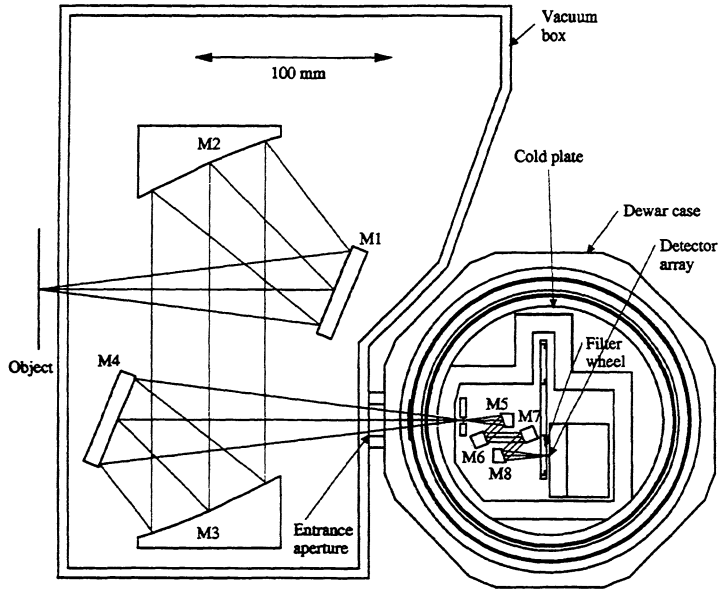

Fig. 1. Schematic layout of the terahertz camera.

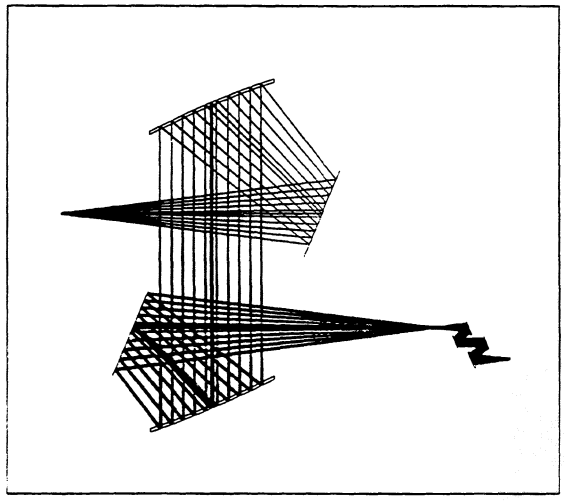

Fig. 2. Ray tracing for designing optics.

optics consists of eight mirrors: mirrors M1, M2, M3 and M4 are in the vacuum box of ~ 10^{-3} Torr at room temperature, and mirrors M5, M6, M7 and M8 are cooled at 4.2 K in a 5-inch helium dewar. The distance between object and M1 is 150 mm. The beam is collimated by M2 and forwarded to the decollimator of M3 which focuses again at an entrance aperture of the dewar via the flat mirror of M4. An expanding beam inside the dewar is collimated by M5, and forwarded to the flat mirrors of M6 and M7, the latter of which is aperture stop. The decollimator of M8 reflects and focuses the beam on the 20 × 3 Ge:Ga detector array through the filter wheel. A long axis of the detector array is perpendicular to a plane on which the optical axis of the beam is arranged. The flat mirror of M1 is continuously scanned in the horizontal direction and it is shifted in the

vertical direction by 6 times to take an image of 120 × 120 pixels, and the offset paraboloid mirror of M2 is straightly scanned on the optical axis to the M1 in order to adjust the focal depth. Ray tracing indicates that spot sizes (Fig. 3) are less than 0.25 mm even for the worst (off-axis edge) pixels, well below the pixel size of 0.5 mm square, and the image distortion is about 10 % of the pixel size even for the worst pixels. This implies that the performance of this optics is sufficient for the required resolution and the distortion. A field of view (60 × 60 mm^2) will be useful in observing biological and biomedical objects, such as a leaf or a skin of a human being.

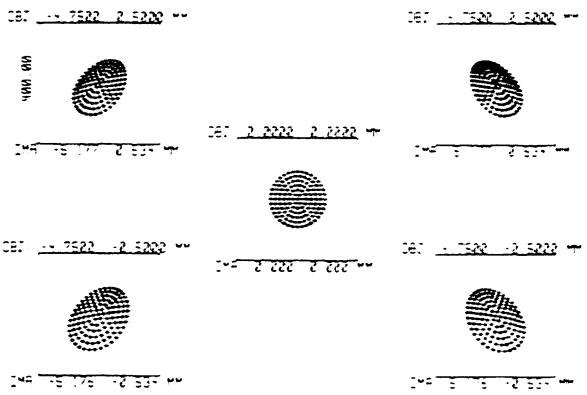

Fig. 3. Spot diagrams for the camera optics. OBJ is the position of object point, and IMA is the image point. The squares are 0.4 mm in size.

Better spatial resolution up to the wavelength of light can be obtained by decreasing a F-ratio of the input optics down to one-fifth of the present design.

ESTIMATED PERFORMANCE OF TERAHERTZ CAMERA

The camera will be used to map spatial variation in the terahertz properties of objects such as dielectric constants, emissivity, absorbance, and temperature, including the spectral properties of dielectrics and semiconductors, superconductors, biological objects, liquids, and gases. We estimate that noise equivalent temperature difference (NETD) at a background of 300 K is 0.09 K (Table I) for each area of 0.45 × 0.45 mm^2 with emissivity of 1.0, when it is measured with the object space of F-number of 4.1, spectral range of 300 GHz, and a integration time of 0.2 ms, which corresponds to a frame rate of 1.7 Hz. The optical quantum efficiency of the detector is supposed to be about 0.2. In the measurement of biological objects, we can, for example, detect the water content of a leaf because the emissivity of the water is different from that of leaf. We will obtain a signal-to-noise ratio of 49 dB for emissivity of 0.96 (water) and 0.90 (leaf). Better NETD can be obtained by increasing the integration time, decreasing the F-ratio of the input optics and increasing the spectral range. We can, for example, obtain NETD of 0.009 K by adopting an integration time of 6.1 ms and an input optics's F-ratio of 0.9. Using illumination of terahertz light, we will be able to have much higher contrast, because the water content inside the leaf causes strong absorption of far-

infrared light. If far-infrared light of 1 mW is illuminated at behind the sample, a signal-to-noise ratio will increase to 79 dB.

TABLE I
Specifications and performance of the terahertz camera

Resolution of each detector	0.45×0.45 mm^2
F-number of object space	4.1
Field of view	60×60 mm^2
Format of array	20×3
Quantum efficiency	0.2
Spectral range	300 GHz
Minimum integration time	0.2 ms
Background	300 K
Emissivity of object	1.0
NETD (Noise equivalent temperature difference)	0.09 K

CONCLUSION

In this paper, we proposed a novel concept for the terahertz imaging system using Ge:Ga photoconductor array. The camera will have high performance for taking terahertz images with high resolution, high responsivity, and high S/N ratio. Construction of the camera system is progressing and applications to imaging of various materials including biological and biomedical objects will be carried out in the future work.

REFERENCES

[1] B. B. Hu and M. C. Nuss, "Imaging with terahertz waves," Opt. Lett. vol. 20, no. 16, pp. 1716-1719, 1995.

[2] S. Hunsche, D. M. Mittleman, M. Koch and M. C. Nuss, "New dimensions in T-ray imaging," IEICE Trans. Electron., vol. E81-C, no. 2, pp. 269-275, 1998.

[3] N. Hiromoto, M. Fujiwara, H. Shibai, T. Hirao, T. Nakagawa, and M. Kawada, "Ge:Ga far-infrared photoconductor 2D direct hybrid array," SPIE 3354, pp. 48-56, 1998.

[4] M. Fujiwara, N. Hiromoto, H. Shibai, T. Hirao, and T. Nakagawa, "Fabrication of Ge:Ga far infrared photoconductor two-dimensional array," Conf. Digest of 23rd Int. Conf. on IR&MMW, pp. 210-211, Sept.1998.

[5] N. Hiromoto, M. Fujiwara, H. Shibai, and H. Okuda, "Ge:Ga far infrared photoconductors for space applications," Jpn. J. Appl. Phys. vol. 35, no. 3, pp. 1676-1680, 1996.

A folded Fabry-Perot diplexer of triangular shape.

Herman van de Stadt

Space Research Organization Netherlands,
SRON, PO box 800, 9700 AV Groningen, The Netherlands.

fax +31 503634033, h.vandestadt@sron.rug.nl

10th Space THz Symposium, Charlottesville, March 16-18, 1999.

ABSTRACT.

In this paper we present a novel triangular, multiple-beam diplexer. Its properties are compared with existing square diplexers. Our triangular folded Fabry-Perot (FFP) diplexer is a ring-interferometer consisting of two partially-transparent mesh filters and a slightly concave mirror. The reflector is tunable in position and the three components are mounted in the shape of a triangle with 60-degree angles. The purpose of the diplexer is to superimpose a signal and a local oscillator (LO) beam with frequencies of order 1 THz and a difference frequency of order 10 GHz.

INTRODUCTION.

The operation of a THz heterodyne receiver in space requires a large IF bandwidth in order to increase the speed of line surveys and to allow observation of broad weak line emission from distant galaxies. For example the HIFI instrument on board of FIRST will have a 4 GHz IF bandwidth for RF frequencies ranging from 480 GHz to over 2.5 THz [1].

For efficient coupling of the signal and the local oscillator (LO) power to the mixer one often uses diplexers to combine the signal and LO beams. A diplexer is an interferometer allowing nearly loss-less superposition of two beams of different frequency. The optical path length in the interferometer, L_{opt}, is related to the difference, or intermediate frequency IF by:

$$L_{opt} = c / (2\ IF) \qquad (1)$$

The usual diplexer in heterodyne receivers is a dual-beam, polarizing Martin-Puplett [2] interferometer, (MP). However, its transmission is sinusoidal as a function of frequency, which makes this interferometer less suitable for wide IF bandwidths. Wide

bandwidths have been achieved with multiple-beam interferometers of the Fabry-Perot type in a folded version, originally proposed by Gustincic [3]. General properties of the mentioned interferometers are described in ref [4].

In table I we give the calculated efficiency (i.e. transmission) of a loss-less MP diplexer in the case of a 6 and a 10 GHz IF center frequency and 4 GHz bandwidth. Also given is the efficiency (i.e. reflection) of a loss-less FFP diplexer for the same IF frequencies and for mirror reflectivities of 67% and 77%, i.e. a finesse of 7.8 and 12.0, respectively .

Diplexer type	Efficiency @ IF center frequency	Efficiency @ IF center freq. ± 2 GHz
Martin-Puplett @ IF= 6 GHz	1.0	0.75
Idem @ IF=10 GHz	1.0	0.90
Fabry-Perot, R=0.67 @ IF= 6 GHz	0.961	0.949
Idem, @ IF=10 GHz	0.961	0.957
Fabry-Perot, R=0.77 @ IF= 6 GHz	0.983	0.978
Idem, @ IF=10 GHz	0.983	0.981

Table I: Calculated efficiency of loss-less diplexers with 4 GHz bandwidth.

In practice diplexers are never loss-less. Some sources of loss can be:
- coupling losses because of small diplexer size as compared to QO beam size,
- scattering or absorption losses at wire grids or mesh filters,
- coupling losses due to imperfect re-imaging of multiple beams,
- imperfect angular alignment of diplexers' optical components.

Design aspects of our triangular diplexer will be discussed in this paper against the background of the mentioned loss mechanisms. Some measurements illustrate its performance.

DESIGN AND QUASI-OPTICAL PROPERTIES .

Figure 1 gives a schematic diagram of the triangular FFP. The signal beam is reflected upon incidence on the first mesh filter, while the LO is transmitted by the FFP after incidence on the other mesh. Note that the reflector and the meshes have a width W and that the roundtrip path of the multiple reflected beams is:

$$L_{opt} = 3\ W / 2 \qquad (2)$$

The curvature of the reflector is such that it re-images the minimum beam waist, w0, of the quasi-optical beams at a distance z_f from the center of the mirror, where

$$z_f = 3\ W / 4 \qquad (3)$$

Note however that this does not mean that the focal distance of the mirror is z_f, except in the case that the FFP is used in the far-field region of the propagating beams. We will come back to this later on.

Figure 2 is a graph of the calculated reflection of LO and signal beams for an FFP with R=0.67. The figure illustrates the case that ΔIF is 2/3 of the center IF frequency, representing a bandwidth of one octave.

Propagation of a wavefront with beam radius w(z) at distance z from the (minimum) waist w0 goes as:

$$w(z)^2 = w0^2 (1 + z^2/z_R^2) \qquad (4)$$

, where $z_R = \pi\, w0^2 / \lambda$ is the confocal or Rayleigh distance, see ref [4], eq. (2.21b), and w0 is the beam waist radius. If we require that the mirror must have a projected size sufficiently large for 4 beam radii, we have approximately:

$$W = 4\, w(z_f)\, 2 / \sqrt{3} \qquad (5)$$

Combination of eqs. (5) and (4) with $z = z_f$ (3) gives:

$$(w0)^4 - 3\, W^2\, (w0)^2 / 64 + 9\, W^2\, \lambda^2 / (16\, \pi)^2 = 0 \qquad (6)$$

Solving this equation for w0 gives the two values of w0 for the extreme cases of near- and the far-field. The minimum value of the expression yields the size of w0 for the case of confocal imaging.

As an example we take IF = 6 GHz and f = 800 GHz, i.e. λ = 0.375 mm. This yields L_{opt} = 25 mm, W = 16.67 mm and z_f = 12.5 mm. In table II we summarize the values for w0 and $w(z_f)$ for the near-field, confocal field and the far-field. This is further illustrated in figure 3, where the propagating beam waists at – w and –w are drawn.

	w0 (mm)	$w(z_f)$ (mm)	z_R (mm)
Near-field	3.58	3.61	107.6
Confocal	1.22	1.73	12.5
Far-field	0.42	3.61	1.45

Table II: Quasi-optical parameters of a triangular FFP with IF = 6 GHz and f = 800 GHz.

From table II and figure 3 it can be seen that in the confocal case the beam does not use the corners of the diplexer and allows ample space for mechanical support of the mesh filters. In the near-field and far-field however there is no space for mechanical support, making these extreme cases not realistic for beam diameters of 4 waists. In other words the efficiency of the diplexer will be reduced by truncation of the beams.

The question is whether there will always be a confocal situation possible. The answer is that this depends on frequency: there will be a lowest frequency where 4 beam waists are just transmitted by the diplexer. The minimum frequency is determined by calculating the value of λ for which eq. (6) has a single root. This gives:

$$f_{min} = 96\ IF / \pi \qquad (7)$$

For IF = 6 GHz we find 183 GHz as the minimum frequency of a triangular diplexer. This is much lower than the value of 489 GHz, which we find for an equivalent square diplexer.

MIRROR CURVATURE.

The radius of curvature, R(z), of a Gaussian beam propagating along the z axis is described by the following equation:

$$R(z) = z\,(1 + z_R^2 / z^2) \qquad (8)$$

, where z_R is the confocal distance as before. The mirror of the diplexer should have an elliptical shape in order to match the Gaussian beam wavefront, see ref [5]. For a triangular diplexer the angle of incidence is 30°, which means that the semi-major axis of the ellipse is $a = R_f = R(z_f)$, where R_f is the radius of curvature of the wavefront when it hits the mirror. This is further illustrated in figure 4. Note that R_f is always larger than z_f, except in the far-field, where R_f is approaching z_f because $z >> z_R$. The effective radii of curvature of the elliptical mirror in the horizontal and vertical direction are:

$$R_{hor} = 2\,R_f/\sqrt{3} \qquad \text{and} \qquad R_{vert} = R_f\sqrt{3}/2 \qquad (9)$$

For example in the earlier case with IF = 6 GHz and f = 800 GHz we find the following values:

	Confocal distance, z_R (mm)	Wavefront radius of curvature, R_f (mm)	Horizontal radius of ellipse, R_{hor} (mm)	Vertical radius of ellipse, R_{vert} (mm)
Near-field	107.6	939.3	1085	813
Confocal	12.5	25	28.88	21.65
Far-field	1.45	12.67	14.63	10.97

Table III: Properties of the elliptical mirror in a triangular diplexer for IF = 6 GHz and f = 800 GHz.

POLARIZATION.

The resonant frequencies in a triangular diplexer are polarization dependent because of the odd number of reflections. This is not a problem in general, since the LO and signal beams need to have identical polarizations (linear in horizontal or vertical direction) anyway. For the LO beam it means that the cross-polarized component of the beam is not transmitted by the triangular diplexer.

BEAM SYMMETRY.

Off-axis beams propagate through the triangular FFP in an asymmetric way. This is illustrated in figure 5, which gives the trajectories for the central beam and one off-axis beam. After multiple reflections inside the interferometer the off-axis beam propagates alternately above and below the central beam. For symmetric beam modes this is not a problem, since the round-trip optical path is independent on the amount of offset. However, asymmetric modes with 180° phase difference between the upper and lower halves of their mode pattern will be attenuated by this phenomenon.

COMPARISON BETWEEN TRIANGULAR AND SQUARE FFPs.

In the preceding sections we have derived equations for triangular FFPs. Similar equations have been derived for square FFPs (ref [5]) and can be derived for modified versions of triangular FFPs.

In table IV, at the end of this paper, we give parameters of four different FFPs:
1. a square FFP with a single curved mirror,
2. the same as 1, but with 2 curved mirrors,
3. the triangular FFP as described in this paper,
4. a diamond FFP with 60° top angle.

Relevant parameters have been mentioned in the preceding chapters. To quantify the various parameters in the table we calculated the values for the case IF=6 GHz and f=800 GHz, which may be applicable to the HIFI instrument of FIRST.

In order to get a feel of the optical aperture of the beams we added to the table the so-called F-ratio. This parameter, F/D, corresponds to an 11 dB edge taper, i.e. we assumed an "optical diameter", D, for which the beam waist radius in the far field is w = 0.889 D/2. This applies e.g. to the quasi-optical beam at the secondary mirror of the FIRST telescope.

From table IV we can see that the triangular FFP has the lowest f_{min} and consequently the widest range of possible F/D ratios. The diamond shaped FFP can be regarded as a deformed square FFP with the advantage that the focal distance, z_f, of the mirrors is more than 4 times larger. This means that the mirror in the diamond FFP will

be much less strongly curved than in the square case. Moreover, the resonances of the diamond FFP are independent of polarization, in contrast to the triangle FFP.

The square FFP with a single curved mirror offers a minimum of flexibility for the chosen frequency: in its confocal case we have w0 = 1.22 mm, which means that 4 beam radii at the mirror (4 w0 $\sqrt{2}$ = 6.9 mm) is larger than the projected mirror size (W $\sqrt{2}$ = 5.72 mm). This is equivalent to saying that only 3.6 beam radii fit instead of the desired 4 beam radii.

ALTERNATIVE CONFIGURATIONS.

Many alternative configurations of FFPs can be thought of. However, it is not possible to combine any set of FFPs like with a box of bricks, because the images of multiple beams must be coinciding.

We want to mention one version consisting of two triangles in series: see figure 6. Effectively this is a 3-mirror FFP, discussed in the literature [6] and actually tested at 490 GHz [7, 8]. One advantage of this configuration is that the transmission peak for the LO becomes wider without reducing the reflection of the signal. Thus the required tuning accuracy is reduced. Another advantage is that the two outer reflectors can have a much-reduced reflectivity, R1 = R3 = 0.243, so that presumably scattering and/or absorption losses in the 2 outer grids will be reduced. Moreover, the asymmetry for off-axis beams, as was illustrated in figure 5 for a single triangular FFP, is now removed.

However, disadvantages of the setup of figure 5 are as follows. The 2 triangles need to have identical optical pathlengths and the tuning mechanism must maintain this equality. Also, in this design the difference in resonances between the two linear polarizations still exists.

EXPERIMENTAL RESULTS.

The use of a square FFP was recently reported [9] at IF = 6 GHz and f=640 GHz. Another application of square FFPs can be found in ref [10], describing the heterodyne instrument in UARS-MLS, where an FFP is used for frequencies of 205 and 268 GHz.

At SRON we have built a prototype triangular FFP using 2 inductive, nickel mesh filters of 150 lines/inch providing a reflectivity of about 73% and a plane reference reflector. The measured reflection and transmission as a function of mirror position are given in figure 7 for a frequency of about 345 GHz.

The magnitude of scattering and absorption losses in mesh filters are not well known, but will certainly be present. In this respect further tests on triangular FFPs need to be performed in the future.

CONCLUSIONS.

THz heterodyne receivers in space require the use of diplexers in order to efficiently couple the available LO power to the mixer. Application of a folded Fabry-Perot (FFP) diplexer is especially useful in heterodyne receivers requiring a wide IF bandwidth for a relatively low IF center frequency.

In this paper we described the properties of an FFP with triangular cross-section. The main advantage over the usual FFP with square cross-section is the larger size of the triangle, allowing accommodation of a much wider range of different beam sizes. We have demonstrated the feasibility with a prototype triangular FFP.

ACKNOWLEDGEMENTS.

The author wants to thank Th. de Graauw, N. Whyborn and P. Zimmermann for stimulating this research and D. Beintema for carefully reading the manuscript.

REFERENCES.

[1] N.D. Whyborn, "The HIFI heterodyne instrument for FIRST: Capabilities and Performance", Proc. of ESA symp The Far Infrared and Submillimetre Universe, Grenoble, ESA SP-401, p.19-24, Aug 1997.

[2] D.H. Martin and E. Puplett, "Polarised Interferometric Spectroscopy for the Millimetre and Sub-millimetre Spectrum", Infrared Phys., 10, 105 (1969).

[3] J.J. Gustincic, "A quasi-optical receiver design", IEEE-MTT-S Int. Microwave Symp. Dig., 99-101, 1977.

[4] P.F. Goldsmith, "Quasi-Optical Systems", IEEE press, ISBN 0-7803-3439-6, 1998.

[5] H.M. Pickett and A.E.T. Chiou, "Folded Fabry-Perot Quasi-Optical Ring Resonator Diplexer: Theory and Experiment," IEEE Trans. Microwave Theory Tech. **MTT-31**, 373 (1983).

[6] M.M. Pradhan, "Multigrid Interference Filters for the Far Infrared Region", Infr. Phys., Vol. 11, 241-245, 1971.

[7] H. van de Stadt and J.M. Muller, "Multimirror Fabry-Perot interferometers", JOSA, A2, 1363-1370, 1985.

[8] S.J. Hogeveen and H. van de Stadt, "Fabry-Perot interferometers with three mirrors", Appl. Opt, 25, 4181-4184, 1986.

[9] P.H. Siegel et al. , "A 640 GHz Planar-Diode Fundamental Mixer/Receiver", preprint, June 1998.

[10] "Eos MLS Instrument Conceptual Design", ESA conference report, Appendix B-1, 1997.

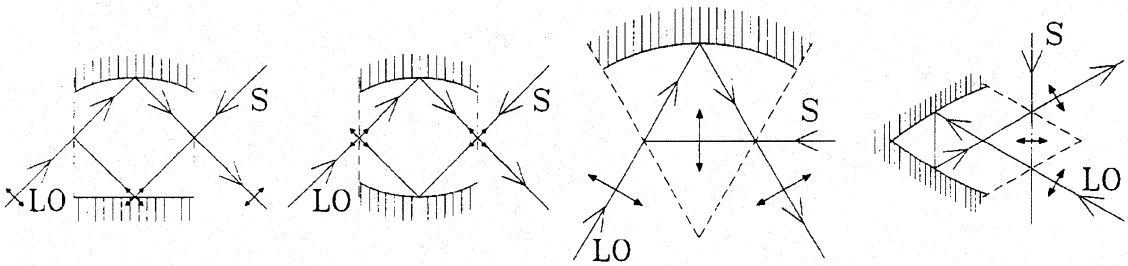

Square 1 Square 2 Triangle Diamond

	Square 1	Square 2	Triangle	Diamond
Size W	W1 = c / (4√2 IF)	W2 = W1	W3 = c / (3 IF)	W4 = c / (6 IF)
Optical Path L_{opt}	2 W1 √2	2 W2 √2	3 W3 / 2	3 W4
Focal distance z_f	W1 √2	W2 / √2	3 W3 /4	5 W4 / 4
Minimum freq. f_{min}	512 IF / π	256 IF / π	96 IF / π	320 IF / π
Values for IF=6 GHz and f = 800 GHz				
W	8.84 mm	8.84 mm	16.67 mm	8.33 mm
Zf	4.42 mm	2.21 mm	12.50 mm	10.41 mm
f_{min}	978 GHz	489 GHz	184 GHz	612 GHz
wO for Near field	-	1.48 mm	3.58 mm	1.64 mm
wO for Confocal	(1.22 mm) *	0.86 mm	1.22 mm	1.12 mm
wO for Far field	-	0.51 mm	0.42 mm	0.76 mm
F/D for beam with 11 dB edge taper.				
F/D for Near field	-	5.51	13.35	6.09
F/D for Confocal	-	3.22	4.55	4.15
F/D for Far field	-	1.88	1.55	2.83

Table IV: Summary of properties of different types of folded Fabry-Perot diplexers. The *symbol indicates that the design frequency is lower than the minimum frequency.

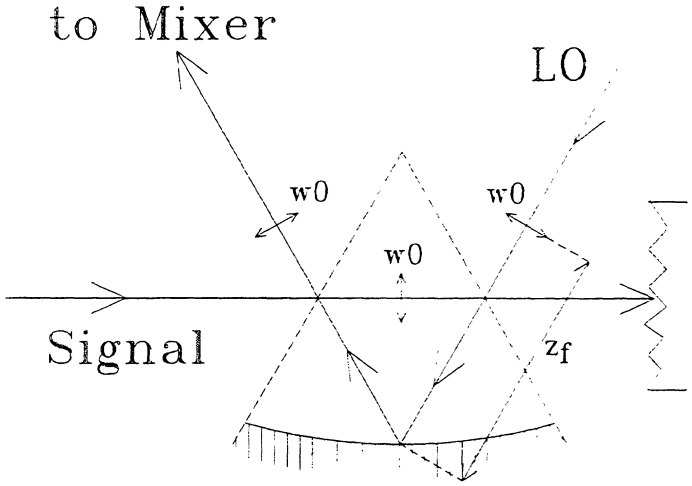

Figure 1: Schematic diagram of a triangular FFP.

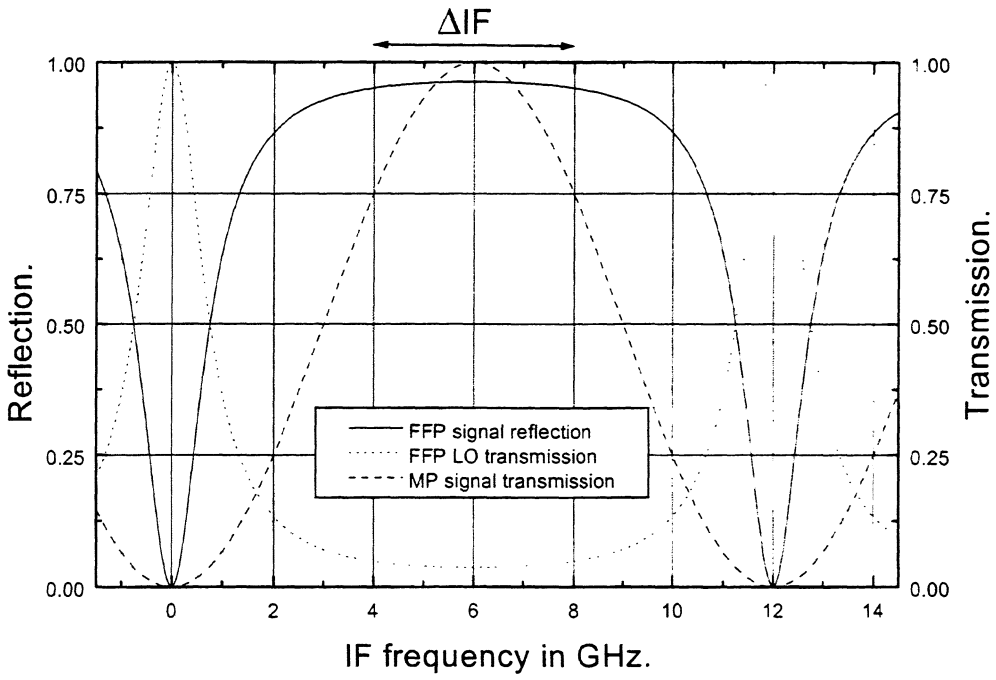

Figure 2: Calculated reflection of the signal beam and transmission of LO beam in a FFP with R = 0.67. For comparison we also give the transmission of a Martin Puplett interferometer.

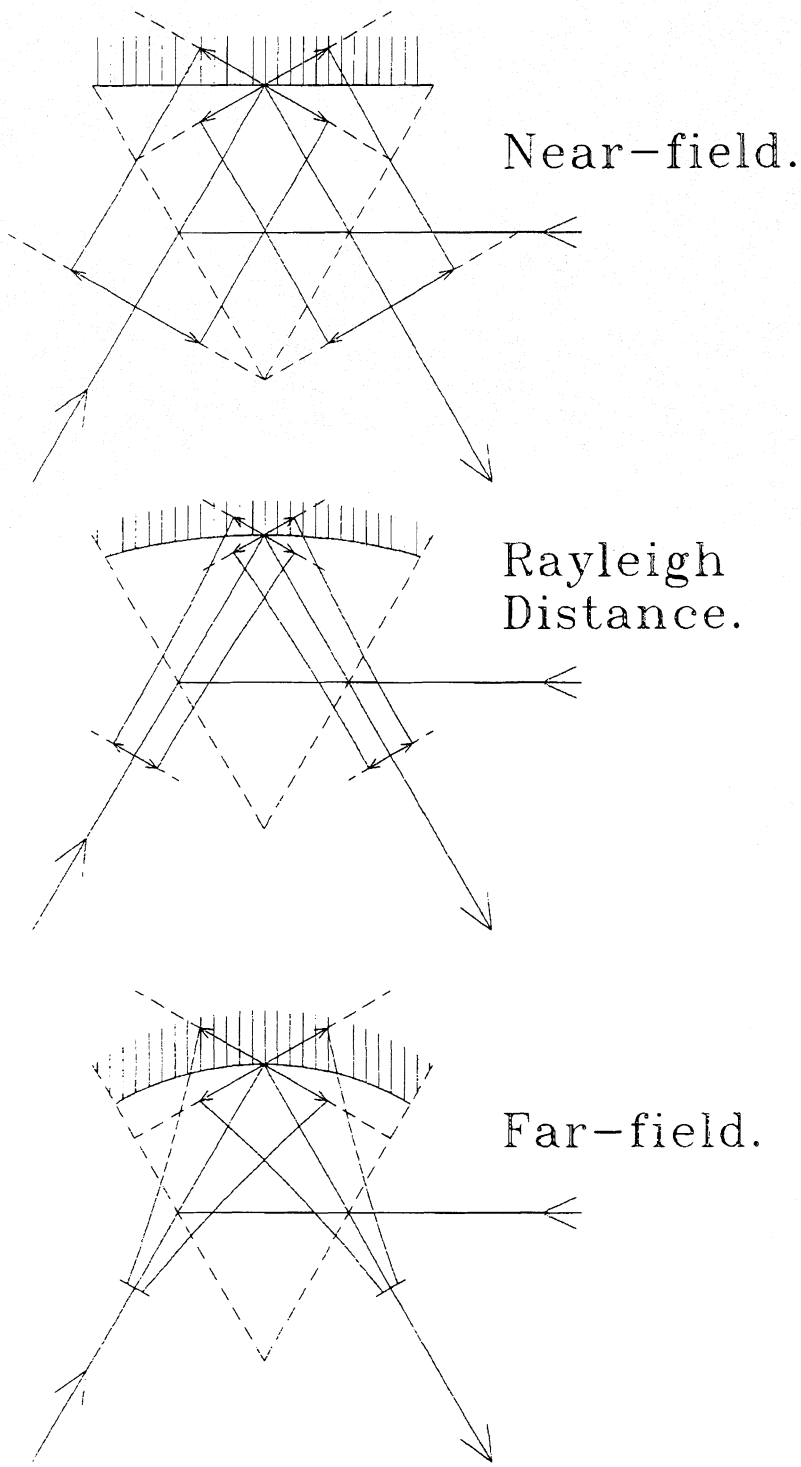

Figure 3: Quasi-optical beam trajectories in a triangular FFP for IF = 6 GHz and f = 800 GHz. The pictures are an illustration of the values in Table II.

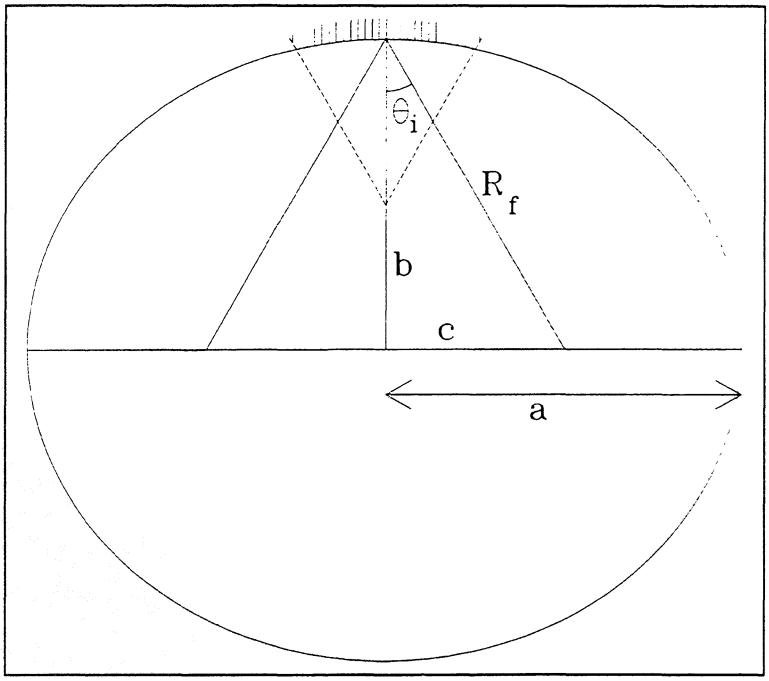

$\theta_i = 30°$

$a = R_f = 2\,c \qquad \epsilon = 0.5$

$c = a/2 \qquad b = a\sqrt{3}/2$

Figure 4a: Geometry of the elliptical reflector in a triangular FFP with $\theta_i = 30°$.

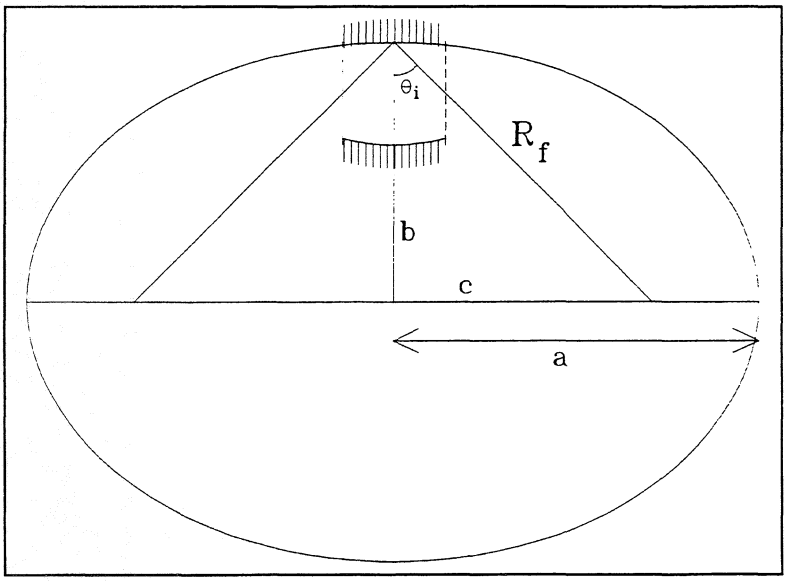

$\theta_i = 45°$

$a = R_f = c\sqrt{2} \qquad \epsilon = 1/\sqrt{2}$

$c = b = a/\sqrt{2}$

Figure 4b: Geometry of the elliptical reflector in a square FFP with. $\theta_i = 45°$.

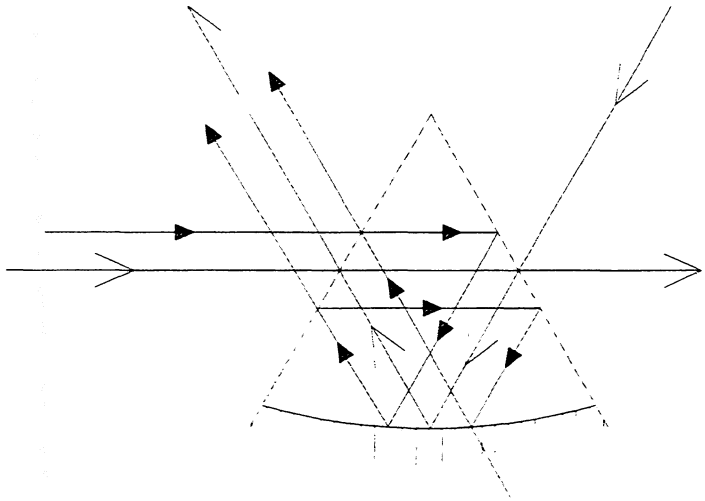

Figure 5: Trajectories of off-axis beams in a triangular FFP.

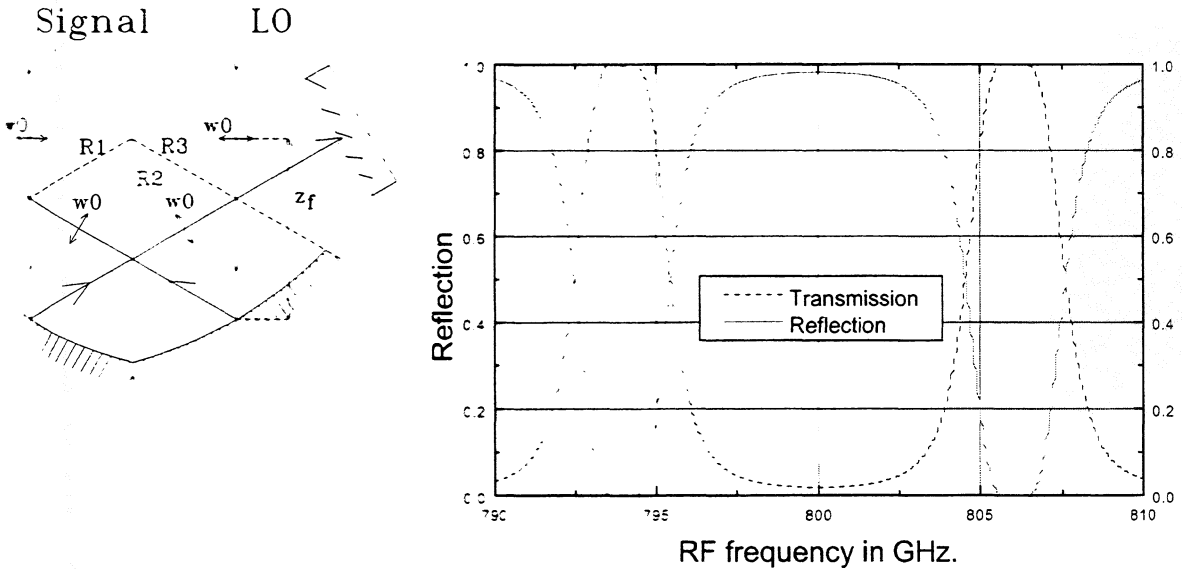

Figure 6: Configuration with 2 triangular FFPs in series. Transmission is calculated for R1 = R3 = 0.243 and R2 = 0.664.

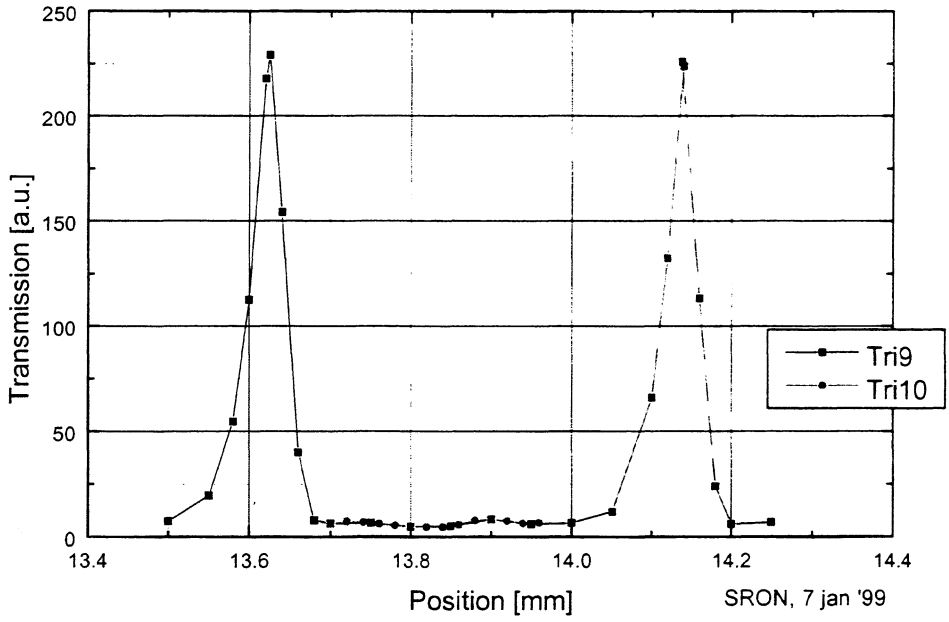

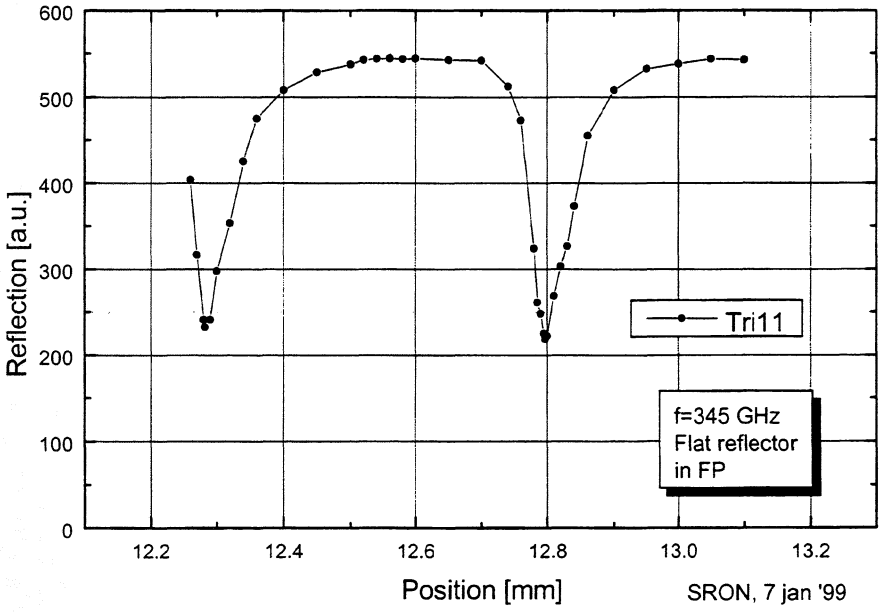

Figure 7: Transmission & reflection measured with prototype of triangular FFP at f ≅ 345 GHz.

THEORETICAL ANALYSIS OF THE POTTER HORN-REFLECTOR ANTENNA FOR SUBMILLIMETRE-WAVE APPLICATIONS

G. YASSIN, S. WITHINGTON, P. KITTARA AND K. G. ISAAK
Department of Physics, University of Cambridge,
Madingley Road, Cambridge CB3 OHE, UK

ABSTRACT We present a new horn-reflector feed design for SIS mixers. The antenna comprises an offset parabolic reflector fed by a Picket-Potter horn. The horn is easy to machine, and yet still preserves the desirable electrical properties of a corrugated horn, namely low cross polarisation and low sidelobe level, albeit over a reduced bandwidth. We calculate the aperture field distribution and the scattering matrix of the horn using the modal matching method and provide design curves which show the dependence of the beamwidth and the cross polarisation level on the antenna design parameters.

INTRODUCTION

The horn-reflector antenna is an offset parabolic reflector fed by a metallic horn. This arrangement is used to increase the aperture efficiency of the antenna without using lenses. When fed by a corrugated horn, the antenna has the additional advantage of low cross polarisation and sidelobe level. In a previous publication (Withington *et. al*, 1996) we demonstrated that this antenna is suitable for SIS mixer optics, guaranteeing efficient coupling between the telescope and the SIS detector over a large bandwidth. Such good performance, however, can only be achieved if a high rate of corrugations is maintained deep in the throat of the horn in order to prevent the excitation of higher order modes. Clearly, machining of corrugations in the horn throat at submillimetre-wavelengths is difficult, and the practical realisation of this unique design becomes very awkward at THz frequencies, and very expensive and time consuming for imaging arrays.

In this paper we present a new horn-reflector antenna design which employs a Picket-Potter horn, which is essentially a smooth-wall conical horn, with a single step at the throat. We show that this horn, clearly much easier to manufacture than the corrugated horn, has comparable electrical characteristics over a 15% fractional bandwidth.
We have developed software which allows us to predict accurately the performance of the Potter horn-reflector antenna. This is done by calculating the scattering matrix and the aperture field distribution of the horn using a modal matching technique, followed by the conformal mapping of the horn fields onto

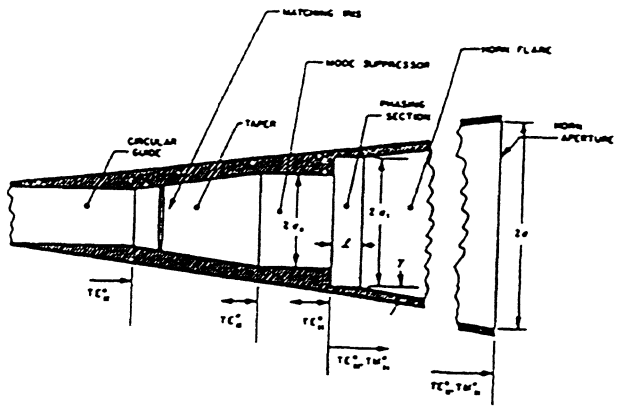

FIGURE I The Potter horn

the projected aperture of the antenna. These results are then used to derive expressions for the gain and the beam efficiency of the antenna and to calculate the co-polar and cross-polar antenna radiation patterns. In particular, we investigate the useful bandwidth of the antenna for high performance SIS split-block mixers. This will allow us to incorporate a high performance and yet easy-to-machine horn into our split-block technology, one which we have been developing over the past few years.

THE POTTER HORN

The conventional Potter Horn

The idea of synthesising a field distribution over the aperture of a horn by combining orthogonal waveguide modes was first suggested and successfully implemented by Potter (Potter, 1963). Potter demonstrated that a dual-mode horn could be realised by exciting both the TE_{11} and the TM_{11} modes at the throat of the horn. He showed that the radiation pattern of the horn becomes circular if the two modes reach the horn aperture with a particular relative amplitude and phase. This means that the horn beamwidth becomes independent of polarisation and the sidelobes become low in both the E-plane and H-plane. By converting a small percentage of the incident power carried by the TE_{11} mode into the TM_{11} mode, the E-plane sidelobes cancel. This results in an E-plane beam pattern which is almost identical to the H-plane pattern which in itself is unaffected by the step discontinuity. Potter presented a detailed empirical procedure for designing dual-mode horns shown in Fig. 1. First, the TE_{11} and TM_{11} modes are launched at the step discontinuity with a relative amplitude α and relative phase . The two modes are then allowed to propagate in a straight circular waveguide section. As the modes propagate, the phase difference between the modes is reduced prior to being launched into the conical horn of semi-flare angle θ_o. The length of the phasing section is chosen so that the TE_{11} and TM_{11} modes are in phase at the horn aperture. It is this requirement of zero phase difference between modes at the horn aperture that limits the horn bandwidth. As an example, if we require the cross-polar level to be less than -20 dB, we find that horn has a bandwidth of 10%. The bandwidth increases to

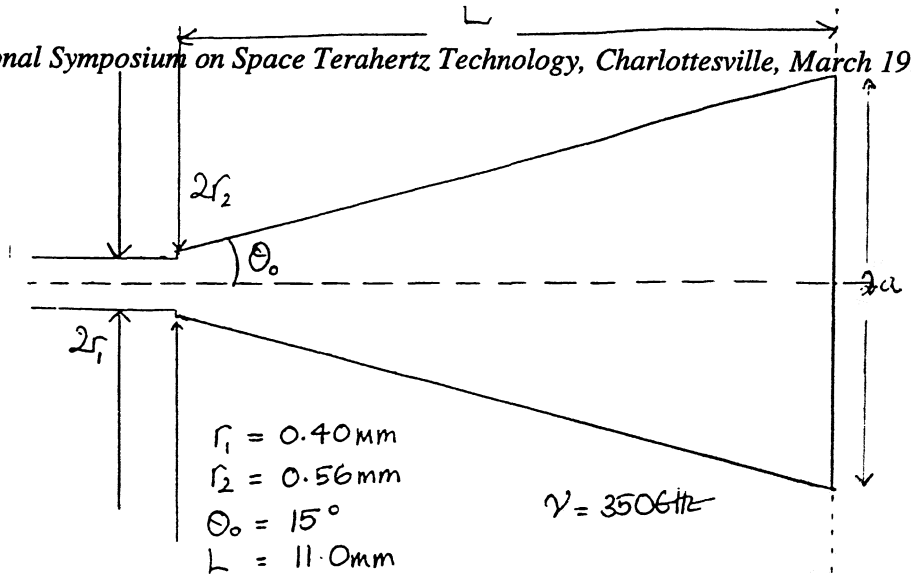

FIGURE II The Pickett-Potter horn

20% if the tolerance on the cross-polar level is relaxed to -16dB.

The Pickett-Potter horn

A simplified version of the conventional Potter horn was first introduced by Pickett *et. al* (Pickett, Hardy and Farhoomand, 1984). Here, the phasing section is removed, leaving a single step discontinuity at the throat of the horn (see Fig. 2). This simplifies greatly the horn fabrication, however, the relative phase between the modes can now only change as the modes propagate along the horn itself. As a result, the horn dimensions, normally chosen to obtain a pre-determined beam shape, are now constrained by the requirements of minimum phase difference between the two modes. We shall show later that this in turn restricts the minimum allowed semi-flare angle and thus tends to increase the length of the horn. In all other respects, the electrical properties of this simplified horn should be identical to the original Potter horn.

Calculation of the electrical properties of the Pickett-Potter horn

We have calculated the field distribution across the aperture of the Potter horn using the well-known modal matching method. To do this, the horn is divided into discrete sections. At each junction a scattering matrix is calculated by matching the expansion coefficients of the field on either side of the junction and applying the constraint of conservation of power. The overall scattering matrix of the horn is calculated by cascading the matrices of the individual sections. In particular, the scattering matrix of the horn contains information about the complex mode coefficients across the horn aperture and the reflection coefficient at the horn input. Once the field distribution across the field aperture has been found, the radiation pattern of the horn can easily be calculated.

We have developed software to analyse the behaviour of the Pickett-Potter horn to be used for SIS mixer applications. The following parameters were used to define the horn: a centre frequency of 350 GHz, a semi-flare angle at 15° and an aperture diameter of a few millimetres. To simplify the calculation procedure, in particular for the horn-reflector antenna, we calculated the radiation pattern of the Pickett-Potter horn by assuming that the field at the aperture is given by that of a cylindrical waveguide, multiplied by the spherical phase error factor,

$\exp -j\frac{kr^2}{2L}$, where r is the radial distance in the horn aperture. k is the free space wavenumber and L is the horn length. The phase difference between the two modes as they propagate along the horn is given by

$$\Delta\phi = \int \frac{dz}{\lambda_{gTE}(z)} - \frac{dz}{\lambda_{gTM}(z)} \tag{1}$$

where z is axial distance along the horn. We have used this method in the past to calculate the radiation pattern of a corrugated horns and have obtained agreement between the computed and measured results down to -40 dB. Using Kirchhoff's aperture diffraction theory to calculate the radiated far fields we obtain:

$$E_\theta = \frac{jk\exp -jkR}{4\pi R}(1+\frac{\beta\cos\theta}{k})[f_x\cos o + f_y\sin o] \tag{2}$$

$$E_\phi = -\frac{jk\exp -jkR}{4\pi R}(\cos\theta+\frac{\beta}{k})[f_x\sin o - f_y\cos o] \tag{3}$$

where R,θ and ϕ are the spherical coordinates of the plane of observation, β is the guided propagation constant and $f_{x,y}$ are the far field components of the $E_{ax,y}$ aperture field components and can be written as:

$$\underline{\mathbf{f}} = \int_0^{2\pi}\int_0^a \underline{\mathbf{E}a}(r',\phi')\exp[jkr'\sin\theta\cos(\phi-\phi')]r'dr'd\phi' \tag{4}$$

The co-polar and cross-polar patterns can then be written using Ludwig's third definition of cross polarisation as:

$$\begin{pmatrix} E_{cp} \\ E_{xp} \end{pmatrix} = \begin{pmatrix} \sin\theta & \cos\phi \\ \cos\theta & -\sin\phi \end{pmatrix}\begin{pmatrix} E_\theta \\ E_\phi \end{pmatrix} \tag{5}$$

An example of these calculations is shown in Fig. 3 where we have computed the radiation pattern at three frequencies. Note that the pattern quality at the optimum frequency (350 GHz) is comparable to that of a corrugated horn. By 380 GHz, however, the cross-polarisation level has already increased to -15 dB. A plot of the -3 dB and -10 dB beamwidths of the Pickett-Potter horn as a function of frequency is shown in Fig. 4. The best indicator of the bandwidth of the Pickett-Potter horn is the cross-polarisation level,(the sidelobe level is low over a very wide band). We have therefore plotted the cross-polar level as a function of frequency in Fig. 5, where the horn dimensions have been chosen to match those used in Fig. 3. We see that, over this frequency range, the cross polarisation level is comparable to that of a corrugated horn of similar dimensions and, unsurprisingly, much better than that of a diagonal horn over much of the frequency band of comparison.

A very useful design tool is the plot of the relative beamwidth of the horn ($\frac{\Delta\theta}{\theta_o}$) as a function of the phase error parameter Δ which defined as

$$\Delta = \frac{a}{\lambda}\tan\frac{\theta_o}{2} \tag{6}$$

An example design curve, which was computed for a fixed semiflare angle of 15° is given in Fig. 6.

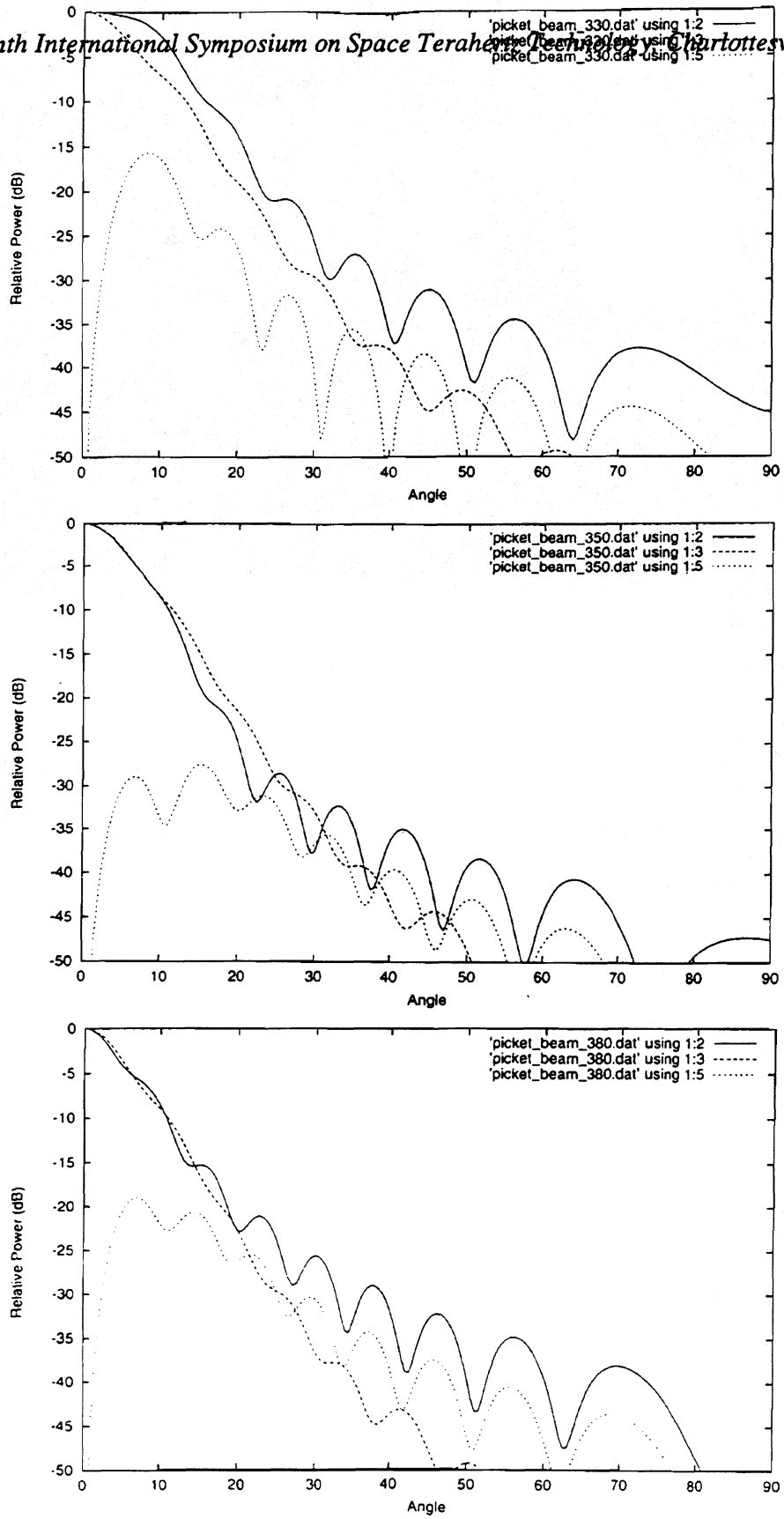

FIGURE III Pickett potter horn radiation patterns over the frequency range 330-380 GHz for a horn with semi-flare angle of 15° and length 11.6 mm . (a) 330 GHz (b) 350 GHz (c) 380 GHz.

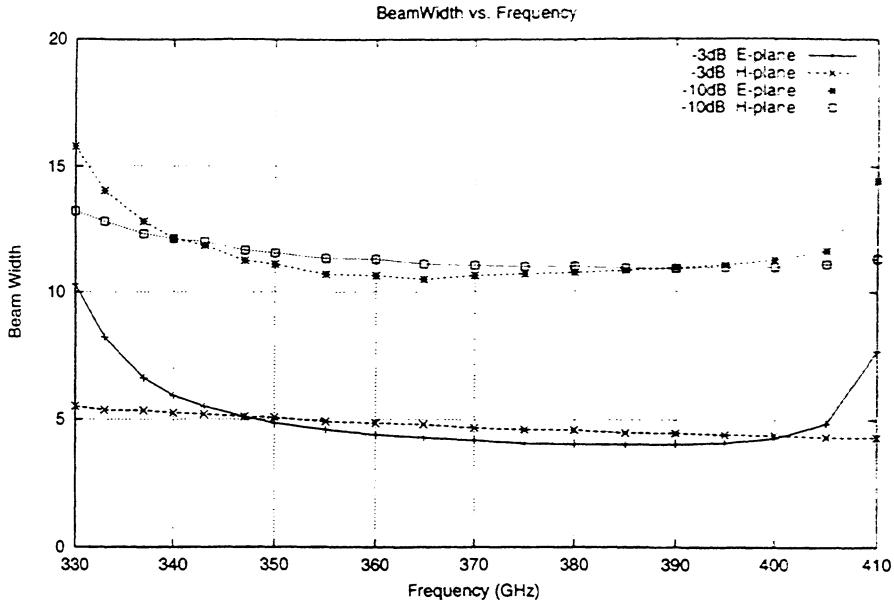

FIGURE IV -3 dB and -10 dB widths of the Potter horn

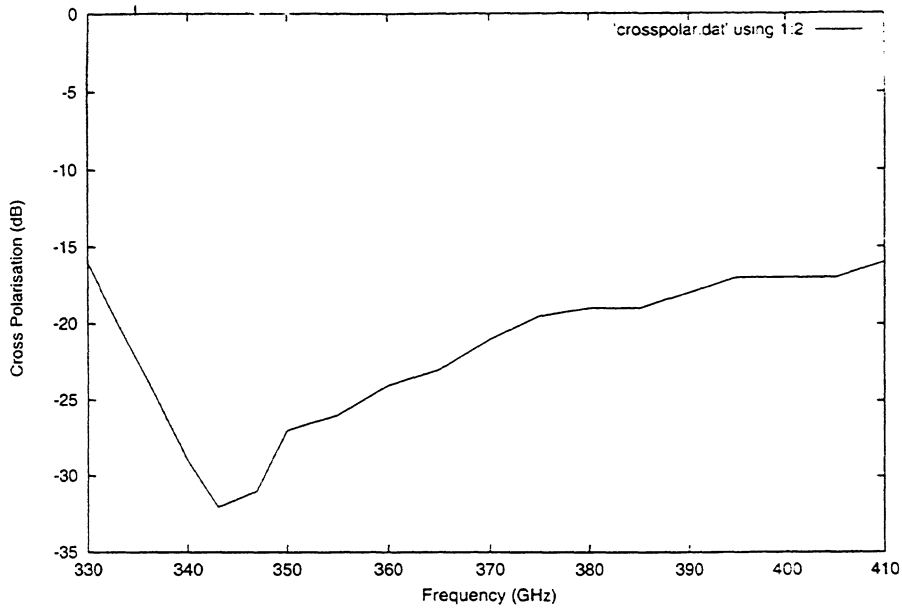

FIGURE V Cross polarisation level as a function of frequency for the Potter horn in Fig. 3

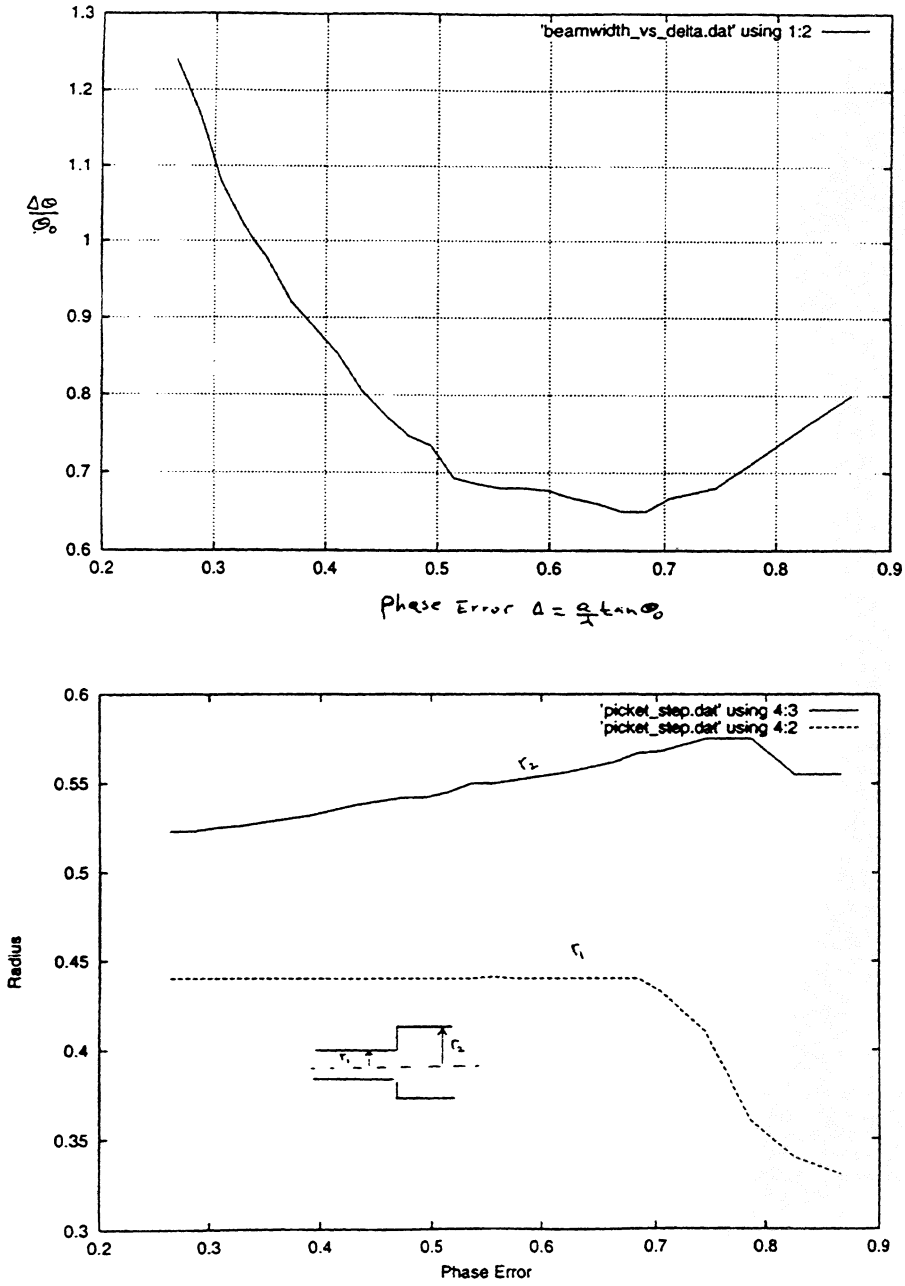

FIGURE VI A plot of the beamwidth of the Pickett-Potter horn as a function of the phase error, Δ, as defined by eqn. 6. The semi-flare angle of the horn was fixed at 15°

It should be noted that at each point on the plot the dimensions of the step were adjusted (by varying r_1, r_2) to give optimum performance (minimum cross-polarisation). It is interesting to note that the plot has a minimum which corresponds to the minimum beamwidth for a given horn semi-flare angle. A similar minimum occurs for corrugated horns, where the horn design becomes "optimum" in the sense of having maximum gain. Less encouraging was the discovery that the dynamic design range is severely compromised by the absence of the phasing section. This is why the phase error parameter cannot be increased to the values obtained by corrugated horns. In spite of this, it can be seen from Fig. 6 that a Pickett-Potter horn that is not diffraction-limited can still be realised using a moderately small flare angle.

THE POTTER HORN-REFLECTOR ANTENNA

Beams shape

The radiation pattern of a horn-reflector antenna fed by a conical horn is calculated by assuming that the parabolic reflector removes the spherical error of the horn. It is therefore assumed that the fields mapped onto the projected aperture are those of a cylindrical waveguide. This implies that an optimised horn design would automatically yield a good horn-reflector antenna pattern. This is because if the two modes reach the horn aperture in phase, then, assuming that the reflector only removes the quadratic phase error, they will also be in phase at the projected aperture plane. It should, however, be emphasised that if the length of the horn is changed, for example, to obtain a different beamwidth, then the step dimensions will also have to be changed in order to re-phase the two modes. Our analysis nevertheless shows that it is indeed feasible to realise a horn-reflector fed by a Pickett-Potter horn with performance comparable to that of a corrugated horn-reflector, however, a longer horn is required. This is demonstrated in Fig. 7 where we plotted the radiation pattern of the Potter horn-reflector antenna at two different frequencies. The patterns were computed for longitudinal input polarisation for either longitudinal (LL)or transverse (LT)observation planes (Yassin *et al*, 1993). It can be seen that the bandwidth of the antenna is at least as good as that of the horn and that the main beam shape resemble that of a corrugated horn. In Fig. 8 we compare the pattern of a horn-reflector antenna fed by a Potter horn with those when the antenna is fed by either a corrugated horn or a smooth-wall conical horn. We notice that the sidelobes of the Potter antenna are comparable to those of the corrugated horn and are much lower than those obtained in the E-plane of the smooth wall conical horn. Finally, we would like to emphasise that in spite of the difficulties that arise from the phase error removal discussed above, the circularity of the Potter horn-reflector beam is insensitive to changes in the horn length. Apart from the expected change in beamwidth, the difference between the LL and LT main beams is very small as the length of the horn is increased from 2 cm to 6 cm. This can easily be understood by noting that the additional phase created at the aperture of the horn is a combination of the spherical phase error and the phase deference which results from the difference in the propagation constants of the TE_{11} and the TM_{11} modes. When the length of the horn is further increased the phase error change is removed, as usual, by the reflector and the

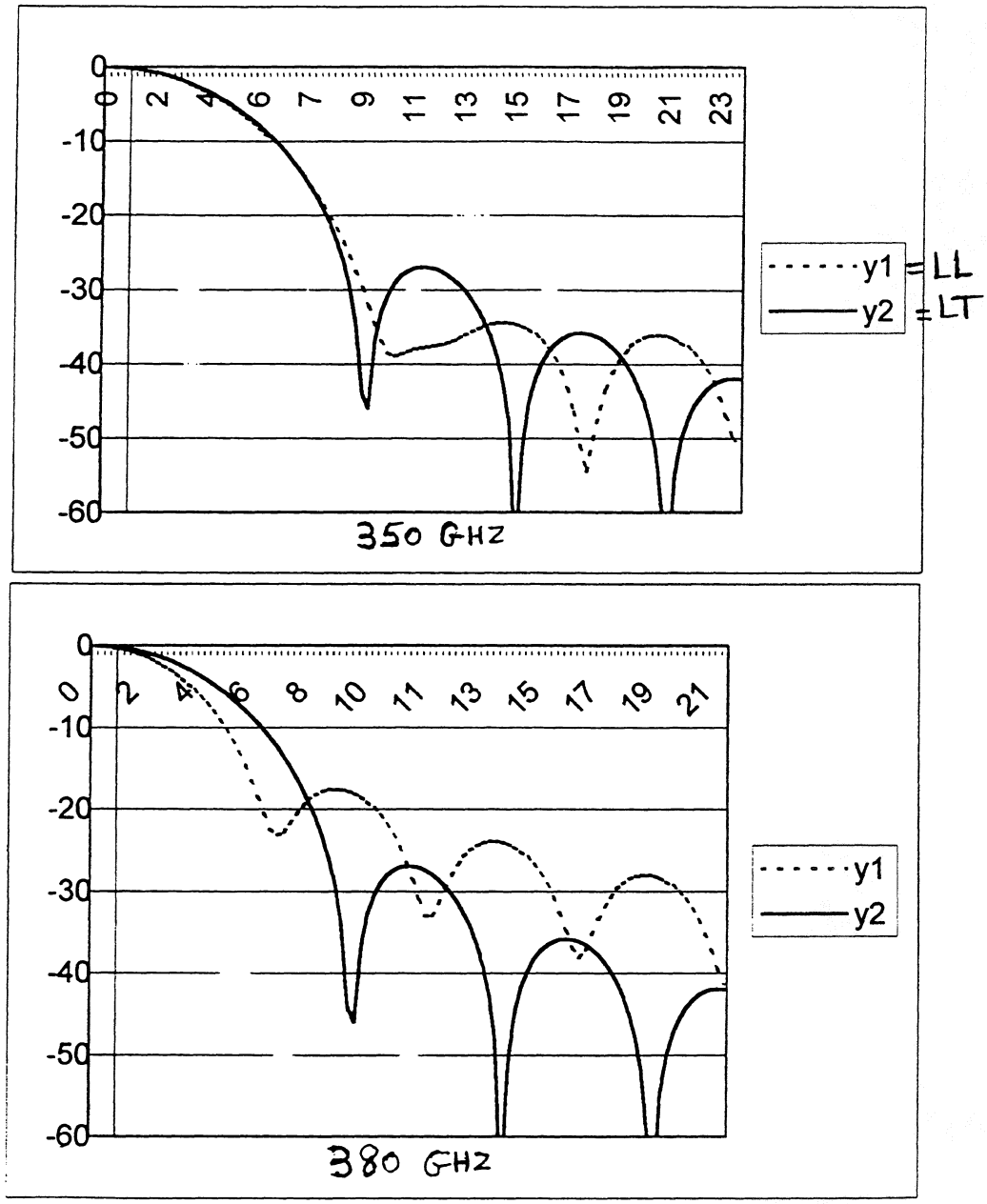

FIGURE VII Radiation patterns of the Potter horn-reflector antenna in the frequency range 330-380 GHz for a horn with semiflare angle of 15° and horn length of 1.65 cm for longitudinal polarisation. (a) 350 GHz (b) 380 GHz .

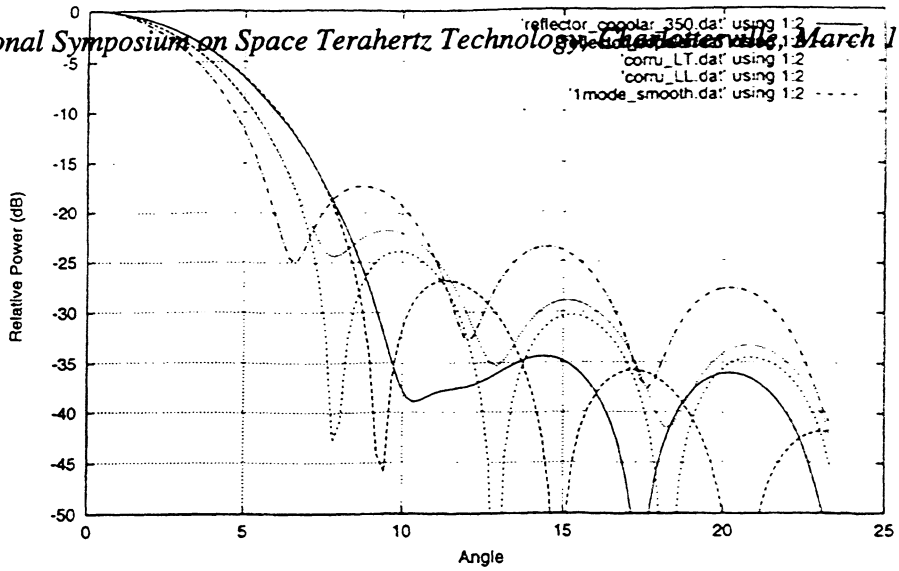

FIGURE VIII Comparison of the radiation patterns of the Potter horn-reflector antenna with those of corrugated and smooth wall conical horns.

change resulting from the difference in the propagation constant is very small. As a result, the phase change in the projected aperture remains very small and consequently the beam circularity is maintained. In contrast, the diameter of the projected aperture, which in fact determines the beamwidth, is proportional to the horn diameter, hence the beamwidth is substantially changed.

Design recipe

The procedure to design a Pickett-Potter horn-reflector antenna is similar to that would be used to design a corrugated horn-reflector. The following approximate design formulas are provided for the reader's convenience. The relation between the projected aperture diameter D and the full beamwidth is, for moderate semi-flare horn angles, is given by:

$$\Delta\theta \approx 1.2\frac{\lambda}{D} \tag{7}$$

The design of the horn reflector antenna can be realised as follows:

- Determine the diameter of the projected aperture according to the required beamwidth from the above formula
- Calculate the horn aperture diameter, d, according to the relation:

$$D = d[\frac{1+\sin\theta_o}{\cos\theta_o}] \tag{8}$$

- Design a potter horn with a semiflare angle $10° - 20°$ with optimum performance around the band centre frequency.
- Determine the focal length of the 90° offset parabolic reflector using the relation

$$D = 4f\tan\theta_o \tag{9}$$

- Calculate the radiation patterns of the antenna and refine the step discontinuity dimensions to achieve maximum beam circularity.

CONCLUSION

We have shown that the Pickett-Potter horn can be employed in conjunction with horn-reflector antennas, provided that the TE_{11} and TM_{11} modes reach the projected aperture in phase. Although the absence of a phasing section in the Picket-Potter version restricts the horn design flexibility, our study showed that practical horn-reflector antenna dimensions suitable for submillimetre-wave array receivers can still be found. The bandwidth of the antenna is clearly dependent on the specified cross- polarisation level. For example, a -20 db cross-polar level can be maintained over a fractional bandwidth of 10%, while -15 db level can be achieved over a fractional bandwidth of 25 %.

REFERENCES

Withington, S., Yassin, G., Buffey, M. and Norden, C. (1997): "A Horn-Reflector antenna for high performance submillimetre imaging arrays," *Int'l J. IR and MM Waves*, vol. 18, no. 2, pp. 341-358, 1997.

Potter, P. D. "A new horn antenna with suppressed sidelobes and equal beamwidths." *Microwave J.*, **6** pp. 71-78, 1963. finline mixer for astronomical imaging arrays ," Elctron. Lett. Vol. 33, PP. 498–500, 1997.

Pickett, H. M., Hardy, J. C. and Farhoomand, J., "Characterisation of a dual-mode horn for submillimetre wavelengths," *IEEE Trans. Microwave Theory Tech.* MTT–32, no. 8, pp. 936-937, 1984.

Silver, S. *Microwave antenna theory and Design*, McGraw-Hill Book Co., Inc., New York, 1949, pp. 162.

Yassin, G., Robson, M. and Duffett–Smith, P. J. "The electrical characteristics of a conical horn–reflector antenna employing a corrugated horn", *IEEE Antennas and propagation*, vol. AP-41, pp. 357–361, April 1993.

THE GAUSSIAN BEAM MODE ANALYSIS OF PHASE GRATINGS

Créidhe O'Sullivan[1], J. Anthony Murphy[1], Neil Trappe[1], William Lanigan[1], Ruth Colgan[1] & Stafford Withington[2]

[1]Experimental Physics Department, National University of Ireland, Maynooth, Co. Kildare. Ireland
[2]Cavendish Laboratory, Cambridge University, Madingley Road, Cambridge CB3 0HE. England

Abstract: Phase gratings find useful application in array receivers as passive multiplexing devices in the local oscillator injection chain. In particular, the Dammann phase grating is one of the simplest class to model and manufacture, and can be used to generate multiple images of a single input beam in a quasi-optical system. It is a binary grating consisting of a regular arrangement of milled slots or recesses in some suitable transparent dielectric or conducting block of material. The basic operation of the phase grating can be understood in terms of Fourier optics. However, Gaussian beam mode analysis is a powerful tool when investigating the limitation of the grating in a real submillimeter system of finite throughput and bandwidth. This is especially the case when evaluating the coupling to an array of horn antenna feeds. In this paper we present the results of our investigation into the modelling of phase gratings using Gaussian beam modes analysis and discuss new experimental measurements.

Introduction

Phase gratings are now being incorporated into submillimeter-wave array receivers as low loss multipliers in the local oscillator injection optics [1-3]. Such quasi-optical devices have the advantage in the submillimeter waveband of being straightforward to manufacture, the required tolerances being relatively easy to achieve compared with their visible-wavelength counterparts. As well as the possibility of manufacturing reflection gratings, there are also a number of dielectric materials whose mechanical and optical properties in the far infrared make them ideal candidates for use in transmission phase gratings [4]. In our investigations we have concentrated on the Dammann Grating (DG) which is a binary optical component, that is the optical path length through the grating takes on just two values ideally separated by half a wavelength [5-8].

The theoretical analysis of phase grating multiplexers is important in determining the practical limitations of such devices in quasi-optical LO injection schemes. Ultimately, it is important to be able to produce quasi-uniform power coupling across an array of mixer feed horns over some useful bandwidth (typically of the order of 10% for ground based astronomical systems covering a submillimeter atmospheric window). Since Gaussian beam mode analysis is ideally suited to the analysis of coupling efficiencies in the case of typical horn antennas [9], and is also useful in analysing submillimeter optical systems of finite throughput [10], it was chosen as the optical analysis tool in this investigation.

In this paper we also report on experimental measurements made on transmission Dammann phase gratings. Three different gratings, designed to produce 2 × 2, 3 × 3 & 5 × 5 uniform two-dimensional arrays of images at 100GHz, were manufactured and tested as quasi-optical multiplexers. It was decided to test the principles involved at this frequency since both the manufacture and experimental measurements are easier. Such phase gratings can, of course, be designed for the submillimeter/terahertz wavebands. The test facility consisted of a simple Fourier 4-*f* optics set-up with a conical horn antenna fed by a Gunn diode source of variable frequency (90-105 GHz). The results presented confirm such gratings to be particularly suitable multiplexers for sparse arrays of finite bandwidth.

Basic Theory of Multiplexer

As indicated above, the basic operation of a phase grating multiplexer can be understood in terms of Fourier optics. The grating is best illuminated by a quasi-collimated incident field $\psi(x,y)$ produced by the source feed, this being achieved by arranging that the source beam has a waist at the grating (Figure 1). A Dammann grating consists of a two dimensional array of identical basis cells, with the transmission function of the (on-axis) basis cell being given by $t(x,y)$. Since a binary grating implies a phase step difference of π then $t(x,y) = \pm 1$. In the example of the basic period of a one-dimensional cut through a grating shown in Figure 2, the free parameters are $\pm x_1$, $\pm x_2$, $\pm x_3$, etc. The transmission of an entire grating with rectangular symmetry is then given by a sum of the form: $\Sigma_{m,n}\, t(x-m\Delta x, y-n\Delta y)$, where Δx and Δy are the grating periods in the x and y directions, respectively. The grating then produces a strong corrugated modulation of the quasi-planar wavefront of the incident field, severely affecting the resulting beam pattern. At the Fourier plane of the grating an array of beams is produced as predicted by the Array Theorem, the intensity of the beams being determined by the diffraction pattern (i.e. the Fourier Transform) of a single cell $T(u,v)$.

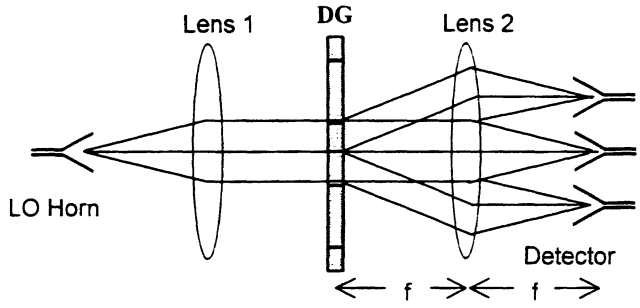

Figure 1 Optical set-up for beam multiplexing with a Dammann Grating.

At the output focal plane of the system illustrated in Figure 1 (the Fourier plane of the plane where the grating is placed), the diffraction pattern resulting is given by:

$$E(u,v) = \{T(u,v).\sum_{n,m=-\infty}^{\infty}\delta(u-m\Delta u, v-n\Delta v)\} * \Psi(u,v),$$

where $\Psi(u,v)$ is the Fourier Transform of $\psi(x,y)$, the incident field at the grating, and capital symbols represent Fourier Transforms [11]. The pattern can thus be described mathematically as an array of spots (delta functions) convolved with the output LO beam that would have been obtained directly in the absence of the grating. The spatial frequencies u and v are related to the co-ordinates in the output plane through $u = x_o/\lambda f$ and $v = y_o/\lambda f$, f being the focal length of the lens. The array of beams are separated by a common distance of $\Delta u = 1/\Delta x$ in the x-direction and $\Delta v = 1/\Delta y$ in the y-direction, and correspond to the different diffraction orders of a uniformly illuminated grating. In the x-direction for example, the different grating orders are centred at $u = m\ \Delta u$, where m is some integer, equivalent, of course, to the usual grating formula: $n\lambda = d \sin\theta$.

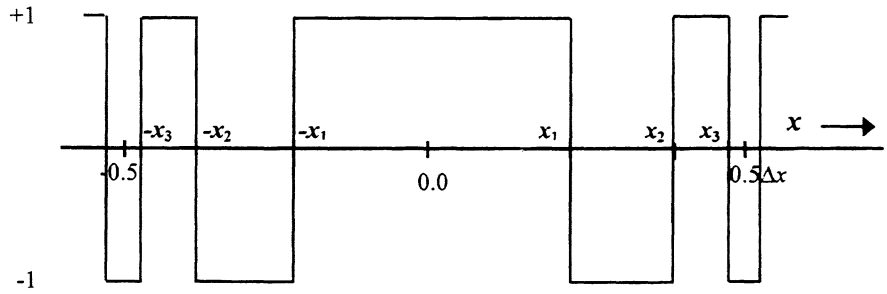

Figure 2 One-dimensional, symmetric binary function with period Δx.

The grating will usually possess rectangular symmetry, so that one can write $t(x,y)=t(x)t(y)$, and only the one-dimensional response of the grating need be considered. Then, if we require a $2M+1$ array of non-overlapping images of the source beam of equal intensity in the x-direction, $T(u)$, must satisfy $|T(m\Delta u)|=|T(0)|$ for m between $-M$ and M (giving $2M+1$ diffraction orders of equal intensity), and $T(m\Delta u) \approx 0$, otherwise, for high efficiency. To ensure this in terms of a Dammann grating the values of $\pm x_1$, $\pm x_2$, $\pm x_3$, etc. mentioned above must be chosen for a single period (cell) of the grating. This is discussed in detail in [5], where various solutions are tabulated for different values of M. Given that $t(x) = \pm 1$, one can show that $T(u)$ is given by:

$$T(u) = \frac{1}{\pi u}\sum_{n=0}^{N}(-1)^n(\sin 2\pi u x_{n+1} - \sin 2\pi u x_n),$$

where N is the number of transition points between $x = 0$ and $\Delta x/2$.

If an even number of output spots is required then neighbouring elements must be out of phase by π. This will cause the grating maxima to lie not in the direction given by $n\lambda = d \sin\theta$, but rather $(n + \frac{1}{2})\lambda = d \sin\theta$, where d is the original cell size, and an even number of equal intensity diffraction spots is obtained [12].

Design of Grating

Now we consider applying the above theory to the design of the multiplexer shown in Figure 1 to produce an array of output beams arranged on a square grid. The position and widths of the slots making up the basis cell determine the number of beams in the array. If we require a diffraction order spacing (the inter-beam spacing on the output plane) of Δx_o, then the grating period Δx is determined by $\Delta x = \lambda f / \Delta x_o$. The number of gratings cells illuminated by the source beam determines the ratio of the output beam spacing to beam width. If one assumes a transmitting scalar feed (corrugated horn) as the source, then, to a good approximation the resulting propagating beam can be considered to have a simple Gaussian field distribution, whose form does not change as the beam propagates. At the grating we can write the incident field $\psi(x,y) \propto \exp(-(x^2+y^2)/W_G^2)$, where W_G is the usual Gaussian beam waist radius for the source beam. At the output Fourier plane $\psi(x_o,y_o) \propto \exp(-(x_o^2+y_o^2)/W_F^2)$, where for this Fourier arrangement $W_F = \lambda f/\pi W_G$. This implies $W_G/\Delta x = [\pi(W_F/\Delta x_o)]^{-1}$, so that the incident beam width to cell size ratio at the grating is inversely proportional to the beam width to inter-beam spacing for the array of images at the output plane.

Consider, for example, the situation where we want to couple the output array of beams from the multiplexer to an array of closely spaced diagonal horns (a typical scenario for quasi-optical local oscillator injection in an astronomical heterodyne array receiver system). The best-fit Gaussian beam to the field at the mouth of a diagonal horn has a radius given by: $W = 0.43a$ [13]. For a horn of finite length the beam waist radius at the horn phase centre will be somewhat less than this, a typical value for a horn of moderate length being: $W_{oh} = 0.38a$. Thus, to match this radius to the incident LO beams ($W_F = W_{oh} = 0.38\Delta x_o$), the corresponding beam width, W_G, at the grating must be: $W_G = \lambda f / \pi W_F = \lambda f / \pi(0.38a) = 0.837\Delta x$. The Gaussian beam radius is of order the grating period! The implications of this for the phase array is that we only need a *small number* of periods in the grating, reducing the complexity for manufacture.

The theoretically predicted resulting set of image Gaussian beams is shown in Figure 3, for the case where the total number of periods in the DG equals 4×4. The grating is designed to produce a 5×5 array of images with the slot edges of the basis cell in

the x-direction at $x_1 = \pm 0.132\Delta x$ & $x_2 = \pm 0.480\Delta x$. For comparison, a set of 5 Gaussian beams is shown in intensity and, as can be seen, the coupling is high. Since about 77.4% of the power is contained in the central orders for the one-dimensional case [5], the total LO coupling loss is of the order of 60% (in two dimensions). This power is lost into higher diffraction orders than 2, and so some power spills round the side of the array of diagonal horns. However, this power can be easily terminated using an absorbing microwave material around the array. It should also be possible to reduce loss by having a basic grating cell with more grooves (more degrees of freedom).

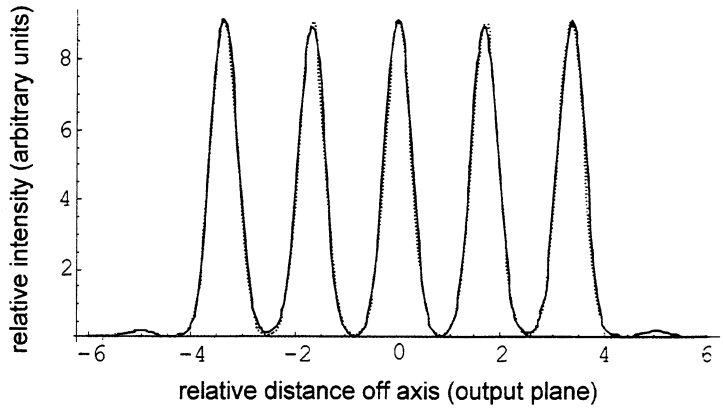

Figure 3 Array of Gaussian beams (dotted line) superimposed on DG beam array.

Gaussian Beam Mode Analysis of Multiplexer Performance

As described in the last section the basic operation of a phase grating is understood in terms of straightforward Fourier optics. However, Gaussian beam mode analysis is a powerful tool when investigating the limitation of the grating in a real submillimeter system of finite throughput and bandwidth[14]. A serious consideration in millimetre/submillimetre-wave systems is that compact optics may result in some of the spatial frequencies in the beam being truncated in the optical train between the grating and the final output plane where an array of image beams is to be delivered. Ultimately, what one is interested in is evaluating the coupling to the horn antenna feeds of the detector array. From a multimode beam viewpoint the grating has the effect of seriously disturbing the lower order modes making up the incident quasi-Gaussian beam, thus scattering significant power into very high order modes.

Because of the Cartesian symmetry of the grating array the fields can be most conveniently expressed in terms of Hermite-Gaussian beam modes, ψ_{mn}:

$$E(x,y) = \sum_{m=0}^{\infty} \sum_{n=0}^{\infty} a_{mn} \psi_{mn}(x,y),$$

where $\psi_{mn}(x,y)$ are given by the usual expression [16]:

$$\psi_{mn}(x,y,z) = h_m(x;W) h_n(y;W) \exp(-ik(z + (x^2 + y^2)/2R) + i\Delta\phi_{mn}),$$

with

$$h_m(s;W) = \left[2^m m! \sqrt{\pi W^2/2}\right]^{-1/2} H_m(\sqrt{2}s/W) \exp(-s^2/W^2),$$

and H_m a Hermite polynomial of order m. The beam width parameter, phase radius of curvature and phase slippage terms, W, R and $\Delta\phi_{mn}$, respectively are functions of position z, which is taken to be zero at a waist (at the grating, in this instance).

Crucial to the efficiency of the Gaussian beam mode approach in analysing the system is the choice of the optimum beam mode set. We require that the array of beams scattered by the grating can be described accurately by a finite sum of as few modal contributions as possible. At first sight one might think that a large number of on-axis modes will be required to accurately describe the array of beams at the output plane, since, of course, in the absence of the grating just one on-axis beam is produced. In fact, a naïve extension of a multi-moded analysis using a beam set appropriate for a single on-axis beam can lead to computational and numerical difficulties as too many modes have to be included. However, as shown in [15] there exits a mode set of modest size in terms of which one can to a good approximation describe all of the off-axis beams with adequate sensitivity. The beam waist radius for the best choice mode set at the output plane is given by:

$$W_o^2 \approx \sqrt{\frac{A}{\pi}} \frac{W_{oh}}{N},$$

where A is the area of the array of beams at the output plane, W_{oh} is the corresponding equivalent waist width of a simple Gaussian approximation to one of the beams on the output plane and N is the maximum diffraction order of the beams that we want to describe. Thus, for a 5 × 5 array with $W_{oh} = 0.38\Delta x_o$, $N = 2$, and $A = (5\ \Delta x_o)^2$, one obtains $W_o = 0.73\ \Delta x$. Clearly, in order for the system to operate efficiently as a

multiplexer, the throughput of the optics (between the grating and the output plane) must be such that the highest order mode transmitted extends spatially over a region that includes all of the array of images of the feed horn in the output plane.

Having chosen the mode set, the amplitude coefficients for the source horn feed are determined by performing the relevant overlap integral at the aperture of the source feed to determine the mode coefficients: $a_{mn} = \iint \psi_{mn}(x,y)^* E(x,y)\, dxdy$. The change in the form of the beam as it propagates away from this plane is determined by the evolution of the phase slippage term $\exp(i\Delta\phi_{mn}(z))$. This term does not depend on (x,y) and can conveniently be included in the amplitude coefficient $A_{mn} = a_{mn} \exp(i\Delta\phi_{mn}(z))$.

The effect of the grating on the source beam can be understood in terms of the scattering of the power carried by the component modes into higher order modes:

$$\psi^S_{mn} = \sum_{m',n'} S_{mm',nn'} \psi_{m'n'},$$

where

$$S_{mm',nn'} = \iint dxdy \exp(i\phi(x,y)) h_m(x;W) h_n(y;W) h_{m'}(x;W) h_{n'}(y;W)$$

and the phase term has been absorbed into the amplitude coefficients. Note that $\phi(x,y)$ represents the phase modulation introduced by the grating. The field scattered by the grating is given by:

$$E(x,y) = \sum_{mn} A_{mn} [\psi_{mn}(x,y)]^S = \sum_{mn} \sum_{m'n'} A_{mn} S_{mm',nn'} \psi_{m'n'}(x,y).$$

Thus, the new mode amplitudes for the transmitted beam are given by:

$$b_{m'n'} = \sum_{mn} S_{mm',nn'} A_{mn}.$$

As the beam the propagates away from the grating the phase slippage terms $\exp(i\Delta\phi_{mn})$ further evolves. For propagation to the Fourier plane of the grating, $\Delta\phi_{mn} = (m+n+1)\pi/2$, so that on the output plane the amplitude coefficients are given by $B_{mn} = i^{(m+n+1)} b_{mn}$. However, if the optics between the grating and the output plane truncates the system of diffracted beams to any extent then some modal filtering takes place. This process can also be described in terms of the scattering of the component modes as discussed in [10].

Grating Bandwidth

To evaluate the performance of a grating as a multiplexer, one can calculate the coupling efficiency of the system of image beams to a test receiver horn moved about the output plane. We can conveniently represent the beam pattern of any of the receiver array horn antennas in terms of a sum of on-axis modes, the amplitudes of the modes depending on the position of the horn on the image plane. Clearly, it is most convenient to expand the fields of the test horn antenna aperture in terms of the same mode set as is used for the array of images $E_h = \sum c_{mn} \psi_{mn}$. For optimum coupling to the array of image beams the phase centre of the horn should be located on the image plane, and the beam width should closely match those of the array of images. The coupling of the horn antenna to the field is then given by: $\eta = | \sum_{mn} (B_{mn})^* C_{mn} |^2$, where $C_{mn} = \exp(i\Delta\phi_{mn}) c_{mn}$, takes into account the phase slippage between the horn aperture and its phase centre.

As with all binary optics the DG will only operate correctly over a finite bandwidth. This may pose a limitation for certain applications as noted in the introduction. We therefore investigated a frequency detuning of the order of 10% using Gaussian beam modes. Two effects occur if the wavelength of the LO beam is not at the design wavelength of the grating:

(i) The actual inter-beam diffraction order separation in the output plane will change implying some of the beams will no longer couple well to the detector array as they will be misaligned with the horn centres. Realignment, however, can be achieved easily by designing some variable magnification into the LO path optics.
(ii) The two binary phase delays for the grating are wavelength dependent, and so the grating will only produce the required phase modulation of $\phi(x,y) = \pm 1$ at the design frequency.

These effects reduce the idealised coupling to an array of test horns both in terms of the uniformity of the intensities and the displacement of the array of image beams with wavelength. Gaussian beam mode analysis can again be applied to determine the deterioration in the power coupling characteristics for an array of test horns. The results of the analysis for a 5 × 5 grating are presented in Figure 4. It is worth noting that SIS mixer sensitivity to local oscillator power for optimised performance is usually not so critical that such a variation would cause a significant deterioration in performance across the array.

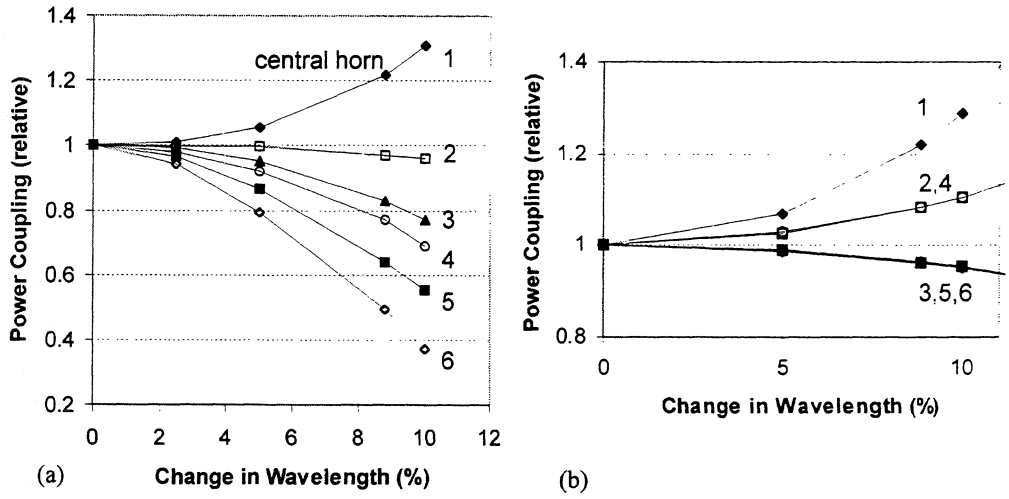

Figure 4 Power coupling to horns at six distances from the centre of a 5×5 array (b) with and (a) without variable magnification.

Experimental Measurements

The practical feasibility of using DGs was evaluated at Maynooth using a 100-GHz test facility. 2×2, 3×3 and 5×5 gratings were designed for use at this frequency and Figure 5 shows a cross-section along one of the axes for each grating. The gratings were manufactured from 112mm×112mm slabs of fused quartz by the Lithuanian optics company, Eksma.

The DGs were tested using the Fourier 4-*f* set-up shown in Figure 6. A 100-GHz Gunn oscillator was used with a conical horn-antenna feed as the source. The horn phase centre was placed at the focal point of an off-axis ellipsoidal mirror, M1, with an angle-of throw of 45°. The gratings were mounted on a perspex holder at the common focal point of the two mirrors M1 and M2 where the source beam had a waist. The mirror M2 was used to image the output of the grating onto the detector plane. The crystal detector was mounted on a computer-controlled XY raster-scanner centred on the focal point of M2. The scanner was capable of covering an area of 550mm × 550mm with a step resolution of 0.03mm. Eccosorb was used to avoid unwanted reflections from component mountings.

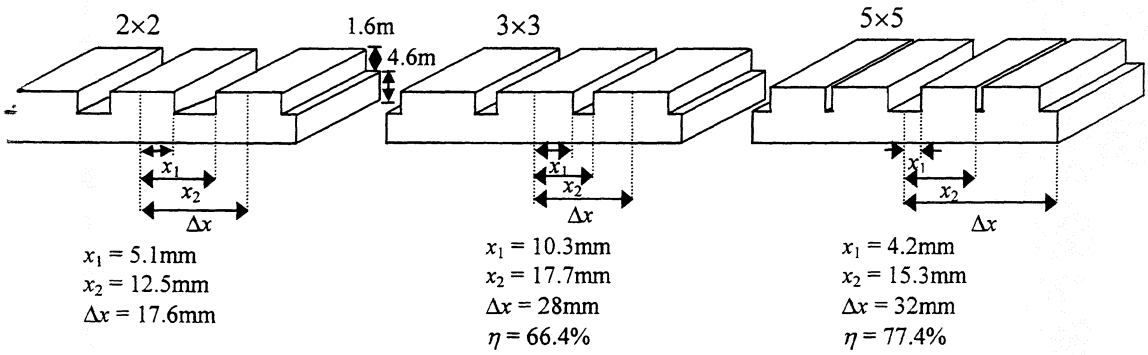

Figure 5 Designs for 2×2, 3×3 and 5×5 DGs. Designs for the 3×3 and 5×5 gratings were based on the calculations of Dammann & Klotz [5]. 6×6 grating periods were used in the 2×2 grating, and 4×4 periods in the other two. The efficiencies, η, refer to the 1-dimensional case. (The tolerance on each dimension was ±0.1mm).

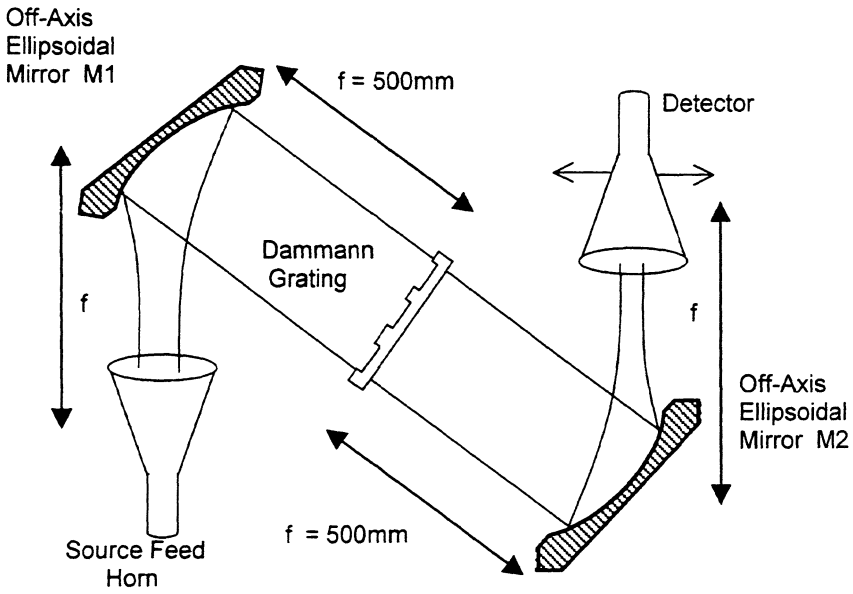

Figure 6 4-*f* set-up to test the Dammann gratings.

The beam patterns obtained with the three gratings are presented in Figure 7. These are to be compared with the theoretical patterns predicted using the Gaussian beam mode analysis discussed previously and shown in Figure 8.

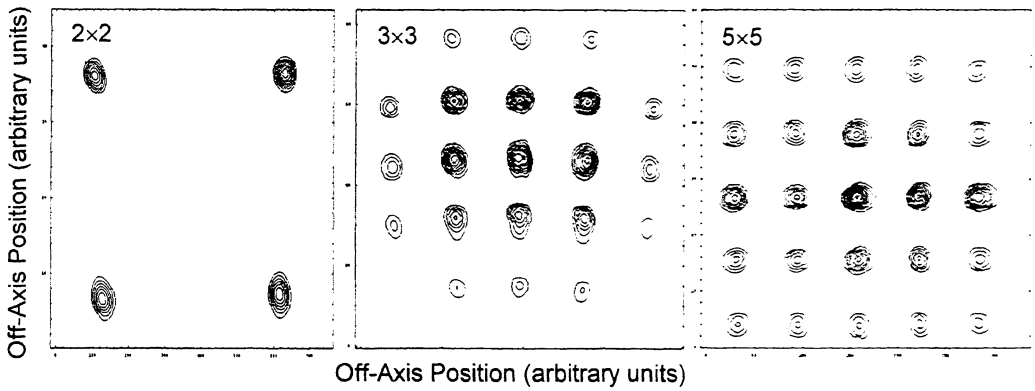

Figure 7 Output intensity patterns obtained with the 2×2, 3×3 and 5×5 gratings (contours are linear)

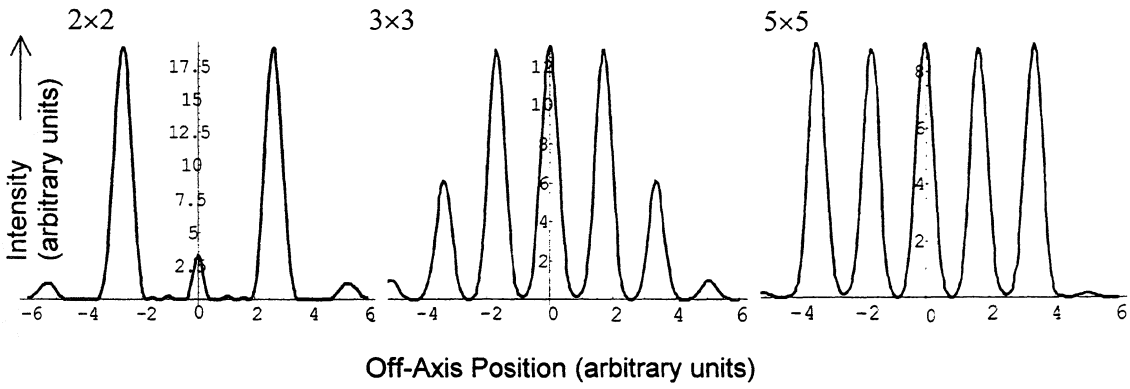

Figure 8 Cross section of the expected beam pattern from the 2×2, 3×3 and 5×5 gratings

In all cases a 2-dimensional grid of beams is obtained. The long focal length of our mirrors meant that the beam waist at the grating was ~$2\Delta x$. From the previous discussion, the predicted beam-separation to beamwidth ratio at the output plane is then ~ 3:1, in agreement with what was found. For our particular choice of 3×3 grating both the theoretical and experimental plots show that the next highest order diffraction peaks are not completely suppressed. The output grid spacings are as expected for a square array reflected through 45° by an ellipsoidal mirror. The overall efficiency of the 2×2 and 5×5 gratings is higher and in these cases the central grid of peaks is far more intense than the higher orders. In practice we found that for the 5×5 array, the bottom row of 5 beams was consistently of a lower intensity than the other four rows,

this we attribute to the fact that our mirrors were not large enough to cover the entire output beam pattern. For the 5×5 measurements, therefore, we replaced the mirrors M1 and M2 in Figure 6 with HDPE lenses (f = 250mm).

In order to investigate the bandwidth limitation of DGs, the 100-GHz Gunn diode was replaced with one whose frequency could be varied over the range 90 – 105 GHz and the measurements repeated.

Measurements on the 3×3 grating at 90.4 GHz are presented along with the theoretical prediction in Figure 9. As expected the inter-beam spacing increases by a factor of $\Delta\lambda/\lambda_0$ and the intensity of the central beam increases at the expense of the other eight.

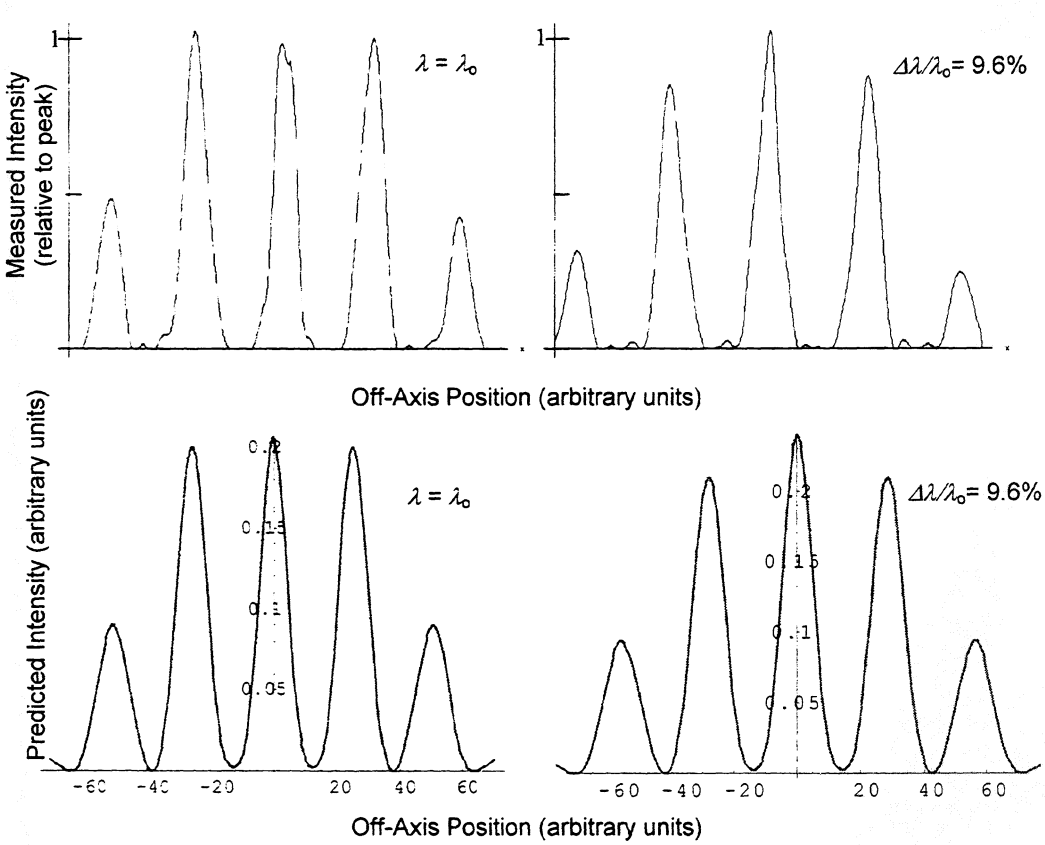

Figure 9 Cross-section of the measured and predicted beam patterns from the 3×3 grating. The output for the design wavelength and a 9.6% detuning are shown. Calculations were made using the Gaussian beam mode analysis discussed in this paper.

The uniformity of the 2×2 and 5×5 beam patterns was also found to remain high over the bandwidth investigated. Figure 10 shows the output from the 5×5 grating at $\Delta\lambda/\lambda_0$ = 5%.

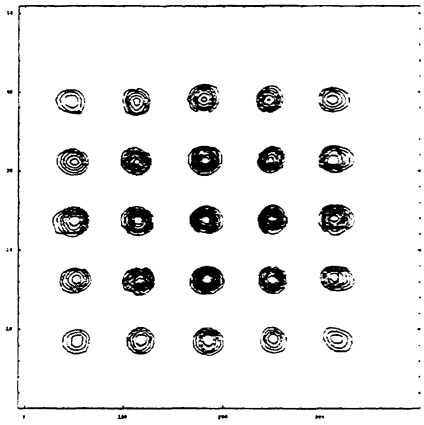

Figure 10 Output intensity patterns (linear contours) obtained with the 5×5 grating at 95.2 GHz.

Conclusions

In this paper we have presented a study of the feasibility of using Dammann gratings for beam multiplexing at millimeter and submillimeter wavelengths. We have shown from a theoretical study that at the design wavelength we get good diffraction efficiencies of around 60% for a 5 × 5 array, with the missing power being channelled into higher diffraction orders which can easily be terminated.

The theoretical bandwidth of such a grating would be of the order of 15%, which is typical of astronomical array receivers operating in the submillimeter waveband.

In the case of the astronomical receiver, an LO multiplexing scheme would work best for the case where mixer characteristics are very similar, so that the LO requirement of individual mixers is the same. The scheme is particularly suitable for sparse arrays.

We also investigated the practical feasibility of producing a 2×2, 3×3 and 5×5 grating at submillimeter wavelengths for the scenario referred to above, and presented measurements of a prototype grating.

Since with the transmission grating there may be some reflection loss, we are also looking into reflection grating designs. These would have to be operated off-axis to prevent beam vignetting.

Acknowledgements

The authors would like to thank Forbairt (The Irish Science and Technology Board) and the Board of the JCMT for financial support of this project.

References

[1] Klein T., Ediss G.A., Gusten R., Hauschildt H. & Kasemann C., "LO beam array generation at 480GHz by use of phase gratings," *Eighth International Symposium on Space Terahertz Technology*, Harvard, 1997

[2] Graf U.U., Haas S., Honingh C. E., Jacobs K., Schieder R. & Stutzki J., "Array receiver development at KOSMA for the sub-millimeter and terahertz spectral range", in *Advanced Technology Millimetre Wave, Radio and Terahertz Telescopes*, Thomas G. Phillips, Editor, Proceedings of SPIE Vol. 3357, 159-166 (1998)

[3] Gusten et al, "CHAMP: The carbon heterodyne array of the MPIfR," in *Advanced Technology Millimetre Wave, Radio and Terahertz Telescopes*, Thomas G. Phillips, Editor, Proceedings of SPIE Vol. 3357, 167-177 (1998)

[4] Belousov V.I., Denisov G.G. and Peskov N. Yu., "Quasi-optical multiplexing based on reflecting diffraction grating," *Int. J. IR & MM Waves*, 12, 1035, 1991

[5] Dammann H. and Klotz E., "Coherent optical generation and inspection of two-dimensional periodic structure," *Optica Acta*, 24, 505, 1977

[6] Jahns J., Downes M.M., Prise E.M., Streibl N. and Walker S.J., "Dammann gratings for laser beam shaping," *Optical Engineering*, 28, 1267, 1989

[7] J.A. Murphy, S. Withington & H. van de Stadt, "Dammann Gratings for Local Oscillator Beam multiplexing," in *Multi-feed Systems for Radio Telescopes*, (ed. D.T.Emerson and J.M. Payne) A.S.P. Conf. Ser. Vol. 75, (1995)

[8] J.A. Murphy, S. Withington and M. Heanue, "Local oscillator splitting using Dammann phase gratings," *Proceedings of the 3rd International Workshop on Terahertz Electronics*, Zermatt, Switzerland, (Sept. 1995)

[9] J.A. Murphy, M. McCabe and S. Withington, "Gaussian beam mode analysis of the coupling of power between horn antennas," *International Journal of Infrared & Millimeter Waves*, vol. 18, 501 (1997)

[10] J.A.Murphy, S. Withington & A. Egan, "Mode conversion at diffracting apertures in millimetre and submillimetre-wave optical systems," *IEEE Trans. Microwave Theory and Techniques*, vol.41, 1700-1702 (1993)

[11] Goodman J.W., *Introduction to Fourier Optics*, McGraw Hill, New York, 1968

[12] Morrison R.L. 1992, *J. Opt. Soc. Am. A*, **9**, 464

[13] S. Withington & J.A.Murphy, "Analysis of diagonal horns through Gaussian-Hermite modes," *IEEE Trans. Antennas & Propagation*, **40**, 198-206 (1992)

[14] S. Withington. & J.A.Murphy, "Modal Analysis of Partially Coherent Submillimetre-wave Quasi-optical Systems." *IEEE Trans. Antennas & Propagation*, vol. 46, 1650-1658, 1998

[15] J.A. Murphy & S. Withington, "Gaussian-beam-mode analysis of multibeam quasi-optical systems," in *Advanced Technology Millimetre Wave, Radio and Terahertz Telescopes*, Thomas G. Phillips, Editor, Proceedings of SPIE Vol. 3357, 97-104 (1998)

[16] Goldsmith P.F., "Quasi-optical techniques at millimeter and submillimeter wavelengths", in *Infrared and Millimeter Waves*, **8**, 227, 1982

SUBMILLIMETER CRYOGENIC TELESCOPE WITH ANDREEV TYPE MICROBOLOMETER FOR THE INTERNATIONAL SPACE STATION. PROJECT SUBMILLIMETRON

A. Vystavkin[1], D. Chouvaev[3], T. Claeson[3], D. Golubev[2,3], V. Gromov[2], N. Kardashev[2], A. Kovalenko[1], V. Kurt[2], L. Kuzmin[3], M. Tarasov[1], A. Trubnikov[2], M. Willander[3]

[1]Institute of Radio Engineering and Electronics of Russian Academy of Sciences (RAS) , 11 Mokhovaya Str., 103907 Moscow, Russia;
[2]Astro Space Center of P.N. Lebedev Physical Institute of RAS, 84/32 Profsoyuznaya Str., 117810 Moscow, Russia;
[3]Department of Microelectronics and Nanoscience, Chalmers University of Technology, S-412 96 Gothenburg, Sweden.

vyst@hitech.cplire.ru, gro@asc.rssi.ru, kuzmin@fy.chalmers.se

Abstract. The tasks of the celestial sphere observations in the Terahertz (500-3.000 GHz) frequency band are analyzed and the place of wideband microbolometers in these tasks is determined. Among such microbolometers the Andreev type is one of most promissing. It is based on the heating electrons in the thin film of normal metal with superconducting electrodes (the S-LN-S structure, where "S" means the superconductor and "LN" means the long film of normal metal), cooled down to temperatures of order of 100 mK. Preliminary estimations and measurements [1, 2] show the possibility to reach the noise equivalent power of such bolometer down to 10^{-18} W/ $Hz^{1/2}$ at least in the part of the THz frequency band. The Astro Space Center of the P.N. Lebedev Institute of the Russian Academy of Sciences is developing the Submillimetron Project [3] that includes a submillimeter wave cryogenic telescope with the Andreev microbolometer as one of receiver candidates to be mounted at the International Space Station.

1. Introduction. One of the fundamental problems of the contemporary physics, in general, and the astrophysics, in particular, is the problem of the investigation of the electromagnetic radiation of the celestial sphere in the terahertz frequency region (0.5 - 3.0 THz), as a result of what they are expecting an abundant information which will bring us forward to the significant broadening of our ideas about the Universe and events taking place in it.

First of tasks on this way is the systematic observation of definite regions of the celestial sphere with the purpose to map the brightness of a distributed radiation and compile catalogues of discrete sources keeping in mind the finding objects unknown earlier as well as the obtaining the ranging of sources in accordance with their intensity and other characteristics what is necessary for the understanding the structure of the Galaxy and the Universe as a whole. The gap between the observation data of the celestial sphere radiation in the centimeter and infrared waveband regions is too big to permit at least slightly reliable oncoming extrapolation into the region of millimeter and submillimeter waves (or terahertz frequency band).
Next task is the investigation of the background radiation solving which, one may discover characteristics of as the distributed objects (the radiation of interstellar and interplanetary dust, initial background radiation) so the total radiation of spatially unresolved objects. Main goal

Presented at the 10-th Intern. Symp. on Space THz Technology, 16-18 March, 1999, Charlottesville, VA, USA.

here is the investigation of the initial background radiation (3 K) and its anisotropy on scales less than 10 angle degrees up to 5 angle minutes in Wien region of electromagnetic spectrum.

Further we have to indicate tasks of investigation of selected objects: spectra of discrete sources (stars, galaxies, quasars, active galaxy nuclei); radiation intensity time variations of quasars and active galaxy nuclei; the atmosphere radiation observation of planets and their satellites; the investigation of dust in the Solar System, the Galaxy and extragalactic formations.

Here we have indicated just some of tasks of the contemporary terahertz radio astronomy. One may find the impressive description of these and many other tasks in the said region of spectrum in the Proceedings of the European Space Agency Symposium named "The Far Infra-Red and Submillimetre Universe", taken place in Grenoble, France, on April 15-17, 1997 [4]

Geophysical tasks are adding to the astrophysical tasks in the terahertz frequency region [5]: the global monitoring of the Earth ozone sphere, including the study of the ozone content distribution in the Earth atmosphere and its variations; the global monitoring of the anthropogenic Earth atmosphere pollution etc.

To attack mentioned above tasks the receivers of the radiation in various bands of the terahertz frequency region, having highest sensitivity and different frequency resolution: high, medium and low, are necessary. To the present time three groups of such receivers have become clear as the result of the research and developments of many institutions. We are describing below these three groups after the example of the already formed groups of the receivers for multi-chanel ***FIRST*** telescope (Far InfraRed and Submillimeter Telescope) of the European Space Agency

1) The superheterodyne receivers based on SIS-mixers at frequencies 0.5-1.25 THz and on superconducting hot-electron bolometers at frequencies 1.25 - 2.5 THz. The achieved characteristic noise temperatures here are: 80 K at 0.5 THz, 750 K at 1.0 THz and 1900 K and 2500-3000 K at 1.3 and 2.5 THz correspondingly; the frequency resolution: $R = f/\Delta f = 1.2 \times 10^7$; the operating temperature of these receivers - 4.2 - 2.0 K [6].

2) Direct detection receivers based on bolometers at frequences 0.5 - 1.5 THz. The characteristic noise equivalent powers estimated in accordance with measurements on dc (so-called electrical NEP) here are $\sim 2 \times 10^{-18}$ W/Hz$^{1/2}$; the frequency resolution $R \sim 10^3$ when working together with grating or Fabry-Perot spectrometers; the time constant is 65 ms; the operating temperature of bolometers is ~0.1 K [7, 8].

3) Direct detection receivers based on photoconductors at frequencies 1.5 - 3.5 THz. The achieved characteristic noise equivalent powers (NEP) here are $\sim 4 \times 10^{-18}$ W/Hz$^{1/2}$; the frequency resolution $R \sim 2 \times 10^3$ - 2×10^4 when working together with Fabry-Perot spectrometer; operating temperature is ~1.7 K [9].

The direct detection receivers based on photoconductors are only ones being most sensitive of known now receivers at frequency region ~1.5 - 3.5 THz. The selection of two types of receivers for frequency region 0.5 - 1.5 THz, superheterodyne and direct detection types, is led

mainly to the reason that when they are observing weak but broadband radiation sources it may occure that the integral sensitivity of narrowband superheterodyne receivers could be not enough and at the same time the bolometer owing to its very wide frequency band will detect this radiation. Besides as bolometers don't need heterodyne pumping it is much easier to construct on their basis multi-element receiving structures for an observation spatially inhomogeneous distributed radiation sources though having not too high frequency resolution.

The Earth-based operation of all considered receivers is limited by the atmosphere that is not enough transparent in 0.5 - 3.0 THz frequency region. At the same time all measures right up to cool receivers down to 0.1 K are taking as regards to achieve ultimate low noise equivalent power. Measures are taking also to cool antennae and radiation guided elements to reduce significantly their thermal noise coming

Thus it can be concluded that the receivers based on bolometers are playing among other receivers their own important part in the terahertz radio astronomy.

2. The Submillimetron Project. The Submillimetron Project [3] is dedicated to solve most of said above tasks of terahertz radio astronomy using the Cryogenic Telescope located on the Russian segment of the International Space Station (ISS). The Astro Space Center of the P.N. Lebedev Physical Institute of the Russian Academy of Sciences is responsible for developing the Submillimetron Project. The Project was selected by the Russian Academy of Sciences in 1997 along with seven other Russian experiments as candidates for scientific radioastronomical payloads on the Russian segment of the International Space Station (Fig. 1). Currently the Astro Space Center is carrying out pre-project study under the contract with Russian Space Agency. If the Project will succeed experiments with the onboard cryogenic telescope can be performed between the years 2001 and 2004. Besides said above tasks the secondary goal of the Submillimetron Project is to provide a test bed to perform the technological experiments needed to develop follow on projects.

The Submillimetron Project intends to fill the time gap between the IRAS, COBE and the follow on projects SIRTF, FIRST and PLANCK. If it succeeds it can provide information on research targets for these projects as well as test/resolve some technological issues needed to build these telescopes.

The uniqueness of the proposed telescope lies in the deep cooling of the entire telescope and even deeper cooling of the detectors (bolometers and photoconductors) to achieve a high sensitivity at terahertz frequency band. Comparative sensitivity performances of the telescopes of the flown project (IRAS and COBE) and projects under development (SIRTF. FIRST, PLANCK) and Submillimetron Telescope are given in Fig.Fig. 2 and 3.

Telescope concept. The telescope payload consists of the Cryogenic Telescope itself and the Data Registration and Processing Unit.

The telescope will be positioned on the Russian Segment of the International Space Station (Fig.4). The telescope assembly shall be oriented in such a way as to preclude interference from the thermal radiation of the station elements, and the Sun and Earth. The angle between the optical axis of the telescope and the directions to these objects shall be larger than 60 degrees in all possible telescope pointing positions.

The data registration and processing block will be located in one of the scientific modules of the Station and connected with the telescope assembly by a cable.

The Cryogenic Telescope parameters are:

Diameter: D = 0.6 m,
Focal length: F = 4 m,
Wavelengths:
- submillimeter band: 0.3, 0.4, 0.5, 0.6, 0.8, 1.0 and 1.5 mm,
- infrared band: 3, 10, 30, 100, 200 μ m.

Cooling:
- telescope as a whole: 5 K,
- detectors (bolometers): down to 0.1 K,

Detectors:
- bolometer arrays.

Number of elements in the detector arrays:
- about 100 at wavelengths shorter than 0.5 mm,
- 7 elements at the wavelength 1.5 mm.

Angular resolution:
- submillimeter band: 5-20 min of arc,
- infrared band: 5 min of arc.

Sensitivity of the detectors:
- submillimeter band: 10^{-18} W/Hz$^{1/2}$,
- infrared band: 10^{-17}-$3 \cdot 10^{-16}$ W/Hz$^{1/2}$.

Sensitivity of the telescope (integration time = 1 s):
- submillimeter band: 3-12 mJy,
- infrared band: 6-40 mJy.

Cryogenic Telescope (see Fig. 5) includes following main units:

	Mass (kg)/Power (W)
- Optic Cryogenic Assembly (OCA)	300/40,
- Active Cooling System (ACS)	30/300,
- Telescope Electronics Assembly (TEA)	10/10,
- Telescope Pointing System (TPS)	90/80,
- Star Tracker (STR)	10/10,
Total	440/440.

Technical Requirements on Active Cryogenic System (ACS):

-The ACS system shall provide cooling of the internal screens of the Optic Cryogenic Assembly (OCA) from 300-350K to the screens operating temperature of 20K,
- Load temperature = 20 K,
- Minimum heat load = 1 W,
- Power consumption = 300 W,
- Maximum mass = 30 kg,
- Power voltage = 23-34 V.

Technical Requirements on Star Tracker (STR):

-The Star Tracker shall define the telescope optical axis pointing information (two perpendicular axes in the plane perpendicular to the optical axis and the rotation angle) and provide the correction signals to the Telescope Pointing System (TPS),
- Accuracy of the telescope pointing axes = ±10 arc sec,
- Accuracy of the telescope rotation angle axis = ±1 deg,

Telescope pointing data rate = 1 point per 10 sec,
- Power consumption = 10 W,
- Maximum mass = 10 kg.

Bolometric array concept. Scientific objectives connected with observation of extremely distant objects determines main features of the instruments and requirements for the detectors. In accordance to the main goal of the experiment - to achieve extremely high sensitivity in spectral density of continuum emission, this features includes: wide spectral bands and simultaneous observation in all spectral and spatial channels, maximum number of spatial elements in field of telescope, minimum instrumental thermal emission of cryogenic optics comparable with extraterrestrial background. Spectral region 0.3 -1.5 mm correspond to minimum in spectral density of this background. Corresponding requirements are the following:

- Wavelengths: 0.3, 0.4, 0.5, 0.6, 0.8, 1, 1.5 mm,
- Bandwidth: 10 - 30% of the observing frequency,
- Number of elements in the bolometer arrays:
  - about 100 at wavelengths 0.3 - 0.4 mm,
  - 7 elements at the wavelength 1.5 mm,
- Sensitivity of the bolometers: $\leq 10^{-18}$ W/Hz$^{1/2}$.

The last figure corresponds to measure of fluctuations in number of quanta in background radiation and can be achieved only with thermal detectors (bolometers). For phase sensitive receiver (heterodine mixer) in accordance to indefinity principle the noise temperature is restricted by a value about hf/k.

3. Normal-metal hot-electron microbolometer based on Andreev reflection effect. Taking into account the said above requirements to the bolometer receiver for the Terahertz Cryiogenic Telescope we have chosen one of most promissing bolometers - the normal-metal hot-electron microbolometer [1, 2] based on the Andreev reflection fenomenon [10] which is based on the heating electrons in the thin film of normal metal with electrodes of metal-superconductor (in the so-called S-LN-S structure (Fig. 6), where "S" means the superconductor and "LN" means the long film strip of normal metal), cooled down to extremely low temperatures of order of 100 - 200 mK. Briefly, the construction of the said microbolometer is the following: the comparatively simple structure consisted of normal metal strip (Cu, Cr or some other normal metal) with the dimensions: length - 3 - 12 μm, width - 0.1 - 0.3 μm and thikness - ~40-75 nm - with the Al or Pb superconducting electrodes at the ends and with S-I-N (superconductor-insulator-normal metal) tunnel junction at the central part of the strip - is evaporated under three angles onto the silicon substrate obtained by means of the usual electron-beam lithography using shadow evaporation technique. The radiation is absorbed by electrons in the strip of normal metal. Two circumstaces lead to the effective heating of electrons by the radiation: (a) the super low temperature (0.1 - 0.3 K) owing to what the interaction between electrons and substrate through electron-phonon collisions and therefore the energy transfer from electrons to the substrate lattice (low heat conductance G) is extremely low and (b) the phenomenon of Andreev reflection of electrons at the normal metal - superconductor boundary which takes place without the energy transfer of electrons to the superconducting electrodes at all [10]. At temperatures < 1 K the electrical resistance of the normal metal strip doesn't depend on temperature. By this reason the temperature increment of electrons in the strip is measuring by means of the mentioned above S-I-N tunnel junction. For the best matching of the bolometer with an incident radiation beam including the providing the maximum capture of the receiving radiation as in case of single so in case of multi-element receiver the log-periodic antenna (Fig.7) is integrated on the same substrate. The bolometer is placed in the center of the antenna.

The estimation of noise equivalent power (NEP) of the normal-metal hot-electron bolometer (NHEB). The shape of IV curve of the S-I-N tunnel junction depends on the electron temperature in the normal part, and by biasing the junction with a constant current and measuring voltage on it we can get a responce $\Delta V(T)$ linear in a rather wide range.

There are three major components contributing to the NEP of NHEB according to the expression:

$$NEP=\left[\ 4k_B T_e^2 G+\frac{V_j^2}{S^2}+\frac{V_n^2}{S^2}\ \right]^{1/2}, \qquad (1)$$

where T_e is the temperature of electrons in the absorber (thin metal film), $G=dP/dT$ is the thermal conductance for the outflow of signal-induced heat, $S=dV/dP= dV/dT\cdot G^{-1}$ is the power responsivity of the bolometer, V is voltage noise of the SIN-junction and V_n is voltage noise of an amplifier. The first term describes the electron temperature fluctuations in the absorber and sets the fundamental noise limit for a given device at a given temperatire. It is clear from the expression above that it is mostly the small G that provides comparatively low NEP in this type of bolometer.

For an experimental verification of the NEP several test samples of the NHEB were fabricated. We performed measurements of IV curves of the SIN-junction at different temperatures and with different dissipated power from the signal current (Fig.8). The dependence of the voltage V at constant bias current through the junction on the signal current I_{ABS} in the absorber was measured at constant temperature for two devices with different absorber lengths. The corresponding curves $V(I)$ for the two devices are almost overlapped (Fig.9). The derivative dV/dI_{ABS} directly related to the form of the curve can be expressed via temperature responsivity, inverse thermal conductivity and dP/dI_{ABS}:

$$\frac{dV}{dI_{ABS}}=\frac{dV}{dP}\cdot\frac{dP}{dI_{ABS}}=\frac{dV}{dT}\cdot\left(\frac{dP}{dT}\right)^{-1}\cdot\frac{dP}{dI_{ABS}}.$$

One can find from the Joule law

$$P=P_{Joule}=I_{ABS}^2 R\Rightarrow\frac{dP}{dI_{ABS}}=2RI_{ABS}..$$

The inverse thermal conductance can be found from the expression for the heat excange in case of the hot-electron effect:

$$P_{e\to ph}=\Sigma U\left(T_e^5-T_{ph}^5\right)\Rightarrow\frac{dP}{dT}=5\Sigma UT^4, \qquad (2)$$

where Σ is a material-specific parameter and we assume equilibrium, $P_{Joule}=P_{e\to ph}$. After substitution we get

$$\frac{dV}{dI_{ABS}}=\frac{dV}{dT}\cdot\left(\frac{2I_{ABS}R}{5\Sigma T^4U}\right)\propto\frac{R}{U}. \qquad (3)$$

The overlapping of the curves means then, that increase of dissipated power (P) due to higher resistance (R) has been exactly compensated by increase of the heat conductance due to larger volume (U), i.e. no substantial thermal transport through the NS-contacts has been present. The dependence $V(I_{ABS})$ was then re-calculated to give $V(P)$. Maximal power responsivity at an optimal I_{bias} = 0.3 nA was found to be $S_{max}=|dV/dP|=3\cdot10^7$ V/W. Combining the data $V(I_{bias},T)$ and $V(I_{bias},P)$ the dependence $P(T_e)$ could be calculated (Fig.10).

From a fit to the expression (2) we could find the parameter $\Sigma = 3 \cdot 10^{-9}$ nW·K^{-5}·μm^{-3} and consequently the thermal conductance $G = 6 \cdot 10^{-12}$ W/K at 300 mK. This value is twice as low as the one which can be calculated using the data from [1]. This decrease was due to the smaller volume of the absorber in our case. The thermal fluctuation component of the NEP (1) calculated for the value of G is about $5 \cdot 10^{-18}$ W/Hz$^{1/2}$. At 100 mK the thermal conductance was considerably decreased to $G = 7 \cdot 10^{-14}$ W/K. This value of G gives a thermal fluctuation noise component of the total NEP$= 2 \cdot 10^{-19}$ W/Hz$^{1/2}$ which is well below the requirements for the Cryogenic Telescope (see the paragraph 2) as well as the ESA requirements for the total NEP for future spaceborn bolometers [11].

The thermal time constant can be computed as $\tau = C/G$ where C is the electron heat capacity. For the obtained value of Σ we get $\tau = 5T^{-3}$ ns. At T=300 mK the time costant $\tau = 0.2$ μs and at T=100 mK the time costant $\tau = 5$ μs which is considerably shorter as what is typically required and much lower of 1 s what is the integration time of the Cryogenic Telescope (see the paragraph 2).

The recently measured sensitivity of the Andreev microbolometer about $5 \cdot 10^{-18}$ W/Hz$^{1/2}$ is presented in detail in separate paper at this Symposium [12].

REFERENCES

[1] **Ultrasensitive hot-electron microbolometer**, M. Nahum and John M. Martinis, Appl. Phys. Lett., **63** (22), 29 November 1993, pp. 3075-3077.

[2] **Andreev reflection based normal metal hot-electron bolometer for space applications,** A. Vystavkin, D. Chouvaev, L. Kuzmin, M. Tarasov, P. Sundquist, M. Willander and T. Claeson, Proc. of 4th International Conference on Millimeter and Submillimeter Waves and Applications, July 20-23, 1998, San Diego, USA, pp. 441-448.

[3] **Development of a Submillimeter Wave Criogenic Telescope for the Russian Segment of the International Space Station (ISS). Project Submillimeteron.** L. Kuzmin, N. Kardashev, V. Kurt, V. Gromov, A. Trubnikov, V. Altunin, M. Tarasov, D. Chouvaev, D. Golubev, A. Vystavkin, M. Willander, T. Claeson, The 2nd European Symposium on the Utilization of the International Space Station, ESTEC, Noordwijk, The Nethernds, November 16-18, 1998.

[4] **The Far InfraRed and Submillimetre Universe,** An ESA Symposium devoted to the Far InfraRed and Submillimetre Telescope (FIRST) mission, 15-17 April, 1997, Institut de Radio Astronomie Millimetrique (IRAM), Grenoble, France, complete volume.

[5] **The Choice of Main Spectral Characteristics of the Limb Spectrometer for Small Atmosphere Gas Components Measurements,** V.D. Gromov, E.N. Kadygrov, A.S. Kosov, M.G. Sorokin, I.A. Strukov, The Investigation of the Earth from the Space, 1991, N 5, pp. 16-21 (In Russian).

[6] **The HIFI Heterodyne Instrument for FIRST: Capabilities and Performance,** N.D. Whyborn, [4], pp. 19-24.

[7] **The Design of a Bolometer Instrument for FIRST**, M.J. Griffin, [4], pp. 31-35.

[8] **A Monolithic Bolometer Array Suitable for FIRST**, J.J. Bock, H.G. LeDuc, A.E. Lange, J. Zmuidzinas, [4], pp. 349-352.

[9] **An Optimised Photoconductor Instrument for FIRST**, A. Poglitsch, [4], pp. 25-30.

[10] **Thermal Conductivity of the Intermediate State of Superconductors**, A.F. Andreev, Sov. Phys. JETP, 1964, November, **19**, pp. 1228-1231.
[11] **ESA Tender AO3288 "Hot-electron Microbolometers Technology for IR and Sub-mmw Application",** Open Date: October 2, 1997.
[12] **Optimization of the normal metal hot-electron mictobolometer,** D. Chouvaev, D. Golubev, M. Tarasov, L. Kuzmin, T. Claeson, this Symposium, page ...

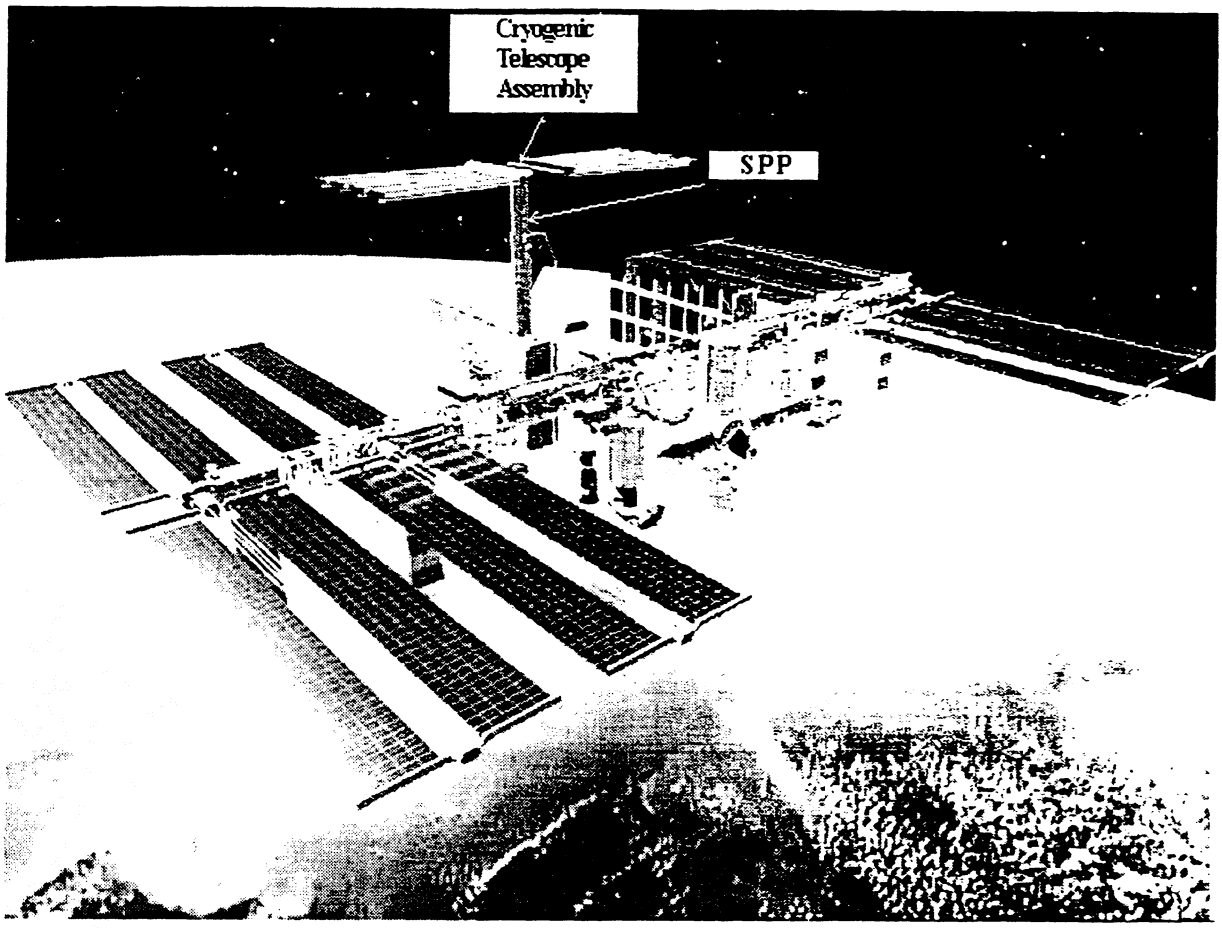

Figure 1. The International Space Station. General view shows a position of the Cryogenic Telescope Assembly and Science-Power Platform (SPP).

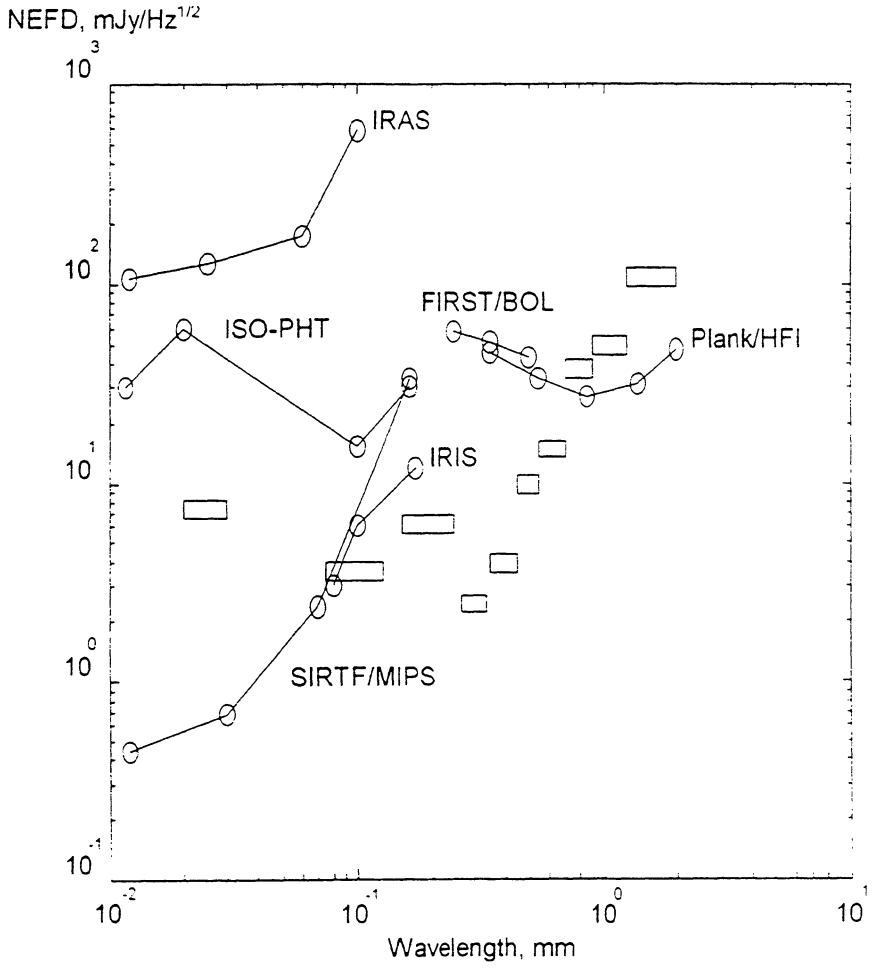

Figure 2. The sensitivity related to discrete sources. Rectangles - the Submillimeteron Project, circles - other projects. NEFD - noise equivalent flux density.

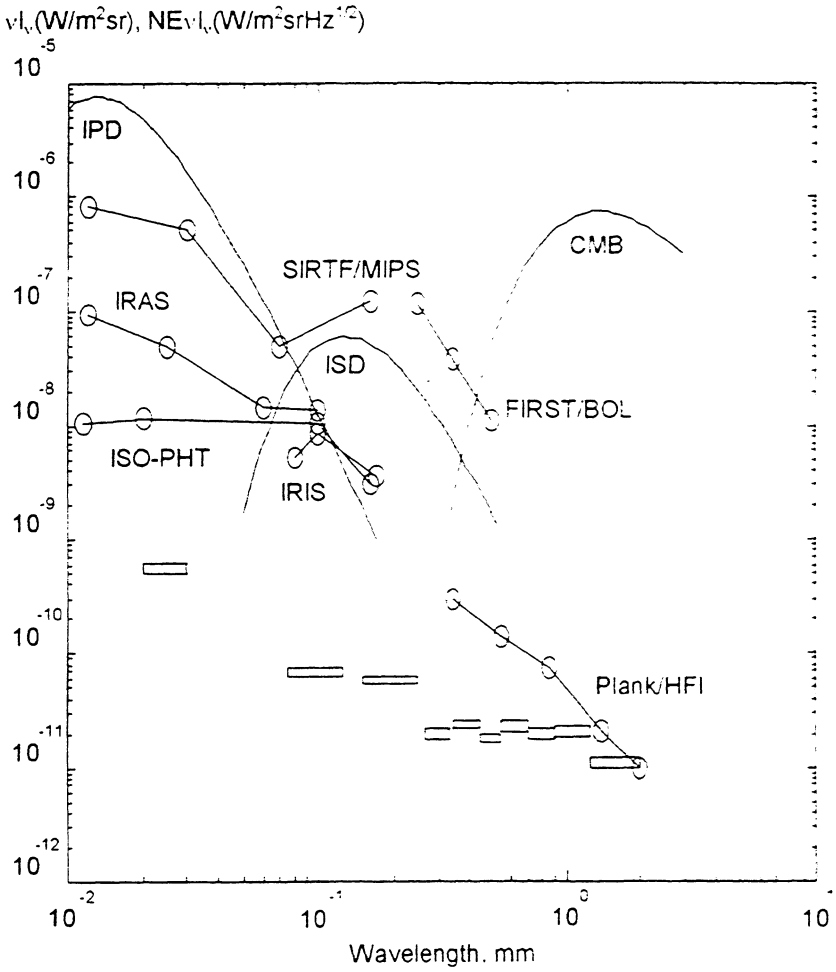

Figure 3. The sensitivity related to brightness of extended sources. Rectangles - the Submillimetron Project, circles - other projects. NE νI_ν - noise equivalent brightness with S/N=1. The brightness of sources given for comparison: CMB - cosmic microwave background, ISD - interstellar dust emission, IPD - interplanetary dust emission.

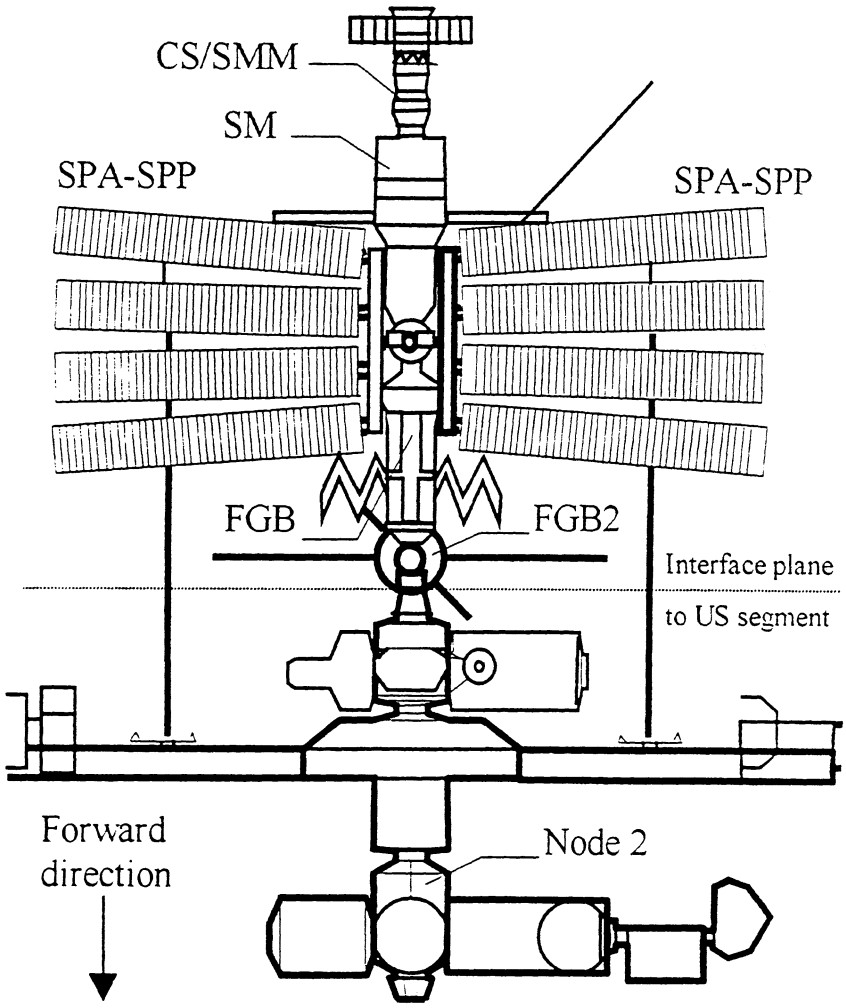

Figure 4. International Space Station. Top view. CS/SMM - Cargo Ship "Progress" (the Submillimetron telescope in the special transport bay); SM - Service Module with remote manipulator; SPA - Solar Power Array; SPP - Science-Power Platform. Large SPA's on both sides of US segment are not shown.

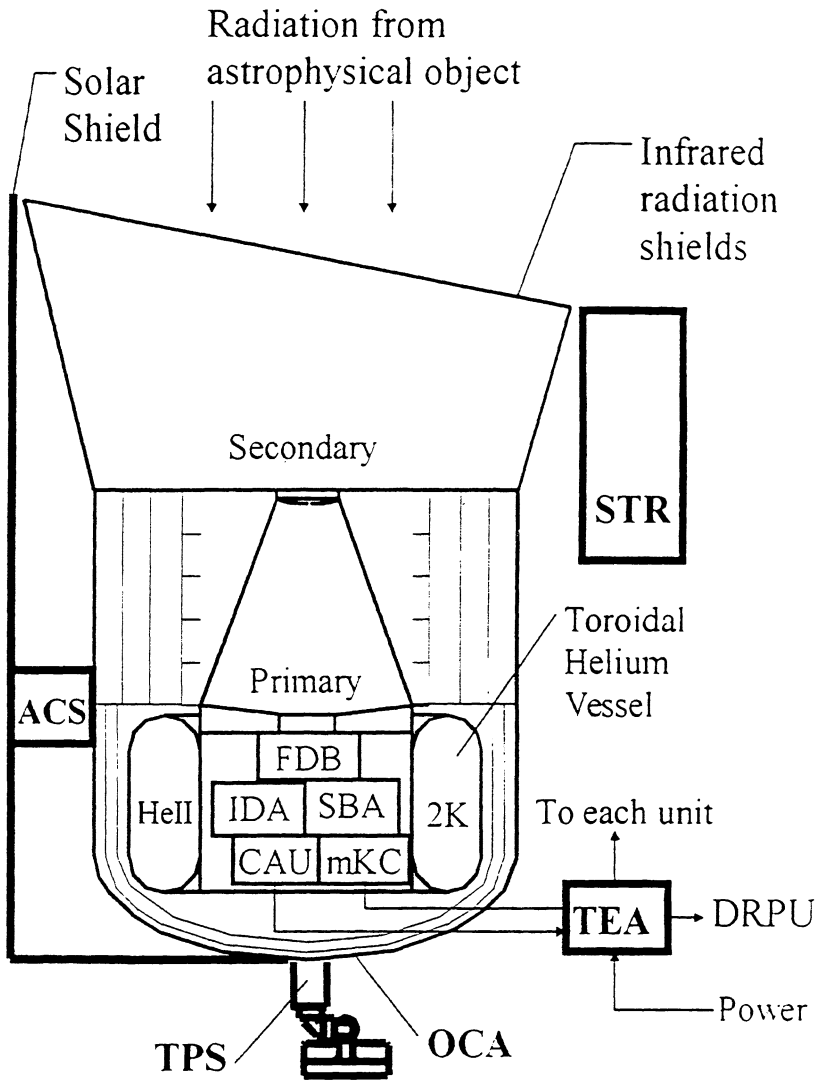

Figure 5. Block-diagram of the Cryogenic Telescope. FDB - Focal Dichroic Beam-splitters assembly; IDA - Infrared Detector Array; SBA - Submillimeter Bolometer Array; CAU - Cool Amplifiers Unit; mKC - milli-Kelvin Cooler (100-300 mK); DRPU - Data Registration and Processing Unit.

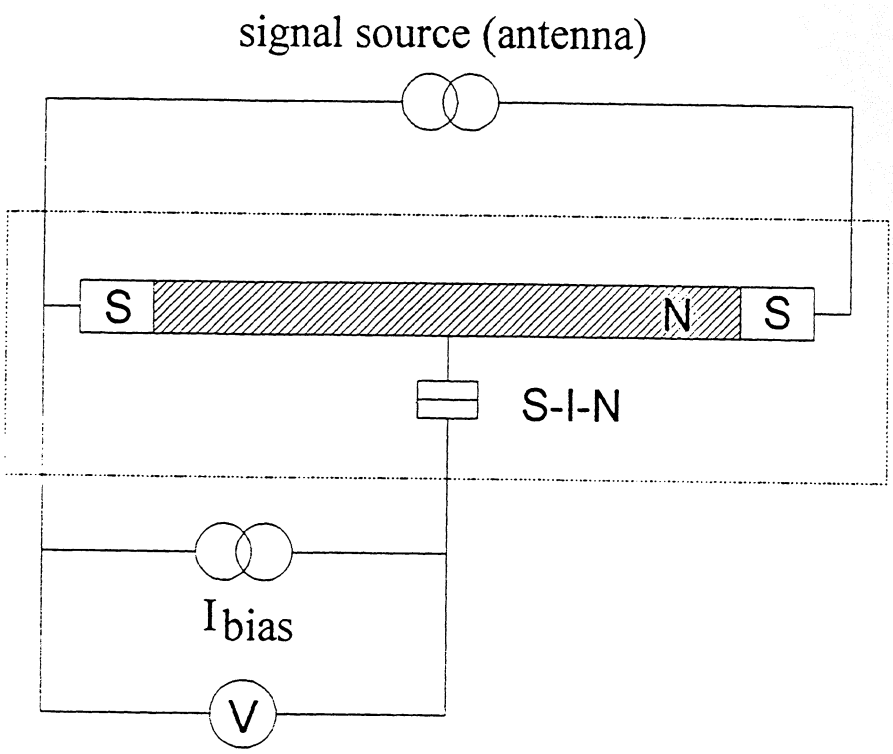

Figure 6. Schematic of the microbolometer: the SIN junction is biased at a small constant current. A junction voltage depends on the smearing of the IV-curve which is used to measure the electron temperature in the normal metal absorber (hatched).

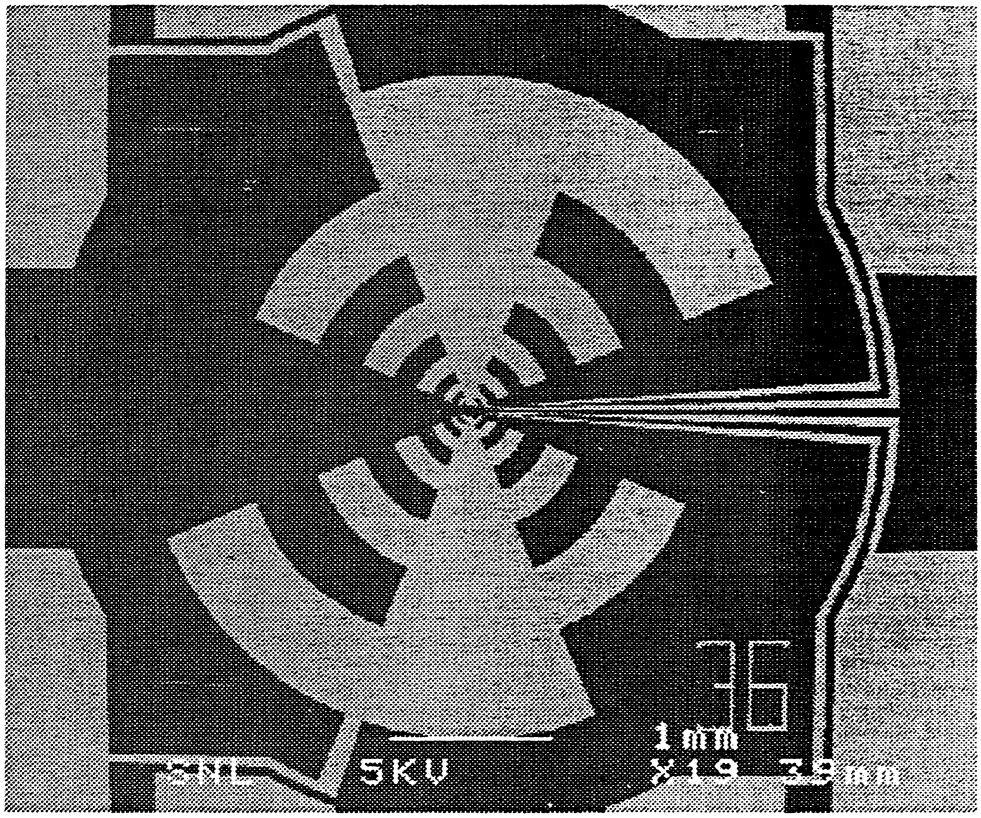

Figure 7. View of a chip with a planar log-periodic antenna and the microbolometer in the focus of the antenna designed for device tests at 100-1000 GHz.

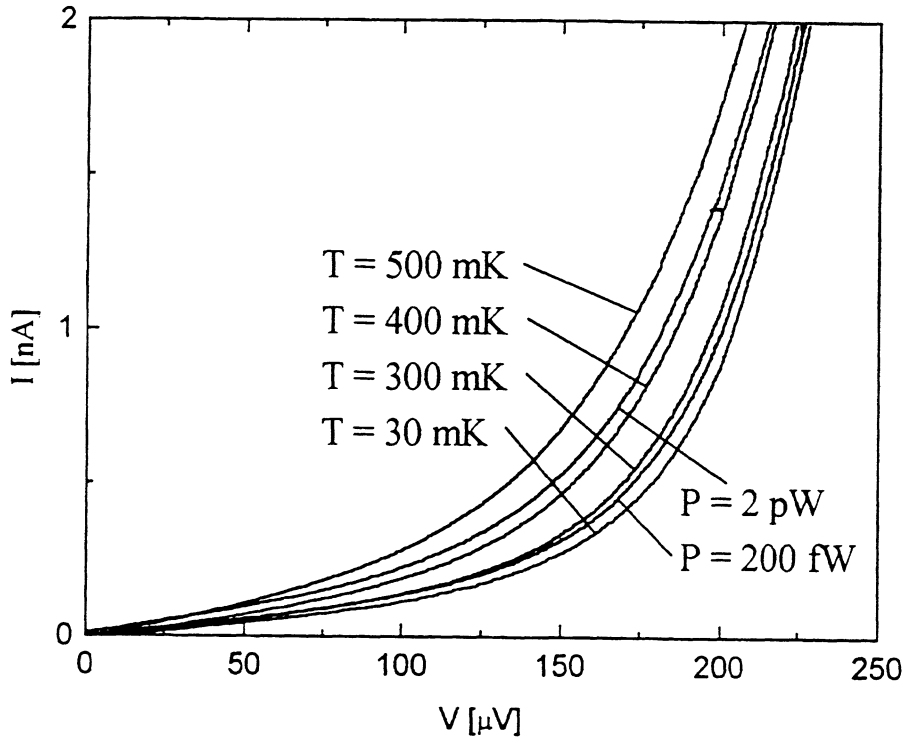

Figure 8. IV-curves of the SIN junction measured for different temperatures without any signal current and for two different powers dissipated by the signal current at the base temperature of 30 mK.

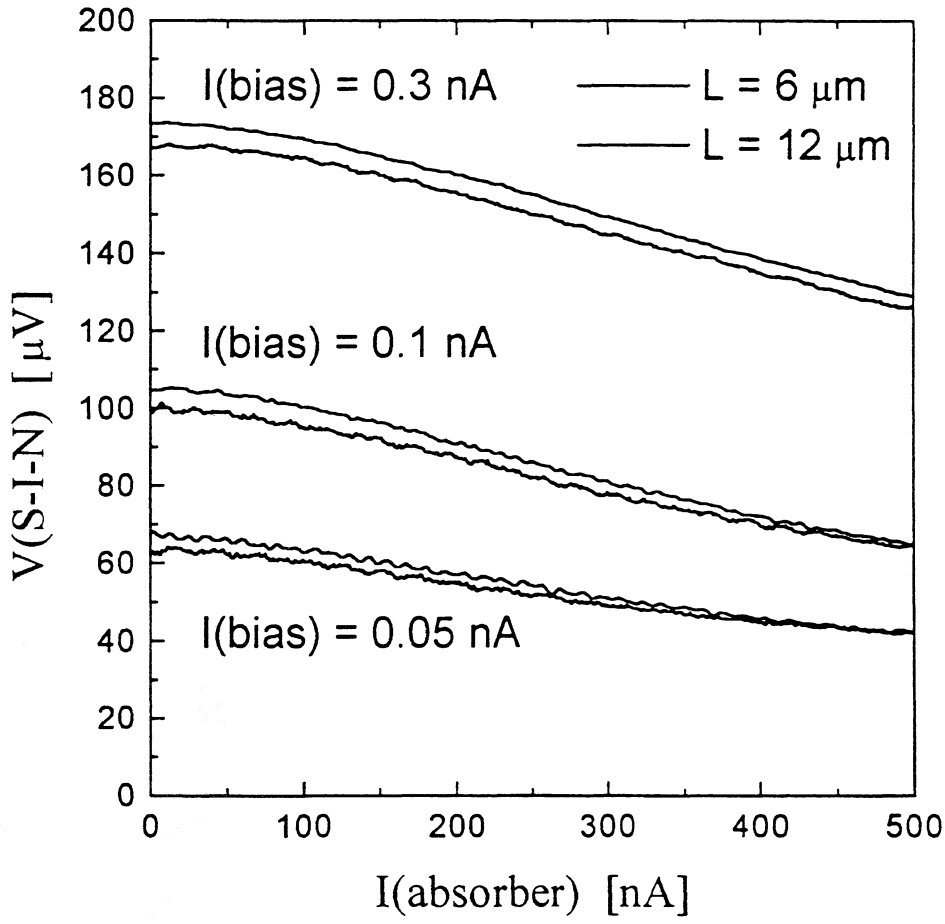

Figure 9. The junction voltage V at constant bias current I_{bias} through the junction as a function of the signal current I_{ABS} for two devices with different absorber lenght 6 μ m and 12 μ m at T=30mK.

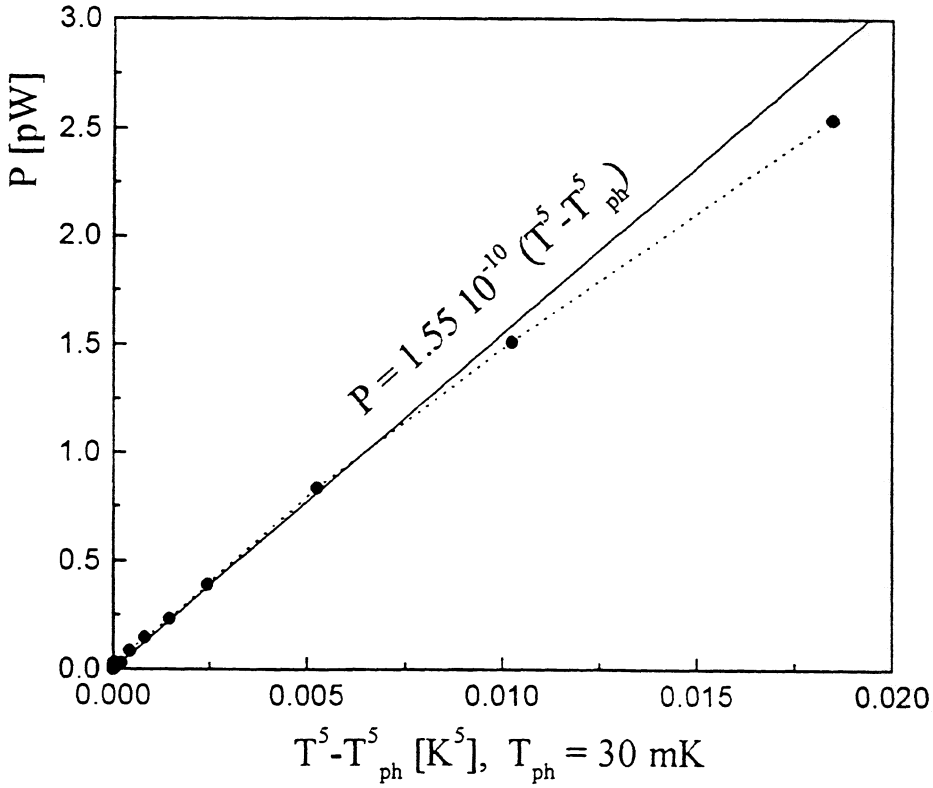

Figure 10. Power dissipated in the absorber vs. $(T^5 - T_{ph}^5)$ where T is temperature of electrons deduced from measurements $V(I_{bias}, T)$ and T_{ph}=30 mK is temperature of the lattice (measured temperature of the sample holder). Linear fit corresponds to the relation (2).

CHARACTERIZATION OF THE ELECTRON ENERGY RELAXATION PROCESS IN NbN HOT-ELECTRON DEVICES

K. S. Il'in, G. N. Gol'tsman,* and B. M. Voronov
Physics Department, Moscow State Pedagogical University, Moscow 119435, Russia
*email: goltsman@rpl.mpgu.msk.su

Roman Sobolewski
Laboratory for Laser Energetics and Department of Electrical and Computer Engineering
University of Rochester, 250 East River Road, Rochester, NY 14623-1299

Abstract

We report on transient measurements of electron energy relaxation in NbN films with 300-fs time resolution. Using an electro-optic sampling technique, we have studied the photoresponse of 3.5-nm-thick NbN films deposited on sapphire substrates and exposed to 100-fs-wide optical pulses. Our experimental data analysis was based on the two-temperature model and has shown that in our films at the superconducting transition 10.5 K the inelastic electron-phonon scattering time was about (10±2) ps. This response time indicated that the maximum intermediate-frequency band of a NbN hot-electron phonon-cooled mixer should reach (16+4/−3) GHz if one eliminates the bolometric phonon-heating effect. We have suggested several ways to increase the effectiveness of phonon cooling to achieve the above intrinsic value of the NbN mixer bandwidth.

Introduction

In the terahertz frequency range, hot-electron mixers (HEM) have reached noise temperatures lower than the other mixer types, such as superconductor–insulator–superconductor tunnel junctions or Schottky diodes. Both Nb diffusion-cooled and NbN phonon-cooled devices demonstrate roughly the same noise temperatures. For a phonon-cooled, 3.5-nm-thick NbN mixer, the 4-GHz gain bandwidth has been demonstrated[1] at 140-GHz and 660-GHz frequencies, and the noise bandwidth at 620 GHz has been found to breach twice the gain bandwidth.[2] For a diffusion-cooled Nb HEM, the 9-GHz gain bandwidth has been measured at 600 GHz.[3]

In the HEM device, the rate of electron cooling controls the bandwidth of the intermediate frequency output; thus, the intrinsic bandwidth of an ideal phonon-cooled HEM corresponds to the inverse of the inelastic electron-phonon scattering time. In real

HEM's, unfortunately, nonequilibrium phonons hamper the device performance. Re-absorption of excited phonons by electrons slows the electron cooling, leading to the increased response time and the decrease of the HEM bandwidth. This explains why numerous experimental studies of NbN ultrathin HEM's resulted in a measured bandwidth smaller than one would expect from the value of the electron-phonon scattering time determined in independent experiments. Thus, secondary processes, such as phonon re-absorption and phonon escape from the film to the substrate, directly affect the results of frequency-domain HEM measurements.

In this work, we report our direct measurements of the electron energy relaxation time in a 3.5-nm-thick NbN HEM using a time-domain electro-optic (EO) sampling technique with 300-fs resolution.[4] EO sampling does not require the response signal to be transmitted out of the cryostat; instead, the signal is measured *in situ*, in the close vicinity (less than 100 μm) to HEM integrated into a coplanar waveguide. As compared to frequency-domain methods, EO sampling provides much more accurate data on the intrinsic picosecond response of the device. Our studies show that the intrinsic gain bandwidth of the NbN HEM is up to 16 GHz, which is sufficient for most coherent terahertz detection applications.

Experimental

Films with a 3.5-nm thickness were deposited on sapphire substrates by reactive dc magnetron sputtering in the Ar+N_2 gas mixture.[5] The largest values of both the critical current density J_c and the transition temperature T_c were achieved at the discharge current of 300 mA, the partial N_2 pressure of 1.1×10^{-4} mbar, and the substrate temperature 850°C. The Ar pressure proved to have no substantial impact on the film deposition rate or film composition, and for this reason, the 4.8×10^{-3}-mbar pressure was selected to maintain a stable discharge. The deposition rate was 0.5 nm/s, defined as the ratio between the film thickness (measured with a mechanical profilometer) and the deposition time.

A typical experimental configuration, used for the EO sampling measurements, is shown in Fig. 1. The test structure was patterned into a 4-mm-long coplanar waveguide (CPW) with a 30-μm-wide central line, separated by 5-μm-wide gaps from the ground planes. The tested HEM consisted of 25 parallel, 2-μm-wide strips, located in the middle of the CPW, between the central line and grounds. Vanadium strips terminated both ends of the CPW to assure 50-Ω output impedance of our device. Typically, after processing, the device exhibited the midpoint of the superconducting transition (definition of T_c) at 10.3 K, with ~1.0-K transition width, and a critical current density J_c at 4.2 K of 10^6 A/cm^2.

The sample was mounted on a copper cold finger inside an exchange-gas, liquid-helium dewar, with optical access through a pair of fused-silica windows. During our measurements, the sample was in the He exchange gas with the temperature regulated in the range from 4.2 K to 12 K and stabilized to 0.2 K. One end of the CPW was grounded, while the other was wire-bounded directly to a 50-Ω coaxial cable connected through a bias-tee to the 14-GHz sampling oscilloscope. To facilitate EO measurements the entire waveguide structure was overlaid with an electro-optical $LiTaO_3$ crystal.

A block diagram of our experimental setup is shown in Fig. 2 and described in detail in Ref. 4. A commercial self-mode-locked Ti:Al_2O_3 laser, pumped by an Ar-ion laser, was used to excite picosecond pulses in the HEM and, simultaneously, to electro-optically measure the resulting electrical transient propagating in the CPW line. The laser provided a train of ~100-fs-wide optical pulses with 800-nm wavelength and 76-MHz repetition rate at an average power of >1 W. The train was split into two beams by a 70/30 beamsplitter. The first (excitation) beam was frequency doubled in a nonlinear crystal, intensity modulated, and focused by a microscope objective to an ~100-μm-diam spot to excite the HEM structure. The microscope objective was also a part of the viewing arrangement that allowed us to observe the sample during beam positioning. The average power of the 400-nm excitation beam measured outside the dewar was ~0.75 mW. By calculating the amount of light absorbed and reflected by two dewar windows and the $LiTaO_3$ crystal, as well as taking into account reflectivity and transmissivity of the NbN film, we estimate that the power actually absorbed by the HEM was only 4.5 μW, which is equivalent to approximately 1.5×10^{16} 3-eV photons per cm^3, and induced below 0.1 K permanent heating of the device area. The second (sampling) beam traveled through a computer-controlled delay line and was focused to a < 10-μm-diam spot inside the $LiTaO_3$ at the gap between the center and ground CPW lines, less than 100 μm from the HEM (see Fig. 1). The transient birefringence introduced in the $LiTaO_3$ crystal by the electric field associated with the HEM photoresponse was detected by the sampling beam, which allowed us to measure the time evolution of the photoresponse voltage signal.[4] From the operational point of view our EO system can be regarded as a sampling oscilloscope featuring <200-fs time resolution and <150-μV voltage sensitivity, which are well below the characteristics of the transients reported here.

Results and Discussion

A typical response of our device measured with our EO-sampling technique is presented in Fig. 3. We note that the signal (solid line) contained a large amount of noise, but it was acquired at low bias current, 175 μA, and at temperature 10.5 K, right at the superconducting-resistive transition. The dashed-dotted line represents the response of the sample calculated for the single-pulse input on the basis of the two-temperature (2T) model.[6] Since the reflection-free time window for our experiments, due to limited length of the CPW and large signal propagation velocity on sapphire, was only about 40 ps, the reflections from the CPW ends contributed to the measured EO sample response and had to be included in simulations. The dashed line in Fig. 3 shows the result of our 2T model calculations that took those reflections into account.

The 2T model assumes a very short thermalization time of quasiparticles. Fast thermalization occurs at high energies via both electron-electron interactions and electron-optical-phonon scattering, while at low energies it is mainly due to electron-electron scattering. For phonons the single-temperature approximation remains reasonable for a relatively weak coupling between phonons and the substrate. For low-temperature superconductors, it is well known that establishment of the phonon nonequilibrium temperature occurs via electron-phonon interactions.

In our simulations, we considered a superconducting film carrying a constant current that drives the sample into the resistive state at the temperature T_b very close to T_c. Under this condition the energy gap is very small as compared to $k_B T_b$, and the quasiparticle energy spectrum is close to that of electrons in a normal metal. Consequently, the inelastic scattering of quasiparticles, as well as their recombination into Cooper pairs, can be described by the electron-phonon interaction time. We assume that the film is uniformly illuminated by radiation and that the bias current is uniformly distributed over the bridge's cross-section area. We also neglect joule heating by the biasing current and consider only small deviations from equilibrium.

The time-dependent effective temperatures T_e and T_{ph} are obtained as a solution of the 2T coupled linear heat-balance equations:

$$C_e \frac{dT_e}{dt} = \frac{\alpha P_{\mathrm{in}}(t)}{\mathrm{V}} - \frac{C_e}{\tau_{e-\mathrm{ph}}}\left(T_e - T_{\mathrm{ph}}\right),$$

$$C_{\mathrm{ph}} \frac{dT_{\mathrm{ph}}}{dt} = \frac{C_{\mathrm{ph}}}{\tau_{\mathrm{ph}\text{-}e}}\left(T_e - T_{\mathrm{ph}}\right) - \frac{C_{\mathrm{ph}}}{\tau_{\mathrm{es}}}\left(T_{\mathrm{ph}} - T_b\right), \tag{1}$$

where C_e and C_{ph} are the electron and phonon specific heats, α is the radiation absorption coefficient, V is the volume of the bridge, and T_b is the sample temperature. $P_{in}(t)$ is the incident optical power, in our case modeled as a Gaussian-shaped pulse. The equations also contain the characteristic times $\tau_{e\text{-ph}}$ for electron-phonon scattering, and τ_{es} for phonon escape to the substrate. The energy balance equation is $\tau_{e-ph} = \tau_{ph-e}\left(C_e/C_{ph}\right)$, where $\tau_{ph\text{-}e}$ is phonon-electron scattering time. To obtain the corresponding time evolution of the device voltage response, we invoked the methods described in detail in Ref. 6.

A diagram of energy relaxation processes taking place in a metal film under the influence of the electromagnetic radiation is presented in Fig. 4. For the ideal $\tau_{e\text{-ph}} << \tau_{ph\text{-}e}$ and $\tau_{es} << \tau_{ph\text{-}e}$ case, the electron energy relaxation back to equilibrium is essentially due to the inelastic electron scattering with phonons. Thus, the voltage signal decay should occur according to the exponential law with a single characteristic time constant $\tau_{e\text{-ph}}$. For real NbN films at $T \approx 10$ K, $C_e = 1.7 \times 10^{-3}$ J cm^{-3} K^{-1}, and $C_{ph} = 1.1 \times 10^{-2}$ J cm^{-3} K^{-1}, which leads to $\tau_{ph\text{-}e} = 6.5\ \tau_{e\text{-ph}}$. In addition, $\tau_{es} = 13 \times d$(nm) ps, which for our 3.5-nm-thick films results in $\tau_{ph\text{-}e} = 1.7\ \tau_{es}$. Consequently, in our case, the energy flow from electrons to phonons dominates over the re-absorption of nonequilibrium phonons by electrons; however, the energy backflow cannot be neglected. Compared to the ideal device, the shape of the response for a real HEM has a more complicated waveform that cannot be described by the single-time-constant exponential law. In this case, it is only possible to determine the "average" decay time (see Fig. 3), which is given by the time that elapses from the pulse arrival until the magnitude of the response decreases down to $1/e$ from its maximum value. Using this criterion, we obtained for our device the 30-ps relaxation time which corresponds to the HEM gain bandwidth of 5.3 GHz.

The $\tau_{e\text{-ph}}$ value was obtained as the fitting parameter in the 2T equations, which provided the best agreement (dotted and dashed lines in Fig. 4) with the experimental transient and was determined to be (10±2) ps. This value can be regarded as the intrinsic electron-phonon scattering time and limits the maximum gain bandwidth of the 3.5-nm-thick phonon-cooled NbN HEM's to (16+4/–3) GHz.

There are several possible ways to increase the current experimental 5.3-GHz bandwidth limit to the intrinsic 16-GHz value. Further technological development of NbN film deposition (e.g., epitaxial growth) should result in decreased film thickness without degrading its operational parameters, such as T_c and J_c. This should increase the escape rate of nonequilibrium phonons from the film. Phonon escape τ_{es} also depends on the transparency of the film–substrate interface; using substrate materials that provide better acoustic matching with NbN films (e.g., MgO) one would additionally lower τ_{es}. Out-diffusion of hot electrons into the metal contact pads bounded to the superconducting

bridge is commonly used in Nb devices (so-called diffusion-cooled HEM's) to increase their gain bandwidth.[7] The same approach could be implemented for NbN structures, despite NbN's very small electron diffusivity. Finally, it might be beneficial to deposit an acoustically matched, low-loss dielectric layer on top of the device to act as an additional channel for the phonon escape.

Conclusions

We have measured the 30-ps photoresponse of NbN ultrathin films at 10 K and calculated the corresponding (10±2)-ps inelastic electron-phonon scattering time. This latter value imposes the fundamental limit of (16±4/–3) GHz to the intermediate frequency bandwidth of phonon-cooled NbN HEM's. We have also indicated the possible ways to approach this maximal bandwidth in real devices.

Acknowledgment

This work has been supported by Russian Program on Condensed Matter (Superconductivity Division) under Grant N 98062, the U.S. Office of Naval Research Grant N00014-97-1-0696, and the NATO Linkage Grant CRG.LG974662.

References

1. S. Cherednichenko, P. Yagoubov, K. Il'in, G. Gol'tsman, and E. Gershenzon, in *The Proceedings of the 8th International Symposium on Space Terahertz Technology* (Cambridge, MA, 1997), p. 245.
2. H. Ekström, E. Kollberg, P. Yagoubov, G. Gol'tsman, E. Gershenzon, S. Yngvesson, Appl. Phys. Lett. **70** (24), 3296–3298 (1997).
3. B. S. Karasik, A. Scalare, R. A. Wyss, W. R. McGrath, B. Bumble, H. G. LeDuc, J. B. Barner, and A. W. Kleinsasser, Proceedings of the 6th International Conference on Terahertz Electronics, Leeds, UK, September 1998, in press.
4. M. Lindgren, M. Currie, C. A. Williams, T. Y. Hsiang, P. M. Fauchet, R. Sobolewski, S. H. Moffat, R. A. Hughes, J. S. Preston, F. A. Hegmann, IEEE J. Sel. Top. Quantum Electron. **2** (3), 668–678 (1996).
5. P. Yagoubov, G. Gol'tsman, B. Voronov, L. Seidman, V. Siomash, S. Cherednichenko, and E. Gershenzon, "The Bandwidth of HEB Mixers Employing Ultrathin NbN Films on Sapphire Substrate," in *The Proceedings of the 7th International Symposium on Space Terahertz Technology*, (Charlottesville, VA, 1996), p. 290.
6. A. D. Semenov, R. S. Nebosis, Yu. P. Gousev, M. A. Heusinger, K. F. Renk, Phys. Rev. B **52** (1), 581–590 (1995).
7. D. E. Prober, Appl. Phys. Lett. **62** (17), 2119–2121 (1993).

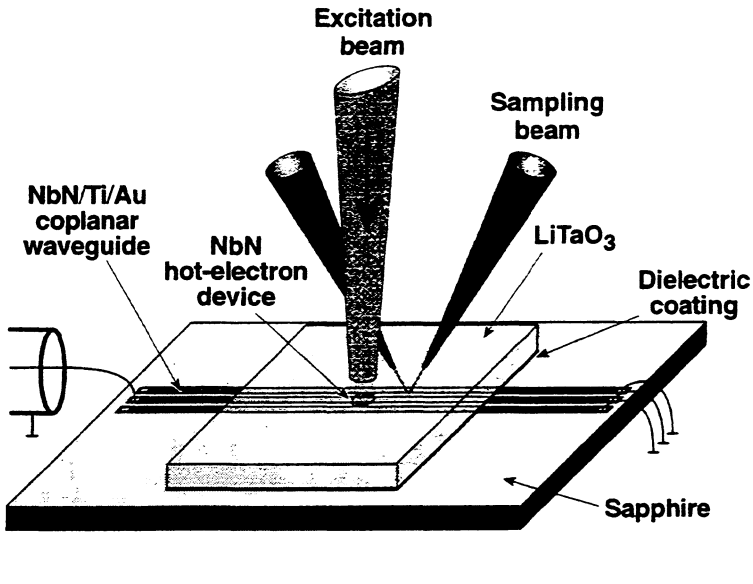

Fig. 1. Experimental configuration for EO sampling testing of a NbN HEM.

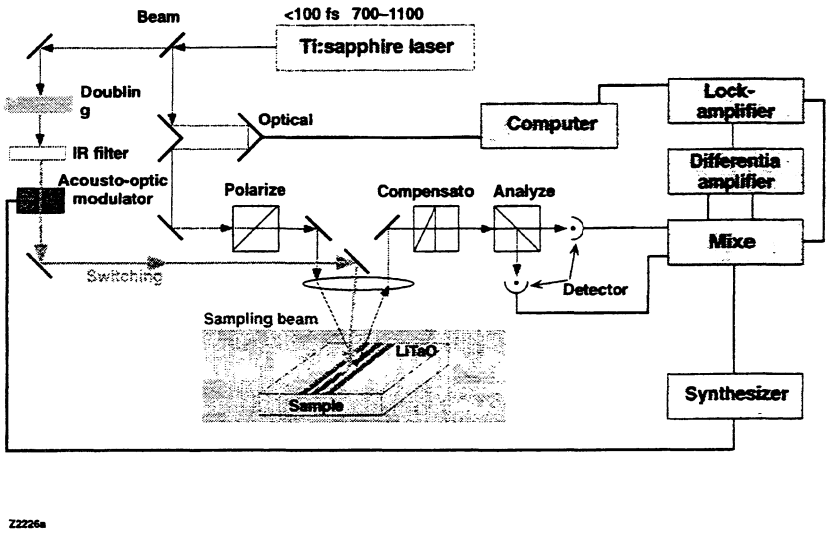

Fig. 2. Block diagram of the EO sampling system.

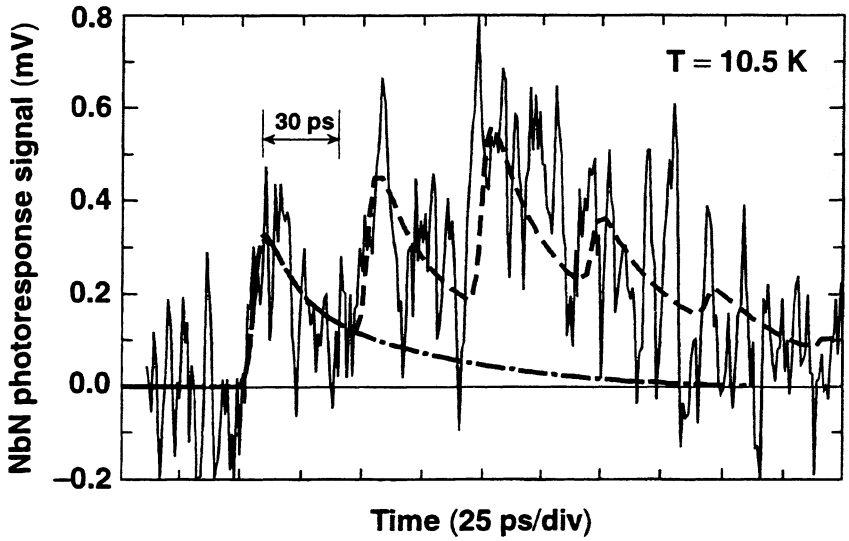

Fig. 3. Time-resolved response of a NbN HEM to a 100-fs optical excitation pulse. Temperature was 10.5 K.

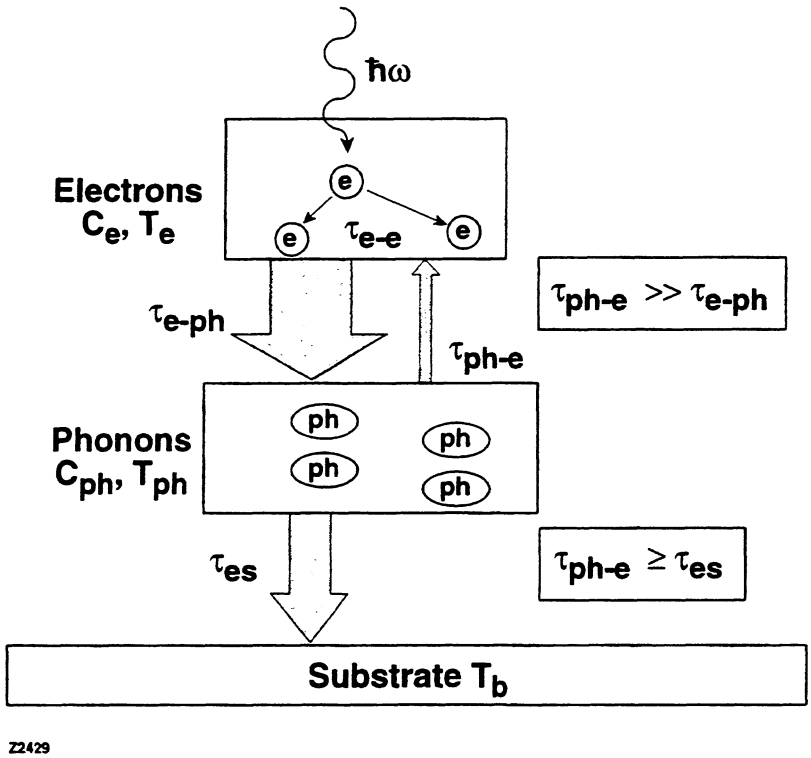

Fig. 4. Schematics of the energy flow diagram for the hot-electron effect.

SUBMILLIMETER SIS MIXERS USING HIGH CURRENT DENSITY Nb/AlN/Nb TUNNEL JUNCTIONS AND NbTiN FILMS

J. Kawamura, D. Miller, J. Chen, J. Kooi and J. Zmuidzinas
California Institute of Technology, 320-47, Pasadena, CA 91125

B. Bumble, H. G. LeDuc, and J. A. Stern
Center for Space Microelectronics Technology,
Jet Propulsion Laboratory, Pasadena, CA 91108

Abstract—We are currently exploring ways to improve the performance of SIS mixers above 700 GHz. One approach is to use NbTiN in place of Nb for all or some of the mixer circuitry. With its high gap frequency and low losses demonstrated up to 800 GHz, it should be possible to fabricate an all-NbTiN SIS mixer with near quantum-limited noise performance up to 1.2 THz. Using a quasioptical twin-slot two-junction mixer with NbTiN ground plane and wiring and hybrid Nb/AlN/NbTiN junctions, we measured an uncorrected receiver noise temperature of $T_{RX} \approx 500\,\mathrm{K}$ across 790–850 GHz at 4.2 K bath temperature.

Our second approach is to reduce the RC product of the mixer by employing very high current density Nb/AlN/Nb junctions. By using these we will greatly relax the requirement on tuning circuits, which is where substantial losses occur in mixers operating above the Nb gap frequency. These junctions have resistance-area products of $R_N A \approx 5.6\,\Omega\,\mu\mathrm{m}^2$, good subgap to normal resistance ratios, $R_{sg}/R_N \approx 10$, and good run-to-run reproducibility. From FTS measurements we infer that $\omega R_N C = 1$ at 270 GHz in these junctions. This is a substantial improvement over that available using Nb/AlO_x/Nb technology. The sensitivity of a receiver incorporating these high current density mixers is $T_{RX} = 110\,\mathrm{K}$ at 533 GHz using a design for lower J_c mixers, which is close to the best we have measured with lower J_c Nb/AlO_x/Nb mixers.

I. Introduction

SIS mixers have now developed to the point where their noise performance under 700 GHz (the gap frequency of niobium) is nearly quantum-limited, and near 1 THz their sensitivity is still better than those of competing technologies. Though it is clear that SIS mixers using Nb junctions can work efficiently above 700 GHz, resistive loss in the tuning circuit ultimately limits their performance. Indeed, the best results at 1 THz were achieved by using tuning circuits made with good normal metal conductors; however, even in this case the power coupled to the junctions is only about 20% [1]. There are two major ways to improve the performance of SIS mixers above 700 GHz: 1) Use low-loss superconducting films with T_c higher than Nb, and 2) reduce the RC product of the junctions. We are pursuing both of these options.

We recently began an effort to use NbTiN film in our quasioptical SIS mixers. Our previous work with these mixers has convincingly demonstrated that NbTiN films can have very low loss at frequencies as high as 800 GHz, and thus may be suitable for use in mixers operating up to its gap frequency, $2\Delta/h \approx 1.2$ THz. For example, a mixer with

Nb/AlO_x/Nb junctions, Nb wiring and NbTiN ground plane gave very impressive performance: $T_{RX} = 110\,\mathrm{K}$ at 638 GHz [2]. This measurement showed that the loss in the ground plane near 650 GHz is at least as low as in a Nb ground plane. Fourier transform spectrometer (FTS) characterization of a mixer made entirely from NbTiN film indicated that the surface resistance of the mixer wiring was $R_S < 0.03\,\Omega$ at 500 GHz, and had an upper limit of roughly $R_S < 0.1\,\Omega$ at 800 GHz [3]. These measurements support the claim that NbTiN films are not as lossy at submillimeter wavelengths as NbN films. In the past year considerable progress has been made in the fabrication process [4],[5], and we presently report on measurements made near 800 GHz on a mixer with NbTiN ground plane, NbTiN wiring, and Nb/AlN/NbTiN junctions.

Kleinsasser et al [6] studied the use of AlN as a barrier material for extremely high current density Josephson junctions. The practical difficulty in fabricating AlO_x junctions with high current densities, say $J_c \gg 10\,\mathrm{kA\,cm^{-1}}$, is that the quality of the junctions, as indicated by the subgap to normal resistance ratio, degrades rapidly with increasing J_c. Using AlN as the barrier material, however, it is now possible to reliably produce very high current density junctions while maintaining their quality. In addition, the material parameters for AlN and AlO_x are similar, so AlN-based junctions are amenable for incorporation into existing designs based on AlO_x barriers in contrast to using MgO, which has a much higher specific capacitance for the same current density. We presently demonstrate the operation of a low-noise receiver incorporating high current density Nb/AlN/Nb junctions with an input bandwidth of about 300 GHz.

II. Receiver Setup

The mixer configuration we use is a quasioptical planar twin-slot antenna coupled to a two junction tuning circuit [7]. The antenna and junctions are fabricated simultaneously on the same Si substrate. This substrate is attached to a hyperhemispherical Si lens, which is anti-reflection coated with Al_2O_3-loaded epoxy. The lens/substrate combination is clamped into a mixer block assembly, which is mounted in a liquid helium-cooled cryostat. The beam passes through a high-density polyethylene lens at 4.2 K, and several layers of porous Teflon on the 77 K radiation shield. A 25 μm mylar film serves as the vacuum window. This receiver setup is nearly identical to that used for prior measurements and is known to give excellent receiver performance up to 1 THz [1],[8].

III. Mixers with NbTiN Ground Plane and Wire, Nb/AlN/NbTiN Junctions

The NbTiN film used for the ground plane is deposited on unheated Si and has $T_c \approx 15\,\mathrm{K}$, $\rho(T_c) = 80\,\mu\Omega\,\mathrm{cm}$ and $\lambda_L \approx 230\,\mathrm{nm}$. The mixer layout was designed using these as nominal values. The wiring layer NbTiN film is deposited on SiO, and has slightly lower T_c and higher resistivity, which together imply a larger penetration depth. The junctions are defined to dimensions of $2.6 \times 0.25\,\mu\mathrm{m}$, and are made to stretch across the width of the tuning inductor while preserving an area of $0.65\,\mu\mathrm{m}^2$. This junction geometry is used instead of square junctions to lessen the impact of non-ideal behavior stemming from spreading inductance.

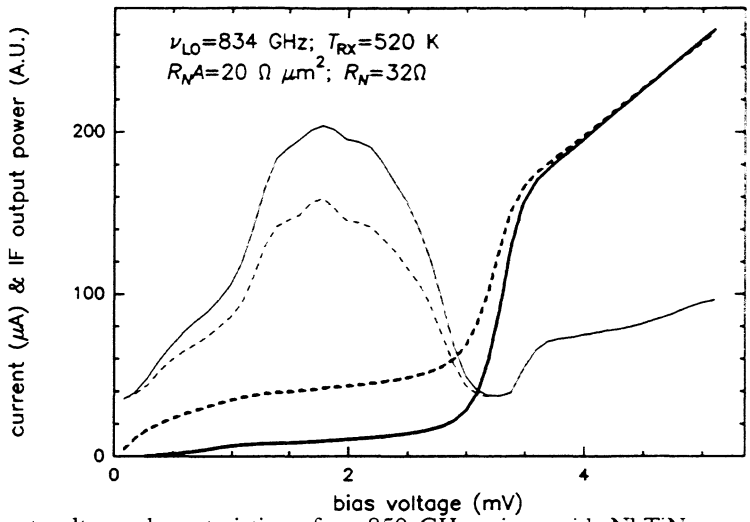

Figure 1: Current-voltage characteristics of an 850 GHz mixer with NbTiN ground plane and wiring and Nb/AlN/NbTiN junctions. Shown are the IV curve traced with (dashed heavy) and without (solid heavy) LO power applied at 4.2 K bath temperature. The IF power in response to 295 K (solid light) and 77 K (dashed light) loads are shown as a function of changing bias. The mixer is normally biased at 2.0 mV. For this particular measurement, a 25 μm Mylar beam splitter was used to couple the optimum amount of LO power to the mixer, and $T_{RX} = 520$ K.

The current-voltage curve of an 850 GHz mixer with is shown in Fig. 1. The junction's quality is good, $R_{sg}/R_N \approx 12$, but for the mixers in this batch, the gap voltage is only $V_g \approx 3.2$ mV. This is about 0.3 mV lower than seen in mixers produced in other batches. These are still significantly lower than the 4.0 mV gap we expect from this hybrid junction. We do not presently understand why the gap in these junctions is so much smaller than the sum gap value. Note that the gap is further reduced under LO pumping. We speculate that this is caused by LO-injected quasipartilces trapped near the junction.

The spectral response of an 850 GHz mixer was measured with an FTS, and is shown in Fig. 2. The response agrees reasonably well with a model that assumes that there is no loss in the ground plane and that there is an excess surface resistance in the wiring layer, $R_S \approx 0.1\,\Omega$ at 900 GHz. This value tolerable, but further measurements are needed to better quantify this value. Nevertheless, the width of the resonance indicates that the excess surface resistance cannot exceed $R_S < 0.3\,\Omega$, which is still better than the surface resistance of polycrystalline NbN film [9].

Heterodyne tests were performed following the FTS test, and their results are summarized in Table 1. For the 850 GHz mixer it was necessary to use a 25 μm mylar beam splitter, with transmission of about $t \approx 76\,\%$, to couple enough LO power for optimal noise performance. The best receiver noise temperature was $T_{RX} = 520$ K at an LO setting of 834 GHz. Generally, using a 13 μm beam splitter ($t \approx 92\,\%$) improved the noise performance even though the mixer was LO starved. The best noise temperature thus achieved was $T_{RX} = 460$ K at an LO frequency of 824 GHz. For the 550 GHz mixers enough LO

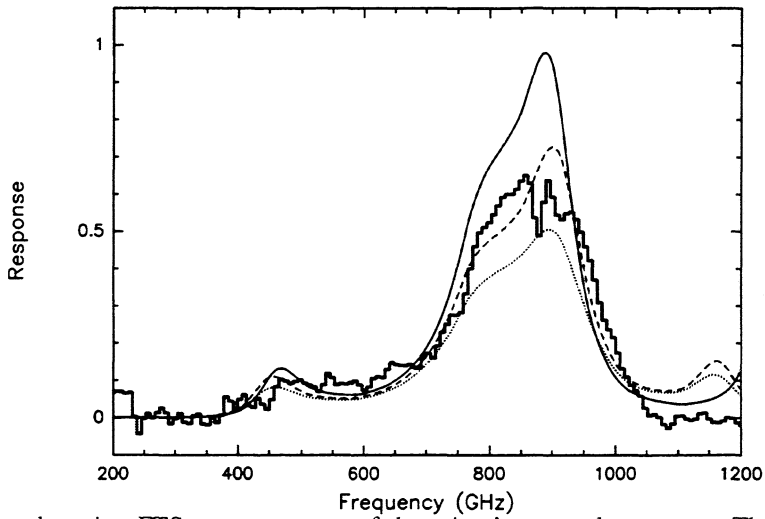

Figure 2: Direct detection FTS measurements of the mixer's spectral response. The measured response is shown as a histogram. The absorption feature near the peak of the response at 875 GHz is a measurement artifact. Model calculations are plotted as follows: a circuit model that assumes no loss in either the NbTiN ground plane or wiring is shown as a solid line; the dashed line assumes an excess surface loss in the wire layer of $R_s = 0.1\,\Omega$ at 900 GHz; and the dotted line, $R_s = 0.3\,\Omega$.

power was coupled using a 13 μm beam splitter ($t \approx 97\,\%$). Though we have some problems understanding the spectral response of the 550 GHz mixers, their noise performance is still quite respectable.

It is quite clear from our measurements that substantial improvements can be made to the receiver's sensitivity, especially for the 850 GHz mixer. For this receiver the 25 μm beam splitter accounts for approximately 200 K of the total receiver noise temperature. We forsee immediate improvement in the receiver performance by upgrading the optics to a similar configuration used in the 850 GHz CSO waveguide receiver [10]. Furthermore, since the circuit design was optimized for mixers using NbTiN ground plane and Nb wiring, we should see some improved performance with a new design.

Mixer's peak frequency response (GHz)	LO frequency (GHz)	$T_{RX,DSB}$ (K)
530	536	160
550	536	160
850	834	520
"	824	460

Table 1: Noise performance of mixer with NbTiN ground plane and wiring, and Nb/AlN/NbTiN junctions. For the measurement in the last line, a 13 μm mylar beam splitter was used.

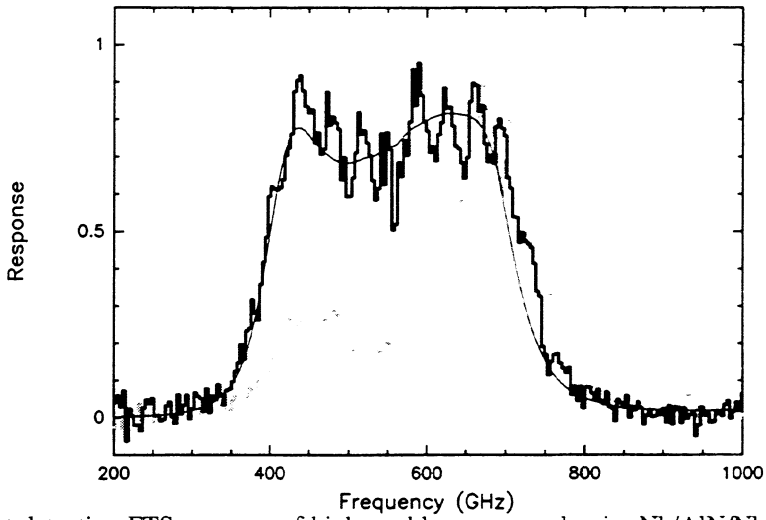

Figure 3: Direct detection FTS response of high- and low-current density Nb/AlN/Nb mixers designed for the same frequency band. The histograms are the measured receiver responses, and the lines are model fit to these. Those shown in black are the response of high current density mixer with $R_N A = 5.6\,\Omega\mu\mathrm{m}^2$; grey, the low current density mixer with $R_N A = 20\,\Omega\mu\mathrm{m}^2$. For the high current density mixer, we infer $\omega RC = 1$ at 270 GHz, whereas for the low current density mixer, $\omega RC = 1$ at 110 GHz. The rather large ripples on the response are caused by reflections between layers of new infrared filters, which have since been replaced.

IV. High-current density Nb/AlN/Nb junctions

The high current density mixers were fabricated using an existing design for low current density Nb/AlO_x/Nb SIS mixers which gave good performance and whose behavior was well-understood [8]. However, in place of the AlO_x barriers, AlN barriers are formed by plasma nitridation following the Al deposition. The junctions are square, with a nominal area of $A = 1.7\,\mu\mathrm{m}^2$. The mixers used in our study have $J_c \approx 30\,\mathrm{kA\,cm}^{-2}$, yielding junctions with $R_N A = 5.6\,\Omega\,\mu\mathrm{m}^2$ and good quality, $R_{sg}/R_N \approx 10$. To allow a direct comparison, a batch of mixers with low current density was also fabricated, with $R_N A = 20\,\Omega\,\mu\mathrm{m}^2$. These mixers have very similar R_{sg}/R_N ratios as the high current devices.

The spectral response of 650 GHz mixers of each kind was measured with an FTS, and the results are shown in Fig. 3. The difference in response between the two types of junctions is dramatic and impressive. The response of the high current mixer spans nearly an octave! Nevertheless, the curves are well-modeled, and provide tight constraints to the value of the junction capacitance. Combined with the junction normal resistance, which is trivially determined from DC measurements, we derive that $\omega R_N C = 1$ at 270 GHz. Similarly, for the low current density mixer, we find $\omega R_N C = 1$ at 110 GHz.

Measurements of the receiver noise temperature followed the FTS experiments. The best performance was recorded for a 550 GHz mixer, where $T_{RX} = 110\,\mathrm{K}$ at 530 GHz. We stress that the mixer circuit design was optimized for a junction with $R_N A \approx 20\,\Omega\,\mu\mathrm{m}^2$, so that the coupling is not optimal at either the IF or RF. Regardless, the performance

at 530 GHz is still competitive with the best receivers employing lower J_c Nb/AlO_x/Nb mixers.

The use of high current density mixers in SIS mixers should greatly advance the development of low-noise mixers above 1 THz. Mixers using Nb junctions and normal metal tuning circuits could see an improvement in their sensitivity by a factor of about 2. Even for millimeter-wave mixers, the the large bandwidth made possible by these mixers offers obvious advantages.

V. Conclusions

We have made conclusive measurements that show NbTiN-based mixers will work with low-noise performance up to at least 900 GHz Modest improvements to the receiver optics should allow us to demonstrate a receiver with a noise temperature near $T_{RX} \approx 300\,\mathrm{K}$ across 800–900 GHz with the existing set of mixers. Tests are on-going to determine whether or not this type of mixer will work comparably well up to 1.2 THz. The spectral response of a 1 THz mixer is shown in Fig. 4.

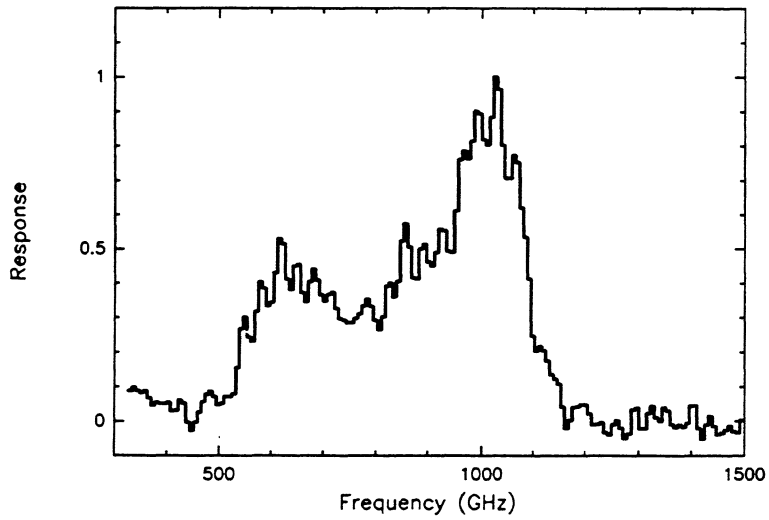

Figure 4: Spectral response of a 1 THz mixer measured with an FTS.

In addition, we demonstrated low-noise performance of a mixer with a very high-current density AlN junction. Generally, this technology will allow the development of SIS mixers with very wide bandwidth operation. Most notably, reliance on tuning circuits will be relaxed; and clearly, this has important consequences for mixers with normal metal turning circuits operating near 1 THz. But it is obvious that the development of low-loss tuning circuits using NbTiN does not diminish the advantages gained by using high current density junctions: rather, we soon hope to develop a mixer that draws the benefits from each approach, a terahertz mixer with low-noise performance and wide bandwidth operation.

This work was supported in part by NASA/JPL and its Center for Space Microelectronics Technology, by NASA grants NAG5–4890, NAGW–107, and NAG2–1068, by the

NASA/USRA SOFIA instrument development program, and by the Caltech Submillimeter Observatory (NSF grant AST–9615025).

References

[1] M. Bin, M. C. Gaidis, J. Zmuidzinas, T. G. Phillips, and H. G. LeDuc, "Low-noise 1 THz niobium superconducting tunnel junction mixer with normal metal tuning circuit," *Appl. Phys. Lett.*, vol. 68, pp. 1714–1716, 1996.

[2] J. W. Kooi, J. A. Stern, G. Chattodpadhyay, H. G. LeDuc, B. Bumble, and J. Zmuidzinas, "Low–loss NbTiN films for THz SIS mixer tuning circuits," *Int. J. IR and MM Waves*, vol. 19, pp. 373–383, 1998.

[3] J. Zmuidzinas, J. Kooi, J. Kawamura, G. Chattopadhyay, B. Bumble, H. G. LeDuc, and J. A. Stern, "Development of SIS mixers for 1 THz," in *Proc. SPIE* (T. G. Phillips, ed.), vol. 3357, pp. 53–62, 1998.

[4] B. Bumble, H. G. LeDuc, and J. A. Stern, "Fabrication of Nb/Al-N_x/NbTiN junctions for SIS mixer applications above 1 THz," in *Proc. of the 9th Int. Symp. on Space THz Tech.* (W. R. McGrath, ed.), pp. 295–304, 1998.

[5] J. A. Stern, B. Bumble, H. G. LeDuc, J. W. Kooi, and J. Zmuidzinas, "Fabrication and DC-characterization of NbTiN based SIS mixers for use between 600 GHz and 1200 GHz," in *Proc. of the 9th Int. Symp. on Space THz Tech.* (W. R. McGrath, ed.), pp. 305–313, 1998.

[6] A. W. Kleinsasser, W. H. Mallison, and R. E. Milller, "Nb/AlN/Nb josephson junctions with high critical current density," *IEEE Trans. Applied Superconductivity*, vol. 5, pp. 2318–2321, 1995.

[7] J. Zmuidzinas, H. G. LeDuc, J. A. Stern, and S. R. Cypher, "Two-junction tuning circuits for submillimeter SIS mixers," *IEEE Trans. Microwave Theory Tech.*, vol. 42, pp. 698–706, 1994.

[8] M. C. Gaidis, H. G. LeDuc, M. Bin, D. Miller, J. A. Stern, and J. Zmuidzinas, "Characterization of low-noise quasi-optical SIS mixers for the submillimeter band," *IEEE Trans. Microwave Theory Tech.*, vol. 44, pp. 1130–1139, 1996.

[9] S. Kohjiro, S. Kiryu, and A. Shoji, "Surface resistance of epitaxial and polycrystalline NbCN films in the submillimeter wave region," *IEEE Trans. Applied Superconductivity*, vol. 3, pp. 1965–1767, 1993.

[10] J. W. Kooi, J. Pety, B. Bumble, C. K. Walker, H. G. LeDuc, P. L. Schaffer, and T. G. Phillips, "A 850 GHz waveguide receiver employing a niobium SIS junction fabricated on a 1 μm Si_3N_4 membrane," *IEEE Trans. Microwave Theory Tech.*, vol. 46, pp. 151–161, 1998.

TRANSMISSION PROPERTIES OF ZITEX IN THE INFRARED TO SUBMILLIMETER

D.J. BENFORD[1]
California Institute of Technology
Mail Code 320-47, Pasadena, CA 91125

M.C. GAIDIS
NASA-Jet Propulsion Laboratory
Mail Stop 168-314, Pasadena, CA 91109

J.W. KOOI
California Institute of Technology
Mail Code 320-47, Pasadena, CA 91125

contact: dbenford@stars.gsfc.nasa.gov

ABSTRACT

The results of measurements of the refractive index and power absorption coefficient of Zitex at 290K and 77K in the spectral region from 1 to 1000 microns are presented. Zitex is a porous Teflon sheet with a filling factor of $\sim 50\%$, and is manufactured in several varieties as a filter paper. Zitex is found to be an effective IR block, with thin (200μm) sheets transmitting less than 1% in the 1-50μm range while absorbing $\lesssim 10\%$ at wavelengths longer than 200μm. Some variation in the cutoff wavelength is seen, tending to be a shorter wavelength cutoff for a smaller pore size. Additionally, the thermal conductivity of Zitex at cryogenic temperatures has been measured, and is found to be roughly one-half that of bulk Teflon.

1. INTRODUCTION

To reduce the loading on cold optical elements operating in the far infrared, room temperature radiation must be blocked efficiently while allowing the desired wavelengths to pass unattenuated[1, 2]. Commonly used materials include blackened polyethylene and Quartz. Unfortunately, the transmittance of black polyethylene is dependent on the size, concentration, and form of the carbon used to blacken it, and varies substantially in its far-infrared properties[3]. Quartz is a low-loss material when a suitable antireflection coating like Teflon is applied, but this is difficult and restricts the wavelengths over which it can be used as a highly transmissive element[4]. Teflon itself is a good IR block, but transmits power in the 5-10μm range and longward of 50μm, limiting its usefulness. Several more absorbing materials, such as Fluorogold and Fluorosint, have been used for low frequency applications, but their slow spectral cut-off characteristics are not ideal for receivers operating near 1 THz[4, 5].

Zitex is a sintered Teflon material with voids of 1-60μm and a filling factor of 50%. Several different varieties are

[1]Present address: Code 685, NASA-Goddard Space Flight Center, Greenbelt, MD 20771

available, divided into two categories by manufacturing process. Zitex A[6] is designed to reproduce filter paper, and so has many narrow linear paths through it and is a rough but soft sheet. It is available in 11 grades with effective pore sizes ranging from 3μm to 45μm and in thicknesses from 0.13mm (0.005") to 0.64mm (0.025"). Zitex G is made of sintered Teflon spheres of small sizes, resulting in a denser, smoother material. Available in 5 grades, the pore sizes range from 1.5μm to 5.5μm and is available in standard thicknesses of 0.10mm (0.004") to 0.38mm (0.015"), although larger thicknesses are available.

Zitex is similar in geometry to glass bead filters, in which dielectric spheres are embedded into a suspending material with a different index of refraction. A single sphere of radius a will scatter strongly for wavelengths $\lambda \lesssim \pi a(n-1)$[7]. Thus, for Teflon ($n = 1.44$[8]), a sphere of radius 10μm produces a shadow for wavelengths shortward of 15μm. At short wavelengths, then, a perfectly scattering screen will redistribute the optical power in an incident beam equally in all directions, resulting in a large loss for well-collimated beams.

2. MEASUREMENTS

Because of the large wavelength range involved, three FTS instruments were used to characterize Zitex. For the near- to mid-infrared (1 - 80 μm; 10000-125 cm^{-1}) a commercially available Nicolet 60SX spectrometer[9] was used. The far-infrared (50 - 200 μm; 200 - 50 cm^{-1}) measurements were made on a Bruker interferometer at JPL. The submillimeter data (200-1000 μm; 50-10 cm^{-1}) was obtained on an FTS at Caltech[10]. The focal ratio of the spectrometers was roughly $f/4$. A perfectly scattering surface would yield a transmission of roughly 0.4% in this case. Table 1 lists the samples we measured.

3. TEFLON

In order that we might characterize qualitatively the difference between bulk Teflon and Zitex sheets, we measured one thin (0.25mm) and one thick (0.75mm) sample of plane-parallel Teflon sheet. Figure 1 shows the results of a measurement of the far-infrared transmission of the thick sample near the cut-on region at 50-100μm. The sample was measured at room temperature and liquid nitrogen temperature, showing a slight improvement in the transmission when the sample is cold. Figure 2 shows the mid-infrared transmission of the thinner sample, which highlights the fairly narrow regions near 10-20μm where the absorption is large.

4. ZITEX G104, G106, G108, G110, G115, A155

The samples of G104 and G106 were measured in the near- to mid-infrared to derive a transmission and an effective absorption coefficient, as shown in figure 3. The absorption coefficient α for a sheet of thickness h is calculated from the transmission T as $-\mathrm{Ln}(T)/h$. Since some wavelength-dependent fraction of the loss $(1 - T)$ is from scattering and some from absorption, the absorption coefficient cannot be used to estimate the transmission of arbitrary thicknesses. It does, however, provide a useful means of comparison with other, more purely absorptive, materials.

Combining sets of data in the near- through far-infrared for samples of G108 and G110 allows us to build a more complete picture of the profile of the cut-on

Table 1. Zitex samples measured.

Grade	Pore Size (μm)	Thickness (mm)	Filling Factor*	NIR data	FIR data	Submm data
G104	5-6	0.10	0.45	X		
G106	4-5	0.16	0.50	X		
G108	3-4	0.20	0.55	X	X	
G110	1-2	0.25	0.60	X	X	
G115	1-2	0.41	0.60	X		
G125	~3	3.53	~0.5	X		X
A155	2-5	0.27	0.40	X		

* Relative density of Teflon.

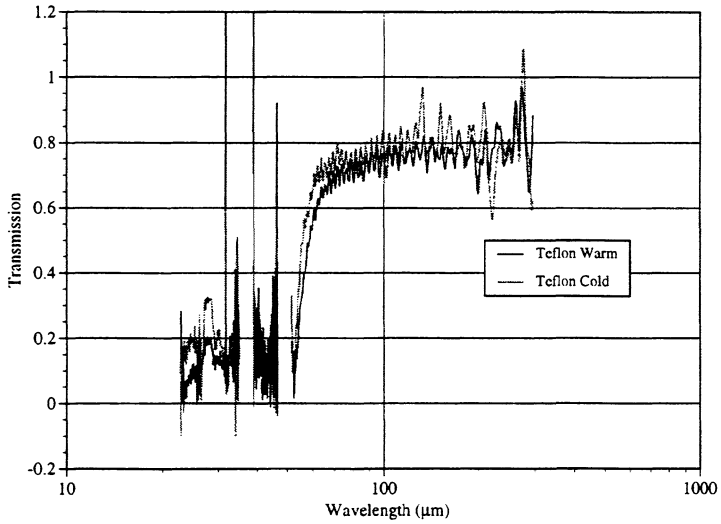

Fig. 1.— Far-Infrared transmission of the thick slab of Teflon at 300K and 77K.

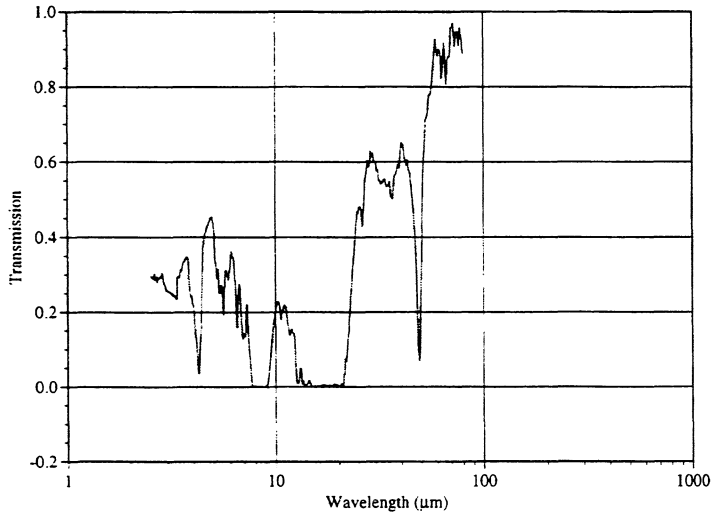

Fig. 2.— Mid-Infrared transmission of a 0.25mm thick Teflon sheet, highlighting the regions of good absorption.

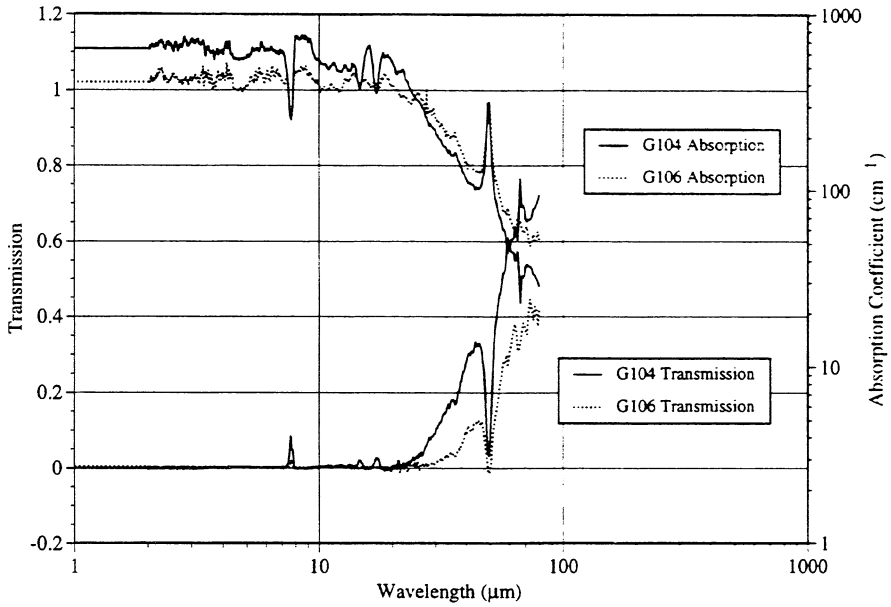

Fig. 3.— Transmission and absorption coefficient in nepers/cm of Zitex G104 and G106.

of Zitex near 100μm, as shown in figure 4. Measurements of G115 and A155 are shown in figure 5. A marked shortening of the cut-on wavelength can be seen in the A155 sample, presumably as a result of its different structure.

5. ZITEX G125

As the thickest of all the samples, the G125 sheet of Zitex was used for the longest wavelengths, covering 400 and 1600 GHz (188 and 750μm). Even with a 3.5mm thick slab, the loss was small enough to be below detectability at longer wavelengths. The sample was cooled to 2K in order to determine its suitability as a mid-infrared blocking filter for helium-cooled cryostats. The transmission and effective absorption coefficient are shown in figure 6. The 1400 GHz absorption feature is known as an absorption band seen in cold Teflon[8].

Combining the data on G125 near 1 THz with data at shorter wavelengths allows us to determine a broadband transmission and absorption coefficient, as shown in figure 7, for the range 20-1000μm (300 GHz-15 THz). The effective absorption coefficient as well fit by $\alpha = 23\exp[(\lambda_{\mu m}/37)^{0.77}]$ nepers/cm. The transmission, neglecting the absorption band, follows $T = \exp(-7000\lambda_{\mu m}^{-1.8})$.

6. MULTIPLE LAYERS

A helium-cooled receiver is likely to have several layers of infrared-blocking filtration in the optical path. As a result, it is natural in the case of a scattering material like Zitex to question its efficacy in a multilayer application. Layering single-, double-, and triple-ply sheets of Zitex in close proximity (limited only by the natural wavy contours of the thin sheets) yields the transmission measurements shown in figure 8. Because the transmission drops more slowly that for

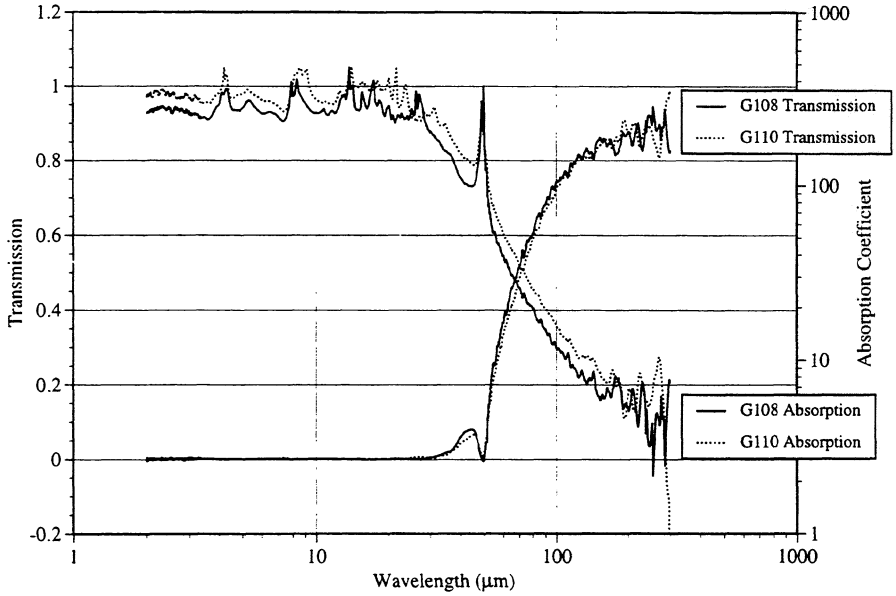

Fig. 4.— Transmission and absorption coefficient in nepers/cm of Zitex G108 and G110 using near-, mid-, and far-infrared data.

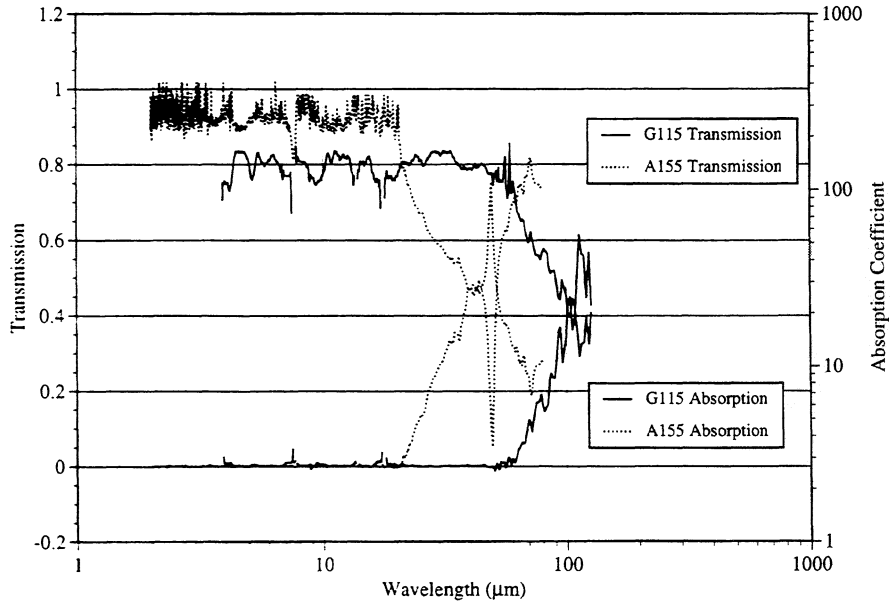

Fig. 5.— Transmission of Zitex G115 & A155 in the near- to mid-infrared.

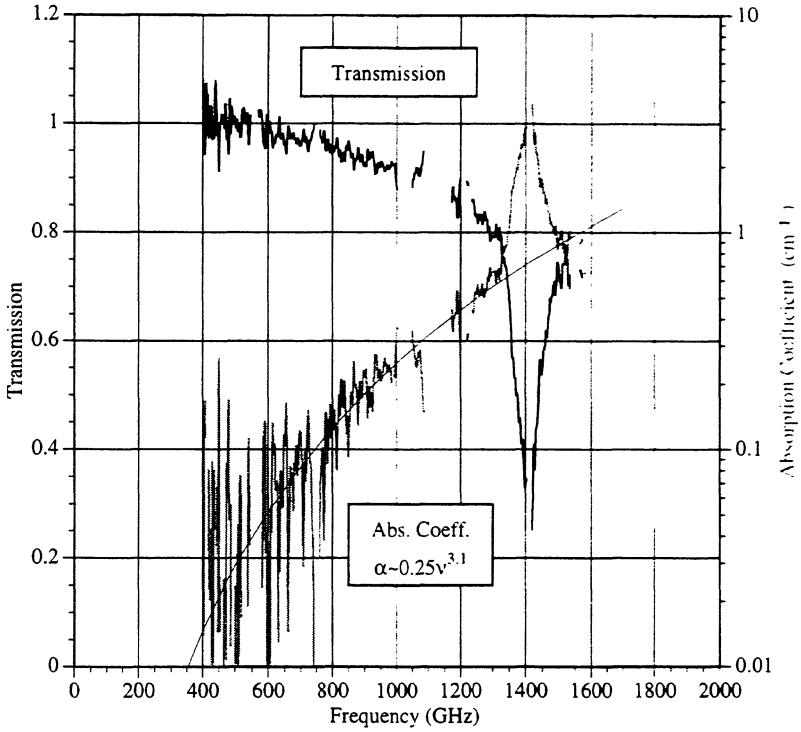

Fig. 6.— Transmission and absorption coefficient in nepers/cm of Zitex G125 between 400 and 1600 GHz (188 and 750μm).

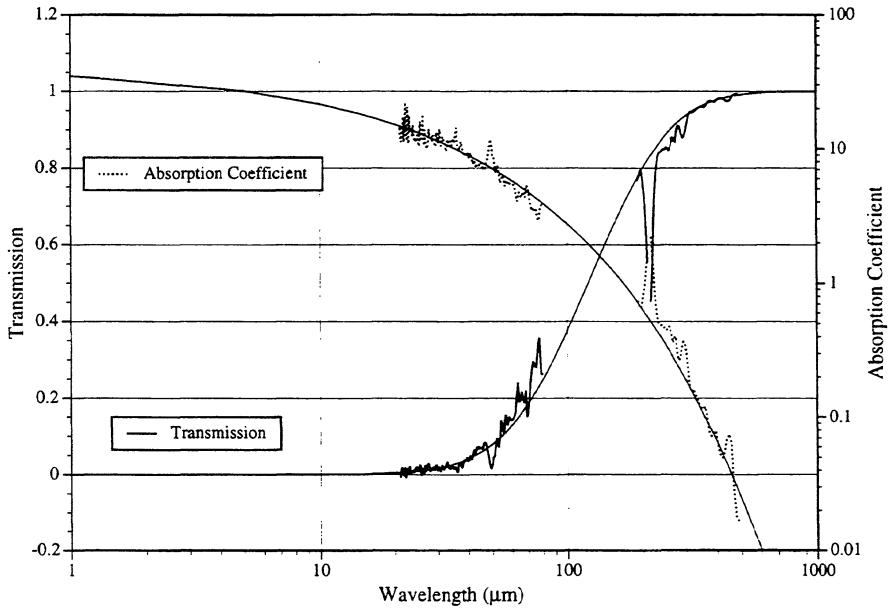

Fig. 7.— Transmission and absorption of Zitex G125.

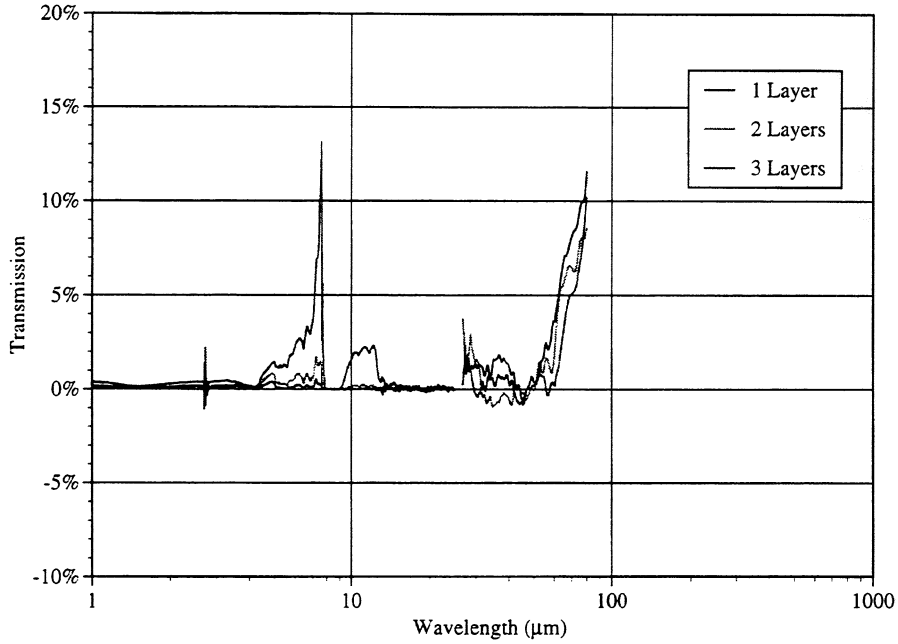

Fig. 8.— Transmission of single, double, and triple layers of Zitex in close proximity. The transmission drops more slowly than for a pure absorbing medium, implying strong scattering.

a pure absorbing medium (i.e. $T_3 = T_1^3$ and $T_2 = T_1^2$) in the mid-infrared, we can infer than scattering is the dominant loss mechanism and that multiple sheets are not substantially more effective than single sheets.

If, however, we separate the layers slightly and look at longer wavelengths, the picture changes. Using Zitex A155 sheets spaced by roughly 5mm, we find find the transmission shown in figure 9. At mid-infrared wavelengths, the Zitex still appears to be dominated by scattering, whereas at far-infrared wavelengths, the transmission appears to be increasingly determined by absorption (presumably in the bulk of the Teflon).

7. TEMPERATURE VARIATION

In the case of many materials (e.g., quartz), the absorption of mid-infrared radiation is known to vary as the temperature changes[11]. To determine if there was any temperature effect in the transmission of Zitex, we measured the transmission of samples of G110 at 300K and 77K in the far-infrared near the cut-on region. No significant variation in the transmission was seen upon cooling (figure 10), which is to be expected for dielectric scattering.

8. REFRACTIVE INDEX

Measuring the refractive index of a material of low dielectric constant is difficult near 1 THz for a nondispersive FTS. Only the thick sample of G125 could be measured, via a determination of the fringe spacing in the 3.5mm thick slab. The fringe spacing, averaged between 13 and 45 cm^{-1} (200-800 μm or 400-1350 GHz), was 1.18 cm^{-1}. This yields a refractive index for Zitex of is $n = 1.20 \pm 0.07$ at a temperature of 2K. This

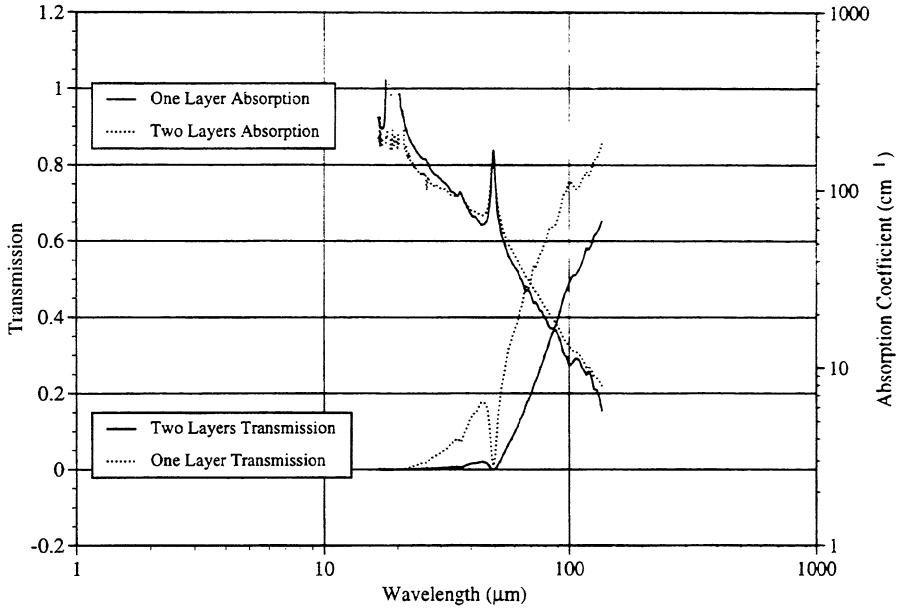

Fig. 9.— Transmission of single and double layers of Zitex in an $f/4$ beam with 1cm spacing. At mid-IR wavelengths, the Zitex acts as two scattering surfaces; at far-IR wavelengths, like an absorber.

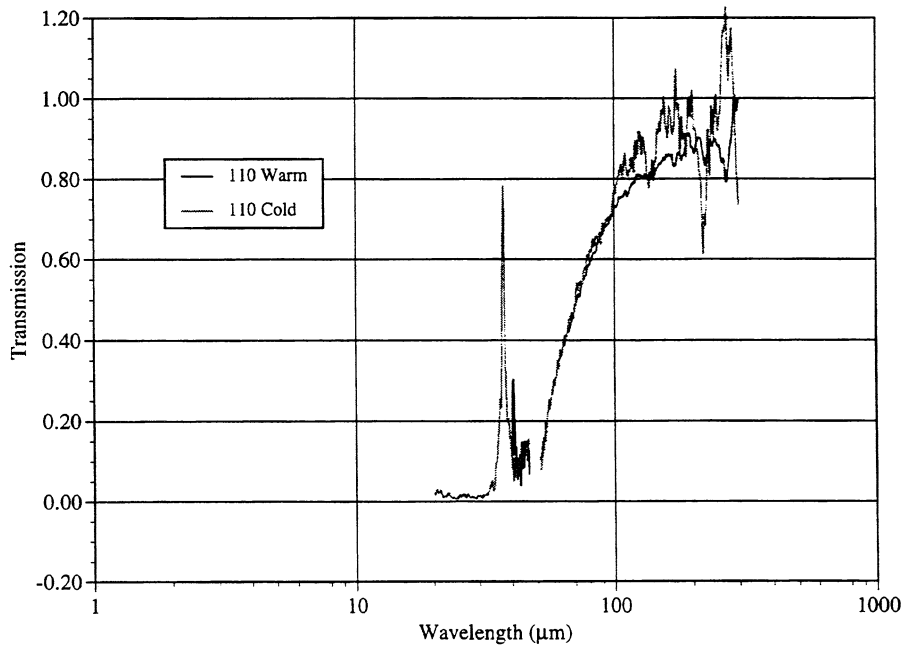

Fig. 10.— Far-Infrared transmission of Zitex at 300K and 77K. No substantial variation is seen.

can be compared to Teflon, which has $n = 1.44$[8]; with a filling factor of $\sim 50\%$, the expected refractive index is $n = 1.22$, exactly as measured.

9. THERMAL CONDUCTIVITY

The thermal conductance of a thick slab of Zitex was measured in the direction along the sheet using an apparatus developed for the purpose[12]. At cryogenic temperatures ($T \leq 150$K), the conductivity of Zitex is found to be well fit by $K(T) = 0.01\,T^{0.58}$ W K^{-1}m^{-1}. This value is half the bulk conductivity of Teflon, indicating that the porous nature of Zitex does not substantially affect its thermal conductance beyond the geometric reduction. However, since Zitex sheets tend to be thin ($\sim$ 0.3mm), even the small power incident on Zitex when used as a near-infrared blocking filter will raise its temperature by a significant fraction. This suggests the use of two layers for good blocking, whereas one Teflon layer might have been sufficient to handle the optical loading. However, since the loss in Zitex at long wavelengths is so low, this solution is likely to be more efficient than the use of Teflon.

10. CONCLUSIONS

We have measured the refractive index and power absorption coefficient of Zitex at 290K and 77K in the spectral region from 2 to 200 microns. Its absorption at wavelengths longer than this is found to be extremely small, and with an index of refraction of $n = 1.2$, there is very little reflection loss. Zitex is an effective IR block when used at wavelengths longward of 200μm, having lower absorption/reflection losses than black polyethylene or quartz and better IR blocking characteristics than Teflon.

REFERENCES

[1] Hunter, T.R., Benford, D.J. & Serabyn, E. 1996. *PASP*, 108, 1042

[2] Kooi, J.W., Chan, M., Bumble, B., LeDuc, H.G., Schaffer, P.L. & Phillips, T.G. 1995. *Infrared & Millimeter Waves*, v.16, n.12, 2049

[3] Blea, J.M., Parks, W.F., Ade, P.A.R. & Bell, R.J. 1970. *J. Opt. Soc. America*, v.60, n.5, 603

[4] Benford, D.J., Kooi, J.W. & Serabyn, E. 1998. *Proc. Ninth Int. Symp. on Space Terahertz Technology*, p. 405

[5] Lamb, J.W. 1996. *Int. J. IR MM Waves*, v.17, n.12, pp.1997–2034

[6] Norton Performance Plastics, Wayne, New Jersey, (201) 696-4700

[7] Sato, S., Hayakawa, S., Matsumoto, T., Matsuo, H., Murakami, H., Sakai, K., Lange, A.E. & Richards, P.L. 1989, *Applied Optics*, v.28, n.20, p. 4478

[8] Kawamura, J., Paine, S. & Papa, D.C. 1996, *Proc. Seventh Int. Symp. on Space Terahertz Technology*, p. 349

[9] Nicolet 60SX spectrometer, Nicolet Instruments, 5225 Verona Rd., Madison, WI 53711; (800) 232-1472

[10] Bin, M., Gaidis, M.C., Benford, D.J., Büttgenbach, T.H., Zmuidzinas, J. & Phillips, T.G., 1999. *Int. J. IR MM Waves*, v.20, n.3, in press.

[11] Bréhat, F. & Wyncke, B. 1997 *Int. J. IR MM Waves*, v.18, n.9, pp.1663–1679

[12] Benford, D.J., Powers, T.J. & Moseley, S.H. 1999. *Cryogenics*, in press

WEB-BASED SIMULATION OF MIXERS, MULTIPLIERS AND OSCILLATORS

Venkat Veeramachaneni, Sandeep Ranade, Tim O'Brien, Stephen Jones, Greg Tait*
{vsv8v, ssr4d, tmo9d, shj2n}@virginia.edu
Department of Electrical Engineering, University of Virginia, Charlottesville, VA
**Department of Electrical Engineering, Virginia Commonwealth University, Richmond, VA*

Abstract - The Applied Electrophysics Laboratory at the University of Virginia has developed a web based device simulation environment to accurately model and simulate high frequency mixers, multipliers and oscillators. The simulation environment uses a three-tier client server architecture to free the user from low level computing details. The user interfaces for the devices being simulated have been developed in Java. A major benefit of Java programs is that they can be run on any hardware architecture for which a Java virtual machine exists, allowing our simulation programs to run on a variety of platforms. The simulation environment has been successfully implemented, and is being used by researchers for simulation and design of high frequency devices. This environment hides the less important details of simulation and lets the researcher concentrate on the most important parameters. This environment has the additional benefit of allowing researchers to run simulations from any computer connected to the Internet.

I. INTRODUCTION

Computer simulation is widely used in many fields for design, development, and research. Semiconductor researchers in particular employ a wide variety of tools to simulate material processing and device performance. The millimeter and submillimeter-wave regions of the electromagnetic spectrum continue to be areas of increasing interest. Millimeter waves correspond to the frequencies between 30GHz and 300GHz, while the submillimeter-wave range is defined to be the region between 300GHz and 3THz. In recent years, scientists and engineers have intensified their efforts to create more complex systems at millimeter and submillimeter wavelengths affording improved range, increased frequencies, frequency stability, and durability. In order to effectively design these complex systems, which consist of highly nonlinear circuits such as large-signal amplifiers, frequency converters such as mixers and multipliers, or oscillators, various accurate and fully self-consistent computer aided simulation tools have been developed.

In general these simulation tools operate as computationally intensive Fortran programs. Expensive and powerful computing hardware is required to run these tools effectively. Many of these simulation tools are potentially reusable for related research efforts and educational purposes. However, they tend to be used only at the places where they were developed because of limited availability of required resources and the

problems inherent to porting and distributing software. The complex nature of these Fortran codes coupled with the cost of the necessary computing hardware makes the large-scale distribution of these codes impractical and inefficient. Hence, an ability to quickly access and run such tools via the Internet would be very beneficial to designers.

The main aim of this research is to develop a simulation environment that allows designers and researchers around the world to run these tools quickly and effectively without the need to maintain expensive and powerful computing hardware. We describe a simulation environment which allows for accurate modeling and simulation of high frequency devices and circuits. The applications developed under this simulation environment include Heterostructure Barrier Varactors (HBV), GaAs Schottky Barrier Diode Mixers (SBM), GaAs Schottky Barrier Diode Varactors (SBV), InP & GaAs Transfer Electron Oscillators (TEO), and high frequency Bipolar Junction Transistors (BJT).

These applications are divided into three categories: Local Applications, Relatively Fast Network Applications and Slow Network Applications. The Local Applications, also known as Quick Design applications, are developed to aid in the HBV and SBV full simulations. Prior to the submission of a full simulation, the user can run the corresponding Quick Design application, which returns results in few seconds. Though the Quick Design application results are less accurate than the full simulation results, they provide insight into the optimal embedding impedance values and device parameters. After the iterative process of using the Quick Design application to estimate the results of full simulation, the user can then run the full simulation to obtain more accurate results. The HBV and SBV full simulations, which are Slow Network Applications, have simulation times as high as few hours. The Local Applications are run exclusively and entirely on the end-user's system and do not make use of the network for simulation purposes.

The Relatively Fast Network Applications and the Slow Network Applications are network-aided applications. Actual simulations are run on high-end Unix machines, which reside at the University of Virginia. These applications use a client-server architecture to transfer data between the simulation clients and the compute servers running the actual simulations. The input parameters and results are transferred between the client and the server over the network, which in our case happens to be the Internet. The Relatively Fast Network Applications have faster computation times than the Slow Network Applications.

The simulation environment has been developed in Java using a client-server architecture. The platform independence of Java programs allows the applications in our simulation environment to be run from a variety of platforms. This environment allows a worldwide workgroup of design and research engineers to concurrently share the same computational resources without getting lost in the minute details of computing.

II. APPLICATIONS DEVELOPED

We have developed six applications – two Local Applications, three Relatively Fast Network Applications and one Slow Network Application. All applications are up and running and can be downloaded from our web-site. The Schottky Barrier Varactor (SBV) Quick Design for design of 50-600 GHz GaAs SBV frequency doublers and the Heterostructure Barrier Varactor Quick Design for design of 100-900 GHz AlGaAs/GaAs HBV frequency triplers are the two Local Applications. The SBV Quick Design employs the equivalent circuit model proposed by Jones and Lipsey [1] with the semi-empirical coefficients derived from the Monte-Carlo Harmonic Balance (MCHB) simulator. The HBV Quick Design employs the equivalent circuit model proposed by Jones and Stake [2] with the design coefficients derived from the Drift-Diffusion Harmonic Balance (DDHB) simulator. The simulation times for both these applications are on the order of a few seconds and the results are displayed in text format.

Transferred Electron Oscillator (TEO) Design, Bipolar Junction Transistor (BJT) Design and Schottky Barrier Diode Mixer (SBM) Design are the three Relatively Fast Network Applications. For these three applications a combination of textual, tabular, and graphical results are displayed on the end-user's machine once the simulations are completed on the high-end Unix workstations. The TEO Design is for analysis and design of 50-200 GHz InP and GaAs transferred electron devices. It employs the integrated DDHB simulator developed by Jones and Zybura [3]. The simulation time varies with the tolerance parameter – the lower the tolerance, the higher the simulation time. The simulations take from a couple of minutes to a maximum of ten minutes depending on the tolerances. The BJT Design is for analysis and design of bipolar transistors. It employs the Vertical Bipolar Inter-Company (VBIC) [4], which is an equivalent circuit model. VBIC was defined by a group of representatives from the IC and CAD industries as an industry standard replacement for the Spice Gummel-Poon (SGP) model. VBIC is public domain and the complete source code is available at **http://www-stall.rz.fht-esslingen.de/institute/iafgp/neu/VBIC/**. The simulation time for this application varies from 30 seconds to a couple of minutes. The SBM Design is for analysis and design of 100-1000 GHz Schottky diode mixers. This application employs the integrated Equivalent Circuit/Harmonic-Balance (ECHB) simulator proposed by Siegel and Kerr [5]. The simulation time for this application is comparable to the BJT Design. It varies from 30 seconds to a couple of minutes.

Heterostructure Barrier Varactor (HBV) Design, the Slow Network Application, is for analysis and design of 100-1000 GHz GaAs/AlGaAs HBV frequency multipliers. This application employs the integrated DDHB simulator developed by J.R. Jones and S.H. Jones [6]. The simulation time for this application depends on the tolerance parameter. It varies from a few minutes to a couple of hours. It is impractical to expect the user to be logged on and wait for the results for this amount of time. Hence, the results are sent to the user by email once the simulations are completed.

III. SIMULATION ENVIRONMENT ARCHITECTURE

In this section we discuss the details of the simulation environment. Figure 1 gives a graphical description of our system. The simulation environment uses a three-tier client server architecture comprising of simulation clients, simulation servers, and middle-ware to connect the client and server. The simulation client consists of a graphical user interface (GUI) where the simulation parameters are entered. These clients have been implemented as Java applications. We have developed clients for the high frequency devices mentioned above.

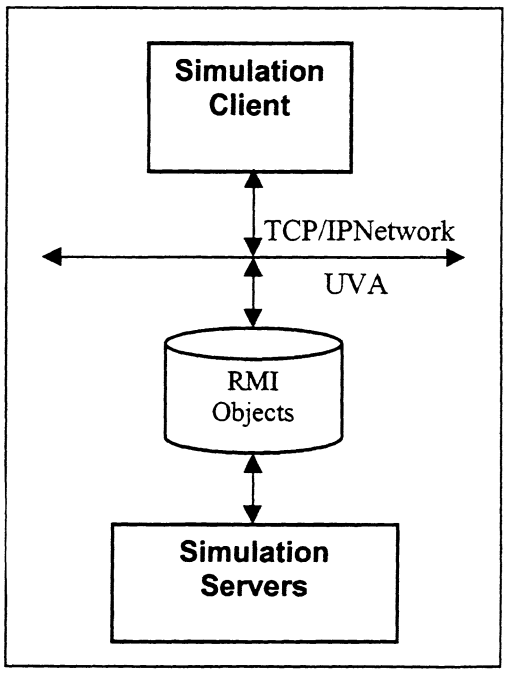

Figure 1 Simulation Environment Architecture

The simulation servers are where the actual execution of the simulations takes place. These machines are powerful UNIX servers running the Fortran programs developed for the devices.

The RMI objects allow for communication between the clients and the servers. RMI (Remote Method Invocation) is a Java technology that allows Java objects to invoke methods on other Java objects residing on different machines. This allows our simulation clients, residing on any machine connected to the Internet, to start simulations on machines residing at UVA. This also allows the simulation servers to return results back to the clients. Each simulation application has a RMI object on the simulation servers listening for messages from the respective simulation client.

The steps that take place in executing a simulation in this environment are as follows. The user starts the client associated with the particular device being simulated. The parameters are entered into the input fields of the client application. The simulation is then initiated. If the simulation is a Quick Design, the computation takes place on the user's machine and the results are displayed in a few seconds. If the simulation is a Network Application, the user is presented with a list of machines on which that particular simulation is available. The user then selects one machine on which the simulation will take place.

Once a machine has been chosen, the client invokes a method on the RMI object residing on the selected machine, requesting the execution of a simulation. This method invocation also results in the input parameters being transferred to the RMI object. The RMI object then uses the input parameters to create a input file for the simulation. The RMI object then starts the simulation engine for the device being simulated. Once the simulation is completed, the RMI object collects the results and returns it to the client. The Slow Network applications email the results back to the user, as it is unreasonable to expect the user to wait a few hours for the results.

In order to use this simulation environment, the software for the clients needs to be downloaded from our web site. We currently have a convenient client installation program available for users running Windows 95/98 and Windows NT on their machines. Users on Unix platforms currently have to manually install the client software on their machines (An automatic install option is currently being developed).

Our simulation environment is advantageous to the researcher for several reasons. We are able to offer an ever increasing library of device simulation programs. All that is required of the researcher is a one-time download of the client software. Moreover, the clients can be run from any platform and from any computer connected to the Internet. The three-tier architecture also gives us flexibility in maintaining the simulation servers. We are able to quickly bring in newer, more powerful servers into the environment without bringing down the entire simulation environment. Overall, this simulation environment gives researchers a powerful, virtual compute center for carrying out an array of high frequency device simulations.

IV. DEMONSTRATION APPLICATION

This section gives a walk-through of the simulation environment using one of the device simulations. Accurate and efficient analysis of InP & GaAs 50-200 GHz Transferred Electron Oscillators can be obtained with the TEO Design application. This application employs the integrated drift and diffusion device/harmonic-balance (DDHB) nonlinear circuit simulator developed by Jones and Zybura. When the application is started, the GUI window shown in Figure 2 is displayed. The device parameters such as the length of the device, diameter, anode and cathode doping, the initial condition (J/JC), fundamental frequency, dc bias, and the impedances and tolerances at different

harmonics are entered through this window. This application allows the analysis of two types of TEDs: the conventional Gunn diode and the Standard Depletion Layer (SDL) TED. The Gunn diode employs a n^+-n-n^+ epitaxial doping profile whereas the SDL TED employs a n-n^+ epitaxial doping profile. The semiconductor material for these TEDs can be either Gallium Arsanide (GaAs) or Indium Phosphide (InP). Users can select the diode type and the material for the diode from the GUI window.

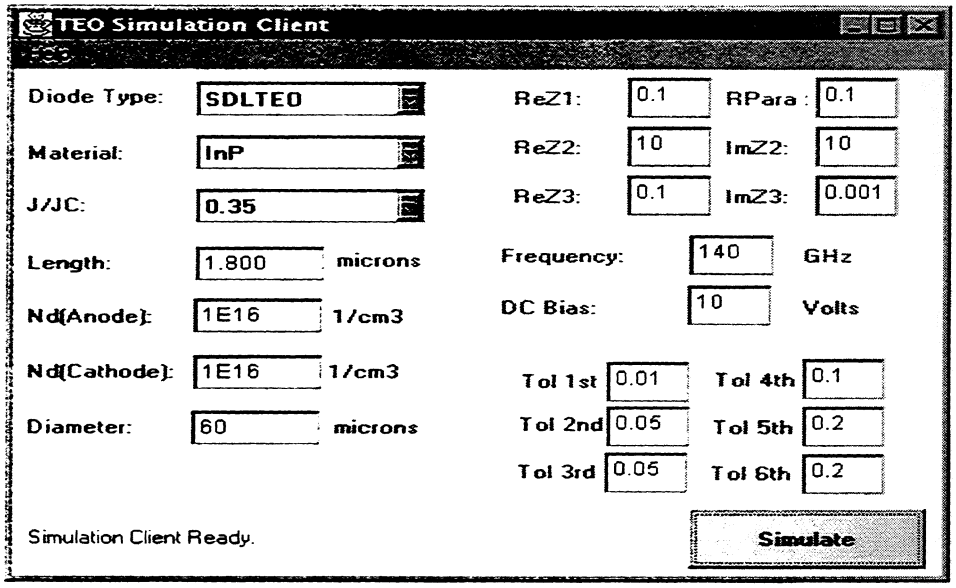

Figure 2 TEO Simulation Client GUI

After entering all the necessary parameters, the simulation is started by clicking the "Simulate" button. After the "Simulate" button is clicked, a machine selection dialog box is displayed. The machine selection dialog box along with the GUI window is shown in Figure 3. This dialog box has a list of machines on which the simulations can be run. The user can select a particular machine depending on the level of computation necessary for the simulation.

Once the machine has been selected, the simulation is started on that particular machine. The results are sent back to the client on the end-user's system after the simulation has finished execution. When the client has received the results, the window shown in Figure 4 is displayed. This window contains device data such as the power, voltage, impedance and admittance values at the six harmonics, starting and ending temperature of the active layer, and the D.C. current and voltage values. Other results can be viewed by selecting the options provided on this window. This window has options for displaying graphs and tabular data for the following results:

- Terminal Currents (i) Vs. position (x), time (t)
- Electron concentration (n) Vs. x, t
- Voltage (P) Vs. x, t
- Electric Field (E) Vs. x, t

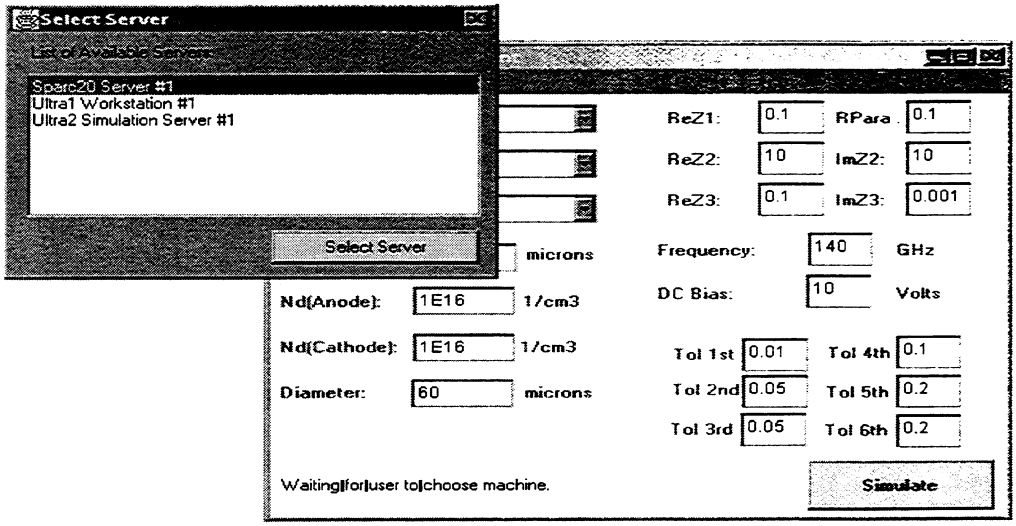

Figure 3 TEO Application Machine Selection

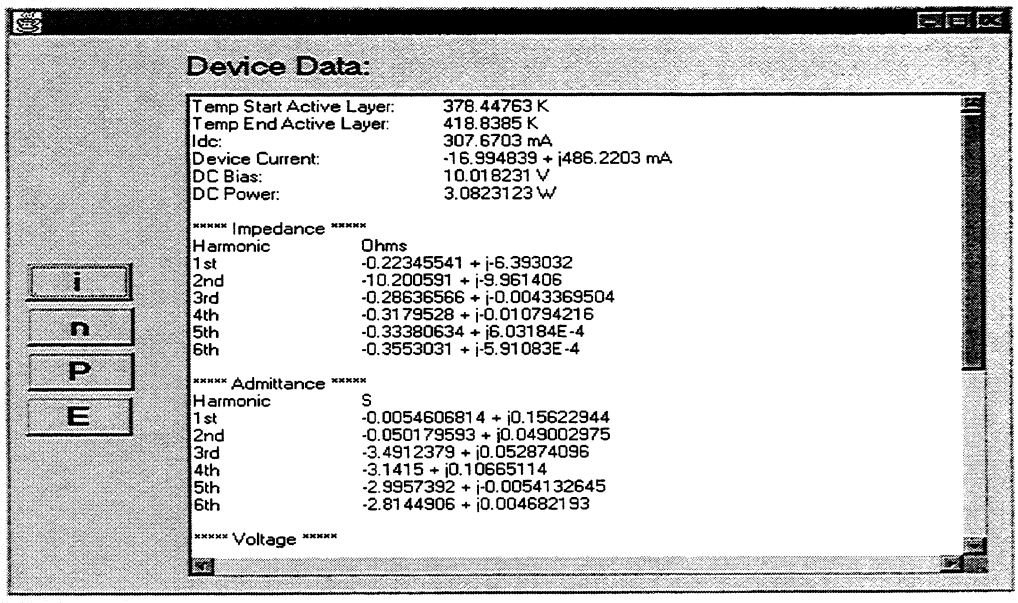

Figure 4 TEO Application Results Summary

The TEO application has demonstrated the feasibility of our simulation environment. Using the simulation environment, researchers concentrate on the most important simulation parameters while not having to deal with minor computing details. The client uses a simple GUI to gather information from the user. The platform-independence of Java programs allows the simulation client to be run from a variety of hardware platforms. Finally, the user is able to submit simulations from any computer connected to the Internet.

V. CONCLUSION

We have described a new simulation environment for the simulation of high frequency mixers, multipliers, and oscillators. Existing device simulation applications run as stand alone applications on expensive Unix servers. The complex nature of these codes and the effort involved in porting them to other platforms prevents large-scale distribution of these applications. Our approach uses a three-tier architecture of simulation clients, simulation servers, and Java RMI middleware to connect the clients and the servers. Using our simulation clients, users can initiate device simulations from any computer connected to the Internet. Users also have access to an expanding library of device simulation applications. Our simulation environment allows researchers all over world to execute an array of device simulations without having to buy expensive computing hardware or maintain complex simulation codes.

ACKNOWLEDGEMENTS

This work was supported in part by the National Science Foundation and by the IBM Corporation.

REFERENCES

1. R.E. Lipsey and S.H. Jones, "Accurate Circuit and Device Equations for Designing 50-600 GHz GaAs Schottky Diode Vàractor Frequency Doublers," Eigth Int. Symp. Space Terahertz Technology, March 1997, Boston, pp. 166-177.
2. Jan Stake, S.H. Jones, L. Dillner, C. Mann, and E. Kollberg, "Design of 100-900 GHz AlGaAs/GaAs Planar Heterostructure Barrier Varactor Frequency Tripplers,' 1998.
3. M.F. Zybura, "A Theoritical and Experimental Contribution to the Design of 100-200 GHz Transferred Electron Oscillators,' Ph.D. Dissertation, Univ. of Virginia, 1996.
4. McAndrew, et al, "VBIC95: An improved Vertical, IC Bipolar Transistor Model," Proc. IEEE BCTM, 1995, pp. 170-177.
5. P.H. Siegel, A.R. Kerr, and W. Hwang, "Topics in the Optimization of Millimeter Wave Mixers," NASA Tech. Paper No.2287, Mar. 1984.
6. J.R. Jones, "CAD of Millimeter Wave Frequency Multipliers: An Experimental and Theoretical Investigation of the Heterostructure Barrier Varactor," Ph.D. Dissertation, Univ. of Virginia, 1996.

COMBINED CIRCUIT-DEVICE TIME DOMAIN SIMULATION OF 2.5 THZ GAAS SCHOTTKY DIODE MIXERS

Haoyue Wang[1], Stephen H. Jones[1], Gregory B. Tait[2], Chris Mann[3]

[1]University of Virginia, Department of Electrical Engineering, Charlottesville, VA 22903
[2]Virginia Commonwealth University, Department of Electrical Engineering, Richmond, VA 23284
[3]Rutherford Appleton Laboratory, Didcot, Oxon, UK

ABSTRACT — In this paper we describe a novel drift-diffusion and time-domain analysis for GaAs Schottky diode mixers operatiing at THz frequencies. The simulator allows for transient analysis and multiple non-commensurate driving tones typical of down-converters.

I. INTRODUCTION

The simulation of THz mixers requires a better understanding of the strong interaction between the nonlinear active device and the linear embedding circuit. As such, mixer numerical simulation techniques must incorporate a combination of a non-linear device simulator and a linear circuit simulator. Simulations should accurately calculate the conversion loss, noise temperature, absorbed and reflected power, device impedances, and time varying current and voltage waveforms, as well as the electron and electric field distributions verses time and position.

In this paper we describe the development of an accurate and efficient simulation tool for THz GaAs Schottky diode mixers. This novel simulation technique incorporates a detailed drift-diffusion device simulator coupled to a time-domain circuit simulator.

II. TIME DOMAIN AND HARMONIC BALANCE METHODS

Traditionally, mixer simulations use harmonic balance techniques to analyze the nonlinear diode embedded in the linear circuit. The diode is typically modeled using a small signal, quasi-static equivalent circuit model. In a harmonic balance circuit simulator (HB) [1], only those frequency components associated with the harmonics of the local oscillator (LO) tone are considered. In the HB frequency domain analysis, only steady-state properties are considered when solving for the device large-signal current and voltage waveforms. Then, small-signal approximations are used to calculate the properties of the down-converted intermediate frequency (IF) signal.

Given the limited frequency components strictly related to the LO, the HB technique is unable to account for complex nonlinear device and circuit interactions during transient conditions. Also, detailed and self-consistent analysis of the current and voltage waveforms cannot be completed using HB since it is impossible to include multiple and non-commensurate frequency signals. At extremely high frequencies one would prefer to use the most complete and

detailed analysis of the mixer in order to better understand the complex mixer behavior.

A time domain method (TD) [2] allows for complete transient analysis, the incorporation of multiple and non-commensurate driving tones, and the self-consistent, direct calculation of down-conversion. However, it is computationally intensive and requires efficient implementation to be practical.

Time domain methods are usually convolution based. Unlike HB, where only circuit impedance or admittance is required for the analysis, the time-domain analysis requires the entire embedding circuit frequency response from DC to at least twice the LO frequency. During the simulation the frequency response is converted to the impulse response using the fast Fourier transform (FFT). The convolution of the impulse response and the device current determines the driving terminal voltage, which is then iteratively applied to the device at each time interval. By this process, the diode current and voltage are consistently calculated as functions of time.

Several techniques were proposed to realize the time domain method efficiently [2]. Combined with a drift-diffusion device simulator, this general technique was employed to study transferred electron oscillator (TEO) circuits.

III. Device Models and Combined Circuit-device Simulation

Often, the diode can be represented as an equivalent circuit model (EC) of lumped elements [1]. Though simple and fast, an equivalent circuit based code fails to predict proper device performance at high frequencies and drive levels. The model cannot inherently account for phenomena such as current saturation, velocity saturation, and transit time effects. To cope with these difficulties and provide a means for studying the internal physics occurring within the device, more complex drift-diffusion numerical device simulators (DD) and Monte Carlo numerical device simulators (MC) have been incorporated in HB algorithms [3, 4, 6].

The drift-diffusion technique is based on a numerical solution to the first two moments of the Boltzmann transport equation coupled to Poisson's equation [3, 4].

The Monte Carlo technique actually simulates the motion of electrons in both k-space and real space [5, 6]. The Monte Carlo technique offers increased accuracy over the drift-diffusion technique owing to its direct modeling of carrier transport, but suffers lengthy run times and convergence problems.

The three different device simulators have been coupled to harmonic balance methods to simulate complete diode circuits [3, 4, 6].

The numerical ECHB simulation technique developed by Siegel and Kerr is widely used to simulate Schottky diode mixers [1]. First employing a harmonic balance technique, the diode terminal current and voltage waveforms are determined in a large-signal analysis. Then in a small signal analysis, the lumped element values for the equivalent circuit model are extracted, and the conversion loss and noise temperature are calculated.

The DDHB and MCHB codes were developed for Schottky barrier varactor (SBV) frequency multipliers [3, 4, 6].

Both the DDHB and MCHB codes allow for the self-consistent study of device electron transport phenomena and circuit performance. Besides terminal current and voltage waveforms, internal physics are also calculated with excellent computational speed and convergence properties. However, the DD and MC codes have not been implemented in mixer HB simulators to date.

IV. Drift Diffusion-Time Domain Simulation of 2.5 THz GaAs Schottky Diode Mixers

The goal of this research is to implement the combined drift-diffusion and time-domain (DDTD) simulation tool for submillimeter wave mixers. At such high frequencies, accurate simulation is very important for the design and optimization of mixers. The task requires the synergistic integration of the drift-diffusion device simulator and the time domain circuit simulator. The DDTD mixer analysis is the first fully self-consistent analysis of high frequency mixers that directly and accurately predicts mixer conversion loss. This analysis will also allow us to observe the electron transport within these devices at high frequencies.

The flow chart of the DDTD code is shown in Fig. 1. The device voltage signal is applied to the DD device model, and the device current signal and internal physics parameters are calculated. A new device voltage is then derived from the TD convolution.

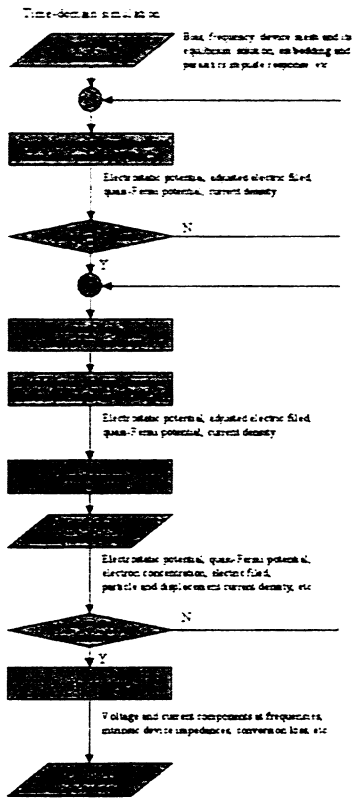

Fig. 1. Flow chart of the DDTD code

The intrinsic device voltage is calculated, via convolution, as

$$V_d(t) = V_{LO}\sin(2\pi f_{LO}t) + V_{RF}\sin(2\pi f_{RF}t) - [h_e(t) + h_p(t)] * I_d(t)$$

where $I_d(t)$ is the device current, $h_e(t)$ is the embedding impulse response, $h_p(t)$ is the parasitic impulse response, and V_{LO}, V_{RF}, f_{LO}, and f_{RF} are the LO voltage, RF voltage, LO frequency, and RF frequency, respectively. The equations modeling the device are

$$\frac{\partial n(x,t)}{\partial t} = \frac{1}{q}\frac{\partial J_n(x,t)}{\partial x}$$

$$J_n(x,t) = -q\mu_n(x,t)n(x,t)\frac{\partial \phi_n(x,t)}{\partial x}$$

$$\frac{\partial}{\partial x}[\varepsilon(x)\frac{\partial \psi(x,t)}{\partial x}] = q[n(x,t) - N_D(x)]$$

$$n(x,t) = n_{i,ref} \exp[\frac{q}{kT}(\psi(x,t) + V_n(x) - \phi_n(x,t)]$$

where J_n is the electron particle current density, n is the electron density, ϕ_n is the electron quasi-Fermi potential, ψ is the electrostatic potential, k is Boltzmann's constant, q is the electron charge, T is the absolute temperature, $n_{i,ref}$ is the intrinsic electron density in the reference maetrial (GaAs), and V_n, μ_n, ε, and N_D are the alloy potential, electron mobility, dielectric permittivity, and donor impurity concentration, respectively. Combined with the appropriate metal-semiconductor interface and ohmic contact boundary conditions, the carrier transport equations are solved via the coupled-equation Newton-Raphson finite difference technique.

The time step of $V_d(t)$, $I_d(t)$, $h_e(t)$, and $h_p(t)$ should be smaller enough than the LO cycle.

The DDTD code was used to simulate a 2.5 THz Schottky diode mixer incorporating the UVa IT2 GaAs mixer diode [7]. The LO and RF frequencies are 2.511 THz and 2.524 THz, respectively. The diode has parameters of area = 0.28 μm^2, epilayer doping = $5x10^{17}$ cm^{-3}, epilayer thickness = 0.055 μm. The diode is driven by a DC bias voltage of 0.8 V and available LO power of 1 mW and an RF power of 0.4 μW. The time step is 20 fs and much smaller than 1/2.5 THz = 400 fs. The mixer block frequency response has been estimated and is shown in Fig. 2.

Over a relatively long time scale, the entire process from turn-on transient to steady state, as a function of time, is self-consistently and autonomously simulated (Fig. 3). The voltage and current waveforms in a LO cycle are shown in Fig. 4. Sampled uniformly in a LO cycle, electron concentration, electric field, and electron potential energy are calculated to give insight into the internal physics of the device (Fig. 5). By simulating in the time domain, the IF signal is naturally created (see low frequency ripples in the waveform of Fig. 3) and the conversion loss from the incoming frequency to the IF is directly calculated without using any standard small signal analysis. The conversion loss predicted by the DDTD code is 17 dB.

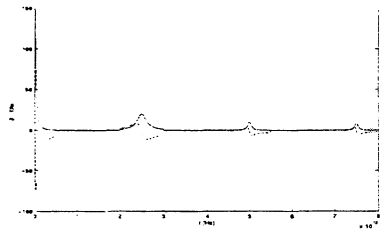

(a)

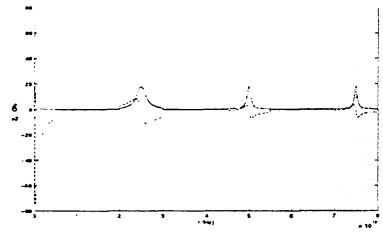

(b)

Fig. 2 Frequency-dependent impedances (solid: real part, dashed: imaginary part) (a) Embedding impedance. (b) Parasitic impedance.

The time domain method can also be combined with a Monte Carlo algorithm to enable more accurate device modeling.

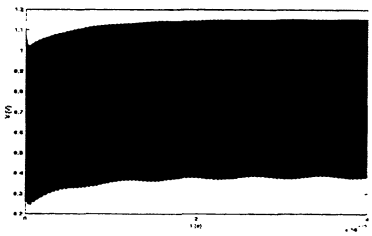

Fig. 3. Device voltage: from turn-on transient to steady state

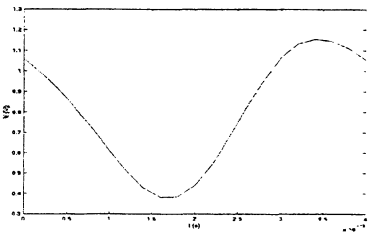

(a)

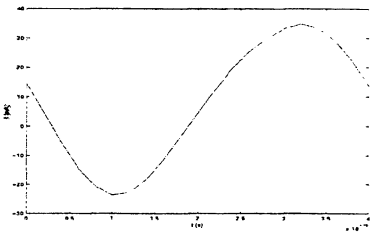

(b)

Fig. 4. Device voltage and current (a) Voltage. (b) Current.

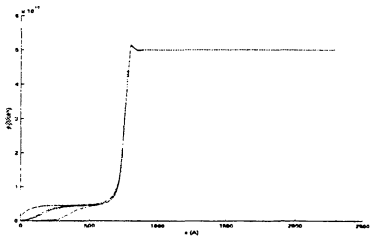

(a)

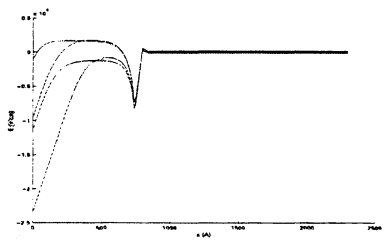

(b)

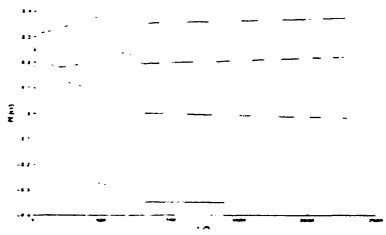

(c)

Fig. 5. Snapshots of the internal parameters of the diode. (a). Electron concentration. (b) Electric field. (c) Potential energy.

V. Summary and Conclusions

A combined drift-diffusion time domain simulator that allows for transient analysis, the direct calculation of mixer down-conversion, and insight into the internal physics of the device has been demonstrated for the first time. The time domain method can also be combined with a Monte Carlo device model to enable more powerful simulation tools. Continued research is on going to calculate noise temperature and compare simulation results with the actual 2.5 THz mixer.

References

[1] P. H. Siegel, A. R. Kerr, and W. Hwang, "Topics in the Optimization of Millimeter-Wave Mixers," *NASA Tech. Papers*, No. 2287, March 1984.

[2] G. B. Tait and S. H. Jones, "Transient Simulation of Harmonic TEO Circuits," *Proc. Ninth Int. Symp. Space Terahertz Technol.*, March 1998.

[3] J. R. Jones, S. H. Jones, and G. B. Tait, "Self-Consistent Physics Based Numerical Device/Harmonic-Balance Circuit Analysis of Heterostructure Barrier and Schottky Barrier Varactors Including Thermal Effects," *Proc. Sixth Int. Symp.*

Space Terahertz Technol., March 1995, pp. 423-441.

[4] L.F. Horvath, J. R. Jones, S. H. Jones, and G. B. Tait, "Numerical Device/Harmonic-Balance Circuit Analysis of Schottky Barrier Varactors," *Proc. 1995 Int. Dev. Research Symp.*, Vol. 1, Dec. 1995, pp. 259-262.

[5] U. V. Bhapkar, "Monte-Carlo Simulation of GaAs Schottky Diodes for Terahertz Frequencies," Doctoral Dissertation, University of Virginia, 1995.

[6] R. E. Lipsey, "Computer Aided Design of Schottky Barrier Varactor Frequency Multipliers," Master's Thesis, University of Virginia, May 1997.

[7] C. M. Mann, D. N. Matheson, B. N. Ellison, M. L. Oldfield, B. P. Moyna, J. J. Spencer, D. S. Wilsher, and B. J. Maddison, "On The Design And Measurement of a 2.5 THz Waveguide Mixer," *Proc. Ninth Int. Symp. Space Terahertz Technol.*, March 1998.

A DUAL FREQUENCY (810/492 GHz) SIS RECEIVER SYSTEM FOR THE AUTHENTIC SUBMILLIMETER TELESCOPE & REMOTE OBSERVATORY (AST/RO)

C.K. Walker, Jacob Kooi, Karl Jacobs

Steward Observatory, Caltech, KOSMA

We have constructed a dual frequency receiver system for AST/RO. AST/RO is a 1.7 m, submillimeter telescope located at the geographic South Pole. Through polarization diplexing, the receiver can observe simultaneously at 492 and 810 GHz. The 492 GHz mixer utilizes a corrugated feedhorn with a transition into full height rectangular waveguide. The impedance match to the junction is achieved through an on-chip impedance transformer and by adjusting two waveguide backshorts. The 492 GHz junction was fabricated at JPL. The 810 mixer and junction were constructed by KOSMA. The signal is fed into the mixer via a Potter horn. The SIS junction is matched to the waveguide by an on-chip tuner and a single, fixed backshort. The system is now in operation at the South Pole.

A Moderate Cost 2.5THz High Performance Feedhorn

D S Wilsher[1], J J Spencer[1] , C M Mann[1], M C Gaidis[2]

[1]Rutherford Appleton Laboratory, Chilton, Didcot, Oxon, OX11 0QX

[2]California Institute of Technology, Jet Propulsion Laboratory, Pasadena, CA 91109

Abstract

Corrugated waveguide feedhorns operating at terahertz frequencies were first demonstrated in 1994 and have been used successfully since this time. Whilst offering unrivalled performance their production requires state of the art precision machining and can be time consuming. Also, each has to electroformed around an aluminium mandrel. Feedhorn fabrication is carried out on a one for one basis as the mandrel is eventually destroyed as part of the manufacturing process. The cost of the end product is therefore very high.

A modified version of the Potter horn was demonstrated to operate at these frequencies in 1998 but these feedhorns whilst being easier to machine than their corrugated counterparts were still fabricated using an aluminium mandrel. We have now developed the machining and electro-forming procedure to allow such horns to be made using an extractable stainless steel mandrel that incorporates the circular to reduced height waveguide transition. This approach has so far allowed six identical feedhorns to be made from one mandrel which has subsequently shown no sign of damage or degradation.

The resulting horns radiation characteristics have been measured and are found to be in excellent agreement with theory.

In addition, we have developed a technique that allows the feedhorn to be removed and replaced whilst maintaining near perfect alignment of the waveguides.

This paper describes the manufacturing process and presents the radiation properties of the horn.

Introduction

Since the introduction of corrugated feedhorns at true terahertz frequencies in 1994[1], it has become possible to realise terahertz receivers that have near perfect Guassian coupling efficiency[2]. This is of paramount importance for microwave limb sounding where the field of view of the radiometer must be more or less completely restricted that

portion of the limb being observed. However, the cost associated with such feedhorns is still very high as the fabrication process requires the machining of a complicated aluminium former or mandrel that possesses micron scale features. The electro-forming process that must be used necessitates the removal of this mandrel via chemical etching. Therefore horns are realised on a one for one basis.

An alternative design[3] that also offers adequate performance for limb sounding has also been fabricated and demonstrated in working 2.5THz mixers [4,5].However, whilst this design of horn in principle allows the mandrel to be extracted it was still machined from aluminium because of its desirable machining properties. This paper describes how a new manufacturing process has been realised whereby the mandrel is machined from stainless steel which allows the mandrel to be released after electro-forming allowing it to be subsequently re-used. So far six feedhorns have been pulled from the same mandrel with no apparent wear . This process has several advantages, firstly, it promises to dramatically reduce the future cost of terahertz feedhorns fabricated in this way and also ensures that provided the master mandrel has been machined correctly the tight tolerances required are easily maintained .All horns produced are effectively identical to the master. Finally there is no degradation of the surface finish of the horn as the stainless steel mandrel requires no pre-treatment etch of its surface prior to gold electroplating as is the case with aluminium.

The Fabrication Process

Firstly the circular sections of the stainless steel mandrel are machined on a precision lathe. This lathe is fitted with high precision positional slides that allow tool placement to within +/-1μm. The tool used is a conventional lathe turning tool fabricated using a precision grinder and hand lapped to a point. The lathe is also fitted with high performance microscopes with large working distances and magnifications of 50-100X.

In order to machine the rectangular waveguide section and circular to rectangular taper the mandrel is then moved to a ultra high precision milling machine. This can achieve repeated tool placement to within +/- 0.5μm. This detail is machined using a 150μm diameter carbide endmill. An optical non-contacting measurement system is used at all stages to ensure that the tight tolerances required by this design are met. Dimensions can be determined to an accuracy of +/-1μm. The finished 2.5THz stainless steel mandrel with a human hair to give an idea of scale is shown below in figure 1.

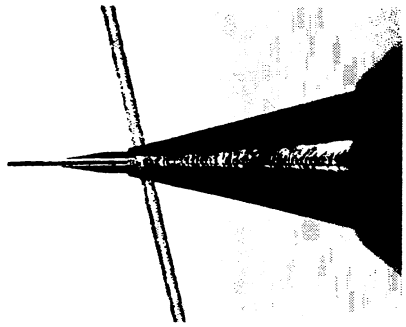

Figure 1: A finished 2.5THz stainless steel mandrel and human hair

Once machined and inspected the mandrel is coated in a 2μm thick layer of electroplated gold followed by copper electro-forming. Compared to the electro-forming of aluminium the process is quicker, more straightforward and has less risk associated with it as the solutions are near neutral pH. The only area of uncertainty is in obtaining sufficient adhesion between the mandrel and the gold to stop the gold lifting but allow the mandrel to be easily extracted. Once the required thickness of copper has been formed the profile of the feedhorn package is machined and the mandrel extracted. For extraction a simple non-rotating sliding pulling mechanism is employed. Very little force is required for the removal as the surface area of the horn is so low.

The basic construction of the mixer is the same as that described in Ref:4. The backshort waveguide section that also houses the RF circuit and Schottky diode is formed in two parts. A machined waveguide/RF filter channel and micromachined diode pill package which is soldered in to form the waveguide roof. However, whereas in the earlier design the feedhorn had to be optically realigned each time the mixer was modified for the Engineering Model mixers this was not possible because of the requirement for an integrated bias circuit and the mixer mounting scheme adopted. Therefore it was decided to use a self aligning approach whereby the feedhorn is automatically aligned to the waveguide upon assembly. This is achieved by the use of two 0.7mm stainless steel dowels. An external clamping fixture is used to hold the feedhorn securely in place. An assembly drawing is shown in figure 2 alongside a photograph of a finished mixer block.

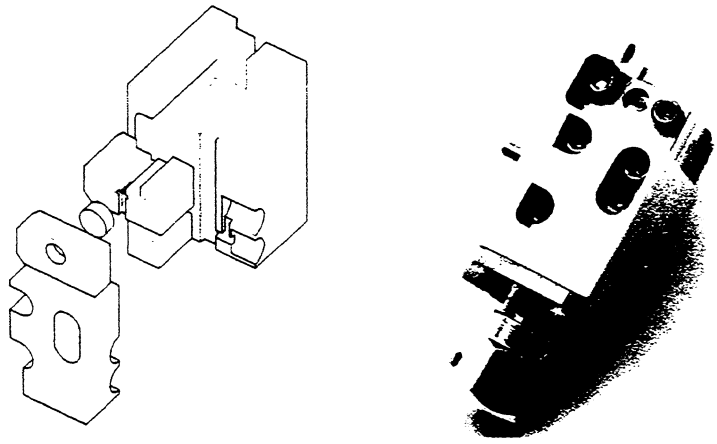

Figure 2: An assembly drawing and photograph of a 2.5THz mixer block

To achieve the alignment required, +/-1μm, the feedhorn is backlit and moved whilst observing through a powerful microscope. When the waveguide in the feedhorn and the mixer are aligned it is clamped and the two dowel holes are drilled and reamed. Some care was required to obtain a sufficiently close fit between the dowels and holes to allow easy removal and replacement without the loss of positional accuracy. In order to check that the feedhorn could be removed and replaced without the waveguides becoming mis-aligned it was carried out several times and checked visually. A series of photographs showing the alignment of the waveguides before and after removal and replacement are shown below in figure 3. The entrance to the filter channel can also be seen.

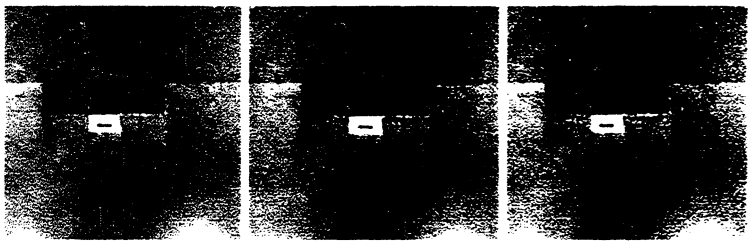

Figure 3: The alignment between feedhorn and waveguide after removal 3 times

A photograph of the finished horn is shown below in figure 4 alongside a view of the waveguide aperture. For scale a human hair is shown, the waveguide dimensions are 27.5x105μm. The feedhorn alignment dowels can be clearly seen to the left and right of the horn aperture.

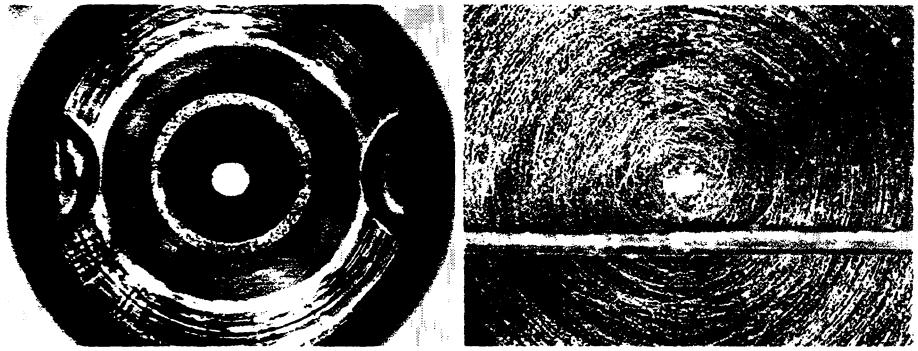

Figure 4: The feedhorn and waveguide apertures.

An early mixer was assembled which could then be used to carry out beam pattern measurements at JPL. The diode was used to detect the applied signal for a far infrared laser operating at 2.5THz whilst the mixers field of view was scanned in 2 axis. A photograph of the measurement system is shown below in figure 5. The laser is fired through a pinhole in order to shape the beam, then through a beam splitter to separate a small amount for power level reference. A chopper is using to modulate the beam and the bias of the mixer is used to determine the power level seen by the mixer.

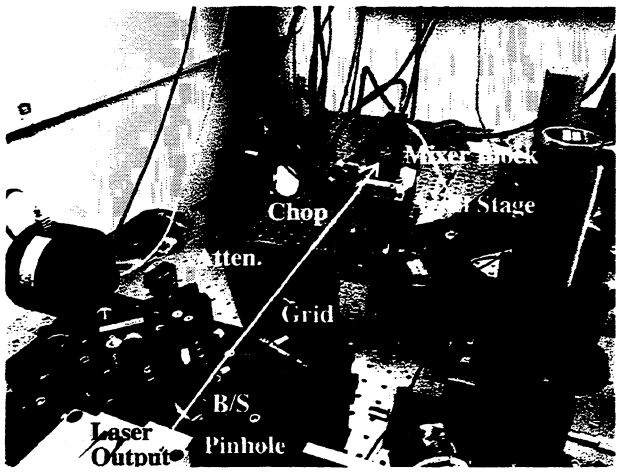

Figure 5: The measurement set-up used to determine the radiation pattern

The horns radiation pattern is shown below in figure 6.

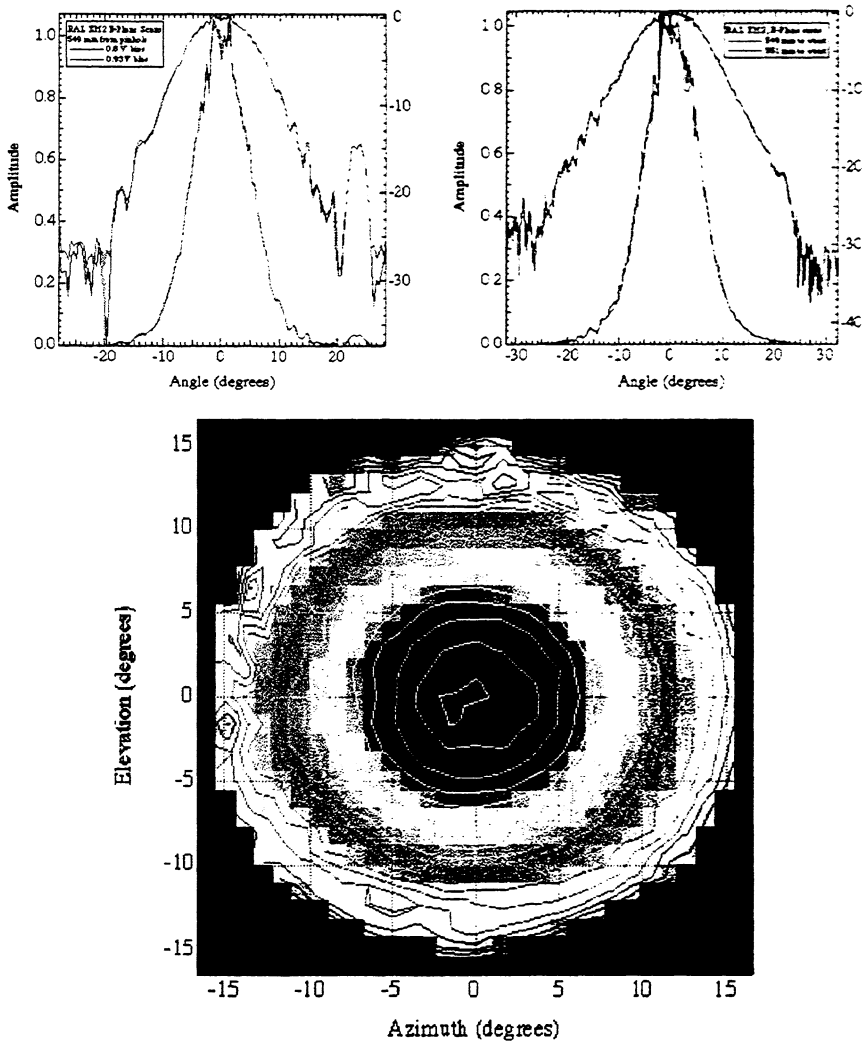

Figure 6: The measured radiation pattern of the feedhorn at 2.5THz

From the plots it can be seen that the horn as a very high quality radiation pattern. Some asymmetry exists between the E and the H plane, also, a spurious side lobe is present in the E-plane. This lies outside the antenna's field of view in the 2.5THz EOS-MLS system and its origin is at present unknown. More measurements will be required on subsequent mixers in order to determine if it is a characteristic of all horns extracted from this mandrel.

Discussion

The ability to automatically align the feedhorn to waveguide combined with the reduced cost allows the possibility of a miniature mixer package. The mixer and feed horn can be simply assembled and fixed together with adhesive. The potential exists for the

completed mixer to be simply included in the backend low noise amplifier housing. This in term may allow the realisation of compact imaging arrays.

Conclusion

A new fabrication process has been demonstrated that can produce at moderate cost high quality waveguide feedhorns. It is expected that the technique could be extended to at least 5 THz. In addition to the reduced cost, the technique also has the advantage that each subsequent horn is an exact copy of the original therefore maintaining radiation properties between different horns.

Finally the removal of the need for a mixer block type housing by incoporporating automatic alignment opens the way forward for small compact terahertz imaging arrays.

Acknowledgements

This work was supported by the Jet Propulsion Laboratory under contract number: 000750008.

---

[1] 'Corrugated Feedhorns at Terahertz Frequencies - Preliminary Results', B.N.Ellison, M.L.Oldfield, D.N.Matheson, B.J.Maddison, C.M.Mann and A.F.Smith, The Fifth International Symposium on Space Terahertz Technology, Ann Arbor, May 1994.

[2] 'First Results for a 2.5 THz Schottky Diode Waveguide Mixer', B.N.Ellison, M.L.Oldfield, D.N.Matheson, B.J.Maddison, C.M.Mann, S.Marazita, T.W.Crowe, P.Maaskant, W.M.Kelly, 7th International Symposium on Space Terahertz Technology, University of Virginia, March 1996.

[3] 'Characterisation of a Dual-Mode Horn for Submillimetre Wavelengths', H.M.Pickett, J.C.Hardy, J.Farhoomand,IEEE Transaction on Microwave Theory and Techniques, Vol. MTT-32, NO. 8, August 1984

[4] C. M. Mann, D. N. Matheson, B. N. Ellison, M. L. Oldfield, B. P. Moyna, J. J. Spencer, D. S. Wilsher, and B. J. Maddison, 'On The Design And Measurement Of A 2.5THz Waveguide Mixer' 9th International Conference on Space THz Technology, Pasadena, CA, March 1998

[5] *'2.5THz GaAs Monolithic Membrane-Diode Mixer'*, P. H. Siegel, M. Gaidis, S. Martin, J. Podosek, U Zimmermann, 9th International Conference on Space THz Technology, Pasadena, CA, March 1998

640 GHz SIS RECEIVER SYSTEM FOR JEM/SMILES ON INTERNATIONAL SPACE STATION

M. Seta, H. Masuko, and T. Manabe
Communications Research Laboratory (CRL), Koganei, Tokyo 184-8795, Japan
TEL: +81-42-327-5367, FAX: +81-42-327-6110, E-mail: seta@crl.go.jp

J. Inatani
National Space Development Agency of Japan (NASDA), Tsukuba, Ibaraki 305-8505, Japan

JEM/SMILES mission team
NASDA, CRL

ABSTRACT

We are developing a superconductor-insulator-superconductor (SIS) receiver for a submillimeter-wave limb emission sounder (SMILES) on the Japanese Experiment Module (JEM) of the International Space Station. SMILES is a sensitive heterodyne spectrometric radiometer in 640 GHz band, and observe thermal emission lines of stratospheric trace molecules in the limb sounding method. SMILES operates two SIS mixers simultaneously in single-sideband (SSB) mode using only one local source. For the SSB filter we employ a frequency selective polarizer (FSP), which consists of two sets of a wire grid and a flat mirror and operates in the principle of Martin-Puplett interferometer. The SIS mixers and the first low noise amplifiers will be cooled to 4.5 K and 20 K, respectively, by a compact Stirling refrigerator combined with a Joule-Thomson circuit. We succeed in demonstrating the cooling capability of 20 mW at the 4-K stage, 200 mW at the 20-K stage, and 1000 mW at the 100-K stage with a power consumption of 250 W. We expect a system nose temperature below 500 K in the SSB mode. In 2003 SMILES will become the first SIS receiver flown on space.

INTRODUCTION

Stratospheric minor constituents (e.g., O_3, ClOx, NOx) play an important role in the Earth environmental change such as ozone depletion. Although we know that the basic ozone depletion process are caused by man-made chemical substances such as chlorofluorocarbons, researches on the complicated chemical network of the ozone depletion are still in progress. We need data of global distributions of these minor gases and their diurnal and seasonal variations with a high altitude resolution. We are now developing a highly sensitive submillimeter-wave limb emission

sounder (SMILES) to promote sciences related to the ozone depletion (e.g., Masuko *et al.* 1997; Manabe *et al.*, 1998). SMILES will be installed on the exposed facilities of the Japanese Experiment Module (JEM) of the International Space Station (ISS). In the limb sounding method, thermal emission from the stratospheric molecules are observed by a sounder on the orbit (e.g., Barrath *et al.*, 1993). Figure 1 shows the schematic drawing of the limb sounding observation by SMILES. We expect to start a operation of SMILES in 2003 for at least one year, and now we are in the final design trade-off of the system. This paper mainly describes the current instrumental design of the 640 GHz SIS receiver system, and also reports some experimental results.

OVERVIEW OF JEM/SMILES

Table 1 summarizes the basic specifications of JEM/SMILES, and Figure 2 shows the signal flow diagram of SMILES. We employ a highly sensitive heterodyne superconductor-insulator-superconductor (SIS) receiver, and observe twelve emission lines of stratospheric molecules as listed in Table 2. The SIS receiver makes it possible to detect extremely weak emissions and reduce the observational time for each observational positions. We retrieve the altitude profile of the molecules at a high altitude resolution over a wide altitude range together with their global diurnal and seasonal variations from the sensitive data set.

A 60 cm x 30 cm main reflector gathers the thermal radiation from the atmospheric limb region at an altitude resolution of 2 km. The 638.4 GHz fixed frequency LO signal is injected into the RF signal by wire grids. In order to measure the intensity of the signal in one sideband precisely, we use the receiver in single-sideband mode (SSB) by a quasi-optical SSB filter. We operate two SIS mixers simultaneously, one for upper sideband (USB) and the other for lower sideband (LSB) detection. The IF signals of 9.8 -14.8 GHz are further down-converted in frequency and amplified to a power level large enough for spectroscopy. In the IF subsystem only frequency ranges around the molecular emission lines of interest are chosen to save the band width of the spectrometer. We use three acousto-optical spectrometers (AOSs) for high resolution spectroscopy. The system noise temperature is expected to be less than 500 K in SSB mode, which gives a sensitivity of 1.3 K for an integration time of 0.2 sec and a spectral resolution of 1.4 MHz.

SUBMILLIMETER ANTENNA

We require several technical specifications in the antenna of SMILES for demonstrating a highly sensitive limb emission technique from the space. First requirement is an altitude resolution of 2 km with precise pointing accuracy of 0.01°. We use an offset Casegrain type elliptical (60 cm x 30 cm) antenna. The long axis of 60 cm is chosen to realize an altitude resolution of 2 km, and another axis is reduced to 30 cm for compactness. The main reflector of the antenna will be polished aluminum, and special attention is paid in the frame structure of the main reflector and thermal insulation around the antenna for minimizing the thermal distortion. We drive the pointing elevation angle of the antenna in a step size smaller than 0.01°. The altitude pointing of the antenna

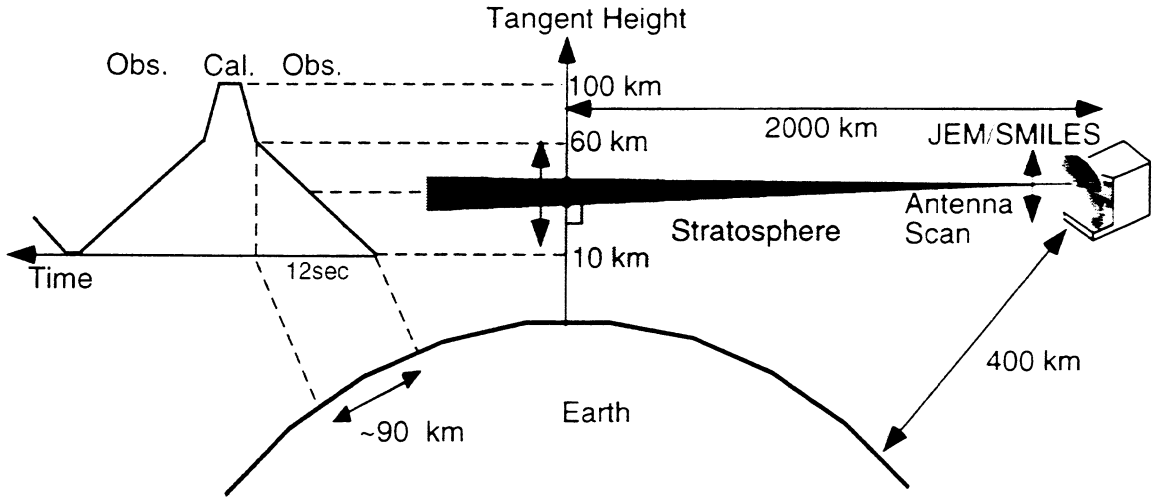

Fig. 1. Schematic view of the limb sounding observation by JEM/SMILE.

Table 1. Basic Specifications of JEM/SMILES

Receiver	Heterodyne Spectrometric-Radiometer
Observation Scheme	Limb Sounding
Observation Platform	International Space Station
Orbit Altitude	~400 km. 51° inclination
Observable Latitude Observation Altitude Altitude Resolution	65°N - 38°S h = 10 - 60 km. Δh = 2 km
Antenna Type Size & Beam width	Offset Cassegrain 60 cm. 0.055°(El.), 30 cm. 0.117° (Az.)
Pointing Accuracy	0.01°(El.)
Signal Frequency	624 - 629 GHz (LSB) 649 - 654 GHz (USB)
SSB Separation Method	Quas- optical SSB filter FSP
LO Source	Gunn diode (109.4 GHz) doubler+tripler
Mixer Operation Temp. Low noise Amps.	PCTJ type Nb/AlOx/Nb @4.5K HEMT amps@20K,100K
Spectrometer Spectral Resolution	Acousto-Optical Spectrometer (AOS) 1.4 MHz
System Noise Temp.	500 K (SSB)
Mission Life Time	1 year
Weight & Power	500 kg, 500 W
Size	0.8 x 1 x1.9 m
Launch Date	2003

Table 2. Observing Molecular Species

Species	Frequency (GHz)	Brightness Temp. (K)	Comments
O_3	650.733	220	Ozone Layer,Global Warming
$O^{18}O$	627.773	80	*T* and *P* measurement
ClO	649.45	20	Ozone Depletion
HCl	625.90-93	100	Cl Reservoir
HOCl	628.46	3	Cl Reservoir
NO	651.772	8	Ozone Depletion
N_2O	652.834	30	NOx Reservoir
HNO_3	650.279	5	NOx Reservoir
HO_2	649.701	5	Ozone Depletion
H_2O_2	627.087	0.3	HOx Reservoir
BrO	624.77	0.3	Ozone Depletion
SO_2	624.344	0.2	Aerosol Source

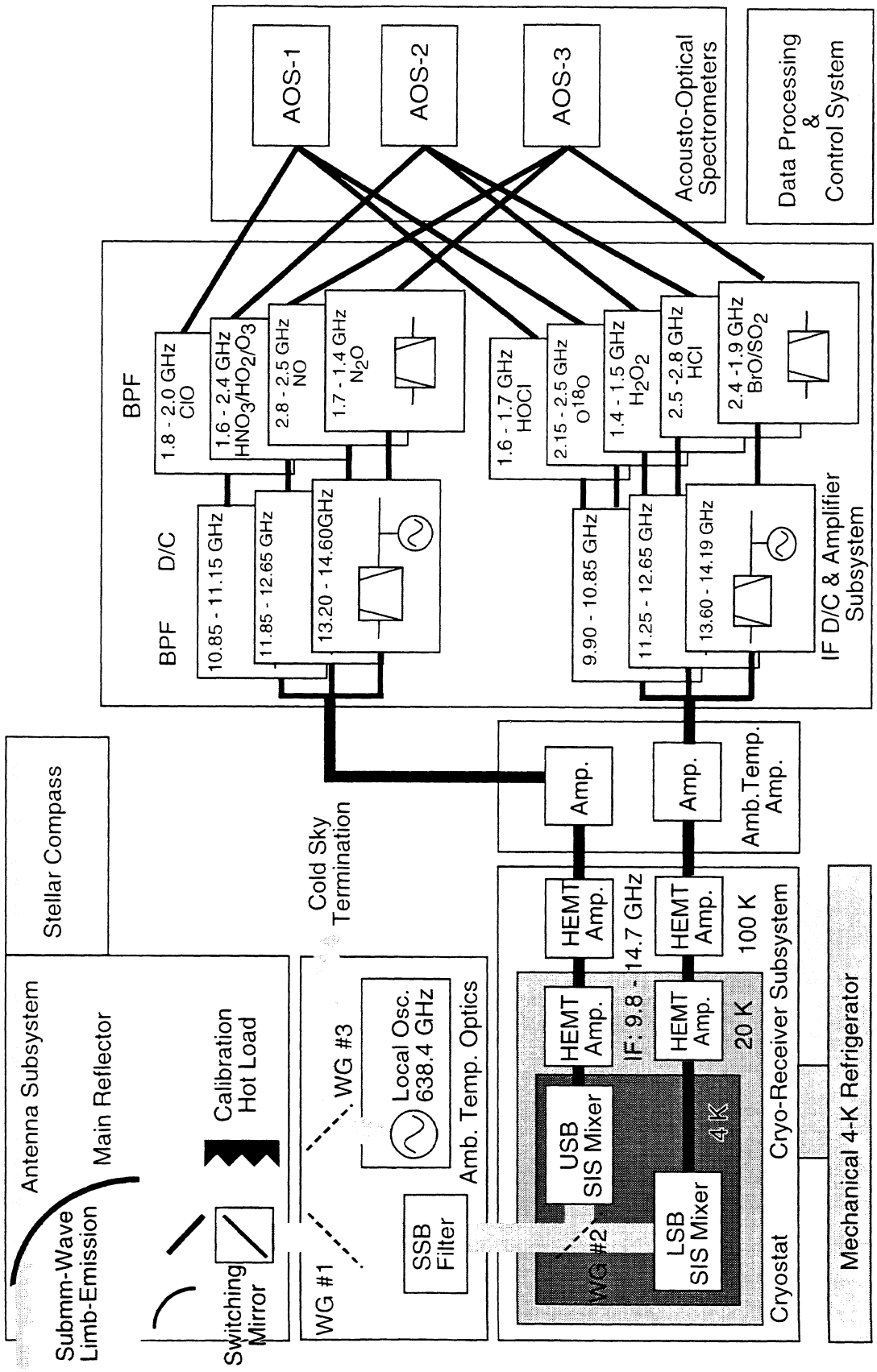

Fig. 2. Signal flow diagram of JEM/SMILES.

support structure is monitored by a stellar compass installed very close to the antenna. We will be able to determine the positions of the antenna with an accuracy of 0.01°.

Second requirement is precise intensity calibration. We require a high main beam efficiency of 95 % so that undesirable emission from the sidelobe should be reduced. The shape of the main reflector is modified to produce the high efficiency main beam, and its surface is polished with an accuracy better than 10 μm to reduce the level of sidelobe. We use a temperature monitored submillimeter-wave absorber at an ambient temperature for a hot load calibration, but we use the main antenna itself for cold load calibration by pointing upward directions. We expect a precise cold load calibration compared with a system looking cold sky by a switching mirror in the beam transportation system, because effect from the surroundings of the optics is kept same during operation. The baseline ripple which appears in the observed spectra due to undesired reflection within the system is also a source for reducing the reliability of calibration. We choose offset type antenna for avoiding the beam reflection in the antenna which may cause baseline ripple in the spectra. We expect a precise intensity calibration better than 10 % in error.

QUASI-OPTICS

Figure 3 is the schematic drawing of the receiver optics of SMILES. Optical system is designed to realize easy alignment and reduce the risk of misalignment caused by variation of environmental condition on space. The optics are divided into two main components: the optics on 4-K stage and that in ambient temperature. The ambient temperature optics guide the beam from the antenna subsystem into the cooled optics. The 638.4 GHz LO signal is injected into the wire grid in the ambient optics. Typical physical size of the mirror is ranging from 30 mm in the 4-K stage and 60 mm on the ambient optics. They are settled around the center of cryostat as close as possible. The center of the cryostat is stable in terms of mechanical structure and thermal conditions, and concentration of them toward the center is suitable for keeping the good alignment conditions.

An outstanding feature of the optics is the realization of SSB operation of two SIS mixers simultaneously using only one local source (Inatani *el al.*, 1998). Two mixers on the 4-K stage receive two perpendicular polarizations each other. One mixer looks at the antenna port in the USB band, while it looks at the cold sky though the LO port in the LSB band. At the same time, the other mixer looks at the antenna port in the LSB band and the cold sky in the USB band. This SSB operation is realized by a quasi-optical SSB filter on the ambient temperature optics. The band suppression ratio of 17 dB is expected at the band edge frequency.

The SSB filter is a key component of the optics. We use a frequency selective polarizer (FSP) as an SSB filter which use the principle of Martin-Puplett interferometer (MPI) (Seta *et al.*, 1999). The FSP consists of two pairs of a flat mirror and a wire grid. Figure 4 shows the operational principle of the FSP comparing that of traditional MPI consisting of two roof-top mirrors and a wire grid shown in Figure 5. The wire grid (WG) #4, whose wire direction is oriented at 45° with respect to the incident linear polarization, divides the input signal into two components. The reflected and transmitted signals are combined again in WG #5 after traveling two different path

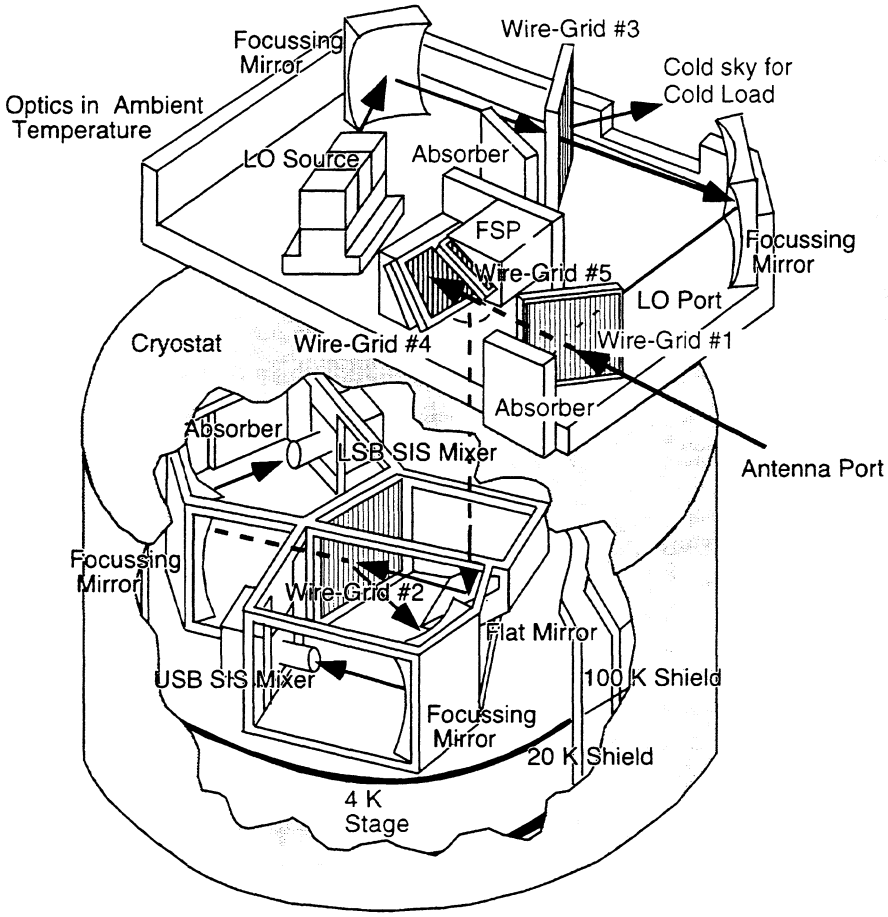

Fig. 3. Schematic view of receiver optics of JEM/SMILES.

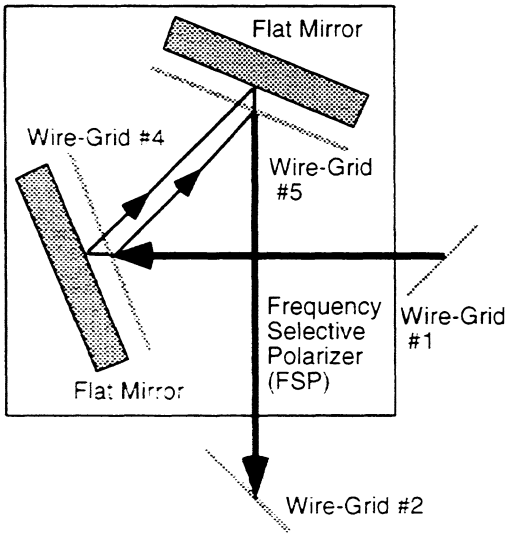

Fig. 4. Schematic drawing of our proposed new type of SSB filter operating in the principle of MPI.

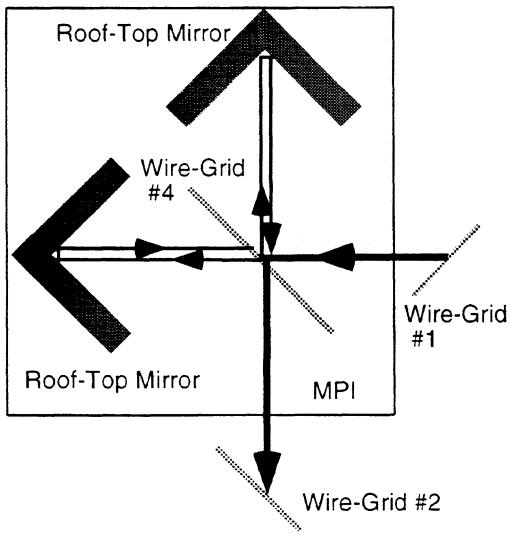

Fig. 5. Schematic drawing of a conventional MPI.

lengths. We can tune the transmission characteristics in frequency from a linearly polarized input signal to a linearly polarized signal in the output port by adjusting the traveling path length difference. The path lengths is adjusted by a gap between the flat mirror and the wire grid, while in the conventional MPI the path difference is controlled by the relative distance difference between the WG #4 and each roof top mirror.

The FSP is superior to the traditional MPI in two reasons for our purpose. Since we use the SSB filter for a fixed frequency, we do not need tuning mechanism. A mechanical tuner may be harmful by increasing possibilities of mechanical troubles in space. So we will use a fixed tuned SSB filter without moving mechanical structure. We adjust the position of the mirror in the ground which works as a tuner, and fix the position tightly once it is tuned. The required alignment accuracy of the mirror is estimated to be 2 μm. In the traditional MPI we must achieve this accuracy for a traveling path length of 50 mm, and this is too difficult to achieve without mechanical tuning structure. On the other hand in case of FSP, we can adjust the mirror position in a accuracy of 2 μm for a path length of 2 mm, which is achieved with careful machine work. The second advantage of the FSP is elimination of standing waves generated on the MPI. In the conventional MPI, the input signal partially returns to the input port due to undesirable transmission and reflection of the wire grid. The returned signal becomes a source of standing wave. This level is estimated to be 20 dB assuming the undesired reflection and transmission of the wire grid is 1%, and it is harmful to our sensitive spectroscopic observation. Although in the FSP we cannot avoid the undesirable reflection and transmission of the wire grid, this component never comes back to the input port.

The LO signal at 638.4 GHz is generated in a phase-locked Gunn diode oscillator followed by a doubler and a tripler, and injected into the FSP through the WG #3. The direction of wires in WG #3 is tilted 10° from the linear polarization plane of the LO source, so that the local power is injected into the FSP by 3 % , while each mixer, in its image band, looks at the cold sky by 97 %. The injected LO power is equally supplied into two mixers. The LO output power, which is expected to be around 200 μW, is sufficient for operation of two 640-GHz SIS mixers.

SUBMILLIMETER SIS MIXERS AND LOW NOISE AMPLIFIERS

The SIS is the ultimate device for sensitive millimeter and submillimeter observations especially for 100 - 1000 GHz. Up to now only a Schottky barrier diode type mixer is used in the space (e.g., Barath *et al.* 1993). SMILES employs the SIS mixer for the first time in the space. We use simple and stable SIS mixers for increasing reliability of the mission.

We use a parallel-connected-twin-junctions (PCTJ) type SIS mixer composed of 1.25-micron scale Nb/AlOx/Nb junctions, which are developed at the Nobeyama Radio Observatory (Noguchi *et al.*, 1995; Shi *et al.*, 1997; 1998). The mixer with this device achieves a broad-band performance without a mechanical tuning structure. We place the SIS device in a wave guide type mixer-mount in a typical size of 20 mm. A corrugated type feed horn is attached to the mount, and superconducting magnets are integrated in the mount to suppress the Josephson current. One model of the mixer covers both USB (649-654 GHz) and LSB (624-629 GHz), which is

advantageous in performing space qualification tests such as vibration and radiation. The mixer block is attached to the rigid 4K-optics directly with screws. An independent battery will be used for a DC bias of the mixer for stable operation. Our experiment already demonstrated the mixer noise of Tmix = 60-140 K in DSB in the frequency range of 600-650 GHz (Irimajiri *et al.*, 1998).

We require broad band and low power consumption low noise amplifiers for IF amplifiers. SMILES requires a bandwidth of 5 GHz in the 640 GHz band to detect important molecules listed in Table 2. and the IF amplifiers should be low noise over the frequency band for high sensitivity. The power consumption of IF amplifiers should be low for using compact refrigerator. We are developing a high-electron-mobility transistor (HEMT) amplifier with a bandwidth of 5 GHz. We expect a noise temperature below 25 K and a gain of 20 dB with a power dissipation of 20 mW at the operational temperature of 20 K. We succeed in demonstrating this performance in the engineering model of the HEMT amplifiers.

CRYOSTAT AND MECHANICAL REFRIGERATOR

The SIS mixer needs to be operated below 4.5 K. We chose mechanical refrigerator as a cooling system. The mechanical refrigerator is superior to liquid helium type cooler for space use mainly for two reasons, even though it needs lager electric power. First it can be made smaller and lighter, because we do not need large helium tank. Second there is possibilities to expand the life time keeping its smallness and lightness.

We have been developing a compact and low power consumption type refrigerator for space use. Inatani *et al.* (1997) reported the experimental results of thermal prototype of the refrigerator, and concluded that an SIS receiver cooled by a compact 4-K mechanical refrigerator is feasible for space use. Based on this successful experiment we are developing an advanced type of a compact refrigerator system for JEM/SMILES, which satisfies the launching condition of SMILES. Figure 6 shows the schematic view of our cryostat. In the cryostat, we place two SIS mixers, two HEMT amplifiers, other two HEMT amplifiers on the 4-K, 20-K, and 100-K stages, respectively. The cryostat is equipped with a Joule-Thomson circuit and a two-stage Stirling refrigerator (Kyoya *et al.*, 1994). Table 3 shows the thermal analysis of the cryostat. The 4-K stage is surrounded with radiation shields at 20 K and 100 K, and the effect of thermal radiation is minimized with a set of carefully installed multi-layer insulators. For reducing the thermal radiation through an RF signal window, we place two IR filers made of porous polytetrafluoroethylene (PTFE) between the 100-K stage and the outer shell. The cooling capacity is designed to be 20 mW at the 4-K stage, 200 mW at the 20-K stage, and 1000 mW at the 100-K stage with an electric power consumption less than 250 W at the AC power supply to the refrigerator system.

Mechanically the three stages are supported by a number of glass-fiber reinforced plastics (GFRP) straps from the outer shell of the cryostat. The 4-K and 20-K stages are connected by poles made of carbon-fiber-reinforced plastic (CFRP) and 20-K and 100-K stage is connected by poles of GFRP. The GFRP and CFRP keep the thermal conductance as small as possible while surviving the vibrating environment during the launch. Mylar film is used for outer shell window

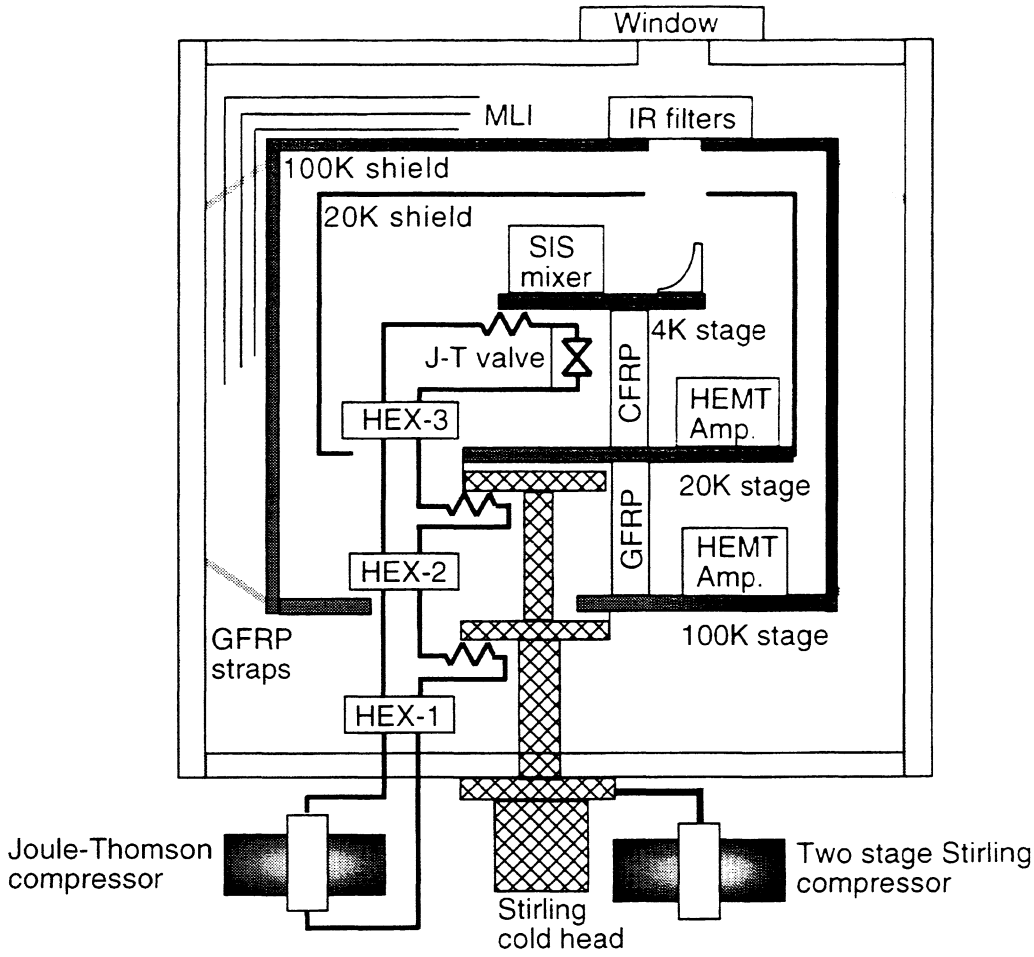

Fig. 6. Schematic view of a small Joule-Thomson circuit combined with two stage String refrigerator.

Table 3. Calculated thermal balance of 640 GHz receiver for SMILES

Items	Types	Heat load at each stage (mW)		
		100-K stage	20-K stage	4-K stage
RF input window	radiation	150	3	2.4
Wall (with MLI)	radiation	370	19	0.1
Supporting structure	conduction	230	47	2.4
IF cables	condition	90	42	13
DC bias cables	conduction	28	5	0.6
Bias current	heat source	9	3	1
Monitor cables	conduction	11	4	0.6
HEMT amps	heat source	30	20	-
J-T gas cooling	heat source	170	87	-
Total load (mW)		970	210	20
Equilibrium temperature (K)		99	22	4.5

to keep the vacuum of cryostat during testing of the receiver on the ground.

By using the engineering model of our cryostat we succeeded in demonstrating the cooling capability and also demonstrated that the vibration expected during the launch did not change the capability. The detail of the refrigerator will be given elsewhere (Narasaki *et al.*, in preparation).

IF SUBSYSTEM AND SPECTROMETER

In retrieving altitude profiles from the spectral data, frequency resolution restricts the altitude resolution in the profile, and the frequency bandwidth restricts the lower altitude limit of the profile. We employ AOS for getting high spectral resolution and wide bandwidth. AOS is superior in terms of weight, size, and power consumption compared with other frequently used digital or filter-bank type of spectrometers. We use three AOSs and achieve a total bandwidth of about 4 GHz with a frequency resolution of 1.4 MHz. We convert a readout data of the CCD in the AOS into a 16 bit digital data every 10 msec, and we integrate it for 200 msec.

In order to save the bandwidth of the spectrometer, only limited frequency ranges of molecular lines of interest are chosen from the broad band width of 5 GHz, and band-pass-filtered into sub bands. The divided band is again combined into three AOS input ports for spectroscopy. We realize observational bandwidth of 800 MHz for O_3 using this technique.

CONCLUDING REMARKS

In this paper we reported the basic design of the 640 GHz submillimeter receiver system of the JEM/SMILES mission, and also reported some experimental results of the engineering model. SMILES employs a sensitive 640 GHz SIS receiver. We operate two SIS mixers simultaneously in the SSB mode. We use a frequency selective polarizer (FSP) as an SSB filter. The SIS mixer will be cooled 4 K by a compact Joule-Thomson circuit combined with two stage String refrigerator. In the engineering model of the refrigerator, we demonstrated the cooling capability of 20 mW at the 4-K stage, 200 mW at the 20-K stage and 1000 mW at the 100-K Stage. We use three AOSs for spectrometer, and achieve a frequency resolution of 1.4 MHz and total bandwidth of 4 GHz. We expect a system noise temperature of 500 K in the SSB mode.

We are now making a final design trade-off for JEM/SMILES, and the specifications described here may be subject to minor changes. In 2003, SMILES will be transported to ISS by a Japanese transporter vehicle HTV launched by the H-IIA rocket. The SMILES will observe twelve stratospheric molecules and reveal interesting phenomena relating to the ozone chemistry. This mission will also demonstrate the feasibility and effectiveness of the SIS receiver as a sensitive system for monitoring trace gases in the stratosphere. The success of this new technique will open new possibilities of submillimeter wave observation in earth science and in astronomy.

ACKNOWLEDGEMENT

We acknowledge Mitsubishi Electric Corporation for system design of JEM/SMILES, Sumitomo

Heavy Industries, Ltd. for development of the refrigerator. Nihon Tsushinki Co. Ltd. for development of HEMT amplifiers. Paris-Meudon Observatory for design of AOS. Thomas Keating Ltd. for design of optics. Radiometer Physics GmbH for design of LO system. and space instrumentation group of Technical University of Denmark for design of stellar compass. In developing SIS junctions we are collaborating with Nobeyama Radio Observatory (NRO). We thank Dr. S.-C. Shi and Dr. T. Noguchi of NRO for technical support and discussions.

REFERENCES

F. T. Barath *et al.*, The Upper Atmosphere Research Satellite Microwave Limb Sounder Instrument, *J. Geophys. Res.*, 98, D6, 10751, 1993.

J. Inatani *et al.*, A Submillemeter SIS Receiver Cooled by a Compact Stirring-JT Refrigerator, Eighth Int. Symp. on Space Terahertz Tech., Harvard Univ., March, 1997.

J. Inatani, S.C. Shi, Y. Sekimoto, H. Masuko, and S. Ochiai, Single Sideband Mixing at Submillimeter Wavelengths, Ninth Int. Symp. on Space Terahertz Tech., Pasadena CA. March, 1998.

Y. Irimajiri, T. Manabe, H. Masuko, S. Ochiai, M. Seta, Y. Kasai, T. Noguchi, and S.C. Shi, Waveguide Heterodyne SIS Receiver for Balloon-borne Superconducting Submillimeter-Wave Limb Emission Sounder at 640-GHz-band., 23rd. Int. Conf. on IR and MM Wave, Essex, September, 1998.

M. Kyoya, K. Narasaki, K. Ito, K. Nomi, M. Murakami, H. Okuda, H. Murakami, T. Matsumoto, and Y. Matsubara, Development of Two Stage Small Stirling Cycle Cooler for Temperature below 20 K, *Cryogenics*, 34, No5, 431, 1994.

T. Manabe *et al.*, Space-Station Borne Submillimeter-Wave Limb-Emission Sounder for Observing Stratospheric Minor Constituents, URSI Commission F Int. Triennial Open Symp. Wave Propagation and Remote Sensing, September, Aveiro, 1998.

H. Masuko, S. Ochiai, Y.irimajiri, J. Inatani, T. Noguchi, Y. Iida, N. Ikeda, and N. Tanioka, A Superconducting Sub-millimeter Wave Limb Emission Sounder (SMILES) on the Japanese Experiment Module (JEM) of the Space Station for Obsrving Trace Gases in the Middle Atmosphere, Eighth Int. Symp. on Space Teraherzt Tech., Harvard, MA, March, 1997.

T. Noguchi, S.-C., Shi, and J. Inatani, An SIS Mixer Using Two Junctions Connected in Parallel, *IEEE trans. Appl. Supercond.*, 5, 2228, 1995.

M. Seta, T. Manabe, H. Masuko, J. Inatani, H. Harada, T. Noguchi, S.-C. Shi, K. Narasaki, and Y. Abe., Submillmemeter -Wave SIS Receiver System for JEM/SMILES, Advances in Space Research, in press, 1999.

S.C. Shi, T. Noguchi, and J. Inatani, Analysis of the Bandwidth Performances of SIS Mixers with Distributed Junctions Arrays, Eighth Int. Symp. on Space Terahertz Tech., Harvard Univ., March, 1997.

S.C. Shi, T. Noguchi, J. Inatani, Y. Irimajiri, and T. Saito, Experimental Results of SIS Mixers with Distributed Junction Arrays, Ninth Int. Symp. on Space Teraherzt Tech., Pasadena, CA. March, 1998.

CONCEPT OF A SUPERCONDUCTING INTEGRATED RECEIVER WITH PHASE-LOCK LOOP

Sergey V. Shitov, Valery P. Koshelets, Lyudmila V. Filippenko, Pavel N. Dmitriev
Institute of Radio Engineering and Electronics (IREE)
Russian Academy of Sciences
103907 Moscow, Russia

Andrey M. Baryshev, Willem Luinge
Space Research Organization of the Netherlands (SRON)
9700 AV Groningen, the Netherlands

Jian-Rong Gao
Space Research Organization of the Netherlands (SRON),
Department of Applied Physics and Materials Science Center,
University of Groningen, the Netherlands

Abstract — A new chip for the sub-millimeter quasioptical heterodyne receiver with an externally phase-locked superconducting local oscillator is designed and being studied. An integrated circuit of the chip contains an ultra-low-noise SIS mixer, FFO, a harmonic SIS mixer and a SIS multiplier (optional). A scheme of the chip is presented along with numerical simulation of the circuitry. The first experimental samples that were pre-tested did show encouraging performance.

INTRODUCTION

Integration of a free-running flux-flow oscillator (FFO) and a SIS mixer into a single-chip Superconducting Integrated Receiver (SIR) is a proven technique. The receiver noise temperature below 100 K (DSB) and a good beam pattern of the double-dipole antenna (sidelobes below –16 dB) have been measured at 500 GHz [1]. To estimate the ultimate performance of the receiver, the detailed tests on a reference

chip which contained only the lens-antenna SIS mixer showed a noise temperature of about 40 K at 470 GHz [2]. A densely packed imaging array seems to be the natural niche for a SIR. The feasibility of such an imaging array was demonstrated as well [1]. Since a SIR is a complicated multi-device chip, a special acquisition system IRTECON has been developed for effective test and optimal control of both the local oscillator and the SIS mixer [1, 3].

To be useful in practice as a narrow-band spectrometer, SIR has to have a narrow linewidth of its internal local oscillator (LO). A technique to stabilize the superconducting integrated oscillators [4] was developed recently into the real PLL circuit using room temperature electronics. An externally phase-locked FFO was realized *in Fiske mode* ($f_{LO} < 440$ GHz) with a measured linewidth as narrow as 1 Hz in the frequency range 230 – 440 GHz for samples of special design [5, 6]. The experimental data on spectra of the locked FFO are presented in Fig. 1. Taking into account that Fiske steps (FS) are almost overlapping at higher voltages, a complete tuneability might be achieved. In summary, it seems possible to use such LO for radio astronomy now already. A PLL circuit for the FFO operation in so-called flux-flow mode ($f_{LO} > 500$ GHz) still has to be developed and studied.

SCHEMATIC OF THE CHIP

To combine a SIS mixer and a *phase-locked* FFO on the same substrate, a new design of the chip has been developed; its scheme is presented in Fig. 2. The chip contains a combination of circuits which principles have been tested already, namely, a PLL circuit to narrow the linewidth of the FFO [5, 6] and a quasioptical SIS mixer with the integrated circuit for LO power injection (see Fig. 3). The harmonic SIS mixer and the SIS multiplier (not shown in Fig. 2) are parts that are added to the chip of the earlier SIR [1, 3].

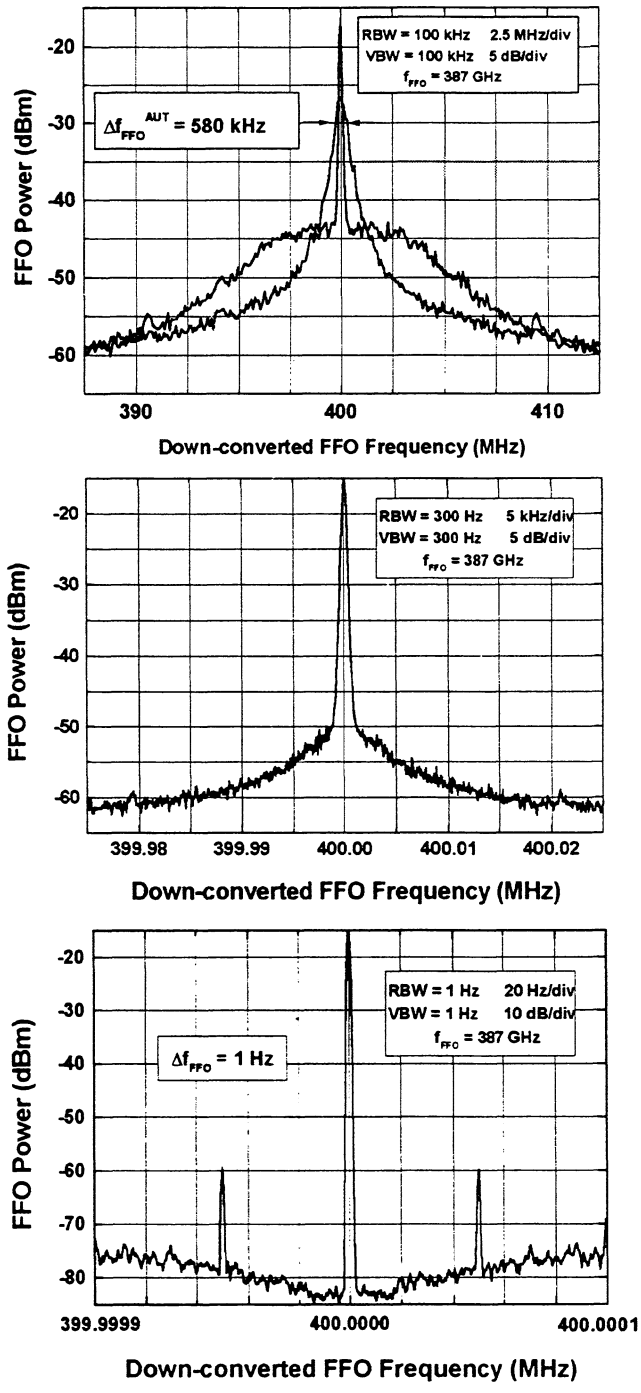

Fig. 1. *IF* power spectra of FFO phase-locked at 387 GHz recorded at different frequency spans.

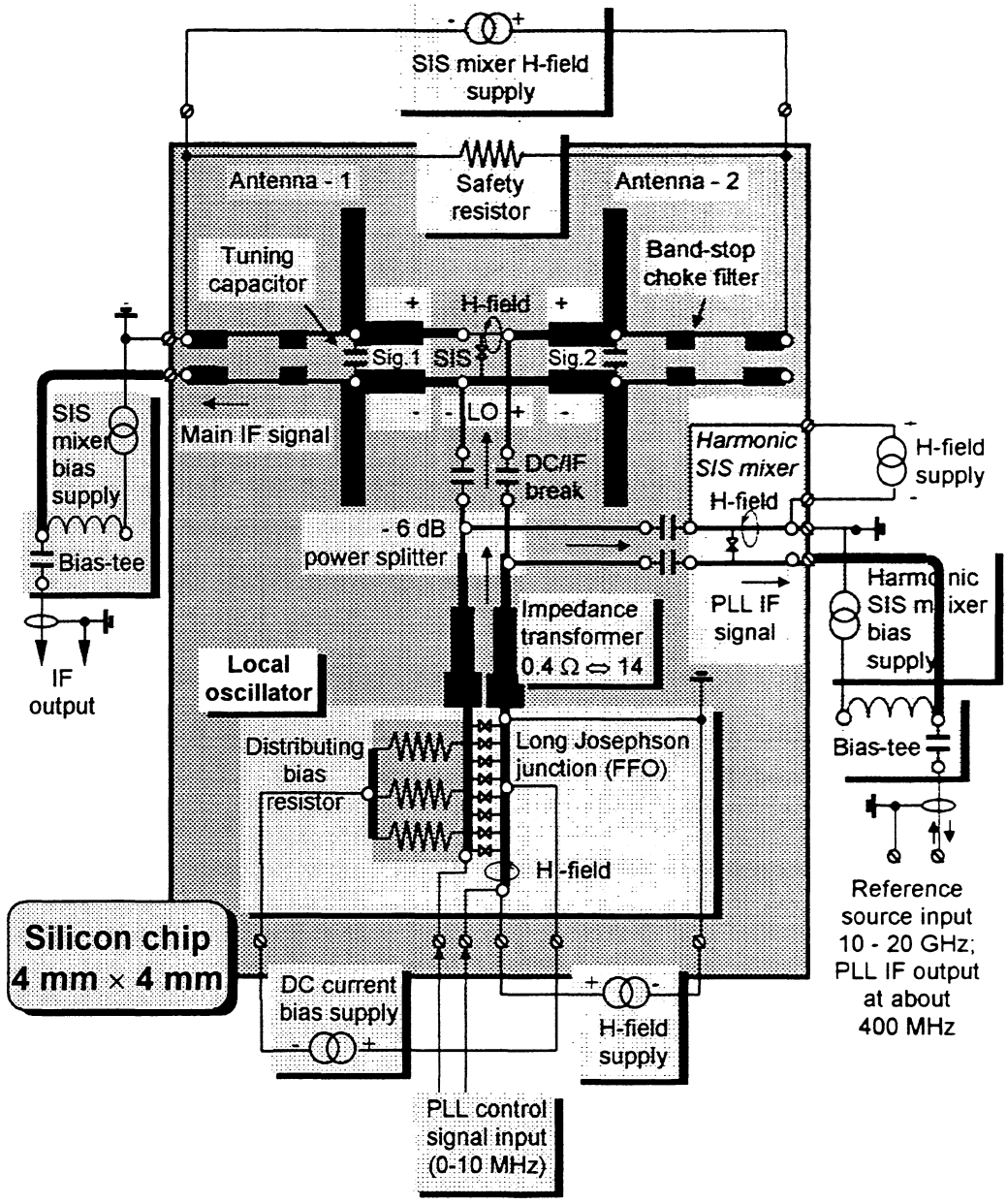

Fig. 2. Simplified equivalent diagram of external supplies and connections necessary to operate the chip of Superconducting PLL Receiver.

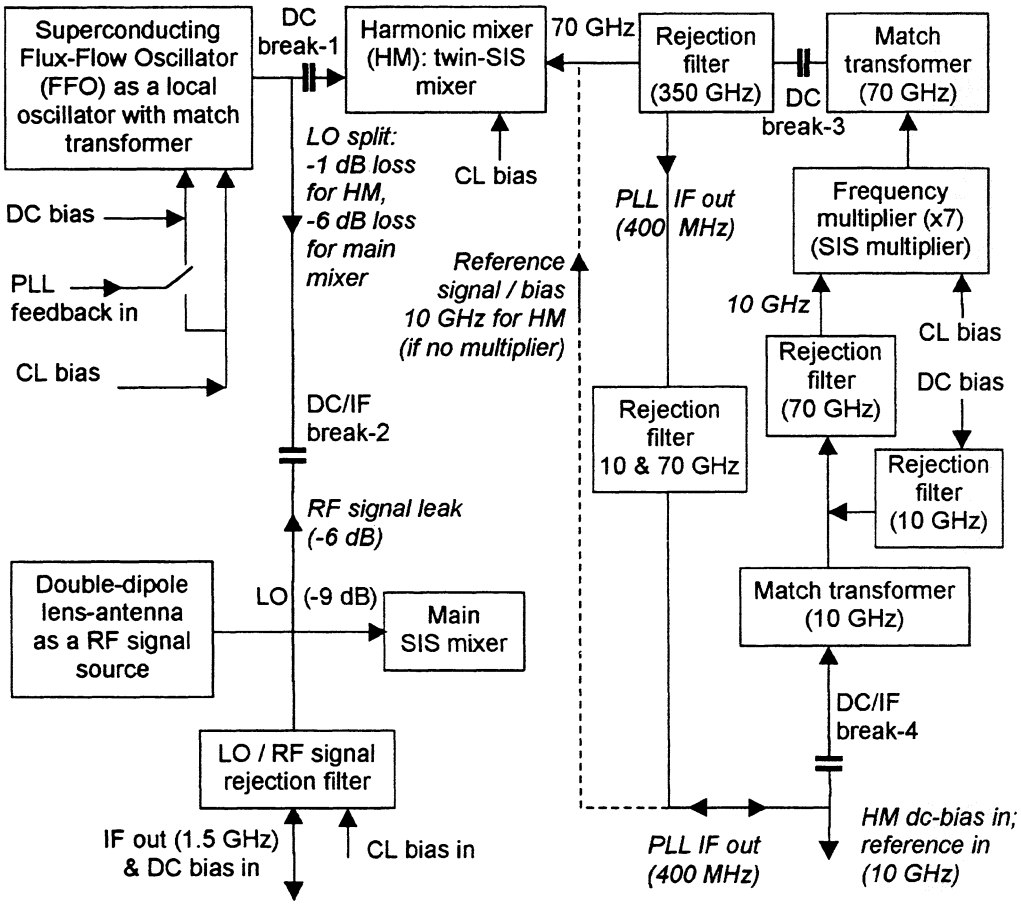

Fig. 3. Simplified block-diagram showing elements located at the chip of Superconducting PLL Receiver (parameters indicated for operation at 350 GHz).

A. Power Balance of Local Oscillator

When one FFO feeds two devices the balance of LO power is very important. The power from the FFO is split unequally between the harmonic mixer and the receiver part. To avoid too much signal loss towards the LO source, only 25-30 % of the power that is available from FFO can be coupled to the receiver SIS mixer. Taking into account that the mixing SIS junction and FFO are coupled effectively to the antenna and the harmonic mixer respectively, the portion of FFO power available at the receiver SIS junction is further reduced to about 12-15 %. This is twice as low in comparison with the previous SIR design [1, 3]. A result of numerical simulation on distributing of the signal and LO power is presented in Fig. 4. To make the level of LO power sufficient for both mixers, either more powerful FFO or smaller receiver SIS junction has to be employed in the PLL receiver.

B. Layout of the Chip

To avoid a reduced yield due to the growing complexity of the chip, special attention was paid not to use micron-sized elements which were present in the earlier SIR design [1, 3]. The narrowest strip width now is about 4 micrometers and the smallest gap is about 3 micrometers. However, the receiver SIS junction has to be small enough, proportional to the available LO power. The area of SIS junctions for both the receiver mixer and the harmonic mixer is chosen to be 1.5 by 1.5 micrometers, so a reasonable reproducibility can be expected.

C. Design of FFO

The power available from FFO seems to be proportional to the width of the long junction. Since characteristic impedance of such a Josephson transmission line (JTL) is reduced with increasing width, the coupling circuit (mainly the impedance transformer) has to provide higher ratio, that may narrow the coupling bandwidth. The increase of the FFO width is restricted because of a transverse mode can be generated

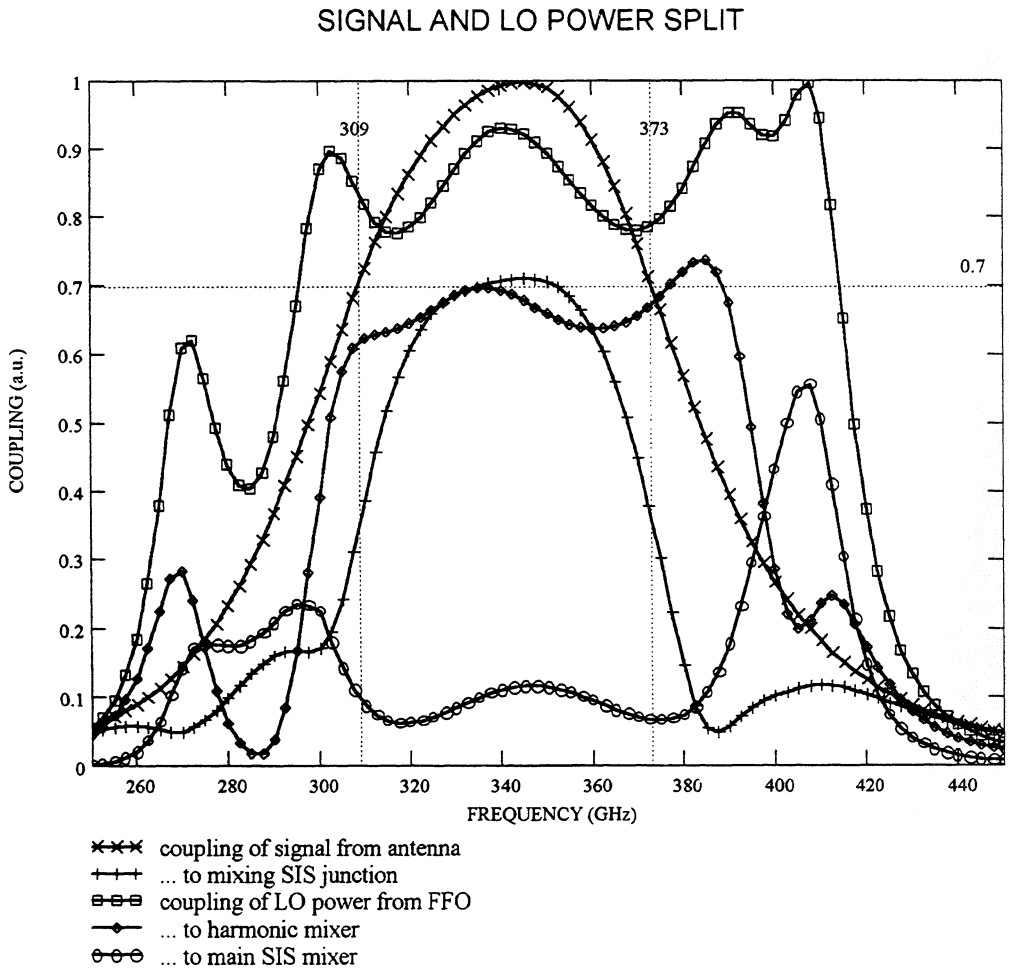

Fig. 4. Example of calculated distribution of signal (x's and +'s) and local oscillator power (box's and dimond's) in the PLL receiver circuitry. Fraction of LO power used by main SIS mixer presented at the bottom by o's. The data calculated for central frequency of 350 GHz.

in the JTL. Three different FFO widths are used in experimental samples: 4, 6 and 9 micrometers. A compact single-section impedance transformer is used.

The PLL receiver will be tested first at about 350 GHz in the Fiske mode. The length of FFO is chosen in the range of 600 ± 50 micrometers that provide voltage separation of FS small enough for continuous coverage of the RF signal band using a 4 GHz IF amplifier and picking different side-bands. The experimental samples for 350 and 560 GHz are fabricated, and preliminary tests are showing reasonable pump level at about 500 GHz.

D. Harmonic Mixer

It was demonstrated that the most efficient regime of the harmonic mixer (tested up to 50^{th} harmonic) can be realized in the Josephson mode using high order Shapiro steps [4 - 6]. However, Josephson mixing is known to be quite noisy [7] and can be the reason for the unwanted noise floor in the experimental PLL loop. Unfortunately, the experimental harmonic mixer operated in a low-noise SIS mode (Josephson effect was suppressed by magnetic field) appeared to be inefficient, at least at high order harmonics. To try mixing at lower harmonics (5th or 8th), a SIS multiplier was integrated on the chip as a source of LO power at 70 GHz. A SIS junction of area 10 by 10 micrometers is used in the multiplier. The part of the chip relevant to the multiplier is shown in Fig. 5.

Use of the multiplier essentially complicates the chip circuitry demanding a few selective filters. Since a reference signal (10 GHz) is applied via IF coaxial cable of the harmonic mixer (see Fig. 2), leak of the reference power has to be suppressed well below the level of its 7^{th} harmonic generated by the SIS multiplier. The multiplier feed circuits (both RF and dc bias) are arranged to provide a good coupling of the reference signal and avoid loss of the harmonic at about 70 GHz. A fragment of the multiplier-related circuit and its numerical simulation are presented in Fig. 5 and Fig. 6 respectively. The calculation demonstrates a reasonable match to the IF port at 400 - 1000 MHz, good rejection of 10 GHz reference signal, reasonably wide

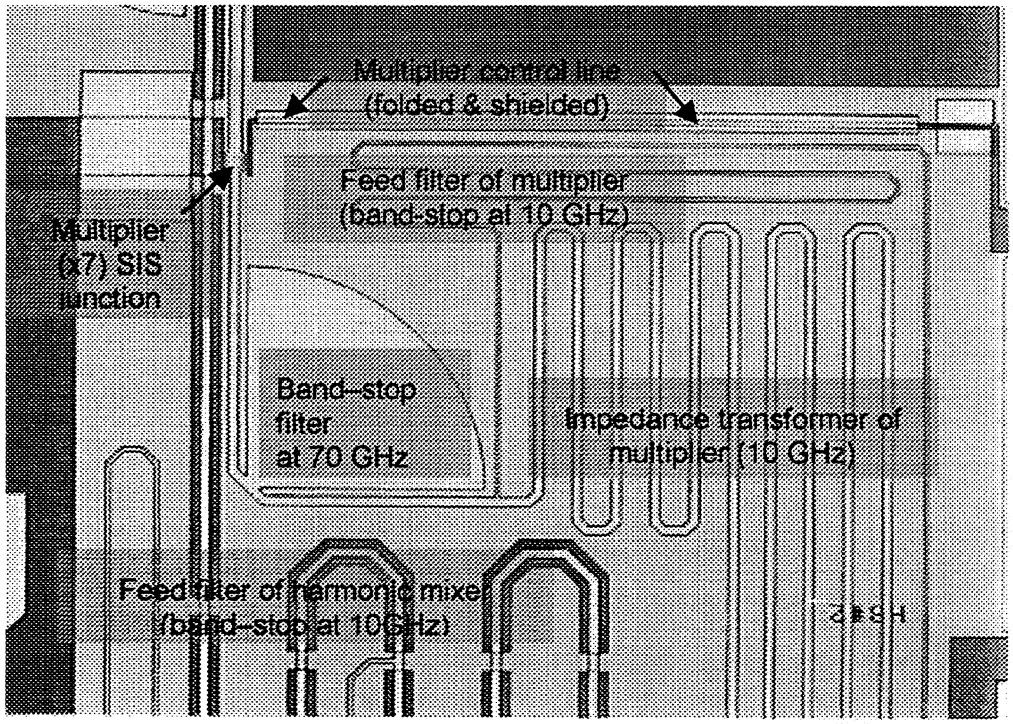

Fig. 5. Partial view of the integrated receiver chip. Folded striplines are feed filters at 10 GHz and 70 GHz used for the SIS multiplier and for the harmonic mixer. Field of view is about 900 x 600 micrometers.

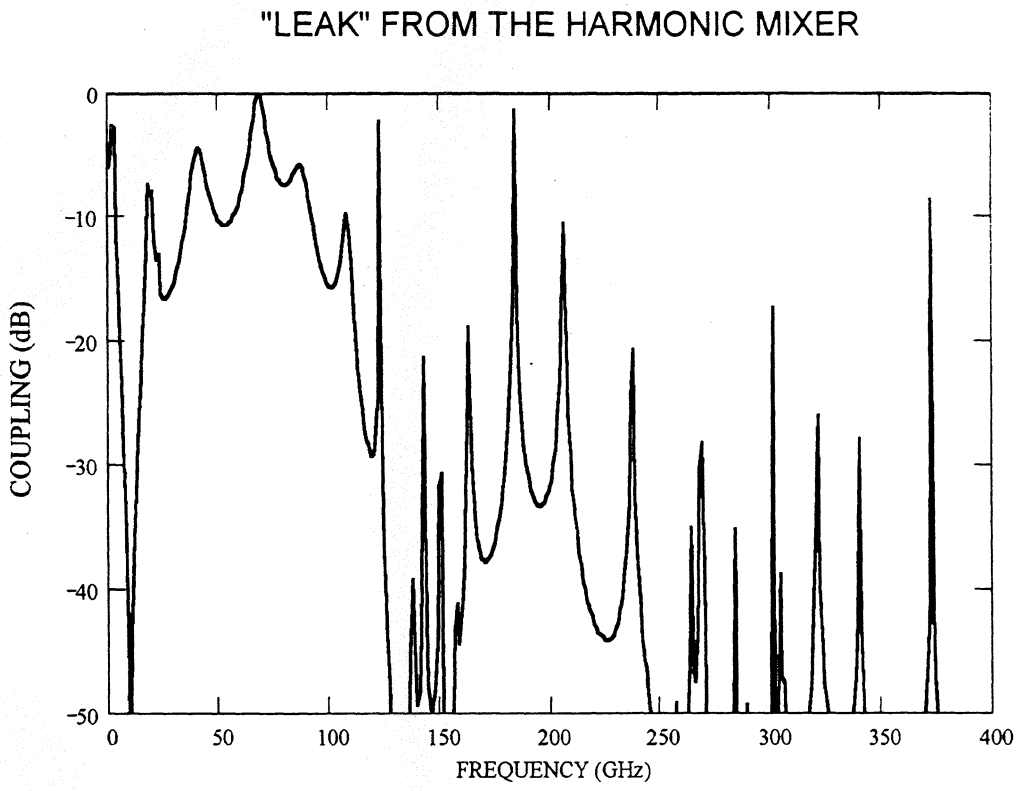

Fig. 6. Reflection loss at the harmonic mixer towards its IF port and towards the SIS multiplier (if used). Coupling to FFO that is, by definition, strong *excluded* from this calculation.

coupling at about 70 GHz and no essential leak within LO/signal range at about 300 – 400 GHz.

CONCLUSION

The concept of a superconducting integrated receiver with phase-lock loop is developed, has passed extensive numerical simulation and is implemented in experimental devices on the basis of recent progress on quasioptical SIS mixers and locked FFO. Preliminary test of experimental samples is, so far, encouraging: sufficient pump level is obtained at about 500 GHz for both mixers. More experimental details are expected soon.

ACKNOWLEDGMENTS

The work was supported in parts by the Russian Program for Basic Research, the Russian SSP "Superconductivity", the grant from *Netherlandse Organisatie voor Wetenshappelijk Onderzoek* (NWO) and ESA TRP contract 11/653/95/NL/PB/SC.

REFERENCES

[1] S. V. Shitov, V. P. Koshelets, A. B. Ermakov, L. V. Filippenko, A. M. Baryshev, W. Luinge, J.-R. Gao, "Superconducting Chip Receivers for Imaging Application", *20-th Applied Superconductivity Conference*, Palm Springs, CA, September 13-18, 1998, report EMA-09.

[2] A. M. Baryshev, W. Luinge, V. P. Koshelets, S. V. Shitov, T. M. Klapwijk, "Three-photon noise quasioptical superconductor-insulator-superconductor receiver at 500 GHz," Submitted to *Applied Physics Letters* (1998).

[3] S. V. Shitov, A. B. Ermakov, L. V. Filippenko, V. P. Koshelets, W. Luinge, A. M. Baryshev, J. - R. Gao, P. Lehikoinen, "Recent Progress on the Superconducting Imaging Receiver at 500 GHz," *Proceedings of Ninth International Symposium on Space Terahertz Technology*, March 17-19, 1998, Pasadena Hilton, Pasadena, California, USA, pp. 263-272.

[4] V. P. Koshelets, S. V. Shitov, A.V. Shchukin, L. V. Filippenko, and J. Mygind, "Linewidth of Submillimeter Wave Flux-Flow Oscillators," *Appl. Phys. Lett.*, **69** (5), pp. 699 - 701 (29 July, 1996).

[5] V. P. Koshelets, S. V. Shitov, A. V. Shchukin, L. V. Filippenko, P. N. Dmitriev, V. L. Vaks, J. Mygind, A. B. Baryshev, W. Luinge, H. Golstein, "Flux-flow oscillators for sub-mm wave integrated receivers," *20-th Applied Superconductivity Conference*, Palm Springs, CA, September 13-18, 1998, report EQB-04.

[6] V. P. Koshelets, S. V. Shitov, L. V. Filippenko, V. L. Vaks, J. Mygind, A. M. Baryshev, W. Luinge, N. Whyborn, "External Phase Locking of 270-440 GHz Josephson Flux Flow Oscillator", Submitted *to Applied Physics Letters* (1998).

[7] R. J. Schoelkopf, J. Zmuidzinas, and T. G. Phillips, "Measurements of noise in Josephson-effect mixers," *Proceedings of Fifth International Symposium on Space Terahertz Technology*, March 1994.

Tenth International Symposium on Space Terahertz Technology, Charlottesville, March 1999

A BROAD BAND LOW NOISE SIS RADIOMETER

Alexandre Karpov, Jacques Blondel
Institut de Radioastronomie Millimétrique, St. Martin d'Hères, France

Pavel Dmitriev, Valery Koshelets
Institute of Radio Electronics and Engineering, Moscow, Russia

Abstract—**A new type of ultra broad band SIS low noise radiometer has been developed. The SIS receiver instantaneous band of about 30% is significantly increased compared to traditional designs. We avoid a restriction related to the limited band of the Intermediate Frequency (IF) low noise amplifier by using a multifrequency heterodyne power source. In this regime the frequency mixing is performed simultaneously in a big number of the subbands and the IF signals are combined in a common amplifier. A low noise operation in this regime is possible due to the quantum nature of the frequency mixing in SIS quasi particle tunnel junctions.**

The SIS receiver covers 25 GHz band centered at 90 GHz with an equivalent noise temperature of about 50 K. The receiver uses a fixed tuned SIS mixer with Nb/Al Ox/Nb junctions. The critical Josephson current density is about 2.6 KA/cm² and the junction area is of about 1.5 μm². The limits to further improvement of the radiometer and the possibilities for extension of the technique to the sub millimeter band are discussed.

I. INTRODUCTION

The development of ultra low noise millimeter wave broad band radiometers is required for several different applications, particularly for the detection of weak radiation of distant objects in radio astronomy. The sensitivity ΔT of a radiometer may be characterized by a relation:

$$\Delta T_{Rec} = T_{Rec}\sqrt{\frac{1}{2\tau B}} \qquad (1)$$

where *Trec* is an equivalent receiver noise temperature, *B* is the receiver bandwidth and τ is the integration time. Optimizing the operation of a radiometer according to (1), one has to try to increase the receiver bandwidth B and to reduce the receiver noise *Trec*.

During the last decade the best receiver noise at short mm and sub millimeter wavelength was obtained using SIS heterodyne receivers [1], achieving a noise temperature close to 2hυ/k [2,3].

There are two main limitation to the bandwidth of an SIS receiver. The input SIS receiver bandwidth is limited due to a large SIS junction capacitance. The output receiver bandwidth is limited by the bandwidth of the low noise IF amplifier.

Normally the problem of a relatively broad band coupling of the SIS junction with the signal source may be solved, using a super conductive integrated matching circuit [4,1]. A real limitation of the SIS receiver bandwidth is imposed by the difficulty of development of a broad band low noise intermediate frequency (IF) amplifier. The problem arises from an increase of the IF amplifier noise with the enlargement of the IF bandwidth.

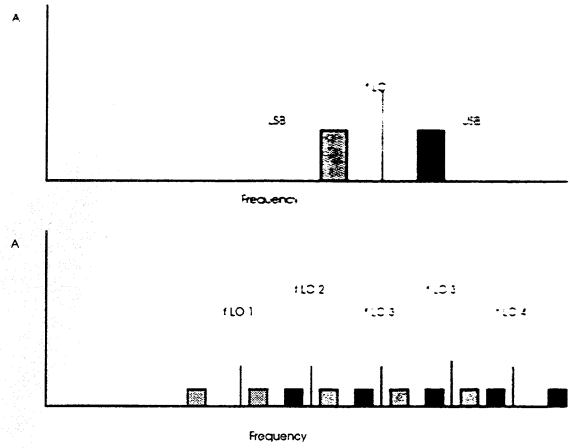

Fig. 1. The frequency diagram of a common heterodyne receiver (upper drawing) with the local oscillator frequency *f lo* and with low and upper side bands (USB and LSB). The lower diagram illustrate the operation of a heterodyne receiver with a multifrequency local oscillator. The bandwidth of the receiver is increased, proportionally to the number of the components in the spectrum of local oscillator.

In this work we present a method of increasing the receiver bandwidth *B* by a factor of 10-100, thus improving the receiver sensitivity wile using a single common IF amplifier chain.

First we discuss the principle of the new mode of SIS receiver operation. Then we describe a fixed-tined SIS mixer developed for this experiment and the test set up. At the end we give the description of the receiver tests and the perspective for further development.

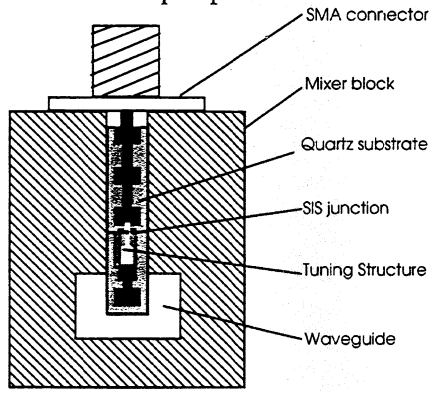

Figure 2. A fixed tuned SIS mixer design. It is a single backshort mixer block with a full height 2.3×1.15 mm waveguide. The printed circuit is coupled to the waveguide with a matching probe in the 70 - 130 GHz band. The non contacting backshort position once adjusted remains fixed in the waveguide.

II. Approach

We propose a new mode of broad band operation of a mixer with a SIS quasi particle tunnel junction using simultaneous mixing of the signal with the local oscillator having a multiline spectrum. In this way the effective receiver RF bandwidth is increased by the

number of the components in the spectrum of the local oscillator (Fig. 1). There the upper drawing represents the operation of a receiver in a common mode, with a monochromatic local oscillator signal. Below is presented frequency diagram of the proposed receiver. A new approach allows one to use a relatively low intermediate frequency in a broad band SIS radiometer and to benefit from the low noise of an ultra low noise cryogenically cooled HEMT amplifier. This mode of operation is not efficient with a classical mixer, where one needs to increase significantly the total power of a local oscillator to keep a sufficient amplitude of each component of the local oscillator.

An efficient multifrequency mixing in SIS junction is possible due to a quantum nature of the mixing mechanism. The non linear properties of an SIS quasi particle tunnel junction do not strongly depend on the amplitude of the local oscillator, but on the photon energy. At the each frequency of the local oscillator the power may be low, providing a sufficiently large conversion gain.

For example, in our experiment the monochromatic local oscillator of a broad band fixed tuned SIS receiver is replaced by a harmonic generator. Using a 1.2-1.8 GHz IF band and a 2 GHz spacing of the local oscillator frequencies across the 75-120 GHz frequency range we obtain the operation of a receiver with the RF bandwidth increased 22 times, of about 27 GHz in total.

III. SIS MIXER DESIGN

The waveguide mixer design is presented in Fig. 2. The SIS mixer comprises a microstrip Nb circuit with SIS junction

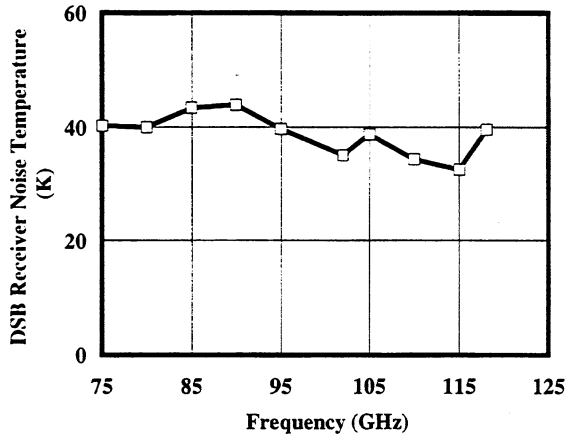

Figure 3. Fixed-tuned SIS mixer operation with a monochromatic local oscillator. The 1.2 - 1.8 GHz band of the intermediate frequency amplifier defines the limits of the receiver bandwidth.

printed on a 0.2 mm thick quartz substrate and a mixer block. The mixer block uses a single backshort in a full height 2.3×1.15 mm waveguide. The printed circuit is coupled to the waveguide with a matching probe in the 70 - 130 GHz band [5]. The non-contacting backshort position once adjusted remains fixed in the waveguide.

The printed circuit of the mixer is optimized for the junction normal resistance of about 50 Ohm and $R_N\omega C \approx 4$. The Nb-Aloxide-Nb SIS junction has an area of 1.5 μm^2. The coplanar inductive tuning circuit is connected to the junctions as part of the top electrode layer in the junction fabrication process (Fig. 2). The coplanar design gives a wider operation band and a better tolerance of the manufacturing imperfections of Nb printed circuit [6]. Coplanar line parameters are calculated with GPLINES program and the circuit was developed using the EESOF Libra program. The bandwidth of the SIS junction match in the mixer is expected to be about 50 GHz.

IV. TEST RECEIVER

The receiver comprises a liquid helium cryostat, a SIS mixer, a cooled HEMT IF amplifier, an ambient temperature amplifier and the local oscillator.
In experiment we used two different type of local oscillator. A 3 mm harmonic source pumped with a 2 GHz signal was used for the broad band mode of operation. In the normal mode of operation a Gunn device was used as a local oscillator. The local oscillator power was injected at the mixer input by a cooled waveguide coupler. The cooled intermediate frequency amplifier used in the experiment had about 5 K noise temperature in the frequency range of 1.2-1.8 GHz [7]. An isolator was fitted between the SIS mixer and the first IF amplifier. The receiver input window with anti-reflection grooves is made of polyethylene and an infrared filter of expanded polystyrene foam was fixed to the 77 K shield. The mixer block was at a temperature of about 4.5 K.

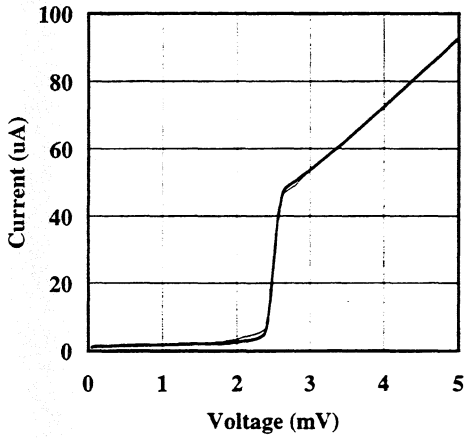

Fig. 4. Current-voltage characteristic of the SIS junction with and without multifrequency local oscillator power.

The design of the test receiver has the same features as a real receiver: the same windows and infrared filters on the way of the signal beam to the SIS mixer, the same amplifier and the same temperature at the mixer block. The receiver performance observed in laboratory may be reproduced without constraints at a radio telescope.

V. FIXED TUNED SIS RECEIVER OPERATION

A. Monochromatic local oscillator

The fixed-tuned SIS mixer was tested first with a monochromatic local oscillator power source. The receiver double sideband noise temperature versus frequency dependence was determined in a standard experiment with the ambient temperature (295 K) and the 77 K liquid nitrogen cooled loads (Fig. 3). The receiver DSB noise temperature of 40 K was nearly constant in the 75 - 118 GHz frequency range.
This confirms the design expectation of a broad, about 50%, bandwidth for the SIS junction coupling to the signal source. The two sidebands of a broad band SIS receiver have to be in balance in a major part of the band. The total receiver bandwidth at each frequency of the local oscillator is limited by the IF chain and is about 1.2 GHz.

B. SIS receiver with a multifrequency heterodyne source

In this experiment we used as a local oscillator a harmonic generator pumped with a 2 GHz signal. Across the 75-120 GHz range the number of the harmonics produced by this source is about 22. In the next subsection we will demonstrate the mixing of a broad band signal with each component of the local oscillator spectrum.

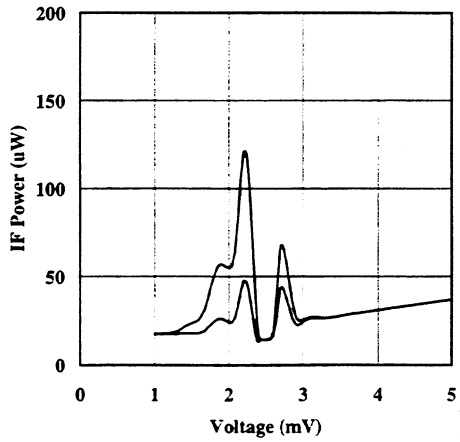

Fig. 5. Receiver IF power versus bias voltage with the multifrequency local oscillator power source. The upper and lower curves are measured respectively with the 295 K and with the 77 K loads in front of the receiver.

The current - voltage characteristics of the SIS junction measured with and without radiation from the multifrequency local oscillator is shown in Fig. 4. The receiver IF power versus bias voltage measured with the multifrequency local oscillator is shown in Fig. 5. The upper and lower curves are measured respectively with the ambient and with the liquid nitrogen temperature loads in front of receivers. The current detected in the SIS junction of about 4.5 μA was lower, compared to the experiments with the monochromatic local oscillator, which was typically about 10 μA. Nevertheless the receiver noise temperature

measured in the new regime is only 55 K, close to the receiver noise temperature in a usual narrow band mode of operation.

C. Receiver spectral response with the multifrequency local oscillator

We verified the reality of the simultaneous mixing with a large number of local oscillator frequencies by injecting a signal of a small amplitude from a second harmonic generator (Fig. 6). The harmonic source producing the local oscillator power was pumped with a 2.000 GHz signal. The signal harmonic source was pumped at a frequency 2.030 GHz, producing signals in the upper sideband of the all subbands of the receiver (upper drawing in Fig. 6). The measured response across the IF band is in the lower part of Fig. 6. The number of spectral lines corresponds to the number of the subbands in the receiver.

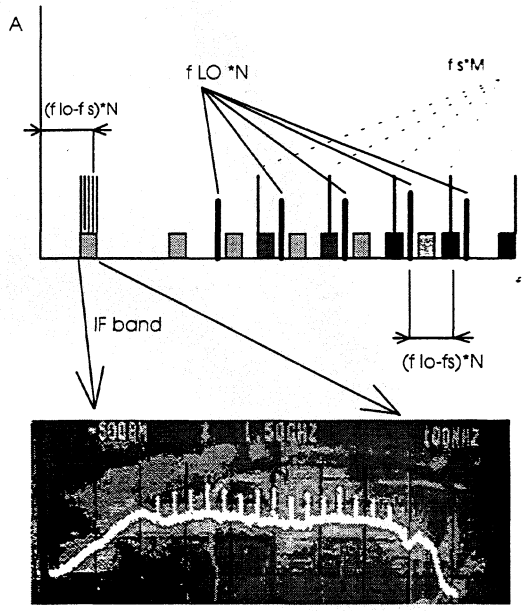

Fig. 6. The receiver with a harmonic source as a local oscillator receive a signal from a second harmonic source, pumped at a slightly different frequency. Upper drawing gives the diagram of the signals, local oscillator and intermediate signal frequencies. Below is a measured IF spectrum. The number of the component in the IF spectrum corresponds to the number of the local oscillator frequencies and confirms the expected mode of receiver operation.

V. SUMMARY

We have demonstrated a possibility of making a low noise SIS radiometer with a detection bandwidth many tens of times larger than in the standard design. The new type of a broad band operation of a mixer with a SIS quasi particle tunnel junction uses the simultaneous mixing at the different frequencies of the local oscillator with a comb type spectrum. This allows one to use a relatively low intermediate frequency in a broad band SIS radiometer. The efficient multifrequency mixing in a SIS junction is possible due to the quantum nature of the mixing mechanism. In the experiment a monochromatic local oscillator of a broad band SIS

receiver was replaced by a multifrequency harmonic source. Using a 1.2-1.8 GHz IF band and a 2 GHz spacing of the local oscillator frequencies we obtained an operation of the receiver with a RF 25 - 30 GHz bandwidth around 100 GHz with a 55 K noise temperature.

REFERENCES

1 J. E. Carlstrom, J. Zmuidzinaz, "Millimeter and submillimeter techniques", in "Review of radio science 1993 - 1995", ed. W. Stone, Oxford, The Oxford University Press, 1996.

2 A. Karpov, J. Blondel, M. Voss, K. H. Gundlach, "Four photons sensitivity heterodyne detection of submillimeter radiation with superconducting tunnel junctions", *IEEE Transactions on Applied Superconductivity*, Vol. 5, No. 2, pp. 3304-3307, 1995.

3 R. Blundell, C.-Y. E. Tong, D. C. Papa, J. W. Barrett, S. Pain, X. L. Zhang, J. A. Stern, H. G. LeDuc, and B. Bumble, "A fixed-tuned SIS receiver for the 450 GHz frequency band", *Proceedings of the 6 th International Symposium on Space Terahertz Technology*, Pasadena, CA, USA, March 21 - 23, 1995, pp. 123-133.

4 S. K. Pan, A. R. Kerr and M. J. Feldman, "Integrated tuning elements for SIS mixers", *International Journal of Infrared and Millimeter Waves*, Vol. 9, No 6, pp. 203-212, Feb. 1988.

5 A. Karpov, J. Blondel, P. Pasturel, K. H. Gundlach, "A 125-180 GHz fixed-tuned SIS Mixer for Radioastronomy", , *IEEE Transactions on Applied Superconductivity*, Vol. 7, N 2, pp. 1073-1076, 1997.

6 A. Karpov, J. Blondel, C. Grassl, K. H. Gundlach, "A full height waveguide SIS mixer for waveguide band operation", *Proceedings of the 17 th International Conference on the Infrared and Millimeter Waves*, ed. R. J. Temkin, SPIE-P/1929, p. 212 - 213, 1993.

7 J. D. Gallego, M. W. Pospieszalski, "Design and performance of cryogenically coolable ultra low noise L-band amplifier", Electronic division internal report No. 286, NRAO, Charlottesville VA, USA, March 1990.

A 200 GHz Broadband, Fixed-Tuned, Planar Doubler

David W. Porterfield

Virginia Millimeter Wave, Inc.
706 Forest St., Suite D
Charlottesville, VA 22903

Abstract - A 100/200 GHz planar balanced frequency doubler has been designed and tested. The doubler is designed for high output power and efficiency over a wide bandwidth without relying on mechanical tuners of any kind. The only available tuning mechanism is through an external electronic DC bias supply. The doubler employs a six anode planar Schottky Barrier varactor array fabricated at the University of Virginia Semiconductor Device Laboratory.

INTRODUCTION

The multiplier was designed as part of a local oscillator (LO) chain for the European Space Agency's (ESA) Far Infrared and Submillimeter Telescope (FIRST). Instruments on FIRST will require LO sources in seven bands covering a large part of the spectrum between 480 GHz and 2.7 THz. Since the instruments must be space qualified, the LO sources should be solid state, rugged, reliable, efficient and low noise.

The 100/200 GHz doubler described here was designed as part of an LO multiplier chain for Band 5 which covers the spectrum from 1.12-1.25 THz. It is estimated that approximately 50 μW is needed at these frequencies to pump either an SIS mixer or an HEB. Much less power is actually required by the mixers, but there are substantial optical coupling losses associated with the cryogenic dewars. The table below shows the makeup of the LO chain for Band 5. The estimated multiplication efficiencies are for room temperature operation. However, the LO chains on FIRST may be cooled to 80 K which will result in a significant increase in the multiplication efficiencies and output powers.

Table 1. Proposed LO chain for Band 5 on FIRST.

Input frequency/power	Component	Estimated efficiency	Output frequency/power
100 GHz /	MMIC amp		100 GHz / 200^{+} mW
100 GHz / 170 mW	Doubler	30 %	200 GHz / 50 mW
200 GHz / 50 mW	Doubler	14 %	400 GHz / 7 mW
400 GHz / 7 mW	Tripler	0.7 %	1.2 THz / 50 μW

SCHOTTKY BARRIER VARACTOR

The nonlinear device used in the 100/200 GHz frequency doubler is a GaAs planar Schottky barrier varactor fabricated at the University of Virginia (UVA) Semiconductor Device Laboratory (SDL). The varactor chip comprises 6 anodes in an antiseries arrangement as shown in Fig. 1. The epitaxial doping is 2×10^{17} cm^{-3}, the reverse breakdown voltage is measured to be 9.5 V/anode at 50 μA and the series resistance is estimated to be approximately 4 Ω/anode. Three versions of the varactor chip were fabricated as specified in Table 2. The values for the anode diameter, D, the zero biased junction capacitance, C_{j0}, the input frequency embedding impedance, Z_{IN}, and the output frequency embedding impedance, Z_{OUT}, are for the individual anodes. The input power required for optimum multiplier efficiency, P_{IN}, is the total for the 6 anode chip.

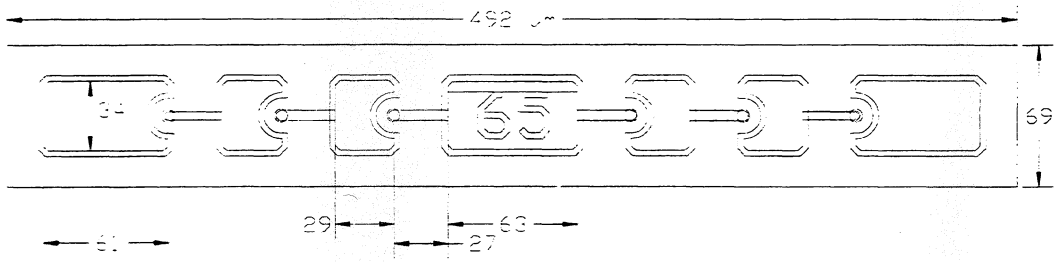

Figure 1. Sketch of the UVA planar varactor chip.

Table 2. Varactor parameters for a pump frequency of 100 GHz.

UVA type	D (μm)	C_{j0} (fF)	Z_{IN} (Ω)	Z_{OUT} (Ω)	P_{IN} (mW)
SB6T3	6.0	42	11 + j70	18 + j35	130
SB6T4	6.5	49	10 + j60	15 + j30	160
SB7T5	7.0	56	8 + j52	13 + j26	190

EMBEDDING CIRCUIT

The embedding circuit comprises a quartz circuit and varactor chip housed in a split waveguide block. This basic circuit topology can be traced back to a novel design described by Erickson in the literature [1-3]. The original architecture was later successfully modified to remove all mechanical tuners without sacrificing bandwidth [4,5]. This was achieved by mounting the planar varactor chip on a quartz circuit rather than directly across a split waveguide block. The photolithographic process used to fabricate the quartz circuits results in a high degree of control over circuit dimensions and thus significant control over the embedding impedances.

The varactors are situated in the input waveguide as illustrated in Figure 2. Input radiation is incident on the varactors in a balanced mode (TE_{10}) in reduced-height waveguide. However, the input radiation can propagate beyond the varactor chip toward the output waveguide. HFSS simulations indicate that the center conductor and quartz dielectric in this quasi-coaxial region only slightly perturb the TE_{10} mode. At a point between the varactor chip and the output waveguide, the width of the quasi-coaxial waveguide section is sufficiently reduced to cut off propagation of the TE_{10} mode, creating a reactive termination (backshort) at the input frequency. The reduced-width section, more appropriately termed as enclosed suspended microstrip, extends to the output waveguide. The position of the backshort and the length of the reduced-height waveguide section between the varactors and the full-height input waveguide are design parameters that were used to obtain an acceptable input frequency embedding impedance. The output frequency is generated by the varactors in an unbalanced mode (TEM) and is free to propagate to the output waveguide. Since the input waveguide is overmoded at the output frequency, the output radiation from the varactors can couple to the TM_{11} mode. However, this unwanted coupling can be eliminated by sufficiently reducing the input waveguide height in the region near the varactor chip.

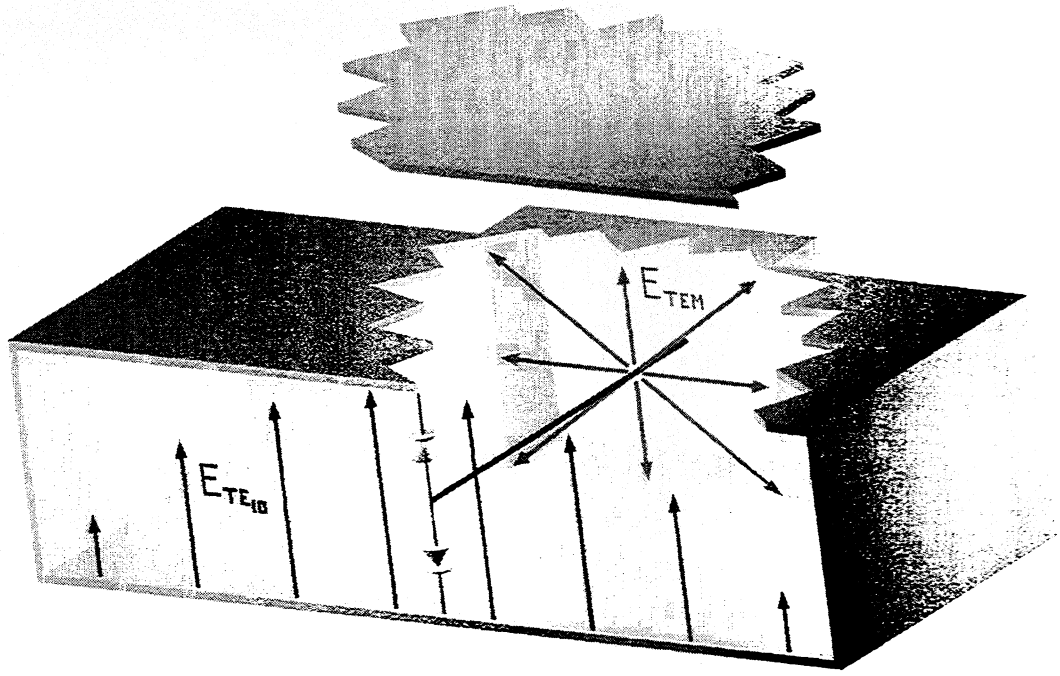

Figure 2. Conceptual sketch of the input and out electric field distributions.

A sketch of the 100/200 GHz doubler is shown in Figure 3. The input waveguide (WR-10) and output waveguide (WR-5) flanges are on opposite sides of the block and are offset by 0.3 inches. An SMA connector (not shown) is provided for DC biasing of the varactor chip. The quartz circuit sits in a groove machined in the lower half of the block. The quartz circuit comprises an output embedding circuit, a probe for a microstrip-to-waveguide transition and a low-pass hammerhead filter for an external DC bias network.

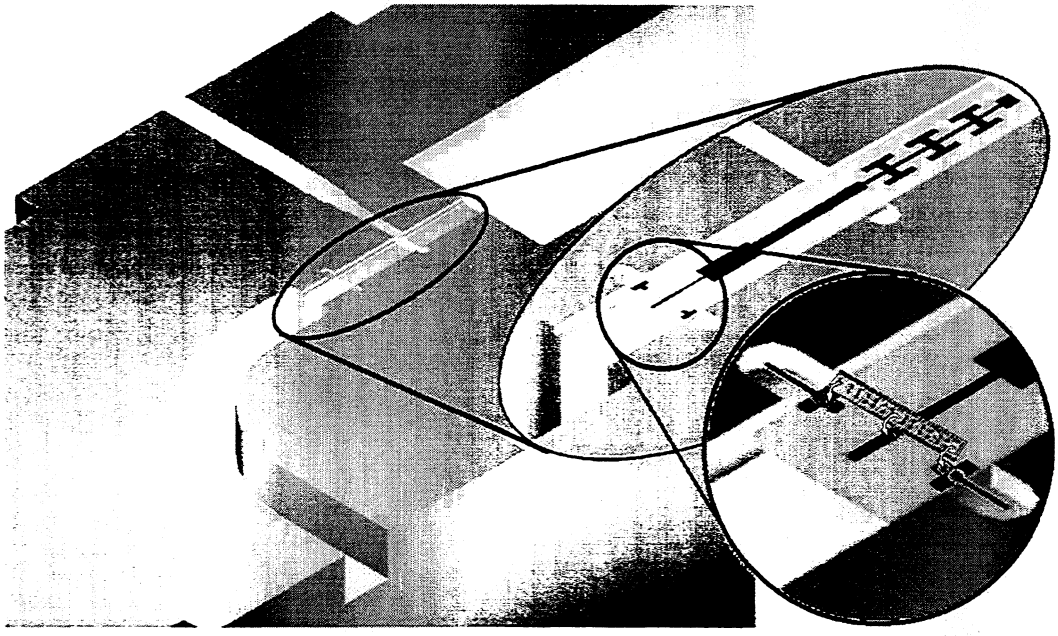

Figure 3. Sketch of the lower half of the 100/200 GHz frequency doubler block. The quartz circuit and varactor chip are shown in the magnified inserts.

The assembly process is relatively simple. First, 2 bondwires are attached to the circuit pads located at the two ends of the varactor chip and a third bondwire is attached to the large pad at the far end of the circuit beyond the hammerhead filter. The varactor chip is then soldered to 3 pads on the quartz circuit as shown in the sketch in Figure 3. The circuit is then placed in the lower half of the block, the two bondwires near the varactor chip are attached to the block and the third bondwire is attached to the center pin of the SMA connector. Finally, the two halves of the block are assembled.

EMBEDDING CIRCUIT DESIGN

The optimum embedding impedances were determined using the nonlinear analysis of Penfield and Rafuse and verified with harmonic balance simulations. The input and output embedding circuits were analyzed using Ansoft's High Frequency Structure Simulator (HFSS). Ports were attached to probes on each anode so that the individual

embedding impedances for each varactor could be monitored directly. The final HFSS simulation results are shown in the graph of Figure 4. The data for the input embedding circuit covers the frequency range from 92-106 GHz and the data for the output embedding circuit covers the frequency range from 184-212 GHz. The simulated embedding impedances are nearly optimal at the center of the bands and vary slowly with frequency. The 3 dB ouput power bandwidth of the doubler is estimated to be approximately 15 %.

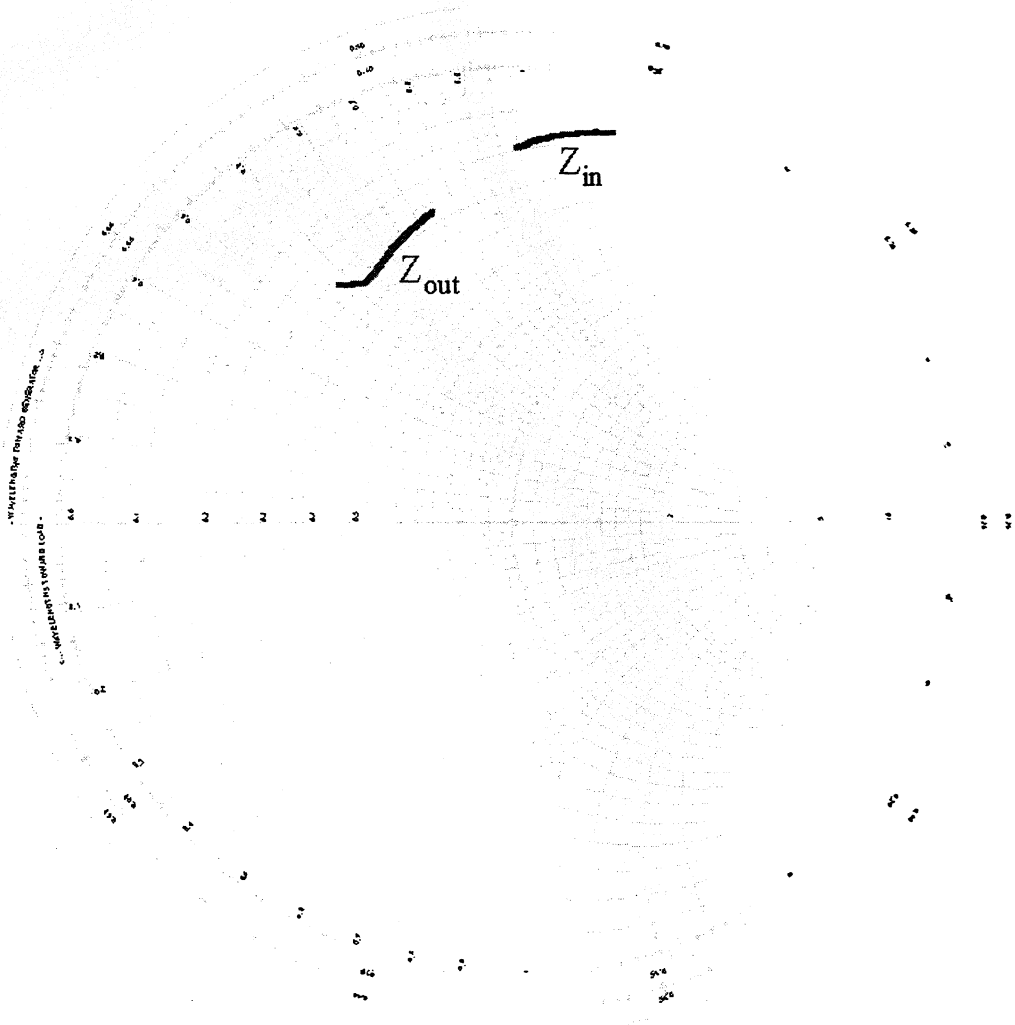

Figure 4. HFSS simulated embedding impedances.

EXPERIMENTAL RESULTS

The data shown in Figure 5 was taken at the University of Massachusetts at Amherst. Input power was provided by an IMPATT oscillator operating at 100 GHz. The varactor chip was a UVA type SB6T4 with 6.5 μm diameter anodes. The peak output power is approximately 36 mW and the corresponding efficiency is 15 %. The data was taken with the DC path open circuited so that the varactor chip was self-biased and the DC current was zero. For an available input power of 200 mW, the reflected input power was measured to be 33 mW.

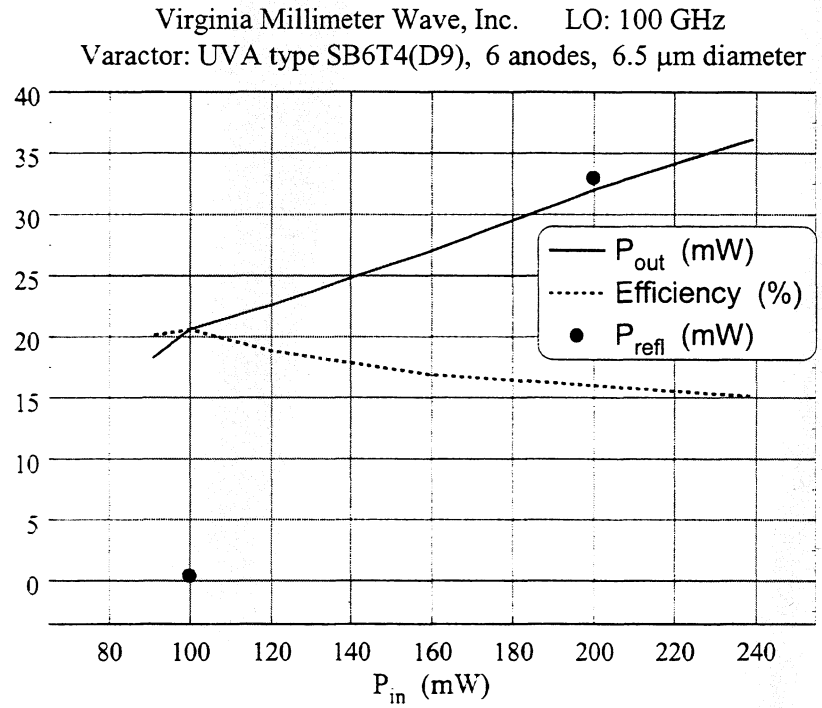

Figure 5. Measured data for the SB6T4 varactor.

Figure 6 shows measured output power and efficiency at 92/184 GHz and 100/200 GHz using a UVA type SB7T5 varactor with 7 μm diameter anodes. The data at 100/200 GHz was taken at the University of Massachusetts at Amherst using an IMPATT oscillator at 100 GHz to pump the doubler. The data at 92/184 GHz was taken at the Jet Propulsion Lab using a YIG oscillator and MMIC amplifier at 92 GHz to pump the doubler. The peak output power at 92/184 GHz was 24 mW with an input power of 148 mW and an efficiency of 17 %. The peak output power at 200 GHz was 23.5 mW with an input

power of 250 mW and an efficiency of approximately 10 %. The reflected input power for the 100/200 GHz data was measured at several points and found to be approximately 20-25 % of the available input power for pump powers above 180 mW. Peak efficiency was achieved at all points with a DC current of almost zero, indicating that the doubler was operating in an almost purely varactor mode.

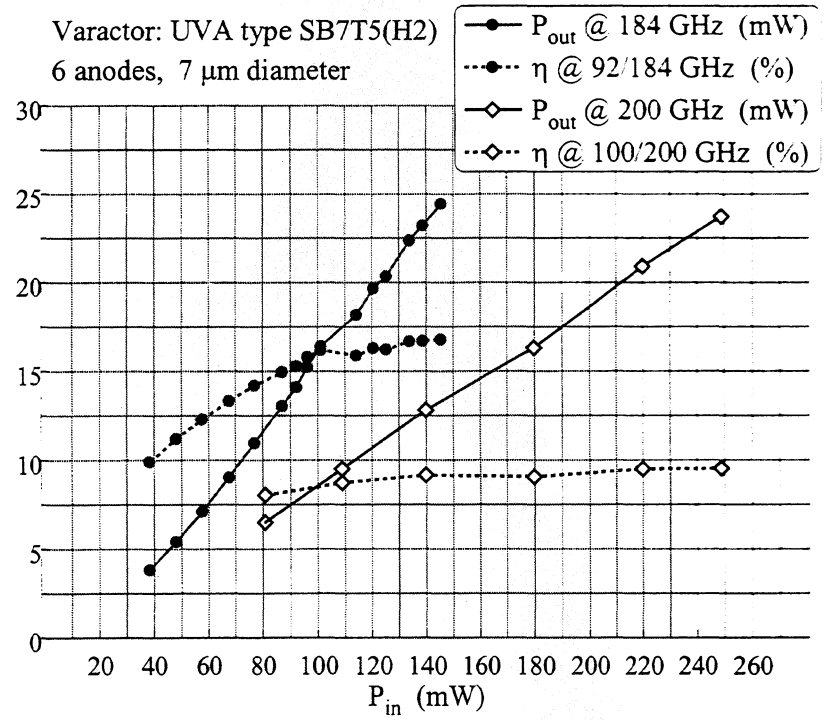

Figure 6. Measured data for the UVA type SB7T5 varactor.

The data shown in Figure 7 was taken at the University of Virginia Far-Infrared Receiver Lab in Charlottesville. Input power was provided by a commercially available Gunn effect oscillator operating over the band from 85-105 GHz. Input power levels from the Gunn ranged from a low of 35 mW at 90 GHz to a high of 95 mW at 103 GHz. The Gunn was used to drive 3 different varactor chips mounted in 3 separate blocks. The embedding circuits were identical except for small perturbations in the varactor chip and quartz circuit alignment.

Peak output power ranged from 6 mW for the SB7T5 (7 μm anodes) to 8 mW for the SB6T3 (6 μm anodes). The peak output power occurred at 96/192 GHz for all 3 varactor chips. The measured 3 dB bandwidth was approximately 9 % for the 7 μm anodes, 10 % for the 6.5 μm anodes, and 15 % for the 6 μm anodes. All 3 chips were under-pumped and thus the efficiencies were less than optimal. The increase in bandwidth for smaller anode varactors is attributable to the fact that the smaller anode varactor requires less pump power and therefore operates at higher efficiency across the band.

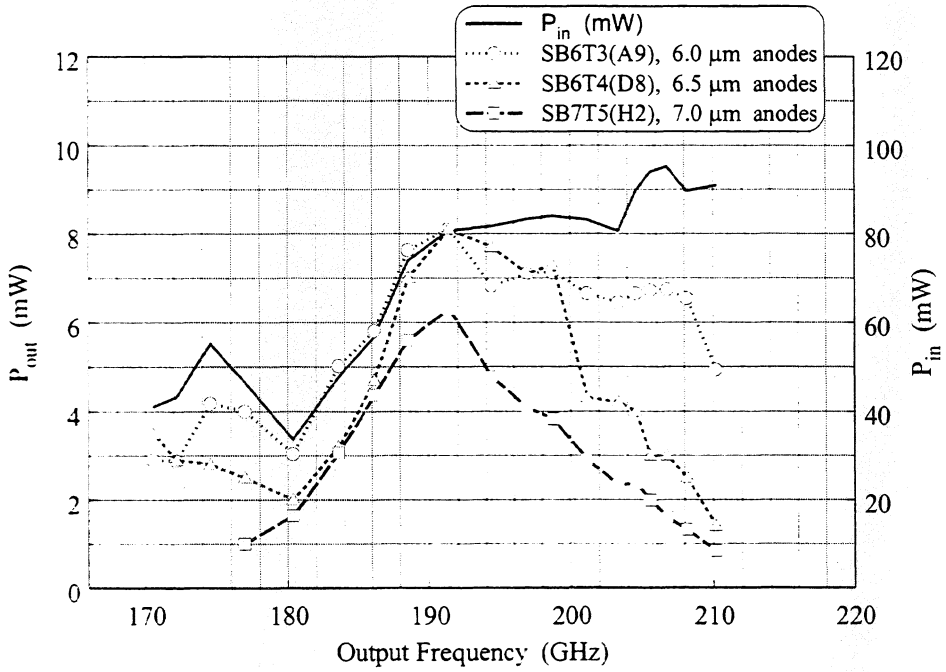

Figure 7. Measured data for 3 different varactor chips pumped with a commercially available Gunn effect oscillator.

CONCLUSION

A 100 200 GHz frequency doubler was designed and tested. The nonlinear device is a GaAs planar Schottky barrier varactor chip fabricated at the University of Virginia. The embedding circuit comprises a quartz circuit housed in a split waveguide block. The high power and large bandwidth requirements of ESA's FIRST project were the determining

factors in the design of the 100/200 GHz doubler. For optimal efficiency, the doubler requires 170 mW pump power across the band from 92-106 GHz. The source for this input drive is proposed to be a MMIC amplifier currently under development at the Jet Propulsion Lab. Since the amplifier was unavailable at the time of this report, it was impossible to fully test the multiplier. However, other high power sources were found at 92 GHz and 100 GHz and these sources were used to partially test the device.

The peak measured output power was 36 mW at 200 GHz with an input power of almost 250 mW provided by an IMPATT oscillator at 100 GHz. The peak measured output power at 184 GHz was 24 mW with an input power of 148 mW from a MMIC amplifier and YIG oscillator operating at 92 GHz. The corresponding peak efficiency was 17 %. The bandwidth was found to be approximately 15 % at drive levels below 100 mW.

There are some known problems with the current implementation of the 100/200 GHz doubler. A 20 % machine error was found in the location of the TE_{10} backshort. This error was repeated in all four manufactured blocks and was the result of an error in the CNC code. The error in the code has been fixed and new blocks will be fabricated. There were also 2 errors in the artwork for the quartz circuit. Both errors have been corrected and new photomasks have been produced. A new batch of quartz circuits will be fabricated in the coming months.

ACKNOWLEDGEMENTS

I would like to thank Dr. Imran Mehdi of the Jet Propulsion Lab, Dr. Thomas Crowe of the University of Virginia, and Dr. Neal Erickson of the University of Massachusetts for their support of this work.

REFERENCES

[1] N. Erickson, "High Efficiency Submillimeter Frequency Multipliers," IEEE/MTT-S Int. Microwave Symp. Dig., pp. 1301-1304, 1990.

[2] N. Erickson, B. Rizzi, T. Crowe, "A High Power Doubler for 174 GHz Using a Planar Diode Array," Proc. 4th Int. Space THz Tech. Symp., pp. 287-296, March 1993.

[3] P. Koh, W. Peatman, T. Crowe, N. Erickson, "Novel Planar Varactor Diodes," Proc. 7th Int. Space THz Tech. Symp., pp. 143-156, May 1994.

[4] D. Porterfield, T. Crowe, R. Bradley, N. Erickson, "A High-Power, Fixed-Tuned, Millimeter-Wave Balanced Frequency Doubler," to be published in IEEE Trans. Microwave Theory Tech., Vol. 47, No. 4, April 1999.

[5] D. Porterfield, T. Crowe, R. Bradley, N. Erickson, "An 80/160 GHz Broadband, Fixed-Tuned Balanced Frequency Doubler," 1998 MTT-S Symp. Dig., Vol. 2, pp. 391-394.

PROGRESS IN PLANAR DIODE BALANCED DOUBLERS

N.R. Erickson
Dept. of Physics and Astronomy
University of Massachusetts
Amherst, MA 01003

T.W. Crowe and W.L. Bishop
Dept. of Electrical Engineering.
University of Virginia
Charlottesville, VA 22904

R.P. Smith and S.C. Martin
Jet Propulsion Lab
4800 Oak Grove
Pasadena, CA 91109

Abstract

New developments in higher performance planar diode balanced doublers are reported. These include higher output power, higher efficiency, wider bandwidth, and simpler, more reliable construction. An output power of 80 mW was produced at 140 GHz using a new planar diode array designed to handle very high power. An efficiency of 25% was achieved at 270 GHz with 14 mW output. A wideband doubler has been designed which is extremely simple and easy to assemble, using a new planar diode with on-chip matching. All of these new designs are mechanically improved and should survive cooling to 80K. On those devices where tests have been made, the efficiency at 80 K improves by 30-36% relative to the room temperature value.

Introduction

In work reported last year [1], a wideband fixed-tuned balanced doubler was described using planar diodes with typically 26% efficiency over the band 130-165 GHz. This doubler used an array of four diodes and worked best at 120 mW input power. In this new work, the same basic doubler circuit has been duplicated and improved in a number of ways. A new six diode array has been used in the doubler, and while not tested over any bandwidth, has produced a record high power. A similar circuit has been used with a four diode array in the 270-340 GHz band and works well, with very high efficiencies at 270 and 330 GHz. A cascaded pair of these doublers has been tested over a 5% bandwidth with good results. The general layout of a planar balanced doubler is shown in Figure 1.

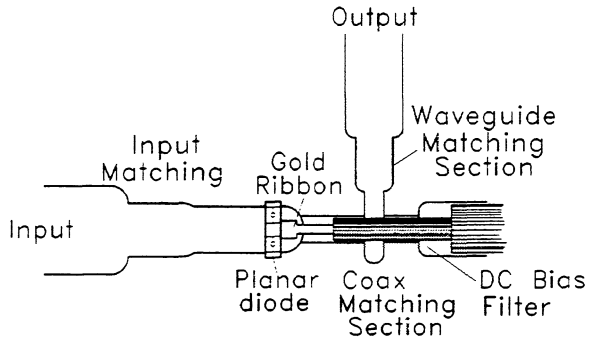

Figure 1. Balanced doubler using planar diode array, in a generic form. This circuit shows the essential elements and does not represent any real circuit.

These circuits are now more easily and reliably assembled using wire bonding techniques and higher temperature solder. This enables them to work at high power levels, where diode heating is a problem, without degadation. This assembly also reduces the strain on the diode at low temperature extremes. A 280 GHz planar diode doubler is being built for long duration space flight use in the Microwave Instrument for the Rosetta Orbiter (MIRO), a mission to a comet.

A doubler circuit has been designed using a new planar diode layout, which incorporates output impedance matching into the diode itself. As a result the circuit is simpler and more readily assembled, and is predicted to work better, with very flat efficiency over a 20% band.

Improved methods of assembly

Early versions of these planar diode doublers followed closely upon their whisker contacted predecessors, using coaxial pins connecting the center pad of the diode to the output circuit. This makes it easy to produce a wide range of impedances but leads to a type of construction in which three solder joints must be completed at once. It is very difficult to be sure that all points are really soldered properly. In addition the rather stiff center pin is strong enough to break the diodes if it flexes, and this usually happens to some extent in cooling to 80K. This method of construction has been improved in some designs by replacing the coaxial circuit with a quartz substrate microstrip circuit, [2,3] which reduces the strain but still presents some assembly difficulties. Present designs use a thin ribbon to connect to the diode so that strain is not a problem. In addition, it is easy to thermo-compression bond this wire to the diode if a pure gold ribbon is used, and this eliminates the potential problem with one solder joint. These solder joints can be a problem as was seen on one doubler that failed after being driven at 250mW for three days. The solder joints were found to be severely degraded, apparently because the diodes ran so hot that the indium solders used either oxidized or melted. After experiencing the high power failure, subsequent doublers have been built with bonded ribbons and a higher melting temperature solder (MP 149C) between the diode and the waveguide wall.

High power diodes

In an effort to build a diode able to handle very high power, a six anode diode was designed for use in the 150 GHz range. The diode was intended as a replacement for the existing four anode diode, in a chip with the same overall length. A combination of impedance matching and moding concerns makes it essential that the waveguide height used with these diodes not be too large, and the 0.66 mm height used with the existing diodes is about as large as is believed optimal for this frequency band. Design of such a diode is not as easy as for four anode devices because the space available for the diodes becomes smaller and the parasitic elements more important. This design was also intended to improve the impedance matching to the diode over a wide band. The simplest design, with 6 anodes spaced nearly evenly across the waveguide, showed serious problems

because the input power divided unevenly between the diodes, while the output coupling showed even larger variations. The cure for this problem is to space the diodes much more closely, since the parasitics depend on their location within the waveguide, and also to space the diodes unevenly. The general approach to the design was to place all of the diodes near the waveguide wall, where it would be easier to heatsink them, and then to adjust the spacing until all diodes coupled equally to the external circuit. This results in very little space for the ohmic contact pads and special problems in the fabrication of the diodes.

The method of design was to simulate the circuit of the input waveguide (split in half due to symmetry) in HFSS [4] with an input waveguide port, an output TEM port, and 3 diode ports, and to attempt to achieve a uniform impedance environment for the three diode ports. Simulations were performed for both the input and output frequencies. Testing the design required terminating the diode ports in this simulation with actual varactor impedances and determining how uniformly the power split to the ports. These impedances were determined using a nonlinear simulator to optimize a single diode circuit at the expected drive level [5]. It is important to not compare the S parameters into 50 Ω. 50Ω comparisons can be very misleading since the diodes are so reactive, and the port power balance is very sensitive to capacitance. In general these simulations showed that the output frequency presents the most difficult problem, and that the variation in power becomes worse with increasing frequency. There is no really perfect solution, but a power imbalance of 0.5 dB is certainly not serious, and simulations seem to indicate that even a 1 dB imbalance has no major consequences. The one thing that is difficult to simulate is the division of bias voltage across the diodes when the circuit impedances are not matched. All simulations assumed equal bias voltage on each anode. The final design uses a relatively long contact finger to the first diode on each side, with this finger length decreasing for the second diode and even more for the third. The remaining space to the center pad is taken up with a high impedance line to add as much inductance as possible.

This diode was originally laid out for fabrication at JPL, where the diode process is able to make almost exactly the designed shape. However, the diodes made at JPL had relatively poor properties, and while they worked in the doubler and could handle high power, the efficiency was only 23%. The design was not so compatible with the UVa process, because the finger length for the innermost diode is too short for the UVa surface channel etch process, and also because the optimized ohmic pad sizes are too small as well. Therefore, the diode that eventually was produced was not exactly the optimized design, but was believed to be close enough to try out the idea. These diode layouts are shown in Figure 2.

The diodes were successfully processed at UVa (batch SB8T1), but no DC parameters were available since the measured R_s is too strongly influenced by heating effects. The diodes were installed into the wideband doubler designed for a 4 anode

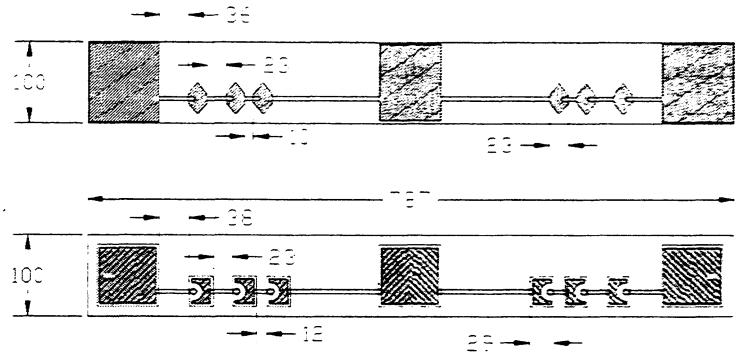

Figure 2. Six anode diode designed for optimum use in the 140-170 GHz band (top), and the diode made at UVa as a compromise to utilize their fabrication process (bottom). Dimensions are in μm.

chip [1], since no doubler designed for these new diodes was available. The doubler was tested at input frequencies between 70 and 85 GHz using high power IMPATT sources. The best performance in terms of circuit matching was seen at 70 GHz. At this frequency the input reflection was about 20%, while the source power was nearly 300 mW, so delivering sufficient power to drive the input was not a problem. The output match was optimized with a single Teflon quarter wave transformer in the output waveguide. The diode was installed into the circuit by bonding a gold ribbon to the diode center pad, and then soldering the diode outer pads to the waveguide walls with Indalloy #2 solder (MP 149C). The diode survived the full 300 mW input power available, with nearly 250 mW actually absorbed by the diode. The output power at this drive was 80 mW, and this power level was sustained for a period of 1 day. In this time the diode IV curve changed slightly, but showed no signs of leakage, which normally occurs if a diode is seriously overdriven. At a lower power of 210 mW absorbed, and 70 mW output, the test was carried out for 1 week, so it appears that this is a safe operating power. The peak efficiency occurs at 150 mW absorbed power, where the efficiency, corrected for input mismatch, is 35%. This efficiency is typical of that of other good diodes produced at UVa, and tested at similar frequencies, although somewhat lower than the best (40%). Therefore, it seems that the power combining in the three series diodes is fairly efficient, and that the fabrication compromises are not too serious. However, all of the problems are expected to become worse at the higher end of the design band near 170 GHz, and no tests have been done here since the diode matches the existing circuit so poorly. This doubler was tested at ~80 K with only 215 mW input power (196 mW absorbed) due to the loss of the stainless steel waveguide required to thermally isolate it from the room temperature source. At room temperature before cooling the output power was 64 mW, while the cold output power was 85mW, an increase of 33%. The cold efficiency (corrected for input mismatch) is 43%.

High efficiency doublers for 270-340 GHz

A similar doubler for twice this frequency has also been completed, using four anode diodes. This more conservative design requires tuning the output backshort in order to cover the full 270-340 GHz band, but the bandwidth is ~20 GHz with fixed tuning. It also uses a 2 mil wide gold ribbon for strain relief in the connection between the planar diode and the output waveguide. At room temperature the efficiencies achieved with this doubler are much better than with the previous model [6]. The best results at 270 GHz are 14 mW output at an efficiency >25% using a diode fabricated at JPL, and at 330 GHz, 7.0 mW output at an efficiency of 18% using a UVa diode. It works well at 80K, with an efficiency improvement (using the JPL diode) of 35% relative to the room temperature value. The bandwidth of this doubler is not optimized for fixed tuning but shows the potential for wideband operation. Figure 3 shows the power output with a Gunn oscillator pump (without an isolator between the Gunn and doubler) over a moderate band. In this test, a Teflon tuner was added in the input waveguide very close to the diode to improve the match. While there is a lot of power ripple due to the interaction with the Gunn, the power at the peaks of the ripple is large and the bandwidth is broad enough to be quite useful. Presumably the ripple would go away with an isolator in the circuit, but this was not attempted because the doubler works best at the highest input power available (~50 mW), and the loss of the present isolators drops the power to a sub-optimal level.

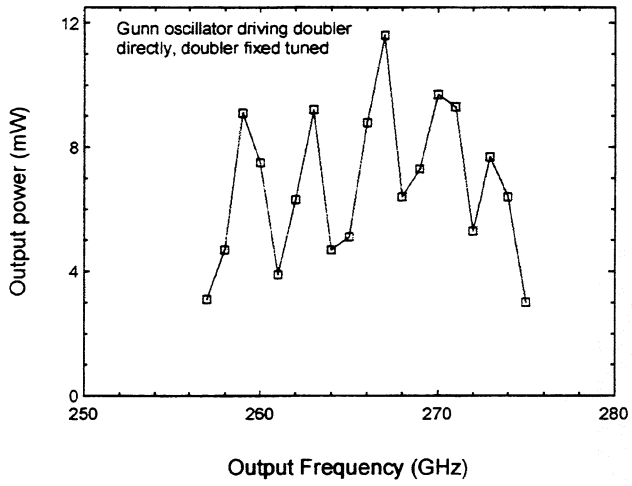

Figure 3. Output power from doubler and Gunn with no isolator, and fixed doubler tuning. The power ripple is due to the interaction between the Gunn oscillator and the doubler input match.

We have cascaded two of these doublers to produce a 330 GHz source. This source produced a peak power of 7.0 mW, and a minimum power of 5 mW over a band of 325-335 GHz, with an input power of 130 mW, all at room temperature. The diodes in both doublers were from UVa (batches SC6T6 and SB3T2). Figure 4 shows the performance measured over an extended band using higher input power at some of the

extreme points. Despite the lack of an isolator between doublers, there is little ripple in the output power over most of the band, showing that over a limited band, doublers can be matched quite well. However, this is much more difficult over a wider band.

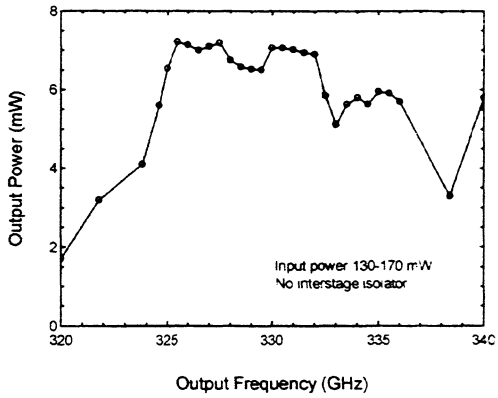

Figure 4. Cascaded doubler performance at room temperature with mechanical tuning fixed. No isolator was used between the doublers. The match between stages is good enough over the midband that the power ripple is minimal.

Wideband doubler using improved diode layout

To make the assembly of these doublers easier, we have designed a new set of planar doubler diodes intended for use near 280 GHz. These incorporate on-chip wideband matching to optimally couple into a circuit having relatively high impedance. This potentially eliminates the need for any microstrip circuit, since the output circuit can be just a gold ribbon connecting to the output waveguide. The starting point for this work was the diode mask designed at UMass a few years ago and fabricated at UVa as the successful batch SB3T2. This layout produces a fairly serious power imbalance at frequencies above 300 GHz, and requires that the first section of the output matching circuit have a low impedance for matching over a wide band. The low impedance line is needed to add capacitance to the output to compensate for the excess inductance in the diode. Reducing the diode inductance is not practical because the input matching depends on a large inductance.

It was found that simply adding some metal area to the diode center pad is all that is required to eliminate the low impedance line, but the method of adding this area is critical because it seriously affects the parasitics for the individual diodes. In particular, adding metal which closely approaches the small midpad in the diode pair causes the inner diode's parasitics to increase, so a pad was developed which flares out as a trapezoid as it leaves the critical region. In addition, the other side of the pad was also enlarged slightly. In principle, even more capacitance may be added as a stub line on this side, but it was not found to work well in practice. The final layout is shown in Figure 5.

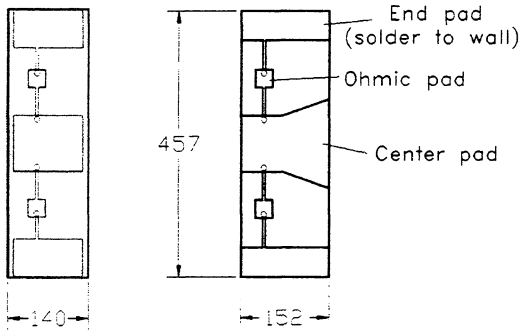

Figure 5. Original SB3T2 diode layout (left) and the new design with better output matching. Diode locations are shown by small circles. Dimensions are in μm.

All of this design was done with the assumption of a GaAs thickness of 37 μm. This thickness makes it easy to handle the diodes and appears to have only a minor effect on the circuit bandwidth. The dominant effect of varying substrate thickness is to change the optimum capacitance of the diode for a given circuit design. If diodes are made in a few capacitance values it should be possible to correct for errors in thickness, or vice versa. With the added area, the diode power match was not seriously affected, and in fact the outer diode was still found to have the larger parasitic capacitance so its outer pad was moved out to the very edge of the waveguide. All of this design work was done in much the same way as for the six anode diode described above, while investigating the diode match into a nearly ideal circuit. No full circuit optimization is practical, due to its complexity, until one arrives at a final diode design.

After the diode was designed, the optimized output impedance was quite high, and best coupled as directly as possible into waveguide, which is better suited for high impedance circuits than TEM media. This was facilitated by the optimized input circuit, which favored placing the diode extremely close to the waveguide backwall. The required connecting wire turned out to be quite short, only slightly longer than that required to extend from the diode to the far wall of half height output waveguide. Thus this wire becomes more of an interconnection than a circuit element. The output waveguide circuit was optimized and a two section step transformer to full height was placed at an optimized distance from the transition. The final circuit was quite simple, yet the predicted output match shows a 14 dB return loss over an 18% bandwidth. Bias to the diode is still required, but without the need for any other circuitry, the bias may be decoupled from the output by bonding the ribbon to a capacitor at the far wall of the waveguide. The circuit is shown in Figure 6.

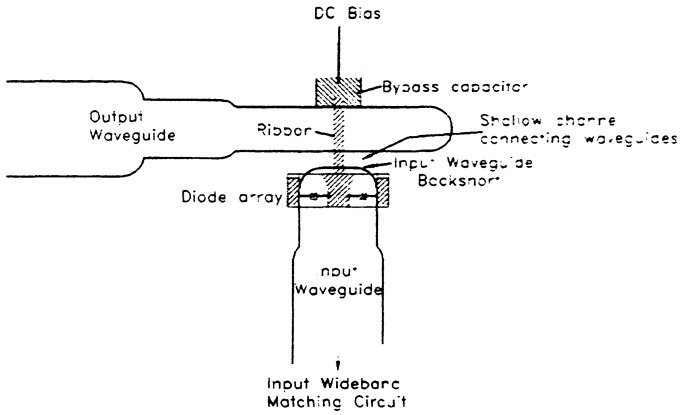

Figure 6. Cross section of planar diode doubler using a new diode incorporating output matching into the diode itself. The diode is shown with a transparent substrate in order to show hidden details. Input matching waveguide sections are not shown. This circuit operates from 250-300 GHz with fixed tuning.

The input circuit is always the more difficult to match because the diode Q is higher, but it is also entirely a waveguide circuit so assembly is not an issue in the design. The only constraints are that the TM11 mode at the output frequency be suppressed for a sufficient distance from the diode, and that the various waveguide sections be machinable. The final design is somewhat odd looking, with a section of greater than full height waveguide used as a half wave resonator for broadbanding, but it is quite simple to machine. The predicted input match is a return loss of 10-11 dB across the same band (assuming a perfect output match), which is about as good as seems possible. The complete circuit was then simulated in HFSS to produce a full set of S parameters for all of the real circuit elements, and these were then modeled in HP-MDS with a realistic nonlinear diode model, to predict the full performance. This prediction is shown in Figure 7a, which is done at a constant input power and bias voltage across the band. This prediction may be compared to the upper curve, which is the best possible efficiency for the same diode in an ideal circuit under the same conditions. This shows that the design process works well, and that nonlinear simulation is not required except as a verification of performance. The simplicity of the final circuit makes it suitable for frequencies up to 450 GHz, by using a frequency scaled version of the diode, and a set of appropriately scaled diodes have been fabricated at JPL. Since the circuit is very compact and fully planar, it appears suitable for further integration, placing the bond ribbon and bypass capacitor onto a single substrate with the diodes. With this level of integration, and beam leads for grounding, such a design should be workable up to 1 THz.

Despite the apparently good match to the external circuit, this doubler is still quite sensitive to input and output mismatch, and a VSWR of as little as 2:1 causes serious ripple in the efficiency as shown in Figure 7b. This simulation is done with a 2:1 VSWR

mismatch on the input and output separately, with the mismatch as close to the input and output as possible. While the ripple due to the output VSWR is about what is expected for a linear circuit, the input is much more severe. This large effect occurs in part because of the nonlinearity of the circuit, which causes the output power to decrease more rapidly than the input power. Also the input match (as simulated with a perfectly matched output) becomes a poorer match in the presence of the real output circuit. This interaction is similar to that expected in the cascade of two doubler stages, and demonstrates that these circuits will never be well suited for system use without isolators between stages if reasonably flat output power is required. This limitation may be overcome by reducing the bandwidth, but probably a severe reduction is necessary for cascading with acceptably flat power.

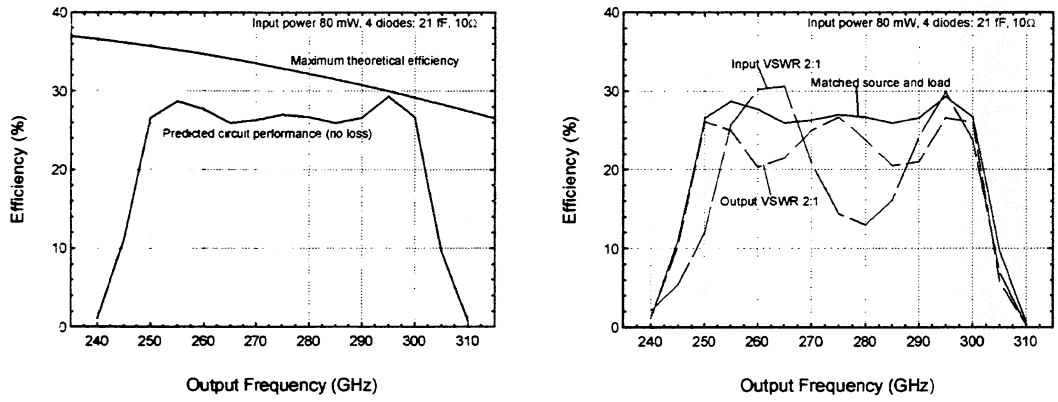

Figure 7. (a) Predicted performance of wideband planar diode doubler at fixed input power and bias. Upper curve is the efficiency of the same diode in an ideal optimized circuit.
(b) Effect of input and output mismatch on the doubler of (a). A VSWR of 2:1 was simulated on the input and output separately.

Conclusions

We have reported on several new developments in balanced doublers using planar diodes. These include 80 mW output power using a six diode array at 140 GHz, 25% efficiency at 270 GHz and a wideband high efficiency doubler using an improved diode design. Circuits are now more reliable for operation at sustained high power levels. All of the new doublers work well at cryogenic temperatures, with increased efficiency over the room temperature value. We have also pointed out some limitations on wideband matching of these circuits. All of these developments and others are making this a very versatile doubler for applications from 140-450 GHz, and in the future this circuit may be pushed up to near 1 THz. The performance exceeds that possible with whisker contacts, and is far easier to assemble. The newest design is sufficiently compact that a fully integrated diode with output matching circuit seems practical.

References

[1] "Wideband High Efficiency Planar Diode Doublers," N.R. Erickson, *Ninth International Symposium on Space Terahertz Technology*, pp. 473-480, Mar. 98

[2] "An 80/160 GHz Broadband, Fixed-tuned, Balanced Frequency Doubler," D.W. Porterfield, T.W. Crowe, R.F. Bradley and N.R. Erickson, *IEEE 1998 Int'l Microwave Symposium*, Baltimore.

[3] "A High Power Fixed-Tuned MM-Wave Balanced Frequency Doubler," D.W. Porterfield, T.W. Crowe, R.F. Bradley and N.R. Erickson, to be published in *IEEE Trans. Microwave Theory and Tech., May 99.*

[4] High Frequency Structure Simulator, Ansoft Corp.and Hewlett Packard Corp.

[5] "Wideband Fixed-Tuned Millimeter and Submillimeter-Wave Frequency Multipliers," N.R. Erickson, *Eighth International Symposium on Space Terahertz Technology*, pp. 137-148, March 97.

[6] "Novel Planar Varactor Diodes," P.J. Koh, W.C.B. Peatman, T.W. Crowe and N.R. Erickson, *Proceedings of the Seventh Int'l. Symposium on Space Terahertz Tech.*, pp. 143-156, 1996.

IMPROVED DIODE GEOMETRY FOR PLANAR HETEROSTRUCTURE BARRIER VARACTORS

Jan Stake[1], Chris Mann[2], Lars Dillner[1], Mattias Ingvarson[1], Stephen H. Jones[3], Stein Hollung[1], Henini Mohamed[4], Byron Alderman[4], Martyn Chamberlain[4], and Erik Kollberg[1]
[1]Chalmers University of Technology, SE-412 96 Göteborg, Sweden
[2]Rutherford Appleton Laboratory, Chilton, Oxon, UK
[3]Virginia Semiconductor, Inc., Fredericksburg VA 22401, USA
[4]School of Physics and Astronomy, University of Nottingham, Nottingham NG7 2RD, UK
Email: stake@ep.chalmers.se

***Abstract*—We report state-of-the-art performance of tripler efficiency and output power for a new design of AlGaAs-based heterostructure barrier varactor diodes. The new diodes were designed for reduced thermal resistance and series resistance. An efficiency of 4.8% and a maximum output power of 4 mW was achieved at an output frequency of 246 GHz.**

***Index Terms*—HBV, varactor frequency tripler, self-heating.**

I. INTRODUCTION

Recent progress in planar Heterostructure Barrier Varactor (HBV) design [1], has given performance comparable to Schottky varactor diodes at output frequencies below 400 GHz. The first planar HBVs were fabricated with a non-optimal diode geometry with high thermal resistance (~2 K/mW) [2] as well as high conduction current due to a low barrier height (0.17 eV). Consequently, self-heating of these HBVs [3], resulted in an increased conduction current as the temperature increased, and hence, reduced multiplier efficiency. As thermionic emission dominates the electron transport across the barrier region of standard $Al_{0.7}GaAs/GaAs$ HBVs, lattice matched InP material systems have been used to significantly reduce the conduction current in these devices [4]. However, to grow many stacked barriers and very thick epitaxial layers in an InP material system is difficult and expensive. Furthermore, the conversion efficiency critically depends on the parasitic series resistance which generally increases with temperature. The effect of current saturation is also increased with temperature due to a lower maximum electron velocity [5, 6]. A GaAs system is cheaper and is easier to process.

In this paper, we present a new batch of $Al_{0.7}GaAs/GaAs$ HBV (CTH-NU2003) diodes. The new diodes were designed for reduced thermal resistance and parasitic resistance. Experimental tripler results for the new design (hbv-3a) show state-of-the-art performance for $Al_{0.7}GaAs/GaAs$ based HBVs.

II. THE DEVICE

A. Fabrication

The $Al_{0.7}GaAs/GaAs$ epitaxial structure (NU2003), MBE grown on semi-insulating GaAs substrate by the University of Nottingham, consists of two barriers, and an n^{++} $InAs/In_{1.0-0.0}Ga_{0.0-1.0}As/GaAs$ epitaxial capping layer to improve the specific contact resistance of the resulting ohmic contacts (see Table I). This material design is similar to the UVA-NRL-1174 HBV material [2]. The measured I-V and C-V characteristic are shown in Figure 1. Simple test structures were fabricated and the measured I-V and C-V characteristics are consistent with the results from the UVA-NRL-1174 material. A back-to-back geometry, shown in Figure 2, has been utilised to double the number of barriers and to compensate for any asymmetries. The HBVs were fabricated using standard photolithography techniques for isolation and ohmic contact patterning, Cl-based reactive ion beam etching for anode definition, and wet etching for the mesa/pad isolation [2]. The surface channel was planarised prior to airbridge formation using a low-viscosity thermosetting epoxy and a planarising superstrate [2, 7]. The fingers were Au-electroplated to a thickness of ~4 μm. Special attention was given to the ohmic contact formation and the anode isolation etch, since these steps affect the series resistance, and thus the tripler performance, drastically. The Au/Ge/Au/Ni/Au ohmic metallic scheme [8] was alloyed for one minute at 400°C. The resulting specific contact resistance is less than 50 $\Omega\mu m^2$. The HBVs were diced into individual chips with the overall dimensions of 20 x 150 x 60 μm^3.

TABLE I: NU2003 LAYER STRUCTURE

Material	Doping [cm^{-3}]	Thickness [Å]
InAs	1×10^{19}	100
$In_{1\rightarrow0}GaAs$	1×10^{19}	400
GaAs	1×10^{19}	3000
GaAs	8×10^{16}	2500
GaAs	Undoped	35
$Al_{0.7}GaAs$	Undoped	200
GaAs	Undoped	35
GaAs	8×10^{16}	5000
GaAs	Undoped	35
$Al_{0.7}GaAs$	Undoped	200
GaAs	Undoped	35
GaAs	8×10^{16}	2500
GaAs	1×10^{19}	40000
GaAs	SI	-

B. Parasitic resistances analysis

The new planar HBV design incorporates a shorter finger with a larger cross section area, mainly to reduce the thermal resistance of the diode. Changing the anodes from an almost circular to a rectangular shape will both reduce the thermal resistance and the spreading resistance between the anodes. Furthermore, reducing the distance between the anodes from 5 μm (hbv-o) to 3 μm (hbv-3a) will also reduce the series resistance.

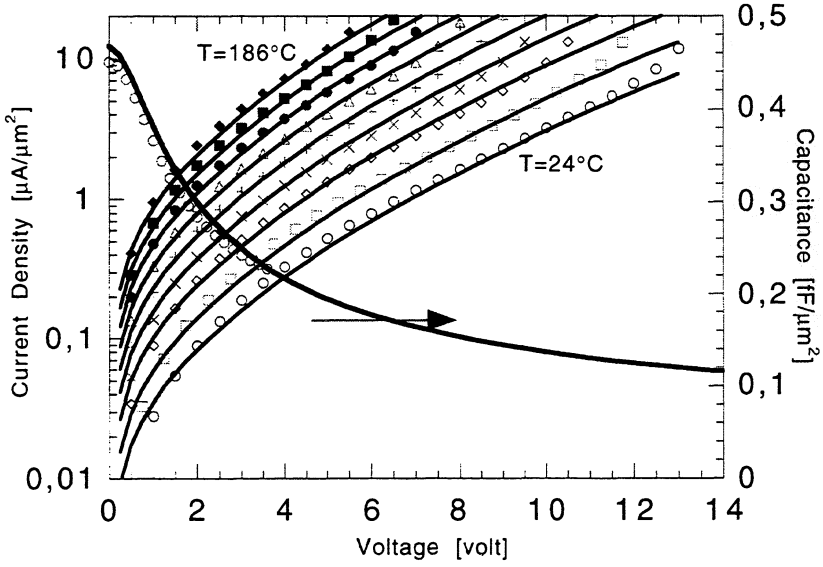

Figure 1: Measured I-V and C-V characteristics (UVA-NRL-1174 material).

The parasitic series resistance is the sum of the resistance of the undepleted active layers, the spreading resistance, and the ohmic contact resistance. All these resistive elements have different temperature dependence. In general, it is difficult to determine the series resistance of HBVs or back-to-back Schottky varactor diodes from DC-measurements, given the large junction resistance over the normal operating range of the device. For the HBVs described and with a specific contact resistance of ~ 50 $\Omega\mu m^2$, a room temperature series resistance of 12 Ω was estimated for hbv-o and 10 Ω for hbv-3a, see TABLE II. These values were calculated using standard expressions for contact resistance, mesa resistance and spreading resistance in the n^{++} island that connects the two diodes, as well as using impurity dependent mobility values for GaAs [9].

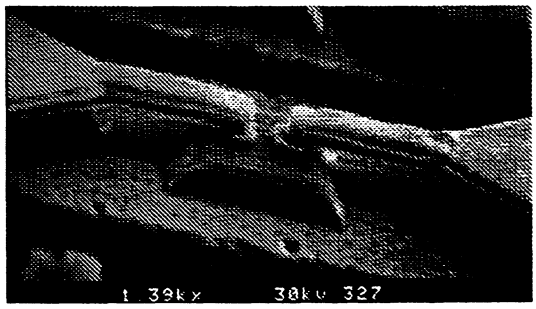

Figure 2: SEM picture of the new planar design (hbv-3a).

Assuming a point heat-source in the middle of the active region, Jones [10] has estimated the thermal resistance through the finger and the GaAs substrate to $R_t \approx 2\ K/mW$ for the old device geometry, by using a combination of analytical models and FEM-simulations. The same technique was used to estimate the thermal resistance of the new HBV diode design. The theoretical parasitic resistance and thermal resistance for the new diode design and the original planar HBV design [2] are summarised in TABLE II. Room temperature material data has been used for the calculations.

TABLE II: PARASITIC RESISTANCES

HBV / Batch	Area [μm²]	R_s [Ω]	R_t [K/mW]	Finger size [μm³]
3a / CTH-NU2003J	52	10	0,7	17x4x5
o / UVA-NRL-1174	57	12	2	50x4x4

III. TRIPLER MEASUREMENTS

The tripler block used was a Rutherford Appleton Laboratory (RAL) block (HBVII) which was designed for use with symmetric varactor diodes. Compared to a conventional varactor tripler block, there is no need for idler cavity or DC-bias line. The planar HBV chip was lapped to a thickness of about 20 μm and mounted across the output waveguide. The tripler block is equipped with two input tuners and two output tuners.

Input power was provided by a J.E. Carlstrom (H270) Gunn oscillator which can be tuned over a frequency range of 75 - 90 GHz. For the higher frequency range, 90 - 110 GHz, an ELVA BWO was used. Sufficient power was available so that an isolator, an attenuator and directional couplers could be included in the input chain to determine input and reflected power levels. Input and output powers were measured using separate Anritsu power heads and meter type ML 83A, which had previously been compared with a Thomas Keating power meter and had been found to agree to +/- 5%. In order to match the output waveguide to that of the output power head it was neces-

sary to include a waveguide transformer section. The additional loss the transformer section introduced was not corrected for.

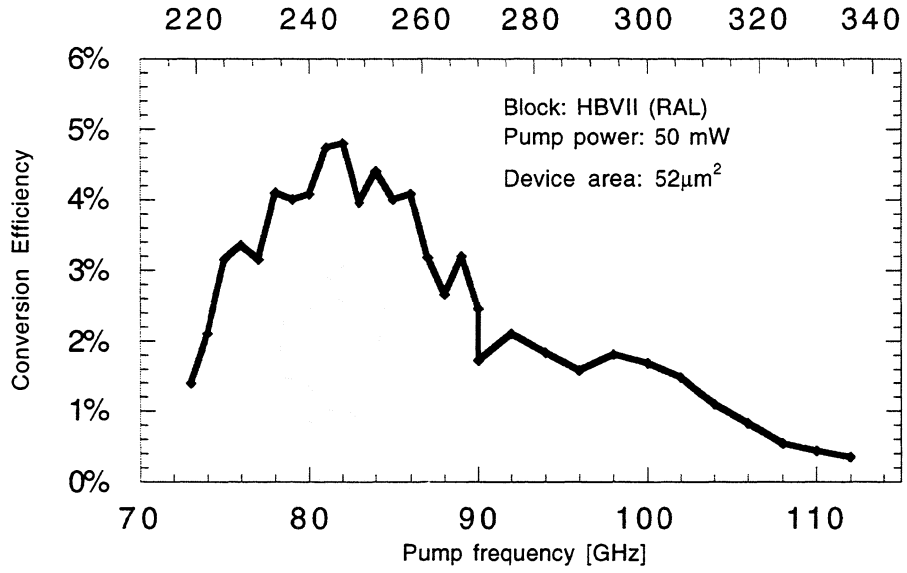

Figure 3: Conversion efficiency versus pump frequency for an input power of 50 mW (hbv-3a).

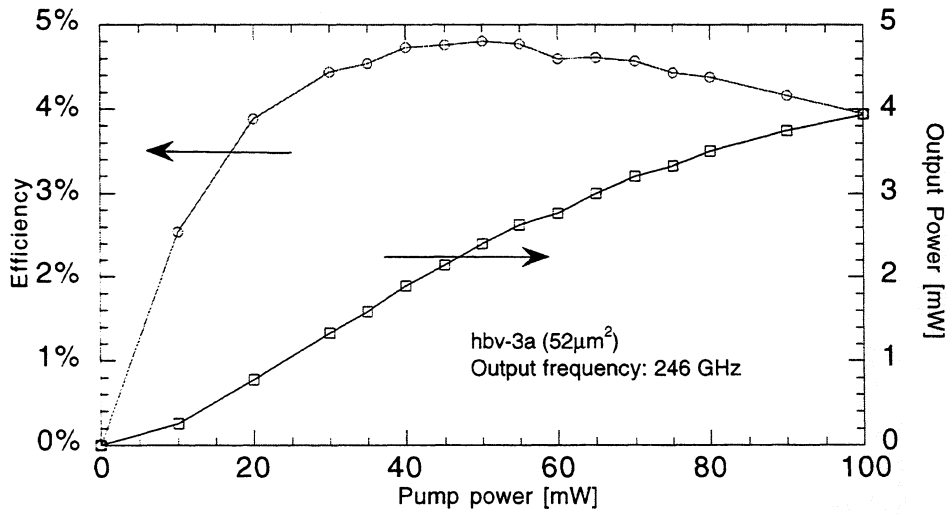

Figure 4: Output power and tripler efficiency versus pump power (hbv-3a).

IV. Results and Discussion

For an input power of 50 mW, the maximum output power was obtained at a pump frequency of 82 GHz for hbv-3a, see Figure 3. A maximum output power of 4 mW was generated at 246 GHz and a peak flange-to-flange efficiency of 4.8% was achieved at an available input power of 50 mW, see Figure 4. These results should be compared with an efficiency of 3.1 % and a maximum delivered output power of 2 mW achieved with hbv-o in TABLE II (UVA-NRL-1174-17) [3]. The improvement is expected to be due to a lower series resistance and thermal resistance.

V. Conclusions

In this paper we have reported an improved planar HBV diode geometry. The thermal resistance and series resistance have been reduced with the new design and hence the tripler efficiency has been improved. Also, the use of InGaAs spacer layers to improve the effective barrier height [11, 12], reduces the conduction current and improves the elastance modulation ratio. This should improve the overall tripler performance.

VI. Acknowledgment

The authors would like to thank Emmanuil Choumas and Göran Reivall for their support during device fabrication.

References

[1] X. Mélique, C. M. Mann, P. Mounaix, J. Thornton, O. Vanbésien, F. Mollot, and D. Lippens, "5 mW and 5 % Efficiency 216 GHz InP-based Heterostructure Barrier Varactor Tripler," *IEEE Microwave and Guided Wave Letters*, vol. 8, pp. 384-386, 1998.

[2] J. R. Jones, W. L. Bishop, S. H. Jones, and G. B. Tait, "Planar Multi-Barrier 80/240 GHz Heterostructure Barrier Varactor Triplers," *IEEE Trans. Microwave Theory Tech.*, vol. 45, pp. 512-518, 1997.

[3] J. Stake, L. Dillner, S. H. Jones, C. M. Mann, J. Thornton, J. R. Jones, W. L. Bishop, and E. L. Kollberg, "Effects of Self-Heating on Planar Heterostructure Barrier Varactor Diodes," *IEEE Trans. on Electron Devices*, vol. 45, pp. 2298-2303, 1998.

[4] E. Lheurette, P. Mounaix, P. Salzenstein, F. Mollot, and D. Lippens, "High Performance InP-based Heterostructure Barrier Varactors in Single and Stack Configuration," *Electronics Letters*, vol. 32, pp. 1417-1418, 1996.

[5] J. G. Ruch and W. Fawcett, "Temperature Dependence of the Transport Properties of Gallium Arsenide Determined by a Monte Carlo Method," *J. Appl. Phys.*, vol. 41, pp. 3843-3849, 1970.

[6] J. T. Louhi, A. V. Räisänen, and N. R. Erickson, "Cooled Schottky Varactor Frequency Multipliers at Submillimeter Wavelengths," *IEEE Trans. on Microwave Theory and Techniques*, vol. 41, pp. 565-571, 1993.

[7] W. L. Bishop, K. McKiney, R. J. Mattauch, T. W. Crowe, and G. Green, "A Novel Whiskerless Schottky Diode for Millimeter and Submillimeter Wave Applications," presented at 1987 IEEE MTT-S International Microwave Symposium Digest, Las Vegas, 1987, pp. 607-610.

[8] P. A. Verlangieri, M. Kuznetsov, and M. V. Schneider, "Low-Resistance Ohmic Contacts for Microwave and Lightwave Devices," *IEEE Microwave and Guided Wave Letters*, vol. 1, pp. 51-53, 1991.

[9] S. M. Sze, "Carrier Transport Phenomena: mobility," in *Physics of Semiconductor Devices*, 2nd ed. Singapore: JOHN WILEY & SONS, 1981, pp. 27-38.

[10] J. R. Jones, S. H. Jones, and G. B. Tait, "Self-Consistent Physics-Based Numerical Device/Harmonic-Balance Circuit Analysis of Heterostructure Barrier Varactors Including Thermal Effects," presented at Sixth International Symposium on Space Terahertz Technology, Pasadena, California, 1995, pp. 423-441.

[11] J. R. Jones, S. H. Jones, and G. B. Tait, "GaAs/InGaAs/AlGaAs Heterostructure Barrier Varactors for Frequency Tripling," presented at Fifth International Symposium on Space Terahertz Technology, Ann Arbor, Michigan, 1994, pp. 497-513.

[12] V. Duez, X. Mélique, O. Vanbésien, P. Mounaix, F. Mollot, and D. Lippens, "High capacitance ratio with GaAs/InGaAs/AlAs heterostucture quantum well-barrier varactors," *Electronic Letters*, vol. 34, pp. 1860-1861, 1998.

A 141-GHz QUASI-OPTICAL HBV DIODE FREQUENCY TRIPLER

Stein Hollung, Jan Stake, Lars Dillner and Erik Kollberg

Chalmers University of Technology
Department of Microelectronics ED
Microwave Electronics Laboratory
SE-41296 Göteborg, Sweden

Abstract — A 141-GHz quasi-optical heterostructure barrier varactor (HBV) diode frequency tripler is presented. The tripler consists of two slot antennas loaded with HBV diodes and located at the focal plane of a dielectric lens. A quasi-optical high-pass filter is used at the output to improve the conversion efficiency and act as a tuning element for the slot antennas. The tripler demonstrates an effectively isotropic radiated power (EIRP) of 2.24 W at 141 GHz with an input power of 143 mW. The corresponding radiated power is 11.5 mW and the tripler conversion efficiency is about 8%.

I. INTRODUCTION

The increasing demand for inexpensive sources for millimeter- and submillimeter-wave applications has motivated the use of solid-state devices such as varactor diodes to generate higher harmonics from less expensive low-frequency sources. Quasi-optical grid multipliers are capable of producing high output power [1]-[3], but are often inefficient due to large diffraction losses and require bulky dielectric lenses and powerful sources. Several waveguide mounted tripler circuits have been reported with good efficiency [4]-[6], but machining of these waveguide circuits can be both complicated and expensive. An integrated planar antenna multiplier can provide an inexpensive, less complicated and efficient transmitter front-end. While a variety of millimeter-wave and submillimeter-wave receivers with double-slot antennas fabricated on dielectric lenses have been presented to date [7]-[11], few transmitters have been reported.

Here we present a quasi-optical frequency tripler with four heterostructure barrier varactor (HBV) diodes soldered across two slot antennas and located at the focal plane of a dielectric lens as shown in Fig. 1. The slot antennas are fed from a WR-22 waveguide connected to a Gunn oscillator. A quasi-optical high-pass filter is used to tune the slot impedance and increase the conversion efficiency. The symmetric capacitance-voltage and asymmetric current-voltage characteristics of the HBV diodes only allows odd harmonics of the applied signal to be generated, and thus simplifies the frequency tripler design [12]-[13].

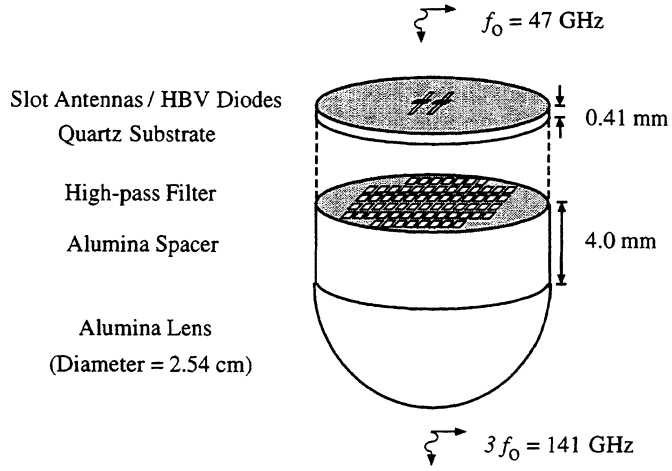

Fig.1. The quasi-optical tripler circuit consisting of two slot antennas loaded with four HBV diodes on a quartz substrate, a quasi-optical high-pass filter, an alumina spacer and a 2.54-cm diameter spherical alumina lens.

II. DESIGN

The planar four-barrier GaAs/$Al_{0.7}$GaAs HBV diodes (UVA-NRL-1174-17) [5] used for this circuit has a device area of 57 μm^2. The optimum embedding impedances at the fundamental (47 GHz) and third harmonic (141 GHz) frequency of two of these devices in parallel were found from harmonic balance simulations [13] to be 16+j126Ω and 22+j53Ω, respectively. Two diodes are soldered in parallel across each of the two slot antennas to lower the required input impedance of the slots and increase the power handling capability of the tripler.

The input impedance of the slot antennas on a layer structure as shown in Fig. 1 and with a CPW feed, was simulated using HP Momentum as shown in Fig. 2. The optimal embedding impedances of the HBV diodes at the fundamental and third harmonic frequency can be seen to match the input impedance of a short slot antenna. This property was first recognized and used by Arcioni *et al.* [3] for a quasi-optical HBV grid tripler design. The fabricated slot antennas are 1.36 mm long, 0.07 mm wide, spaced by 0.387 mm, and fabricated on a quartz substrate with permittivity ε_r = 4.6. A quasi-optical high-pass filter is used to tune the impedance of the slot antennas as well as improve the input coupling efficiency. The high-pass filter consists of an array of 0.4-mm square slots with a period of 0.45 mm. A 0.41-mm-thick stack of quartz substrates separates the filter and slot antennas. The slots were fabricated on a quartz substrate, to achieve sufficiently high input impedance. A 4-mm-thick alumina spacer is used to locate the high-pass filter at the hyperhemispherical point of a 2.54-mm-diameter alumina lens with permittivity

ε_r = 9.8. The slots are thus located at a distance 0.41 mm behind the hyperhemispherical extension length resulting in a slightly higher directivity [9].

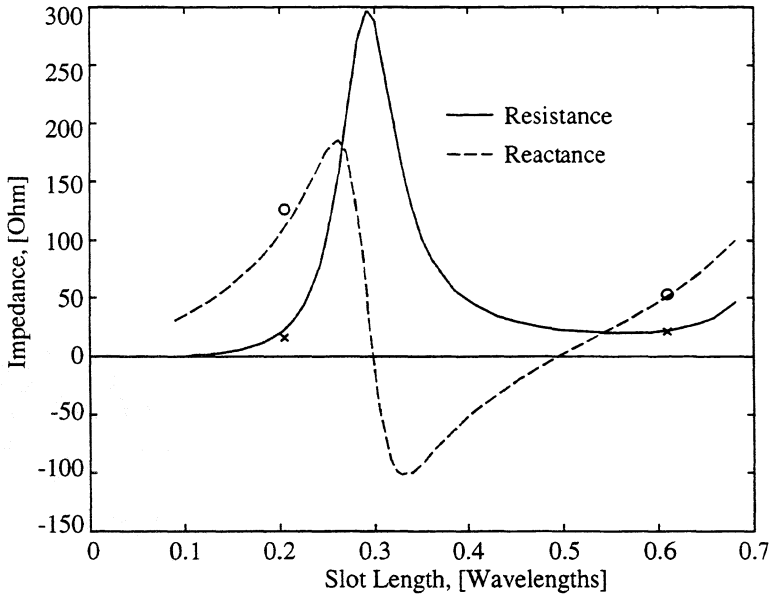

Fig. 2. Simulated input impedance of a slot antenna as a function of slot length. The slot width is 5 % of the slot length. The simulated optimum embedding impedances of two HBV diodes in parallel at the fundamental and the third harmonic are also indicated for a pump frequency of 47 GHz.

The conversion efficiency of the tripler as a function of embedding impedance at the fundamental and third harmonic frequency was simulated using an harmonic balance model of the HBV diodes [13] as shown in Fig. 3. The maximum conversion efficiency of the tripler is 25.1% with a pump power of 100 mW at 47 GHz. Included are also the simulated input impedances of the slot antennas as a function of frequency around the fundamental and third harmonic frequency. Notice that the input match at the fundamental frequency limits the bandwidth of the tripler. An estimated 3-dB bandwidth of about 10% can be seen from the figure.

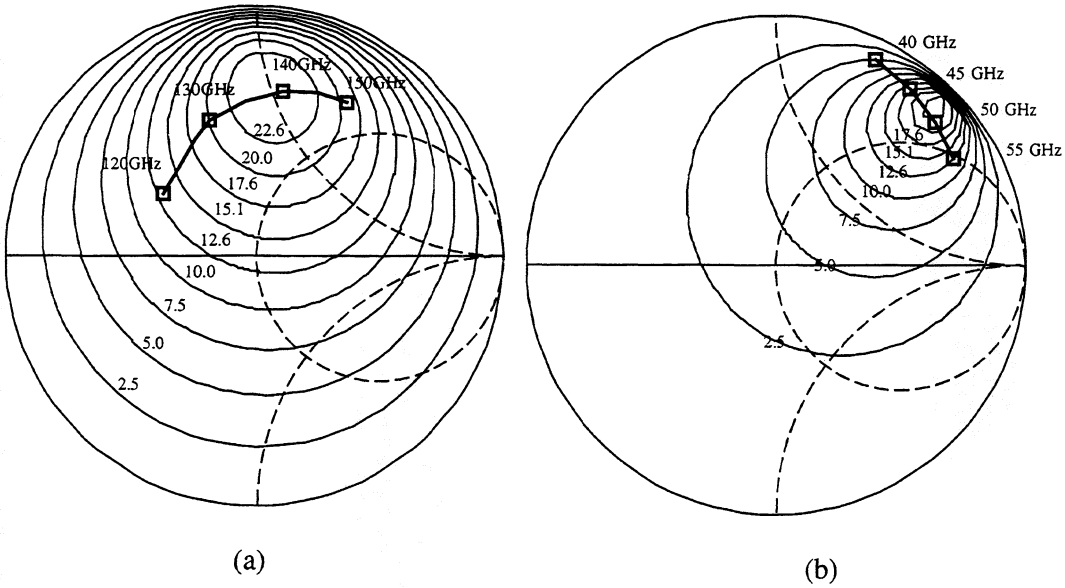

Fig. 3. Simulated conversion efficiency of an HBV tripler as a function of embedding impedance at the a) fundamental frequency and b) the third harmonic for a pump frequency of 47 GHz. The maximum efficiency is 25.1% and each contour describes a 10 % reduction in efficiency. The simulated input impedance of a slot antenna as a function of frequency is also shown.

III. EXPERIMENTS

The open end of a WR-22 waveguide with an *E*- and *H*-plane tuner connected to a Gunn-diode oscillator was used to feed the slot antennas as shown in Fig. 4. While the input impedance calculations assume a plane-wave feed, the slot antennas are located at the plane of the open-ended waveguide during the experiments to minimize spillover loss. The *E-H* tuner is then used to optimize the input coupling to the slots. An *F*-band horn antenna located in the far-field of the lens and connected to an Anritsu power sensor is used to measure the radiated power at the third harmonic. The tripler demonstrates an effectively isotropic radiated power (EIRP) of 2.24 W at 141 GHz for an input power of 143 mW as shown in Fig. 5.

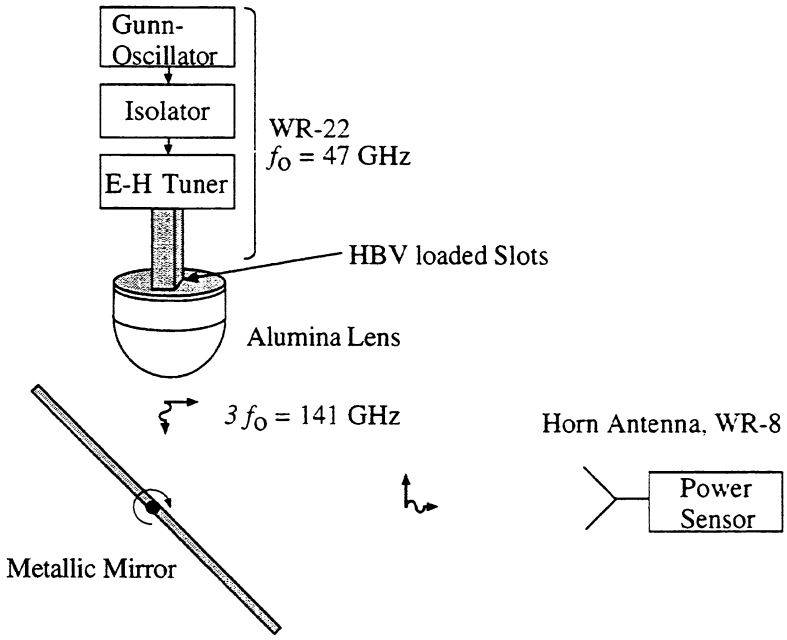

Fig. 4. Experimental set-up for the quasi-optical tripler measurements.

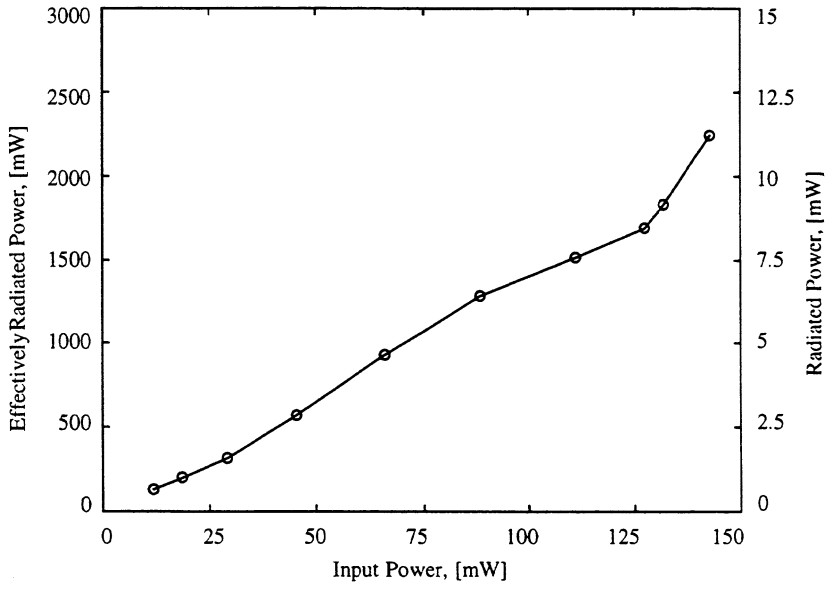

Fig. 5. Effectively isotropic radiated power (EIRP) and estimated radiated power from the tripler at 141 GHz.

Using the simulated radiation patterns of the double-slot antenna into the dielectric lens from Momentum simulations, the radiation patterns from the lens was calculated using a ray tracing technique [11]. Both measured and simulated *E*- and *H*-plane radiation patterns for the lens at 141 GHz are shown in Fig. 6.

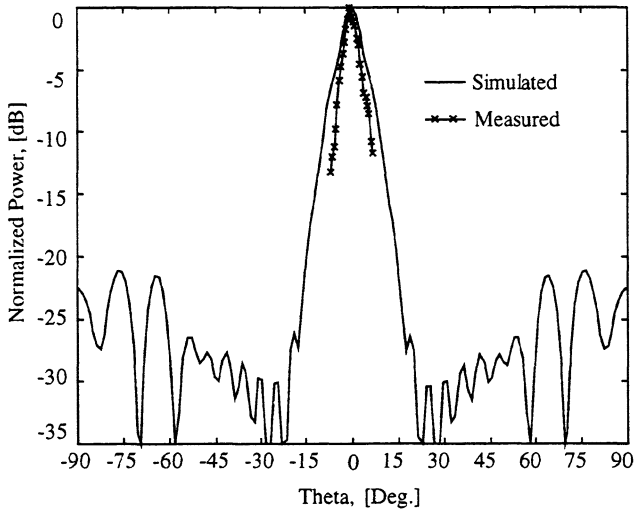

(a)

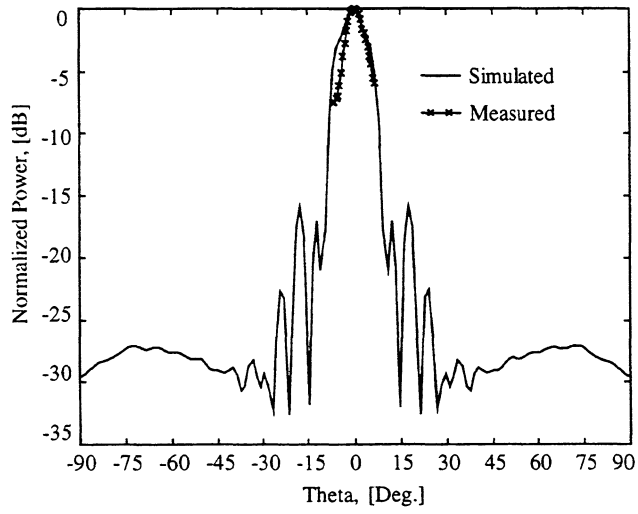

(b)

Fig. 6. Measured and simulated (a) *E*-plane and (b) *H*-plane radiation pattern for the tripler at 141 GHz.

The measured cross-polarized signal was below the detector sensitivity level, or more than 10 dB relative to the co-polarized on-axis power level, for all angles in both planes. The measured 3-dB beamwidth in the *E*- and *H*-plane are 6 and 7 degrees, respectively. From the measured radiation patterns, a directivity of 22.9 dB can be estimated for the slot-fed lens.

A radiated output power of about 11.5 mW, with a corresponding conversion loss of 10.9 dB can be estimated. The conversion loss is defined as the available power from the input waveguide at the fundamental frequency to the power radiated from the lens at the third harmonic. A slightly better conversion loss of 10.5 dB was measured with 110-mW input power as shown in Fig. 7.

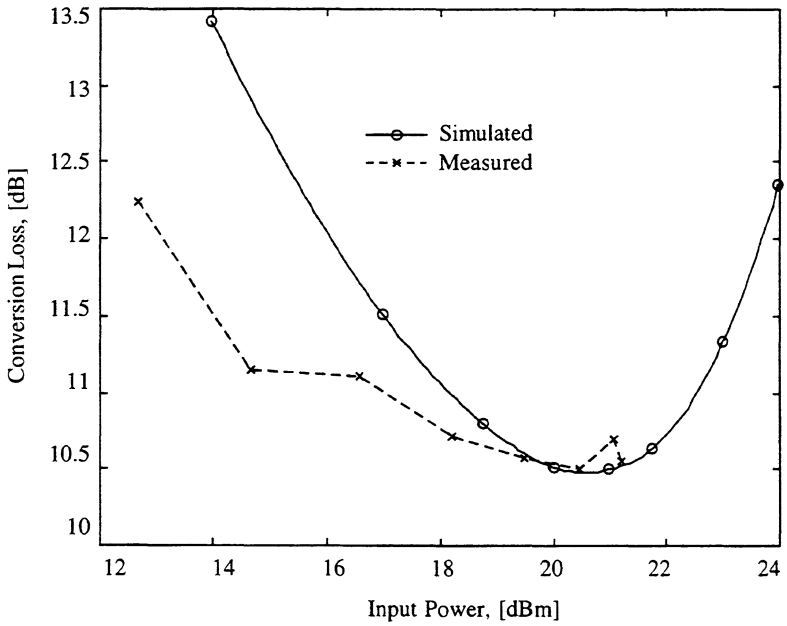

Fig. 7. Measured and simulated conversion loss for the tripler circuit. The conversion loss is defined as the available power at the fundamental from the waveguide to the power radiated from the lens at the third harmonic.

The conversion loss of the four HBV diodes as a function of pump power was calculated using the device model presented in [13]. The calculated conversion loss of the four HBV diodes is 6 dB (25.1% efficiency) for a pump power of 100 mW at 47 GHz assuming optimum embedding impedances and room temperature operation. An estimated loss of 1.0 dB at the input and 3.5 dB at the output was added to the diode conversion loss to approximate the measured conversion loss. The output loss can be due to reflection losses at the lens surface (0.5 dB was estimated from ray tracing), losses in

the dielectric and high-pass filter, misalignment of the receive horn, mirror, lens and slot antennas, overestimated gain of the receive horn, and mismatch of the diodes at the output. No significant power was measured radiating from the substrate edges due to substrate modes. The input loss is due to coupling loss from the waveguide to the slots as well as mismatch losses of the diodes at the fundamental frequency. At the fundamental, an effectively isotropic radiated power of 1.4 W was measured. If a directivity of 17 dB is assumed for the slot-fed lens at 47 GHz, a radiated power of 28 mW from the lens at the fundamental frequency can be estimated.

IV. Acknowledgment

The authors would like to thank G. Rebeiz for use of the dielectric lens. This work was supported by the INTERACT program.

References

[1] C. F. Jou, W. W. Lam, H. Z. Chen, K. S. Stolt, N. C. Luhmann Jr., and D. B. Rutledge, "Millimeter-wave diode grid frequency doubler," *IEEE Trans. Microwave Theory Tech.*, vol. 36, pp. 1507-1514, Nov. 1988.

[2] A. Moussessian, M C. Wanke, Y. Li, J.-C. Chiao, F. A. Hegmann, S. J. Allen, T. W. Crowe, and D. B. Rutledge, "A terahertz grid frequency doubler," *IEEE MTT-S Int. Microwave Symp. Dig.*, Denver, CO, vol. 2, pp. 683-686, Jun. 1997.

[3] P. Arcioni, M. Bozzi, G.Conciauro, H. L. Hartnagel, L. Perregrini, E. Sacchi, M. Shaalan, and J. Weinzierl, "A 430.5 GHz quasi-optical HBV frequency tripler," *Proc. Ninth Int. Symp. on Space Terahertz Tech.*, Pasadena, CA, pp. 493-500, Mar. 1998.

[4] N. Erickson and J. Tuovinen, "A waveguide tripler for 800-900 GHz," *Proc. Sixth Int. Symp. on Space Terahertz Tech.*, Pasadena, CA, Mar. 1995.

[5] J Stake, L. Dillner, S. H. Jones, C. Mann, J. Thornton, J. R. Jones, W. L. Bishop, and E. Kollberg, "Effects of self-heating on planar heterostructure barrier varactor diodes," *IEEE Trans. Electron Devices.*, vol. 45, no. 11, pp. 2298-2303, Nov. 1998.

[6] X. Mélique, A. Maestrini, E. Lheurette, P.Mounaix, M. Favreau, O. Vanbésien, J. M. Goutoule, G. Baudin, T. Nähri, and D. Lippens, "12% efficiency and 9.5 dBm output power from InP-based heterostructure barrier varactor triplers at 250 GHz," *IEEE MTT-S Int. Microwave Symp. Dig.*, Anaheim, CA, to be published 1999.

[7] D. B. Rutledge, and M. S. Muha, "Imaging antenna arrays," *IEEE Trans. Antennas and Prop.*, vol. AP-30, no. 4, pp. 535-540, Jul. 1982.

[8] G. M. Rebeiz, "Millimeter-wave and terahertz integrated circuit antennas," *Proc. IEEE*, vol. 80, no. 11, pp. 1748-1770, Nov. 1992.

[9] T. H. Buttgenbach, "An improved solution for integrated array optics in quasi-optical mm and submm receivers: the hybrid antenna," *IEEE Trans. Microwave Theory Tech.*, vol. MTT-41, no. 10, pp. 1750-1761, Oct. 1993.

[10] H. H. G. Zirath, C.-Y. Chi. N. Rorsman, and G. M. Rebeiz. "A 40-GHz integrated quasi-optical slot HFET mixer," *IEEE Trans. Microwave Theory Tech.*, vol. MTT-42, no. 12, pp. 2492-2497, Dec. 1994.

[11] D. F. Filipovic, G. P. Gunthier, S. Raman, and G. M. Rebeiz, "Off-axis properties of silicon and quartz dielectric lens antennas," *IEEE Trans. Antennas and Prop.*, vol. AP-45, no. 5, pp. 760-766, May 1997.

[12] E. Kollberg, and A. Rydberg, "Quantum-barrier-varactor diodes for high-efficiency millimeter-wave multipliers," *Electron. Lett.*, vol. 25, no. 25, pp. 1696-1698, Dec. 1989.

[13] J Stake, L. Dillner, S. H. Jones, C. Mann, and E. Kollberg, "Design of 100-900 GHz AlGaAs/GaAs planar heterostructure barrier varactor diodes," *Proc. Ninth Int. Symp. on Space Terahertz Tech.*, Pasadena, CA, pp. 359-366, Mar. 1998.

A FAST AND SENSITIVE SUBMILLIMETER WAVEGUIDE POWER METER

Neal Erickson
Department of Physics and Astronomy
Lederle 619, Univ. of Mass.
Amherst, MA 01003

Abstract
A sensitive, fast and stable power meter has been developed which responds over a frequency range extending from 75 GHz up to the THz range. The method of measurement is essentially calorimetric, but with feedback circuitry added to speed up the response. The measurement time constant is 0.5 sec for power levels from 2-100 mW, but increases to 9 sec below 50 μW. The drift level is 2-5 μW in a typical measurement, while accuracy is better than 3%.

Introduction

Measurement of power at frequencies in the mm and submillimeter wave range has always been problematic. Power sensors suffer from a number of problems, all of them worsening as frequency increases. These include poor sensitivity, slow response time, poor impedance match and frequency dependent calibration. At this time commercial sensors are available which largely eliminate these problems up to 110 GHz, but at higher frequencies there are no fully satisfactory measurement options. This leads to a situation where it is not known within a factor of two or more the power required to operate SIS or HEB mixers, and where errors in the measurement of multiplier efficiencies can be comparably large.

In fact, it has always been possible to make accurate measurements at any frequency through the use of calorimetric power measurement [1,2,3]. The problem with these instruments is that they are very slow in response, with sufficient zero drift that accuracy suffers severely below a power of 50 μW. The accousto-optic sensor [4] can offer fast response and reasonable accuracy, but requires careful matching to an optical beam and requires correction for input reflection and partial absorption. Its drift level is also fairly large, and it requires a chopped signal. Other very sensitive detectors such as cooled bolometers are also fast, but are nearly impossible to calibrate with any accuracy.

The goal of this work was to develop a power sensor which could be used like a conventional waveguide power sensor at any frequency in the ~100GHz to THz range, with fast enough response to permit its use in tuning a source. The sensor had to have minimal frequency variation to its response and a sufficiently good input match that the error due its VSWR would be insignificant even in the measurement of a source with a VSWR of 4:1. In addition it had to be sensitive enough to reliably measure a power level

of a few microwatts, since this is a typical power level for submillimeter sources. This sensor incorporates a number of features used in the calorimeter of refs [1,2], but uses a construction much more optimized for response speed.

Fundamentals of calorimetry

The only method of power measurement that is frequency insensitive is calorimetry, that is, simply measuring the temperature rise of a well-matched wideband absorber in response to applied power. In principle, this is a very simple technique and is easily calibrated because the same absorber can be heated using a known amount of power applied through other means. It is important in this calibration that the reference heat produce the same response as the microwave power. In practice, the difficulty is in making a sensor with a fast response time and uniform temperature, while maintaining acceptable sensitivity. In addition, drift due to ambient temperature variations is very difficult to control. The usual technique to reduce drift is to use a matched pair of sensors having nearly identical thermal environments, and to use one as the measurement sensor and the other as a reference. So long as the sensors are identical, they show no response to common mode temperature variations, but this requires extreme care in their fabrication.

The response time, τ, of the sensor is determined by the heat capacity of the sensor load, C, and the thermal resistance to thermal ground, ρ:

$$\tau = C \times \rho$$

while the temperature rise ΔT is given by:

$$\Delta T = \rho \times P, \text{ where P is the absorbed power.}$$

Since a large ΔT response is desired, ρ must be made fairly large, and the only way a fast response can then be achieved is by making the heat capacity (and thus the mass) of the sensor as small as possible, but a practical sensor can not be made arbitrarily small. A sensor must be large enough to be an efficient absorber with no frequency resonances. In practice this means that a slowly tapered load is required, and the load material must be thick enough that no power can pass through it. In addition the load must include a temperature sensor and a heater resistor for calibration.

The accuracy of power measured in this way is quite good if the input loss is small. In the case where the input loss is negligible, it is obvious that all of the power must appear as heat in the load, and that this heat can easily be calibrated by heating the load with a known power. The problem when the loss is high is that it is not easy to determine exactly how much of the input power dissipated in the waveguide loss is also heating the load. However, this factor is calculable assuming the waveguide loss is uniform over its length. In practice, the inaccuracy in the use of a calorimeter of this type is dominated by the much more uncertain loss in the tapers used to transition into WR10 waveguide.

Within the 75-110 GHz band the input loss is small enough to introduce an uncertainty of only 1-2%.

Calorimeter sensor

The geometry of the sensor used in this work is shown in figure 1. The input was chosen to be WR10 waveguide so that cross calibration could be done against commercial sensors, while being small enough to keep the heat capacity low. It is quite practical to couple from this waveguide into any smaller size using linear tapers. While many submillimeter sources are optically coupled, nearly all use waveguide internally, and are easily coupled back into waveguide. An unconventional waveguide termination geometry was chosen which places the load entirely on the outside of the waveguide, where it is easy to attach the thermometer and heater. The load itself is a simple slab with no critical shape. The waveguide cutoff angle was chosen as 10° to give a VSWR better than 1.2:1 for the best available load material in the WR10 band. A variety of materials have been tested as loads including several ferrite loaded resins and other lossy materials. The best found so far in having a good match with very low mass is a sandwich of 2 silicon wafers. The inside layer is a 100 Ω/□ metal film deposited on a moderate resistivity silicon wafer with a thickness of 0.2 mm. The outer layer is a highly doped silicon wafer with a thickness of 0.3 mm. The metal film provides a well matched load while the very lossy silicon top layer absorbs all of the energy that leaks through the film. All of the edges of the inside wafer are coated with conductive epoxy to eliminate loss of power, and the absorber is carefully sealed to the waveguide without any gaps where power can be lost. Silicon is an excellent substrate material because it is a good heat conductor, is easily coated with metal films, and is readily available in various dopings.

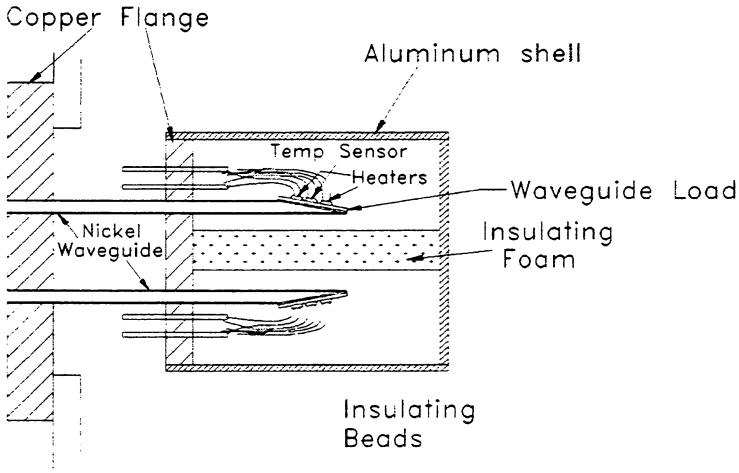

Figure 1. Diagram of the power sensor head, showing the waveguide loads, heaters and temperature sensors.

The waveguide is electroformed nickel with a gold plated interior. Nickel is a fairly poor thermal conductor, and is readily electroplated with good mechanical properties. The waveguide must be very thin so that it has sufficient thermal resistance in a short length, and so that its heat capacity is small compared to that of the load. A numerical simulation shows that the effective heat capacity of the load includes a contribution of one third of the heat capacity of the full waveguide length. A practical minimum waveguide thickness is ~60 μm and a reasonable length is 10-15 mm. For this sensor, the waveguide adds about 10% to the effective heat capacity of the load. The time constant of this type of load is found to be 9 sec for a responsivity of ~500K/W. While this is faster than typical calorimeters, it is still too slow for a primary power sensor.

Stainless steel would be better for use in the waveguides since its thermal conductivity is 20% that of Ni, but it is only available in 0.25 mm thickness, and must be thinned to be useful. Thinning this small waveguide in a reproducible manner is possible but tedious. Stainless steel waveguide also must be plated on the interior to reduce the loss, and this process is somewhat variable in its results.

The temperature sensors used must be very linear if the sensor is to work over a wide power range, and they also must have very low drift and noise. Thin film Pt resistance sensors have been found to be stable to <0.2 mK, with noise determined largely by the readout electronics. The only problem with these sensors is that the smallest standard package is somewhat large, and adds 20% to the mass of the load.

Drift due to external temperature fluctuations is a serious problem with such a small responsivity. To minimize this problem the sensor uses a second stage of thermal isolation by connecting the waveguides together at their midpoint with a copper plate. Any differential heat leaking in along the waveguides is short circuited at this point, and the mass of the midplate leads to a very slow propagation of this (now common mode) heat to the sensors. The sensors are isolated from any differential heating from other directions by enclosing them in a metal shell, so that any external influence is nearly entirely common mode. One subtle source of drift is heat generated in the temperature sensors due to the current used to measure their resistance. Convection currents from one load to the other cause drift which depends on the orientation of the sensors. To eliminate this effect the sensors must be thermally isolated from each other by an insulator, which completely blocks any convection within the metal shell.

Feedback circuit for faster response

Improvement in the speed of response can be obtained electronically with the readout circuit. While in principle the readout response can be tuned to give an apparent increase in sensor speed, in practice this results in overshoot of the measured power, and very unpredictable responses while tuning. An alternative method is to use the readout circuit to maintain a nearly constant temperature for the load. This can be done by biasing the temperature of the loads (both sensor and reference) to a point somewhat above that which would be produced by the highest power that is to be measured. As RF power is applied, the heater power is reduced to maintain a constant temperature. Rather than

measuring temperature rise, one then measures the change in heater power. If the feedback circuit maintaining the temperature has a gain, G, then the change in temperature for a given RF power is reduced by a factor of G, and the response time is decreased by the same factor. There is no problem in this case with spurious behavior in the indicated power, no matter how the RF power is varied, and arbitrarily fast response may in principle be obtained. However there are practical limits to speed because the sensor noise, for frequencies > $1/\tau$, is increased by a factor of G, and also because the response can not be faster than the thermal equilibrium time within the load element (due to the thermal resistance between the heater and the thermometer). For the load used in these sensors, a gain of 20 works well, giving a time constant of 0.45 sec, and faster response is probably possible. However, this gain is only practical with the present circuit for measurements above 2 mW. At lower power levels the gain is reduced for lowest noise and highest stability.

A block diagram of the readout electronics is shown in Fig 2. The feedback circuit is somewhat complicated because the error voltage from a linear temperature sensor applied to a heater resistor produces a $V^2 \propto \Delta T^2$ response. Such a nonlinear loop response is difficult to compensate. To simplify the loop response and to provide a linear readout, an analog square root module is included within the loop. These modules are now so accurate that their response has no measurable affect on the overall linearity of response. The electronics module uses a bridge circuit to measure the temperature imbalance of the two loads, with AC excitation of the bridge to minimize drift in the following amplifier. The AC imbalance signal is amplified and the synchronously detected to minimize noise. Following DC amplification, the square root is taken and the output is then offset from the full scale error voltage. This offset error is then fed back to the active sensor to heat it in response to its difference in input power from full scale. The reference sensor is always heated with a power equivalent to full scale input.

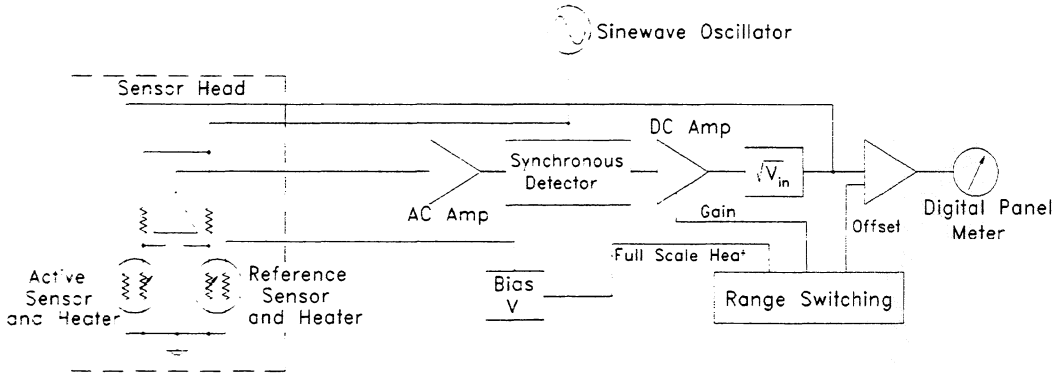

Figure 2. Block diagram of the readout electronics with feedback to increase the response speed.

The feedback loop requires that there be a heater resistor on the load, and in addition there needs to be a second heater resistor for calibration purposes. These resistors add mass to the sensor, and their functions could all be performed by metal films deposited directly on the silicon load, but this would require an investment in masks and lithography.

The stability of this type of sensor depends critically on maintaining a constant heat path to thermal ground for both waveguide loads. Since the bias temperature is somewhat greater than full scale power, any variation in the thermal path will cause a significant zero drift. For this reason, it is necessary to change the bias heat when changing measurement scales so that the drift will be only a fraction of each full scale reading. Changing scales requires changing several gains and offsets in the electronics.

Performance

The actual performance achieved in the prototype meter built using this technique is not optimized, but the meter still is an extremely useful instrument. This sensor used waveguides with relatively poor thermal match, having 10% difference in responsivity, and thus significant common mode response. The maximum power level that can be measured is 100 mW, limited mainly by concerns for the sensor stability if operated continuously at higher temperatures, as is necessary due to the bias heat used. At the bias point, the sensor temperature is 70 C. Other scales provided are 20 mW, 2.0 mW and 200 μW FS, using a $3^1/_2$ digit panel meter. On the 100 mW scale, the drift is negligible, being <0.2 mW over several months. On the 20 mW scale, the drift is ~0.1 mW over the same time, with much smaller short term drift. For both of these scales the gain is 20 so the time constant is 0.45 sec. For the 2.0 mW scale the gain is reduced to 5 giving a time constant of 1.8 sec. This scale is useful down to a power level of 50 μW with good stability, with a typical drift and noise level of 5-10 μW. The 200 μW scale operates open loop for best stability, and has a typical drift level <2 μW during a typical measurement interval, if the sensor is not thermally disturbed. However, most measurements introduce a thermal disturbance due to the common mode response, and the drift becomes ~5 μW typically. This can be reduced if the sensor remains connected to the source for a time so that the transient dies out.

The large change in bias heat when changing scales leads to the only obvious difference in use between this meter and a more conventional power sensor. Upon changing scales, there is a large thermal transient that must die away before the sensor is stable once more. This stabilization time depends on the inherent time constant of the sensor element, and when switching scales to a lower power, at least five time constants (45 sec) are required for stabilization. This problem would be less if the two loads were closely matched so that they both settle at the same rate. When switching scales upward in power the settling time is quite short.

The potential for much higher stability is apparent from another sensor (without feedback), which was made using stainless steel waveguides that were electropolished

down to a thickness of 80 μm and matched in their thermal conductivity. They also have a longer length and significantly lower thermal conductivity. However, the overall time constant is only twice as large, in part because the waveguide conductivity is only a part of the total heat loss of the sensor. In this sensor the typical drift level is <0.5μW over a period of 5 minutes without perturbation, and <1 μW during typical measurements. If such low drift were present in a sensor with fast response, then the instrument would be extremely useful for most submillimeter work. These refinements are planned for future versions of this instrument.

Conclusions

A very wideband power meter has been built which is fast and stable. The useful power range is 10 μW-100 mW with a measurement time constant of 0.5-9 sec depending on power. Construction is somewhat complex, but could be simplified in production. This meter already is useful for a wide range of measurements on LO sources, and with some refinements could fill an even larger range of needs.

References

[1] "Broad-band Calorimeter for Precision Measurement of Millimeter and Submillimeter-Wave Power," B. Volwinkle, *IEEE Trans. on Instrumentation and Measurement*, Vol 29, pp. 183-189, 1980.

[2] "Precision Measurement of Power at Millimeter and Sub-Millimeter Wavelengths Using a Waveguide Calorimeter," B. Vowinkel and H.P. Roser, *Int'l J. of Infrared and Millimeter Waves*, Vol 3, pp 471-487, 1982.

[3] "A Microwave Microcalorimeter," A.C. Macpherson and D.M. Kerns, *Rev. Sci. Instr.*, vol. 26, pp. 27-33, 1955.

[4] Thomas Keating Ltd, Billingshurst, W. Sussex, England.

AN ACCURATE EXPRESSION FOR THE INPUT IMPEDANCES OF ONE-SIDED MICROSTRIP PROBES IN WAVEGUIDE

S. Withington, G. Yassin, J. Leech, and K.G. Isaak

Department of Physics,
University of Cambridge,
Madingley Rd, Cambridge.

Abstract

In previous work we established a general procedure for calculating the input impedances of one-sided microstrip probes in waveguide. The *one-sided* configuration, where the probe extends only part way across the waveguide, contrasts with the *two-sided* configuration, where the probe extends the whole way across the waveguide. We demonstrated that because of the way in which the different current distributions couple to the waveguide modes, the one-sided probe is intrinsically lower impedance and more broadband than the two-sided probe. This observation has important consequences for the design of THz SIS waveguide mixers.

Previously, we had to make an approximation when evaluating the integral for the complex radiated power, and this led to a corresponding approximation in the final expression for the input impedance. We have now evaluated this integral rigorously, and we have shown that the original approximation breaks down to third order in the width of the probe, an effect we have seen experimentally. In this paper, we review the technique for calculating the impedances of one-sided microstrip probes, and we present a more accurate expression based on a rigorous analytical evaluation of the power integral. This expression is compared with complex impedances measured on a scale model at 5GHz, and excellent agreement is found.

1 Introduction

The planar waveguide probe has become the standard way of coupling SIS tunnel junctions to rectangular waveguides in conventional low-noise submillimetre-wave mixers. In the most popular configuration, the tunnel junction is placed at the centre of a thin conducting strip that extends the whole of the way across the waveguide [1]. This arrangement has the disadvantage that it is is not possible to obtain low values of input impedance (50 Ω or less) without reducing the height of the waveguide. This property is intrinsic to the "two-sided" geometry, and is a consequence of the fact that the contributions from the evanescent waveguide modes add up in parallel and influence the real part of the input impedance in an complicated way. An alternative approach is to use a metallisation that extends only part way across the waveguide: a "one-sided" probe. In this case, the contributions from the waveguide modes add up in series, and only the propagating fundamental mode couples to the resistive part of the input impedance. As a consequence, the input impedance is low,

and does not exhibit the complicated frequency dependence of the two-sided arrangement. The ease with which it is possible to couple low-impedance devices to one-sided probes in full height waveguide has important consequences for the design of THz SIS mixers.

In a previous paper [2], we established a general procedure for calculating the input impedances of one-sided microstrip probes in waveguide. The approach was based on the reciprocity theorem and the spectral-domain method [3]. The main feature of the theory is that the Fourier transforms of the current and field distributions are related—through the spectral dyadic Green's function—by an algebraic rather than an integral equation. Moreover, the expression for the spectral Green's function is much simpler and easier to obtain than the space-domain version—especially for dielectrically-loaded waveguide. Originally, we had to make an approximation when evaluating the integral for the complex radiated power, and this led to a corresponding approximation in the expression for the input impedance. We have now evaluated this integral rigorously and have shown that the original approximation was accurate to only second order in the width of the probe. Indeed, the original expression was accurate for narrow probes only, an effect we had seen experimentally.

In this paper, we present an accurate expression for the input impedance of one-sided microstrip probes. The expression is based based on a rigorous analytical evaluation of the power integral. The physical significance of the various terms in the final expression is clear. Through this work we have found that a broadband match can be achieved by using a radial probe. We describe how, by using the Fast Fourier Transform, the basic technique can be extended to cover any geometry for which the current distribution is approximately known.

2 Theoretical Analysis

In Fig. 1, we show the geometry of a microstrip probe in waveguide. The probe is assumed to be fed by a current source I_{in}, which is connected between the base of the probe and the wall of the waveguide. This source causes a potential difference V_{ab} to be established, through which the input impedance can defined:

$$Z_{in} = \frac{V_{ab}}{I_{in}} \; . \tag{1}$$

Using the reciprocity theorem [4],[5], we can derive an expression for V_{ab} in terms of the current density on the surface of the probe J_x and the tangential electric field in the waveguide E_x; in this way, we obtain

$$Z_{in} = -\frac{1}{I_{in}^2} \int\int\int E_x(r) J_x(r) dV \; . \tag{2}$$

When evaluating the above integral we assume that the current is distributed sinusoidally over the length of the probe. This assumption allows a great deal of simplification and eventually leads to a closed-form solution for the input impedance. All of our detailed experimental measurements show that this first-order guess at the current distribution gives extremely accurate results. We therefore write

$$J_x(x,y,z) = J_0 \delta(y-d) u(z) \sin k(x_1 - x) \tag{3}$$

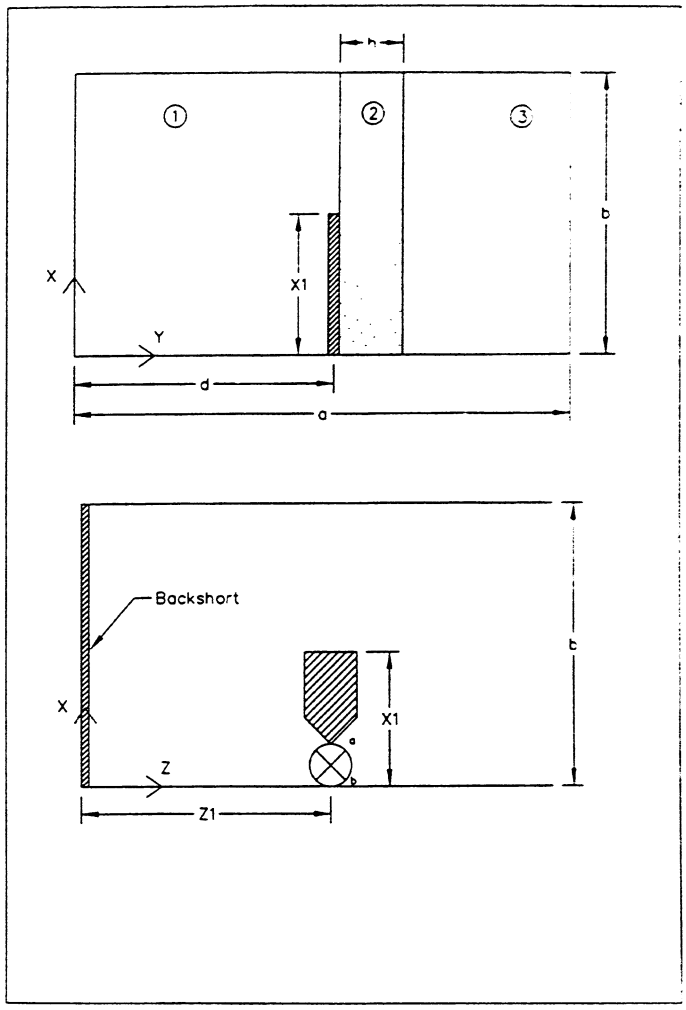

Figure 1: A one-sided microstrip probe in waveguide

for $x < x_1$ and zero otherwise. $u(z)$ describes the current density distribution across the width of the probe. Previously, we used an expression of the form

$$u(z) = \frac{1}{\pi} \frac{1}{\sqrt{1 - (\frac{z - z_1}{w})^2}} \qquad |z - z_1| < w \ , \tag{4}$$

where w is the half width of the probe, to take into account the singularity that exists, in the case of infinitely thin metallisation, at the edge of the strip. In this paper, we simply assume that the current is constant across the width of the strip and goes to zero at the edges: $u(z) = 1$ for $|z - z_1| < w$ and zero otherwise. For all practical purposes, these two current distributions are identical. Notice that we are assuming that the plane of the probe lies in the E-plane of the waveguide. In a previous paper we proved analytically that the input impedance is insensitive to the orientation of the probe. In the following treatment, we shall neglect the transverse components of the current J_z and the electric field E_z. Rigorous theoretical analyses of microstrip lines suggest strongly that this approximation, which significantly simplifies the solution, is a good one for geometries of practical interest.

To apply the spectral-domain method to our problem, we first replace the current and field in (2) by their Fourier transforms and apply Parseval's theorem in two dimensions to obtain

$$Z_{in} = -\frac{1}{8\pi b} \frac{1}{I_{in}^2} \sum_{n=-\infty}^{+\infty} \int_{-\infty}^{+\infty} \tilde{E}_x(\alpha_n, \beta, d) \tilde{K}_x^*(\alpha_n, \beta) \, d\beta, \tag{5}$$

where $\tilde{K}_x(\alpha_n, \beta)$ is the two-dimensional Fourier transform of the current distribution. At this stage, the boundary conditions at the top and bottom of the waveguide have effectively been introduced by the method of images: forcing the Fourier parameter α to be discrete.

The input impedance can now be calculated by using the spectral-domain relationship between the current and field distributions. Neglecting the transverse component of the field and current we obtain

$$\tilde{E}_x(\alpha_n, \beta, d) = \tilde{G}_{xx}(\alpha_n, \beta, d) . \tilde{K}_x(\alpha_n, \beta) \tag{6}$$

where

$$\tilde{G_{xx}}(\alpha, \beta, d) = \frac{\alpha^2}{\alpha^2 + \beta^2} Z^e + \frac{\beta^2}{\alpha^2 + \beta^2} Z^h \ . \tag{7}$$

In the above equations $\tilde{G_{xx}}(\alpha, \beta, d)$ is the longitudinal component of the dyadic Green's function, evaluated at d. Z^e and Z^h are the Green's functions associated with the LSE and LSM modes and expressions for them may be found in several places [6]. We can, if desired, take into account the effect of the supporting dielectric substrate simply by using the appropriate Green's function.

Substitution then gives

$$Z_{in} = -\frac{1}{4\pi b} \frac{1}{I_{in}^2} \sum_{n=-\infty}^{+\infty} \int_{-\infty}^{+\infty} \tilde{G}(\alpha_n, \beta, d) \left| \tilde{K}_x(\alpha_n, \beta) \right|^2 \, d\beta, \tag{8}$$

where for convenience we have dropped the subscript on the Green's function.

To proceed with the analysis, we need the spectral domain dyadic Green's function for an empty waveguide and the Fourier transform of the current distribution. To derive an expression for the Fourier-transformed current distribution we can use the method of

images; that is to say we replaced the wall of the waveguide by a virtual probe. The virtual probe is identical to the actual probe, but points in the opposite direction. We then find,

$$\tilde{K_x}(\alpha_n,\beta) = I_{in}\frac{2k}{(k^2-\alpha_n^2)}\left[\frac{\cos\alpha_n x_1 - \cos kx_1}{\sin kx_1}\right]\left[\frac{\sin\beta w}{\beta w}\right], \tag{9}$$

where boundary conditions require

$$\alpha_n = \frac{n\pi}{b}. \tag{10}$$

Substituting the current distribution into the expression for the impedance we find

$$\begin{aligned} Z_{in} &= \frac{-1}{2\pi b}\sum_{n=0}^{+\infty}\delta_n\frac{k^2}{(k^2-\alpha_n^2)^2}\left[\frac{(\cos\alpha_n x_1 - \cos kx_1)}{\sin kx_1}\right]^2 \\ &\int_{-\infty}^{+\infty}\tilde{G}(\alpha_n,\beta,d)\left[\frac{\sin\beta w}{\beta w}\right]^2 d\beta, \end{aligned} \tag{11}$$

and $\delta_n = \begin{cases} 1 & \text{for n=0} \\ 2 & \text{otherwise} \end{cases}$.

To make further progress we need an expression for the spectral Green's function of empty waveguide. Using the immittance method, and assuming that the probe is at the centre of the waveguide, we find

$$\tilde{G}(\alpha_n,\beta,d) = \frac{jkRo}{2\gamma}\left[\frac{k^2-\alpha_n^2}{k^2}\right]\tanh\gamma d, \tag{12}$$

where R_0 is the impedance of free space, and γ is the propagation constant in the transverse direction.

Substituting the expression and using an expansion for the hyperbolic tangent, we arrive at

$$\begin{aligned} Z_{in} &= \frac{-jkR_0}{\pi ab}\sum_{n=0}^{+\infty}\sum_{m=1}^{+\infty}\delta_n\frac{1}{(k^2-\alpha_n^2)}\left[\frac{(\cos\alpha_n x_1 - \cos kx_1)}{\sin kx_1}\right]^2 \\ &\sin^2\left(\frac{m\pi}{2}\right)\int_{-\infty}^{+\infty}\frac{1}{(\beta^2-\beta_{mn}^2)}\left[\frac{\sin\beta w}{\beta w}\right]^2 d\beta. \end{aligned} \tag{13}$$

In the above equation, β_{mn} are the poles of $\tilde{G}$ which satisfy the relation

$$\beta_{mn}^2 = k^2 - \gamma_m^2 - \alpha_n^2 \tag{14}$$

where the propagation constant in the transverse direction is given by

$$\gamma_m = \left(\frac{m\pi}{a}\right). \tag{15}$$

For functions of this kind the value of the integral is determined by the poles of the integrand. In the case of propagating modes, the β_{mn} are real, and the poles lie on the real axis of the complex plane and contribute to the real part of the input impedance through the singularities that exist when integrating along the real line from $-\infty$ to $+\infty$. In the case of non-propagating modes, the poles lie on the imaginary line and contribute to the reactive part of the input impedance—they do not produce singularities on the real line. Hence, we

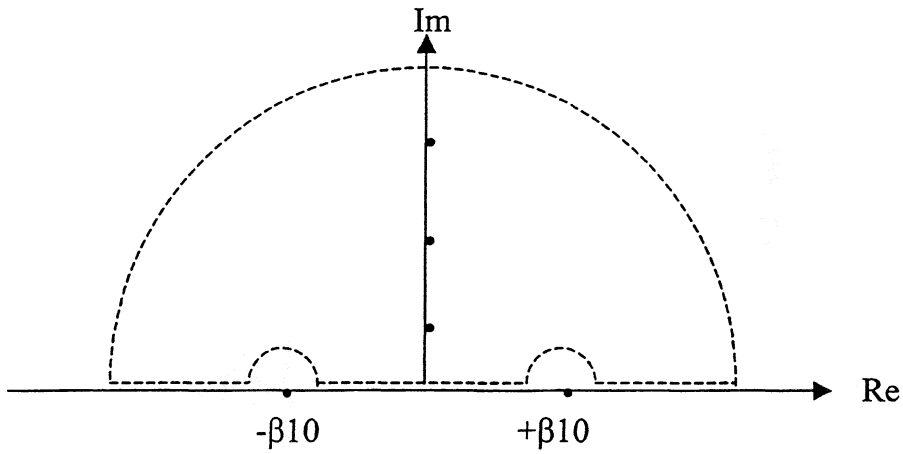

Figure 2: Poles of the power radiation integral in the complex plane. The poles on the real line correspond to the propagating modes, and the poles on the imaginary line correspond to the evanescent modes.

should perform the integrals for the propagating and none propagating modes separately. For convenience, we shall assume that the size of the waveguide has been chosen so that only the lowest-order mode can propagate. In this case, only β_{10} is real. The situation is shown in Fig. 2.

We can now use the residue theorem easily to get the input resistance of a free-standing one-sided microstrip probe in waveguide:

$$R_{in} = \frac{R_0}{abk\beta_{10}} \tan^2\left[\frac{kx_1}{2}\right]\left[\frac{\sin\beta_{10}w}{\beta_{10}w}\right]^2 . \tag{16}$$

This expression is identical to our early one apart form the appearance of a sinc-squared function rather than a Bessel function due to the different assumption about the transverse current distribution.

In the case of the imaginary part, the integral in (14) becomes

$$X_{in} = \frac{kR_0}{ab}\left[\sum_{m=2}^{+\infty} X_{m0} + \sum_{n=1}^{+\infty}\sum_{m=1}^{+\infty} X_{mn}\right] \tag{17}$$

$$X_{mn} = \delta_n \frac{1}{(k^2-\alpha_n^2)}\frac{1}{\beta_{mn}} \left[\frac{\cos\alpha_n x_1 - \cos kx_1}{\sin kx_1}\right]^2 \sin^2\left(\frac{m\pi}{2}\right) \left[\frac{2\beta_{mn}w - 1 + \exp^{-2\beta_{mn}w}}{2(\beta_{mn}w)^2}\right] . \tag{18}$$

This equation is similar to the approximate expression for the reactive part of the input impedance derived previously. Now, however, the sinc-squared function in $\beta_{mn}w$ is replace by the last term in square brackets of (23). For all real probes $\beta_{mn}w$ is less than unity.

Expanding the sinc-squared function and the exponential function as power series and comparing the two, we find that the third-order term in our original expression is incorrect; an effect which we see experimentally when the width of the probe becomes large.

Clearly, the propagating mode does not make a contribution to the reactive part of the input impedance. Also it can be seen that the contributions of the different modes to the overall reactance change sign depending on whether or not $k > \alpha_n$. In fact the contributions are inductive for $n = 0$ and capacitive for $n > 0$. Hence, the overall input impedance can be inductive or capacitive depending on the height of the waveguide and the frequency.

Finally, we would like to include the effect of a backshort in the analysis. There are various ways in which this can be achieved. To a good approximation we can simply multiply the Green's function associated with the unterminated waveguide by the factor

$$\tau = 2j \sin \beta z_1 \exp -j\beta z_1 \ , \tag{19}$$

where z_1 is the distance between the centre of the probe and the backshort. In addition, we only include this factor in the integration over β when considering the propagating mode, and we ignore the effect on the non-propagating modes. This assumption makes the integral easy to evaluate and has physical justification because the backshort is usually sufficiently far from the probe that the near-field effects of the non-propagating modes are negligible. It is the reactive contribution of the lowest-order mode that can be used to cancel the reactive effects of the non-propagating modes in order to tune the probe for any frequency.

Finally, the input impedance, $Z_{in} = R_{in} + jX_{in}$, of a free-standing centred, one-sided probe with backshort is given by

$$R_{in} = \frac{2R_0}{abk\beta_{10}} \tan^2\left[\frac{kx_1}{2}\right]\left[\frac{\sin\beta_{10}w}{\beta_{10}w}\right]^2 \sin^2(\beta_{10}z_1) \tag{20}$$

$$X_{in} = X_{10} + \frac{kR_0}{ab}\left[\sum_{m=2}^{+\infty} X_{m0} + \sum_{n=1}^{+\infty}\sum_{m=1}^{+\infty} X_{mn}\right] \tag{21}$$

$$X_{10} = \frac{R_0}{abk\beta_{10}} \tan^2\left[\frac{kx_1}{2}\right]\left[\frac{\sin\beta_{10}w}{\beta_{10}w}\right]^2 \sin(2\beta_{10}z_1) \tag{22}$$

$$X_{mn} = \delta_n \frac{1}{(k^2-\alpha_n^2)}\frac{1}{\beta_{mn}} \left[\frac{\cos\alpha_n x_1 - \cos kx_1}{\sin kx_1}\right]^2 \sin^2\left(\frac{m\pi}{2}\right) \left[\frac{2\beta_{mn}w - 1 + \exp^{-2\beta_{mn}w}}{2(\beta_{mn}w)^2}\right] . \tag{23}$$

In all of these equations β_{mn} corresponds to $|\beta_{mn}|$, that is to say we use the modulus of the propagation constant regardless of whether the mode is propagating or not.

In general, we see that for the microstrip probe the real part of the input impedance is due solely to the lowest-order propagating mode; whereas for the two-sided probe, the real part of the input impedance is influenced by a large number of high-order non-propagating modes. This basic and important difference results in the one-sided probe being characterised by a high value of input impedance whereas the microstrip probe is characterized by a relatively low value of input impedance. In order to reduce the input impedance of the two-sided probe, and also to increase the bandwidth, the height of the waveguide is usually reduced by a factor of about 4, but this modification increases the conduction losses

and the manufacturing complexity—both of which are extremely important if one wants to manufacture components for the THz frequency range.

3 Experimental Results and Discussion

To investigate the above theory, we manufactured a scale model of a 400-500GHz mixer block. The waveguide had dimensions of a=47mm and b=22mm, and the probe was fed by an SMA connector which was inserted into the centre, ($d = a/2$), of the broad wall. The central conductor of the SMA connector penetrated 0.5mm into the waveguide and a copper-foil probe was soldered to the end. A major advantage of this arrangement is that a short circuit can be applied at the wall of the waveguide in order to establish a well-defined reference plane for the impedance measurements. It is substantially more difficult to do well-calibrated impedance measurements on a two-sided probe. In order to separate out the intrinsic behaviour of the probe from the behaviour of the probe-backshort combination, we performed measurements on a waveguide that was terminated by two matched loads. The real and imaginary parts of the input impedance were then measured by using a Vector Network Analyser.

In Fig. 3 we show the input impedance of a doubly-matched probe as a function of frequency. In this case the probe was 3mm wide, $2w$. As can be seen, the measurements are in excellent agreement with the theory over the whole range of frequencies tested. An important observation is that the microstrip probe is essentially a low-impedance structure with a typical input resistance in the range 10-100Ω. This range is ideally suited to the characteristic impedances of microstrip lines. From the point of view of SIS mixers, the probe can be used for feeding SIS tunnel junctions over broad ranges of frequency without the need to reduce the height of the waveguide.

We also notice in Fig. 3 that the agreement between theory an experiment is extremely good apart from the resistive component of the longest probe. In fact, as the length of the probe was increased further, so that it became significantly longer than half of the waveguide height, the agreement between theory and experiment deteriorated even more. We attribute the inability of our theory to predict the behavior of very long probes as being due to the fact that the assumption of a one-term sinusoidal current distribution along the length of the probe breaks down.

Because the derivation of the analytical result is rather involved, we have checked the result by evaluating the integral in (11) numerically after substituting the expression for the Green's function given by (12). This reactance has also been plotted in Fig. 3. Clearly, the two are in agreement showing the integrity of our analytical expressions.

Overall, the above result shows that whereas the two-sided probe is essentially a high-impedance structure, the one-sided probe is a low-impedance structure. Moreover, wide-band operation can be obtained with a one-sided probe without the need to reduce the height of the waveguide. In fact, wideband operation with low impedance levels can be obtained with *increased-height* waveguide, and this implies that the upper frequency limit to which waveguide mixers can be manufactured can be extended well into the THz frequency range.

Because of the intrinsic advantages of the one-sided probe, we have started to look at other shapes of metallisation. Shown in Fig. 4 is the input return loss of a radial probe on a quartz substrate. The scale model had a waveguide size of 22×47mm, a radius of 9mm, and a quartz substrate measuring 7×12.5mm. The probe had an opening angle of 90°, and the

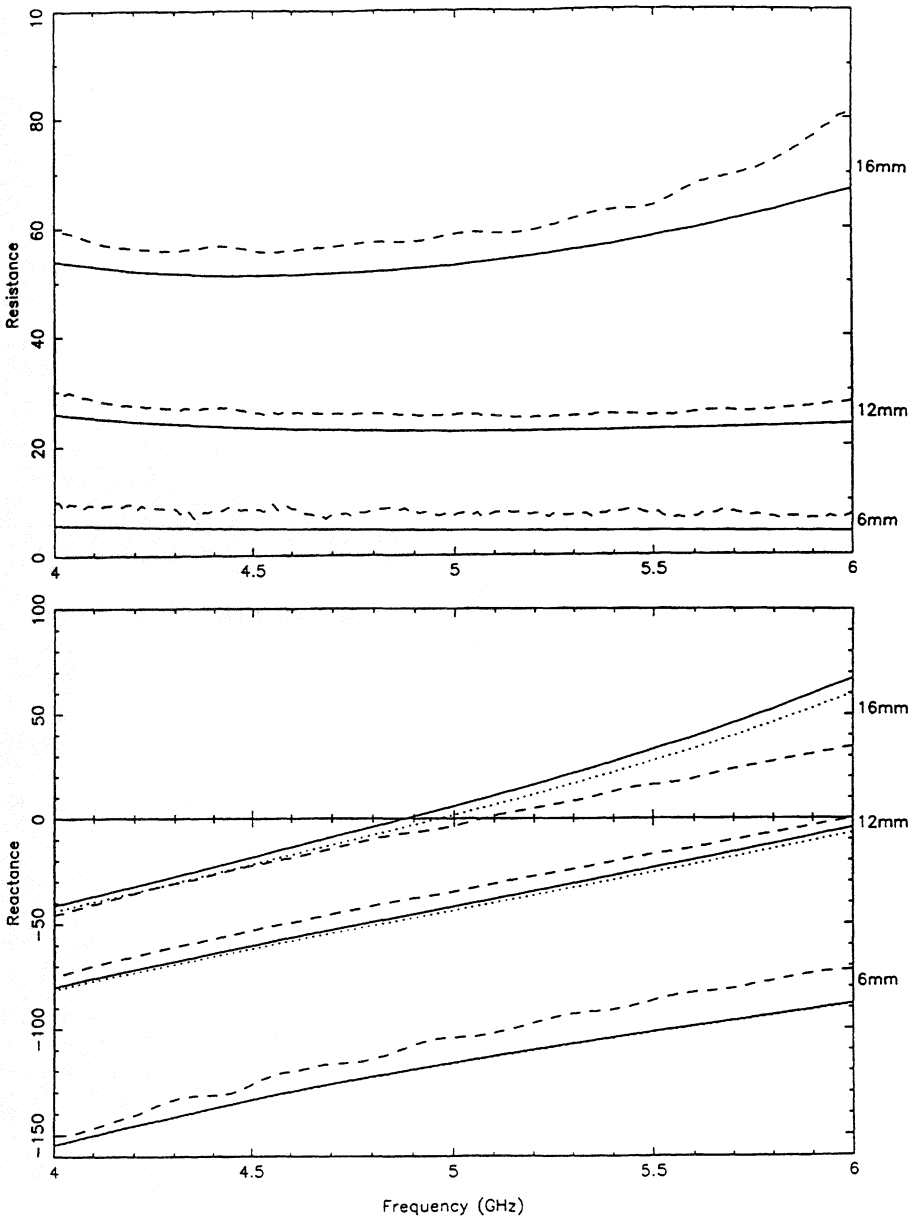

Figure 3: The input impedance of a doubly-matched microstrip probe as a function of frequency for $2w$ =3mm. The waveguide measured 47mm×22mm, and the probe was in the centre of the waveguide. The dashed lines correspond to the experimental data, the dotted lines to the numerical integration, and the solid lines to the analytical expressions.

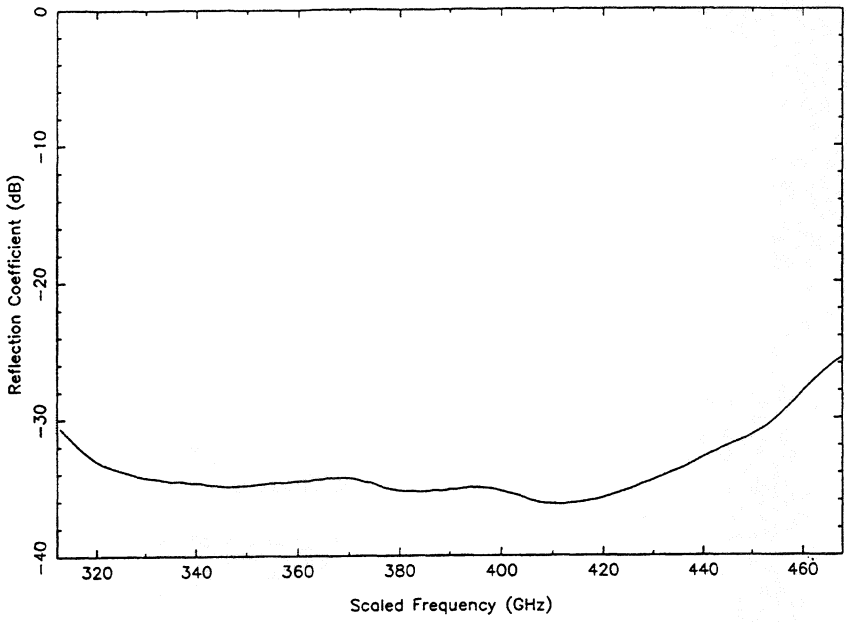

Figure 4: The input reflection coefficient, normalised to 30Ω, of the radial probe described in the text. The frequency scale is that of the final device rather than the model.

backshort was at a distance of 10mm relative to the centre of the probe. This type of probe has the remarkable property that its input impedance is purely real over a very wide range of frequencies, and the resistance is low and can be adjusted merely by changing the length of the probe. In order to investigate this design, and also the hammer-head arrangement used by Kerr [7], theoretically, we have generalised our procedure to handle more complicated current distributions. This has been achieved by evaluating the integral in (8) numerically after calculating the current distribution by means of a Fast Fourier Transform. The results for the rectangular probe described above are the same as the analytical expression derived here, and we are now employing this method to study more complicated geometries.

4 Conclusions

We have derived an analytical expression for the input impedances of one-sided microstrip probes in waveguide, where the integral for the complex radiated power has been evaluated rigorously. We find that, compared to our previous work, where an approximation was made, there is a small difference in the expression for the reactive contributions of the evanescent waveguide modes. The error is, however, only third order in $\beta_{mn}w$, where β_{mn} is the modulus of the propagation constant and w the half-width of the probe.

We conclude that combined with our previous work, we have a rigorous way of calculating the input impedances of one-sided microstrip probes. The supporting dielectric substrate can be taken into account by using the appropriate Green's function. It is important to include the effect of the substrate in submillimetre-wave components, where the substrate

can occupy a significant fraction of the waveguide.

By using a procedure based on the Fast Fourier Transform, we are now extending our analysis to cover other probe geometries, and other current distributions, such as that of the radial probe.

References

[1] R.L. Eisenhart and P.J. Khan, "Theoretical and experimental analysis of a waveguide mounting structure," IEEE Trans. Microwave Theory Tech., vol. MTT-19, pp. 706-717, 1971.

[2] G. Yassin and S. Withington, "Analytical Expression for the Input Impedance of a Microstrip Probe in Waveguide," Int. J. Infrared and Millimetre Waves, vol. 17, pp.1685-1705, 1996.

[3] T.Q. Ho and Yi-Chi Shih, "Spectral-domain analysis of E-plane waveguide to microstrip transition," *IEEE Trans. Microwave Theory Tech.*, vol. MTT-37, pp. 388-392, 1989.

[4] W.L. Weeks, it Electromagnetic Theory for Engineering Applications, John Wiley & Sons, Inc.: New York, 1964.

[5] V.H. Rumsey "Reaction concept in electromagnetic theory," Phys. Rev., vol. 94, pp. 1483-1491, 1954.

[6] Q. Zhang and T. Itoh, "Spectral-domain analysis of scattering from E-plane circuit elements," IEEE Trans. Microwave Theory Tech., vol. MTT-35, pp. 138-150, 1987.

[7] A.R. Kerr and S.-K. Pan, "Some recent developments in the design of SIS mixers," Int J. Infrared Millimetre Waves, vol. 11, pp. 1169-1187, 1990.

LOW COST DIRECT MACHINING OF TERAHERTZ WAVEGUIDE STRUCTURES

G. Narayanan[1], N. R. Erickson, and R. M. Grosslein
Five College Radio Astronomy Observatory, University of Massachusetts, Amherst, MA 01003

ABSTRACT

We present a low cost technique of direct machining of precision waveguide structures on metal blocks. The micro machine setup employs compact, precision numerically controlled (NC) stages to automate the machining process. Endmills are held in high speed pneumatic spindles, while other features are made by scraping ("broaching") in repeated small passes. We can set up two endmills and three broaches at the same time. The fabrication process is monitored under a microscope, while the ambient temperature conditions are controlled. The NC code is generated from a combination of AutoCAD drawings, commercially available CAD/CAM software and simulation software we developed for this process. Both halves of a reasonably complex tripler block can be fabricated in under 3 hours, including setup time. An estimate of the machining accuracy is about 7 μm, the accuracy being principally limited by the difficulties in visually inspecting the microscopic machined features and correcting the small tool offsets. We also discuss methods to extend this technique to the fabrication of THz waveguides.

1 Introduction

Traditional metal blocks manufactured using conventional machining techniques are used in most successful receiver systems in the submillimeter wavelength range. The components of such receiver systems include oscillators, multipliers and mixers, which mostly incorporate waveguides and their associated transitions. The waveguide is a well characterized, low-loss transmission medium, which affords easy and excellent coupling of the freespace modes to electronic circuit elements. As the desired wavelength of operation becomes smaller, so do the dimensions of waveguide and quasi-optical elements that comprise a receiver system. On the one hand, the small sizes are advantageous in the fabrication of high-resolution focal-plane imaging receiver systems. Such arrays have applications like radio astronomy, commercial and industrial applications like the extension of millimeter technology to collision avoidance

[1]e-mail: gopal@fcrao1.phast.umass.edu

radars, aircraft guidance and landing, contraband detection and personal communication systems, all of which benefit from having a large number of elements in a compact, practical sized system. However, as the sizes of components scale down, the cost of fabrication goes up. Indeed, the fractional cost of machined metal blocks containing waveguide electromagnetic elements in the overall budget of receiver systems, especially those that involve arrays, becomes prohibitively high with increasing frequency.

In the past decade or so, non-traditional techniques that can be collectively called "micromachining" are demonstrating practical means for producing a variety of submillimeter and terahertz frontend components [1]. Micromachining as a class is derived from manufacturing tools based on batch thin and thick film fabrication techniques of the electronic industry [2]. Many novel micromachining methods such as silicon wet etching [3], laser micromachining [4, 5], mold replication by the method of mastering, molding and casting [6] have demonstrated examples of components with performance equalling that produced by conventional machining. These new techniques, although offering great potential for the future, have many drawbacks, most of which are primarily due to the relative youth of such technologies.

At least for the submillimeter and low terahertz frequencies, conventional machining of metal, which has a long history of manufacturing engineering, can be used to fabricate receiver components. The method often used is the so-called "split-block" technique, where the circuit structures are machined on two (or more) metal blocks and then mated together to form complete components. The split-block technique offers the advantage that the machining is in principle straightforward. In addition, circuit components such as RF chokes, diodes and coupling structures can be easily placed on the split blocks prior to assembly of the complete piece. In the past, the main problems of conventional machining as applied to the fabrication of submillimeter and terahertz receiver systems have been (1) the high cost of machine tools and equipment, (2) the high level of expertise required of the machinist and (3) the fabrication time requirements. In this paper, we present a low cost technique of direct machining of waveguide structures on metal blocks that addresses all three of the aforementioned problems.

2 Micro NC Machine Setup

2.1 Positional Stages and Tooling

A schematic view of the machining setup is shown in Figure 1. The block to be machined is held in a metal plate that is attached to linear, compact, precision XYZ positioners [7]. The positioning stages employ precision ground leadscrews which have 5 μm of accuracy over the full 2 inches of travel. The resolution of movement of the stages is 0.1 μm, while the grating period and readout of the linear optical encoders sets the effective resolution to 1 μm. The drive systems for these positioners

employ DC servo motors with rotary encoders for closed loop positioning feedback. The stages are made out of special-alloy aluminum tooling plate for good stiffness and long-term stability.

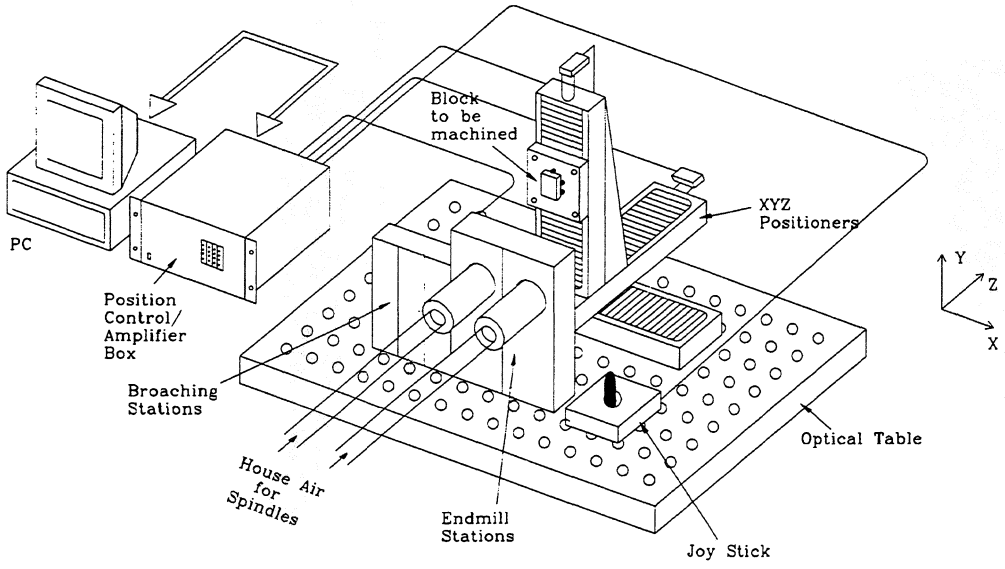

Figure 1: Schematic view of the micro NC machine.

Motion control of the positioning stages is accomplished with the PC-bus based Unidex 500 series controller [7]. The U500 interface card in the PC is connected to the DR500 amplifier/drive chassis. The amplifier and control box has cabling to control the XYZ drives. A digitizing joystick is also part of the system. The joystick allows the user to control the stages for coarse adjustments, tool registration and workpiece inspection. During actual machining, the joystick is disabled. The Windows based toolkit software has the option of loading user-supplied NC code and the option of single-stepping or free-running modes of operation.

Depending on the actual features to be cut, the removal of metal is accomplished with three different machining strategies and five different tools: milling with two endmills, broaching with an endmill insert, and scraping with two saws. Figure 2 shows a photograph showing the top view of the five tool holders.

The endmills are held in high speed, precision air bearing spindles that run at

Figure 2: Top view showing arrangement of tools.

70,000 rpm [8]. Air bearing spindles have low vibration and exhibit smaller temperature rise compared to electric motor driven spindles. For a given tool and workpiece material, there is an optimal cutting speed (CS) of machining, which is available from a machinery handbook [9]. For a given CS, measured in feet per minute (fpm), the spindle speed required, N, is given by $N = 3.82\frac{CS}{D}$ rpm, where D is the diameter of the cutting tool in inches. For small diameter endmills, required spindle speeds can be quite high. If higher spindle speeds are not available, the feed rate needs to be proportionately slower, resulting in increased time for machining. For high speed steel (HSS) endmills on brass, nominal CS is 100 fpm [9]. The required spindle speed for a 5 mil endmill is 76400 rpm. With regards to precision machining, the high spindle rpm that is a necessity for fabrication with small tools has some ancillary benefits as well: (1) High spindle speeds also has the effect of reducing the chip size by requiring a smaller feed rate per tooth, f_T (since $f_T \propto \frac{1}{N}$). Smaller chip loads result in improved surface finish. Good surface finishes are crucial for cutting down on waveguide losses. (2) High spindle rpm can reduce or eliminate secondary operations (such as deburring, or using finish passes) by improving surface finish of the workpiece in the primary machining operations. (3) The reduced cutting forces due to high spindle rpm gives better control while machining thin walls or brittle materials. (4) Reduced cutting

forces reduces the heat transfer into the workpiece. A greater percentage of the heat generated by cutting is carried away with the chip in high speed machining. Reduced workpiece distortion leads to more accurate parts. (5) The high level of precision in the motion of the positioning stages is achieved in the absence of significant loads on the stages. High spindle speeds with small radial feeds are helpful in reducing the load, and hence in maintaining accuracy of the finished work. (5) High spindle speed is less likely to excite vibrations in the workpiece.

Dry, purified house air is used to power the turbines of the air bearing spindles to a constant speed of 70,000 rpm. The house air which usually has a pressure range between 85 to 105 psi is sent to a refrigerated air dryer [10]. Coalescing compressed air filters [11] are used at the inlet and outlet of the dryer. After passing through additional filters to remove any remaining particulates, the air enters a regulator which sets the output pressure to 80 PSI. A pressure switch/alarm detects any drop in pressure from the house air supply. Air for the spindle bearings is sent through a check valve. A backup nitrogen tank container is used to provide air for the spindle bearings should the house air fail during machining operations. The nitrogen tank can provide 25 minutes of bearing air in the absence of house air, so that spindles can be spun down safely. The spindle turbines are run directly from the regulated house air supply. As shown in Figures 1 and 2, two spindles are available for machining. The house air pressure is adequate for powering both spindles at the same time. However, the usual machining operation proceeds by using one of the spindles at one time.

The smallest endmill available commercially is of the order of 4 mils in diameter. Another problem machining with endmills is that they are not effective in cutting pockets where the depth is large compared to the diameter of the tool used. The typical cutting length of commercial endmills is only about 2 diameters (lengths of upto 3 diameters are sometimes available on special order). Thus endmills cannot be used for small and/or deep waveguide sections. For features smaller than 5 mils, thin saws are used in the micro NC machine. Small amounts of material are removed in repeated passes by "scraping" (broaching) type of operations where the workpiece is moved against a single saw tooth of a stationary blade. By exposing more of the tooth from the clamp, deeper cuts can be achieved. For example, a 5 mil saw was used to cut a waveguide section 18 mils deep. The saws, however are only capable of cutting straight sections of waveguide. Two saws of thickness 5 mils and 2 mils are used in the machine. The two saw blades are oriented so that their cutting motion is 180° from each other, that is, one saw cuts in the positive Y direction, while the other cuts in the negative Y direction.

Another tool that is used in the micro NC machine is a special order carbide milling insert with a sharp 90° corner [12]. This tool is used to cut diagonal feedhorns [13]. The insert was clamped in a stationary mount, and the horns cut by moving the workpiece in linear ramping motions only in the X-Z plane.

During actual fabrication, there are no tool changes involved. The workpiece is carried by the precision positioning stages to each tool. The relative coordinates of the tool positions to the workpiece are initially carefully measured by using target marks made at the same location by all tools on a corner of the workpiece. An electrical edge-finder is also used to determine tool offsets from the edges of the workpiece. In conventional milling machines many tool changes are required to fabricate parts, which can result in considerable errors in the fabricated parts.

For the sake of clarity, two other components that make up the precision machine system are not shown in Figure 1: a lubrication arrangement and a microscope viewing station. Lubrication for the machining operation is provided using a biostable, water soluble machine oil [14] that is delivered onto the work using a fixed clamp. The lubricant carries out the chips to a collecting pan and is recycled for use within a closed cycled system consisting of a gear pump, a water aspirator, a filter and a reservoir. Antifoaming additives are added to the lubricant mix to prevent foaming of the water soluble oil mixture. A specialized adjustable microscope mount allows the user to watch the actual machining operation with appropriate magnification. The microscope is mounted parallel to the Y-axis to allow for continuous monitoring of the machining operation.

2.2 Temperature Control

One of the crucial issues in precision machining is maintaining a constant temperature of the positional stages and the tool holders. At the tolerance levels required for fabricating high frequency waveguide structures, temperature changes of a few degrees can result in considerable errors. In this respect, the high speed air bearing spindles offer another advantage compared to conventional electric motor driven spindles which exhibit temperature increases of several tens of degrees during operation. The temperature rise in the air bearing spindles is only a couple of degrees centigrade after half an hour of operation, after which it remains stable. In order to understand the temperature stability of the room while operating the machine, temperature was monitored at eight different locations in and around the micro NC machine and careful records were kept.

After repeated experiments machining with and without temperature control, it was found that a closed loop temperature control system significantly improved machining accuracy and repeatability. A heater on the metal blocks that house the spindles (seen on top of the spindles in Figure 2) forms part of the control loop. Before commencing actual machining the machine is usually run for ten to twenty minutes to reach temperature equilibrium. Several fans and blowers are run around the machine to provide adequate circulation of air. At present, although the temperatures of the positional stages and workpiece are monitored, they are not controlled. The closed loop system maintains the temperature of the spindles to within half a degree of the temperature set point, 26° C, which is a few degrees above ambient.

2.3 Software Issues

The numerical control (NC) code to operate the stages is in "G-code" format, which is an industry standard. The initial design from 3-d Autocad drawings is imported into a commercial CAD/CAM package called Surfcam[15]. Surfcam is capable of generating NC code for 2-axis and 3-axis milling and for turning (lathe operations). Rectangular pockets and grooves are defined as 2-axis paths, while surface machining (where the feature bottoms could have ramps) are defined as 3-axis toolpaths. After chaining features to define the toolpaths, the NC code is generated within the software. Surfcam also has a graphical simulator to view the tool motions involved in the machining operation. A postprocessor that is specific to our chosen geometry and coordinate system was written. Running the postprocessor produces the required NC code. At present the NC code for the broaching operations is written manually. In order to test and troubleshoot the final NC program, a software program was written to convert NC code to a 3-d Autocad script file, which is subsequently run and viewed within Autocad to perform final verification. The combination of reasonably inexpensive commercially available software and overall ease of use of complimentary in-house software helps further reduce the normally high cost of precision machining.

3 Fabrication of Receiver Components

The micro NC machine described above has been used to fabricate several state-of-the-art receiver components. We have successfully fabricated several blocks of a 810 GHz tripler. The electromagnetic design for the tripler is outlined in [16]. Figure 3a shows a photograph of the split block of the fabricated tripler. Five different tools were used in the fabrication: two endmills of diameter 8 mils and 4 mils respectively, two saws of thickness 5 mils and 2 mils respectively, and the horn broach described above. Figure 3b shows a magnified view of the features in one half of the tripler block. The smallest feature of the tripler block is a 2 mil wide, 6 mil deep waveguide section. This section, that is part of the output waveguide, was cut using the 2 mil saw. The fabrication proceeded with the preliminary roughing operations with the endmills, followed by broaching with the horn broach and the saws. Subsequently, final deburring passes were required to remove chips generated by the broaching operations. After a few trial runs with dummy blocks, several fully functional units were fabricated. Careful inspection of the resultant metal blocks revealed a maximum error of ~ 7 μm. Including setup time, both halves of the tripler block were fabricated in under three hours. The performance of the tripler fabricated with the micro NC machine was found to be comparable to a previous tripler fabricated with conventional machining. One of the finished tripler blocks now forms part of the LO system for a 810 GHz SIS receiver system being used currently at the South Pole AST/RO facility.

With this low cost precision machining technique, it is now possible to consider the construction of large format arrays of high performance heterodyne waveguide receivers. The first test SIS mixer block of a seven element 345 GHz focal plane

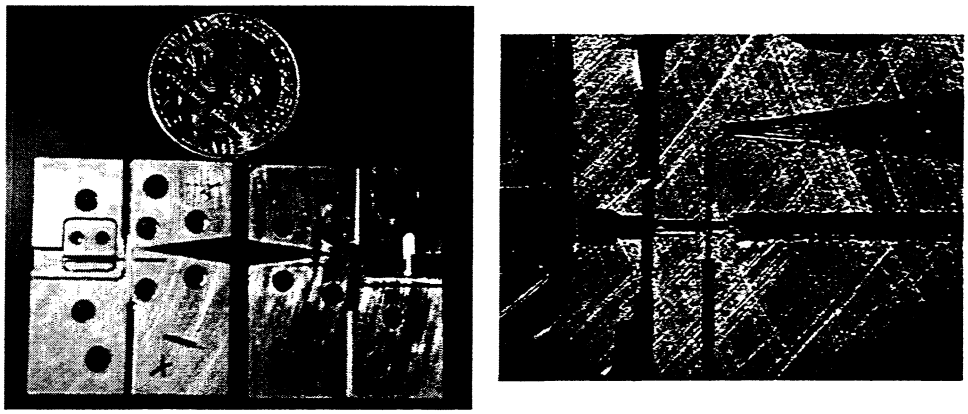

Figure 3: (a) Photograph of split blocks of a 810 GHz tripler fabricated using the micro NC machine. (b) Magnified view of one half of the tripler block showing details of the waveguide features. For details of the electrical design see [16].

array [17] for the HHT was fabricated with the micro NC machine. Figure 4(a) shows the fabricated split blocks and Figure 4(b) shows the magnified details of one half of the split block. The mixer employs a diagonal feed horn to half-height rectangular waveguide transition. A suspended stripline substrate channel orthogonal to the waveguide houses the SIS junction. The 345 mixer block was machined with the horn broach described above and a 6 mil endmill. The maximum error in the machined mixer blocks is ~ 8 μm.

The micro NC machine has also been used as a precision lathe to turn coaxial pins to be used in multiplier circuits. The pin is held in the high speed spindle and one tooth of a saw blade held in the XYZ positioners was used as the turning tool. Preliminary results of this procedure indicates that the remaining problems to overcome in making precision, micro diode pins are mostly related to software issues.

4 Fabrication Considerations for Terahertz Components

The resolution and accuracy of the positional stages in the present system can be upgraded with commercially available stages. However, one of the principal limitations to extending this technology to terahertz waveguides is the requirement for small tools. For example, the dimensions of a half-height 2.5 THz waveguide are $\sim 96 \times 24\mu$m. To fabricate such a waveguide, one would need a cutter smaller than 1 mil in diameter. Grinding down saws to small thicknesses should be feasible by using the high-speed spindles as a microgrinder. Only straight sections of waveguide can be fabricated with these tools. The rigidity of a tool is inversely proportional to the third power of its thickness. In order to prevent breakage of thin saws, the toolholder will

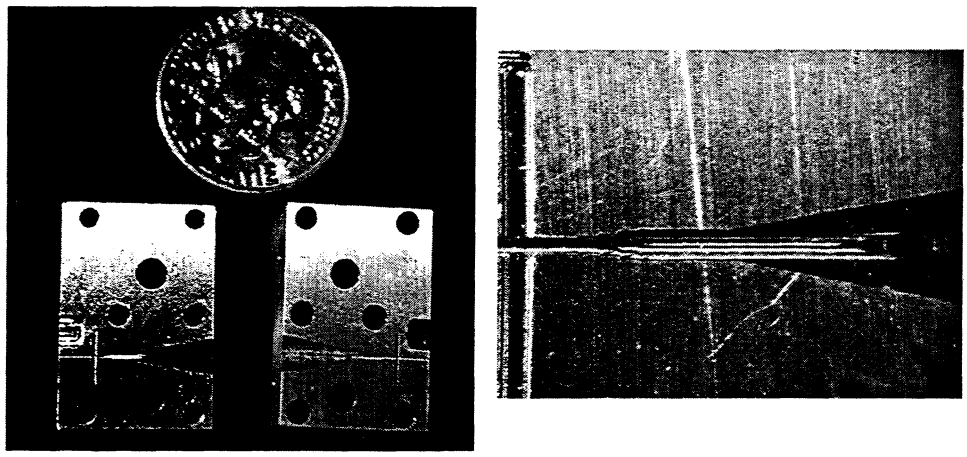

Figure 4: (a) Photograph of split blocks of a 345 GHz SIS mixer block fabricated using the micro NC machine. (b) Magnified view of one half of the mixer block showing details of the transition from diagonal feedhorn to half-height waveguide. For details of the electrical design see [17].

need to clamp the tool closer to the cutting edge, which in turn causes the maximum cutting depths to become shallower. One alternative is to make custom endmills, which when used in the high speed spindle does not suffer the rigidity problems of stationary tools.

Another challenge in the fabrication of terahertz structures is maintaining the temperature of the workpiece and toolholders. Enclosing the entire machine in a closed chamber and using a closed loop system with less than 0.1 K of absolute change in temperature will result in higher dimensional accuracy of the parts produced.

The features that are produced with the micro NC machine are extremely tiny and stretch the limit of metrology tools associated with conventional microscopes. One of the limitations of the current system is the difficulty of measurement of test target features to identify tool coordinates with respect to the workpiece. Good relative tool registration between tools and the work is crucial in the production of useful terahertz components. A metrology system with a high resolution digital camera attached to high magnification scopes and coupled with an image processing software package will be required to improve the accuracy of measurement and thus correction of relative tool positions.

5 Summary

1. A low cost technique for the fabrication of terahertz waveguide components by direct machining on metal has been presented. The machine setup uses high

speed air bearing spindles, precision positioning stages and NC programming to cut down costs, fabrication time and expertise levels required for the fabrication of high frequency components.

2. This novel micro NC machine has been used to fabricate a 810 GHz tripler and elements of a 345 GHz focal plane array.

3. With relatively minor improvements, this technology has potential to be extended to produce reliable terahertz receiver components up to 2.5 THz.

6 References

[1] V. M. Lubecke, K. Mizuno, and G. M. Rebeiz, "Micromachining for Terahertz Applications", IEEE Trans. on Microwave Theory and Techniques, vol 46, No. 11, pp 1821-1831, November 1998.

[2] M. Madou, "Fundamentals of Microfabrication", CRC Press New York, 1997.

[3] R. McGrath, C. K. Walker, M. Yap, and Y. Tai, "Silicon Micromachined Waveguides for millimeter-wave and submillimeter-wave frequencies", IEEE Microwave and Guided Wave Letters, vol 3, 61, 1993.

[4] C. K. Walker, G. Narayanan, A. Hungerford, T. Bloomstein, S. Palmacci, M. Stern, J. Curtin, J., "Laser Micromachining of Silicon: A New Technique for Fabricating TeraHertz Imaging Arrays", Astronomical Telescopes and Instrumentation, SPIE Symposium, Kona, Hawaii, 1998.

[5] C. K. Walker, G. Narayanan, T. M. Bloomstein, "Laser Micromachining of Silicon: A New Technique for Fabricating Terahertz Waveguide Components", 1997, 8th International Symposium on Space Terahertz Technology, eds. Blundell and Tong, Harvard University.

[6] T. W. Crowe, P. J. Koh, W. L. Bishop, C. W. Mann, J. L. Hesler, R. W. Weikle, P. A. D. Wood, and D. Matheson, "Inexpensive Receiver Components for Millimeter and Submillimeter Wavelengths", 1997, 8th International Symposium on Space Terahertz Technology, eds. Blundell and Tong, Harvard University.

[7] Aerotech, Inc., Pittsburgh, PA 15238.

[8] Westwind Air Bearings Ltd., Dorset, England.

[9] Machinery's Handbook, 1996, Industrial Press.

[10] TK20A Air Dryer, General Pneumatics, Ocala, FL 34474.

[11] Wilkerson M30-04-F00 coalescing air filter, D. L. Thurott Inc., South Windsor, CT 06074.

[12] Lovejoy Tool Co. Inc., Springfield, VT 05156.

[13] J. F. Johansson, and N. D. Whyborn, "The Diagonal Horn as a Submillimeter Wave Antenna", IEEE Trans. on Microwave Theory and Techniques, vol 40, No. 5, pp 795-800, May 1992.

[14] Astro-cut 2001 A, Monroe Fluid Technology, Hilton, NY 14468.

[15] Surfcam v7.1, Surfware Inc., Westlake Village, CA 91362.

[16] Erickson, N. R., and Tuoivinen, J., "A Waveguide Tripler for 720-880 GHz", Proceedings of the Sixth Int'l Symposium on Space Thz Tech., pp 191-198, Mar 1995.

[17] G. Narayanan, C. K. Walker, H. Knoepfle, and J. Capara, "Design Of Mixer Elements For The HHT 345 GHZ Heterodyne Array Receiver", Proceedings of the Ninth Int'l Symposium on Space Thz Tech., pp 433-442, Mar 1998.

A HIGH RESOLUTION SPECTROMETER FOR THE INVESTIGATION OF MOLECULAR STRUCTURES IN THE THZ RANGE

G.W. Schwaab
Physical Chemistry II, Ruhr-Universität Bochum
Universitätsstraße 150, Build. NC 7/71, D-44801 Germany

H.-W. Hübers, J. Schubert, Patrik Erichsen
DLR Institute of Space Sensor Technology
Rudower Chaussee 5, D-12489 Berlin

G. Gol'tsman, A. Semenov, A. Verevkin, S. Cherednichenko, E. Gershenzon
MSPU, 1, M. Pirogowskaya St., 119435 Moscow, Russia

Abstract

A status report on the design study of a novel tunable far-infrared (TuFIR) spectrometer for the investigation of the structure of weakly bound molecular complexes is given. The goal is a sensitive TuFIR spectrometer with full frequency coverage from 1-6 THz. To hit the goal, advanced sources (e.g. p-Ge lasers) and detectors (e.g. superconducting hot electron bolometric (HEB) mixers) shall be employed to extend the technique of cavity ringdown spectroscopy, that is currently used at optical and infrared frequencies to the FIR spectral range. Critical for such a system are high-Q resonators that still allow good optical coupling, and wideband antireflection coatings to increase detector sensitivity and decrease optical path losses. 2^{nd} order effective media theory and an iterative multilayer algorithm have been employed to design wideband antireflection coatings for dielectrics with large dielectric constants like Ge or Si. Taking into account 6 layers, for Si bandwidths of 100% of the center frequency could be obtained with power reflectivities below 1% for both polarizations simultaneously. Wideband dielectric mirrors including absorption losses were also studied yielding a bandwidth of about 50% with reflectivities larger than 99.5 %.

Introduction

Recent advances in terahertz (THz) technology allow the construction of improved tunable far-infrared (TuFIR) spectrometer systems, that can be used for the investigation of the structure of small molecular clusters. Ideally, such a system would cover several octaves (e.g. 0.5 to 6 THz) with a linewidth considerably below 1 MHz, and a sensitivity close to the quantum limit. If one wants to employ rapid detection or heterodyne detection, one needs a broad band low noise temperature mixer as detector and a widely tunable radiation source as local oscillator.

From the mixer side, superconducting hot electron bolometric (HEB) mixers have revolutionized heterodyne detection in the THz range, because they work as quantum detectors with low noise temperature and low local oscillator power needs (< 1 μW). Two possible realizations of the HEB differ according to the type of electron cooling mechanism used, either heat transfer to phonons via electron-phonon-interaction (phonon cooled HEB mixers)[1] or out-diffusion of hot electrons from the device (diffusion cooled HEB mixers)[2]. Recently, with a single phonon-cooled HEB mixer mounted in a spiral antenna on an elliptical Si lens low noise temperatures have been measured from 700 GHz to 5.2 THz[3]. Part of the optical losses (about 30% or 1.5 dB) are due to the reflection of the radiation at the Si-air surface.

From the local oscillator side several options are possible like BWOs (direct or multiplied), laser sideband generation[4,5,6], optical mixers[7,8], or p-type Ge lasers[9]. While laser sideband generation has been in use for more than a decade now, p-Ge lasers provide the most promising aspects for an improved spectrometer for the frequency range between 1 and 4 THz, since they are solid state devices with their maximum output power in the frequency range needed and they can be easily tuned by changing the magnetic field. The draw-backs of p-Ge lasers are their pulsed operation and their internal mode spacing which is defined by the length of the laser crystal. Improved systems should therefore be operated with an external resonator and anti-reflection coated front surfaces.

For spectroscopic applications, the pulsed laser still can be used. This has for example been done in the field of cavity ringdown spectroscopy[10], where instead of directly measuring the absorption of a gas, the Q-factor of a resonator cavity is measured with and without an absorbing gas. Briefly, a high-Q resonator is illuminated by a short laser pulse. At the resonator output an exponentially decaying series of signal pulses appears whose decay time is a measure of the resonator quality. An absorbing gas in the resonator will change this decay time in a way that the absorption coefficient can be calculated. The sensitivity of this method is extremely dependent on the reflectivity of the end mirrors. The higher the reflectivity, the more sensitive the spectrometer.

Summarizing, to be able to develop a new type of TuFIR spectrometer, two optical problems have to be tackled: first, the fabrication of wide-band anti-reflection coatings for the surfaces of Si lenses or the surface of a p-type Ge laser, and second, the design of wideband high-reflectivity FIR mirrors. To be able to theoretically study these problems, a computer program has been developed, that includes iterative handling of multilayer optical problems and second order effective media theory to simulate artificial dielectrics. In the following, the underlying theory of the code is described and some applications to wideband antireflection coatings and high-reflectivity FIR mirrors are shown.

Recursive Formalism for Multilayer Optics

The reflection and transmission of a multilayer optics can be calculated recursively by taking into account the reflections and transmissions at the boundaries between different layers and the phase delay within one layer. Figure 1 shows a N-layer system with layer thickness d_i, index of refraction n_i, and propagation angle θ_i for the i-th layer. With the incident electric field E_i, and the reflected electric field E_r, the total field reflection coefficient $\rho_j = \frac{E_r}{E_i}$ of layers j+1 through N is given by[11]

$$\rho_j = \frac{r_{j,j+1} + \rho_{j+1}\, e^{2i\delta_{j+1}}}{1 + r_{j,j-1}\, \rho_{j+1}\, e^{2i\delta_{j+1}}}$$

Here, $r_{j,j+1}$ represents the field reflection coefficient at the boundary of layers j and j+1, which is given by the Fresnel formulae[12], ρ_{j+1} the total field reflection coefficient of layers j+2 through N, i the $\sqrt{-1}$, and δ_{j+1} the phase delay in layer j+1. The phase delay is given by the relationship

$$\delta_j = 2\pi \frac{\nu}{c} n_j\, d_j \cos\vartheta_j$$

with c the velocity of light and θ_j the propagation angle of the radiation in layer j. The θ_j can be calculated from the incident angle θ_i using Snellius' law.

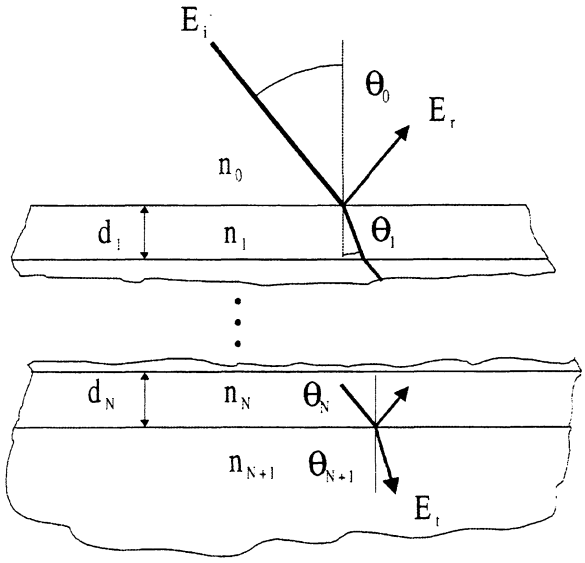

Figure 1: Schematic of a N-layer optics with incident field E_i, reflected field E_r, and transmitted field E_t. Each layer is described by its thickness d, its refractive index n, and its propagation angle θ.

For the total transmission τ_j of the multilayer optics, in a similar way the following formula can be derived:

$$\tau_j = \frac{\frac{n_{j+1}}{n_j}\frac{\cos\vartheta_{j+1}}{\cos\vartheta_j} t_{j,j+1}\,\tau_{j+1}\,e^{i\delta_{j+1}}}{1 + r_{j,j+1}\,\rho_{j+1}\,e^{2i\delta_{j+1}}}.$$

Here, $t_{j,j+1}$ represents the Fresnel field transmission factor at the boundary between layers j and j+1 as calculated by traversing from layer j into layer j+1. Please note, that for the transmission formula the layers are counted just opposite to the labeling in Figure 1 so that the numbers increase looking backward from the transmitted beam.
The power reflection and power transmission coefficients can be calculated from ρ_j and τ_j by taking the absolute square value, respectively. The phase shift is given by the overall argument of the expression. The formulae given here are based on plane-parallel surfaces and take not into account any walk-off effects due to Gaussian beam characteristics or a tilt between the different layers. However, they do include absorption effects: absorption can be characterized by a complex index of refraction, where the imaginary part represents the absorption in the medium. Both the Fresnel formulae and the Snellius law are still valid for complex indices of refraction (although, the angles θ_j become complex and more difficult to interpret).

2nd Order Effective Media Theory

Artificial dielectrics single layer antireflection coatings are well known in microwave technology and have been widely used for example to coat the surface of dielectric lenses[13]. Generally, they consist of a 1- or 2-dimensional periodic structure on the material surface, that is small enough to be seen as an effective dielectric medium by the incident wave. The advantage of artificial dielectric coatings is that they can be fabricated directly from the material in use and are therefore less susceptible to differential thermal expansion problems (e.g. for LHe systems). Also, in the frequency range between 1 and 6 THz there are not many materials available, that show low loss and good thermal behaviour as coatings for Si or other low-loss semiconductor optical elements.
The main disadvantage of such coatings at THz frequencies is their fabrication, since the dimensions necessary are between the dimensions manageable by mechanical means and those that can be etched. Only recently, new techniques, like laser ablation have been demonstrated, that can be used for fabricating those coatings.
The theory of one-dimensional antireflection structured surfaces is described in [11]. Incident radiation propagating in a dielectric with permittivity ε_i is partly transmitted through the surface of a dielectric with permittivity ε_t (see Figure 2). To minimize reflection losses, the surface is ruled with tapered grooves, that are approximated by a 1-dimensional step-function. The period of the grating is Λ, it's grating vector is K.

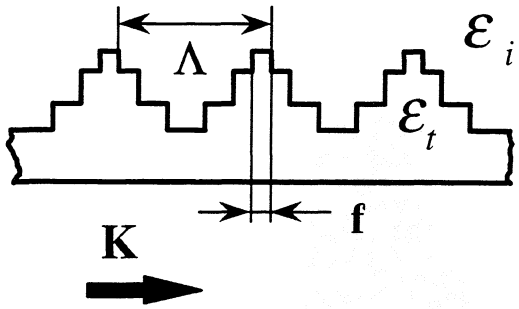

Figure 2: Multilayer antireflection coating between dielectrics with permittivities ε_i and ε_t by one-dimensional periodic surface grating. Λ is the grating period, K the grating vector, and f the filling factor of the grating.

The index of refraction at each level of the step function can be described by second order effective media theory. To be sure that no surface waves are generated by the grating, and that only the 0th diffraction order can be excited, one has to ensure that the design constant β fulfills the relationship

$$\beta = \frac{\lambda}{\Lambda}\frac{1}{n_i + n_t} \geq 1$$

with λ the wavelength of the wave, and n_i and n_t the indices of refraction of the incident and transmitting medium, respectively. For large values of β the grating period Λ becomes small which complicates fabrication of the structure. On the other hand, if β becomes smaller than unity, at certain angles higher orders can be diffracted. Thus, β is typically chosen to be unity (β=1).

One-dimensional surface gratings create birefringence for the two polarizations with the field vector E perpendicular to K and E parallel to K. To second order theory, the relationships are:

$$\varepsilon_{E\perp K}^{(2)} = [f\,\varepsilon_t + (1-f)\,\varepsilon_i]\left[1 + \frac{1}{\beta^2}\frac{\pi^2}{3} f^2 (1-f)^2 \frac{(\alpha_n - 1)^2}{1 + f(\alpha_n^2 - 1)}\right]$$

for E perpendicular to K with f the fraction of the grating period that is filled with permittivity ε_t, and $\alpha_n = n_t / n_i$. For E parallel to K, the expression is

$$\varepsilon_{E\parallel K}^{(2)} = \left[\frac{f}{\varepsilon_t} + \frac{(1-f)}{\varepsilon_i}\right]^{-1}\left[1 + \frac{1}{\beta^2}\frac{\pi^2}{3} f^2 (1-f)^2 \frac{f(\alpha_n^2 - 1)}{\alpha_n^2 - f(\alpha_n^2 - 1)^2}\right]$$

Note, that in both formulae the expression in the left bracket gives the 0th order approximation as it can be found for example in [13].

Wideband Anti-Reflection Coatings for Highly Refractive Materials

To achieve the goal of wideband FIR antireflection coatings, second order effective media theory for one-dimensional surface gratings has been combined with the multilayer formula to optimize the index of refraction gradient.

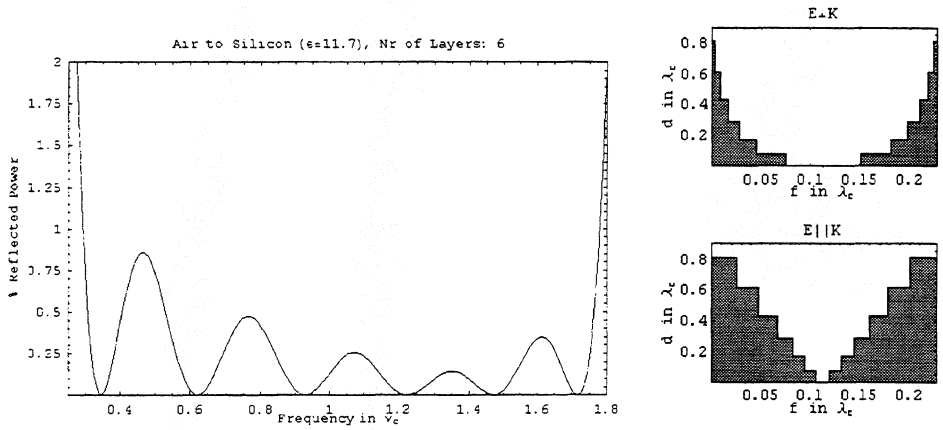

Figure 3: left: Power reflected off an air-silicon transition antireflection coated with a 6 layer one-dimensional surface grating. The coating has been optimized for single polarization radiation, the frequency is given relative to the design frequency ν_c. Right: the optimized shape of the grooves for the E-field perpendicular to the K-vector (above) and parallel to the K-vector (below). All dimensions are relative to the design wavelength λ_c.

In the mm-wave to FIR region most dielectrics change their index of refraction only slightly, if at all[13]. Therefore it is advantageous to calculate optimized grooves in a wavelength independent way; i.e. grating period, layer thickness, layer spacing, and the bandwidth of the coating are given in relative frequencies for a particular index of refraction. The result may then be used to tailor the coating for the application frequency range.

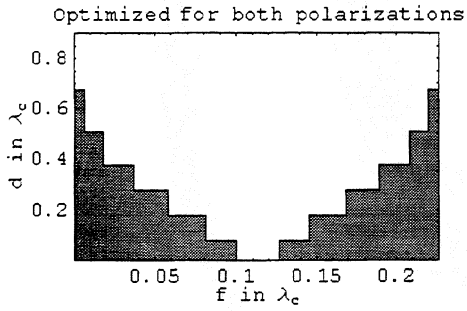

Figure 4: Groove shape optimized for minimum reflection for arbitrary polarization. Dimensions are given in units of the design wavelength

Numerical optimization was used to minimize the power reflection for a given ratio ν_{max}/ν_{min} and to calculate optimized groove sizes. Figure 3 shows the bandwidth that can be achieved for singly polarized radiation for an air-Si (ε=11.7) transition with a 6 layer antireflection coating. While the single surface

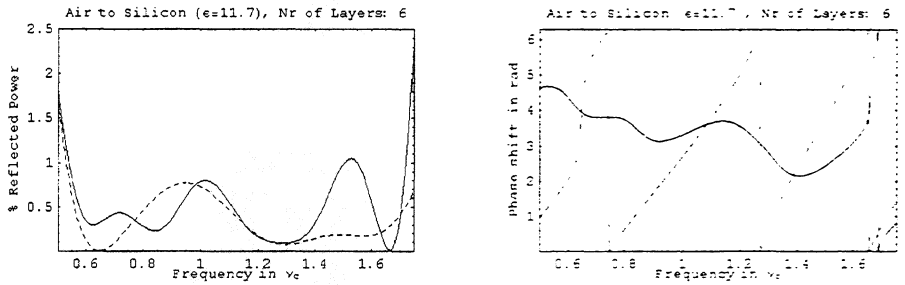

Figure 5: left: Power reflected off an air-silicon transition antireflection coated with the 6 layer one-dimensional surface grating shown for E perpendicular K (solid line) and E parallel K (dashed). The coating has been optimized for minimum reflection for both polarizations. Right: phase shift for both polarizations.

power reflection of an air-Si transition is 30%, a power reflection of less than 1 % can be achieved over $\nu_{max}/\nu_{min} \approx 6$. The birefringent behavior of the method is demonstrated by the different groove shapes necessary for the E-field of the incident light perpendicular and parallel to the K-vector of the grating, respectively, to achieve the same AR-performance.

The same number of AR-layers can also be optimized to achieve minimum reflection for both polarization directions simultaneously. The optimized groove shape is shown in Fig. 4. The total thickness of the AR coating is smaller than that for single polarization coatings, and the shape lies in between those for the two single polarization cases.

The reflected power as well as the phase shift versus frequency for both polarizations is shown in Figure 5. Again, the power reflection is below 1% for both polarizations. However, the bandwidth is reduced to $\nu_{max}/\nu_{min} \approx 3$. Although the reflectivities are about the same for both polarisations, the phase shift versus frequency behaves very different: for E$\perp$K the phase shows only minor changes over most of the frequency band, while for E$\parallel$K the phase is continuously increasing.

Wideband Dielectric Mirrors for High-Q THz Resonators

The multilayer algorithm has also been used to investigate high-reflectivity FIR mirrors as they have to be used in resonators for advanced TuFIR spectroscopy. The simplest possible way to build such a mirror is stacking alternating $\lambda/4$-layers of materials with high and low index of refraction (see Fig. 6, left). Calculations where performed for four $\lambda/4$-layers of Si separated by $\lambda/4$-layers of air. Fig. 6, right shows 1-R of such a system, R being the power reflection coefficient. For lossless material, reflectivities higher than 99.9 percent can be achieved with a relative bandwidth of more than 20%. Introducing a loss tangent of 12×10^{-4} as it has been described in the literature [13] leads to a reduced reflectivity of 99.8% maximum and a bandwidth of about 50% for reflectivities higher than 99.5%.

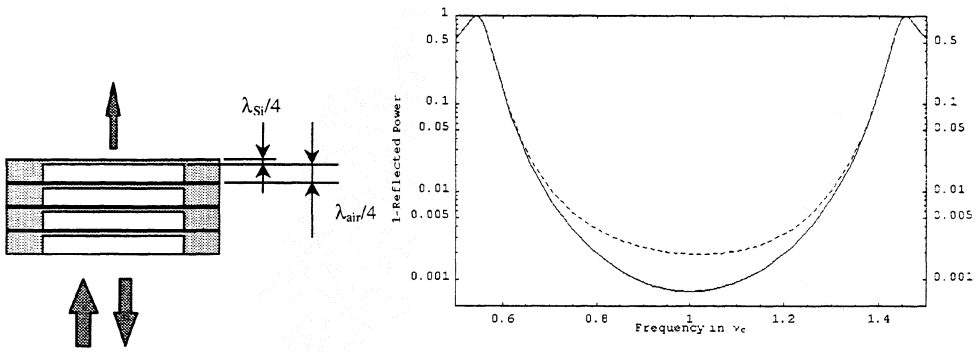

Figure 6: Left: Stack of four λ/4 doublets in air and Si as high-reflectivity FIR mirror. Right: 1-Reflectivity versus relative frequency for lossless Si (solid line) and Si with a loss tangent of 0.0012 (dashed).

Conclusions

Recursive multilayer optics in conjunction with 2nd order effective media theory can be used to design optimized wideband anti-reflection coatings for highly refractive dielectrics, and to design high-reflectivity mirrors for advanced TuFIR spectrometers. The AR coating will allow to get rid of the 30% optical losses in quasi-optical HEB mixers place on Si lenses and also to minimize losses in pressure or cryostat windows in spectroscopic systems. For example, the pressure windows necessary for the HIFI instrument for FIRST could be built of quartz or Si with a 4 to 6 layer antireflection coating on both sides of the window. A single window could cover a frequency range from 450 to 1350 GHz with less than 2% loss at any particular frequency (scaling Fig. 5 with ν_c= 900 GHz). The disadvantage of the coating, the different phase behavior of the polarization directions parallel and perpendicular to the K-vector of the grating can be overcome by using the same groove shape at perpendicular orientations at the front and back side of the window, respectively.
Similarly, taking into account newest results on wide-bandwidth HEB mixers [3], wideband THz receivers as they are currently being built for SOFIA can use the coatings to optimize receiver noise temperature from 1-3 THz or from 2-6 THz. The same holds for wideband sources, as for example optical mixers or p-type Ge lasers in external resonators.
The demonstration of the feasibility of high reflectivity FIR mirrors facilitates the design of new FIR resonators as they are needed for FIR cavity ringdown spectroscopy or for external resonators of p-type Ge lasers.
The next steps towards an advanced TuFIR spectrometer are the experimental verification of the theoretical investigations presented in this paper and their implementation into a spectroscopic system. Eventually, the extension of the frequency and power range accessible to TuFIR spectroscopy will lead to an

improved understanding of molecular systems as they can be found on earth and in space.

Acknowledgements: The Conference visit of G. Schwaab was supported by the Deutsche Forschungsgemeinschaft

References

[1] E.M. Gershenzon, G.N. Goltsman, I. G. Gogidze, Yu.P. Gousev, A.I. Elantiev, B.S. Karasik, A.D. Semenov, Sov. Phys. Superconductivity, **3**(10). 1582. (1990)

[2] D.E. Prober, Appl.Phys.Lett. **62**, 2119 (1993)

[3] J. Schubert, A Semenov, G. Gol'tsman, H.-W. Hübers, G. Schwaab, B. Voronov, E. Gershenzon, „Noise Temperature and Sensitivity of a NbN Hot-Electron Mixer at Frequencies from 0.7 to 5.2 THz", Proceedings of the 10th International Symposium on Space Terahertz Technology, Charlottesville, Virginia, 1999.

[4] D.D. Bicanic, B.F.J. Zuidberg, A. Dymanus, Appl. Phys. Lett. 32. 367 (1978) .

[5] P, Verhoeve, E. Zwart, M. Drabbels, J.J. ter Meulen, W. L. Meerts, A. Dymanus, D. B. McLay, Rev. Sci. Instrum. 61, 1612 (1990) .

[6] G.A. Blake, K.B. Laughlin, R.C. Cohen, K.L. Busarow, D.H. Gwo, C.A. Schmuttenmaer, D.W. Steyert, R.J. Saykally, Rev. Sci. Instrum. 62, 1701 (1991)

[7] S. Matsuura, G.A. Blake, R.A. Wyss, J.C. Pearson, C. Kadow, A.W. Jackson, A.C. Gossard, Traveling-Wave Photmisers Based on Noncollinear Optical/Terahertz Phase-Matching, Proceedings of the 10th International Symposium on Space Terahertz Technology, Charlottesville, Virginia, 1999.

[8] E. Duerr, K. McIntosh, S. Verghese, „Design of a Distributed Photomixer for Use as Terahertz Local Oscillator, . Proceedings of the 10th International Symposium on Space Terahertz Technology, Charlottesville, Virginia, 1999

[9] E. Bründermann, D.R. Chamberlain, E.E. Haller, „Novel Design of Widely Tunable Germanium Terahertz Lasers", to be published in Infrared Physics and Technology, 1999

[10] J.J. Scherer, D. Voelkel, D.J. Rakestraw, J.B. Paul, C.P. Collier, R.J. Saykally, A.O. Keefe, Chem. Phys. Lett 245, 273-280 (1995)

[11] D.H. Raguin, G.M. Morris, Appl. Optics 32, 1154 (1993)

[12] Bergmann-Schaefer, Lehrbuch der Experimentalphysik Band III, Optik, 7th Edition, p. 452, Walter de Gruyter, Berlin 1978,

[13] P.F. Goldsmith, „Quasioptical Systems", Chapter 5.4, IEEE press, New York, 1998

FREQUENCY-DOMAIN ANALYSIS OF DIFFUSION-COOLED HOT-ELECTRON BOLOMETER MIXERS

A. Skalare, W.R. McGrath, B. Bumble, H.G. LeDuc
Center for Space Microelectronics Technology,
Jet Propulsion Laboratory, California Institute of Technology,
Pasadena, CA 91109

Abstract

A new theoretical model is introduced to describe heterodyne mixer conversion efficiency and noise (from thermal fluctuation effects) in diffusion-cooled superconducting hot-electron bolometers. The model takes into account the non-uniform internal electron temperature distribution generated by Wiedemann-Franz heat conduction, and accepts for input an arbitrary (analytical or experimental) superconducting resistance-versus-temperature curve. A non-linear large-signal solution is solved iteratively to calculate the temperature distribution, and a linear frequency-domain small-signal formulation is used to calculate conversion efficiency and noise. In the small-signal solution the device is discretized into segments, and matrix algebra is used to relate the heating modulation in the segments to temperature and resistance modulations. Matrix expressions are derived that allow single-sideband mixer conversion efficiency and coupled noise power to be directly calculated. The model accounts for self-heating and electrothermal feedback from the surrounding bias circuit.

1. Introduction

In the last few years, the superconducting hot-electron bolometer (HEB) has attracted much interest for use as the mixing element in low-noise submillimeter wave spectrometer front-ends for astrophysics. Instruments are now being developed for such missions as the National Aeronautics and Space Administration's airborne SOFIA platform, and the European Space Agency's spaceborne FIRST telescope. One of the key properties that make HEB mixers interesting is their ability to operate significantly above the superconducting gap frequency, which is a materials-related parameter that currently limits competing SIS mixers to frequencies below about 1200 GHz. Even though this is a new heterodyne detector that with one exception [1] has not been used for practical astrophysical observations (primarily because frequencies above 1 THz cannot be observed from ground-based observatories), rapid improvements in measured receiver noise temperatures [2-6], and intermediate frequency (if) bandwidths [6,7], have been reported, primarily in anticipation of upcoming missions such as those mentioned above. Despite these recent encouraging results, further improvements in the noise, and indeed the overall optimization of this mixer, will require an accurate and detailed theoretical model which accounts for the unique operation of this device.

Superconducting HEB mixers have mostly been analyzed using lumped element models that were originally developed for semiconductor bolometers [8-12]. In this approach the bolometer is represented as a single (i.e. "lumped") heat capacitance that is connected to a thermal bath via a heat conductance. While this theoretical model has significant merit, especially for phonon-cooled devices that have a uniform electron temperature [13], it does

not accurately take into account the non-uniform temperature distribution in the diffusion-cooled case [14]. The most obvious complication lies in how to determine an appropriate value for the resistive transition dR/dT, which enters as a square in the lumped-element expression for the mixer conversion efficiency. Inclusion of a non-uniform temperature complicates the model enough, that a closed-form analytic solution for mixer conversion and noise cannot be found. Several methods to avoid this problem have been previously investigated. In one approach, a reduced or "effective" value for dR/dT is calculated numerically taking a non-uniform temperature into account, and this value is then used in the regular lumped-element mixer model [15]. Another solution is the so-called "hot-spot" model, where the device resistance-versus-temperature (RT-) curve is approximated by a step function [16-17]. A third method (previously employed by us) is to discretize the bolometer into segments, and do a brute-force numerical time-domain mixing simulation, calculating heat dissipation and heat flow between the segments within each time step. Results of this method are compared to experiments in [18]. The new frequency-domain method described in this paper has advantages compared to all of these previous efforts: 1) It allows mixer conversion efficiency and output noise to be calculated without making simplifications in the RT-curve; 2) The mixer performance can be determined by straightforward matrix multiplications and inversions, without any equivalent of the time-step dependent instabilities that can occur in time-domain simulations; 3) The dominant noise mechanism is included in the model; and 4) Self-heating and electrothermal feedback are fully included. There are also some issues not currently addressed this new technique. For example, it does not include a method for calculating rf or if saturation effects, and it does not include several effects that are particular to superconductors, such as the coherence length and the differences in heat conductance between superconductors and normal metals. Future inclusion of these effects would affect the first, non-linear, part of the theory. The small-signal part of the theory uses parameters calculated from the non-linear part, but may otherwise remain unaffected.

2 The Mixer Model

The type of HEB device we are modeling consists of a submicron-length strip (microbridge) of a superconductor between two normal metal leads. The pads are assumed to be at a bath temperature T_{amb}. Heat dissipation in the microbridge raises the temperature of the center of the device relative to the ends, creating a non-uniform temperature profile. The bridge length L is assumed short enough that the dominant heat conduction out of the bridge is by diffusion of hot electrons to the cold normal metal pads, rather than by electron-phonon interaction.

2.1 Steady State / Large Signal Model

The large-signal temperature distribution in a diffusion-cooled HEB mixer is a result of the *rf* heating caused by the local oscillator, by the heating from the mixer *dc* bias current, and by internal heat conduction. The heat conduction is assumed to be proportional to the local temperature according to the Wiedemann-Franz law:

$$\Phi = -G_0 \frac{T}{T_0} \nabla T \qquad \text{(Eq.1)}$$

where Φ is heat flow intensity, T is the local temperature, and G_0 is the heat conductivity at a reference temperature T_0. The relation leads to the following one-dimensional integral

equation, where the heat flow towards the ends of the bolometer at a particular distance x from the center is equated to the amount of power dissipated inside of that distance:

$$-\frac{1}{2}\frac{G_0}{T_0}\frac{d\left(T^2\right)}{dx}=\frac{P_{rf}}{w\cdot h\cdot L}x+\frac{I_0^2}{w^2h^2}\int_0^x\rho(x',T(x'))dx' \qquad \text{(Eq.2)}$$

where w,h,L are the width,thickness and length of the bolometer, P_{rf} is the amount of local oscillator power dissipated in the bridge, I_0 is the dc current, and ρ is the local resistivity in the bolometer. Since the device film resistivity is usually a non-linear function of temperature and location, no general closed-form solution can be found to this equation. However, a numerical solution can quite easily be found through a corresponding finite-difference formulation:

$$-\frac{1}{2}\frac{G_0}{T_0}\frac{T_k^2-T_{k-1}^2}{\Delta x}=\frac{P_{rf}}{w\cdot h\cdot L}\cdot\Delta x\cdot(k-1)+\frac{I_0^2}{w^2h^2}\cdot\Delta x\cdot S_k \qquad \text{(Eq.3)}$$

where the integral in the previous expression is approximated by a summation $\Delta x\cdot S_k$, with

$$S_1=0\ ;\ S_2=\rho_1\ ;\ S_k=\frac{1}{2}\rho_1+\sum_{l=2}^{k-1}\rho_l+\frac{1}{2}\rho_{k-1}\ ,\ k=3,4,..,N \qquad \text{(Eq.4)}$$

The finite-difference formulation can be seen as a sub-division of the bolometer into N segments, each with its own temperature T_k, as is illustrated in Fig.1 . Only half of the bolometer needs actually be considered because of symmetry. The finite-difference formulation is computationally fast even when used iteratively to find numerical values of various parameters such as the *dc* current I_0 or the temperature T_1 of the device center segment.

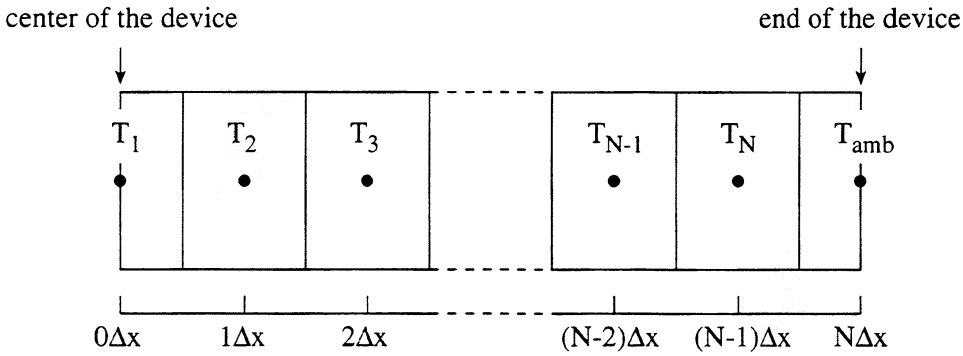

Fig.1; Discretization used in the large- and small-signal models. Because of symmetry only half of the bolometer is analyzed. Therefore the total length of the device is $L=2\cdot N\cdot\Delta x$.

2.2 The Mixer Embedding Circuit

As shown in Fig.2, the discretized bolometer is connected to a Norton equivalent circuit to represent the *dc* bias and intermediate frequency *if* embedding circuits of the mixer. R_0

and I_0 are the steady-state (large signal) resistance and bias current of the device, while ΔR and ΔI are the small-signal modulations representing the modulation of the dissipated *rf* power caused by the combined signal and LO.

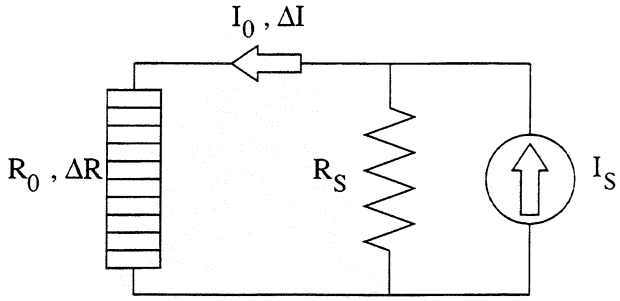

Fig.2; A Norton equivalent circuit is used to represent the dc bias and intermediate frequency circuits.

In the small-signal limit the embedding circuit imposes the following relationship between resistance and current, which must be included in the subsequent mixer theory:

$$\Delta I = -\frac{I_0}{R_0 + R_S}\Delta R \qquad \text{(Eq.5)}$$

, where

$$I_0 = \frac{I_S R_S}{R_0 + R_S} \qquad \text{(Eq.6)}$$

2.3 Mixer Conversion Efficiency Model

In bolometric mixing, the device resistance is varied by the modulation in *rf* power dissipation that is caused by the beating between signal and local oscillator (LO). This modulation in resistance is then detected by an external circuit. In superconducting HEB mixers that are used at frequencies above the superconducting gap frequency, the *rf* heating can be regarded as uniform throughout the device. One can also assume that the signal and local oscillator frequencies are higher than the highest response frequency of the device. In this situation it is convenient to consider the power dissipation from the local oscillator to be constant with time and uniformly distributed throughout the device, and to represent the modulation due to the signal by a uniformly distributed heating function that is modulated at the intermediate frequency, *if*. In the small-signal limit this means that the modulation of the device resistance will occur only at the *if*.

The resistance modulation ΔR is the sum of the modulations ΔR_k in all the segments:

$$\Delta R = \sum_k \Delta R_k = \sum_k \frac{\partial R_k}{\partial T_k}\Delta T_k \qquad \text{(Eq.7)}$$

where ΔT_k is the temperature modulation in segment k. The total heat modulation in segment k is the sum of the contributions from *rf* power dissipation and from the embedding circuit:

$$\Delta P_k = \Delta P_{rf,k} + \Delta P_{emb,k} = \Delta P_{rf,k} + 2R_{0,k} I_0 \Delta I + I_0^2 \Delta R_k \qquad \text{(Eq.8)}$$

The frequency-domain model illustrated in Fig.C is used to calculate the effect that the heating modulations have on the temperatures. In the small-signal limit the thermal model is linear, so heat conductances, heat capacitances and heat sources can be handled by the same complex-notation (i.e. $j\omega$-notation) that is commonly used for small-signal electrical circuits and components. The C_k's in Fig.C are the electronic heat capacitances of the individual segments, which are proprtional to the volume of the segment and to the local temperature T_k. The G_k's are the segment-to-segment heat conductance, which according to the Wiedemann-Franz law is proportional to the electrical conductance and to the local temperature.To handle the many device segments, a matrix notation is introduced (with square brackets denoting matrices and vectors). The relationship between heat dissipation and temperature can be written as an analogue to Ohm's law:

$$[\Delta T_k]_k = [A_{kl}]_{kl} \cdot [\Delta P_l]_l \qquad \text{(Eq.9)}$$

Where $[A]$ is calculated from its inverse, which can be derived according to Fig.3 as :

$$[A^{-1}] = \begin{bmatrix} (j\omega C_1 + G_1) & (-G_1) & 0 & \dots \\ (-G_1) & (j\omega C_2 + G_1 + G_2) & (-G_2) & \dots \\ 0 & (-G_2) & \dots & \dots \\ \dots & \dots & \dots & et\ c. \end{bmatrix} \qquad \text{(Eq.10)}$$

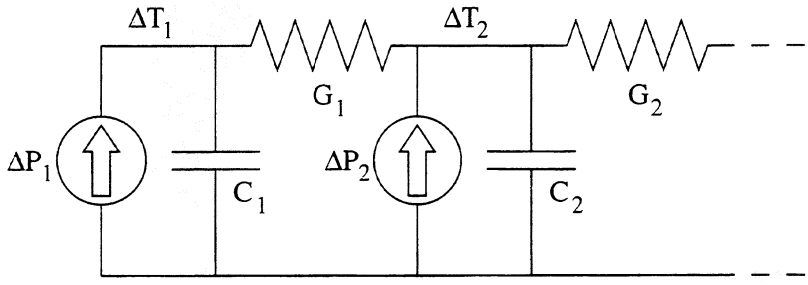

Fig.3; Thermal circuit model, showing heat dissipation sources (ΔP_k), segment heat capacitances (C_k) and segment-to-segment heat conductances (G_k).

The resistance modulation of element k can be written :

$$\Delta R_k = \frac{\partial R_k}{\partial T_k} \Delta T_k = \frac{\partial R_k}{\partial T_k} \sum_l A_{kl} \left(\Delta P_{rf,l} + 2R_{0,l} I_0 \Delta I + I_0^2 \Delta R_l \right) \qquad \text{(Eq.11)}$$

or as the matrix expression (with $\delta_{kl} = 1$ for $k = l$, $\delta_{kl} = 0$ for $k \neq l$.):

$$\left[\Delta R_k\right]_k = \left[B^{-1}\right]_{kl} \cdot \left[\frac{\partial R_l}{\partial T_l} \sum_m A_{lm} \Delta P_{rf,m}\right]_l = \left[B^{-1}\right]_{kl} \cdot \left[\frac{\partial R_l}{\partial T_l} \delta_{lm}\right]_{lm} [A]_{mn} \left[\Delta P_{rf,n}\right]_n \quad \text{(Eq.12)}$$

with:

$$B_{kl} = \delta_{kl} + \frac{\partial R_k}{\partial T_k} \cdot \frac{2I_0^2}{R_0 + R_S} \cdot \left(\sum_m A_{km} R_{0,m}\right) - \frac{\partial R_k}{\partial T_k} I_0^2 A_{kl} \quad \text{(Eq.13)}$$

With the particular discretization illustrated in Fig.1, the heat dissipation in the segments can be written as

$$\Delta P_{rf,1} = \frac{1}{2} \frac{\Delta P_{rf}}{2N} \quad \text{(Eq.14)}$$

$$\Delta P_{rf,k} = \frac{\Delta P_{rf}}{2N} \; ; \quad k = 2,3,...,N \quad \text{(Eq.15)}$$

The matrix expression above provides the connection between the modulation in dissipated *rf* power and the modulation of device resistance. The first of the three terms in the expression for B_{kl} represents the direct response to the *rf* heating. The last term is due to the change in direct ohmic heating when the device resistance changes, while the middle term represents heating due to mismatch between the device and the intermediate frequency load resistor. For convenience, the following response parameter is defined:

$$E = \frac{\Delta R}{\Delta P_{rf}} = \sum_k \Delta R_k \Big/ \sum_k \Delta P_{rf,k} \quad \text{(Eq.16)}$$

In the time domain, the *rf* voltages over the device are

$$V_{LO} \cos \omega_{LO} t + V_S \cos \omega_S t \quad \text{(Eq.17)}$$

and cause a heat modulation at the *if* frequency of:

$$\Delta P_{rf} = \frac{V_{LO} V_S}{R_N} \quad \text{(Eq.18)}$$

The resulting intermediate frequency voltage is:

$$\Delta V = \frac{R_S^2 I_S}{\left(R_0 + R_S\right)^2} \Delta R = \frac{R_S^2 I_S}{\left(R_0 + R_S\right)^2} \cdot E \cdot \frac{V_{LO} V_S}{R_N} \quad \text{(Eq.19)}$$

and, finally, the single-sideband mixer conversion efficiency η can be formulated:

$$\eta = 2 \cdot R_S P_{rf} \left| \frac{I_0 E}{R_0 + R_S} \right|^2 \qquad \text{(Eq.20)}$$

2.4 Thermal Fluctuation Noise

A superconducting bolometer generates both Johnson (or thermal) noise and thermal fluctuation noise. This paper will only treat thermal fluctuation noise in any detail, although a more complete theory should also include Johnson noise. In practice, however, thermal fluctuation noise usually dominates for a diffusion-cooled superconducting *HEB*, when it is operated under the conditions that give minimum receiver noise.

The origin of thermal fluctuation noise is the random exchange of heat carriers between the bolometer and the ambient temperature bath (the normal metal leads), and between different internal parts of the bolometer. In a system in thermal equilibrium with a large reservoir, thermodynamics gives the following well-known expression for the time variance of the energy of that system, where C_V is the heat capacity and k_B is Boltzmann's constant:

$$\left\langle (\Delta E(t))^2 \right\rangle = k_B C_V T^2 \qquad \text{(Eq.21)}$$

In a more relaxed nomenclature this relation can also be expressed as a fluctuation of the system temperature, although this is strictly speaking not correct since temperature is not a fluctuating parameter in a system in equilibrium:

$$\left\langle (\Delta T(t))^2 \right\rangle = k_B T^2 / C_V \qquad \text{(Eq.22)}$$

A real bolometric mixer is per definition *not* in equilibrium with the surrounding medium, since it relies on finite amounts of *dc* and *rf* heat being dissipated inside the device, and of that heat being transported out into the medium. However, if the inelastic electron-electron time is short enough, a local quasi-equilibrium can be established, where any small portion of the device only exchanges heat carriers with the parts of the device that are immediately adjacent to it. The exact conditions under which the expressions above no longer apply are hard to estimate, and in the end a mixer theory for thermal fluctuation noise will need to be compared to experimental results.

For calculating the mixer noise, a circuit model is used, as shown in Fig.4, that is similar to the one used in the conversion efficiency calculation. The heat capacitances and heat conductances are the same as previously discussed, but the heat sources Q_k are arranged differently. The noise heat sources represent exchange of energy between different segments, not dissipation, and are considered incoherent in time (white noise) and uncorrelated with each other. This is a Langevin approach that has similarities to some other formulations found in literature [19]. The method consists of two steps: first the magnitudes of the noise sources are determined, and then the amount of noise power coupled to the output load is calculated.

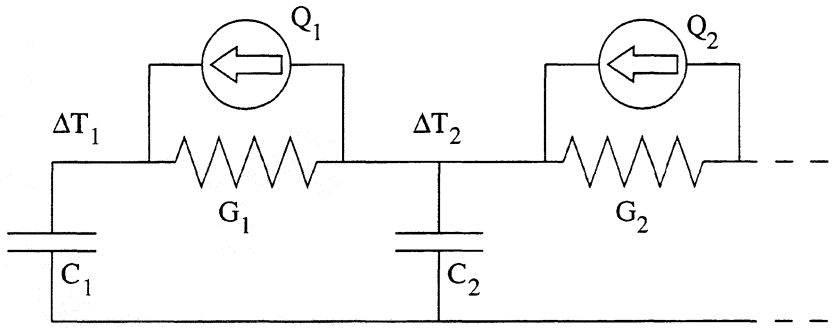

Fig.4; The thermal circuit model used in calculating thermal fluctuation noise.

The expression for the temperature modulation in the segments is (within a small frequency interval *df*):

$$\left[|\Delta T_k|^2 df\right]_k = \left[|F_{km}|^2\right]_{km}\left[|Q_m|^2\right]_m \cdot df \qquad \text{(Eq.23)}$$

, where

$$\left[F_{km}\right]_{km} = \left[A_{kl}\right]_{kl}\left[\delta_{lm} - \delta_{l,m+1}\right]_{lm} \qquad \text{(Eq.24)}$$

The following formula is then used to calculate the source intensities, where the first equality follows from the Wiener-Khinchine theorem and the second one from thermodynamics:

$$\int_0^\infty |\Delta T_k(f)|^2 df = \left\langle |\Delta T_k(t)|^2 \right\rangle = \left[k_B T_k^2 / C_k\right]_k \qquad \text{(Eq.25)}$$

Since the sources are time-incoherent it follows, again from the Wiener-Khinchine theorem, that their frequency-domain representation is frequency-independent. The source distribution can therefore be calculated as the solution to the equation system:

$$\int_0^\infty \left[|F_{km}|^2\right]_{km} df \cdot \left[|Q_m|^2\right]_m = \left[k_B T_k^2 / C_k\right]_k \qquad \text{(Eq.26)}$$

With the noise source distribution known, it is relatively straightforward to calculate the effect on the device resistance:

$$|\Delta R|^2 df = \left[|H_k|^2\right]_k^t \cdot \left[|Q_k|^2\right]_k df \qquad \text{(Eq.27)}$$

, where

$$\left[H_p\right]_p^t = [1]_k^t \left[B^{-1}\right]_{kl} \left[\frac{\partial R_l}{\partial T_l}\delta_{lm}\right]_{lm} [A]_{mn} \left[\delta_{np} - \delta_{n,p+1}\right]_{np} \qquad \text{(Eq.28)}$$

The power delivered to the output load in the small frequency interval df becomes:

$$P_{IF}(f)df = \frac{R_S I_0^2}{\left(R_0 + R_S\right)^2} \left[\left|H_k(f)\right|^2\right]_k^t \left[\left|Q_k\right|^2\right]_k df \qquad \text{(Eq.29)}$$

3. Calculation Example

As an example, a calculation of mixer conversion efficiency was made in order to demonstrate some of the features of our model. Although the method allows an actual experimental resistance-versus-temperature curve to be used, for simplicity the idealized curve in Fig.5 which contains features of actual RT curves was chosen for this example. Two superconducting transition temperatures can be seen in the figure (as is the case in measured RT curves), the higher of which occurs in the central main part of the bridge, while the lower one is present near the ends of the bridge. This is a simplified way of including the suppression of the critical temperature from the proximity effect, that occurs in the regions of the bridge that are contacted by the normal metal leads. The device dimensions used in the calculation are similar to those of our actual HEB mixers: Length $162\ nm$, width $150\ nm$, thickness $10\ nm$, and the heat conductivity $G_0 / T_0 = 0.1\ (W/mK^2)$. The device length included the end regions of the device with the suppressed critical temperature ($12\ nm$). The ambient temperature was chosen to be $4.24\ K$.

Fig.6 shows the current-voltage (IV-) curves calculated for the device, with and without local oscillator power. The overall shape is similar to measured curves for our actual devices. At zero *dc* bias voltage, however, the curves become singular, since the model does not include the limitation on the *dc* supercurrent that is present in real superconductors [20]. The mixer conversion efficiency shown in Fig.6 approaches a maximum at the point where the device cannot be biased in a stable way by the embedding circuit. This is also qualitatively consistent with typical experimental results. The circle in the figure marks approximately the best low receiver noise operating point that would be reachable in a real experiment. In addition, a peak in the conversion efficiency can be seen just above a bias voltage of 3 mV. This effect occurs when enough heat is dissipated in the device so that the end regions of the bridge heat up to their local (suppressed) critical temperature. This is sometimes observed as peaks in the coupled output noise in experimental data. Figure 7 shows the calculated conversion effiency and output noise for the device when operated at the bias point marked in Fig.6. As seen, the conversion effiency curve has the expected single-pole shape, in this case with a 3 dB roll-off frequency of 3-4 GHz. The shape of the output noise curve, however, differs from that calculated from previous "lumped-element" theory [21], according to which it should have the same frequency dependence as that of the conversion efficiency. It should be pointed out that if the number of bolometer segments is reduced to one, the two theories become identical. Also, in a more realistic mixer model the Johnson noise should be included, which has not been done here.

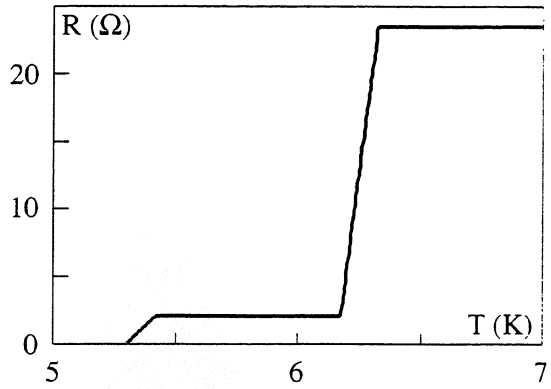

Fig.5; The R-versus-T curve used in the calculation is an idealized curve based on an experimental curve for a niobium HEB.

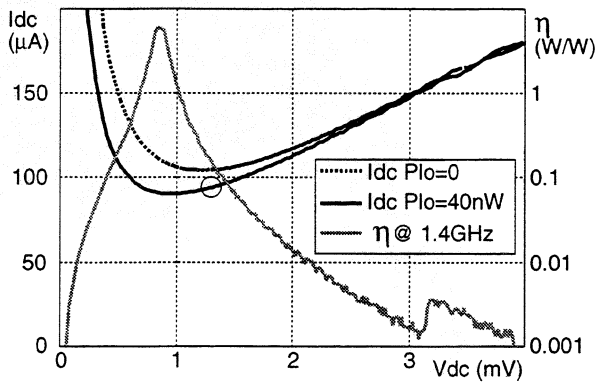

Fig.6; Calculated IV-curves and calculated conversion effiency.

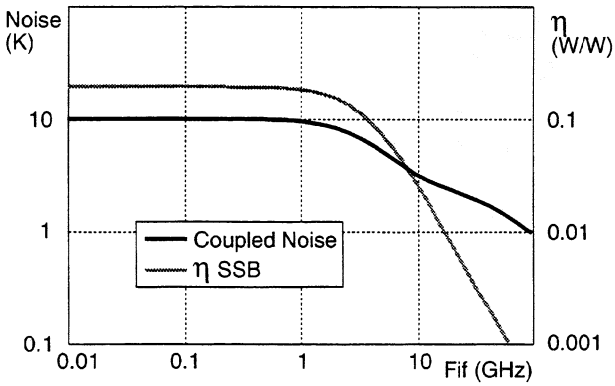

Fig.7; Calculated conversion effiency and coupled output noise as a function of frequency. The noise here is defined as coupled power per Hz to the *if* load resistor, divided by k_B.

Summary

A mixer model for diffusion-cooled hot-electron bolometers has been developed. A non-linear large-signal finite-difference method is used to calculate linearized device parameters, which are subsequently used in small-signal calculations of mixer conversion effiency and noise. The non-uniform temperature distribution inside the bolometer is taken into account both in the large- and small-signal analysis by discretizing the device into a large number of segments, and by assigning a local temperature to each segment. The small signal mixer analysis is done in the frequency domain, using matrix expressions to connect modulations in heating, temperature and resistance. Initial calculations using device parameters that are similar to those of real bolometers give values for conversion and noise that seem reasonable. However, a detailed comparison to experimental data still remains to be done, and will be presented in a future publication. Future work will also include a model for Johnson noise.

Acknowledgments

The research described in this paper was performed by the Center for Space Microelectronics Technology, Jet Propulsion Laboratory, California Institute of Technology, and was sponsored by the National Aeronautics and Space Administration, Office of Space Science.

References

[1] J. Kawamura, R. Blundell, C.-Y.E. Tong, D.C. Papa, T.R. Hunter, G. Gol'tsman, S. Cherednichenko, B. Voronov, E. Gershenzon, "First light with an 800 GHz phonon-cooled HEB mixer receiver", Proc. Ninth Int. Symp. Space Terahertz Tech., 17-19 March 1998, Jet Propulsion Laboratory, Pasadena, CA, pp. 35-43.

[2] B.S. Karasik, M.C. Gaidis, W.R. McGrath, B. Bumble, H.G. LeDuc, "Low noise in a diffusion-cooled hot-electron mixer at 2.5 THz", Appl. Phys. Lett. 71 (11), 15 September 1997, pp. 1567-1569.

[3] P. Yagoubov, M. Kroug, H. Merkel, E. Kollberg, G. Gol'tsman, A. Lipatov, S. Svechnikov, E. Gershenzon, "Quasioptical NbN phonon-cooled hot electron bolometric mixers with low optimal local oscillator power", Proc. Ninth Int. Symp. Space Terahertz Tech., 17-19 March 1998, Jet Propulsion Laboratory, Pasadena, CA, pp. 131-140.

[4] A. Skalare, W.R. McGrath, B. Bumble, H. LeDuc, "Measurements with a diffusion-cooled Nb hot-electron bolometer mixer at 1100 GHz", Proc. Ninth Int. Symp. Space Terahertz Tech., 17-19 March 1998, Jet Propulsion Laboratory, Pasadena, CA, pp. 115-120

[5] B.S. Karasik, A. Skalare, R.A. Wyss, W.R. McGrath, B. Bumble, H.G. LeDuc, J.B. Barner, A.W. Kleinsasser, "Low-noise and wideband hot-electron superconductive mixers for THz frequencies", Proc. Sixth Int. Conf. Terahertz Electronics, 3-4 September 1998, University of Leeds, Leeds, United Kingdom.

[6] R. Wyss et al., these Proceedings

[7] P.J. Burke, R.J. Schoelkopf, D.E. Prober, A. Skalare, W.R. McGrath, B. Bumble, H.G. LeDuc, "Length scaling of bandwidth and noise in hot-electron superconducting mixers", Appl. Phys. Lett. 68 (23), 3 June 1996, pp.3344-3346.

[8] F. Arams, C. Allen, B. Peyton, E. Sard, "Millimeter mixing and detection in bulk InSb", Proc. IEEE, Vol.54, pp.308-318, 1966

[9] J.C. Mather, "Bolometer noise: nonequilibrium theory", Appl. Opt. 21, pp.1125 (1982)

[10] H. Ekström, B.S. Karasik, E.L. Kollberg, K.S. Yngvesson, "Conversion gain and noise of niobium superconducting hot-electron-mixers", IEEE Trans. Microwave Theory Tech., Vol. 43, No.4, April 1995, pp. 938-947

[11] P.J. Burke, "High frequency electron dynamics in thin film superconductors and applications to fast, sensitive THz detectors", Ph.D. dissertation, Yale Univ., New Haven, Connecticut, December 1997.

[12] H.F. Merkel, E.L.Kollberg, K.S.Yngvesson, "A large signal model for phonon-cooled hot-electron bolometric mixers for THz frequency applications,, Proc. Ninth Int. Symp. on Space Terahertz Technology, Jet Propulsion Laboratory, Pasadena, CA, 17-19 March 1998, pp.81-97

[13] E.M. Gershenzon, G.N Gol'tsman, I.G. Gogidze, Y.P. Gusev, A.I. Elant'ev, B.S Karasik, A.D. Semenov, "Millimeter and submillimeter range mixer based on electronic heating of superconducting films in the resistive state", Superconductivity **3** (10), pp. 1582-1597, October 1990.

[14] D. E. Prober, "Superconducting Terahertz Mixer using a Transition-Edge Microbolometer", Appl. Phys. Lett. **62** (17), pp. 2119-2121, (1993).

[15] W.R. McGrath, unpublished

[16] D.W. Floet, J.J.A. Baselmans, J.R. Gao, T.M. Klapwijk, "Resistive behaviour of Nb diffusion-Cooled hot-electron bolometer mixers", Proc. Ninth Int. Symp. on Space Terahertz Technology, Jet Propulsion Laboratory, Pasadena, CA, 17-19 March 1998, pp.63-72

[17] H. Araujo, Presentation at Applied Superconductivity Conference, ASC-98, Palm Desert, California, 1998. To be published in IEEE Trans. Applied Superconductivity.

[18] A. Skalare, W.R. McGrath, B. Bumble, H.G. LeDuc, P.J. Burke, A.A. Verheijen, R.J. Schoelkopf, D.E. Prober, "Large bandwidth and low noise in a diffusion-cooled hot-electron bolometer mixer", Appl. Phys.Lett. 68 (11), 11 March 1996, pp.1558-1560.

[19] R.F. Voss, J. Clarke, "Flicker (1/f) noise : Equilibrium temperature and resistance fluctuations", Phys. Rev. B, Vol.13, No.2, pp.556-573, 15 January 1976.

[20] A.Vl. Gurevich, R.G. Mints, "Self-Heating in Normal Metals and Superconductors", Reviews of Modern Physics, Vol.59, No.4, October 1987

[21] B.S. Karasik, A.I. Elantev, "Analysis of the Noise Performance of a Hot-Electron Superconducting Bolometer Mixer", Proc. Sixth Int. Symp. on Terahertz Technology, pp.229-246, California Inst. of Tech., March 21-23, 1995.

OPTIMIZATION OF THE NORMAL METAL HOT-ELECTRON MICROBOLOMETER

D. Chouvaev, D. Golubev, M. Tarasov*, and L. Kuzmin

Department of Microelectronics and Nanoscience,
Chalmers University of Technology, SE-412 96 Gothenburg, Sweden

**Inst. of Radioengineering and Electronics RAS, Mokhovaya 11, 103907 Moscow, Russia*

Abstract

The purpose of our project is to create a robust fully on-chip integrated antenna-coupled bolometer, competitive in sensitivity for radio-astronomy applications. It must have noise equivalent power (NEP) below 10^{-17} W/Hz$^{1/2}$ and time constant shorter then 1 ms. We call this device a normal metal hot-electron microbolometer (NHEB), because its function is based on the hot-electron effect in a strip of a normal metal at temperatures below 0.5 K.

Until now we have been developing the power sensor for this device. In the beginning we could not operate the sensor at electronic temperatures below 300 mK, presumably because of the high external noise load. Our latest results show how this problem can be solved experimentally. We have achieved noise performance mostly limited by the amplifier, which corresponds to expected detector NEP on the order of $1.5 \cdot 10^{-17}$ W/Hz$^{1/2}$ at 100 mK.

We have also performed a theoretical analysis of temperature readout by NIS tunnel junctions in our device. In particular heat flow fluctuations are discussed as an additional noise component, which needs to be included in the analysis. Our model allows us to calculate optimal ranges of parameters like normal resistance of the junction or optimal bias current, to provide the lowest NEP for given operating conditions (temperature, phonon noise etc.).

1. Introduction

Bolometers are direct broad band detectors of electromagnetic radiation, complementing heterodyne detectors in radio-astronomy research. They are useful, for example, for investigating the cosmic microwave background. Most common bolometers used in radio-astronomy are made with a suspended absorber, being heated by incident radiation, and a semiconducting thermistor. Cooled to 100 mK, they can provide sensitivity better then $3 \cdot 10^{-17}$ W/Hz$^{1/2}$ with time constant down to 10 ms [1]. An alternative to those are superconducting bolometers, where the sensor is a suspended chip with a superconducting

structure. Being kept by electrothermal feedback at the superconducting transition, this system reacts strongly on signal-induced temperature variations around T_c (≈300 mK) [2].

One disadvantage with the existing bolometers is that they compromise sensitivity and speed – to reach NEP < 10^{-17} W/Hz$^{1/2}$ one needs to make the absorbing area large, thus getting also large thermal capacity and, consequently, longer reaction time. The thermal reaction time is defined as $\tau=C/G$, where C is the absorber's thermal capacity and G is thermal conductance from the absorber to the environment.

Another problem is that suspended structures are often fragile, and it is difficult to combine many of them into a 2D detector array. Building a fully planar-integrated 2D array of detectors with sensitivity better then 10^{-17} W/Hz$^{1/2}$ and time constant under 1 ms can be regarded as a challenge in bolometer research.

The device proposed in [3] and later partly implemented [4] can be a promising choice. This is a planar microfabricated bolometer, using an antenna (which can be integrated on the same chip) to receive a signal. The schematic picture of the whole circuit and an SEM-image of a fabricated sensor can be seen in fig. 1. In an antenna-coupled bolometer there is no need to make the sensor itself large to receive more power, instead it can be miniaturized, minimizing also the thermal capacity.

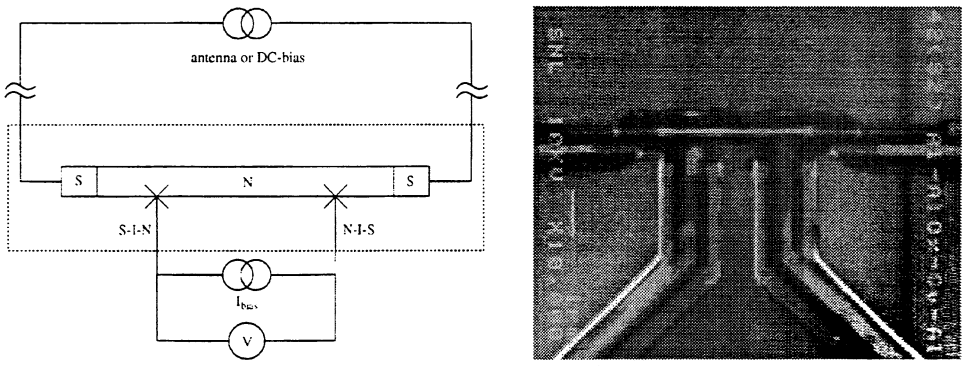

FIG. 1. The original device scheme and an SEM-image of a real sample. Double NIS tunnel junctions are used to increase the response dV/dT and to simplify biasing.

A microwave signal received by the antenna will induce current in a normal-metal resistor (further referred to as "absorber"), this current will dissipate and generate Joule heat. This heat, however, will be delivered not to the whole structure at once, but first to the electron gas in the resistor. At temperatures below 0.5 K, where ultra-sensitive bolometers are operated, the thermal coupling between electrons and phonons is very low, and the electrons will establish their own equilibrium at a temperature above the phonon temperature in the surrounding body (hot electron effect). In this sense, the electron gas in the resistor can be seen as a power absorber, and the thermal conductance to the

environment is then limited by the energy exchange rate between the electrons and the phonons. Thus one does not need to suspend the absorber to thermally isolate it. Furthermore, the thermal capacity of the electrons is much less than the thermal capacity of the whole structure, and this makes the sensor very fast.

The only problem left is that the heated electrons could diffuse back to the antenna instead of exchanging energy with phonons in the resistor. Fortunately this can be avoided by making the antenna superconducting, since a property of a superconductor-normal metal interface is that electric current passes it without transferring the thermal energy of electrons (Andreev reflection).

Finally, very small signal power results in a substantial rise of the electron temperature in the absorber. These temperature variations need to be converted to some electrical response, and this is accomplished using one or two normal-metal/insulator/ superconductor (NIS) tunnel junctions, where the normal electrode is the absorber. Their IV-characteristics get broadened with increasing electron temperature in the N-electrode. When such a junction (or a pair of those) is biased with constant current in the sub-gap region, the voltage over the junction will depend on the thermal smearing, and it will be proportional to the electron temperature in a wide range (fig. 2).

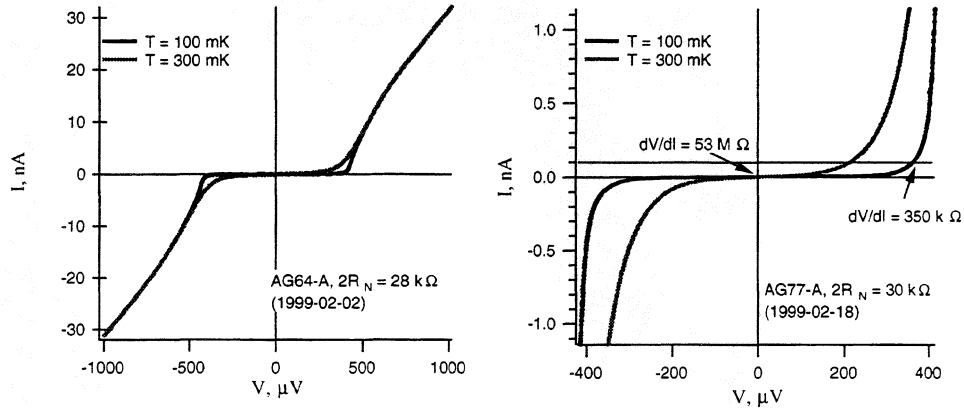

FIG. 2. Principle of measuring electron temperature by means of an NIS or SINIS tunnel junction stucture biased with constant current.

The power responsivity of this sensor is a ratio of two terms: temperature responsivity (dV/dT) and heat conductance from the electrons to the environment ($G = dP/dT$):

$$S = \frac{dV}{dP} = \left|\frac{dV}{dT}\right| \cdot \left|\frac{dP}{dT}\right|^{-1}$$

The temperature responsivity depends on properties of the tunnel junctions and it is nearly constant almost in the whole range of operating temperatures (typically $dV/dT \approx 5\text{-}10 \cdot 10^{-4}$ V/K). The heat conductance depends mostly on properties of the absorber and can be estimated from the ideal energy exchange rate between electrons and phonons in equilibrium at different temperatures:

$$P = \Sigma\Omega(T_e^5 - T_p^5) \quad \rightarrow \quad \frac{dP}{dT} = 5\Sigma\Omega T_e^4 ,$$

where Ω here is the absorber volume and Σ is a specific material parameter. For realistic device parameters (namely for our sample AG77) this gives power responsivity

$$S = \frac{1}{T_e^4} 8 \cdot 10^5 \, {}^{VK^4}\!/_{W} \quad \rightarrow \quad S(0.3\text{K}) = 1 \cdot 10^8 \, {}^{V}\!/_{W} , \quad S(0.1\text{K}) = 3 \cdot 10^9 \, {}^{V}\!/_{W} .$$

Accordingly, a decrease of the operating temperature has great advantages, limited though by the fact that dV/dT rapidly falls below 100 mK. Knowing the power responsivity, we can also estimate the noise equivalent power (NEP) of the detector. Assuming that the total noise is dominated by amplifier noise, and that we use a very good amplifier ($\sqrt{S_V} = 3\text{nV/Hz}^{1/2}$) we get

$$NEP(0.3\text{K}) = 3 \cdot 10^{-17} \, {}^{W}\!/_{\sqrt{Hz}} , \quad NEP(0.1\text{K}) = 1 \cdot 10^{-18} \, {}^{W}\!/_{\sqrt{Hz}} ,$$

which is superior to most of the existing devices.

The thermal reaction time will be determined by the electron-phonon interaction time, estimated to

$$\tau \approx 2 \cdot 10^{-8} \cdot T_e^{-3} \text{sK}^3 \quad \rightarrow \quad \tau(0.3\text{K}) = 0.8\mu\text{s} , \quad \tau(0.1\text{K}) = 20\mu\text{s} .$$

This is also well below of what is usually required (1 ms).

2. Device fabrication and measurement setup

The power sensor ("microcalorimeter") is fabricated by e-beam lithography and shadow metal evaporation. Three metal layers are used – a superconductor for NIS tunnel junctions (aluminum film, 36-38 nm), a normal metal for the power absorber (copper, 58 nm), and one more superconducting layer for the absorber bias leads or eventually the antenna (aluminum, 70 nm). The tunnel junctions are formed by oxidizing the first superconducting layer before deposition of the normal metal on top of it. Typical oxidation conditions are $P(O_2)$ = 0.3-0.4 mbar and t = 0.5-2 min, this results in the junction normal resistance of 5-15 kΩ for area about 0.1 μm^2. The tricky part is to contact the same absorber strip both by an oxidized superconductor (NIS junctions) and by a superconductor with a very transparent interface to the normal metal (absorber bias electrodes). This can be done either by a two-step process with two

lithography/deposition steps and ion beam cleaning in-between, or by our new single-step process where tilting of a sample in two perpendicular planes is employed (fig. 3).

The dimensions of the absorber in the most recent modification of our device are 4.5×0.25 μm^2, thickness 58 nm, copper. Its resistance is about 20 Ω, which is not optimal for matching to an antenna. That is why we are planning to decrease the width to 0.1 μm and increase the length in the future. Changing the absorber material to chromium is another option.

For dc-measurements we have used a current bias to introduce heat into the absorber instead of connecting any antenna. The measurements are done in a dilution refrigerator capable of cooling samples to 25 mK. There is no possibility to irradiate a sample with sub-mm-waves in this cryostat. The current source for the NIS junctions' bias (and the same kind for the absorber bias) is made up of a symmetric voltage source and two high-value (10 or 100 MΩ) resistors in series (at room temperature). Johnson noise in those resistors is the main source of bias noise discussed in part 4.

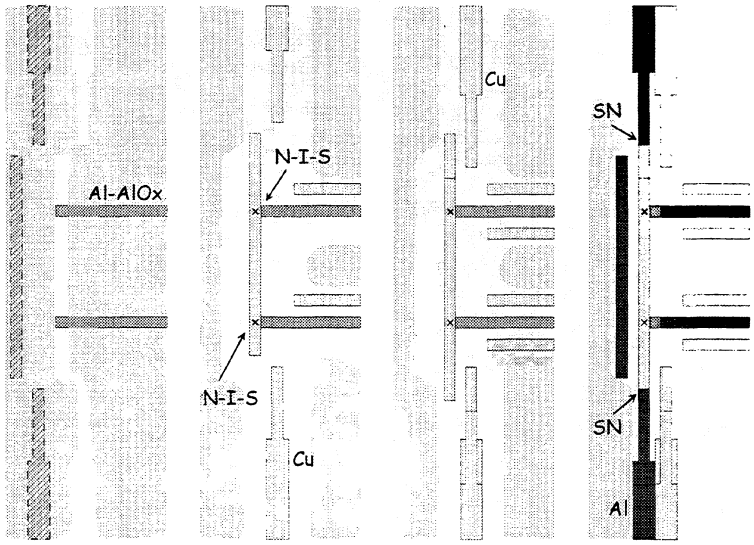

FIG. 3. Schematic picture of the metal deposition process. A double PMMA-copolymer resist is used to make a suspended mask. In the leftmost picture both resist layers are shown by slightly darker areas, on the three others – only the underlying copolymer mask. By tilting the sample in different planes the metal structures are shifted in respect to the original openings in the PMMA-mask, providing also necessary overlaps between subsequently deposited metal layers.

The measurements include a calibration measurement, where the voltage response from the tunnel junctions at the working bias is studied as a function of temperature in the cryostat without applying any additional heating to the absorber. IV-curves of the tunnel junctions at different cryostat temperatures are registered to determine or verify the choice of the working point, as well as for diagnostics of the junction quality. Then we can test the sensor by driving current through the absorber and measuring the response at a fixed cryostat temperature. Finally, noise spectra at different measurement conditions can be taken.

3. Experimental results

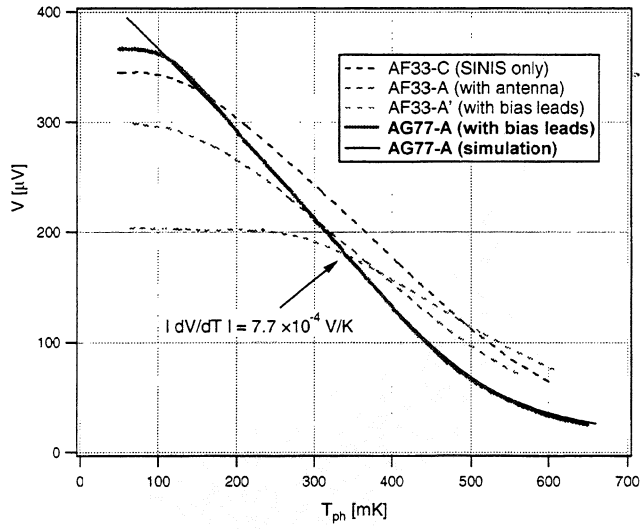

FIG. 4. Comparison of V(T) dependencies for different structures on sample AF33 (older data – dashed curves) and the same dependence for sample AG77, where additional tunnel junctions in the absorber bias circuit have been used (the thick curve). A strong saturation can be seen for the structure with long bias leads on the sample AF33. Saturation is present even for the sample AG77, but only below 100 mK. The thin curve is a theoretical fit for this sample's V(T).

When we started our experiments, we obtained good power responsivity (at the predicted level) at relatively high electron temperatures above 300 mK. However, at first we did not manage to obtain any good results where they were most expected – in the temperature range 100-300 mK. The reason for this was saturation of the response V(T) of the tunnel junctions, apparently seen in the calibration curves (fig. 4). Yet worse, the measured noise level used to be an order of magnitude higher then the noise of our amplifier, which had

modest 30 nV/Hz$^{1/2}$ at 10 Hz. It has taken a while to realize that those phenomena must have had the same cause, namely an intensive and noisy input signal, coupling to the absorber and heating the electrons sometimes above +300 mK. Two clues convinced us of the validity of this hypothesis: a comparison of noise and gain (=power responsivity) of the device (fig. 5a) and the dependence $T_{electron}(T_{phonon})$ of the absorber where $T_{electron}$ had been deduced by fitting IV-curves of the tunnel junctions at different temperatures (fig. 5b).

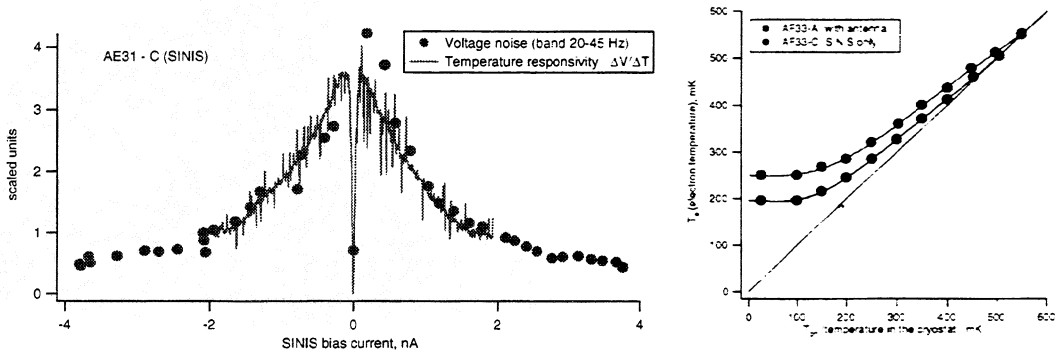

a) b)

FIG. 5. a) Spot noise and dV/dT plotted on the same graph for one of the older samples: both dependencies have very similar shapes, which must indicate that the noise is present already as fluctuations of electron temperature in the absorber, i.e. at the input. b) $T_{electron}$ (deduced from fits of IV-curves for SINIS double junctions) vs. temperature T_{ph} at which those IV-curves have been taken; data for sample AF33 (see also fig. 4).

Once being convinced about the presence of external heating we tried to identify how the noise comes in. Pick-up in the circuit connected for heating the absorber was one suggestion, a microwave "leakage" into the sample cavity was another one. Eliminating the second being a more difficult task, we started by breaking the absorber bias circuit by high-resistive elements close to the absorber. We hoped that the voltage induced in that low-ohmic (R_{abs} = 20 Ω) circuit by microphonics will drop on those high-resistive links, thus not being able to generate any noticeable current. We have chosen NIS tunnel junctions on both sides of the absorber as such protecting links, since they have very high intrinsic resistance in the sub-gap region, and they are very easy to fabricate (fig. 6).

This measure has given surprisingly good results, bringing the V(T) saturation down to 100-130 mK (fig. 4), and the noise level almost to the amplifier level. However, if we look at the noise spectra (fig. 7), we may notice, that connecting wires to the absorber and closing this circuit result in additional noise contributions, thus indicating that even this strong protection is not perfect. Furthermore, even the noise associated with an isolated

"absorber" island (7-10 $nV/Hz^{1/2}$) is clearly higher then what is expected from the thermometry noise (3 $nV/Hz^{1/2}$). We think that some high-frequency leak still exists and that it is responsible for this additional noise. Re-calculated to NEP the measured voltage noise corresponds to about $1.5 \cdot 10^{-17}$ $W/Hz^{1/2}$ at 10 Hz.

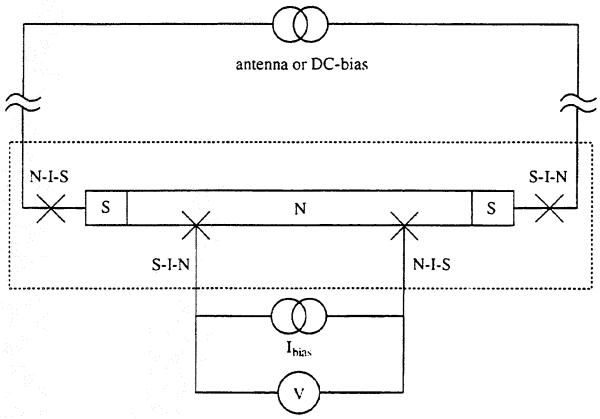

FIG. 6. The modified structure with additional NIS tunnel junctions in the absorber bias circuit.

However, the protection by tunnel junctions distorted completely the heating power calibration at $I_{absorber} > 0$. Earlier we could assume that the dissipated power was $P=P_J=R_{absorber} \times I^2_{absorber}$. Now, as soon as $I_{bias}>0$ high-energy electrons are injected into the superconducting electrode of the protecting NIS-junction, and further to the absorber, where this energy apparently dissipates, giving $P>>P_J$. This effect is similar to the electronic cooling by NIS tunnel junctions described elsewhere [5], but now our object is on the "warm" side of the Peltier cooler. This is the reason why we still can not report the calibrated experimental value of the power responsivity of our device at low temperature (100 mK).

This unfortunate situation does not seem to be a real obstacle. Simply reversing the NIS junctions and thus setting the N-part at the absorber side should be enough to solve the problem. An additional NS-interface between the superconducting electrodes going to the absorber and the N-side of the protecting junctions would interrupt the unwanted energy flow due to the Andreev reflection. Another simple (but probably not as elegant) solution is to use small external resistors, which can be bonded to the chip wiring, instead of tunnel junctions as high-resistive links.

Whatever difficulties can be expected in characterizing the device by applying a dc-current, the new results show that there are no severe problems with the sensor itself. If

we manage to couple the absorber efficiently to an integrated antenna, and place the device in an enclosure with well-controlled input of high-frequency radiation, we expect it to function properly.

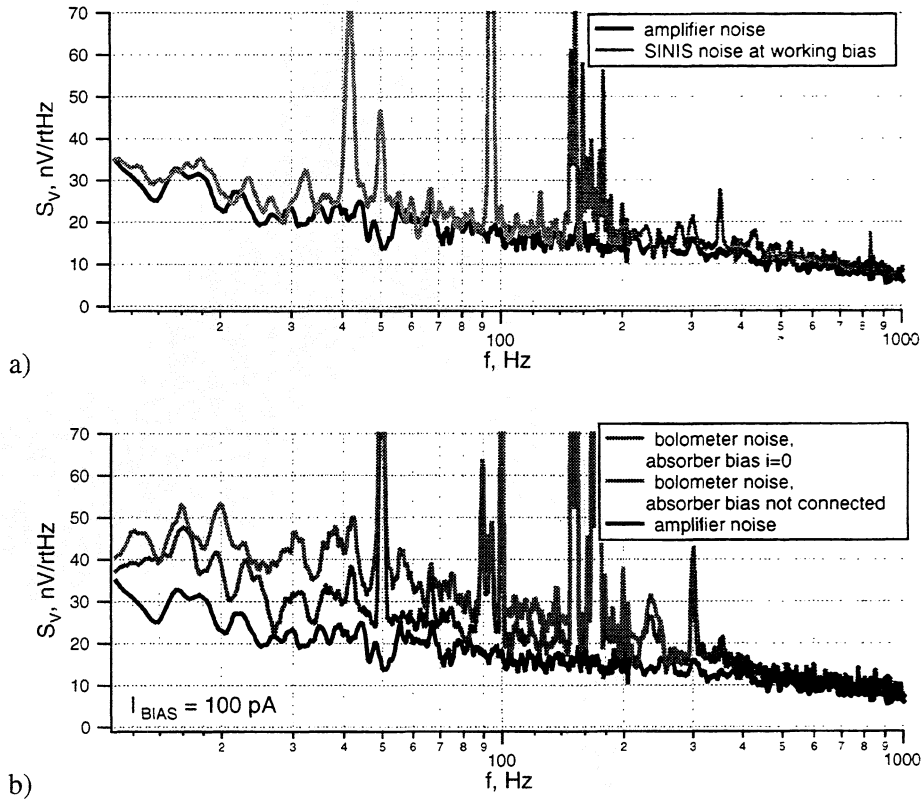

FIG. 7. Noise spectra for a) simple SINIS structure, i.e. without superconducting electrodes connected to the absorber and b) complete microcalorimeter structure equiped with protection NIS junctions and connected to long leads for biasing; the higher noise curve corresponds to leads terminated by a current source. The lowest curve in the both graphs is the amplifier noise.

Disregarding the input noise, the performance of the detector will be limited by thermal fluctuations in the absorber and the noise introduced by the electron temperature readout. The level of thermal fluctuations at a given operating temperature depends on dimensions and material of the absorber. Those, however, can not be varied freely – the absorber length is restricted to a value needed to provide proper impedance for match to the antenna and its width and thickness can not be reduced below certain technological limits. Also, the material choice is bound to the fabrication technology.

On the other hand, the noise from the read-out is a function of many parameters (tunnel junction resistance, number of the junctions, working point, amplifier performance etc.), which can be readily adjusted. Moreover, the noise contribution from the read-out will dominate in all practical configurations. That gives a motivation for optimizing the read-out parameters, and in the following section we will discuss what calculations can aid this process.

4. Optimizing the readout performance

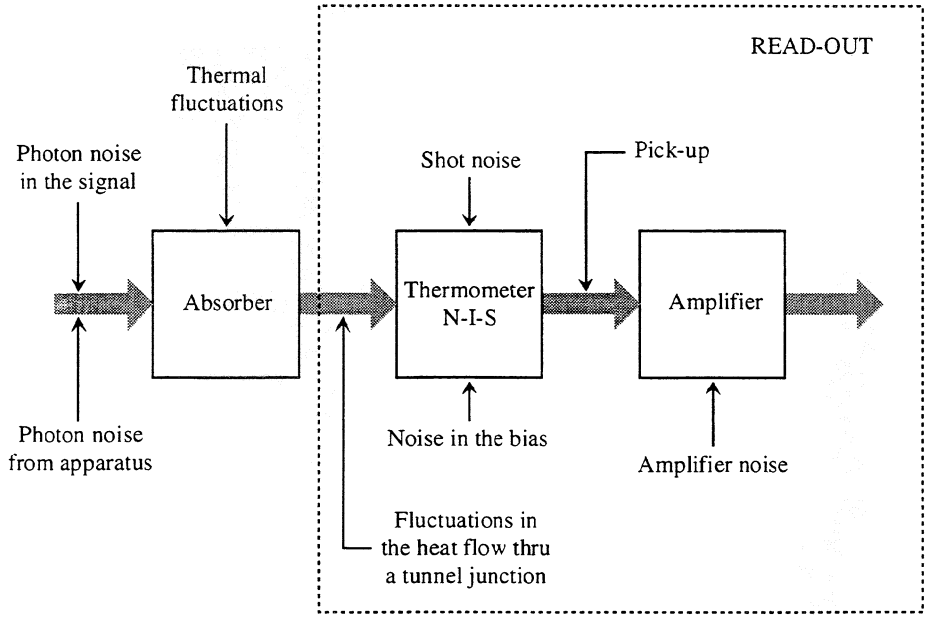

FIG. 8. Scheme of different noise contributions in the NHEB.

Different noise contributions adding to the useful input signal are depicted in fig. 8. The noise equivalent power of the detector can be expressed as

$$NEP^2 = NEP_{IN}^2 + 4k_B T^2 (G - G_{TJ}) + S_P(0) + \frac{S_I^{bias}(0)\left|\frac{dV}{dI}\right|_I^2 + 2eI\left|\frac{dV}{dI}\right|_I^2 + S_V^{ampl}(0) + S_V^{pick-up}(0)}{\left|dV/dT\right|_I^2} G^2$$

where

NEP_{IN}^2 is the photon and other noise coming with the signal to the input,

$4k_B T^2 (G - G_{TJ})$ – noise from thermal fluctuations in the absorber. (G-G_{TJ}) is the thermal conductance from the electron gas in the absorber to the lattice and environment. The thermal conductance due to the tunnel junctions is excluded here, since it is incorporated in the next term,

$S_P(0)$ – "heat flow noise", a component similar to shot noise, but related to the transfer of energy by quasi-particles tunneling through the junction.

$2eI \coth(eV/2T) \approx 2eI$ – current fluctuations due to discreteness of charge (shot noise)

$S_I^{bias}(0)$ – current fluctuations in the external bias applied to the junction

$S_V^{ampl}(0)$ – voltage noise of the amplifier (we assume a high-impedance FET-amplifier)

$S_V^{pick-up}(0)$ – voltage induced in the leads going from the sample to the amplifier (microphonics and rf-field detection)

$|dV/dT|_I$ – temperature responsivity of an NIS-junction at the working bias, and

G – total thermal conductance from the electron gas in the absorber to its environment.

One term here is "new" in the sense that it, to our knowledge, has not been included in any similar analysis before, and this is $S_P(0)$ [6]. If a voltage less then Δ/e is applied over an NIS junction, there will be an energy flow from the normal metal to the superconductor. The effect can be used to cool the normal metal [5] and, accordingly, this energy flow is often called "cooling power":

$$P(V,T_N,T_S) = \frac{1}{e^2 R_N} \int_{-\infty}^{+\infty} d\varepsilon \frac{\theta(\varepsilon^2 - \Delta^2(T_S))|\varepsilon|}{\sqrt{\varepsilon^2 - \Delta^2(T_S)}} (\varepsilon - eV)[f_N(\varepsilon - eV) - f_S(\varepsilon)],$$

where T_N and T_S are temperatures of the normal and superconducting electrodes, $\Delta(T_S)$ is the gap in the superconductor, f_N and f_S are electron distributions in respective electrodes. This expression is very similar to the expression is very for current going through an NIS junction

$$I(V,T_N) = \frac{1}{eR_N} \int_{-\infty}^{+\infty} d\varepsilon \frac{\theta(\varepsilon^2 - \Delta^2(T_S))|\varepsilon|}{\sqrt{\varepsilon^2 - \Delta^2(T_S)}} [f_N(\varepsilon - eV) - f_S(\varepsilon)],$$

but here every tunneling event results in transferring a portion of energy (ε-eV). Since the tunneling events are random and independent, there will be a heat flow noise similar to the usual shot noise. Calculating its spectral density is, however, somewhat more complicated, since the portions of energy are not all the same. The way to do this is to

integrate contributions $dS_{P,\varepsilon} = 2(\varepsilon - eV)\coth(eV/2T)P_e d\varepsilon$ from electrons with a particular energy in the range (ε, ε+dε) over all possible energies:

$$S_P(0) = \frac{2}{e^2 R_N}\coth\frac{eV}{2T}\int_{-\infty}^{+\infty} d\varepsilon \frac{\theta(\varepsilon^2 - \Delta^2(T_S))|\varepsilon|}{\sqrt{\varepsilon^2 - \Delta^2(T_S)}}(\varepsilon - eV)^2[f_N(\varepsilon - eV) - f_S(\varepsilon)] .$$

The heat flow noise is growing with applied voltage, respectively applied current, thus affecting the upper limit of the optimal range of the bias current for the temperature reading.

From the expression for the total noise one can see that the individual contributions from the different noise sources depend on the absorber properties (G), the shape of the NIS junction's IV-curve (dV/dI, dV/dT), and the working point $I=I_{bias}$. It is also worth to notice that in the theoretical calculations the temperature responsivity dV/dT as a function of bias current I can have a logarithmic singularity at $I \to 0$ (be arbitrary large). This may be misleading (suggesting very low bias currents), because this singularity does not exist in nature, being destroyed by fluctuations near $I=0$.

We can use a computer program to simulate the total noise for any given set of parameters. For the integral giving the IV-characteristics of an NIS junction there is a good analytical approximation, which is suitable for fast calculations. But this is not the case for the heat flow integral, and its computing in every point slows down the model a lot. Fortunately we can separate the tasks. Sets of noise data can be pre-compiled for a specific working temperature T, superconductor with energy gap Δ, and tunnel junction quality in terms of sub-gap conductance $r_o = R(0)/R_N$. Then we can combine those half-ready arrays by substituting all the other parameters of the device:

absorber size and material $\Sigma\Omega$,
current bias source with noise $S_{I.bias}(0)$,
amplifier with noise $S_{ampl}(0)$,
input noise NEP_{IN},
normal resistance of tunnel junctions R_N, and
working bias current I_{bias}.

This can be done really fast, and we have actually made a computer program where one can gradually tune any of those parameters and see on a screen in real time how it affects every noise component and the total NEP. Examples of how the different noise components and the total NEP depend on the SINIS bias current are given in fig. 9 for two different values of R_N and two different temperatures.

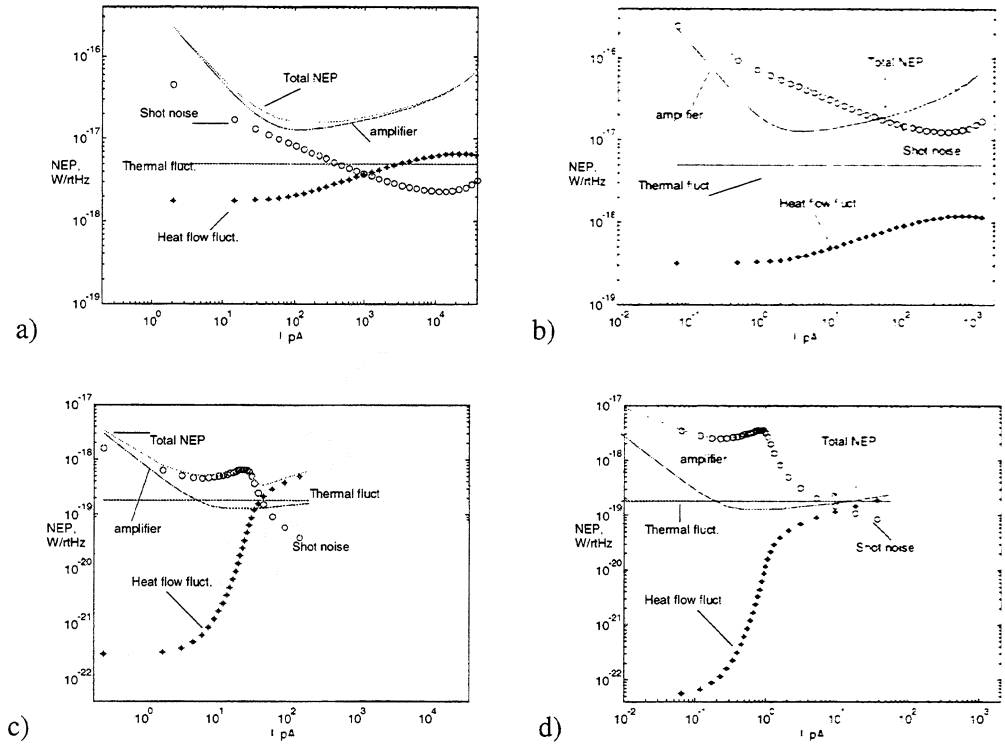

FIG. 9. Different noise components and the total noise calculated as function of SINIS bias current for R_N=1 kΩ (a,c) and R_N = 30 kΩ (b,d) /R_N per one junction/ assuming working temperature of T=300 mK (a,b) and T=100 mK (c,d).

5. Conclusion

We have managed to demonstrate a reasonable performance of the microcalorimeter which we aim to use as power sensor in an integrated antenna-coupled bolometer. We could do this also at temperatures below 100 mK, where the responsivity of the sensor is much higher than in our earlier results (for 300 mK). The measured noise level corresponds to about NEP = $5 \cdot 10^{-18}$ W/Hz$^{1/2}$, and it is dominated by the input noise external to the sensor itself and the amplifier noise. Some refinement of the experiment is still needed to make a fully calibrated characterization of the device.

We considered the noise components determining the practical performance of the future detector, some of them not referred to in earlier analyses of the similar kind. In particular, we payed attention to the heat flow noise, important at higher thermometer bias currents. We also showed how noise optimization can be performed in a model, co-adjusting two or several device and operation parameters at the same time.

References

[1] P.L. Richards, J. Appl. Phys. **76** (1), 1 (1994).

[2] A.T. Lee, S-F. Lee, J.M. Gildemeister, and P.L. Richards, Proc. of the 7th Int. workshop on Low Temperature Detectors, Munich, July-Aug 1997, pp 123-125.

[3] M. Nahum, P.L. Richards, and C.A. Mears, IEEE Trans. Appl. Supercond. **3**, 2124 (1993).

[4] M. Nahum and J. Martinis, Appl. Phys. Lett. **63**(22), 3075 (1993).

[6] M.M. Leivo, J.P. Pekola, and D.V. Averin, Appl. Phys. Lett., **68** (14), 1996 (1996).

[5] L.S. Kuzmin, D.S. Golubev, and M. Willander, *SIN tunnel junction as a temperature sensor*, draft.

OPTIMUM RECEIVER NOISE TEMPERATURE FOR NbN HEB MIXERS ACCORDING TO THE STANDARD MODEL

K. Sigfrid Yngvesson[1] and Erik L. Kollberg[2]

[1]Department of Electrical and Computer Engineering, University of Massachusetts, Amherst, MA 01003

[2]Department of Microelectronics, Chalmers University of Technology, S-41296 Gothenburg, Sweden

INTRODUCTION

This paper addresses the problem of how to find the optimum noise performance of NbN HEB mixers, based on the original model for such devices, the "standard model". The standard model was developed in the work of Arams et al.[1], and also by the group of Gershenzon et al in Russia [2]. The main assumption inherent in this model is that the device is treated as a uniform bolometer with a heat capacity, C_e, and thermal conductance to the heat sink, G_{th}. The bolometer has a resistance which depends on the electron temperature, θ, and equal amounts of DC and RF (LO) power produce identical changes in the electron temperature. The entire device is taken to be at the same electron temperature. More recent uses of this model include that by Yang et al. [3,4] for 2DEG HEBs, and by Ekström et al. [5,6]. The latter two references analyzed measurements taken at about 20 GHz on a phonon-cooled HEB (PHEB) with Nb, and obtained detailed quantitative agreement of the measured and the calculated conversion loss, as the bias voltage was varied. A popular method for "calibrating" the LO power absorbed by the device is also based on the assumption of equal heating effects due to DC or RF power [6]. Recently, analysis of NbN HEBs exposed to RF power at THz frequencies has shown that this model leads to inaccurate results, in terms of being able to predict the absorbed LO power correctly, see Merkel et al., 1998 [7]. This puts into question the validity of the standard model for calculating other quantities, such as conversion loss, output noise temperature, and receiver noise temperature. In this paper we show that the main functional dependence of these quantities on the LO power, as measured for several NbN HEBs, is still in quite good agreement with measured data, based on the standard model, if the operating point is fairly close to the experimentally determined optimum point for lowest receiver noise temperature. The theory uses two adjustable parameters to fit measured data for receiver noise temperature, and output noise temperature. We also compare the theoretical prediction for the conversion loss, which can be derived from the measured noise data. For all devices, the optimum noise temperature is measured to occur for about the same value of the optimum bias current, I_0, normalized to the bias current without LO power, I_{00}, a ratio which is about 0.3 to 0.45. This optimum results from the competing dependencies of the conversion loss, as well as the different noise processes,

upon the LO power, as we discuss in detail below. The model also enables us to make reasonable estimates of the optimum receiver noise temperature which is achievable with this type of devices of the best quality presently available, and to make approximate comparisons with HEBs which use other materials, such as Nb and Al.

DEFINITION OF THE MODEL

The analysis we will use was presented in detail in [5], and [6], and the main equations will be quoted from these references. We refer to these for detailed derivations.

Conversion gain

The conversion gain may be calculated by using measured parameters obtained from the IV-curves of the device, see Figure 1.

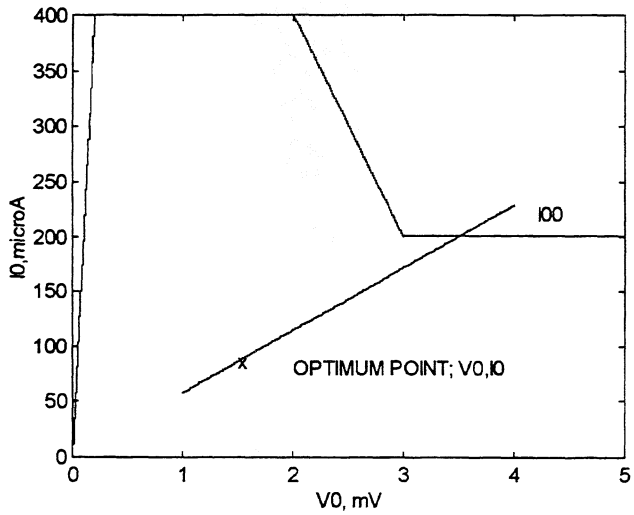

Figure 1. Typical I-V-curve for a NbN HEB device.

The bias currents with and without LO power, respectively, defined along a line of constant resistance, R_0, are I_0 and I_{00}. The quantity $C_0 = dR/dP$ is also assumed to be constant along this line, since it represents a constant electron temperature. The original derivation of the Single Sideband conversion gain of an HEB mixer by Arams et al. [1] yielded the following expression

$$G = 2C_0^2 \frac{P_{LO}P_{DC}}{(R_L + R_0)^2} \frac{R_L}{R_0} \left[1 - C_0 I_0^2 \frac{R_L - R_0}{R_L - R_0} \right]^{-2} \quad (1)$$

where R_L is the IF load resistance. The above equation is equivalent to the one used by Elantiev and Karasik [8, Eq. (17)]. According to the assumptions of the standard model, we can write the local oscillator power P_{LO} as $R_0(I_{00}^2-I_0^2)$, and the DC power dissipated at the bias point, P_{DC}, as $R_0I_0^2$. Inserting these into (1), we obtain

$$G_{dB} = 10\log\left[2C^2x(1-x)\frac{b\sqrt{x}}{\left(b\sqrt{x}+1\right)^2}\left(1-Cx\frac{b\sqrt{x}-1}{b\sqrt{x}+1}\right)^{-2}\right] \qquad (2)$$

Here, we have introduced $b= R_LI_{00}/V_0$, where V_0 is the bias voltage with LO power applied. Also, $C_0I_{00}^2 = C$. We let $x=(I_0/I_{00})^2$ represent the variation with the LO power (P_{L0} goes to zero for x=1).

Temperature Fluctuation Noise

It has been established for both PHEBs and Diffusion-Cooled HEBs (DHEBs) that the main noise mechanism is that due to fundamental fluctuations in the temperature of the bolometer medium, with an equivalent output noise temperature, T_{FL}. The expressions given by different sources are basically equivalent, but differ in some details, partly because they were compared with experiment in situations which allowed some approximations. For example, Ekström and Karasik [9] give the output noise from the device into a matched load, R_L. A careful re-examination reveals that the R_L-dependence for T_{FL} is the same as for G, a conclusion also consistent with that of Elantiev and Karasik ([8], Eq. (27); we assume that $Z(\infty) = R_0$]. We then find the following expression for the temperature fluctuation output noise, T_{FL}:

$$T_{FL} = \frac{I_0^2R_L\left(\frac{dR}{d\theta}\right)^2\left(\Delta T_{FL}\right)^2}{(R_0+R_L)^2\left(1-C_0I_0^2\frac{R_L-R_0}{R_L+R_0}\right)^2} \qquad (3)$$

Here, $dR/d\theta$ is the dependence of R on electron temperature at the actual operating point. It can not be obtained by simply using the measured R/T-curve, but can be found by using IV-curves near the desired point taken at different temperatures, as shown in Ekström et al [10]. Here, we regard it as a fitting parameter. Also, $(\Delta T_{FL})^2$ is known from basic thermodynamics to be $4\ k_B\theta^2/G_{th}$ (per unit bandwidth), where $G_{th}= C_e/\tau_\theta$ is the thermal conductance from the device to the heat sink (C_e is the heat capacity of the device, and τ_θ

the energy relaxation time constant). We can simplify (3) by using the fact [5] that $C_0 = (dR/d\theta)(\tau_\theta/C_e)$, introducing x for $(I_0/I_{00})^2$, and defining a numerical constant $N=4\theta^2 (dR/d\theta)$; hence

$$T_{FL} = \frac{Cb^2x^2}{\left(b\sqrt{x}+1\right)^2}\frac{N}{R_L}\left[1-Cx\frac{b\sqrt{x}-1}{b\sqrt{x}+1}\right]^{-2} \quad (4)$$

Note that the two device parameters which determine the strength of the temperature fluctuation noise through N are $\theta \approx T_c$ ($T_{FL} \propto \theta^2$), and $dR/d\theta$.

It was also demonstrated experimentally in [9] that the time-constant which characterizes the frequency-dependence of the temperature fluctuation noise (τ_θ^*) is the same as the one for the mixer conversion loss (τ_{mix}). These are given by

$$\tau_\theta^* = \tau_{mix} = \frac{\tau_\theta}{1-C\dfrac{R_0-R_L}{R_0+R_L}} \quad (5)$$

where τ_θ is the energy relaxation time of the medium.

Johnson Noise

The Johnson noise can similarly be written as [6]

$$T_J = \frac{4\theta R_0 R_L}{(R_0+R_L)^2}\frac{(1-Cx)^2}{\left[1+Cx\dfrac{R_0-R_L}{R_0+R_L}\right]^2} = \frac{4\theta b\sqrt{x}}{\left(b\sqrt{x}+1\right)^2}\frac{(1-Cx)^2}{\left(1-Cx\dfrac{b\sqrt{x}-1}{b\sqrt{x}+1}\right)^2} \quad (6)$$

Receiver Noise Temperature

The total (intrinsic) Double Sideband (DSB) receiver noise temperature is now obtained from the usual expression

$$T_{RX,DSB} = L_c/2\,(T_{out} + T_{IF}) \qquad (7)$$

$L_c = 1/G$ is found from (2) above, and (4) plus (6) yield

$$T_{out} = T_{FL} + T_J \qquad (8)$$

For low receiver noise temperature situations, we may also need to take into account a term $= 2T_{in}/L_c$ which contributes to T_{out} in (8) (from both sidebands ; T_{in} is usually either 300 K or 77 K).

Elantiev and Karasik [8] derived an expression for the receiver noise temperature , T_m^{TF} , in the idealized special case for which the only noise process included is that due to temperature fluctuations, and the IF amplifier noise is neglected. They found that it is predicted to approach zero as the LO power is increased indefinitely. We can confirm this by calculating the ratio of Equations (5) and (2), by which we recover Eq. (28) in [8].

$$T_m^{TF} = \frac{2\theta^2 G}{P_{LO}} \qquad (9)$$

The receiver noise temperature vanishes despite the fact that the conversion loss goes to infinity. We illustrate this for typical values of the parameters in (2) and (5) in Figure 2 which displays the DSB receiver NT:

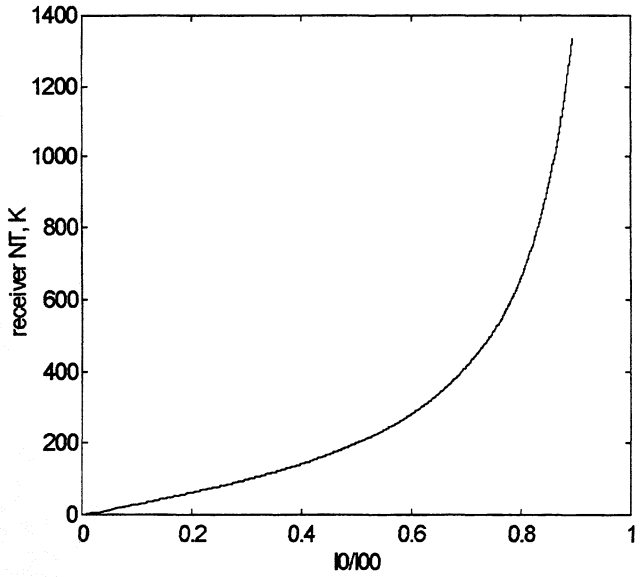

Figure 2. Predicted intrinsic receiver noise temperature for an ideal HEB receiver which has only temperature fluctuation noise.

The parameters used in Figure 2 are typical for NbN PHEBs (C=1, b=4, $dR/d\theta$ = 75 ohms/K, T_c = 10 K, R_L = 50 ohms).

In Figure 3 below, we can clearly see the opposite trends of the two contributions to the output noise, T_{FL} and T_J , as the LO power is changed. Figure 4 indicates that the conversion loss has a minimum for a fairly low LO power, i.e. large I_0/I_{00} (about 0.85).

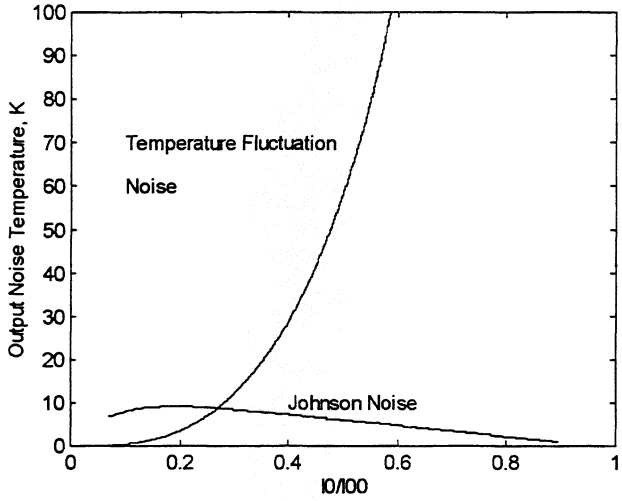

Figure 3. Temperature fluctuation noise and Johnson noise at the output of a typical NbN HEB mixer. Parameters are: C=1, $dR/d\theta$ = 55 ohms/K, b=4, T_c =10K

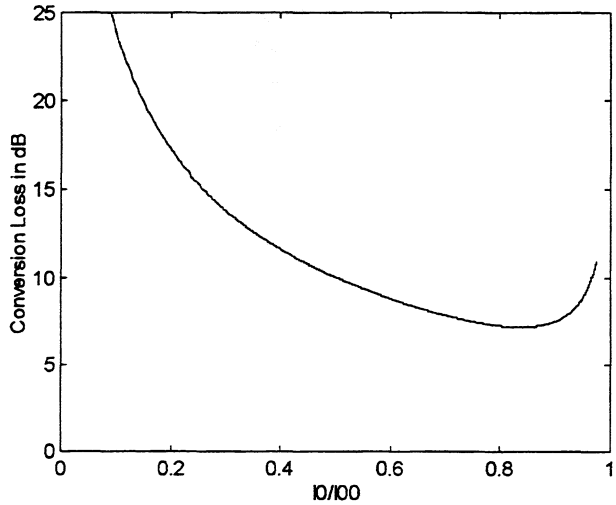

Figure 4. SSB Conversion loss versus normalized current (I_0/I_{00}) for the same HEB mixer as in Figure 3.

Due to the other noise sources in a practical receiver (Johnson noise, IF amplifier noise) beyond the fluctuation noise, increasing the LO power to a very large value will not be the condition for which the receiver noise temperature will be optimized. Conversely, the region of very low LO power, in which the conversion gain has a maximum, will not result in the lowest receiver noise temperature either, since then the temperature fluctuation noise becomes very large. The optimum receiver noise temperature should occur for an LO power in between these extremes. We will explore this question as we compare the predictions from the standard model to experimental data obtained recently on NbN PHEB devices.

COMPARISON WITH EXPERIMENTAL DATA

Many experiments yield data for both T_{out} and $T_{RX,DSB}$ (see [10]). The measured DSB receiver noise temperature is of course the total value, including input losses. One can then also find L_c from (7). This value will be the total SSB conversion loss, from the mixer input (outside the dewar) to the IF amplifier, including all input losses, and mismatch at the RF and the IF. Often, it is possible to either independently measure, or to estimate, the losses outside the mixer itself, and thus one can also find the intrinsic receiver noise temperature, and the intrinsic mixer conversion loss, $L_{c,int}$. These are the quantities calculated in (2) and (7). Experiments can thus obtain data for three quantities:

(i) $T_{R,DSB,int}$;
(ii) T_{out};
(iii) $L_{c,int,SSB}$.

Values for these quantities were obtained from measured data at different points in the IV-diagram, by varying the bias voltage and the LO power, respectively. We have used this procedure for several different NbN devices. We adjusted only the two parameters N and C in order to obtain the best fit between predictions based on the standard model, and the experimental values of the above three variables, measured as a function of LO power. The value of C can be obtained by fitting the conversion loss data, which do not depend on N. This value for C is then inserted in (4) and a fit is obtained to the data for T_{out}. The values of C and N may need to be re-adjusted to obtain a good fit to the data for the intrinsic receiver noise temperature. The noise temperature for the specific IF amplifier used in each experiment was also measured independently, and inserted in the equations. Reasonable fits were possible as the LO power was varied, as shown for one device in Figure 5 though 7. The best fit values of C and N were obtained from similar plots for a total of five devices, measured at frequencies near 650 GHz (devices 1,2,3 and 5) and 1560 GHz (device 4), respectively, as summarized in Table 1. The standard model also predicts well the variation of the output noise temperature with bias voltage at constant LO power, but not the conversion loss and the receiver noise temperature under these conditions, as discussed further below.

TABLE 1. Summary of data derived from a comparison of experimental measurements and calculations based on the standard model.

Dev.#	t,nm	freq. THz	$T_{R,i}$ opt. K	I_0/I_{00} at opt.	$L_{c,i}$ opt dB	T_{out} opt.	C	N times 10^{-4}	dR dθ Ω/K	b	V_0 (mV)
1UM	3.5	0.62	190	0.46	8.5	82	1.2	2.6	65	4.45	2.0
2UM	3.5	0.62	240	0.45	10.2	60	1.1	2.2	55	4.45	2.0
3CTH	3.5	0.60	300	0.32	14	30	1.0	3.0	75	3.79	1.4
4UM	4.0	1.56	435	0.37	12.3	42	1.0	4.84	100	2.4	5
5UM	5.0	0.62	500	0.42	15.7	27	0.8	0.86	15	12.5	2.0

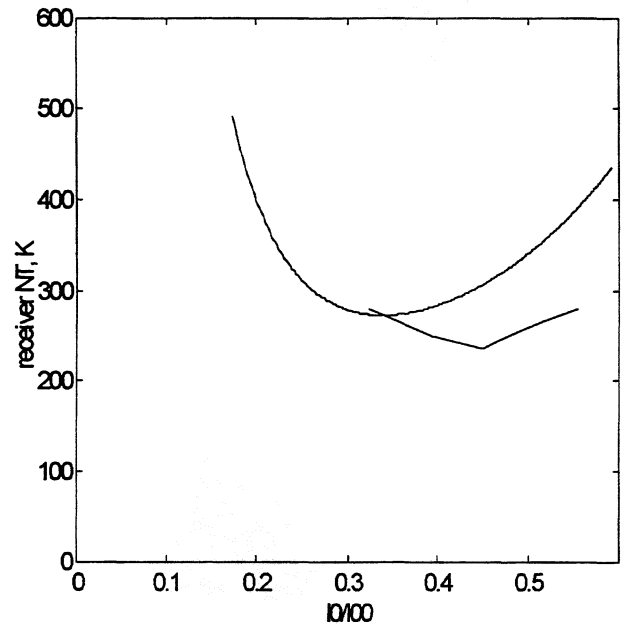

Figure 5: Predicted and measured intrinsic receiver noise temperature versus normalized bias current for device #2 in Table 1. Measurements were done at 620 GHz. In this and the following figures, the smooth curve is the predicted one, if not specifically marked.

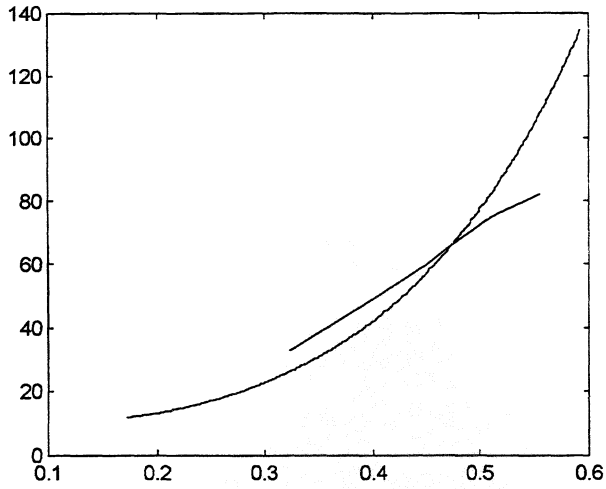

Figure 6: Predicted and measured output noise temperature in K, versus normalized bias current for device #2.

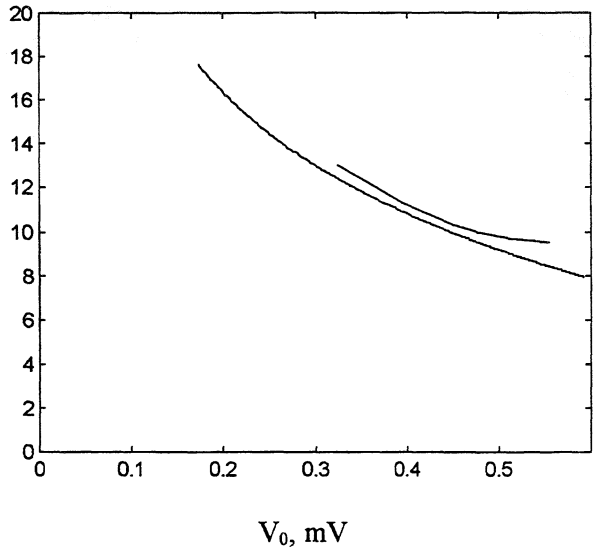

Figure 7: Predicted and measured intrinsic conversion loss (in dB) versus normalized bias current for device #2.

DISCUSSION

The comparison given above between theoretical predictions and experimental data for several devices enables us to draw some general conclusions. Specifically,

1) There is a qualitative agreement between the theoretical and experimental curves of $T_{R,DSB}$, $L_{c,i}$, and T_{out}, as the LO power is varied over the range used in the experiments.
2) The optimum intrinsic $T_{R,DSB}$ is in the range 190 K to 500 K. The thinnest devices consistently yield lower NT.
3) The optimum receiver NT occurs at a very similar I_0/I_{00} value for all devices; the experimental range is 0.32 to 0.46, and this is close to what is predicted from the standard model.
4) The optimum conversion loss is at best 8.5 dB, and more commonly 10-12 dB. The devices with lowest conversion loss typically also have higher output noise temperature. The conversion loss is lower by a sufficiently large factor that $T_{R,DSB}$ is still lower for these devices.
5) The values for $dR/d\theta$ also fall in a fairly narrow range, from 55 to 100 Ω/K, except for the 5 nm device which has $dR/d\theta$ = 15 Ω/K.

We discuss some of these conclusions further below:

C-value and optimum conversion loss.

We can predict the C-value from the standard model by using the slope of the IV-curve for the no-LO case, i.e. at a current of I_{00}, using the following expression from [5]:

$$\frac{dV}{dI} = R_0 \frac{1 + C_0 I_{00}^2}{1 - C_0 I_{00}^2} \quad (10)$$

For all of our recent NbN devices, the slope at this point of the IV-curve is essentially horizontal, i.e. dV/dI is infinite, and $C = C_0 I_{00}^2 \approx 1.0$. This is seen to agree with the C-value derived from our comparison with the experimental data. For C = 1, the optimum conversion loss is 6 dB, but this is attained for a much larger I_0/I_{00}-value than seen in the experiments ($I_0/I_{00} \approx 0.8$ to 0.9). As mentioned before, the low conversion loss at larger normalized current does not lead to the optimum noise temperature, since the fluctuation noise grows rapidly with increasing I_0/I_{00}. The C-value we derive from fitting the experimental data of receiver noise temperature, etc., is close to 1.0 (the range is 0.8 to 1.2). We can therefore assume an effective value for C of 1.0 when assessing the optimum performance of NbN HEBs (this is quite conservative since we have already measured NbN devices with C as high as 1.2, which have lower noise temperature than we claim for NbN in this section).

To avoid confusion, we should mention that Karasik and Elantiev [8] use a different definition of C ($C=C_0I_0^2$, *where I_0 is the current at the operating point*).

N-value and dR/dθ.

The values for N and dR/dθ also fall within a fairly narrow range. One can estimate dR/dθ based on IV-curves for different temperatures, and this was done for a NbN PHEB in reference [10]. A value similar to what we have found here was obtained, dR/dθ = 63 Ω/K. For Nb DHEB devices, dR/dθ was estimated to be in the range 68-250 Ω/K [11], somewhat lower in operating points which yield optimum conversion gain. However, this reference found that it was not generally possible to predict T_{out} for Nb DHEBs from parameters such as dR/dθ and the standard model [11]. We will compare PHEBs and DHEBs later in this paper.

Discussion of Variation with the Bias Voltage

Measured and modeled data for different bias voltages at constant LO power are given in the following three figures. The bias voltage enters the equations through $b = R_L * I_{00} / V_0$. We used the same values for C and N, resp., which were obtained from the fit in Figures 5 through 7. The values of I_0/I_{00} for each point were found from an experimental IV-curve for constant LO power. This curve included the point at which the optimum receiver noise temperature was measured.

It is clear that the standard model does not predict the variation of receiver noise temperature (Figure 8) or conversion loss (Figure 9) with the bias voltage, although the output noise temperature curve shows a good fit (Figure 10). The predicted conversion loss depends only on C, not on N, and it is thus clear that if one wanted to fit the conversion loss versus V_0 with the standard model expression, then C must also vary with V_0. Specifically, C would need to decrease as V_0 increases. This behavior is actually found in the one-dimensional hot spot model of Merkel et al. [7]. In future work, we plan to incorporate the conclusions from [7] explicitly in our model. This will not be pursued further here, however. Instead, we note that close to the optimum, $C \approx 1$ produces a good fit, and that this point occurs for a bias voltage corresponding to a b-value of roughly 4.

Another parameter which changes the value of b in our equations is R_L. Since the b-dependence for receiver noise temperature and conversion loss differs from that of the standard model, we do not at this stage know how to predict how the receiver noise temperature would change if we were to change R_L. We can, however, predict what would happen if we were to change R_L and V_0 by the same factor. In this case, b will be unchanged, and the receiver NT will also not change. There are almost certain to be parameter combinations for which the NT would decrease for a change of R_L from the value of 50 ohms which we assume throughout this paper, however. This offers an intriguing possibility of further lowering the receiver NT of THz HEBs.

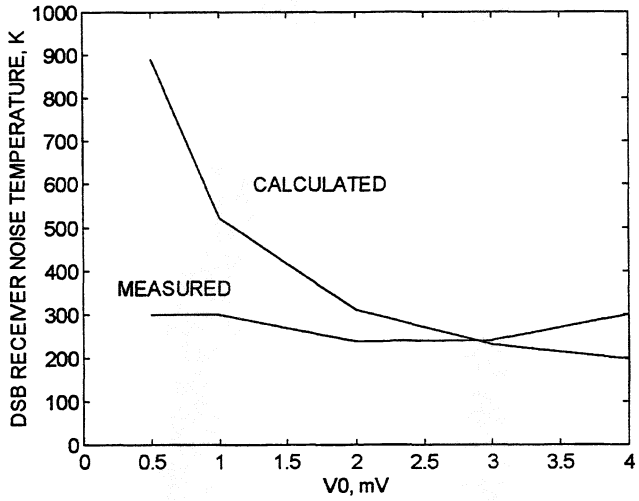

Figure 8: Calculated and measured intrinsic DSB receiver noise temperature versus bias voltage for device #2. The LO power was kept constant for this and the next two plots.

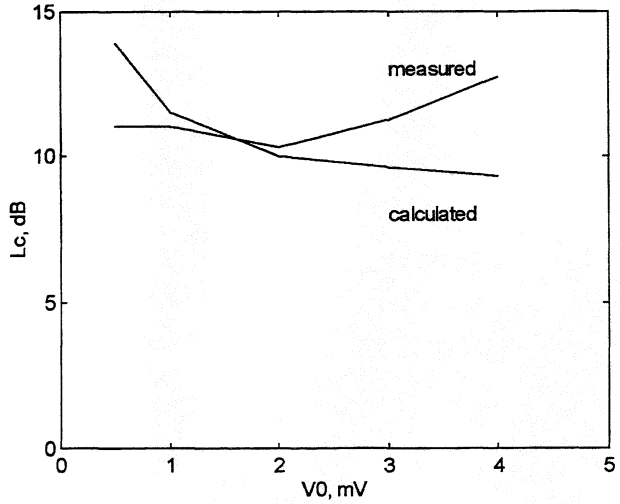

Figure 9: Calculated and measured intrinsic SSB conversion loss versus bias voltage for device #2.

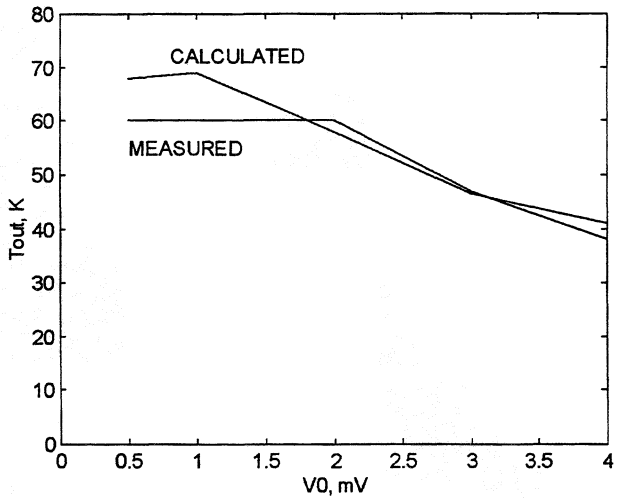

Figure 10: Calculated and measured output noise temperature (K) versus bias voltage (mV) for device #2.

Prediction of Optimum Receiver Noise Temperature for Devices with Different Critical Temperatures.

Based on the above results, we can make some approximate predictions for the expected optimum receiver noise temperature for different materials, such as NbN, Nb, and Al. The detailed model for diffusion-cooled HEBs is certainly different from that of PHEBs, but it is believed that the standard model is still a sufficiently good guide for this estimate. The standard model was, indeed, used for this purpose by Elantiev and Karasik [8], and by Karasik and McGrath [12]. In performing this estimate, we will choose values of C = 1.0, and $dR/d\theta$ = 55 Ω/K, which are typical for the optimum points of NbN devices. The main difference between the different materials then is the transition temperature, θ, for which we take 10 K for NbN, 5 K for Nb, and 1.5 K for Al. Any real receiver would also be somewhat limited in performance by its IF amplifier, and we assume a value for T_{IF} of 5 K, about the best which is presently achievable. Figure 11 shows our predictions for receiver NT for these materials, assuming the same values for the other model parameters. **The conclusion is that a lower transition temperature in principle helps one achieve a lower receiver NT. However, other factors must also be considered, as becomes clear as we compare these predictions with the best experimental data measured so far.** As expected, the optimum receiver noise temperature occurs for a higher value of I_0/I_{00} (0.46 for Nb and 0.75 for Al) as θ is decreased, since the temperature fluctuation noise is lower. The total output noise temperature at the optimum receiver noise point is 13 K for Nb and 6 K for Al. Our predicted optimum receiver noise temperatures are considerably higher than those

obtained by Elantiev and Karasik [8], and later Karasik and McGrath[12]. The latter authors find 50 K for NbN, 12 K for Nb, and 4 K for Al. These estimates utilize approximations which would appear to be equivalent to using a very large C-value (about 6, using our definition), which we believe is unrealistic (see the discussion above). The optimum conversion loss is consequently predicted to be very low (some conversion gain, actually). Conversion gain has been measured in lower frequency HEB mixers [5, 11], and for a NbN PHEB mixer at very low IF (600 kHz) in one case [13]. While HEBs clearly can achieve conversion gain under such special conditions, this has not yet been demonstrated at GHz IF for any THz HEB mixers. Instead, we find a lowest conversion loss of 8.5 dB (see Table 1). In comparing existing measured data for Nb DHEBs with our predictions [11], we note that for the frequencies 533, 1267, and 2540 GHz, the output noise temperature was 41K, 16.6 K, and 10 K, respectively. At the same frequencies, the intrinsic conversion loss was 14 dB, 13 dB, and 18.5 dB. The lowest intrinsic receiver noise temperature was found at 1267 GHz, and would be 210 K, if we assume T_{IF} =5 K. This is comparable to the best NbN results, as are the recent measurements of the total receiver NT at 2.54 THz [14]. The conversion loss at all the above frequencies is higher than for any of the NbN mixers, however, which explains why the measured receiver NT at the present time is roughly comparable for Nb DHEBs and NbN PHEBs. **Thus, low output noise is not sufficient, one also must have low conversion loss, in order to realize the optimum receiver noise temperature performance of which HEB mixers are capable.** Nb DHEBs may also have somewhat higher values of $dR/d\theta$ [11], whereas 55 ohms/K was used for the predicted performance in Figure 11. NbN mixers have higher output noise in general, but also considerably lower conversion loss. For NbN we have included two curves in Figure 11: one with C=1, and another one with C=1.2 and $dR/d\theta$ = 45 ohms/K which approximately matches the best NbN mixer in Table 1 with $T_{R,DSB}$ of 190 K; note that this performance has already been achieved. The situation for Al is of course completely unpredictable at the moment, until experimental data become available. Specifically, it must be clarified whether low conversion loss is at all possible in Al, for which a different process due to bandgap suppression from the hot electrons (Semenov and Gol'tsman, [15]) may be responsible for the HEB conversion gain, (it appears that no electron equilibrium distribution can become established). Other uncertainties in the Al case are the effective value for $dR/d\theta$, and whether there are any difficulties in operating in the optimum region for this material, which requires lower LO power, based on the standard model (instabilities may become a problem). Finally, we should note that the quantum noise limit for any coherent double sideband mixer is hf/2k = 24 K at 1 THz, and 61 K at 2.54 THz. None of the above HEB mixer technologies can of course produce lower noise temperature than hf/2k, and the intrinsic noise temperatures of NbN mixers are presently less than a factor of ten times this limit. As HEB technology develops further, the difference in receiver NT between different versions will matter less and less, and other factors may assume primary importance.

The standard model versus newer models

We have shown that some features in the measured data for NbN PHEBs can be explained quite well by the standard model, whereas others can not. Specifically, we can not model the dependence of the receiver noise temperature on V_0, and as a consequence also do not know the effect of R_L. HEB receiver designers will require a model which covers all important aspects in order to be able to successfully optimize all aspects of the performance of these already very good receivers, however. The standard model is basically a "zero-dimensional" model which can for example be expected to describe an HEB device exposed to sub-bandgap microwave power. The DC power and the microwave power are then absorbed in equal resistances in any given section of the device, and a single heated region ("hot spot") is obtained. On the other hand, at above bandgap frequencies, THz radiation is absorbed in the entire device, whereas DC heating is likely to still create a hot spot (see Merkel et al.,[7]). A more complicated model is clearly required for the THz case. Progress along these lines will require further work in which HEB theory and "diagnostic" measurements of the type we have used, are coupled in order to validate the new HEB models.

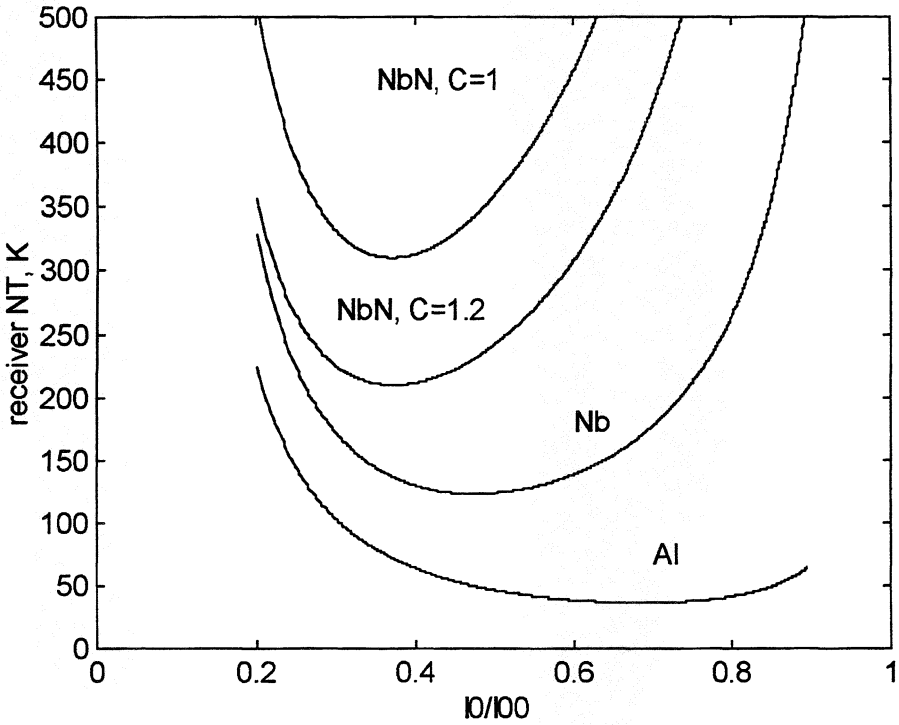

Figure 11. Optimum noise temperature for three different HEB technologies, predicted from the standard model. Parameters assumed are C=1 (additional curve for NbN with C=1.2), b = 4, R_L = 50 ohms, and $dR/d\theta$ = 55 ohms/K. T_c is 10 K, 5 K, and 1.5 K, respectively, for NbN, Nb, and Al.

CONCLUSION

Comparison of experimental data for several NbN PHEBs with calculations based on the standard model indicate good agreement with the variation of receiver NT, output noise and conversion loss as a function of LO power. As the bias voltage (V_0) is varied, it appears that the effective self-heating parameter C decreases with increasing voltage. Further investigations of this problem should be able to include the variation with V_0, and result in predictions of the optimum IF load impedance. It would be interesting to extend the measurements to the IF impedance, and compare this with model predictions. Ultimately, HEB designers need a comprehensive model upon which to base the detailed design of matching circuits, which optimize not only the noise temperature, but the IF bandwidth and the flatness of the receiver NT versus IF frequency as well.

ACKNOWLEDGEMENTS

It is a pleasure to acknowledge collaboration with several other researchers, who provided experimental data which have been used in this paper, or contributed to the paper through many discussions. We would like to especially thank Drs. Eyal Gerecht, Harald Merkel and Pavel Yagoubov.

REFERENCES

[1] F. Arams, C. Allen, B. Peyton, and E.Sard, Proc. IEEE, **54**, 308 (1965).
[2] E.M. Gershenzon, G.N. Gol'tsman, I.G. Gogidze, A.I. Elant'ev, B.S. Karasik, A.D. Semenov, Sov.Phys.Superconductivity, **3**, 1582 (1990).
[3] J.-X. Yang, F. Agahi, D. Dai, C. Musante, W. Grammer, K.M. Lau, and K.S. Yngvesson, IEEE Trans. Microw.Theory Techniques, **MTT-41**, 581 (1993).
[4] J.-X. Yang, Ph.D. thesis, University of Massachusetts at Amherst, Dept. of Electrical and Computer Engineering, Sept. 1992.
[5] H. Ekström, Ph.D. thesis, Chalmers University of Technology, Dept. of Microelectronics (1995).
[6] H. Ekström, B. Karasik, E. Kollberg and S. Yngvesson, "Conversion Gain and Noise of Niobium Hot-Electron Mixers," IEEE Trans.Microw.Theory Techniques, **MTT-43**, 938 (1995).
[7] H.F. Merkel, E.L. Kollberg, and K.S. Yngvesson, Proc. Ninth Intern.Symp.Space THz Technology, p. 81 (1998). Also see paper by Merkel et al. in this conference proceedings.
[8] B.S. Karasik, and A.I. Elantiev, Proc. Sixth Intern.Symp.Space THz Technology, p. 229 (1995).

[9] H. Ekström, and B.S. Karasik, Appl.Phys.Lett, **66**, 3212-3214 (1995).
[10] H. Ekström, E. Kollberg, P. Yagoubov, G.Gol'tsman, E. Gershenzon, and S. Yngvesson, Proc. Eighth Intern.Symp.Space THz Technology, p. 29 (1997).
[11] P.J. Burke, Ph.D. thesis, Yale University, Dec. 1997.
[12] B.S. Karasik, and W.R. McGrath, Proc. Ninth Intern.Symp.Space THz Technology, p. 73 (1998).
[13] E. Gerecht, C.F. Musante, H. Jian, K.S. Yngvesson, J. Dickinson, J. Waldman, G.N. Gol'tsman, P.A. Yagoubov, B.M. Voronov, and E.M. Gershenzon, Proc. Ninth Intern.Symp.Space THz Technology, p. 105 (1998).
[14] R. Wyss, B. Karasik, W.R. McGrath, B. Bumble, and H. LeDuc, "Noise and Bandwidth Measurements ...", this conference proceedings.
[15] A. Semenov and G. Gol'tsman, paper submitted to JAP, 1998.

COMPARISON BETWEEN ELECTRONIC HOT SPOT MODEL AND CURRENT-VOLTAGE CHARACTERISTICS OF SUPERCONDUCTING HOT-ELECTRON BOLOMETERS

D. Wilms Floet[1ab], J.R. Gao[2], T.M. Klapwijk[1], and P.A.J. de Korte[2]

[1]*Department of Applied Physics, Delft University of Technology, Lorentzweg 1, 2628 CJ Delft, The Netherlands*

[2]*Space Research Organization of the Netherlands, 9700 AV Groningen, The Netherlands*

Abstract

We compare theoretical predictions based on the electronic hot spot (EHS) model for hot electron bolometers with experimental results obtained with a Nb diffusion-cooled bolometer. We calculate the current-voltage, I(V), characteristics both analytically and numerically and find a good agreement with unpumped and pumped experimental I(V) curves. Observed deviations can partially be explained by the thermal conductance of the superconducting parts of the microbridge, which is lower than the normal state value assumed in the analytical model. Remaining deviations are attributed to heat-trapping due to Andreev reflection, resulting in a thermal boundary resistance at the interface. Furthermore, the influence of a finite electron-electron interaction time, which prevents complete thermalization of the electrons, is discussed.

I. Introduction

Despite the rapid progress in HEB mixer development from the experimental side, it is not fully clear yet what the limits of their performance are. This question has been a central subject of several studies, in which the bolometer, being essentially a superconducting microbridge contacted by normal conducting banks, is treated as a so-called transition-edge detector (lumped element approach) [1,2]. In these papers a broken-line transition model represents the resistive transition of the microbridge. Recently, however, the authors have shown that the resistive transition of the HEB of the microbridge is only relevant at a bath temperature close to the critical temperature T_c of the microbridge [3].

At low bath temperatures, where the actual mixing experiments are being performed, the lumped element approach is no longer adequate and the presence of a temperature profile in the microbridge has to be taken into account. We have proposed to describe heterodyne operation of the HEB mixer in terms of an electronic hot spot (EHS)

[a] Corresponding address: University of Groningen, Department of Applied Physics, Nijenborgh 4, 9747 AG Groningen, The Netherlands

[b] Electronic mail: wilms@phys.rug.nl

of which the length, and consequently the resistance, oscillates at the intermediate frequency[4,5]. This process is schematically depicted in Fig. 1. The potential importance of hot spot formation in phonon-cooled HEB mixers was also recognized in [6]. From a different perspective others have recently taken into account the temperature profile in the microbridge, but continue to relate the mixing properties to a local temperature dependent resistance [7,8]. In our EHS model, it is the *length of the resistor* that changes.

In this paper we compare analytical and numerical predictions made by the EHS-model with experimental results obtained on a Nb HEB mixer. We will mainly focus on the pumped and unpumped I(V) characteristics. In Section II we discuss the heat balance equations which we use to calculate the I(V) curves of the device. In Section III we present measurements of the pumped I(V) characteristics of the Nb HEB and compare

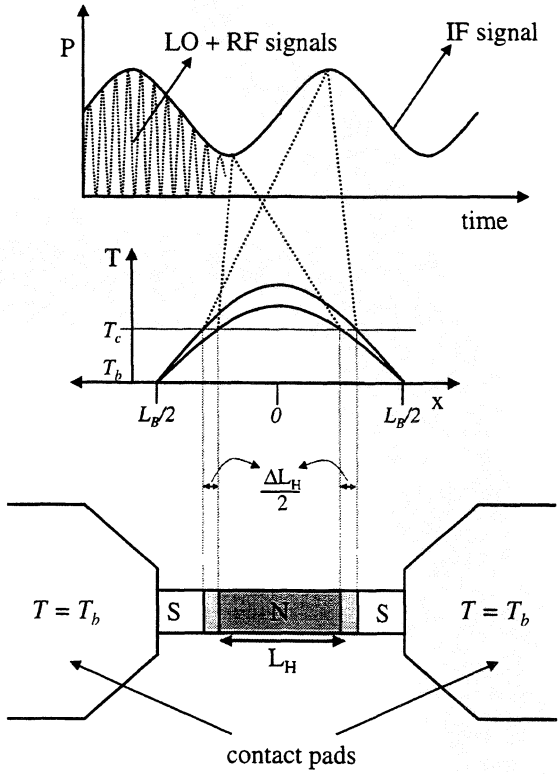

Fig. 1: Schematic representation of the electronic hot spot model. The microbridge is in a normal conducting state in those regions with $T>T_c$ (hot spot region). Beating of the absorbed RF power density at the intermediate frequency leads to a modulation of the length of the hot spot, and thus to a modulated resistance of the mixer.

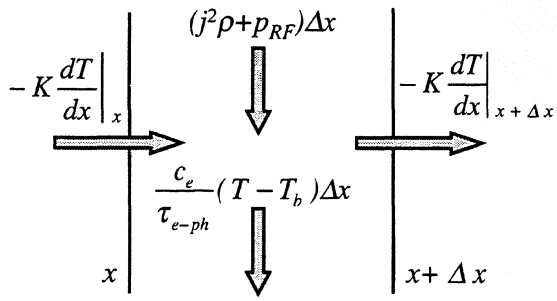

Fig. 2 : Heatflow diagram of a small segment Δx of the microbridge, from which the heat balance equations are derived.

them with the calculations. In Section IV we discuss the deviations between experiment and model.

II. Heat balance equations

If the critical current of the HEB is exceeded, the dc and RF power cause the formation of an electronic hot spot in the center of the otherwise superconducting microbridge [5,9]. With increasing power dissipation, the length of the hot spot, and thus the resistance, will increase and eventually asymptotically approach the normal state resistance of the bridge.

The heat flow inside a small segment Δx of the microbridge is depicted in Fig. 2. Joule heating occurs as a result of absorption of RF radiation and dc dissipation. Direct current dissipation only occurs inside the hot spot, whereas the RF radiation is absorbed homogeneously, because the RF frequency is assumed to be much larger than the gap frequency of the superconductor. The difference between the inflow and outflow of heat K(dT/dx), with K the thermal conductivity, at position x and x+Δx determines the magnitude of the diffusion term. Heat is transferred in the bulk from the electrons to the phonon bath. To parameterize which one of the two dominates for a microbridge with length L_B, it is convenient to introduce a so-called thermal healing length λ_{TH} given by [9]

$$\lambda_{TH} = \sqrt{\frac{K\tau_{e-ph}}{c_e}} = \sqrt{D\tau_{e-ph}} \,. \qquad [1]$$

Here, $\tau_{e\text{-}ph}$ is the electron-phonon energy scattering time, c_e is the electronic heat capacity and D is the electronic diffusion constant. If $\lambda_{TH}>L_B$, the HEB mixer is in the diffusion-cooled limit, in the opposite case it is phonon-cooled. Based on the heat flow diagram of

Fig. 2, we have the following heat-balance equations for a pumped microbridge with a normal state resistivity ρ_n, at a bath temperature T_B, and biased with a current density j:

$$-K\frac{d^2T}{dx^2}+\frac{c_e}{\tau_{e-ph}}(T-T_B)=j^2\rho_n+p_{RF} \qquad \text{(inside hot spot)} \qquad [2]$$

and

$$-K\frac{d^2T}{dx^2}+\frac{c_e}{\tau_{e-ph}}(T-T_B)=p_{RF} \qquad \text{(outside hot spot)} \qquad [3]$$

Here, p_{RF} is the RF power density (per unit volume). We solve these equations by requiring that, at the end of the microbridge, the electron temperature T equals the bath temperature T_B. In addition the electron temperature at the boundary of the hot spot equals the critical temperature of the microbridge T_c. Matching of K(dT/dx) at the hot spot boundary yields the following expression for the current as a function of the hot spot length L_H and p_{RF} :

$$j(L_H,p_{RF})=\sqrt{\frac{c_e}{\rho\tau_{e-ph}}\left[T_C-T_B-\frac{p_{RF}\tau_{e-ph}}{\rho_n}-\frac{\left[T_C-T_B-\frac{p_{RF}\tau_{e-ph}}{\rho_n}\right]\cosh\left[\frac{2L_H-L_B}{2\lambda_{TH}}\right]+\frac{p_{RF}\tau_{e-ph}}{\rho_n}}{\sinh\left[\frac{2L_H-L_B}{2\lambda_{TH}}\right]\tanh\left[\frac{L_H}{\lambda_{TH}}\right]}\right]} \qquad [4]$$

In the calculation, we have made a number of assumptions, which allow an analytical solution of the problem, but do not include the correct temperature dependence of the thermal conductivity and coupling strength between the electron and phonons. Therefore, a numerical calculation was performed [10].

First, in Eqs. 2 and 3, we have taken K independent of temperature, which is not true in reality. The thermal conductivity in the normal parts is described via the Wiedemann-Franz law, which states that the thermal conductivity is linearly dependent on the temperature. Also, in the superconducting parts K rapidly decreases with decreasing temperature due to the decreasing quasi-particle density. In our numerical approach we have used the following relations [11]

$$K=K_0\left(\frac{T}{T_c}\right) \qquad \text{(inside hot spot)} \qquad [5]$$

$$K=K_0\left(\frac{T}{T_c}\right)^3 \qquad \text{(outside hot spot)} \qquad [6]$$

where K_0 is the thermal conductivity at the critical temperature T_c. Note that Eq. 6 is an empirical relation, which is compatible with the microscopic theory in the relevant parameter range, but easier to use in the calculations.

Secondly, the cooling of hot-electrons is not linear in temperature, but is found to be proportional to T^4-T_B^4 [12]. Therefore, the second term in the heat-balance equations is replaced with

$$A\left(T^4 - T_B^4\right), \qquad [7]$$

where A is a constant and equal to ~10^{10}.

Finally, in the analytical model, the transition between the normal conducting parts and superconducting parts is sharply defined, by taking Eq. 2 and 3 in different domains. In reality, we suppose that the resistivity changes gradually from ρ_n to 0 over a certain length ΔL. To model this, we assume that we can express the change of the resistivity as a function of position near the interface by the Fermi-function

$$\rho(x) = \frac{\rho_N}{1 + e^{\frac{x - L_H}{\Delta L}}}. \qquad [8]$$

Since we calculate the temperature as a function of the position, it is convenient to use the following equivalent expression, by which we replace ρ_n of Eq. 2:

$$\rho(T) = \frac{\rho_n}{1 + e^{\frac{T - T_c}{\Delta T}}} \qquad [9]$$

A practical reason why Eq. 9 is used, is that it greatly simplifies the numerical procedure. Note that in the analysis we have assumed that an effective temperature can be attributed to each position in the microbridge, which implies a zero electron-electron interaction time.

III. I(V) characteristics of the pumped HEB

III.A Experimental

We measure the I(V) curves of the hot-electron bolometers as a function of applied RF power density and compare them with the results of the calculated I(V) curves based on the heat-balance equations. Details of the devices can be found in [13]. The bolometer is mounted in a fixed-tuned waveguide, designed for frequencies around 700 GHz and cooled down to 4.2 K. RF radiation is provided by a carcinotron with a doubler and coupled to the mixer via a mirror. The coupled RF power is regulated with an adjustable attenuator in the optical path. The measurements are performed at a frequency of exactly 700 GHz. The critical temperature of the microbridge is ~ 6 K, which corresponds to a

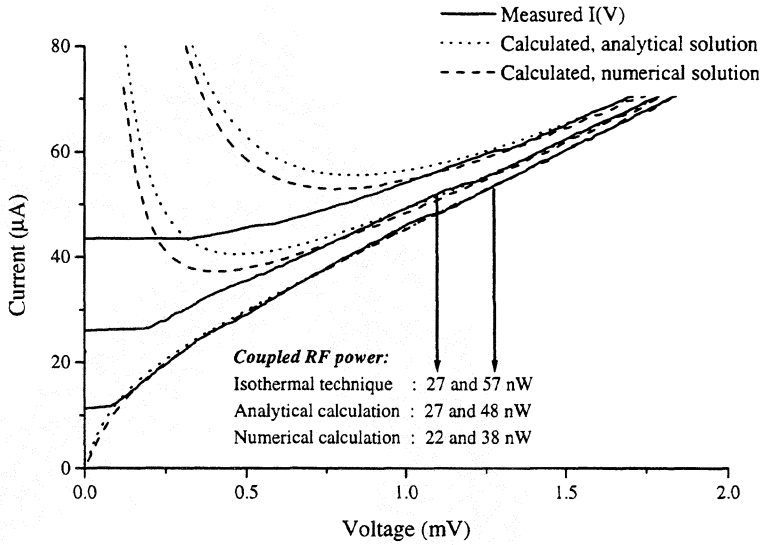

Fig. 3 : Measured and calculated I(V) curves. The solid curves are the measured characteristics, whereas the dotted and dashed curves are the calculated characteristics, resulting from the analytical and numerical solution of the problem, respectively

gap frequency of ~ 470 GHz. This justifies our assumption that the radiation of 700 GHz is absorbed homogeneously in the microbridge.

III. B Results

Fig. 3 shows three measured I(V) curves, together with the calculated ones. The data are obtained by using the dc bias-supply in bias-current mode. Note that this bias-supply, when operated in voltage-bias mode, does not allow measuring the regions of the I(V) curve with a negative differential resistance, due to oscillations. For clarity we only show the part of the I(V) which is recorded from high bias current to zero current. Therefore the hysteresis loop is not visible (the critical current of the unpumped curve is 120 μA). The measured data are corrected for a small series resistance of ~ 1 Ω, which originates from the electrical connection in the mixermount.

The measured curves are compared with the result of the analytical calculation, i.e. Eq. 4, and the numerical calculation. The parameters used for both calculations can be found in Table 1. They are determined by first optimizing the agreement between the unpumped curves. Fixing these values, we then calculate the pumped I(V) curves by adjusting only the absorbed RF power. We find a good agreement between model and measurement if we use 27 nW, 48 nW in the analytical calculations and 22 nW, 38 nW in the numerical calculations. Evidently, the numerical simulation predicts a somewhat

lower minimal current than the analytical result and is in somewhat better agreement with the measured curves.

We have also applied the isothermal technique at high current to determine the coupled RF power [14]. We find 27 nW and 57 nW, which is in reasonable agreement with the values calculated from the heat-balance equation as it should.

Table 1: *Parameters used for the calculated I(V) curves of figure 3.*

	D cm^2/s	c_e J/m^2K	$\tau_{e\text{-}ph}$ ns	T_B K	T_c K	L_B nm	λ_{TH} nm	K_0 W/mK	A W/m^3K^4
Analytical calculation	1.2	2800	1	4.3	5.9	300	350	-	-
Numerical calculation	-	-	-	4.3	5.9	300	-	0.32	$0.3\text{x}10^{10}$

IV. Discussion

A few comments can be made about the outcome of this comparison between measurements and calculations. As emphasized, the RF power densities, which follow from the conventional isothermal technique do hardly differ from those predicted by the EHS-model calculations. The isothermal technique is based on the lumped element approach, which implies that a change in dc power and RF power results in the same change in resistance of the device. At low bias voltage, where the length of the normal EHS is substantially smaller than the length of the microbridge, this is obviously incorrect. At large bias, however, the I(V) is quasi-Ohmic and the EHS boundaries reach to the end of the microbridge, so both dc power and RF power are dissipated along almost the full length of the microbridge. Therefore, the physical state of the microbridge closely corresponds to the state required in the isothermal technique.

It is obvious from Fig. 3, that at low bias, disagreement arises between the measured and calculated I(V) characteristics, in particular in the relevant experimentally accessible regime of positive differential resistance. In the EHS model the I(V) curve "bends up" with decreasing voltage, because the diffusion term in the heat balance equation is of growing importance with decreasing hot spot length (or voltage). The second derivative of the temperature profile increases with decreasing hot spot length. This implies, that as a counter balance, the dc power needed to sustain the hot spot, will decrease slower with decreasing hot spot length (non-Ohmic behavior) and eventually become almost constant. Consequently, the current and voltage become inversely proportional to each other and the differential resistance becomes negative [9].

Experimentally the measured minimum dc power to sustain the hot spot is found to be smaller than the predicted minimum dc power (see Fig. 3). This can only be reconciled within the model by assuming outflow of heat from the microbridge is less than assumed. Indeed, if the reduced thermal conductance in the superconducting parts is included better agreement is obtained. In addition, the interface is electrically conducting but constitutes a thermal boundary resistance for energies below the energy gap, which is the essence of Andreev reflection. This process is schematically represented in Fig. 4. Since there is no energy transfer during this process, heat will be partially trapped in the

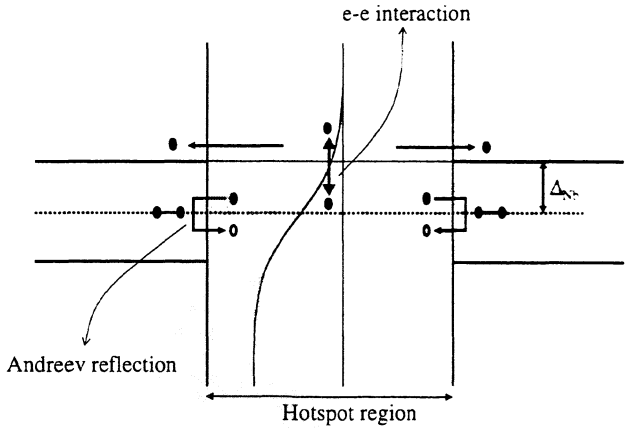

Fig. 4 : Representation of physical processes which are not included in the analysis, but are relevant in the heat transport. Andreev reflection occurs for energies below the gap energy of the superconductor and results in an additional heat transfer barrier at the N/S interface. Moreover, a non-thermal distibution function due to the finite electron-electron interaction time would require an energy dependent analysis of the heat tranport problem.

hot spot. Only those electrons with energies larger than the energy gap have a high probability to diffuse out into the superconducting parts.

Let us finally discuss the effect of a possible incomplete thermalization of the electron system. The electron-electron scattering time can be approximated by [15]

$$\tau_{in}^{-1} = 10^8 R_{sq} T \qquad [10]$$

with R_{sq} the square resistance of the material. This time, using Eq. 9, is ~ 50 ps in our samples at 6 K, which corresponds to an electronic thermalization length of 70 nm. In our analysis we have used as a starting assumption that an effective temperature can be attributed to each position in the microbridge, which implies an infinitely strong electron-electron interaction [5]. The effect of a having non-thermal distribution function is beyond the scope of our current investigations. However, incomplete thermalization is an important issue for the sensitivity of the bolometer, and might cause a reduced mixer conversion gain [16].

V. Conclusions

In conclusion, we have compared I(V) curves of Nb diffusion-cooled HEB pumped above the gap frequency with the electronic hot spot model. We find an excellent agreement at high voltage, whereas deviations at low voltage can be accounted for in a plausible way by pointing out certain simplifications made in the model: the reduced thermal conductance in the superconducting parts of the microbridge and the existence of a thermal barrier as implied by the process of Andreev reflection.

Acknowledgements

Useful discussions with M. Dröge, H. W. Hoogstraten, H. Merkel, B. J. van Wees, and W. F. M. Ganzevles are acknowledged. This work is supported by the European Space Agency (ESA) under Contract No. 11738/95/NL/PB and by the Nederlandse Organisatie voor Wetenschappelijk Onderzoek (NWO) through the Stichting voor Technische Wetenschappen (STW).

References

[1] B. S. Karasik and A. I. Elantiev, Appl. Phys. Lett. 68, 853 (1996).
[2] D.E. Prober, App. Phys. Lett. 62, 2119 (1993).
[3] D. Wilms Floet, J. J. A. Baselmans, T.M. Klapwijk, and J.R. Gao, Appl. Phys. Lett. 73, 2826 (1998).
[4] D. Wilms Floet, J.J.A. Baselmans, J.R. Gao, and T.M. Klawpijk, Proc. 9th Int. Symp. Space THz Technology, Jet Propulsion Laboratory, Pasadena, March 17-19 1998, pp 63-72.
[5] D. Wilms Floet, E. Miedema, T. M. Klapwijk, and J. R. Gao, Appl. Phys. Lett. 74, 433 (1999).
[6] H. F. Merkel, E. L. Kollberg, K. S. Yngvesson, Proc. 9th Int. Symp. Space THz Technology, Jet Propulsion Laboratory, Pasadena, 17-19 March 1998, pp 81-97.
[7] A. Skalare and W. R. McGrath, submitted to the 1998 Applied Superconductivity Conference, Palm Desert, USA (1998).
[8] H. Araújo and G. J. White, submitted to the 1998 Applied Superconductivity Conference, Palm Desert, USA (1998).
[9] The critical current density of the microbridge can be much larger than the minimum current density that is needed to sustain the hot spot. This is the reason why, in a current bias situation, a strong hysteresis effect in the I(V) curve is observed; see also W. J. Skocpol, M. R. Beasley, and M. Tinkham, J. Appl. Phys. 45, 4054 (1974).
[10] Numerical procedure and programm by M. Dröge and H. W. Hoogstraten.
[11] Superconductivity Vol.1, edited by R. D. Parks, Marcel Dekker Inc, New York (1969).
[12] E.M. Gershenzon, G.N. Gol'tsman, A. I. Elant'ev, B. S. Karasik, and S. E. Potoskuev, Sov. J. Low Temp. Phys. 14, 414 (1988).
[13] D. Wilms Floet, J. R. Gao, T. M. Klapwijk, W. F. M. Ganzevles, G. de Lange, and P. A. J. de Korte, presented at the 10th Int. Symp. Space THz Technology, University of Virginia, Charlottesville, March 16-18 (1999).
[14] H. Ekström, B. S. Karasik, E. Kollberg, and K. S. Yngvesson, IEEE Trans. Microwave Theory Techn. 43, 938 (1995).
[15] P. Santhanam and D. E. Prober, Phys. Rev. B 29 3733 (1984).
[16] A. D. Semenov, G. N. Gol'tsmann, submitted to the 1998 Applied Superconductivity Conference, Palm Desert, USA (1998).

A HOT SPOT MIXER MODEL FOR SUPERCONDUCTING PHONON-COOLED HEB FAR ABOVE THE QUASIPARTICLE BANDGAP

Harald Merkel, Pourya Khosropanah, Pavel Yagoubov, Erik Kollberg

Dept. of Microwave Electronics,
Chalmers Univ. of Technology,
S 412 96 Gothenburg , Sweden
harald@ep.chalmers.se

Abstract— A hot spot mixer model for phonon cooled hot electron bolometers is set up to accurately determine the dependence of the bolometer resistance on bias and absorbed LO power. An one-dimensional power balance for the nonequilibrium electrons containing an electron heat conduction term along the film and a loss term due to phonon escape to the substrate is solved. In the device's operating region of interest the absorbed heating power is usually large enough to heat a part of the bolometer bridge above the critical temperature forming a normal conducting hot spot. In this model heating due to the LO is assumed to be uniform whereas bias heating takes place in the hot spot region only. Solving the nonlinear power balance for the hot spot length allows to predict current-voltage characteristics, required heating powers and regions of optimal operation. Applying a small signal model in a given operating point yields an estimate for the intrinsic conversion gain.

I. LARGE SIGNAL MODEL

Existing device models for hot electron bolometers [1,2] treat the bolometer as a lumped element. It is assigned an effective temperature for the phonons and another for the electrons at a given bath temperature. In terms of heating bias power and RF power are equivalent and exchangeable. From this a method [3,4] to calculate the absorbed RF power is derived. This method is referred to as "isotherm" method: Operating points with identical device resistance must have identical temperatures since $R(T_{electron})$ is a single valued monotonous function. Identical temperature implies identical power losses and identical

total absorbed heating power. So the bias power difference of two such points equals their absorbed RF power difference since their heating efficiency is the same.
Applying the isotherm method to an IV-curve with constant incident LO power the calculated absorbed LO power turns out to drop with decreasing bias voltage in a wide range of the bolometer's resistive transition region. For large bias voltages a constant absorbed RF power is observed. Since the applied RF frequency (1.1 THz, 2.5 THz) is larger than the quasiparticle bandgap (about 700GHz at bath temperature) one would expect the RF resistance to be equal to the normal resistance and consequently the antenna matching and RF coupling to the bolometer not to depend on bias voltage at all. Considering optimal operating points the isothermally calculated RF power is about a factor 1.5 to 3 smaller than the absorbed LO power observed for large bias voltages. Calorimetric data [5] evaluated in vicinity of the optimal operating point show an absorbed LO power close to the value obtained for larger voltage by the isothermal method. This discrepancy is explained by taking spatial effects of the heating into account. For frequencies far above the bandgap LO power is absorbed uniformly on the bolometer bridge. Applying typical LO power levels (about 50nW to 250nW) and bias heating powers (about 150nW for short devices) electrons will be heated above the critical temperature in a portion of the bridge. This creates a normal conducting hot spot. Then bias power absorption will be constrained to the normal conducting part of the bridge only. The heating efficiency due to bias is therefore different from the LO heating efficiency. Now it becomes obvious why the discrepancies between the "isotherm" method and experiment occur exactly in the operating regions where the hot spot is small leading to very different heating efficiencies for LO and bias and where the assumption of exchangeable heating powers is consequently not valid. The "isotherm" method and the lumped element approach works well for large bias voltages: There the hot spot covers almost the whole bolometer resulting in very similar absorption regions and therefore similar heating efficiencies for bias and LO power. The "isotherm" method works also for frequencies below the bandgap. There pair breaking for a given LO frequency is restricted to a small fringe around a hot spot. Absorption areas are similar again and consequently the heating efficiencies comparable. In all other cases the isotherm method underestimates the absorbed LO power since bias heating turns out to be more efficient than LO heating. It is therefore indispensable to include spatial effects into a model for the bolometer heating in order to describe the device behavior properly. This is done in the following one-dimensional mixer model.

A. Nonequilibrium heat balance

Here a hot spot mixer model is presented for phonon-cooled hot electron bolometers which is based on the solution of a one-dimensional, nonlinear coupled heat balance for electrons and phonons. Heat balances for hot spot models with analytical closed form solutions and numerical results have been published elsewhere. These balances were either in time domain for a point bolometer [4,6,7], in time domain with one spatial dimensions with a linearized loss term [12], or fully nonlinear one-dimensionally in time domain where no closed form solution is available [13]).

Here a closed form approximated solution of the nonlinear equation system is given where the loss term has not been linearized. The complete steady state partial differential equation system for the electrons (1) and phonons (2) takes the following form:

$$\lambda \frac{d^2}{dx^2} T(x) - \sigma_{electron}\left[T(x)^{3.6} - T(x)_{phonon}^{3.6}\right] + P(x) = 0 \tag{1}$$

$$\lambda_{ph} \frac{d^2}{dx^2} T_{phonon}(x) + \sigma_{electron}\left[T(x)^{3.6} - T(x)_{phonon}^{3.6}\right] - \sigma_{phonon}\left[T(x)_{phonon}^{4} - T_{bath}^{4}\right] = 0 \tag{2}$$

Here x denotes a coordinate parallel to the bolometer bridge, T, T_{phonon}, T_{bath} the electron, phonon and bath temperature. $\lambda, (\lambda_{ph})$ stands for the electron (phonon) thermal conductivity in direction of the bolometer bridge.

$$\sigma_{electron} = \frac{c_{electron}(T)}{3.6 \cdot T^{2.6} \cdot \tau_{electron \to phonon}(T)} \cdot t \cdot w$$

$$\sigma_{phonon} = \frac{c_{phonon}(T_{ph})}{4.0 \cdot T_{ph}^{3.0} \cdot \tau_{phonon\ escape}(T_{ph})} \cdot t \cdot w$$

denote the efficiencies of electron-phonon cooling and of phonon escape as a function of the thermal capacitances and appropriate relaxation times [6]. Numerical values for these parameters in NbN on Si are summarized in Table 1. $P(x)$ is the electron heating power density profile. The thermal conductivity is obtained by applying Wiedemann-Franz law [10] to measured data for the normal film resistance. For the given NbN bridge geometry (c.f. Table 1) the one-dimensional thermal conductivity becomes:

$$\lambda \approx L_{lorenz} \frac{\ell \cdot T}{R_N} \approx 27 T \frac{nW \cdot nm}{K^2}.$$

Since almost all phonons leave the film and escape to the substrate the heat conduction term due to phonons in film direction in the phonon heat balance (2) is neglected reducing it to an algebraic equation. Solving the latter in terms of a power series allows to eliminate the phonon temperature in the electron heat balance (1) leaving a single power balance for the electrons. Inserting the electron heating term assuming uniform absorption of RF power (all along the bridge of length 2L) and restricted dc bias absorption within a hot spot (covering the interval –H to +H) results in the following ordinary nonlinear differential equation remaining to be solved.

$$\lambda \frac{d^2}{dx^2} T - \sigma_{eff} \left[T^{3.6} - T_{bath,eff}^{3.6} \right] + \frac{1}{2L} P_{RF} + P_{bias} \cdot \frac{\Pi_H(x)}{2H} = 0 \qquad (3)$$

P_{RF} and P_{bias} are the RF and bias powers dissipated in the film. $\Pi_H(x)$ is a function being unity inside the interval –H to +H and zero elsewhere. The effective electron cooling efficiency σ_{eff} is given by the "pure" electron-phonon cooling term reduced by a "phonon-escape-bottleneck" term obtained by series expansion of the phonon heat balance:

$$\sigma_{eff} \approx \frac{\sigma_{electron}(T) \cdot t \cdot w}{1 + \dfrac{3.6 \cdot \sigma_{electron}(T)}{4.0 \cdot \sigma_{phonon}(T_{ph}) \cdot \sqrt{T_{substrate}}}} \qquad (4)$$

The effective bath temperature is slightly larger than the physical bath temperature and found to be $T_{bath,eff} = T_{bath}^{\frac{4.0}{3.6}}$.

No closed form solution is available for (3). Therefore attempts have been made to linearize the loss terms [12] which is a valid approach for mixers where the substrate temperatures is close to the critical temperature. This is definitely not the case for NbN bolometers operated at 4.2K with a critical temperature of about 9.9K. In the following a method is presented where the loss terms and heating terms are treated fully nonlinear.

B. Solution procedure

In a first step the dependent variable in (3) is transformed according to $T^{3.6} \rightarrow q$. The loss term is now obviously linear in q. A series expansion of the dependent variable q around an average temperature $q_{average}$ yields an approximation for the thermal conduction term where an effective thermal conductivity λ_{eff} is defined as follows:

$$\lambda \cdot \frac{d^2}{dx^2} T = \lambda \cdot \frac{d^2}{dx^2} \sqrt[3.6]{q} \approx \frac{\lambda}{3.6} \cdot q_{average}^{\frac{1}{3.6}-1} \cdot \frac{d^2}{dx^2} q = \lambda_{eff} \cdot \frac{d^2}{dx^2} q \qquad (5)$$

Applying this the key equation is reduced to a linear differential equation in $T(x)^{3.6}$. Obviously the curvature of the 3.6th root of the temperature profile is much smaller compared to the curvature of a $T(x)^{3.6}$-term improving the solution accuracy considerably. In a second step the remaining differential equation must be solved:

$$\lambda_{eff} \frac{d^2}{dx^2} T(x)^{3.6} - \sigma_{eff} \left[T(x)^{3.6} - T_{bath,eff}^{3.6} \right] + \frac{1}{2L} P_{RF} + P_{bias} \cdot \frac{\Pi_H(x)}{2H} = 0 \qquad (6)$$

with the boundary conditions:

$$T(L)^{3.6} = T(-L)^{3.6} = T_{rand}^{3.6}$$

After a quite lengthy calculation an electron temperature profile is obtained containing an initial guess of the hot spot length H as a parameter. Results for the electron temperature profile (for a NbN phonon-cooled bolometer with the parameters listed in Table 1) are shown below:

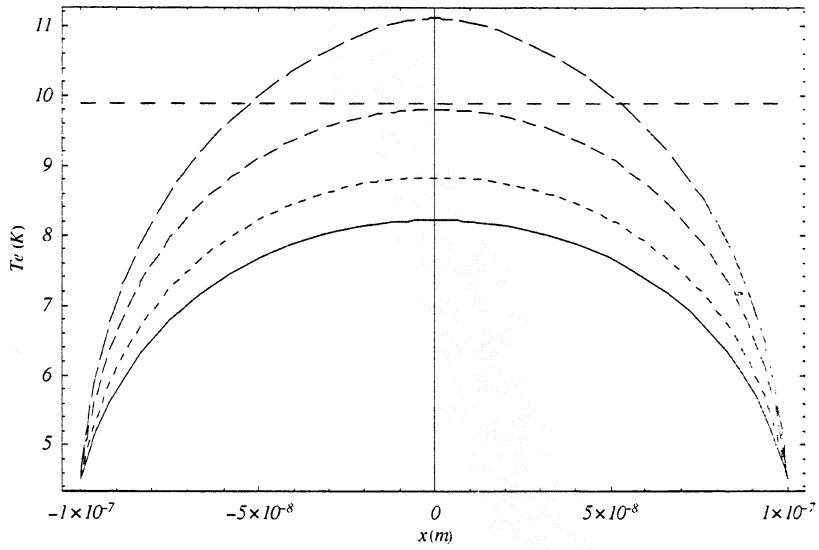

Fig. 1 Electron temperature profile of the reference bolometer (c.f. Table 1) for different LO powers under constant 100nW dc bias heating. The applied LO powers are 50nW (solid line), 100nW (dotted line), 200nW (dashed line), and 300nW (long dashed line) respectively. The horizontal line at 9.9K indicates the critical temperature of the bolometer.

Taking into account a relation for the absorbed bias power $P_{bias} = I_0 \cdot V_0$ and a geometric relation for the device resistance $\frac{R}{R(T_c)} = \frac{H}{L}$ the large signal model is self consistent. In order to obtain a self-consistent hot spot length the initial hot spot length guess must be chosen to give rise to a temperature profile for which the resulting hot spot length is identical to its initial guess. The hot spot length is thus obtained by a simple fixpoint calculation. The hot spot length as a function of heating powers is shown in Fig 2.

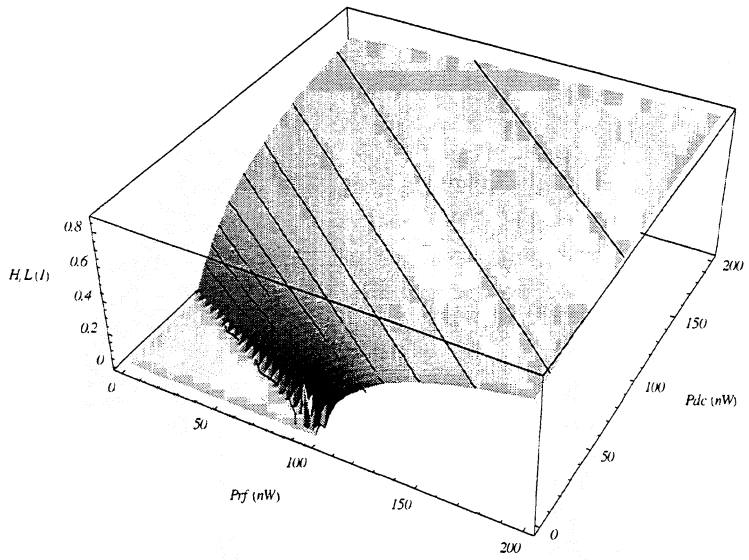

Fig. 2 Relative Hot spot length (normalized by the bolometer bridge length) of a typical (200nm long/1μm wide/35Å thick) NbN bolometer as a function of heating powers.

Based on the hot spot length as a function of heating powers pumped and unpumped IV curves are easily calculated. A Comparison between measured and calculated IV curves is shown in Fig.3.

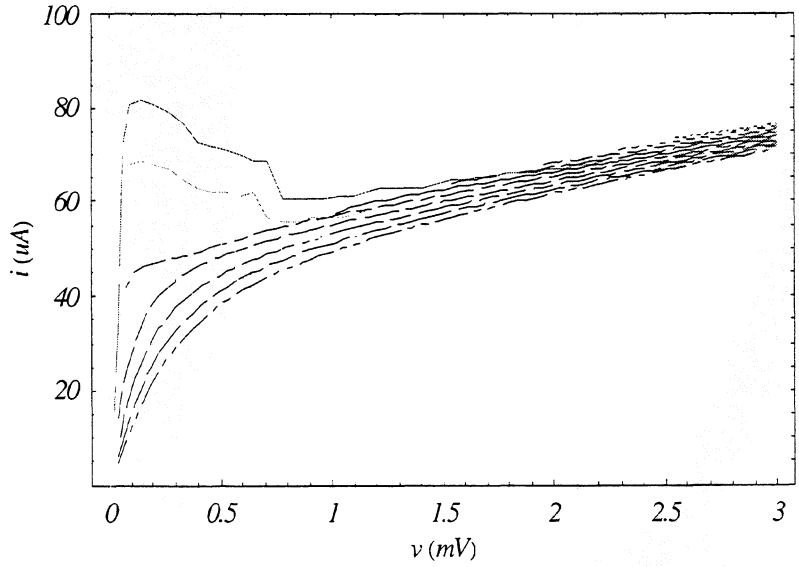

Fig. 3 Measured (gray curves in several shadings) and self-consistently calculated IV curves. The measured curves range from unpumped (top curve, black) to heavily pumping conditions (light gray) where a crude

estimation of the LO power yields 200nW. The calculated curves are obtained for 350nW (bottom curve),310nW, 270nW, 230nW and 190nW (top curve reaching down to zero bias voltage) LO power. There are two more IV curves starting at higher bias voltages for 150nW and 110nW. These curves end where no hot spot is supported by the heating powers. The top measured curve is an unpumped curve

Knowing the hot spot length as a function of heating powers, it can be linearized in vicinity of an operating point resulting in the following total differential for the device resistance:

$$R = R_{b0}(P_{LO}, P_{bias}) + \frac{R(T_c)}{L}\left[\frac{\partial H}{\partial P_{LO}} \cdot p_{LO} + \frac{\partial H}{\partial P_{bias}} \cdot p_{bias}\right] \qquad (7)$$

Here P_{LO}, P_{bias} denote the time averaged heating powers where p_{LO}, p_{bias} are small power amplitudes oscillating at the IF frequency. The resistance changes due to LO and bias power i.e. the heating efficiencies or "slope factors" [9] depend largely on the operating point. Calculated data for the LO heating efficiency for all points on the IV curves from Fig. 3 are summarized in Fig.4.

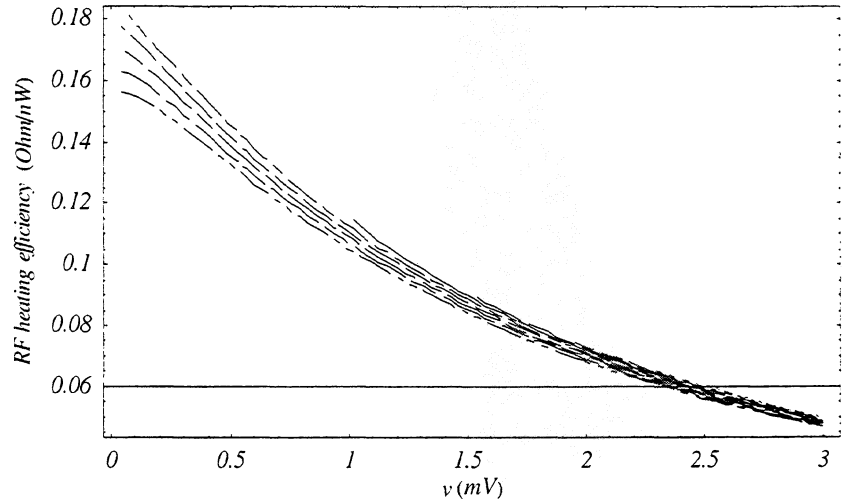

Fig. 4 Calculated LO/RF heating efficiency along the self-consistently calculated IV curves from Fig.3. The curves are obtained for 350nW (bottom curve),310nW, 270nW, 230nW and 190nW (top curve reaching down to zero bias voltage) LO power. There are two more IV curves starting at higher bias voltages for 150nW and 110nW.

As pointed out before, this one dimensional large signal model provides different heating efficiencies for LO and bias heating. The ratio between dc bias and LO heating is shown below. Obviously dc bias heating is always more efficient than LO heating.

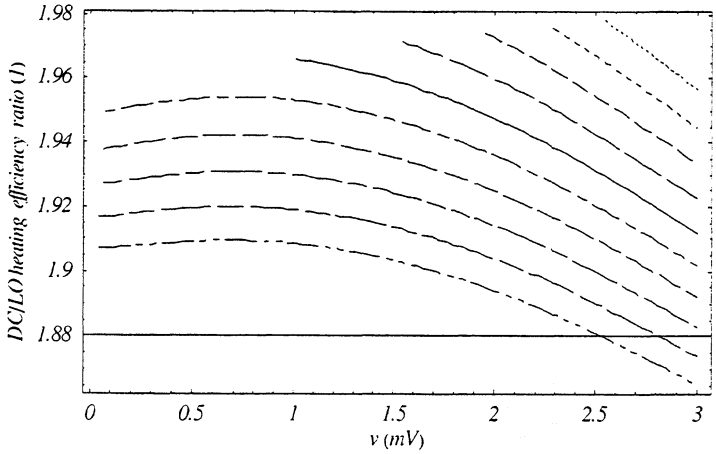

Fig. 5 Calculated ratio of LO and bias heating efficiency along the self-consistently calculated IV curves from Fig.3. The curves are obtained for 370nW (bottom curve),310nW, 270nW, 230nW and 190nW, 150nW, 110nW, 80nW, 60nW and 40nW. In a lumped element approach [9] this ratio is assumed to be unity

In this framework (7) R_{b0} stands for a "pre-heated" dc device resistance which depends on the time averaged heating powers in the operating point as shown in the following figure.

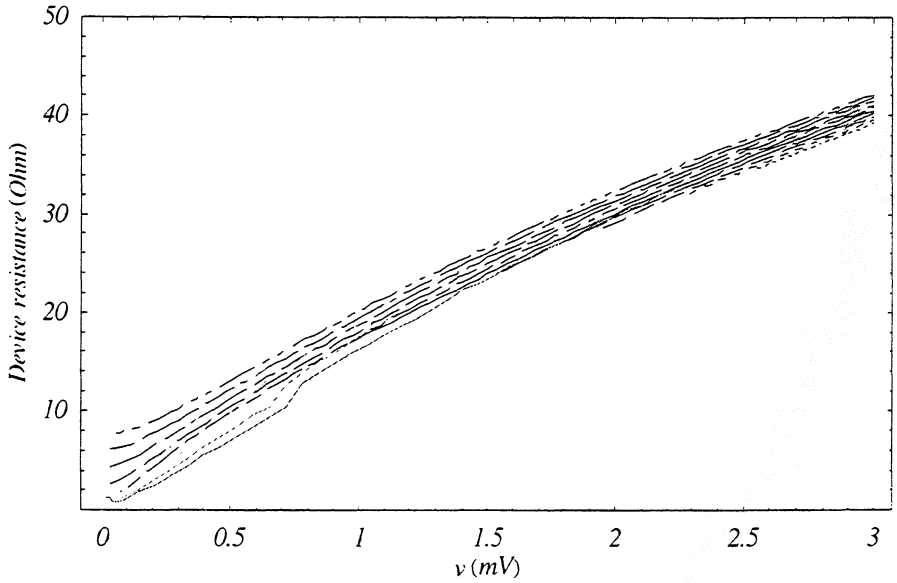

Fig. 6 Measured (gray curves in several shadings) and self-consistently calculated resistance curves as a function of the device voltage following the self-consistent IV curves from Fig. 3. The LO power range is identical to Fig. 3. Obviously increasing LO power corresponds to increased device resistances for the same bias power.

With the knowledge of the above parameters (device resistance and heating efficiencies) a small signal approximation can be made in an operating point where a hot spot exists:

II. SMALL SIGNAL MODEL

Following [9] the bolometer circuit shown in Fig.6 is modeled by three parallel impedances (the bolometer, a bias voltage source in series with a bias resistor and a dc block capacitor in series with a load resistance). RF and LO are fed into the circuit by quasioptical waveguides at one bolometer terminal. This superposition of a LO and a RF signal is absorbed by the bolometer. Since the bolometer cannot follow power variations at LO and RF frequencies it is heated by the time averaged power and by a power signal oscillating at the difference frequency of the LO and RF.

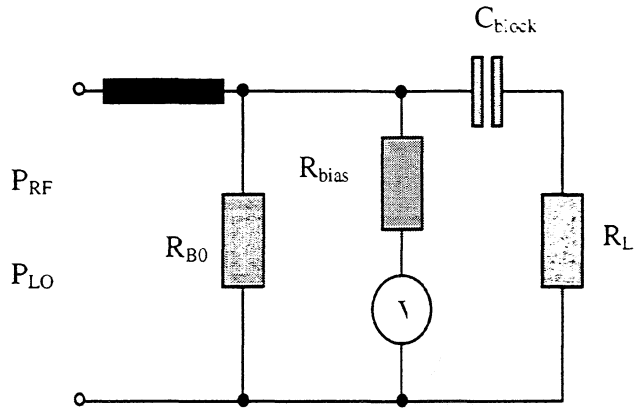

Fig. 6 Mixer circuit. The (pre-heated) bolometer is in series with a bias circuit and the load. The quasioptical feeding is symbolized by a waveguide connection at the upper bolometer terminal.

The heating at IF gives rise to a modulation of the bolometer resistance. Assume the LO signal to be much larger than the RF signal. Then the time average heating (and with it the operating point) are not influenced by the generated small IF signal. For such a "pre-heated" operating point the differential dissipated power in the load resistance due to such a small IF signal can be calculated. In contrast to other small signal models [1,2,3,9] two generally different slope parameters for bias and RF heating are extracted from measured IV curves around the desired operating point (c.f. (7), Fig.4 through 6).

$$C_{rf} = \frac{R(T_c)}{L}\frac{\partial H}{\partial P_{LO}}, \qquad C_{dc} = \frac{R(T_c)}{L}\frac{\partial H}{\partial P_{bias}} \tag{9}$$

Assuming a the bias voltage source to be constant in time and assuming time harmonic variations at the intermediate frequency (IF) for all other currents and voltages, Kirchhoff's

rules specify a complete equation set for all electric parameters. Inserting time varying currents and voltages in the resistance relation (7) products between the small signal voltage and current amplitudes at IF will occur causing new dc terms leading to a shift of the operating point referred to as "thermal runaway" of the bolometer. Here we strictly assume these terms to be negligible which is the case for most mixer applications. When evaluating the power dissipation in the bolometer and load resistance the IF variation of the resistance (i.e. the parametric oscillation) must be taken into account when expanding it into a Fourier series. Last but not least the voltage across the dc blocking capacitor is simply assumed to be such that no dc power is dissipated in the load. Now the bolometer resistance as a function of time (7) becomes

$$R(t) = R_{b0} + \left[C_{rf} \cdot p_{rf} + C_{dc} p_{dc}\right] \cdot \cos(\omega_{IF} \cdot t)$$

$$= R_{b0} + \frac{4C_{rf}\sqrt{\frac{P_{rf}P_{LO}}{R_{b0}}} \cdot \cos(\omega_{IF} \cdot t)}{1 + C_{dc} \cdot \left[\frac{2R_{b0}(R_{bias} + R_L)\left(\frac{R_{bias}R_{b0}V_{bias}}{R_{bias}+R_{b0}} + R_L V_{bias}\right)^2}{(R_{b0}R_L + R_{bias}(R_{b0}+R_L))^3} - \left(\frac{\frac{R_{bias}R_{b0}V_{bias}}{R_{bias}+R_{b0}} + R_L V_{bias}}{R_{b0}R_L + R_{bias}(R_{b0}+R_L)} \right)^2 \right]} \tag{10}$$

Without electrothermal feedback $C_{dc} \rightarrow 0$ the resistance change is solely given by the IF induced resistance oscillation. Now the small signal conversion gain G given by the ratio of the power in the load resistance and RF power is determined:

$$G = \frac{2 \cdot C_{rf}^2 \cdot P_{LO} \cdot R_{bias} \cdot R_L \cdot V_{bias}^2}{(R_{bias}+R_{b0})^2 \cdot (R_{b0} \cdot R_L + R_{bias} \cdot (R_{b0}+R_L))^2 \cdot \left[1 + C_{dc} \cdot \frac{R_{bias} \cdot (R_{b0} - R_L) + R_{b0} \cdot R_L}{(R_{bias}+R_{b0})^2 \cdot (R_{b0} \cdot R_L + R_{bias} \cdot (R_{b0}+R_L))} V_{bias}^2\right]^2} \tag{11}$$

The intrinsic conversion gain obtained at 1THz (for the device from Figures 1 to 3) in the optimal operating point ($V_{bias} \approx 0.9mV$, $I_{bias} \approx 24.5\mu A$, $R_{bias} \rightarrow \infty$) is $G_{opt} = -9.7dB$ where the following parameter values have been used: $R_{b0} = 17\Omega$, $\chi \approx 1.3$, $C_{dc} = 1.1\frac{\Omega}{nW}$, $C_{rf} = 0.7\frac{\Omega}{nW}$. Assuming $C_{dc} = C_{rf} = 1.1\frac{\Omega}{nW}$ one obtains $G_{opt} = -7.4dB$. The lowest

noise temperature of this device was measured in a broad region around $V_{bias} \approx 0.8mV$. The intrinsic conversion gain along the IV curves from Fig. 3 for different absorbed LO power becomes:

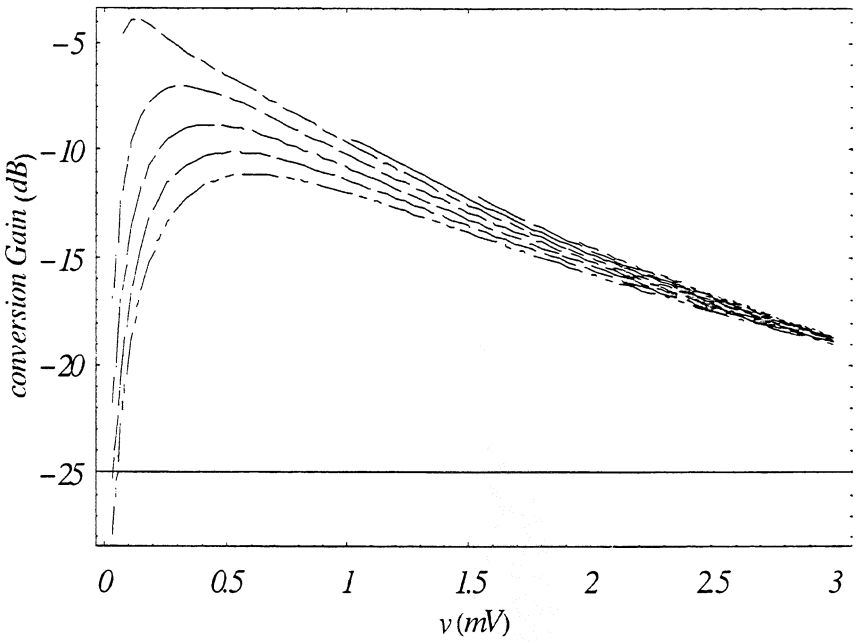

Fig. 7 Intrinsic conversion gain for various LO power. Starting from the lowest line the LO power is 350nW, 310nW, 270nW, 230nW. The curve reaching the absolute maximum was obtained for 190nW.

III. THERMAL FLUCTUATION NOISE

According to an expression for the thermal fluctuation noise [1,2] of a bolometer using a lumped approach this noise contribution is proportional to the change of the resistance with temperature squared.

$$kT_{FL} = \frac{I_0^2 \cdot R_L}{4 \cdot (R_L + R_b)^2} \cdot \left(\frac{dR}{dT}\right)^2 \cdot \frac{4kT_e^2}{c_e V} \cdot \tau_{e,relax} \qquad (12)$$

In the framework of this one-dimensional mixer model it becomes proportional to the inverse square of the slope of the electron temperature profile at the critical temperature. Inserting this result one is left with the following expression for the fluctuation noise temperature:

$$T_{FL} = \left(\frac{1}{1 - C_{dc} \cdot I_0^2 \cdot \dfrac{R_L + R_{b0}}{R_L - R_{b0}}} \cdot \frac{R_N}{L \cdot \left. \dfrac{dT_e}{dx} \right|_{Tc}} \right)^2 \cdot \frac{I_0^2 \cdot R_L}{4 \cdot (R_L + R_b)^2} \cdot \frac{4T_e^2}{c_e V} \cdot \tau_{e,relax} \qquad (13)$$

Results following the self-consistent IV curves are summarized in the following picture for various LO powers. The fluctuation noise depends on the inverse slope of the electron temperature profile which is very large for a small hot spot. Since (12) contains the same thermal feedback factor as the conversion gain. Therefore the fluctuation noise contribution is maximum where the gain is maximum.

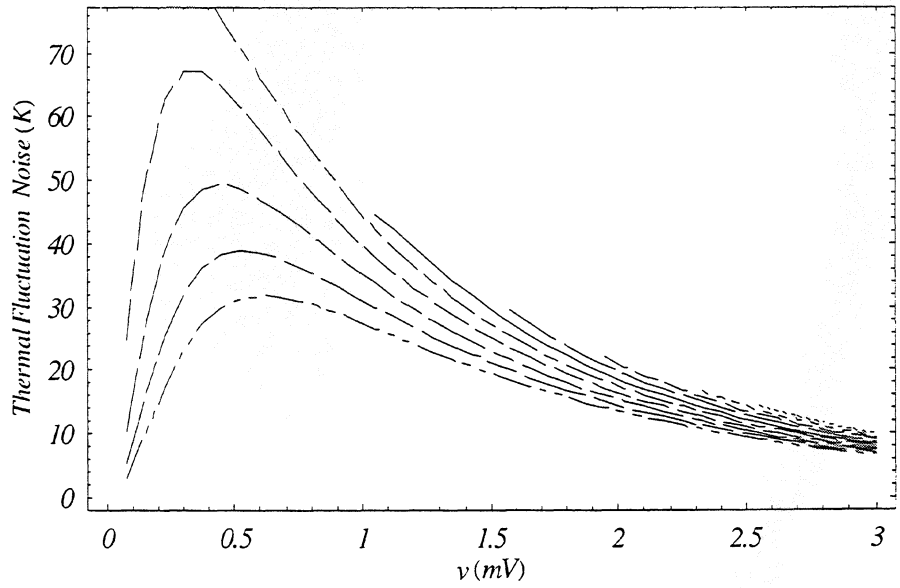

Fig. 8 Thermal fluctuation noise contribution following the self-consistent IV curves from Fig.3. The absorbed LO power starting from the lowest line the LO power is 350nW, 310nW, 270nW, 230nW. The curve reaching the absolute maximum was obtained for 190nW.

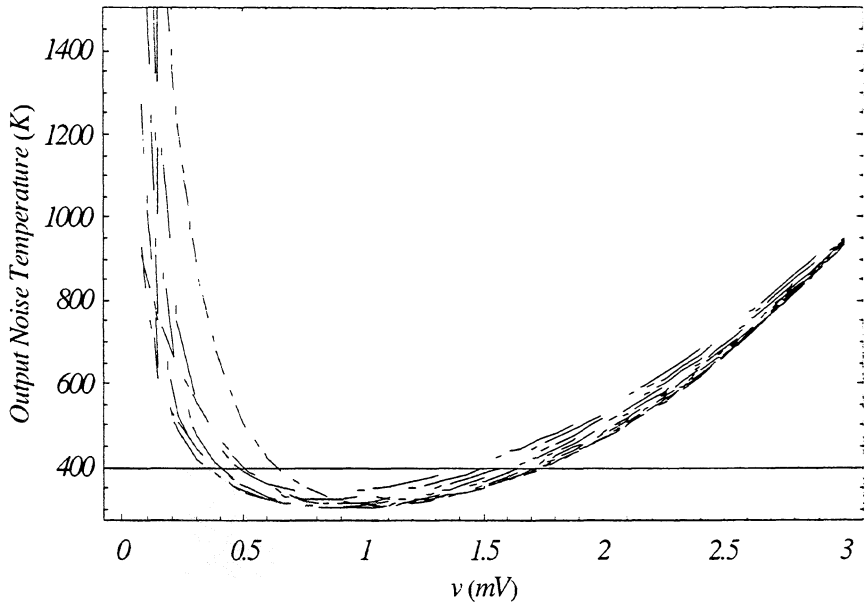

Fig. 9 DSB Output noise temperature following the self-consistent IV curves from Fig,3. The absorbed LO power starting from the top line (dash-dotted at 0.5V) the LO power is 350nW, 310nW, 270nW, 230nW. The curve reaching the absolute minimum was obtained for 190nW at 0.8mV.

IV. Conclusion

In this work a one-dimensional model for a hot spot mixer is presented. It allows to calculate the electron temperature profile and the hot spot length as a function of heating powers in a self consistent way. Knowing the hot spot length as a function of heating powers, the IV curves of the HEB can be predicted. Based on this small signal parameters are calculated as the mixer conversion gain and the fluctuation noise contribution. Now knowing the absorbed RF power the antenna matching of a bolometric mixer can be optimized in terms of device sensitivity and noise temperature.

V. Device Parameter Table

In the following table the parameters for the bolometer, which has been the base of all calculations in this paper, are summarized. These parameters are, unless not otherwise indicated, data measured for a NbN HEB mixer tested at 2.5THz.

Parameter	Name	Value
L, ℓ	Bolometer length	$200nm$
t	Bolometer thickness	$35\AA$
w	Bolometer width	$1\mu m$
R_N	Device resistance at 20K	352Ω
T_{bath}	Bath temperature	$4.5K$
$\tau_{e\rightarrow ph}$	Electron-phonon-interaction time (fitted to data from [8])	$440ps \cdot K^{1.6} \cdot T^{-1.6}$
$\tau_{ph,escape}$	Phonon substrate escape time [8]	$45ps$
$c_{electron}$	Electron thermal capacity [8]	$1.6\times10^{-4} \cdot T \frac{W \cdot s}{cm^3 \cdot K^2}$
c_{phonon}	Phonon thermal capacity [8]	$9.8\times10^{-6} \cdot T^3 \frac{W \cdot s}{cm^3 \cdot K^4}$
T_c	Critical temperature	$9.9K$
L_{lorenz}	Lorenz number [10]	$2.45\times10^{-8} \frac{\Omega W}{K^2}$

VI. Acknowledgment

This work was partly supported by European Space Agency (**#11738/95/nl/mv**). The authors wish to thank Danny Wilms-Floet (RUG Groningen, The Netherlands), K. Sigfrid Yngvesson and Eyal Gerecht (both at UMASS Amherst) for lots of fruitful discussions.

VII. References

[1]H.Ekström, B. Karasik, E. Kollberg, K.S. Yngvesson, IEEE Trans. MTT, 938-947, **43**(4), (1995)

[2]H. Ekström, B. Karasik, E. Kollberg, K.S. Yngvesson, IEEE Microwave Guided Wave Letters 253-255, **4**(7), (1994)

[3]H. Ekström, M. Kroug, V. Belitskij, E. Kollberg, H. Olsson, G. Gol'sman, E. Gershenzon, P. Yagoubov, B. Voronov, K.S. Yngvesson, Proc. 30th. ESLAB Symp. "Submillimeter and Far-Infrared Space Instruments", 24-26 September 1996, Noordwijk, The Netherlands, 207-210, (ESA ESTEC, Noordwijk, The Netherlands , 1996)

[4]S. Svechnikov, A. Verevkin, B. Voronov, E. Menschikov, E. Gershenzon, G. Gol'tsman, Proceedings 9th International Symposium on Space Terahertz Technology , 17-19 March Pasadena, CA, 45-51 (JPL , Pasadena CA , 1998)

[5]P. Yagoubov, M. Kroug, H. Merkel, E. Kollberg, G. Gol'tsman, S. Svechnikov, E. Gershenzon "Noise temperature and LO power requirement of NbN phonon-cooled hot electron bolometric mixers at Terahertz frequencies", Applied Physics. Lett., **73**(19), 9 November 1998

[6]E.M. Gershenzon, G.N. Gol'tsman, I.G. Gogidze, Yu.P. Gousev, A.I. Elant'ev, B.S. Karasik, A.D. Semenov, Sov. Phys. Semicond. **3**. 1582 (1990)

[7]M.N. Özisik "Heat conduction" Wiley, New York (2nd. Ed. 1993)

[8]S. Cherednichenko, P. Yagoubov, K. Il'in, G. Gol'tsman, E. Gershenzon, Proceedings of the 9th International Symposium on
Space Terahertz Technology , March 25-27, Cambridge MA , 245-252, (Harvard Smithsonian Center for Astrophysics, Cambridge MA, 1997)

[9]F. Arams, C. Allen, B. Peyton, E. Sard, Proceedings of the IEEE **54**(3) 308-318 (1966)

[10]K. Kopitzki, "Einfuehrung in die Festkoerperphysik" (german), Teubner, Stuttgart (1985)

[11]A. D. Semenov, R.S. Nebosis, Yu. P. Gousev, M.A. Heusinger, K.F. Renk, Phys. Rev. B-**52(1)** , 581-590 (1995)

[12]D.Wilms-Floet, J.J.A. Baselmans, J.R.Gao, T.M.Klapwijk Proc. 9 Intl. Symp. on Space THz Tech. Pasadena CA 1998, p63-73

[13]H.M.Araùjo, G.J. White (ETA11) Proc. ASC 1998, Deserts Springs CA 1998, p.143

[14]K.S. Yngvesson, et.al. Proc. 10 Intl. Symp. on Space THz Tech. Charlottesville, CA 1999

Tenth International Symposium on
Space Terahertz Technology

Authors and Registered Participants

**********A**********

**********B**********

Andrey Baryshev
SRON
P.O. Box 800
9700 AV Groningen
The Netherlands
andrey@SRON.rug.nl

Robert Bass
University of Virginia
Dept. of Electrical Engineering
Thornton Hall
Charlottesville, VA
rbb7y@virginia.edu

D.A. Beintema
SRON
P.O. Box 800
9700 Av. Groningen
The Netherlands
D.A.Beintema@SRON.Rus.NL

Dominic Benford
California Institute of Technology
M.C. 320-47
Pasadena, CA 91125
dbenford@tacos.caltech.edu

Manju Bhat
University of Virginia
Dept. of Electrical Engineering
Thornton Hall
Charlottesville, VA 22903
msb5u@virginia.eu

William L. Bishop
University of Virginia
Dept. of Electrical Engineering
Thornton Hall
Charlottesville, VA 22903
wlb@virginia.edu

Olga Boric-Lubecke
RIKEN Photodynamics Res. Ctr.
Inst. Physical & Chemical Res.
19-1399 Koeji, Nagamachi
Aoba-Ku, Sendai 980
Japan
olga@postman.riken.go.jp

Willie Bowen
University of Virginia
Dept. of Electrical Engineering
Thornton Hall
Charlottesville, VA 22903
web7c@virginia.edu

Richard Bradley
National Radio Astronomy Observatory
2015 Ivy Rd., Ste. 219
Charlottesville, VA 22903
rbradley@nrao.edu

Jean Bruston
Jet Propulsion Laboratory
California Institute of Technology
MS 168-314
Torrance, CA 90503
bruston@merlin.jpl.nasa.gov

**********C**********

Carey Cates
UCSB
Quantum Instititute
Santa Barbara, CA 93102
isabel@physics.ucsb.edu

Goutam Chattopadhyay
California Institute of Technology
MS 320-47
Pasadena, CA 91125
goutam@caltech.edu

Ming-Tang Chen
Inst. Of Astronomy & Astrophysics
Academia Sinica
Nankang
P.O. Box 1-87
Taipei, Taiwan 115
mchen@asiaa.sinica.edu.tw

Denis Chouvaev
Dept. of Microelectronics & Nanoscience
Chalmers University of Technology
S-412 96 Gothenburg, Sweden
chouvaev@fy.chalmers.se

Tom Crowe
University of Virginia
Dept. of Electrical Engineering
Thornton Hall
Charlottesville, VA 22903
twc8u@virginia.edu

**********D**********

Thijs de Graauw
SRON
P.O. Box 800
Groningen 9700 AV
The Netherlands
tlijsdg@sron.rug.nl

Gerhard DeLange
SRON
P.O. Box 800
9700 AV Groningen
The Netherlands
gert@sron.rug.nl

Marc DeVincentis
University of Virginia
Dept. of Electrical Engineering
Thornton Hall
Charlottesville, VA 22903
mjd9f@virginia.edu

Aaron Datesman
University of Virginia
Dept. of Electrical Engineering
Thornton Hall
Charlottesville, VA 22903
ad3d@virginia.edu

Bascom Deaver
University of Virginia
Physics Dept.
Charlottesville, VA 22903
bsd@virginia.edu

Lars Dillner
Chalmers University of Technology
SE-412 96 Goteborg
Sweden
dillner@ep.chalmers.se

James Duan
University of Virginia
Dept. of Electrical Engineering
Thornton Hall
Charlottesville, VA 22903
zd3g@virginia.edu

Yiwei Duan
University of Virginia
Dept. of Electrical Engineering
Thornton Hall
Charlottesville, VA 22903
yd3v@virginia.edu

Erik Duerr
Massachusetts Institute of Technology
Lincoln Laboratory
244 Wood St., E122F
Lexington, MA 02139
duerr@mit.edu

**********E**********

Jack East
University of Michigan
2301 EECS Building
Ann Arbor, MI 48109
jeast@eecs.umich.edu

Pierre Echternach
Jet Propulsion Laboratory
Center for Space Microelectronics Tech.
4800 Oak Grove Dr.
M/S 302-231
Pasadena, CA 91109
pierre.m.echternach@jpl.nasa.gov

Mick Edgar
California Institute of Technology
Downs Lab of Physics MC 320-47
Pasadena, CA 91125
mick@submm.caltech.edu

John Effland
National Radio Astronomy Observatory
2015 Ivy Rd., Ste. 219
Charlottesville, VA 22903
jeffland@nrao.edu

Neal Erickson
University of Massachusetts
Dept. of Physics and Radio Astronomy
Lederle 619
Amherst, MA 01003
neal@fcrao1.phast.umass.edu

**********F**********

Klebert Feitosa
University of Massachusetts
Dept. of Physics and Astronomy
633 LGRT
Amherst, MA 01003
kfeitosa@phast.umass.edu

Wilms (Danny) Floet
Delft University of Technology
Nyenborgh
9747 AG Groningen
The Netherlands
wilms@phys.rug.nl

**********G**********

Walter Ganzevles
University of Delft
University of Groningen
Nijenborgh 4
Groningen, The Netherlands
ganzevles@phys.rug.nl

Israel Galin
Aerojet
P.O. Box 296
Azusa, CA 91702
galini@ms1.aes.com

J.R. Gao
SRON
P.O. Box 800
9700 AV Groningen
The Netherlands
gao@phys.rug.nl

Boris Gelmont
University of Virginia
Dept. of Electrical Engineering
Thornton Hall
Charlottesville, VA 22903
gb7k@virginia.ed

Eyal Gerecht
University of Massachusetts
Dept. of Physics and Astronomy
817 LGRC
Amherst, MA 01003
gerecht@fcrao1.phast.umass.edu

Eugene Gershenzon
Moscow State Pedagogical University
Department of Physics
29 M. Pirogovskaya Str
Moscow, Russia 119435
geshenzon@rpl.mpgu.msk.su

Gregory Gol'tsman
Department of Physics
Moscow State Pedagogical University
29 M. Pirogovskaya Str
Moscow, Russia 119435
goltsman@rpl.mpgu.msk.su

**********H**********

Oliver Harnack
Jet Propulsion Laboratory
M/S 168-314
4800 Oak Grove
Pasadena, CA 91109
Oliver.Harnack@jpl.nasa.gov

Bert Hayden
University of Virginia
Dept. of Electrical Engineering
Thornton Hall
Charlottesville, VA 22903
ahh3v@virginia.edu

Song "Jackie" He
University of Virginia
Dept. of Electrical Engineering
Thornton Hall
Charlottesville, VA 22903
sh5k@virginia.edu

Jeffrey Hesler
University of Virginia
Dept. of Electrical Engineering
Thornton Hall
Charlottesville, VA 22903
jlh6r@virginia.edu

Neil Horner
National Radio Astronomy Observatory
2015 Ivy Rd., Ste. 219
Charlottesville, VA 22903
nhorner@nrao.edu

Heinz-Wilhelm Hubers
DLR Institute of Space Sensor Technology
Rudower Chaussee 5
D-12489 Berlin, Germany
heinz-wilhelm.huebers@dlr.de

Kai Hui
University of Virginia
Dept. of Electrical Engineering
Thornton Hall
Charlottesville, VA 22903
kh2r@virginia.edu

**********I**********

Mattias Ingvarson
Chalmers University of Technology
SE-412 96 Goteborg, Sweden
ingvarson@ep.chalmers.se

Kate Isaak
University of Cambridge
Cavendish Laboratory
Madingley Rd.
Cambridge, CB3 OHE, UK
isaak@nrao.cam.ac.uk

**********J**********

Brian Jackson
University of Groningen, FDL
9747 AG Groningen
The Netherlands
jackson@phys.rug.nl

Karl Jacobs
KOSMA,
I. Physikalisches Inst.
University of Cologne
Zuelpicher Str. 77
5O937 Cologne, Germany
jacobs@phl.uni-koeln.de

Willem Jellema
SRON
P.O. Box 200
Groningen, The Netherlands 9700AV
w.jellema@sron.nl

Steve Jones
Virginia Semiconductor, Inc.
1501 Powhatan St.
Fredericksburg, VA 22401
shjones@cstone.net

Brian Justin
Ericsson
Mtn. View Road
M/S 2700
Lynchburg, VA 24502
brian.justin@ericsson.com

**********K**********

Boris S. Karasik
Jet Propulsion Laboratory
M/S 168-314
4800 Oak Grove Dr.
Pasadena, CA 91109
boris.karasik@jpl.nasa.gov

Alexandre Karpov
California Institute of Technology
Downs Lab of Physics
MC 320-47
Pasadena, CA 91125
karpov@iram.fr

Jonathan Kawamura
California Institute of Technology
Downs Lab of Physics
MC 320-47
Pasadena, CA 91125
kawamura@submm.caltech.edu

A.R. Kerr
National Radio Astronomy Obs.
2015 Ivy Road, Ste. 219
Charlottesville, VA 22903
akerr@nrao.edu

Pourya Khosropanah
Chalmers University of Technology
Dept. of Microelectronics
Microwave Electronics Lab
S 412 96 Goteborg, Sweden
pourya@ep.chalmers.se

Alan Kleinsasser
Jet Propulsion Laboratory
M/S 302-231
4800 Oak Grove Dr.
Pasadena, CA 91109
klein@vaxeb.jpl.nasa.gov

Satoshi Kohjiro
Electrotechnical Lab
1-1-4 Umezono
Tsukuba, 305-8568 Japan
khjiro@etl.go.jp

Jacob Willem Kooi
California Institute of Technology
M/S 320-47
Pasadena, CA 91125
kooi@submm.caltech.edu

Matthias Kroug
Chalmers University of Technology
Dept. of Microelectronics
S-412 96 Gothenburg, Sweden
kroug@fy.chalmers.se

**********L**********

James Lamb
California Instititute of Technology
P.O. Box 968
Big Pine, CA 93513
lamb@ovro.caltech.edu

Chih-Chien Lee
U.S. Army Research Laboratory
RF & Electronics
Adelphi, MD 20783

Mark Lee
University of Virginia
Physics Department
Charlottesville, VA 22903
ml3g@virginia.edu

Chao-Te Li
University of Virginia
Dept. of Electrical Engineering
Thornton Hall
Charlottesville, VA 22903
cl5g@virginia.edu

Arthur W. Lichtenberger
University of Virginia
Dept. of Electrical Engineering
Thornton Hall
Charlottesville, VA 22903
awl1l@virginia.edu

C.-I. Lin
Institut fur Hochfrequenztechnik
TU Darmstadt
Merckstrasse 25
D-64283 Darmstadt, Germany

Hao Lin
Engineering Physics Department
University of Virginia
Charlottesville, VA 22903
hl8k@virginia.edu

Victor Lubecke
RIKEN Photodynamics Res Ctr
Inst. Physical & Chemical Res
19-1399 Koeji, Ngamachi
Aoba-Ku, Sendai 980
Japan
victor@posmail.nacsis.ac.jp

**********M**********

William R. McGrath
Jet Propulsion Laboratory
M/S 168-314
4800 Oak Grove Dr.
Pasadena, CA 91109
william.r.mcgrath@jpl.nasa.gov

Chris Mann
Rutherford Appleton Laboratory
Chilton, Didcot
Oxfordshire, OX11 0QX
The United Kingdom
c.m.mann@rl.ac.uk

Steve Marazita
University of Virginia
Dept. of Electrical Engineering
Thornton Hall
Charlottesville, VA 22903
smm7k@virginia.edu

Shuji Matsuura
California Institute of Technology
M/S 150-21
Geological & Planetary Sciences
Pasadena, CA 91125
matsuura@gps.caltech.edu

Phil Mavskopf
University of Massachusetts
Dept. of Physics & Astronomy
632 LGRC
Amherst, MA 01003
mavskopf@fcrao1.phast.umass.edu

Imran Mehdi
Jet Propulsion Laboratory
M/S 168-314
4800 Oak Grove Dr.
Pasadena, CA 91109
imran.mehdi@jpl.nasa.gov

Harald Merkel
Dept. of Microelectronics
Chalmers University of Technology
S-412 96 Gothenborg, Sweden
harald@ep.chalmers.se

Dave Miller
California Instititute of Technology
Downs Lab of Physics
M/S 320-47
Pasadena, CA 91125
davem@tarsus.submm.caltech.edu

Norikazu Mizuno
Dept. of Astrophysics
Nagoya University
Chikusa-KU
Nagoya 464-8602 Japan
norikazu@a.phys.nagoya-u.ac.jp

Matthew Morgan
University of Virginia
Dept. of Electrical Engineering
Thornton Hall
Charlottesville, VA 22903
mam3p@virginia.edu

Salez Morvan
Denirn-Observatoire de Paris
77 Avenue Denfert.Rochereau
Paris, France 75016
salez@obspm.fr

Ville Mottonen
Helsinki University of Technology
PL 3000
02015 HUT (EPSOO) Finland
vmo@radio.hut.fi

Urs Mueller
KOSMA
I Physikalisches Institut
University of Cologne
50937, Cologne, Germany
mueller@phl.uni-koeln.de

**********N**********

Gopal Narayanan
University of Massachusetts
Five College Radio Astronomy Observatory
Amherst, MA 01003
gopal@fcrao1.phast.umass.edu

Takashi Noguchi
Nobeyama Radio Observatory
Nobeyama, Minami-Saku
Nagano 384-1305
Japan
noguchi@nro.nao.ac.jp

**********O**********

Paul Ostdiek
AFRL
2241 Avionics Circle
Wright-Patterson AFT, OH 45433
paul.ostdiek@sn.afrl.af.mil

Creidhe O'Sullivan
National University of Ireland, Maynooth
Experimental Physics Department
Co. Kildare, Ireland
creidhe.osullivan@may.ie

**********P**********

Shing-Kuo Pan
National Radio Astronomy Observatory
2015 Ivy Rd., Ste. 219
Charlottesville, VA 22903
span2@nrao.edu

Nagini Paravastu
University of Virginia
Dept. of Electrical Engineering
Thornton Hall
Charlottesville, VA 22903
np4e@virginia.edu

John M. Payne
National Radio Astronomy Observatory
949 N. Cherry Avenue
Campus Bldg. 65
Tucson, AZ 85721-0655
jpayne@nrao.edu

Luca Perregrini
University of Pavia
Dept. of Electronics
Via Ferrata 1
27100 Pavia, Italy
perregrini@ece.unipv.it

Gerry Petencin
National Radio Astronomy Observatory
2015 Ivy Rd., Ste. 219
Charlottesville, VA 22903
gpetenci@nrao.edu

Gernot Pomrenke
AFOSR/NM
801 N. Randolph St.
Arlington, VA 22203
gernot.pomrenka@afosr.af.mil

David Porterfield
Virginia Millimeter Wave
706 Forest St., Ste. D
Charlottesville, VA 22903
porterfield@Cstone.net

Marian Pospieszalski
National Radio Astronomy Observatory
2015 Ivy Rd., Ste. 219
Charlottesville, VA 29203
Mpospies@nrao.edu

**********Q**********

**********R**********

Antti Raisenen
Helsinki University of Technology
P.O. Box 3000
HUT (ESPOO) 02015 Finland
ara@radio.hut.fi

Sanjay Raman
VPI&SU
Electrical & Computer Engineering
340 Whittemore Hall
Blacksburg, VA 24061
sraman@vt.edu

Frank Rice
California Institute of Technology
Submillimeter Astrophysics
M/S 320-47
Pasadena, CA 91125
rice@submm.caltech.edu

Manuel Rodriguez-Girones
Darmstadt Technical University
Merckstrasse 25
Darmstadt, Germany 64283
hfmwe009@hrz2.hrz.tu-darmstadt.de

**********S**********

Chris St. Jean
University of Virginia
Dept. of Electrical Engineering
Thornton Hall
Charlottesville, VA 22903
cs6e@virginia.edu

Kamaljeet Saini
University of Virginia
Dept. of Electrical Engineering
Thornton Hall
Charlottesville, VA 22903
kss4w@virginia.edu

Erich Schlecht
Jet Propulsion Laboratory
M/S 168-314
4800 Oak Grove Dr.
Pasadena, CA 91109
erichs@merlin.jpl.nasa.gov

Gerhard Schoenthal
University of Virginia
Dept. of Electrical Engineering
Thornton Hall
Charlottesville, VA 22903
gss2r@virginia.edu

Karl Schuster
IRAM
300, Rue de la Piscine
38406 St. Martin d'Heres, France
schuster@iram.fr

Gerhard Schwaab
Ruhr-Universitat Bochum
Physical Chemistry Department
D-44801 Bochum, Germany
gerhard.schwaab@ruhr-uni-bochum.de

Masumichi Seta
Communications Research Laboratory
4-2-1, Nukui-Kita-machi
184-8795 Koganei, Tokyo, Japan
seta@crl.go.jp

Sheng-Cai Shi
Purple Mountain Observatory
2 West Beijing Road
Nanjing, JiangSu 21008 China
Shengcai@public1.ptt.js.cn

Sergey V. Shitov
Inst. of Radio Engineering &
Electronics
Russian Academy of Science
103907 Moscow, Russia
sergey@hitech.cplire.ru

Irfan Siddiqi
Yale University
RM 405 Becton Center
15 Prospect St.
New Haven, CT 06520
irfan@siddiqi@yale.edu

Anders Skalare
Jet Propulsion Laboratory
M/S 168-314
4800 Oak Grove Dr.
Pasadena, CA 91109
anders.skalare@jpl.nasa.gov

Jan Stake
Chalmers University of Technology
SE-412 96 Goteborg
Sweden
stake@ep.chalmers.se

Joel Stokolka
KOSMA
I Physikalisches Institut
Universitaei Zu Kofin
Suelpicher Str. 77
50937 Koeln, Germany
stodolka@phl.uni-koeln.de

Larry Suddarth
University of Virginia
Physics Department
Charlottesville, VA 22903
lts7x@virginia.edu

**********T**********

Gregory Tait
Virginia Commonwealth University
Dept. of Electrical Engineering
P.O. Box 843072
Richmond, VA 23284
gtait@vcu.edu

Dorsey "Skip" Thacker
National Radio Astronomy Observatory
2015 Ivy Rd., Ste. 219
Charlottesville, VA 22903
sthacker@nrao.edu

Edward Tong
Harvard-Smithsonian Center
For Astrophysics
60 Garden St.
MS42
Cambridge, MA 02138
Etong@cfa.harvard.edu

**********U**********

Sadik Ulker
University of Virginia
Dept. of Electrical Engineering
Thornton Hall
Charlottesville, VA 22903
su4m@virginia.edu

**********V**********

Herman van de Stadt
SRON
P.O. Box 800
9700 AV Groningen
The Netherlands
herman@SRON.rug.nl

Aleksandr Verevkin
Yale University
Rm. 401, Becton Center
15 Prospect St.
New Haven, CT 06520
Aleksand2.vezerkin@yale.edu

**********W**********

Ming-Tye Wang
Institute of Astronomy & Astro-
Physics
Academia Sinica
Material Science Center
National Tsing Hua University
Shin-Chu, Taiwan, ROC
mijwang@msc.nthu.edu.tw

John Ward
California Institute of Technology
Downs Lab of Physics
MC 320-47
Pasadena, CA 91125
ward@submm.caltech.edu

Ken-ichi Watabe
Communications Research Laboratory
Ministry of Posts and Telecommunications
Optoelectronics Section
Photonic Technology Division
4-2-1 Nukui-kita
Koganei, Tokyo 184-8795 Japan
watabe@crl.go.jp

John Webber
National Radio Astronomy Observatory
2015 Ivy Rd., Ste. 219
Charlottesville, VA 22903
jwebb@nrao.edu

Bobby Weikle
University of Virginia
Dept. of Electrical Engineering
Thornton Hall
Charlottesville, VA 22903
rmw5w@virginia.edu

Nick Whyborn
SRON
P.O. Box 800
9700 AV Groningen
The Netherlands
nick@sron.rub.nl

David Wilsher
Rutherford Appleton Labs
Chilton, Didcot
Oxon, OX11OQX, UK
D.S.Wilsher@rl.ac.uk

S. Withington
Cambridge University
Cavendish Labs
Madingley Rd.
Cambridge CB3 OHE, UK
stafford@mrao.cam.ac.uk

Dwight Woolard
Army Research Office
Research Triangle Park, NC 27709
woolard@aro-emh1.army.mil

Rolf A. Wyss
Jet Propulsion Laboratory
M/S 168-314
4800 Oak Grove Dr.
Pasadena, CA 91109
randwyss@merlin.jpl.nasa.gov

**********X**********

Kecheng Xiao
Astronomy Lab
Dept. of Astrophysics
Nagoya University
Chikusa-Ku
Nagoya 464-8602 Japan
xkc@a.phys.nagoya-u.as.jp

**********Y**********

Pavel Yagoubov
Chalmers University of Technology
Dept. of Microelectronics
S-412 96 Goteborg, Sweden
yagoubov@ep.chalmers.se

Delorne Yan
Denian – Observatoire de Paris
77 Avenue Denfert-Rochereau
75016 Paris, France
delarmo@atoile.obspm.fr

G. Yassin
Cambridge University
Cavendish Laboratory
Madingley Rd.
Cambridge CR3 OHE, UK
ghassan@mrao.cam.ac.uk

Sigfried Yngvesson
University of Massachusetts
Dept. of Electrical and Computer Engineering
Amherst, MA 01003
yngvesson@ecs.umass.edu

Shun-Cheng Yang
The Institute of Astronomy and Astrophysics
Academia Sinica, Nankang
Taipei, Taiwan

**********Z**********

Jonas Zmuidzinas
California Institute of Technology
Downs Lab of Physics
MC 320-47
Pasadena, CA 91125
jonas@submm.caltech.edu

Yan Zhuang
University of Massachusetts
Dept. of Physics and Astronomy
Amherst, MA 01003
uzhuang@acad.umass.edu